PEARSON NEW INTERNATIONAL EDITION

Elements of X-Ray Diffraction

B.D. Cullity S.R. Stock

Third Edition

ALWAYS LEARNING™ PEARSON®

Pearson New International Edition

Elements of X-Ray Diffraction
B.D. Cullity S.R. Stock
Third Edition

PEARSON®

Pearson Education Limited
Edinburgh Gate
Harlow
Essex CM20 2JE
England and Associated Companies throughout the world

Visit us on the World Wide Web at: www.pearsoned.co.uk

ISBN 10: 1-292-04054-8
ISBN 13: 978-1-292-04054-7

British Library Cataloguing-in-Publication Data
A catalogue record for this book is available from the British Library

Printed in the United States of America

Table of Contents

Properties of X-Rays

1 INTRODUCTION

X-rays were discovered in 1895 by the German physicist Röntgen [1][1] and were so named because their nature was unknown at the time. Unlike ordinary light, these rays were invisible, but they traveled in straight lines and affected photographic film in the same way as light. On the other hand, they were much more penetrating than light and could easily pass through the human body, wood, quite thick pieces of metal, and other "opaque" objects.

It is not always necessary to understand a thing in order to use it, and x-rays were almost immediately put to use by physicians and, somewhat later, by engineers, who wished to study the internal structure of opaque objects. By placing a source of x-rays on one side of the object and photographic film on the other, a shadow picture, or *radiograph*, could be made, the less dense portions of the object allowing a greater proportion of the x-radiation to pass through than the more dense. In this way the point of fracture in a broken bone or the position of a crack in a metal casting could be located.

Radiography was thus initiated without any precise understanding of the radiation used, because it was not until 1912 that the exact nature of x-rays was established. In that year the phenomenon of x-ray *diffraction* by crystals was discovered, and this discovery simultaneously proved the wave nature of x-rays and provided a new method for investigating the fine structure of matter. Although radiography is a very important tool in itself and has a wide field of applicability, it is ordinarily limited in the internal detail it can resolve, or disclose, to sizes of the order of 10^{-3} mm. Diffraction, on the other hand, can indirectly reveal details of internal structure of the order of 10^{-7} mm in size, and it is with this phenomenon, and its applications to materials problems, that this book is concerned.

---

[1] Numbers in square brackets relate to the references at the end of the chapter which are organized in two parts: general references ("G" numbers) and specialized references collected by chapter.

From Chapter 1 of *Elements of X-Ray Diffraction*, Third Edition. B.D. Cullity, S.R. Stock.

2 ELECTROMAGNETIC RADIATION

Today it is clear that x-rays are electromagnetic radiation of exactly the same nature as light but of very much shorter wavelength. The unit of measurement in the x-ray region is the angstrom (Å), equal to 10^{-10} m, and x-rays used in diffraction have wavelengths lying approximately in the range 0.5-2.5 Å, whereas the wavelength of visible light is of the order of 6000 Å. X-rays therefore occupy the region between gamma and ultraviolet rays in the complete electromagnetic spectrum (Fig. 1). Other units sometimes used to measure x-ray wavelength are the X unit (XU) and the kilo X unit (kX = 1000 XU). The kX unit, whose origin will be described in Sec. 3-7, is only slightly larger than the angstrom. The approved SI unit for wavelengths in the x-ray region is the nanometer:

$$1 \text{ nanometer} = 10^{-9} \text{ m} = 10 \text{ Å}.$$

This unit has not become popular in x-ray diffraction.

It is worthwhile to review briefly some properties of electromagnetic waves. Suppose a monochromatic beam of x-rays, i.e., x-rays of a single wavelength, is traveling in the x direction (Fig. 2). Then it has associated with it an electric field **E** in, say, the y direction and, at right angles to this, a magnetic field **H** in the z direction. If the electric field is confined to the xy-plane as the wave travels along, the wave is said to be plane-polarized. (In a completely unpolarized wave, the electric field vector **E** and hence the magnetic field vector **H** can assume all directions in the yz-plane.)

In the plane-polarized wave considered, **E** is not constant with time but varies from a maximum in the $+y$ direction through zero to a maximum in the $-y$ direction and back again, at any particular point in space, say $x = 0$. At any instant of time, say $t = 0$, **E** varies in the same fashion with distance along the x-axis. If both variations are assumed to be sinusoidal, they may be expressed in the one equation

$$\mathrm{E} = A \sin 2\rho\alpha\frac{x}{\lambda} - \nu t\beta, \tag{1}$$

where A = amplitude of the wave, λ = wavelength, and ν = frequency. The variation of **E** is not necessarily sinusoidal, but the exact form of the wave matters little; the important feature is its periodicity. Figure 3 shows the variation of **E** graphically. The wavelength and frequency are connected by the relation

$$i = \frac{c}{v}, \tag{2}$$

where c = velocity of light = 3.00×10^{8} m/sec.

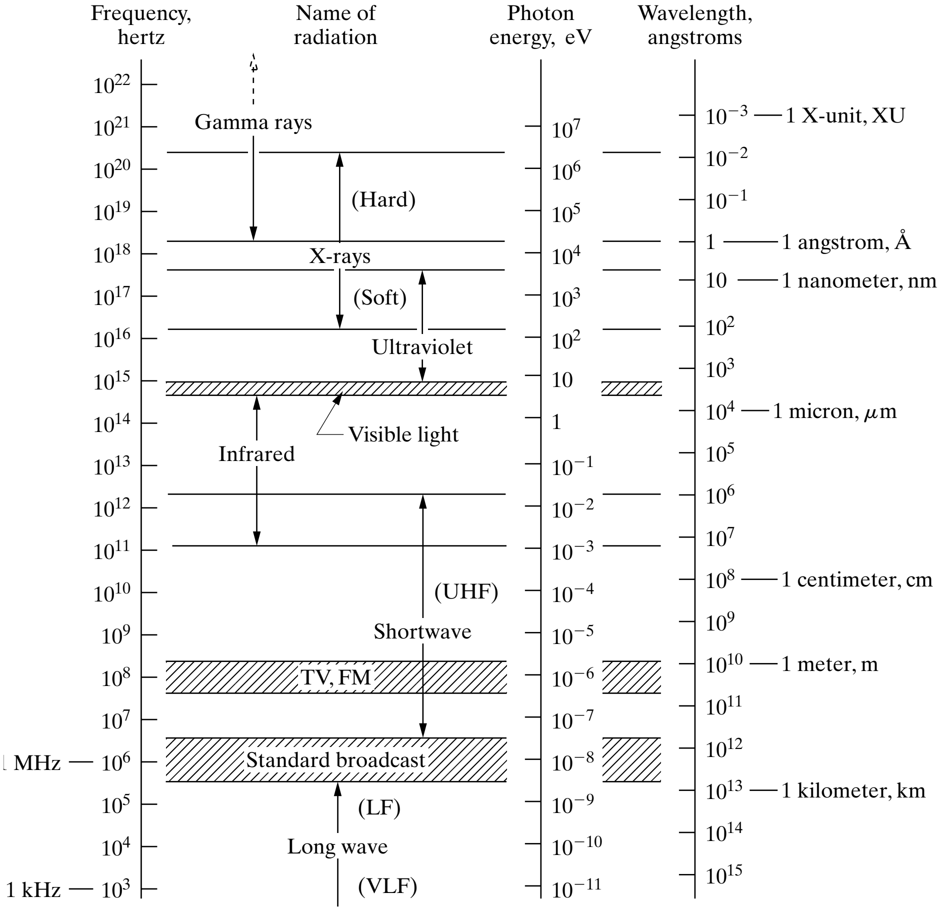

Figure 1 The electromagnetic spectrum. The boundaries between regions are arbitrary, since no sharp upper or lower limits can be assigned. (H. A. Enge, M. R. Wehr, J. A. Richards, *Introduction to Atomic Physics, Addison-Wesley Publishing Company, Reading*, MA, 1972.)

Figure 2 Electric and magnetic fields associated with a wave moving in the x-direction.

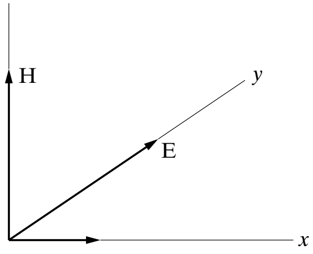

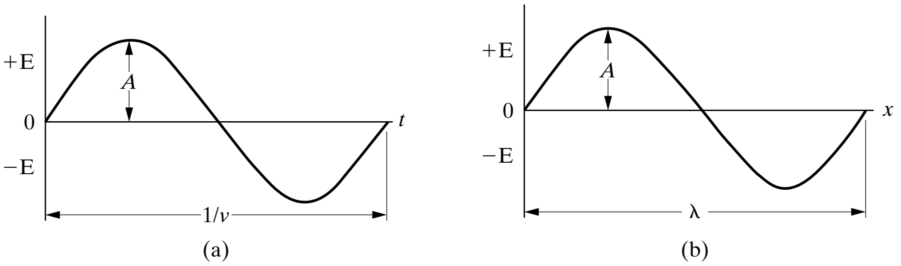

Figure 3 The variation of **E**, (a) with t at a fixed value of x and (b) with x at a fixed value of t.

Electromagnetic radiation, such as a beam of x-rays, carries energy, and the rate of flow of this energy through unit area perpendicular to the direction of motion of the wave is called the *intensity* I. The average value of the intensity is proportional to the square of the amplitude of the wave, i.e., proportional to A^2. In absolute units, intensity is measured in joules/m^2/sec, but this measurement is a difficult one and is seldom carried out; most x-ray intensity measurements are made by counting the number of photons incident on a detector or by measuring the degree of blackening of photographic film exposed to the x-ray beam.

An accelerated electric charge radiates energy. The acceleration may, of course, be either positive or negative, and thus a charge continuously oscillating about some mean position acts as an excellent source of electromagnetic radiation. Radio waves, for example, are produced by the oscillation of charge back and forth in the broadcasting antenna, and visible light by oscillating electrons in the atoms of the substance emitting the light. In each case, the frequency of the radiation is the same as the frequency of the oscillator which produces it.

Thus far electromagnetic radiation has been considered as *wave* motion in accordance with classical theory. According to quantum theory, however, electromagnetic radiation can also be considered as a stream of *particles* called quanta or photons. Each photon has associated with it an amount of energy $h\nu$, where h is Planck's constant (6.63×10^{-34} joule · sec). A link is thus provided between the two viewpoints, because the frequency of the wave motion can be calculated from the energy of the photon and vice versa. Radiation thus has a dual wave-particle character, and sometimes one concept, sometimes the other will be used to explain various phenomena, giving preference in general to the classical wave theory whenever it is applicable.

3 THE CONTINUOUS SPECTRUM

X-rays are produced when any electrically charged particle of sufficient kinetic energy rapidly decelerates. Electrons are usually used for this purpose, the radiation being produced in an *x-ray tube* which contains a source of electrons and two metal electrodes. The high voltage maintained across these electrodes, some tens of thousands of volts, rapidly draws the electrons to the anode, or *target*, which they strike with very high velocity. X-rays are produced at the point of impact and radiate in all directions. If e is the charge on the electron (1.60×10^{-19} coulomb) and V the voltage across the electrodes, then the kinetic energy (in joules) of the electrons on impact is given by the equation

$$\mathrm{KE} = eV = \frac{1}{2}mv^2, \tag{3}$$

where m is the mass of the electron (9.11×10^{-31} kg) and v its velocity in m/sec just before impact. At a tube voltage of 30,000 volts, this velocity is about one-third that of light. Most of the kinetic energy of the electrons striking the target is converted into heat, less than 1 percent being transformed into x-rays.

When the rays coming from the target are analyzed, they are found to consist of a mixture of different wavelengths, and the variation of intensity with wavelength is found to depend on the tube voltage. Figure 4 shows the kind of curves obtained. The intensity is zero up to a certain wavelength, called the *short-wavelength limit* (λ_{SWL}), increases rapidly to a maximum and then decreases, with no sharp limit on the long wavelength side. When the tube voltage is raised, the intensity of all wavelengths increases, and both the short-wavelength limit and the position of the maximum shift to shorter wavelengths. Consider the smooth curves in Fig. 4, which correspond to applied voltages of 20 kV or less in the case of a molybdenum target. The radiation represented by such curves is called *polychromatic, continuous*, or

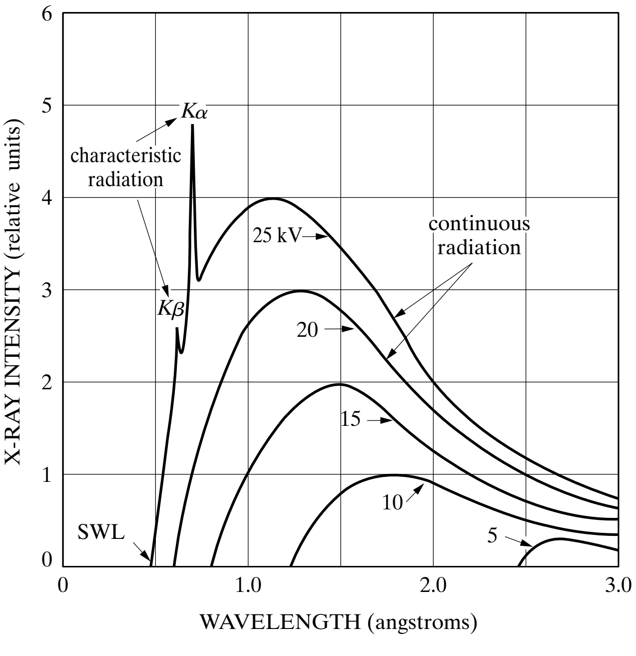

Figure 4 X-ray spectrum of molybdenum as a function of applied voltage (schematic). Line widths not to scale.

white radiation, since it is made up, like white light, of rays of many wavelengths. White radiation is also called *Bremsstrahlung*, German for “braking radiation,” because it is caused by electron deceleration.

The continuous spectrum results from the rapid deceleration of the electrons hitting the target since, as mentioned above, any decelerated charge emits energy. Not every electron decelerates in the same way, however; some stop in one impact and release all their energy at once, while others a deflect this way and that by the atoms of the target, successively losing fractions of their total kinetic energy until it is all spent. Those electrons which are stopped in one impact produce photons of maximum energy, i.e., x-rays of minimum wavelength. Such electrons transfer all their energy eV into photon energy so that

$$eV = hv_{\max}$$

$$\lambda_{\mathrm{SWL}} = \lambda_{\min} = \frac{c}{\nu_{\max}} = \frac{hc}{eV}$$

$$\lambda_{\mathrm{SWL}} = \frac{(6.626 \times 10^{-34})(2.998 \times 10^{3})}{(1.602 \times 10^{-19})\,V} \text{ meter,}$$

$$\lambda_{\mathrm{SWL}} = \frac{12.40 \times 10^{3}}{V}. \tag{4}$$

This equation gives the short-wavelength limit (in angstroms) as a function of the applied voltage V. If an electron is not completely stopped in one encounter but undergoes a glancing impact which only partially decreases its velocity, then only a fraction of its energy eV is emitted as radiation and the photon produced has energy less than $hv_{\max}$. In terms of wave motion, the corresponding x-ray has a frequency lower than $v_{\max}$ and a wavelength longer than λ_{SWL}. The totality of these wavelengths, ranging upward from λ_{SWL}, constitutes the continuous spectrum. The curves of Fig. 4 become higher and shift to the left as the applied voltage is increased, therefore, because the number of photons produced per second and the average energy per photon are both increasing. The total x-ray energy emitted per second, which is proportional to the area under one of the curves of Fig. 4, also depends on the atomic number Z of the target and on the tube current i, the latter being a measure of the number of electrons per second striking the target. This total x-ray intensity is given by

$$I_{\text{cont. spectrum}} = AiZV^{m}, \tag{5}$$

where A is a proportionality constant and m is a constant with a value of about 2 (see [2] for a discussion of this equation; note that a somewhat different form is quoted elsewhere e.g. [G.1]). Where large amounts of white radiation are desired, it is therefore necessary to use a heavy metal like tungsten ($Z = 74$) as a target and as high a voltage as possible. Note that the material of the target affects the intensity but not the wavelength distribution of the continuous spectrum.

4 THE CHARACTERISTIC SPECTRUM

When the voltage on an x-ray tube is raised above a certain critical value, characteristic of the target metal, sharp intensity maxima appear at certain wavelengths, superimposed on the continuous spectrum. Since they are so narrow and since their wavelengths are characteristic of the target metal used, they are called *characteristic lines*. These lines fall into several sets, referred to as *K, L, M*, etc., in the order of increasing wavelength, all the lines together forming the *characteristic spectrum* of the metal used as the target. For a molybdenum target the *K* lines have wavelengths of about 0.7 Å, the *L* lines about 5 Å, and the *M* lines still longer wavelengths. Ordinarily only the *K* lines are useful in x-ray diffraction, the longer-wavelength lines being too easily absorbed. There are several lines in the *K* set, but only the three strongest are observed in normal diffraction work. These are the $K\alpha_1$, $K\alpha_2$, and $K\beta_2$, and for molybdenum their wavelengths are approximately:

$K\alpha_1$: 0.709
$K\alpha_2$: 0.71
$K\beta_2$: 0.632

The α_1 and α_2 components have wavelengths so close together that they are not always resolved as separate lines; if resolved, they are called the *$K\alpha$ doublet* and, if not resolved, simply the *$K\alpha$ line*.[2] Similarly, $K\beta_1$ is usually referred to as the *$K\beta$ line*, with the subscript dropped. $K\alpha_1$ is always about twice as strong as $K\alpha_2$, while the intensity ratio of $K\alpha_1$ to $K\beta_1$ depends on atomic number but averages about 5/1.

These characteristic lines may be seen in the uppermost curve of Fig. 4. Since the critical *K excitation voltage*, i.e., the voltage necessary to excite *K* characteristic radiation, is 20.01 kV for molybdenum, the *K* lines do not appear in the lower curves of Fig. 4. An increase in voltage above the critical voltage increases the intensities of the characteristic lines relative to the continuous spectrum but *does not change their wavelengths*. Figure 5 shows the spectrum of molybdenum at 35 kV on a compressed vertical scale relative to that of Fig. 4; the increased voltage has shifted the continuous spectrum to still shorter wavelengths and increased the intensities of the *K* lines relative to the continuous spectrum but has not changed their wavelengths.

The intensity of any characteristic line, measured above the continuous spectrum, depends both on the tube current *i* and the amount by which the applied volt-

---

[2] The wavelength of an unresolved $K\alpha$ doublet is usually taken as the weighted average of the wavelengths of its components, $K\alpha_1$ being given twice the weight of $K\alpha_2$, since it is twice as strong. Thus the wavelength of the unresolved Mo $K\alpha$ line is

$$\tfrac{1}{3}(2 \times 0.709 + 0.714) = 0.711\text{Å}$$

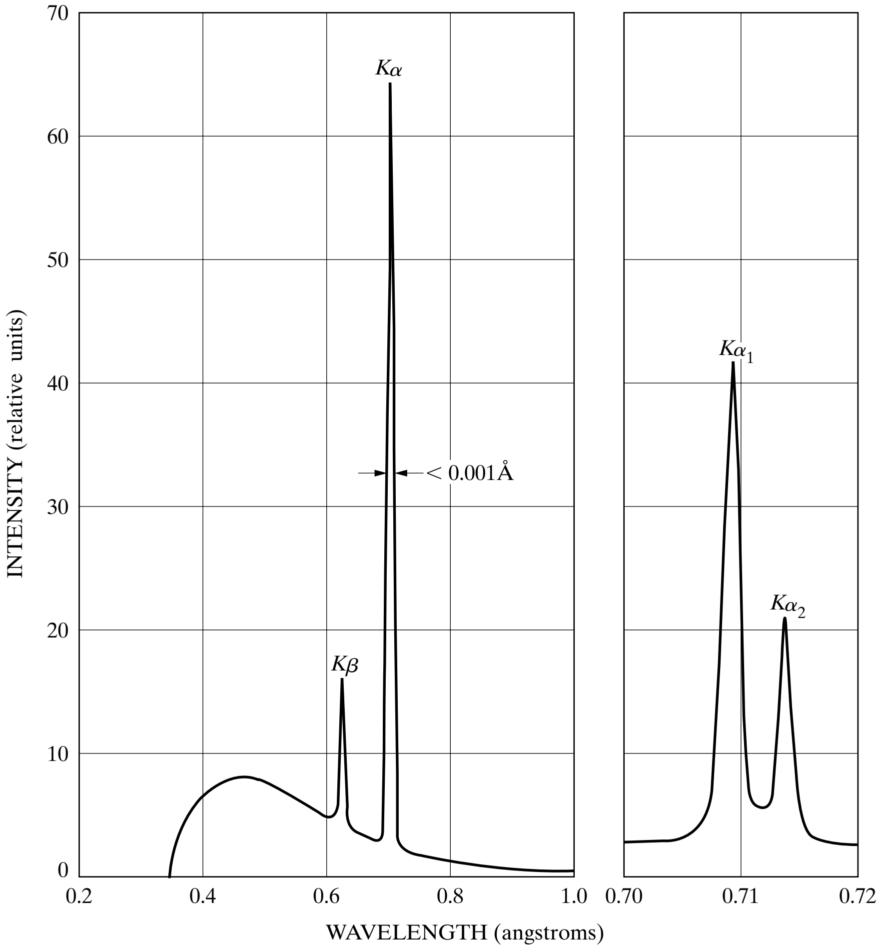

Figure 5 Spectrum of Mo at 35 kV (schematic). Line widths not to scale. Resolved Kα doublet is shown on an expanded wavelength scale at right.

age V exceeds the critical excitation voltage for that line. For a K line, the intensity is given approximately by

$$I_{K\text{line}} = Bi(V - V_K)^n \tag{6}$$

where B is a proportionality constant, V_K the K excitation voltage, and n a constant with a value of about 1.5. (Actually, n is not a true constant but depends on V and varies from 1 to 2 and averages about 1.6 for common tube materials [3].) The intensity of a characteristic line can be quite large: for example, in the radiation from a copper target operated at 30 kV, the $K\alpha$ line has an intensity about 90 times that of the wavelengths immediately adjacent to it in the continuous spectrum.

Besides being very intense, characteristic lines are also very narrow, most of them less than 0.001 Å wide measured at half their maximum intensity, as indicated in Fig. 5. The existence of this strong sharp $K\alpha$ line is what makes a great deal of x-ray diffraction possible, because many diffraction experiments require the use of monochromatic or approximately monochromatic radiation.

The characteristic x-ray lines were discovered by W. H. Bragg [4] and systematized by H. G. Moseley [5] The latter found that the wavelength of any particular line decreased as the atomic number of the emitter increased. In particular, he found a linear relation (Moseley's law) between the square root of the line frequency v and the atomic number Z:

$$\sqrt{v} = C\,(Z - \sigma), \tag{7}$$

where C and σ are constants. This relation is plotted in Fig. 6 for the $K\alpha_1$ and $L\alpha_1$ lines, the latter being the strongest line in the L series. These curves show, incidentally, that L lines are not always of long wavelength: the $L\alpha_1$ line of a heavy metal like tungsten, for example, has about the same wavelength as the $K\alpha_1$ line of copper, namely about 1.5 Å. The wavelengths of the characteristic x-ray lines of almost

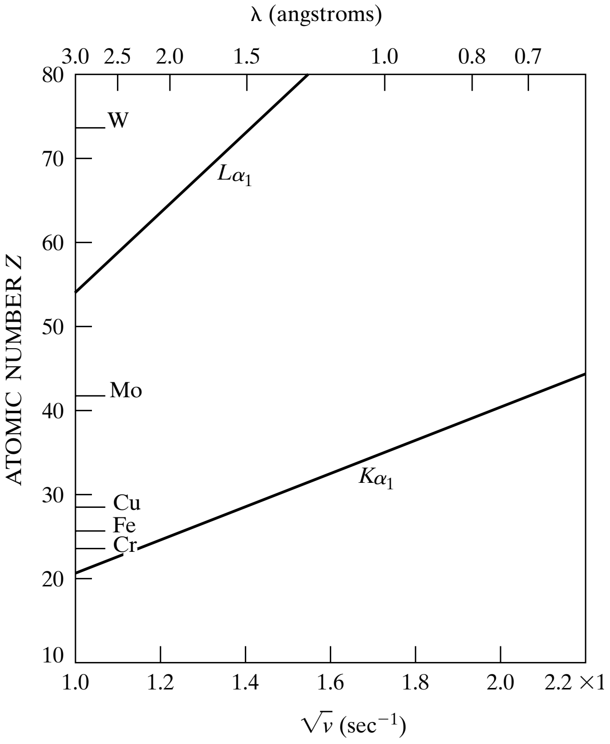

Figure 6 Moseley's relation between, $\sqrt{\nu}$ and Z for two characteristic lines.

all the known elements have been precisely measured, mainly by M. Siegbahn and coworkers. Data on weaker lines can be found in Vol. C of the *International Tables for Crystallography* [G.1]

While the continuous spectrum results from the rapid deceleration of electrons by the target, the origin of the characteristic spectrum lies in the atoms of the target material itself. To understand this phenomenon, it is enough to consider an atom as consisting of a central nucleus surrounded by electrons lying in various shells (Fig. 7), where the designation K, L, M, ... corresponds to the principal quantum number $n = 1, 2, 3, \ldots$ If one of the electrons bombarding the target has sufficient kinetic energy, it can knock an electron out of the K shell, leaving the atom in an excited, high-energy state. One of the outer electrons immediately falls into the vacancy in the K shell, emitting energy in the process, and the atom is once again in its normal energy state. The energy emitted is in the form of radiation of a definite wavelength and is, in fact, characteristic K radiation.

The K-shell vacancy may be filled by an electron from any one of the outer shells, thus giving rise to a series of K lines; $K\alpha$ and $K\beta$ lines, for example, result from the filling of a K-shell vacancy by an electron from the L or M shells, respectively. It is *possible* to fill a K-shell vacancy from either the L or M shell, so that one atom of the target may be emitting $K\alpha$ radiation while its neighbor is emitting $K\beta$; however, it is more *probable* that a K-shell vacancy will be filled by an L electron than by an M electron, and the result is that the $K\alpha$ line is stronger than the $K\beta$ line. It also follows that it is impossible to excite one K line without exciting all the others. L characteristic lines originate in a similar way: an electron is knocked out of the L shell and the vacancy is filled by an electron from some outer shell.

The existence of a critical excitation voltage for characteristic radiation is related to the sharply defined shells of the atoms being bombarded. K radiation, for example, cannot be excited unless the tube voltage provides the bombarding electrons with enough energy to knock an electron out of the K shell of a target atom.

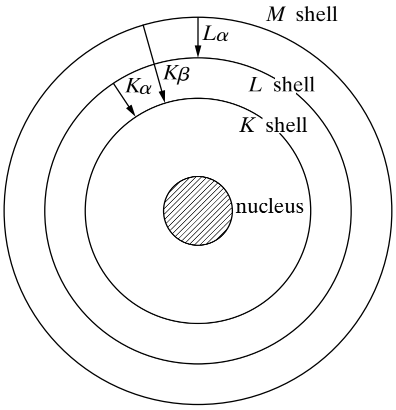

Figure 7 Electronic transitions in an atom (schematic). Emission processes indicated by arrows.

If W_K is the work required to remove a K electron, then the necessary kinetic energy of the electrons is given by

$$\frac{1}{2}mv^2 = W_K. \tag{8}$$

It requires less energy to remove an L electron than a K electron, since the former is farther from the nucleus; it therefore follows that the L excitation voltage is less than the K and that K characteristic radiation cannot be produced without L, M, etc., radiation accompanying it.

5 ABSORPTION

Further understanding of the electronic transitions which can occur in atoms can be gained by considering not only the interaction of electrons and atoms, but also the interaction of x-rays and atoms. When x-rays encounter any form of matter, they are partly transmitted and partly absorbed. Early on Röntgen established that the fractional decrease in the intensity I of an x-ray beam as it passes through any homogeneous substance is proportional to the distance traversed x [1]. In differential form,

$$-\frac{\mathrm{d}I}{I} = \mu \ \mathrm{d}x \tag{9}$$

where the proportionality constant μ is called the *linear absorption coefficient* and is dependent on the substance considered, its density, and the wavelength of the x-rays. Integration of Eq. (9) gives

$$I_x = I_0 e^{-\mu x}, \tag{10}$$

where I_o = intensity of incident x-ray beam and I_x = intensity of transmitted beam after passing through a thickness x.

The linear absorption coefficient μ is proportional to the density ρ, which means that the quantity μ/ρ is a constant of the material and independent of its physical state (solid, liquid, or gas). This latter quantity, called the *mass absorption coefficient*, is the one usually tabulated. Equation (10) may then be rewritten in a more usable form:

$$I_x = I_0 e^{-(\mu/\rho)\rho x}. \tag{11}$$

Values of the mass absorption coefficient μ/ρ appear in "Appendix: Mass Absorption Coefficients μ/ρ (cm2/gm) and Densities ρ" for various characteristic wavelengths commonly used in diffraction and in Vol. C of the International Tables for Crystallography [G.1], for other wavelengths.

It is occasionally necessary to know the mass absorption coefficient of a substance containing more than one element. Whether the substance is a mechanical mixture, a solution, or a chemical compound, and whether it is in the solid, liquid, or gaseous state, its mass absorption coefficient is simply the weighted average of the mass absorption coefficients of its constituent elements. If w_1, w_2, etc., are the weight fractions of elements 1, 2, etc., in the substance and $(\mu/\rho)_1$, $(\mu/\rho)_2$, etc., their mass absorption coefficients, then the mass absorption coefficient of the substance is given by

$$\frac{\mu}{\rho} = w_1\left(\frac{\mu}{\rho}\right)_1 + w_2\left(\frac{\mu}{\rho}\right)_2 + \cdots \qquad (12)$$

The way in which the absorption coefficient varies with wavelength gives the clue to the interaction of x-rays and atoms. The lower curve of Fig. 8 shows this variation for a nickel absorber; it is typical of all materials. The curve consists of two similar branches separated by a sharp discontinuity called an *absorption edge*. Along each branch the absorption coefficient varies with wavelength approximately according to a relation of the form

$$\frac{\mu}{\rho} = k\lambda^3 Z^3, \qquad (13)$$

where k = a constant, with a different value for each branch of the curve, and Z = atomic number of absorber. Short-wavelength x-rays are therefore highly penetrating and are termed *hard*, while long-wavelength x-rays are easily absorbed and are said to be *soft*.

Matter absorbs x-rays in two distinct ways, by scattering and by true absorption, and these two processes together make up the total absorption measured by the quantity μ/ρ. The *scattering* of x-rays by atoms is similar in many ways to the scattering of visible light by dust particles in the air. It takes place in all directions, and

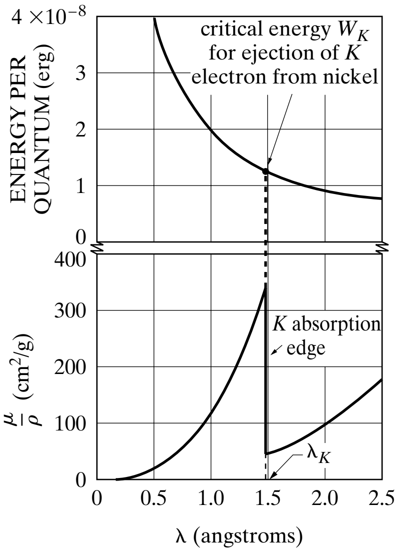

Figure 8 Variation with wavelength of the energy per x-ray quantum and of the mass absorption coefficient of nickel.

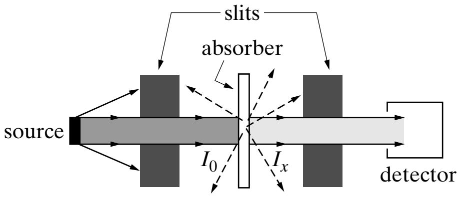

Figure 9 Experimental arrangement for measuring absorption. Narrow slits or pinholes define the beam. The detector measures the intensity I_0 of the incident beam when the absorber is removed and the intensity I_x of the transmitted beam when the absorber is in place. Although the scattered radiation (dashed lines) does not represent energy absorbed in the specimen, it does constitute energy removed from the beam and accordingly forms part of the total absorption represented by the coefficient μ/ρ.

since the energy in the scattered beams does not appear in the transmitted beam, it is, so far as the transmitted beam is concerned, said to be absorbed (Fig. 9). The phenomenon of scattering is beyond the scope of this chapter; it is enough to note here that, except for the very light elements, it is responsible for only a small fraction of the total absorption of x-rays with wavelengths in the range normally used in diffraction. *True absorption* is caused by electronic transitions within the atom and is best considered from the viewpoint of quantum theory. Just as an electron of sufficient energy can knock a *K* electron, for example, out of an atom and thus cause the emission of *K* characteristic radiation, so also can an incident quantum of x-rays, provided it has the same minimum amount of energy W_K. In the latter case, the ejected electron is called a *photoelectron* and the emitted characteristic radiation is called *fluorescent radiation*. It radiates in all directions and has exactly the same wavelength as the characteristic radiation caused by electron bombardment of a metal target. (In effect, an atom emits the same *K* radiation no matter how the *K*-shell vacancy was originally created.) This phenomenon is the x-ray counterpart of the photoelectric effect in the ultraviolet region of the spectrum; there, photoelectrons can be ejected from the outer shells of a metal atom by the action of ultraviolet radiation, provided the latter has a wavelength less than a certain critical value.

To say that the energy of the incoming quanta must exceed a certain value W_K is equivalent to saying that the wavelength must be less than a certain value λ_K, since the energy per quantum is $h\nu$ and wavelength is inversely proportional to frequency. These relations may be written

$$W_K = h\nu_K = \frac{hc}{\lambda_K}, \tag{14}$$

where ν_K and λ_K are the frequency and wavelength, respectively, of the *K* absorption edge. Now consider the absorption curve of Fig. 8 in light of the above. Suppose that x-rays of wavelength 2.5 Å are incident on a sheet of nickel and that this wavelength is continuously decreased. At first the absorption coefficient is about 180 cm^2/g, but, as the wavelength decreases, the frequency increases and so does the energy per quantum, as shown by the upper curve, thus causing the absorption coefficient to decrease, since the greater the energy of a quantum the more easily it passes through an absorber. When the wavelength is reduced just below the critical value λ_K, which is 1.488 Å for nickel, the absorption coefficient suddenly increases about eightfold in value. True *K* absorption is now occurring and a large fraction of the incident quanta simply disappear, their energy being converted into *K* fluorescent radiation and the kinetic energy of ejected photoelectrons. Since energy must be conserved in the process, it follows that the energy per quantum of the fluorescent radiation must be less than that of the incident radiation, or that the wavelength λ_K of the *K* absorption edge must be shorter than that of any *K* characteristic line of the absorber (The eight-fold increase in μ/ρ mentioned above means a tremendous decrease in transmitted intensity, because of the exponential nature of Eq. (11). If the transmission factor I_x/I_o of a particular nickel sheet is 0.1 for a wavelength just longer than λ_K, then it is only 10^{-8} for a wavelength just shorter.)

As the wavelength of the incident beam decreases below λ_K, the absorption coefficient begins to decrease again, even though the production of *K* fluorescent radiation and photoelectrons still occurs. At a wavelength of 1.0 Å, for example, the incident quanta have more than enough energy to remove an electron from the *K* shell of nickel. But the more energetic the quanta become, the greater is their probability of passing right through the absorber, with the result that less and less of them take part in the ejection of photoelectrons.

Plotting the absorption curve of nickel for wavelengths longer than 2.5 Å, i.e., beyond the limit of Fig. 8, reveals other sharp discontinuities. These are the *L, M, N*, etc., absorption edges; in fact, there are three closely spaced *L* edges (L_I, L_{II}, and L_{III}), five *M* edges, etc. (Fig. 10). Each of these discontinuities marks the wavelength of the incident beam whose quanta have just sufficient energy to eject an *L, M, N*,

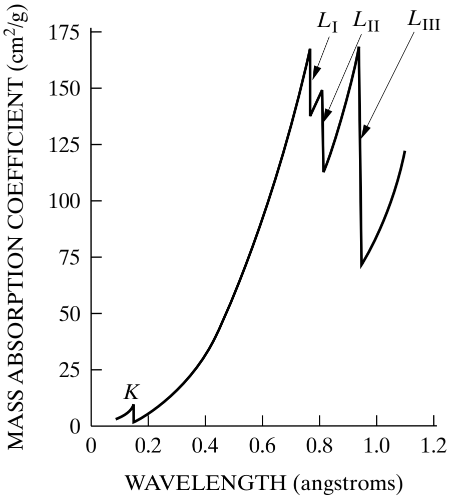

Figure 10 Absorption coefficients of lead, showing *K* and *L* absorption edges [6].

etc., electron from the atom. The right-hand branch of the curve of Fig. 8, for example, lies between the K and L absorption edges; in this wavelength region incident x-rays have enough energy to remove L, M, etc., electrons from nickel but not enough to remove K electrons. Absorption-edge wavelengths vary with the atomic number of the absorber in the same way, but not quite as exactly, as characteristic emission wavelengths, that is, according to Moseley's law.

The measured values of the absorption edges can be used to construct an energy-level diagram for the atom, which in turn can be used in the calculation of characteristic-line wavelengths. For example, if the energy of the neutral atom is defined as zero, then the energy of an ionized atom (an atom in an excited state) will be some positive quantity, since work must be done to pull an electron away from the positively charged nucleus. If a K electron is removed, work equal to W_{K} must be done and the atom is said to be in the K energy state. The energy W_{K} may be calculated from the wavelength of the K absorption edge by the use of Eq. (14). Similarly, the energies of the L, M, etc., states can be calculated from the wavelengths of the L, M, etc., absorption edges and the results plotted in the form of an energy-level diagram for the atom (Fig. 11).

Although this diagram is simplified, in that the substructure of all the levels is not shown, it illustrates the main principles. The arrows show the transitions of the *atom*, and their directions are therefore just the opposite of the arrows in Fig. 7, which shows the transitions of the *electron*. Thus, if a K electron is removed from an atom (whether by an incident electron or x-ray), the atom is raised to the K state. If an electron then moves from the L to the K level to fill the vacancy, the atom undergoes a transition from the K to the L state. The emission of $K\alpha$ characteristic radiation accompanies this transition, and the arrow indicating $K\alpha$ emission is accordingly drawn *from* the K state *to* the L state.

Figure 11 shows clearly how the wavelengths of characteristic emission lines can be calculated, since the difference in energy between two states will equal $h\nu$, where ν is the frequency of the radiation emitted when the atom goes from one state to the other. Consider the $K\alpha_1$ characteristic line, for example. The "L level" of an atom is actually a group of three closely spaced levels (L_{I}, L_{II}, and L_{III}) , and the emission of the $K\alpha_1$ line is due to a K « $\mathrm{L}_{\mathrm{III}}$ transition. The frequency $\mathrm{v}_{\mathrm{K}\alpha_1}$ of this line is therefore given by the equations

$$h\nu_{K\alpha_1} = W_K - W_{L_{\mathrm{III}}},$$

$$h\nu_{K\alpha_1} = h\nu_K - h\nu_{L_{\mathrm{III}}},$$

$$\frac{1}{\lambda_{K\alpha_1}} = \frac{1}{\lambda_K} - \frac{1}{\lambda_{L_{\mathrm{III}}}}, \qquad (15)$$

where the subscripts K and L_{111} refer to absorption edges and the subscript $K\alpha_1$ to the emission line.

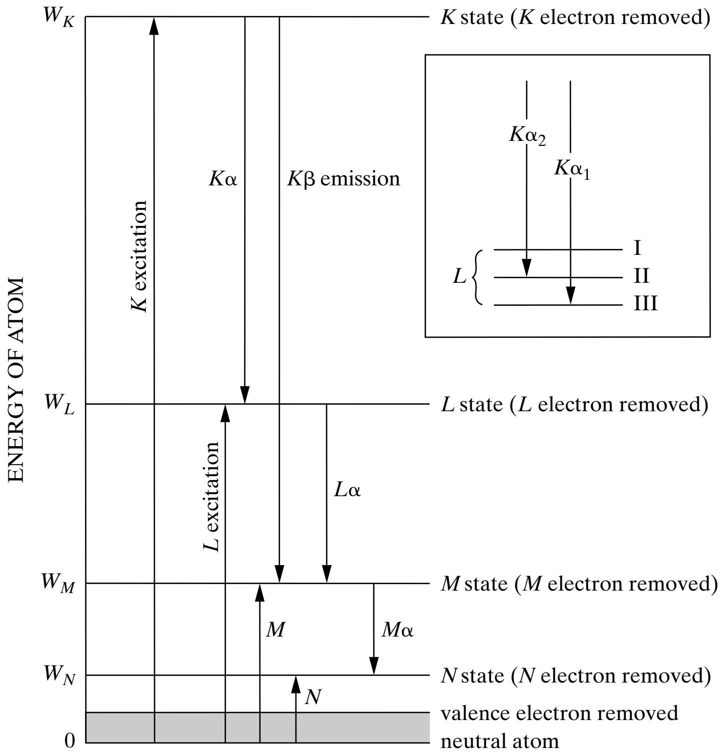

Figure 11 Atomic energy levels (schematic). Excitation and emission processes indicated by arrows. The insert at top right shows the fine structure of the ***L*** state. After Barrett [7].

Excitation voltages can be calculated by a relation similar to Eq. (4). To excite *K* radiation, for example, in the target of an x-ray tube, the bombarding electrons must have energy equal to W_K. Therefore

$$eV_K = W_K = hv_K = \frac{hc}{\lambda_K},$$

$$V_K = \frac{hc}{e\lambda_K},$$

$$V_K = \frac{12.40 \times 10^3}{\lambda_K}, \tag{16}$$

where V_K is the *K* excitation voltage and λ_K is the *K* absorption edge wavelength (in angstroms).

Figure 12 summarizes some of the relations developed above. This curve gives the short-wavelength limit of the continuous spectrum as a function of applied volt-

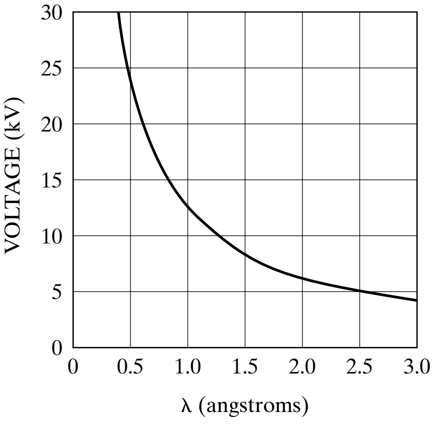

Figure 12 Relation between the voltage applied to an x-ray tube and the short-wavelength limit of the continuous spectrum, and between the critical excitation voltage of any metal and the wavelength of its absorption edge.

age. Because of the similarity between Eqs. (4) and (16), the same curve also allows determination of the critical excitation voltage from the wavelength of an absorption edge.

It might be inferred, from the last two sections, that every atom that has a vacancy in, for example, the K shell will always emit K radiation. That is not so. An atom with a K-shell vacancy is in an ionized, high-energy state. It can lose this excess energy and return to its normal state in two ways: (1) by emitting K radiation ("normal" production of characteristic radiation), or (2) by emitting an electron (*Auger effect* [8, 9]). In the Auger process a K-shell vacancy is filled from, say, the L_{11} level; the resulting K radiation does not escape from the atom but ejects an electron from, say, the L_{111} level. The ejected electron, called an *Auger electron*, has kinetic energy related to the energy difference between the K and L_{11} states.

The Auger effect is by no means a minor one. In fact, atoms with an atomic number Z less than 31 (gallium) are more likely to eject Auger electrons than to emit x-rays. The likelihood of the Auger process can be found from the fluorescence yield ω, which is defined, for the K shell, by

$$\omega_K = \frac{\text{number of atoms that emit } K \text{ radiation}}{\text{number of atoms with a } K\text{-shell vacancy}}. \tag{17}$$

(This quantity is called the *fluorescence* yield, whether the vacancy is caused by incident x-rays or by electrons.) Some values of ω_K are 0.03 for Mg ($Z = 12$), 0.41 for Cu ($Z = 29$), and 0.77 for Mo ($Z = 42$) [G.2, p. 131]. The probability of the Auger process occurring is $(1 - \omega_K)$, which amounts to some 97 percent for Mg and 23 percent for Mo.

Electrons of moderate energy like Auger electrons cannot travel very far in a solid, and an Auger electron emitted by one atom in a solid specimen cannot escape from the specimen unless the atom is situated within about 10 Å of the surface. The electrons that do escape have kinetic energies related to the differences between energy levels of the parent atom, i.e., their energies are characteristic of that atom.

Means are available for measuring these energies, providing a method for chemical analysis of very thin surface layers, called *Auger electron spectroscopy*, used in studies of catalysts, corrosion, impurity segregation at surfaces, etc.

6 FILTERS

Many x-ray diffraction experiments require radiation which is as closely monochromatic as possible. However, the beam from an x-ray tube operated at a voltage above V_K contains not only the strong $K\alpha$ line but also the weaker $K\beta$ line and the continuous spectrum. The intensity of these undesirable components can be decreased relative to the intensity of the $K\alpha$ line by passing the beam through a *filter* made of a material whose K absorption edge lies between the $K\alpha$ and $K\beta$ wavelengths of the target metal. Such a material will have an atomic number one less than that of the target metal, for metals with Z near 30.

A filter so chosen will absorb the $K\beta$ component much more strongly than the $K\alpha$ component, because of the abrupt change in its absorption coefficient between these two wavelengths. The effect of filtration is shown in Fig. 13, in which the partial spectra of the unfiltered and filtered beams from a copper target ($Z = 29$) are shown superimposed on a plot of the mass absorption coefficient of the nickel filter ($Z = 28$).

The thicker the filter the lower the ratio of intensity of $K\beta$ to $K\alpha$ in the transmitted beam. But filtration is never perfect, of course, no matter how thick the

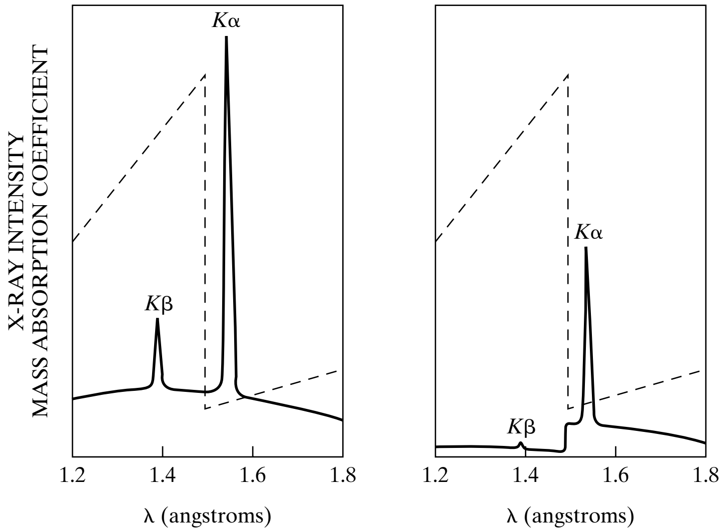

(a) No filter

(b) Nickel filter

Figure 13 Comparison of the spectra of copper radiation (a) before and (b) after passage through a nickel filter (schematic). The dashed line is the mass absorption coefficient of nickel.

filter, and one must compromise between reasonable suppression of the $K\beta$ component and the inevitable weakening of the $K\alpha$ component which accompanies it. In practice, a reduction in the intensity of the $K\alpha$ line to about half its original value decreases the ratio of intensity of $K\beta$ to $K\alpha$ from about 1/9 in the incident beam to about 1/500 in the transmitted beam; this level is sufficiently low for most purposes. Table 1 shows the filters used in conjunction with the common target metals, the thicknesses required, and the transmission factors for the $K\alpha$ line. Filter materials are usually used in the form of thin foils. If it is not possible to obtain a given metal in the form of a stable foil, the oxide of the metal may be used. The powdered oxide is mixed with a suitable binder and spread on a paper backing, the required mass of metal per unit area being given in Table 1.

7 PRODUCTION OF X-RAYS

Since x-rays are produced whenever high-speed electrons collide with a metal target, any x-ray tube must contain (*a*) a source of electrons, (*b*) a high accelerating voltage, and (*c*) a metal target. Furthermore, since most of the kinetic energy of the electrons is converted into heat in the target, the latter is almost always water-cooled to prevent its melting.

All x-ray tubes contain two electrodes, an anode (the metal target) maintained, with few exceptions, at ground potential, and a cathode, maintained at a high negative potential, normally of the order of 30,000 to 50,000 volts for diffraction work. X-ray tubes may be divided into two basic types, according to the way in which electrons are provided: gas tubes, in which electrons are produced by the ionization of a small quantity of gas (residual air in a partly evacuated tube), and filament tubes, in which the source of electrons is a hot filament.

TABLE 1 FILTERS FOR SUPPRESSION OF $K\beta$ RADIATION

Target	Filter	Incident beam* $\frac{I(K\alpha)}{I(K\beta)}$	Filter thickness for $\frac{I(K\alpha)}{I(K\beta)} = \frac{500}{1}$ in trans. beam		$\frac{I(K\alpha)\ \text{trans}}{I(K\alpha)\ \text{incident}}$
			mg/cm^2	in	
Mo	Zr	5.4	77	0.0046	0.29
Cu	Ni	7.5	18	0.0008	0.42
Co	Fe	9.4	14	0.0007	0.46
Fe	Mn	9.0	12	0.0007	0.48
Cr	V	8.5	10	0.0006	0.49

* This is the intensity ratio *at the target* [G.1]. This ratio outside the x-ray tube will be changed somewhat by the differential absorbtion of $K\alpha$ and $K\beta$ by the tube window, typically beryllium, 0.01 inch (0.25 mm) thick.

Gas Tubes

These resemble the original x-ray tube used by Röntgen. They are now obsolete.

Filament Tubes

These were invented by Coolidge in 1913 [1.10]. They consist of an evacuated glass envelope which insulates the anode at one end from the cathode at the other, the cathode being a tungsten filament and the anode a water-cooled block of copper containing the desired target metal as a small insert at one end. Figure 14 is a photograph of such a tube, and Fig. 15 shows its internal construction. One lead of the

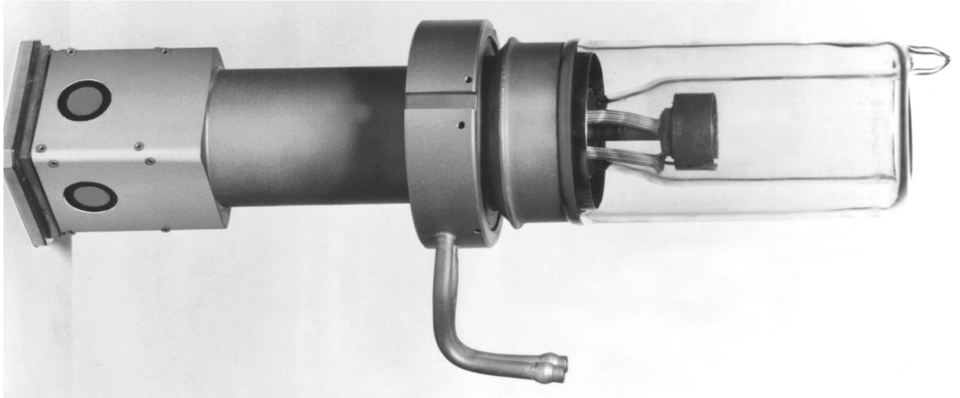

Figure 14 Sealed x-ray tube. Cooling-water tubes at center connect with internal ducts leading to anode at left end. Three windows: two for projecting square focal spots and one for projecting a line focal spot. Focal spots of three sizes are available with this tube (Type A-5): 1.2 × 12.5 mm, 0.75 × 12.5 mm, and 0.45 × 12.5 mm. (Courtesy of Machlett Laboratories, Inc.)

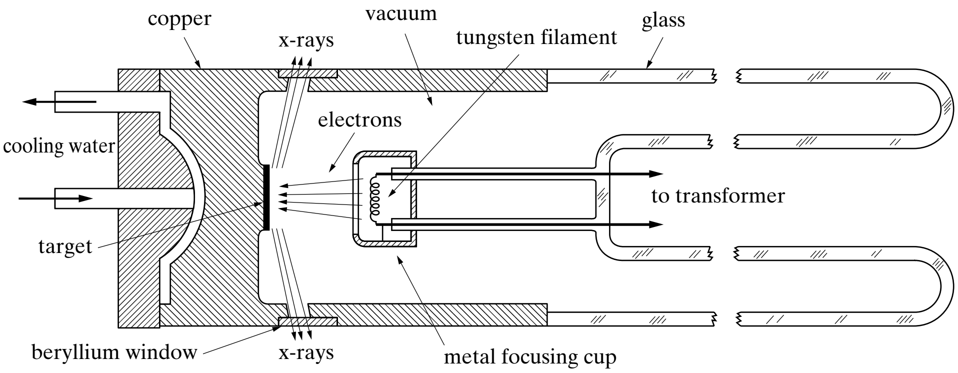

Figure 15 Cross section of sealed x-ray tube (schematic).

high-voltage transformer is connected to the filament and the other to ground, the target being grounded by its own cooling-water connection. The filament is heated by a *filament current* of about 3 amp and emits electrons which are rapidly drawn to the target by the high voltage across the tube. Surrounding the filament is a small metal cup maintained at the same high (negative) voltage as the filament: it therefore repels the electrons and tends to focus them into a narrow region of the target, called the *focal spot*. X-rays are emitted from the focal spot in all directions and escape from the tube through two or more windows in the tube housing. Since these windows must be vacuum tight and yet highly transparent to x-rays, they are usually made of beryllium.

Although one might think that an x-ray tube would operate only from a dc source, since the electron flow must occur only in one direction, it is actually possible to operate a tube from an ac source such as a transformer because of the rectifying properties of the tube itself. Current exists during the half-cycle in which the filament is negative with respect to the target; during the reverse half-cycle the filament is positive, but no electrons can flow since only the filament is hot enough to emit electrons. Thus a simple circuit such as shown in Fig. 16 suffices for many installations, although more elaborate circuits, containing rectifying tubes, smoothing capacitors, and voltage stabilizers, are now the rule. In Fig. 16, the voltage applied to the tube is controlled by the autotransformer which controls the voltage applied to the primary of the high-voltage transformer. The voltmeter shown measures the input voltage but normally is calibrated to read the output voltage applied to the tube. The milliammeter measures the *tube current*, i.e., the flow of electrons from filament to target. This current is normally of the order of 10 to 25 mA and is controlled by the filament rheostat. The rheostat controls the output voltage of the filament transformer; this voltage determines the filament current and, in turn, the temperature of the filament and the number of electrons it can emit per second. Although the filament transformer is a low-voltage step-down transformer, since it

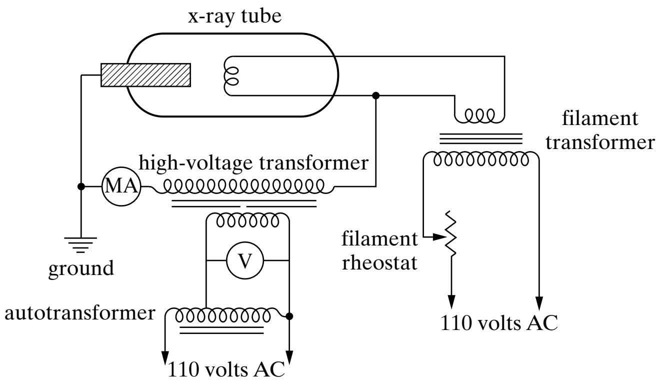

Figure 16 Wiring diagram for self-rectifying filament tube.

need apply only about 5 volts to the filament, it is itself at a high negative voltage relative to ground and must be well insulated.

Two kinds of filament tube exist: sealed and demountable. A sealed tube is evacuated and sealed at the factory. It is by far the easier kind to operate, since no high-vacuum pumping equipment is needed; however, it is expensive (one needs as many tubes as there are target metals required), and the life of the tube is determined by the life of the filament. In demountable tubes, which are used nowadays only for special purposes, both the filament and the target are accessible for replacement; burned-out filaments can be replaced and targets can be interchanged at will. However, the demountable tube must be pumped continuously during operation, and both a diffusion and a mechanical pump are necessary to obtain the required vacuum.

The old gas tube, although tricky to operate, had the advantage of producing the purest radiation available, since the target never became contaminated with a foreign metal. In filament tubes, on the other hand, some tungsten occasionally evaporates from the filament and deposits on the target, and the tungsten then emits characteristic *L* radiation (the *L* excitation voltage of tungsten is only 10,200 volts), as well as the radiation characteristic of the target metal itself.

Focal Spot

The size and shape of the focal spot of an x-ray tube is one of its most important characteristics. Within limits, it should be as small as possible in order to concentrate the electron energy into a small area of the target and so produce an x-ray source of high flux (i.e., intensity per unit area of the x-ray source).

Filament tubes usually have the filament wound in a helix in order to produce a so-called "line focus" which is actually a narrow rectangle (Fig. 17). The total electron energy is thus spread over a rather large focal spot *A*, which helps to dissipate the heat formed; yet the cross section *B* of the beam issuing at a small target-to-beam angle α is that of a small square, and this beam contains more photons per unit area of the source (i.e., is brighter) than one leaving the focal spot at some larger angle α. The best value of the take-off angle α is about 6°, and a good tube will have a projected focal-spot size at this angle of less than 1 mm square. If the tube has a window so arranged that a beam can issue from the focal spot *A* almost

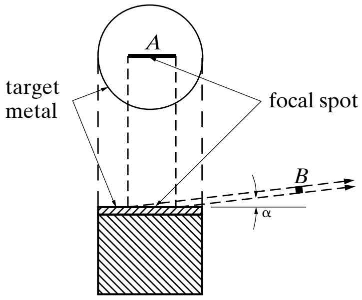

Figure 17 Top and side views of target showing reduction in apparent size of focal spot.

normal to the plane of Fig 17 and at a small angle α, then the cross section of the beam will be an extremely narrow line; such a beam is quite useful in some diffraction experiments.

Power Rating

All x-ray tubes have a maximum power rating which cannot be exceeded without injury to the tube. This limit is fixed by the amount of heat that can be dissipated by the target and is usually stated by the manufacturer in terms of the maximum allowable tube current (in mA) for a given tube voltage (in kV).

Rotating-Anode Tubes

Since an x-ray tube is less than 1 percent efficient in producing x-rays and since the diffraction of x-rays by crystals is far less efficient than this, it follows that the intensities of diffracted x-ray beams are extremely low. In fact, photographic film may require as much as several hours exposure in order to detect them at all. One way of increasing the intensity of the x-ray source is the rotating-anode tube, in which rotation of the anode continuously brings fresh target metal into the focal-spot area and so allows a greater power input without excessive heating of the anode. Figure 18 shows two designs that have been used successfully; the shafts rotate through vacuum-tight seals in the tube housing. Such tubes can operate at a power level 5 to 10 times higher than that of a fixed-focus tube, [11].

Microfocus Tubes

Some diffraction methods require extremely fine x-ray beams. Such beams are most efficiently produced by special demountable x-ray tubes, called microfocus tubes, in which special attention is paid to achieving a very small focal spot. The design problem—fine focusing of the electron beam—is similar to that of the electron microscope or the x-ray microprobe. One focusing method is electrostatic and consists

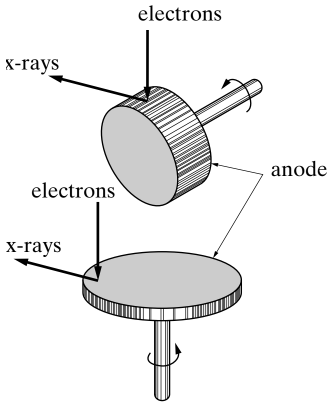

Figure 18 Schematic drawings of two types of rotating anode for high-power x-ray tubes.

simply in maintaining the focusing cup around the filament at a potential of a few hundred volts more negative than the filament, thus concentrating the electrons into a narrower beam.

The focal spots of these tubes have areas of less than 1 percent of those of conventional tubes. Typical sizes are 0.1 × 1 mm for a line focus and 0.05 mm (= 50 μm) diameter for a circular focus, and focal spot diameters smaller than 0.01 mm can be obtained.

Pulsed (or Flash) Tubes

The maximum power at which an x-ray tube can operate continuously is limited by the rate at which the target can be cooled. But if the tube is operated for only a small fraction of a second, a pulse of x-rays can be obtained at a very high power level without any cooling. This can be done by slowly charging a bank of capacitors and then abruptly discharging them across a special x-ray tube. In this way an x-ray pulse lasting about 30 nanoseconds at a peak voltage of 300 kV and a peak current of 5000 amperes has been produced [12]. (Such a brief flash of x-rays is useful only if its results, in radiography or diffraction, can be recorded.)

Miniature Tubes

If increased attention is given, during the design of an x-ray tube, to focusing of the electron beam and to the shape and placement of the target, the intensity of the beam issuing from the tube can be made about as large as that from a conventional tube, but with a power input of one-tenth or less. As a result, water cooling is not needed; air cooling is sufficient. This feature is important for portable apparatus such as those used for in situ residual stress measurements.

Such tubes are commercially available [13]. They are small, only about 4 to 8 in (10 to 20 cm) in length, and operate typically at a voltage of about 50 kV and a tube current of the order of 1 mA, as compared to 10 mA or more in conventional tubes.

High Voltage Tubes and Linear Accelerators

Specialized sealed tubes and linear accelerators are used to produce very penetrating radiation and can be used for x-ray diffraction, but these sources are used primarily in the area of nondestructive evaluation [14].

Synchrotron Radiation

As discussed before, acceleration of charged particles produces electromagnetic radiation; the continuous spectrum emitted from an x-ray tube is one example. If electrons or positrons moving at relativistic velocities (in, say, an accelerator such as an electron synchrotron) are deflected along a curved trajectory by a magnetic field, synchrotron radiation is produced. A continuous spectrum results, spanning from microwaves to very hard x-rays (Fig. 19). Not only is radiation produced in energy ranges where no other usable sources exist, but storage rings emitting synchrotron radiation are the best source of x-rays for many purposes including diffraction.

Several factors give synchrotron radiation an advantage over tube sources for x-ray diffraction. The intensity of x-rays delivered to a sample is far greater than that of other sources, and synchrotron radiation can be tuned to the most advantageous x-ray wavelength. The relativistic character of the synchrotron radiation process confines radiation to directions very close to the plane of electron or positron orbit, and the resulting divergence of the x-ray beam is very small. Therefore, this source of very high flux x-rays has an even higher brightness and spectral brightness (intensity per unit area of source and intensity per unit area per unit solid angle per unit energy bandwidth, respectively). Many diffraction experiments at the frontiers of materials research are feasible only with synchrotron x-radiation.

Several types of devices provide the intense magnetic fields required to produce synchrotron radiation. Bending magnets situated periodically around the storage ring deflect the electrons or positrons and force them to circulate within the ring. Insertion devices placed between the bending magnets and consisting of a relatively closely spaced array of magnets are another source of radiation. There are five storage rings producing x-rays for diffraction in the US alone, along with several other storage rings producing softer radiation; and each ring has its own peculiar combination of ring energy, bending magnets, and insertion devices. Brightness as a function of x-ray wavelength is compared for some of the synchrotron radiation sources in Fig. 19. Values typical of sealed tube and rotating anode sources are also shown. Further details appear elsewhere, e.g., [15, 16], and new reviews appear annually.

Typically a single experiment (and the associated researchers) occupies each station (beamline) at a time; and data collection continues around the clock for the entire period the experiment is on-line (from several days to a month). Activity centers around a radiation-tight enclosure containing the experimental apparatus and connected to the storage ring by radiation transport pipes. Support apparatus including computers cluster around the hutch, and the adjacent beamline and equipment can be as close as a few meters away. Most storage rings have between ten and fifty such stations, some very specialized and some general purpose.

The advantages of synchrotron radiation for materials characterization must be balanced against the limited accessibility (geographic and temporal) and the difficulty of working away from one's own laboratory. New users are generally encouraged by the administration of the different facilities although the how, what and why of a proposed experiment must be evaluated before beam is provided. In many, if not most, circumstances, characterization needs to be done on a day-in, day-out basis. This reason alone is enough to insure that characterization using x-ray tubes continues to flourish.

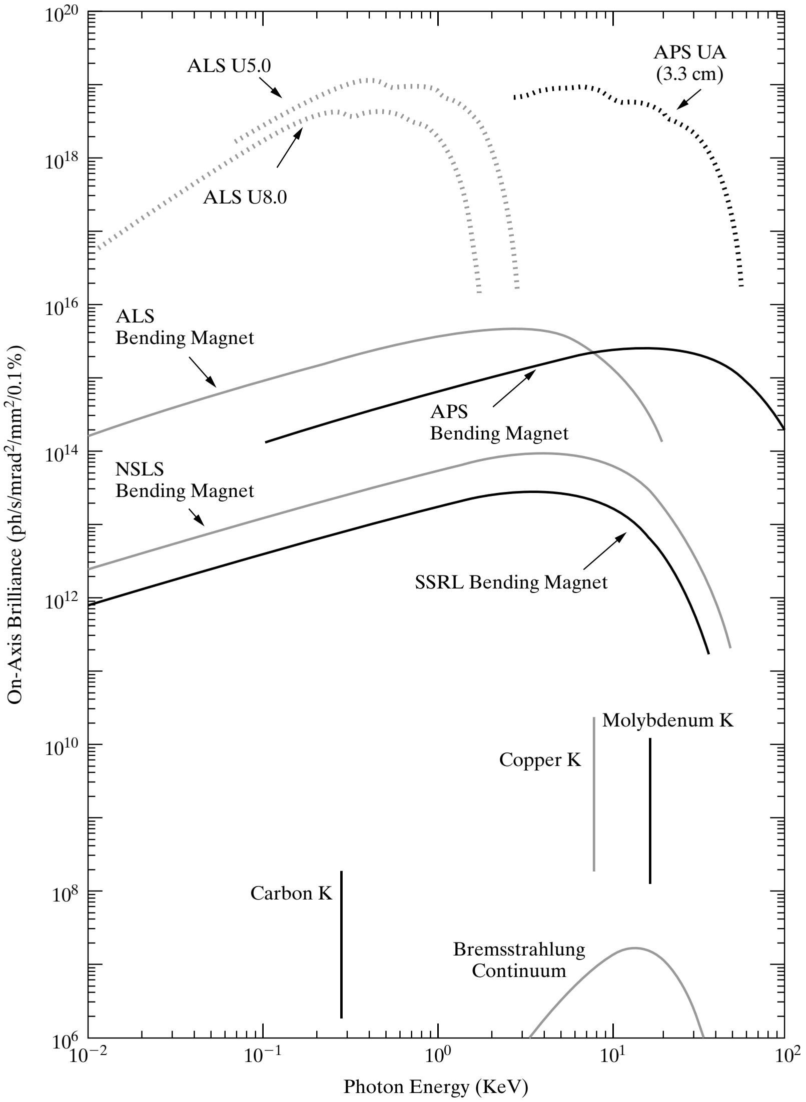

Figure 19 Intensity of synchrotron radiation as a function of photon energy for various sources: ALS (Advanced Light Source, Lawrence Berkeley National Laboratory), APS (Advanced Photon Source Argonne National Laboratory), NSLS (National Synchrotron Light Source, Brookhaven National Laboratory), SSRL (Stanford Synchrotron Radiation Laboratory). Note that Spectra from both undulators and bending magnets are included for ALS and APS, and values typical of laboratory sources are shown for commparison.

8 DETECTION OF X-RAYS

The principal means used to detect x-ray beams are fluorescent screens, photographic film, and electronic detectors. More recently image (storage) plates have become popular as an alternative to photographic emulsions, particularly at synchrotron radiation sources. Discussion of the detectors' interactions with x-rays is beyond the scope of this chapter.

9 SAFETY PRECAUTIONS

The operator of x-ray apparatus is exposed to two obvious dangers, electric shock and radiation injury, but both of these hazards can be reduced to negligible proportions by proper design of equipment and reasonable care on the part of the user. Nevertheless, it is only prudent for the x-ray worker to be continually aware of these hazards.

Electric Shock

The danger of electric shock is always present around high-voltage apparatus. The anode end of most x-ray tubes is usually grounded and therefore safe, but the cathode end is a source of danger. X-ray tubes of the nonshockproof variety (such as the one shown in Fig. 14) must be so mounted that their cathode end is absolutely inaccessible to the user during operation; this may be accomplished by placing the cathode end below a table top, in a box, behind a screen, etc. The installation should be so contrived that it is impossible for the operator to touch the high-voltage parts without automatically disconnecting the high voltage. (i.e., interlocks should be present). Shock-proof sealed tubes are also available: these are encased in a grounded metal covering, and an insulated, shock-proof cable connects the cathode end to the transformer. Being shock-proof, such a tube has the advantage that it need not be permanently fixed in position but may be set up in various positions as required for particular experiments.

Radiation Hazard

The radiation hazard is due to the fact that x-rays can kill human tissue; in fact, it is precisely this property which is utilized in x-ray therapy for killing cancer cells. The biological effects of x-rays include burns (due to localized high-intensity beams), radiation sickness (due to radiation received generally by the whole body), and, at a lower level of radiation intensity, genetic mutations. The burns are painful and may be difficult, if not impossible, to heal. Slight exposures to x-rays are not cumulative, but above a certain level called the "tolerance dose," they do have a cumulative effect and can produce permanent injury. The x-rays used in diffraction are particularly harmful because they have relatively long wavelengths and are therefore easily absorbed by exposed organs such as the skin and eyes.

There is no excuse today for receiving serious injuries as early x-ray workers did through ignorance. There would probably be no accidents if x-rays were visible and produced an immediate burning sensation, but they are invisible and burns may not be felt immediately. If the body has received general radiation above the tolerance dose, the first noticeable effect will be a lowering of the white-blood-cell count, so periodic blood counts are advisable if there is any doubt about the general level of intensity in the laboratory.

Portable detectors, called *radiation survey meters*, are available for surveying various areas around x-ray equipment for possible radiation leaks. Apparatus should be checked for radiation leaks periodically and whenever the instrument's configuration is changed. Film badges should be worn on the torso or wrist of persons who spend a large fraction of their working day near x-ray equipment. Government regulations regarding radiation safety are becoming increasingly severe. Most research institutions have radiation safety offices and require training of radiation workers as well as certification of the safety of apparatus producing ionizing radiation such as x-rays.

Current generations of diffraction apparatus are designed to have no open beam paths or to be operated in radiation enclosures. In both cases, interlocks are included which automatically shut off the x-ray tube if the interlock switch is activated, i.e., the enclosure is opened. Interlocks can be defeated or fail, however, so that the experimenter always needs to be cautious. If an experimenter needs to work with an open beam, say during the alignment of the apparatus, the safest procedure for the experimenter to follow is: first, to check the level of the scattered radiation when the shutter of the x-ray tube is open; second, to locate the *primary* beam from the tube with a small fluorescent screen fixed to the end of a rod and thereafter avoid it; and second, to make sure that he or she is well shielded by lead or lead-glass screens from the radiation *scattered* by the camera or other apparatus which may be in the path of the primary beam. Strict and constant attention to these precautions will go a long way toward insuring safety.

PROBLEMS

***1** What is the frequency (per second) and energy per quantum (in joules) of x-ray beams of wavelength 0.71 Å (Mo $K\alpha$) and 1.54 Å (Cu $K\alpha$)?

2 Calculate the velocity and kinetic energy with which the electrons strike the target of an x-ray tube operated at 50,000 volts. What is the short-wavelength limit of the continuous spectrum emitted and the maximum energy per quantum of radiation?

---

* Answers to starred problems are given at the end of the chapter.

3 Show that the velocity with which electrons strike the target of an x-ray tube depends only on the voltage between anode (target) and cathode and not on the distance between them. [The force on a charge e (coulombs) by a field E (volts/m) is eE newtons.]

4 Graphically verify Moseley's law for the $K\beta_1$ lines of Cu, Mo, and W.

5 Plot the ratio of transmitted to incident intensity vs. thickness of lead sheet for Mo $K\alpha$ radiation and a thickness range of 0.00 and 0.02 mm.

***6** Graphically verify Eq. (13) for a lead absorber and Mo $K\alpha$, Rh $K\alpha$, and Ag $K\alpha$ radiation. (The mass absorption coefficients of lead for these radiations are 122.8, 84.13, and 66.14 cm^2/g, respectively.) From the curve, determine the mass absorption coefficient of lead for the shortest wavelength radiation from a tube operated at 30,000 volts.

7 Lead screens for the protection of personnel in x-ray diffraction laboratories are usually at least 1 mm thick. Calculate the "transmission factor" ($I_{\text{trans.}}/I_{\text{incident}}$) of such a screen for Cu $K\alpha$, Mo $K\alpha$, and the shortest wavelength radiation from a tube operated at 30,000 volts.

***8** (a) Calculate the mass and linear absorption coefficients of air for Cr $K\alpha$ radiation. Assume that air contains 80 percent nitrogen and 20 percent oxygen by weight and has a density of 1.29×10^{-3} g/cm^3. (b) Plot the transmission factor of air for Cr $K\alpha$ radiation and a path length of 0 to 20 cm.

***9** Calculate the K excitation voltage of copper.

***10** Calculate the wavelength of the L_{111} absorption edge of molybdenum.

***11** Calculate the wavelength of the Cu $K\alpha_1$ line.

***12** Plot the curve shown in Fig. 12 and save it for future reference.

***13** What voltage must be applied to a molybdenum-target tube in order that the emitted x-rays excite K fluorescent radiation from a piece of copper placed in the x-ray beam? What is the wavelength of the fluorescent radiation?

In Problems 14 and 15 take the intensity ratios of $K\alpha$ to $K\beta$ in unfiltered radiation from Table 1.

14 Suppose that a nickel filter is required to produce an intensity ratio of Cu $K\alpha$ to Cu $K\beta$ of 100/1 in the filtered beam. Calculate the thickness of the filter and the transmission factor for the Cu $K\alpha$ line.

***15** Filters for Co K radiation are usually made of iron oxide (Fe_2O_3) powder rather than iron foil. If a filter contains 5 mg Fe_2O_3/cm^2, what is the transmission factor for the Co $K\alpha$ line? What is the intensity ratio of Co $K\alpha$ to Co $K\beta$ in the filtered beam?

16 A copper-target x-ray tube is operated at 40,000 volts and 25 mA. The efficiency of an x-ray tube is so low that, for all practical purposes, one may assume that all the input energy goes into heating the target. If there were no dissipation of heat by water-cooling, conduction, radiation, etc., how long would it take a 100-g copper target to melt? (Melting point of copper = 1083°C, mean specific heat = 6.65 cal/mole/°C, latent heat of fusion = 3220 cal/mole.)

***17** Assume that the sensitivity of x-ray film is proportional to the mass absorption coefficient of the silver bromide in the emulsion for the particular wavelength involved. What, then, is the ratio of film sensitivities to Cu $K\alpha$ and Mo $K\alpha$ radiation?

REFERENCES

The following books are listed more or less in the order they are encountered in the text

G.1 *International Tables for Crystallography*, Ed. A.J.C Wilson, Vol. A-C (Dordrecht Kluwer Academic Pub. for International Union of Crystallography, 1995). The reference ''book'' for crystallography and diffraction.

G.2 L.S. Birks. *X-Ray Spectrochemical Analysis*, 2nd ed. (New York: Interscience, 1969). Clear, brief treatment of wavelength and energy dispersive methods, with emphasis on the problems of quantitative analysis. Includes electron-probe microanalysis.

ANSWERS TO SELECTED PROBLEMS

1. $4.23 \times 10^{18}\,\text{sec}^{-1}$, 2.80×10^{-15} J; $1.95 \times 10^{18}\,\text{sec}^{-1}$, 1.29×10^{-15} J

6. 33 cm^2/gm

8. a) 26.97 cm^2/gm, $3.48 \times 10^{-2}\,\text{cm}^{-1}$

b) $I_x/I_0 = 0.50$ for 20 cm of air

9. 8980 volts **11**. 1.541 Å

13. 8980 volts; mainly 1.54 Å (Cu $K\alpha$) and 1.39 Å (Cu $K\beta$)

15. 0.80, 26 to 1 **17**. 3.5 to 1

Geometry of Crystals

1 INTRODUCTION

Turning from the properties of x-rays, consider next the geometry and structure of crystals in order to discover what there is about crystals in general that enables them to diffract x-rays. Particular crystals of various kinds and how the very large number of crystals found in nature are classified into a relatively small number of groups must also be considered. The final sections of the chapter focus on the ways in which the orientation of lines and planes in crystals can be represented in terms of symbols or in graphical form.

Crystallography is a very broad subject and its origins precede the discovery of x-rays by many years. Only the more basic aspects are covered here: how atoms are arranged in some common crystals and how this arrangement determines the way in which a particular crystal diffracts x-rays. Readers who need a deeper knowledge of crystallography should consult such books as those by McKie and McKie [G.3], Borchardt-Ott [G.4], Sands [G.5] or Hammond [G.6].

2 LATTICES

A crystal may be defined as *a solid composed of atoms, ions or molecules arranged in a pattern periodic in three dimensions*. As such, crystals differ in a fundamental way from gases and liquids because the atomic, ionic or molecular arrangements in the latter do not posses the essential requirement of periodicity. Many solids are crystalline; if they are not single-crystals they consist of many contiguous crystals, i.e., they are polycrystalline. Not all solids are crystalline, however; some are *amorphous*, like glass, and do not have any regular interior arrangement of atoms, ions or molecules. There is, in fact, no essential difference between an amorphous solid and a liquid, and the former is often termed an "undercooled liquid." It is important to emphasize that not only are the atom, ion or molecule positions repetitious but also that there are certain symmetry relationships in their arrangement.

In thinking about crystals it is often convenient to ignore the actual atoms, ions, or molecules and to focus on the geometry of periodic arrays. The crystal is then represented as a *lattice*, that is, a three-dimensional array of points (*lattice points*),

From Chapter 2 of *Elements of X-Ray Diffraction*, Third Edition. B.D. Cullity, S.R. Stock.

each of which has identical surroundings. As mathematical constructs, lattices are infinite in extent whereas crystals are not. In practical terms, most crystals consist of enough atoms to render this distinction moot.

Consider first a one-dimensional lattice. The entire "space" is this line with zero thickness. The points of the lattice are separated by a lattice translation vector **a** whose length, the lattice parameter, is written as |a|, a or a_0 (Fig. 1a)[1]. Translation of n**a** from a lattice point, where n is an integer, brings one to another lattice point. Planar or two-dimensional lattices consist of two non-collinear lattice vectors **a** and **b**. These vectors have length a and b and are separated by an angle γ (Fig. 1b). Any translation n**a** + p**b**, where p as well as n are integers, returns one to an equivalent position within the lattice or planar mesh. If a third translation vector **c**, non-coplanar with **a** and **b**, operates on the mesh of Fig. 1b, a three-dimensional or space lattice results (Fig. 1c). Thus, the points of this lattice can be generated solely by applying (repeatedly) the three translation vectors.

Normally **a, b** and **c** are defined in a right-handed sense (if the index finger of the right hand points along **a** and the middle finger is bent to point along **b**, the thumb will point along **c**) The vectors **a, b** and **c** define a unit cell, that is a prism or parallelopiped volume. Stacking the unit cells face-to-face is, in fact, another way of generating a lattice and sometimes offers greater clarity than considering only the translation vectors. Unit cells can also be defined using the six scalar lattice parameters (the lengths of the three lattice translation vectors a_0, b_0 and c_0 and the three inter-axial angles α, between **b** and **c**, β, between **c** and **a**, and γ). Figure 2a shows the relationship between axes and angles which is easy to commit to memory using Table 1. It is important to emphasize that the unit cell (its faces and interior) completely defines the lattice. Adjacent unit cells touch, and eight unit cells share each vertex, four each edge and two each face. Thus, even though there are eight lattice points in the unit cell shown in Fig. 1c, each is shared by eight other unit cells, only one-eighth of each may be attributed to the particular unit cell pictured. Therefore, there is only one lattice point per unit cell, and this and other unit cells, chosen such that they contain only one lattice point, are termed *primitive*.

Translation of the boundaries of the unit cell shown in Fig. 1c by a vector of the type $\pm\mathbf{a}/2 \pm \mathbf{b}/2 \pm \mathbf{c}/2$ centers the unit cell on one of the lattice points (indicated by an open instead of solid sphere) and illustrates that the particular unit cell origin or shape one chooses depends on what is most convenient. In Fig. 2b the arrows show the shift of the unit cell corners from the setting in Fig. 1c, and two of the unit cell body diagonals indicate the relationship between the lattice point and the corners of the unit cells. The gray areas represent projections, along a lattice vector, of a unit cell face onto a plane parallel to that face and containing a plane of lattice points. As a further aid to the eye, the separations of nearest neighbor lattice points from the unit cell faces are indicated with heavy lines. Non-primitive unit cells of some lattices, for example, are employed to illustrate important aspects of perio-

---

[1] Vectors are here represented by boldface symbols. The same symbol in italics stands for the magnitude of the vector.

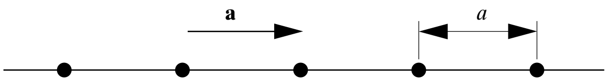

Figure 1 (a) One-dimensional lattice with parameter *a*.

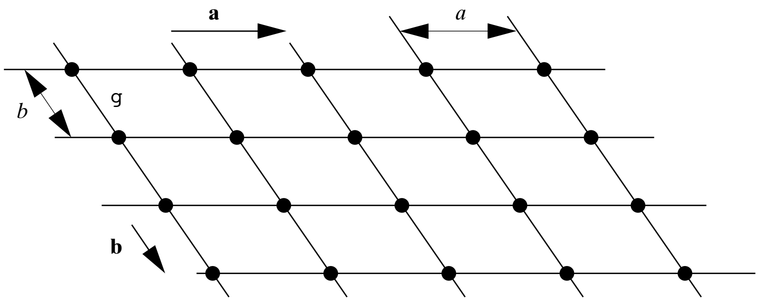

Figure 1 (b) Two-dimensional lattice with lattice translation vectors **a** and **b** and interaxial angle γ.

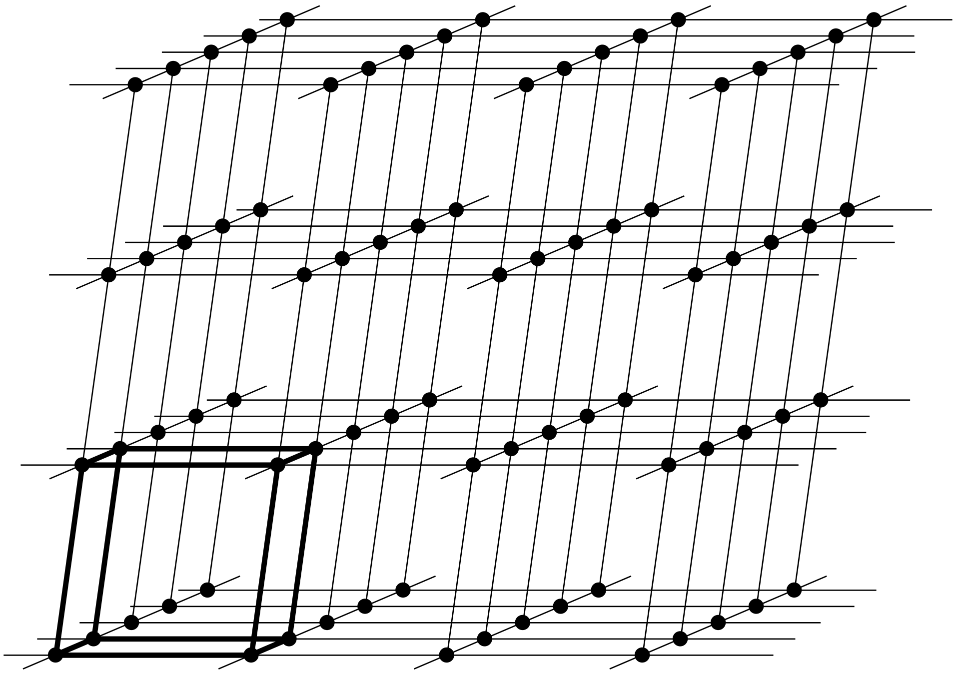

Figure 1 (c) Three-dimensional lattice with a primitive unit cell highlighted in bold. Lattice points are represented by the solid circles/spheres.

dicity or symmetry. Once a particular unit cell or unit cell origin is defined, it must be consistently applied throughout the lattice.

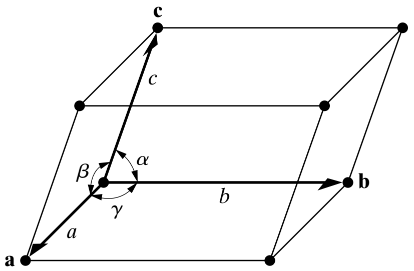

Figure 2 (a) Illustration of lattice vector and interaxial angle designations.

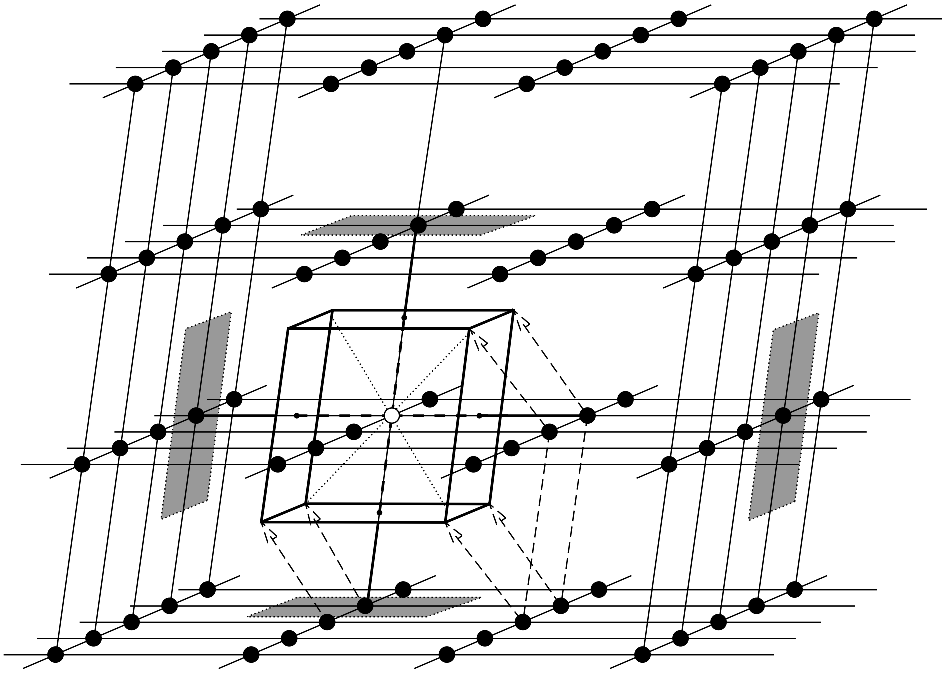

Figure 2 (b) Unit cells with the lattice points located at the cell corners and an alternative unit cell centered on one lattice point.

TABLE 1 DETERMINING WHICH INTER-AXIAL ANGLE IS BETWEEN WHICH PAIR OF AXES. THE ANGLE BETWEEN ANY TWO TRANSLATION VECTORS IS GIVEN BETWEEN THOSE VECTORS ON THE LINE BELOW.

Axis	**a**		**b**		**c**		**a**
Inter-axial Angle		γ		α		β	

A different notation for the lattice vectors uses $\mathbf{a}_1$, $\mathbf{a}_2$ and $\mathbf{a}_3$ in place of **a**, **b** and **c**, respectively. While use of $\mathbf{a}_1$ may seem somewhat more abstract than necessary, this notation can be much more convenient (see Section 4). One or the other of these notations will be used in this book, and what aspects of periodicity are being emphasized will determine which will be used.

3 DESIGNATION OF POINTS, LINES, AND PLANES

Every point within the lattice is uniquely defined with respect to the origin of the lattice by position vector $\mathbf{r} = u'\mathbf{a} + v'\mathbf{b} + w'\mathbf{c}$. If the origin of the lattice lies on a lattice point and if u', v' and w' are integers, the point located by $\mathbf{r}$ must be a lattice point and its coordinates are written simply as an ordered triplet $u'v'w'$. Points in space which are not lattice points have non-integer values of u', v' or w', and it is possible to write $\mathbf{r}$ as the sum of integer multiples n, p and q of the lattice vectors plus fractions u,v and w of the translation vectors:

$$\mathbf{r} = (n + u)\,\mathbf{a} + (p + v)\,\mathbf{b} + (q + w)\,\mathbf{c}. \tag{1}$$

Rearranging terms yields

$$\mathbf{r} = (n\mathbf{a} + p\mathbf{b} + q\mathbf{c}) + (u\mathbf{a} + v\mathbf{b} + w\mathbf{c}), \tag{2}$$

i.e., a vector between lattice points or between corners of equivalent unit cells plus a vector from the corner of a unit cell to a point within the unit cell at position uvw relative to the corner of that unit cell.

The direction of any line in a lattice may be described by first drawing a line through the origin parallel to the given line and then giving the coordinates of any point on the line through the origin. Let the line pass through the origin of the unit cell and any point having coordinates $u'\ v'\ w'$, where these numbers are not necessarily integral. (This line will also pass through the points $2u'\ 2v'\ 2w'$, $3u'\ 3v'\ 3w'$, etc.) Then $[uvw]$, written in square brackets, are the *indices* of the direction of the line. They are also the indices of any line parallel to the given line, since the lattice is infinite and the origin may be taken at any point. Whatever the values of u', v', w', they are always converted to a set of smallest integers by multiplication or division throughout: thus, $[\frac{1}{2}\,\frac{1}{2}\,1]$, [112], and [224] all represent the same direction, but [112] is the preferred form. Negative indices are written with a bar over the number, e.g., $[\bar{u}vw]$. Direction indices are illustrated in Fig. 3. Note how one can mentally shift the origin, to avoid using the adjacent unit cell, in finding a direction like $[120]$.

Directions related by symmetry are called *directions of a form*, and a set of these are represented by the indices of one of them enclosed in angular brackets: for example, the four body diagonals of a cube, [111], $[1\,\bar{1}\,1]$, $[\bar{1}\,\bar{1}\,1]$, and $[\bar{1}\,1\,1]$, may all be represented by the symbol <111>.

The orientation of planes in a lattice may also be represented symbolically, according to a system popularized by the English crystallographer Miller [1]. In the general case, the given plane will be tilted with respect to the crystallographic axes, and, since these axes form a convenient frame of reference, the orientation of the plane might be described by giving the actual distances, measured from the ori-

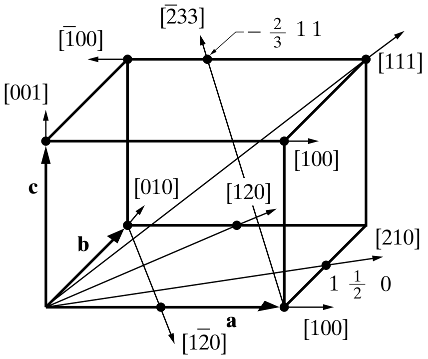

Figure 3 Indices of directions.

gin, at which it intercepts the three axes. Better still, by expressing these distances as fractions of the axial lengths, the numbers become are independent of the particular axial lengths involved in the given lattice. But a difficulty then arises when the given plane is parallel to a certain crystallographic axis, because such a plane does not intercept that axis, i.e., its "intercept" can only be described as "infinity." To avoid the introduction of infinity into the description of plane orientation, the reciprocal of the fractional intercept is used, this reciprocal being zero when the plane and axis are parallel. A workable symbolism results for the orientation of a plane in a lattice, the *Miller indices*, which are defined as *the reciprocals of the fractional intercepts which the plane makes with the crystallographic axes*. For example, if the Miller indices of a plane are (*hkl*), written in parentheses, then the plane makes fractional intercepts of $1/h$, $1/k$, $1/l$ with the axes, and, if the axial lengths are a, b, c, the plane makes actual intercepts of a/h, b/k, c/l, as shown in Fig. 4(a). Parallel to any plane in any lattice, there is a whole set of parallel equidistant planes, one of which passes through the origin; the Miller indices (*hkl*) usually refer to that plane in the set which is nearest the origin, although they may be taken as referring to any other plane in the set or to the whole set taken together.

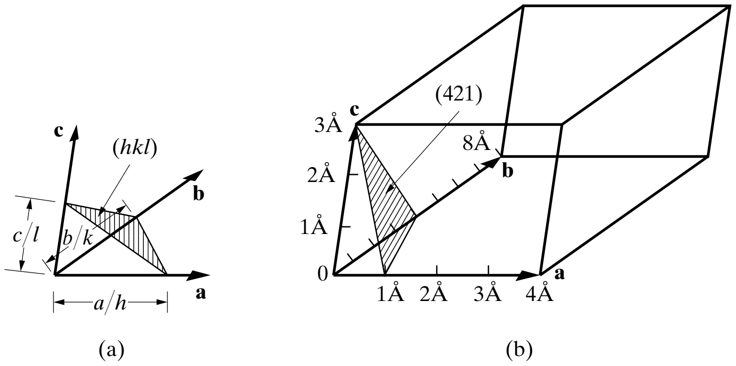

Figure 4 Plane designation by Miller indices.

Determining the Miller indices of the plane shown in Fig. 4(b) requires the following steps.

Axial lengths	4Å	8Å	3Å
Intercept lengths	1Å	4Å	3Å
Fractional intercepts	1/4	1/2	1
Miller indices	4	2	1

As stated earlier, if a plane is parallel to a given axis, its fractional intercept on that axis is taken as infinity and the corresponding Miller index is zero. If a plane cuts a negative axis, the corresponding index is negative and is written with a bar over it. Planes whose indices are the negatives of one another are parallel and lie on opposite sides of the origin, e.g., $(\bar{2}10)$ and $(2\bar{1}0)$. The planes ($nh\ nk\ nl$) are parallel to the planes (hkl) and have l/nth the spacing. The same plane may belong to two different sets, the Miller indices of one set being multiples of those of the other; thus the same plane belongs to the (210) set and the (420) set, and, in fact, the planes of the (210) set form every second plane in the (420) set. In the cubic crystal system it is convenient to remember that a direction [hkl] is always perpendicular to a plane (hkl) of the same indices, but this is not generally true in other crystal systems. Further familiarity with Miller indices can be gained from a study of Fig. 5.

The various sets of planes in a lattice have various values of interplanar spacing. The planes of large spacing have low indices and pass through a high density of lat-

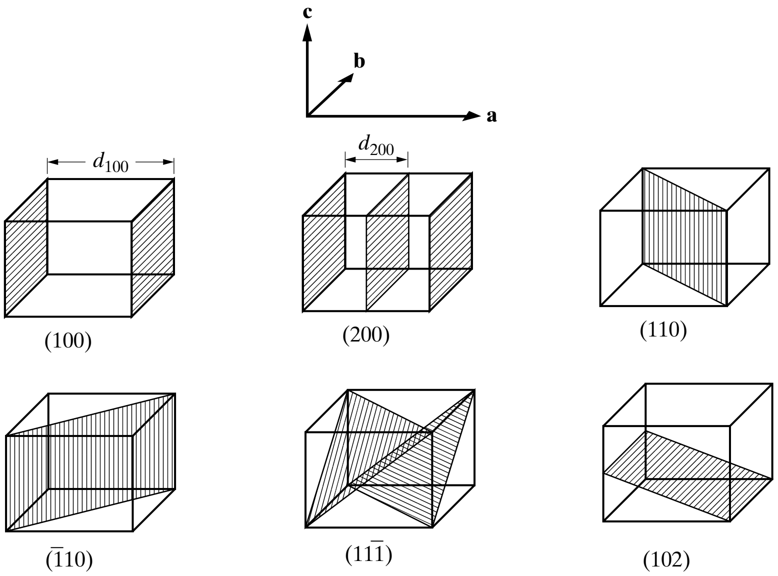

Figure 5 Miller indices of lattice planes. The distance d is the plane spacing.

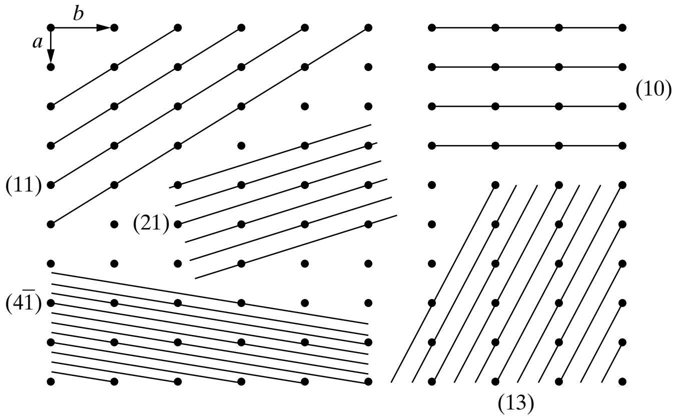

Figure 6 Two-dimensional lattice, showing that lines of lowest indices have the greatest spacing and the greatest density of lattice points.

tice points, whereas the reverse is true of planes of small spacing. Figure 6 illustrates this for a two-dimensional lattice, and it is equally true in three dimensions. The interplanar spacing d_{hkl}, measured at right angles to the planes, is a function both of the plane indices (hkl) and the lattice constants ($a, b, c, \alpha, \beta, \gamma$).

4 RECIPROCAL LATTICE

Vectors $\mathbf{a}_{\mathrm{i}}$ (i.e., **a, b,** and **c**) define the basis vectors of a three-dimensional lattice. This *direct space* lattice, however, is not the only way that the periodicity and symmetry of a given arrangement of lattice points can be represented. As introduced by J. Willard Gibbs [2], a reciprocal lattice $\mathbf{b}_{\mathrm{i}}$ (i.e., a lattice in *reciprocal space*) can be defined for every direct space lattice $\mathbf{a}_{\mathrm{i}}$ by

$$\mathbf{b}_1 = \frac{\mathbf{a}_2 \times \mathbf{a}_3}{\mathbf{a}_1 \cdot \mathbf{a}_2 \times \mathbf{a}_3},$$

$$\mathbf{b}_2 = \frac{\mathbf{a}_3 \times \mathbf{a}_1}{\mathbf{a}_1 \cdot \mathbf{a}_2 \times \mathbf{a}_3} \qquad \text{and}$$

$$\mathbf{b}_3 = \frac{\mathbf{a}_1 \times \mathbf{a}_2}{\mathbf{a}_1 \cdot \mathbf{a}_2 \times \mathbf{a}_3}. \tag{3}$$

The cyclic permutation of the indices in the numerator insures that a right-handed reciprocal lattice is obtained. Strictly speaking, the denominator should be written using the same permutation of indices as the numerator, but this vector product is the volume of the unit cell of the direct space lattice and this volume is the same regardless of the order in which the $\mathbf{a}_i$ are multiplied.[2] One should note that the units of the reciprocal lattice are Å^{-1} and not Å.

The physical significance of the reciprocal lattice in diffraction is due to Ewald [3] and not to Gibbs. The reciprocal lattice has several important properties. First, the cross-product in the numerator means that $\mathbf{b}_1$ is perpendicular to $\mathbf{a}_2$ and $\mathbf{a}_3$, that $\mathbf{b}_2$ is perpendicular to $\mathbf{a}_3$ and $\mathbf{a}_1$ and that $\mathbf{b}_3$ is perpendicular to $\mathbf{a}_1$ and $\mathbf{a}_2$. This relationship means that the reciprocal lattice has the property of orthonormality, i.e.,

$$\mathbf{a}_i \cdot \mathbf{b}_j = \delta_{ij}, \tag{4}$$

where δ_{ij} is the Kroenecker delta and equals 0 if $i \neq j$ and 1 if $i = j$. It can be shown that the volume of the reciprocal lattice unit cell is the reciprocal of the volume of the direct space unit cell. Second, a vector $\mathbf{H}_{hkl}$ drawn from the origin of reciprocal space to any point in reciprocal space having coordinates h,k,l is perpendicular to the plane in direct space whose Miller indices are *hkl*. The length H_{hkl} of the reciprocal lattice vector $\mathbf{H}_{hkl} = h\mathbf{b}_1 + k\mathbf{b}_2 + l\mathbf{b}_3$ equals the reciprocal of the periodicity of (hkl), i.e., $H_{hkl} = 1/d_{hkl}$.

Two examples of direct space lattices and the corresponding reciprocal space lattices appear in Figure 7. Sometimes drawings of the lattices are shown superimposed, but it is best to place the direct space and reciprocal space lattices side-by-side in order to avoid confusion in terms of units, etc. Note that the axes of each pair of lattices are shown in the correct alignment: $\mathbf{b}_2$ is perpendicular to both $\mathbf{a}_3$ and $\mathbf{a}_1$, etc. Also, in both cases, axes $\mathbf{a}_3$ are perpendicular to $\mathbf{a}_1$ and $\mathbf{a}_2$ and to the plane of the paper. The corresponding reciprocal lattices also have $\mathbf{b}_3$ perpendicular to the sheet of paper, and the *hk*0 plane of the reciprocal lattice is shown. In the case of the cubic lattice, $\mathbf{b}_1$ is parallel to $\mathbf{a}_1$ but for the hexagonal lattice $\mathbf{b}_1$ is not parallel to $\mathbf{a}_1$. Several planes in the direct space lattices are indicated along with their Miller indices. In the cubic lattice (110) and (210) are shown, and one can see that the reciprocal lattice vectors $\mathbf{H}_{110}$ and $\mathbf{H}_{210}$ are perpendicular to the corresponding planes. Similarly, in the hexagonal lattice, one can see that $\mathbf{H}_{120}$ is perpendicular to (120) and $\mathbf{H}_{110}$ is perpendicular to (110). Comparing the direct space vector [120] with the orientation of (120) in the drawing of hexagonal lattice demonstrates what should always be remembered: the direct space vector [*hkl*] in non-cubic systems will not necessarily be perpendicular to (*hkl*). One can also demonstrate by direct measurement that the lengths of the reciprocal lattice vectors are equal to the inverse of the spacing between corresponding planes.

In crystallographic terms, all that is needed to uniquely identify a set of parallel lattice planes (*hkl*) is their orientation and their periodicity. These are given by the normal to the planes (a single direction) and the spacing between the planes (d_{hkl}). A single lattice point in reciprocal space, defined by vector $\mathbf{H}_{hkl}$, is sufficient, therefore, to represent the infinite series of physical direct space planes. In other words,

---

[2] If the notation **a**, **b** and **c** is used for the direct space vectors, then $\mathbf{a}^*$, $\mathbf{b}^*$ and $\mathbf{c}^*$ are used for the corresponding reciprocal space vectors.

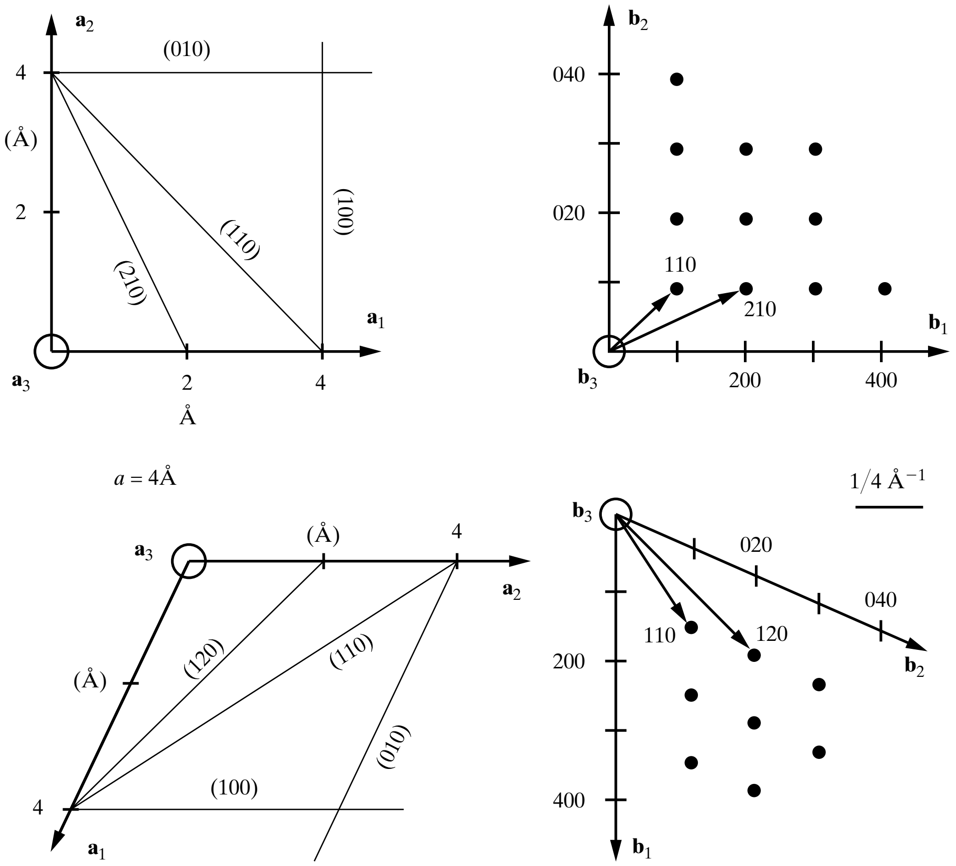

Figure 7 Illustration of crystal lattices (left side) and corresponding reciprocal lattices (right side) for a cubic system (top) and an hexagonal system (bottom).

the transformation from direct space to reciprocal space maps all direct space planes (*hkl*) onto a single point (i.e., the reciprocal lattice point with coordinates *h,k,l*). Note that the symmetry which is present in direct space appears in reciprocal space. The reciprocal lattice representation of a crystal is a powerful tool for understanding diffraction.

5 SYMMETRY

One type of repetition, lattice translation, underlies the periodicity of one-, two- and three- dimensional nets. As mentioned in Sec. 2, the surroundings of each lattice point are identical, not only in kind but also in orientation. Symmetry is the second type of repetition required to define the periodicity of two-dimensional patterns seen in wallpaper or of three-dimensional assemblies of atoms, ions or molecules comprising crystals. The various symmetry operators act to change the orientation of the repeated features or *motifs* which populate a lattice. These operators are required to describe repeating patterns which are more complex than those generated through the simple repetition of lattice translations. For simplicity, the symmetry elements used in crystallography will be introduced distinct from lattices and only later will be incorporated into lattices to produce crystal structures.

Before considering how symmetry is incorporated in lattices, it is necessary to investigate how the symmetry elements operate on their surroundings. If a certain object is at a certain position relative to the symmetry element, the type of symmetry element dictates where to look to find an object identical, except for orientation, to the first. Alternatively, a body or structure is said to be symmetrical when its component parts are arranged in such balance, so to speak, that certain operations can be performed on the body which will bring it into coincidence with itself. For example, if a body is symmetrical with respect to a plane passing through it, then reflection of either half of the body across the *mirror plane* will produce a body coinciding with the other half. Thus a cube has several planes of symmetry, one of which is shown in Fig. 8(a). Points A_1 and A_2 in Fig. 8(a) must be identical because of the mirror plane through the center of the cube; they are related by reflection.

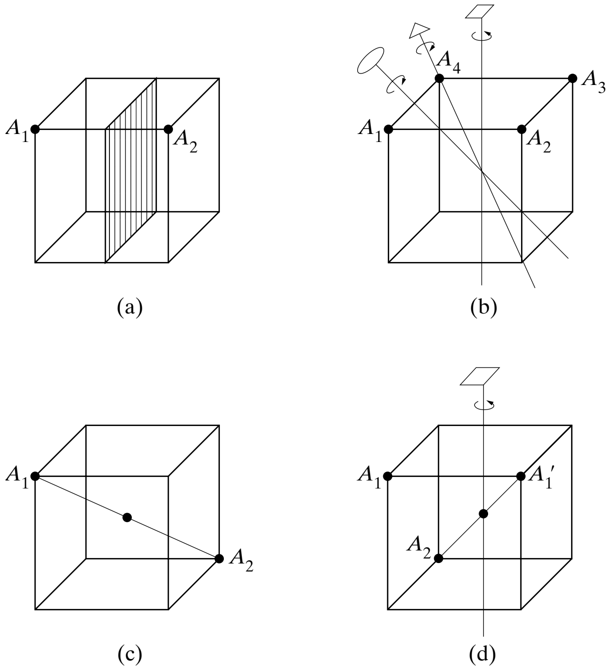

Figure 8 Some symmetry elements of a cube. (a) Reflection plane. A_1 becomes $A_{2.}$ (b) Rotation axes. 4-fold axis: A_1 becomes A_2; 3-fold axis: A_1 becomes A_2; 2-fold axis: A_1 becomes $A_{4.}$ (c) inversion center. A_1 becomes A_2. (d) Rotation-inversion axis, 4-fold axis: A_1 becomes A'_2; inversion center: A'_1 becomes $A2$.

There are in all four macroscopic[3] symmetry operations or elements: *reflection, rotation, inversion* and *roto-inversion*. A body has n-fold rotational symmetry about an axis if a rotation of 360°/n brings it into self-coincidence. Thus a cube has a 4-fold axis normal to each face, a 3-fold axis along each body diagonal, and 2-fold axes joining the center of opposite edges. Some of these are shown in Fig. 8 where the small plane figures (square, triangle, and ellipse) designate the various axes. In Fig. 8(b), points A_1, A_2, A_3, and A_4 are related by the four-fold rotation axis (Fig. 8(b)) while points A_1 and A_4 are also related by the two-fold axis inclined with respect to the four-fold axis. In general, rotation axes may be 1-, 2-, 3-, 4- or 6-fold. Multiple 1-fold axes are present in all objects, and these are normally not shown while a 5-fold axis or one of higher degree than 6 are impossible, in the sense that unit cells having such symmetry cannot be made to fill space without leaving gaps.

A body has an inversion center if corresponding points of the body are located at equal distances from the center on a line drawn through the center. A body having an inversion center will come into coincidence with itself if every point in the body is inverted, or "reflected," in the inversion center. A cube has such a center at the intersection of body diagonals [Fig. 8(c)]. Finally, a body may have a rotation-inversion axis, either 1-, 2-, 3-, 4- or 6-fold. If it has an n-fold rotation-inversion axis, it can be brought into coincidence with itself by a rotation of 360°/n about the axis followed by an inversion in a center lying on the axis. Figure 8(d) illustrates the operation of a 4-fold rotation-inversion axis on a cube.

Consider next all of the positions and orientations an object or motif must take due to the operation of various symmetry elements (Fig. 9). The motif must appear even more frequently if, for example as in Fig. 9(g) and (h), two symmetry operators operate through the same point. The combined operation of a two-fold axis lying within a mirror plane "produces" a second mirror plane, perpendicular to the first mirror and also containing the two-fold axis (i.e., horizontal in Fig. 9(g)). When a four-fold axis lies within a single mirror plane as shown in Fig. 9(h) symmetry requires a total of eight identical motifs (in various orientations) and four mirror planes to be present.

The different symmetry operations acting through a point are termed *point groups*. In two-dimensions there are ten point groups which can be included in lattices. In three-dimensions, the number of point groups increases to thirty-two: unlike in two-dimensions, inversion centers are no longer equivalent to two-fold axes, and combinations such as mirrors perpendicular to rotation axes are possible.[4]

---

[3] So called to distinguish them from certain microscopic symmetry operations which are not of concern here. The macroscopic elements can be deduced from the angles between faces of a well-developed crystal, without any knowledge of the atomic arrangement inside the crystal. The microscopic symmetry elements, on the other hand, depend entirely on atom arrangement, and their presence cannot be inferred from the external development of the crystal.

[4] Texts such as that of Schwartz and Cohen [G.7] and those on crystallography [G.3-G.6] illustrate this topic in considerably greater detail.

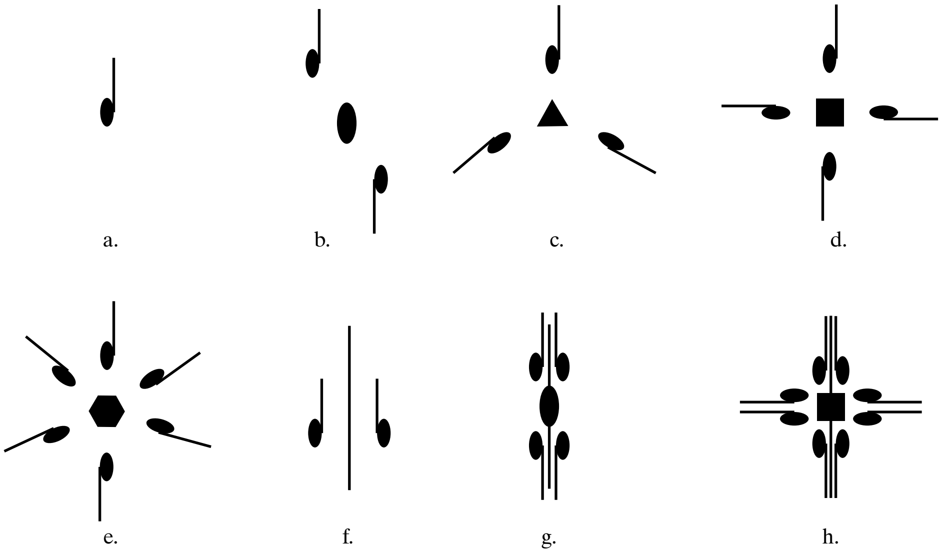

Figure 9 Symmetry operators for crystallography; the point group designations are in quotations. (a)-(h) are 1-fold axis "1", two-fold axis "2", three-fold axis "3", four-fold axis "4", six-fold axis "6", mirror plane "m", mirror plus two-fold axis "2m", mirror plus four-fold axis "4m", respectively.

It is important to emphasize that symmetry elements operate throughout space. The discussion thus far has concentrated on direct space, but all the principles described also apply in reciprocal space.

6 CRYSTAL SYSTEMS

In defining a lattice with three non-coplanar lattice vectors, units cells of various shapes can result, depending on the length and orientation of the vectors. For example, if the vectors **a**, **b**, **c** are of equal length and at right angles to one another, or $\mathbf{a} = \mathbf{b} = \mathbf{c}$ and $\alpha = \beta = \gamma = 90^o$, the unit cell is cubic. Giving special values to the axial lengths and angles, produces unit cells of various shapes and therefore various kinds of point lattices, since the points of the lattice are located at the primitive unit cell corners. It turns out that only seven different kinds of cells are necessary to include all the possible point lattices. These correspond to the seven *crystal systems* into which all crystals can be classified. These systems are listed in Table 2. (Some writers consider the rhombohedral system as a subdivision of the hexagonal, thus reducing the number of crystal systems to six.)

Seven different point lattices can be obtained simply by putting points at the corners of the unit cells of the seven crystal systems. However, there are other arrangements of points which fulfill the requirements of a point lattice, namely, that each lattice point have identical surroundings. The French crystallographer Bravais worked on this problem and in 1848 demonstrated that there are fourteen possible

TABLE 2 CRYSTAL SYSTEMS AND BRAVAIS LATTICES

(The symbol ≠ means that equity is not required by symmetry. Accidental equality may occur, as shown by an example in Sec. 4.)

System	Axial lengths and angles	Bravais lattice	Lattice symbol
Cubic	Three equal axes at right angles $a = b = c, \quad \alpha = \beta = \gamma = 90°$	Simple Body-centered Face-centered	P I F
Tetragonal	Three axes at right angles, two equal $a = b \neq c, \quad \alpha = \beta = \gamma = 90°$	Simple Body-centered	P I
Orthorhombic	Three unequal axes at right angles $a \neq b \neq c, \quad \alpha = \beta = \gamma = 90°$	Simple Body-centered Base-centered Face-centered	P I C F
Rhombohedral*	Three equal axes, equally inclined $a = b = c, \quad \alpha = \beta = \gamma \neq 90°$	Simple	R
Hexagonal	Two equal coplanar axes at 120º, third axis at right angles $a = b \neq c, \quad \alpha = \beta = 90° \quad (\gamma = 120°)$	Simple	P
Monoclinic	Three unequal axes, one pair not at right angles $a \neq b \neq c, \quad \alpha = \gamma = 90° \neq \beta$	Simple Base-centered	P C
Triclinic	Three unequal axes, unequally inclined and none at right angles $a \neq b \neq c, \quad (\alpha \neq \beta \neq \gamma \neq 90°)$	Simple	P

* Also called trigonal.

point lattices and no more [4]; this important result is commemorated by the use of the terms *Bravais lattice* and *point lattice* as synonymous. For example, if a point is placed at the center of each cell of a cubic point lattice, the new array of points also forms a point lattice. Similarly, another point lattice can be based on a cubic unit cell having lattice points at each corner and in the center of each face.

The fourteen Bravais lattices are described in Table 2 and illustrated in Fig. 10. Some unit cells are *simple*, or *primitive*, cells (symbol *P* or *R*), and some are *nonprimitive* cells (any other symbol): primitive cells have only one lattice point per cell while nonprimitive have more than one. A lattice point in the interior of a cell "belongs" to that cell, while one in a cell face is shared by two cells and one at a corner is shared by eight. The number of lattice points per cell is therefore given by

$$N = N_i + \frac{N_f}{2} + \frac{N_c}{8}, \tag{5}$$

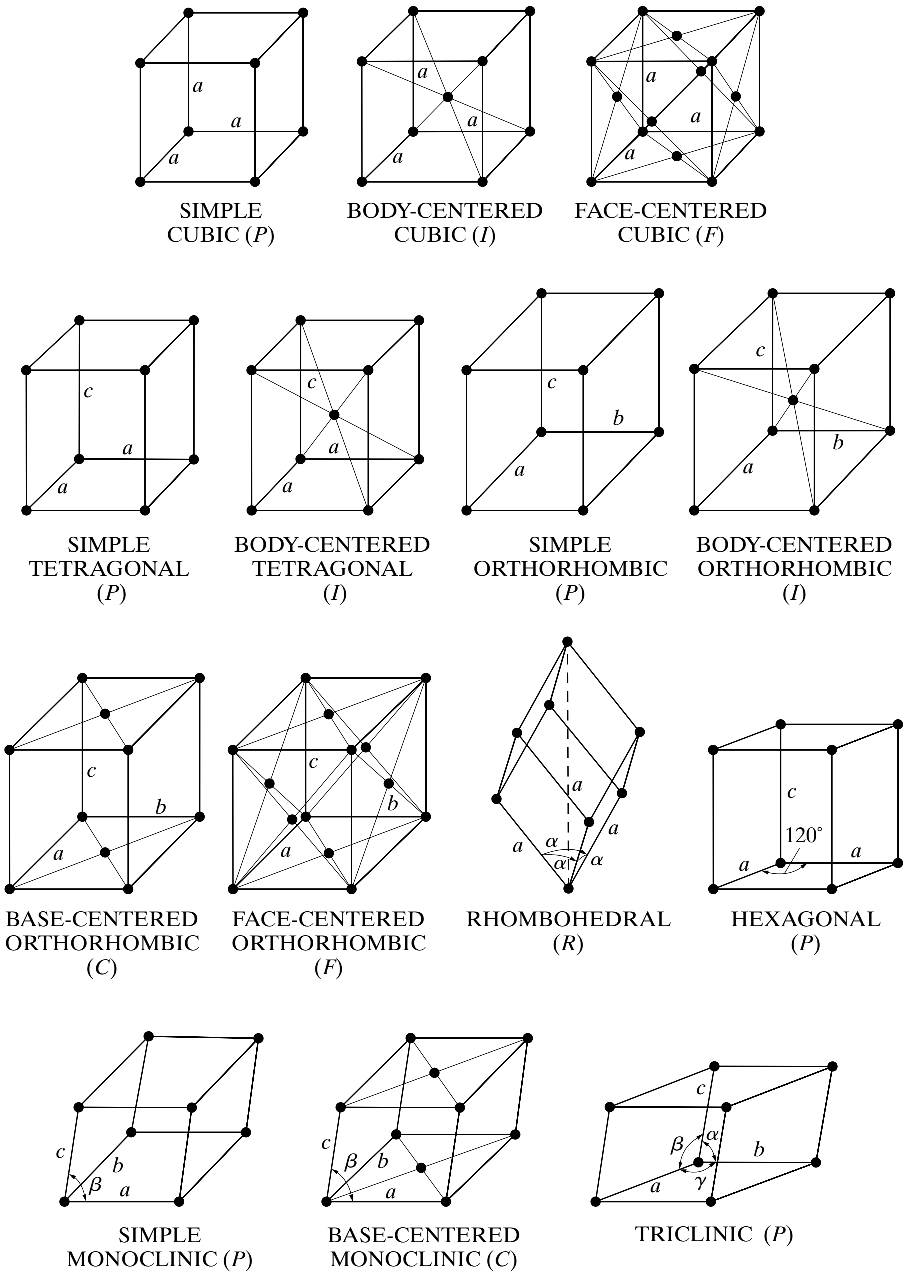

Figure 10 The fourteen Bravais lattices.

where N_i = number of interior points, N_f = number of points on faces, and N_C = number of points on corners. Any cell containing lattice points on the corners only is therefore primitive, while one containing additional points in the interior or on faces is nonprimitive. The symbols *F* and *I* refer to face-centered and body-centered cells, respectively, while *A, B*, and *C* refer to base-centered cells, centered on one pair of opposite faces *A, B*, or *C*. (The *A* face is the face defined by the *b* and *c* axes, etc.) The symbol *R* is used especially for the rhombohedral system. In Fig. 10, axes of equal length in a particular system are given the same symbol to indicate their equality, e.g., the cubic axes are all marked *a*, the two equal tetragonal axes are marked *a* and the third one *c*, etc.

At first glance, the list of Bravais lattices in Table 2 appears incomplete. Why not, for example, a base-centered tetragonal lattice? The full lines in Fig. 11 delineate such a cell, centered on the *C* face, but the same array of lattice points can be referred to the simple tetragonal cell shown by dashed lines, so that the base-centered arrangement of points is not a new lattice. However, the base-centered cell is a perfectly good unit cell and may be used rather than the simple cell. Choice of one or the other has certain consequences.

The lattice points in a nonprimitive unit cell can be extended through space by repeated applications of the unit-cell vectors a, b, c just like those of a primitive cell. The lattice points associated with a unit cell can be translated one by one or as a group. In either case, equivalent lattice points in adjacent unit cells are separated by one of the vectors **a**, **b**, **c**, wherever these points happen to be located in the cell (Fig. 12).

Now, the possession of a certain minimum set of symmetry elements is a fundamental property of each crystal system, and one system is distinguished from another just as much by its symmetry elements as by the values of its axial lengths

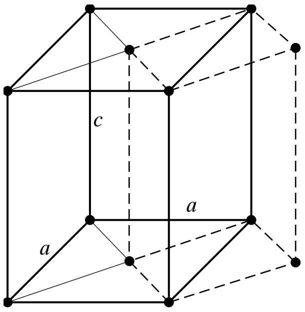

Figure 11 Relation of tetragonal *C* lattice (full lines) to tetragonal *P* lattice (dashed lines).

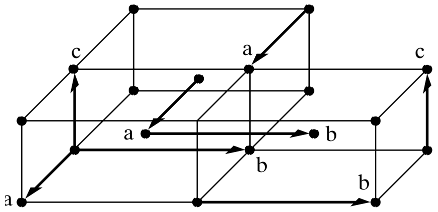

Figure 12 Extension of lattice points through space by the unit cell vectors **a**, **b**, **c**.

and angles. In fact, *these are interdependent*. For example, the existence of 4-fold rotation axes normal to the faces of a cubic cell *requires* that the cell edges be equal in length and at 90° to one another. On the other hand, a tetragonal cell has only one 4-fold axis, and this symmetry requires that only two cell edges be equal, namely, the two that are at right angles to the rotation axis.

The minimum number of symmetry elements possessed by each crystal system is listed in Table 3. Some crystals may possess more than the minimum symmetry elements required by the system to which they belong, but none may have less. The existence of certain symmetry elements often implies the existence of others. For example, a crystal with three 4-fold rotation axes necessarily has, in addition, four 3-fold axes and falls in the cubic system. The converse is not true; there are cubic lattices which do not have three four-fold axes (see the unit cell of AuBe shown in Fig. 23).

Symmetry operations apply not only to the unit cells shown in Fig. 10, considered merely as geometric shapes, but also to the point lattices associated with them. The latter condition rules out the possibility that the cubic system, for example, could include a base-centered point lattice, since such an array of points would not have the minimum set of symmetry elements required by the cubic system, namely four 3-fold rotation axes. Such a lattice would be classified in the tetragonal system, which has no 3-fold axes and in which accidental equality of the *a* and *c* axes is allowed.

Crystals in the rhombohedral (trigonal) system can be referred to either a rhombohedral or a hexagonal lattice. Appendix: The Rhombohedral-Hexagonal Transformation gives the relation between these two lattices and the transformation equations which allow the Miller indices of a plane (see Sec. 8) to be expressed in terms of either set of axes.

7 PRIMITIVE AND NONPRIMITIVE CELLS

In any point lattice a unit cell may be chosen in an infinite number of ways and may contain one or more lattice points per cell. It is important to note that unit cells do not "exist" as such in a lattice: they are a mental construct and can accordingly be chosen for utility. The conventional cells shown in Fig. 10 are convenient and conform to the symmetry elements of the lattice.

TABLE 3 SYMMETRY ELEMENTS

System	Minimum symmetry elements
Cubic	Four 3-fold rotation axes
Tetragonal	One 4-fold rotation (or rotation - inversion) axis
Orthorhombic	Three perpendicular 2-fold rotation (or rotation - inversion) axes
Rhombohedral	One 3-fold rotation (or rotation - inversion) axis
Hexagonal	One 6-fold rotation (or rotation - inversion) axis
Monoclinic	One 2-fold rotation (or rotation - inversion) axis
Triclinic	None

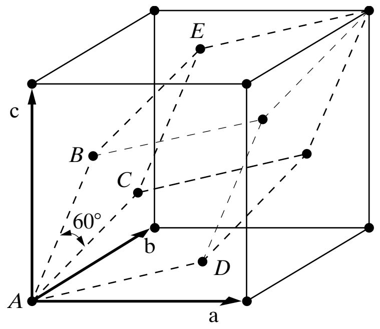

Figure 13 Face-centered cubic point lattice referred to cubic and rhombohedral cells.

Any of the fourteen Bravais lattices may be referred to a primitive unit cell. For example, the face-centered cubic lattice shown in Fig. 13 may be referred to the primitive cell indicated by dashed lines. The latter cell is rhombohedral, its axial angle α is 60°, and each of its axes is $1/\sqrt{2}$ times the length of the axes of the cubic cell. Each cubic cell has four lattice points associated with it, each rhombohedral cell has one, and the former has, correspondingly, four times the volume of the latter. Nevertheless, it is usually more convenient to use the cubic cell rather than the rhombohedral one because the former immediately suggests the cubic symmetry which the lattice actually possesses. Similarly, the other centered non-primitive cells listed in Table 2 are preferred to the primitive cells possible in their respective lattices.

Why then do the centered lattices appear in the list of the fourteen Bravais lattices? If the two cells in Fig. 13 describe the same set of lattice points, as they do, why not eliminate the cubic cell and let the rhombohedral cell serve instead? The answer is that this cell is a *particular* rhombohedral cell with an axial angle α of 60°. In the general rhombohedral lattice no restriction is placed on the angle α; the result is a lattice of points with a single 3-fold symmetry axis. When α becomes equal to 60°, the lattice has four 3-fold axes, and this symmetry places it in the cubic system. The general rhombohedral cell is still needed.

If nonprimitive lattice cells are used, the vector from the origin to any point in the lattice will now have components which are nonintegral multiples of the unit-cell vectors **a**, **b**, **c**. The position of any lattice point in a cell may be given in terms of its *coordinates*; if the vector from the origin of the unit cell to the given point has components $x\mathbf{a}$, $y\mathbf{b}$, $z\mathbf{c}$, where x, y, and z are fractions, then the coordinates of the point are $x\ y\ z$. Thus, point A in Fig. 13, taken as the origin, has coordinates 0 0 0 while points B, C, and D, when referred to cubic axes, have coordinates $0\,\frac{1}{2}\,\frac{1}{2}$, $\frac{1}{2}\,0\,\frac{1}{2}$, and $\frac{1}{2}\,\frac{1}{2}\,0$, respectively. Point E has coordinates $\frac{1}{2}\,\frac{1}{2}\,1$ and is equivalent to point D, being separated from it by the vector **c**. The coordinates of equivalent points in different unit cells can always be made identical by the addition or subtraction of a set of integral coordinates: in this case, subtraction of 0 0 1 from $\frac{1}{2}\,\frac{1}{2}\,1$ (the coordinates of E) gives $\frac{1}{2}\,\frac{1}{2}\,0$ (the coordinates of D).

Note that the coordinates of a body-centered point, for example, are always $\frac{1}{2}\frac{1}{2}\frac{1}{2}$ no matter whether the unit cell is cubic, tetragonal, or orthorhombic, and whatever its size. The coordinates of a point position, such as $\frac{1}{2}\frac{1}{2}\frac{1}{2}$, may also be regarded as an operator which, when "applied" to a point at the origin, will move or translate it to the position $\frac{1}{2}\frac{1}{2}\frac{1}{2}$, the final position being obtained by simple addition of the operator $\frac{1}{2}\frac{1}{2}\frac{1}{2}$ and the original position 0 0 0. In this sense, the vectors between 000 and all body-centered positions in the eight adjacent unit cells, i.e., $\langle\frac{1}{2}\frac{1}{2}\frac{1}{2}\rangle$ are called the "body-centering translations," since they will produce the two point positions characteristic of a body-centered cell when applied to a point at the origin. Similarly, the four point positions characteristic of a face-centered cell, namely, 0 0 0, $0\,\frac{1}{2}\frac{1}{2}$, $\frac{1}{2}\,0\,\frac{1}{2}$ and $\frac{1}{2}\frac{1}{2}\,0$, are related by the face-centering translations $\langle\frac{1}{2}\frac{1}{2}\,0\rangle$. The base-centering translations depend on which pair of opposite faces are centered; if centered on the *C* face, for example, the equivalent positions are 0 0 0, $\frac{1}{2}\frac{1}{2}\,0$ and the C-face centering translations are $[\frac{1}{2}\frac{1}{2}\,0]$ not $[0\,\frac{1}{2}\frac{1}{2}]$ nor $[\frac{1}{2}\,0\,\frac{1}{2}]$. These centering translations, summarized below, should be memorized:

$$\text{body–centering} = \langle\tfrac{1}{2}\tfrac{1}{2}\tfrac{1}{2}\rangle$$

$$\text{face–centering} = \langle\tfrac{1}{2}\tfrac{1}{2}\,0\rangle$$

$$\text{base–centering} = [\tfrac{1}{2}\tfrac{1}{2}\,0] \text{ or } [\tfrac{1}{2}\,0\,\tfrac{1}{2}] \text{ or } [0\,\tfrac{1}{2}\tfrac{1}{2}]$$

Normally one writes "000 + body-centering translation", "000 + face-centering translation" or "000 + base-centering translation" when discussing unit cells with only one atom per lattice point (i.e., Nb, Ni, Cu). Other unit cells have more than one atom per unit lattice point. Silicon, for example, has a face-centered cubic Bravais lattice with atoms at 000 and $\frac{1}{4}\frac{1}{4}\frac{1}{4}$ plus face centering translations, for a total of four lattice points but eight atoms per unit cell. More complex molecular crystals, typical of substances found in biological systems, have large numbers of atoms of different types per lattice point.

Note that the indices of a plane or direction are meaningless unless the orientation of the unit-cell axes is given. This means that the indices of a particular lattice plane depend on the unit cell chosen. For example, consider the right-hand vertical plane of the cell shown by full lines in Fig. 11; the indices of this plane are of the form {100} for the base-centered cell and {110} for the simple cell.

In any crystal system there are sets of equivalent lattice planes related by symmetry. These are called *planes of a form* or a *family of planes,* and the indices of any one plane, enclosed in braces {*hkl*}, stand for the whole set. In general, planes of a form have the same spacing but different Miller indices. For example, the faces of a cube, (100), (010), ($\bar{1}$00), (0$\bar{1}$0), (001), and (00$\bar{1}$), are planes of the form {100}, since all of them may be generated from any one by operation of the 4-fold rotation axes perpendicular to the cube faces. In the tetragonal system, however, only the planes (100), (010), ($\bar{1}$00), and (0$\bar{1}$0) belong to the form {100}; the other two planes, (001) and $(00\bar{1})$, belong to the different form {001}; the first four planes mentioned are related by a 4-fold axis and the last two by a 2-fold axis.[5]

Planes of a zone are planes which are all parallel to one line, called the *zone axis*, and the zone, i.e., the set of planes, is specified by giving the indices of the zone axis. Such planes may have quite different indices and spacings, the only requirement being that they are parallel to a single line. Figure 14 shows some examples. If the axis of a zone has indices $[uvw]$, then any plane belongs to that zone whose indices (hkl) satisfy the relation

$$hu + kv + lw = 0. \tag{6}$$

Any two nonparallel planes are planes of a zone since they are both parallel to their line of intersection. If their indices are $(h_1k_1l_1)$ and $(h_2k_2l_2)$, then the indices of their zone axis $[uvw]$ are given by $[h_1k_1l_1] \times [h_2k_2l_2]$, that is,

$$\begin{aligned} u &= k_1l_2 - k_2l_1, \\ v &= l_1h_2 - l_2h_1, \\ w &= h_1k_2 - h_2k_1. \end{aligned} \tag{7}$$

Before turning to the special system of indexing for hexagonal crystal systems, it is important to revisit the topic of interplanar spacings d_{hkl} for $\{hkl\}$. The exact relation depends on the crystal system involved and for the cubic system takes on the relatively simple form

$$\text{(Cubic)} \qquad d_{hkl} = \frac{a}{\sqrt{h^2 + k^2 + l^2}}. \tag{8}$$

In the tetragonal system the spacing equation naturally involves both a and c since these are not generally equal:

$$\text{(Tetragonal)}\ d_{hkl} = \frac{a}{\sqrt{h^2 + k^2 + l^2(a^2/c^2)}}. \tag{9}$$

In the cubic system, it is important to remember that $[hkl]$ is perpendicular to (hkl). It is equally important never to forget that for all other crystal systems $[hkl]$ generally is not perpendicular to (hkl).

---

[5] Certain important crystal planes are often referred to by name without any mention of their Miller indices. Thus, planes of the form {111} in the cubic system are often called octahedral planes, since these are the bounding planes of an octahedron. In the hexagonal system, the (0001) plane is called the basal plane, planes of the form $\{10\bar{1}0\}$ are called prismatic planes, and planes of the form $\{10\bar{1}1\}$ are called pyramidal planes.

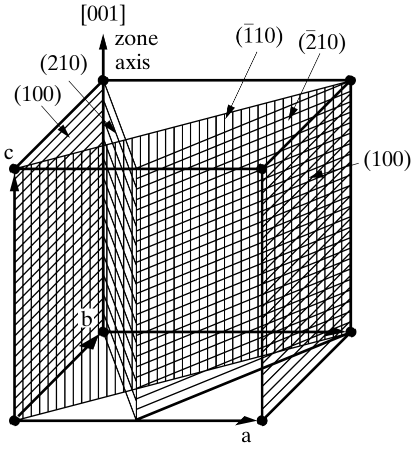

Figure 14 All shaded planes in the cubic lattice shown are planes of the zone {001}.

8 INDEXING IN THE HEXAGONAL SYSTEM

A slightly different system of plane indexing is used in the hexagonal system. The unit cell of a hexagonal lattice is defined by two equal and coplanar vectors $\mathbf{a}_1$ and $\mathbf{a}_2$, at 120° to one another, and a third axis **c** at right angles [Fig. 15(a)]. The complete lattice is constructed, as usual, by repeated translations of the points at the unit cell corners by the vectors $\mathbf{a}_1$, $\mathbf{a}_2$, **c**. Some of the points so generated are shown in the figure, at the ends of dashed lines, in order to exhibit the hexagonal symmetry of the lattice, which has a 6-fold rotation axis parallel to **c**. The third axis $\mathbf{a}_3$, lying in the basal plane of the hexagonal prism, is so symmetrically related to $\mathbf{a}_1$ and $\mathbf{a}_2$

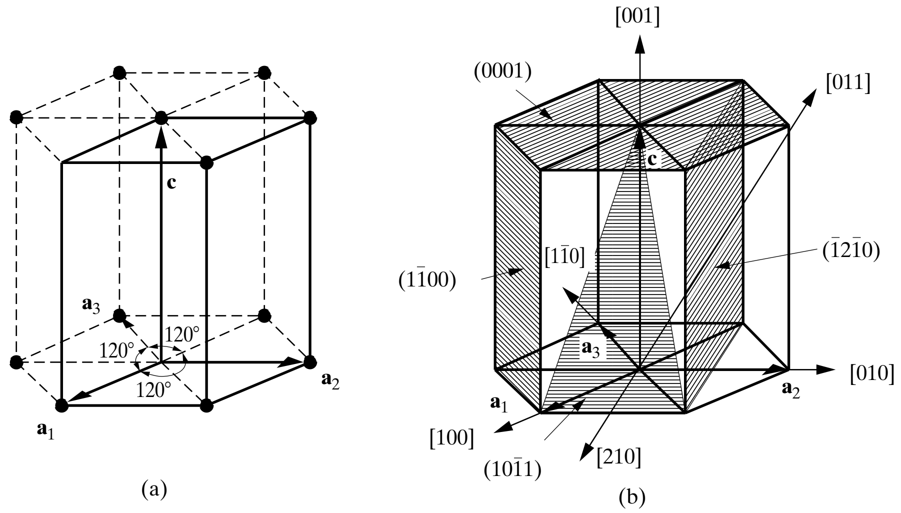

Figure 15 (a) The hexagonal unit cell (heavy lines) and (b) indices of planes and directions.

that it is often used in conjunction with the other two. Thus the indices of a plane in the hexagonal system, called Miller-Bravais indices, refer to *four* axes and are written $(hkil)$. The index i is the reciprocal of the fractional intercept on the $\mathbf{a}_3$ axis. Since the intercepts of a plane on $\mathbf{a}_1$ and $\mathbf{a}_2$ determine its intercept on $\mathbf{a}_3$, the value of i depends on the values of h and k. The relation is

$$h + k = -i. \tag{10}$$

Since i is determined by h and k, it is sometimes replaced by a dot and the plane symbol written $(hk \cdot l)$ Sometimes even the dot is omitted. However, this usage defeats the purpose for which Miller-Bravais indices were devised, namely, to give similar indices to similar planes. For example, the side planes of the hexagonal prism in Fig. 15(b) are all similar and symmetrically located, and their relationship is clearly shown in their full Miller-Bravais symbols: $(10\bar{1}0)$, $(01\bar{1}0)$, $(\bar{1}100)$, $(\bar{1}010)$, $(0\bar{1}10)$, $(1\bar{1}00)$. On the other hand, the abbreviated symbols of these planes, $(10 \cdot 0)$, $(01 \cdot 0)$, $(\bar{1}1 \cdot 0)$, $(\bar{1}0 \cdot 0)$, $(0\bar{1} \cdot 0)$, $(1\bar{1} \cdot 0)$ do not immediately suggest this relationship.

Directions in a hexagonal lattice are best expressed in terms of the *three* basic vectors $\mathbf{a}_1$, $\mathbf{a}_2$, and $\mathbf{c}$. Figure 15(b) shows several examples of both plane and direction indices. Another system, involving four indices, is sometimes used to designate directions. The required direction is broken up into four component vectors, parallel to $\mathbf{a}_1$, $\mathbf{a}_2$, $\mathbf{a}_3$, and $\mathbf{c}$ and so chosen that the third index is the negative of the sum of the first two. Then, if $[UVW]$ are the indices of a direction referred to three axes and $[uvtw]$ the four-axis indices, the two are related as follows:

$$\begin{aligned}
U &= u - t & u &= (2U - V)/3 \\
V &= v - t & v &= (2V - U)/3 \\
W &= w & t &= -(u + v) = -(U + V)/3 \\
& & w &= W.
\end{aligned} \tag{11}$$

Thus, [100] becomes $[2\bar{1}\bar{1}0]$, [210] becomes $[10\bar{1}0]$, etc.

9 CRYSTAL STRUCTURE

So far discussion focused on topics from the field of *mathematical* (*geometrical*) *crystallography* and barely acknowledged actual crystals and the atoms of which they are composed. In fact, all of the above was well known long before the discovery of x-ray diffraction, i.e., long before there was any certain knowledge of the interior arrangements of atoms in crystals.

It is now time to describe the structure of some actual crystals and to relate this structure to the point lattices, crystal systems, and symmetry elements discussed above. The cardinal principle of crystal structure is that *the atoms of a crystal are set in space in some fixed relation to the points of a Bravais lattice.* It follows from this that the atoms of a crystal will be arranged periodically in three dimensions and that this arrangement of atoms will exhibit many of the properties of a Bravais lattice, in particular many of its symmetry elements.

The features associated with each lattice point are termed the *basis* of the lattice, and this applies to one- and two-dimensional lattices as well as three-dimensional crystal structures. Figure 16 shows three different bases for a one-dimensional lattice; the vertical dashed lines mark the end of the unit cells. The basis for lattice (b) is a single dot-dash, with the dot to the right of the dash, that for (c) is a dash-dot dot-dash combination and that for (d) is a dash-dot dash-dot combination. The symmetry in Fig. 16(c) can be represented by mirrors (solid vertical lines in the figure) or by 2-fold rotation axes perpendicular to the page. Note that the mirror at "O" (or the 2-fold axis at "O" in the alternate version) acts throughout the entire one-dimensional space: the features at A and B appear at A' and B'.

The term *space group* defines the entire spatial arrangement of a crystal system, that is, translation (i.e., the vectors which define the size and shape of the unit cell)

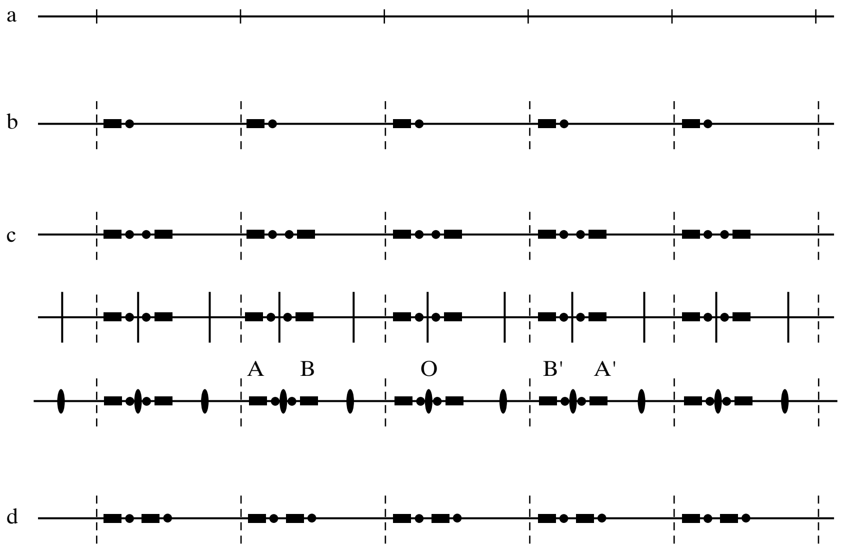

Figure 16 (a) One dimensional lattice with unit cells marked by vertical bars. (b) One-dimensional lattice populated with a "dash-dot" motif and showing one-fold symmetry. The borders of the unit cells are indicated by the vertical dashed lines. (c) Three representations of the same one-dimensional lattice populated with the dash-dot motif. The top line shows only the dash-dot motifs and unit cell boundaries. The middle lattice shows where mirror planes occur in the lattice (vertical bars) while the bottom lattice includes two-fold axes. (d) One-dimensional lattice with a basis consisting of two dash-dot motifs.

combined with the symmetry elements acting through a point (i.e., the point group) specify the space group. There are two point groups and two space groups for one-dimensional lattices, 17 space groups in two-dimensions and 230 unique space groups in three-dimensions. Thus, the combination of symmetry elements with different lattice types (not all symmetry element combinations nor lattice types have been covered here, see [G.3-G.6] for more details) dictate that three-dimensional crystals cannot have any atomic arrangement, only one of the 230 possibilities cataloged in Volume A of the International Tables for Crystallography [G.1]. Instead, different crystals have different bases ranging from single atoms to thousands or millions of atoms.

The simplest crystals imaginable are those formed by placing atoms of the same kind *on* the points of a Bravais lattice. Not all such crystals exist but many metals crystallize in this simple fashion, and Fig. 17 shows two common metal structures based on the body-centered cubic (BCC) and face-centered cubic (FCC) lattices. The former has two atoms per unit cell and the latter four.

The next degree of complexity is encountered when two or more atoms of the same kind are "associated with" each point of a Bravais lattice, as exemplified by the hexagonal close-packed (HCP) structure common to many metals. This structure is simple hexagonal and is illustrated in Fig. 18. There are two atoms per unit cell, as shown in (a), one at 0 0 0 and the other at $\frac{2}{3}\,\frac{1}{3}\,\frac{1}{2}$ (or at $\frac{1}{3}\,\frac{2}{3}\,\frac{1}{2}$, which is an equivalent position). Figure 18(b) shows the same structure with the origin of the unit cell shifted so that the point 1 0 0 in the new cell is midway between the atoms at 100 and $\frac{2}{3}\,\frac{1}{3}\,\frac{1}{2}$ in (a), the nine atoms shown in (a) corresponding to the nine atoms marked with an X in (b). The "association" of pairs of atoms with the points of a simple hexagonal Bravais lattice is suggested by the dashed lines in (b). Note, however, that the atoms of a close-packed hexagonal structure do not themselves form a point lattice, the surroundings of an atom at 000 being different from those of an atom at $\frac{2}{3}\,\frac{1}{3}\,\frac{1}{2}$. Figure 18 (c) shows still another representation of the HCP structure: the three atoms in the interior of the hexagonal prism are directly above the centers of alternate triangles in the base and, if repeated through space by the vectors $\mathbf{a}_1$ and $\mathbf{a}_2$, would also form a hexagonal array just like the atoms in the layers above and below.

The HCP structure is so called because it is one of the two ways in which spheres can be packed together in space with the greatest possible density and still have a periodic arrangement. Such an arrangement of spheres in contact is shown in Fig. 18(d) and appears to have first been noted by Kepler [5], who is better known for

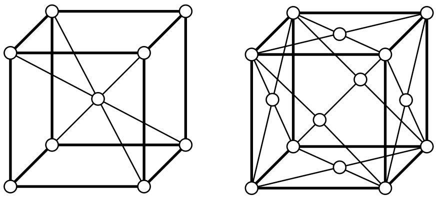
BCC FCC

Figure 17 Structures of some common metals. Body-centered cubic: α-Fe, Cr, Mo, V, etc.: face-centered cubic: γ-Fe, Cu, Pb, Ni, etc.

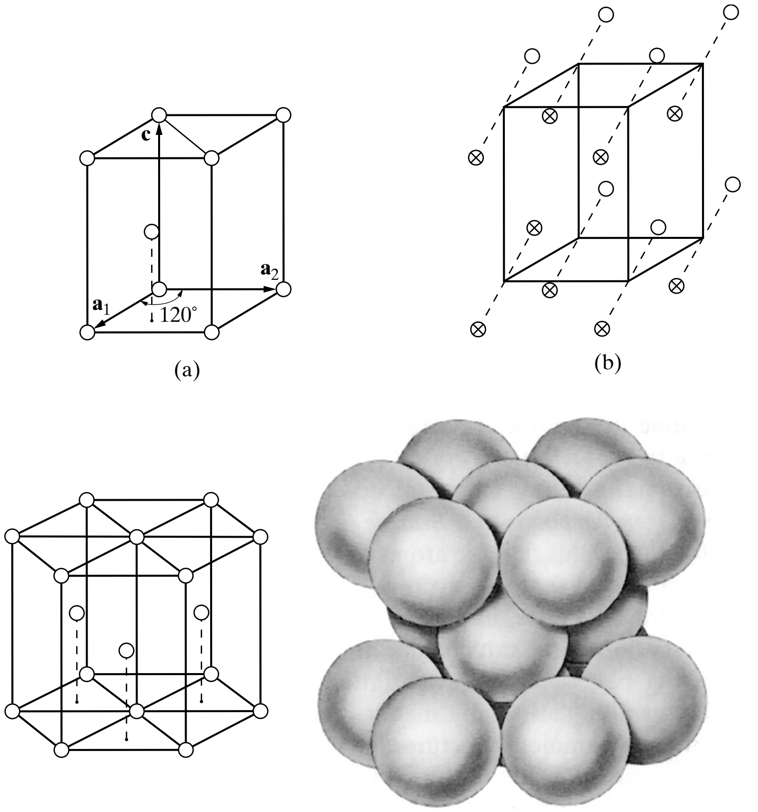

(a) (b)

(c) (d)

Figure 18 The hexagonal close-packed structure, shared by Zn, Mg, Be, αTi, etc.

his work in astronomy. If these spheres are regarded as atoms, then the resulting picture of an HCP metal is much closer to physical reality than is the relatively open structure suggested by the drawing of Fig. 18(c), and this is true, generally, of all crystals. On the other hand, it may be shown that the ratio of *c* to *a* in an HCP structure formed of spheres in contact is 1.633 whereas the *c/a* ratio of metals having this structure varies from about 1.58 (Be) to 1.89 (Cd). As there is no reason to suppose that the atoms in these crystals are not in contact, it follows that they must be ellipsoidal in shape rather than spherical.

The FCC structure is an equally close-packed arrangement. Its relation to the HCP structure is not immediately obvious, but Fig. 19 shows that the atoms on the (111) planes of the FCC structure are arranged in a hexagonal pattern just like the atoms on the (0002) planes of the HCP structure. The only difference between the two structures is the way in which these hexagonal sheets of atoms are arranged above one another. In an HCP metal, the atoms in the second layer are above the hollows in the first layer and the atoms in the third layer are above the atoms in the

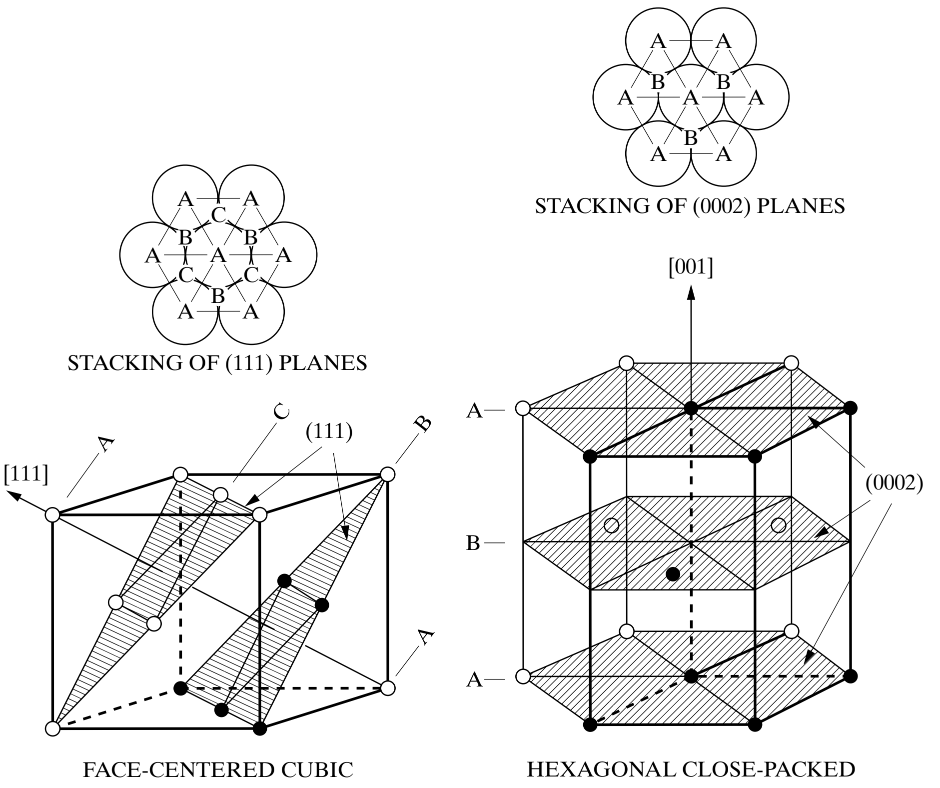

Figure 19 Comparison of FCC and HCP structures. The black atoms in the FCC drawing delineate half a hexagon, which is completed on the same plane extended into the next unit cell below (not shown).

first layer, so that the layer stacking sequence can be summarized as $A\ B\ A\ B\ A\ B\ldots$. The first two atom layers of an FCC metal are put down in the same way, but the atoms of the third layer are so placed in the hollows of the second layer that not until the fourth layer does a position repeat. FCC stacking therefore has the sequence $A\ B\ C\ A\ B\ C\ldots$. These stacking schemes are indicated in the plan views shown in Fig. 19.

Another example of the "association" of more than one atom with each point of a Bravais lattice is given by uranium. The structure of the form stable at room temperature, α-uranium, is illustrated in Fig. 20 by plan and elevation drawings. In such drawings, the height, of an atom (expressed as a fraction of the axial length) above the plane of the drawing (which includes the origin of the unit cell and two of the cell axes) is given by the numbers marked on each atom. The Bravais lattice is base-centered orthorhombic, centered on the C face, and Fig. 20 shows how the atoms occur in pairs through the structure, each pair associated with a lattice point. There are four atoms per unit cell, located at $0\ y\ \frac{1}{4}$, $0\ \bar{y}\ \frac{3}{4}$, $\frac{1}{2}(\frac{1}{2}+y)\frac{1}{4}$, and $\frac{1}{2}(\frac{1}{2}-y)\frac{3}{4}$. Here is an

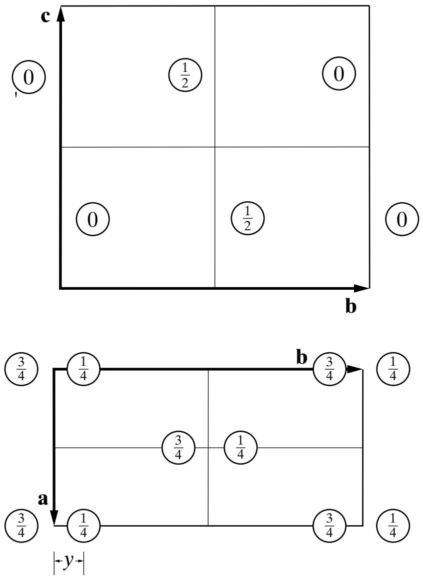

Figure 20 The structure of α-uranium, after

example of a variable parameter *y* in the atomic coordinates. Crystals often contain such variable parameters, which may have any fractional value without destroying any of the symmetry elements of the structure. A quite different substance might have exactly the same structure as uranium except for slightly different values of *a, b, c,* and *y*. For uranium *y* is 0.105 ± 0.005.

Turning to the crystal structure of *compounds* of unlike atoms, structures are built on the skeleton of a Bravais lattice but that certain other rules must be obeyed, precisely because there are unlike atoms present. Consider, for example, a crystal of A_xB_y which might be an ordinary chemical compound, an intermediate phase of relatively fixed composition in some alloy system, or an ordered solid solution. Then the arrangement of atoms in A_xB_y must satisfy the following conditions:

1. Body-, face-, or base-centering translations, if present, must begin and end on atoms of the same kind. For example, if the structure is based on a body-centered Bravais lattice, then it must be possible to go from an A atom, say, to *another* A atom by the translation $\frac{1}{2}\frac{1}{2}\frac{1}{2}$
2. The set of A atoms in the crystal and the set of B atoms must separately possess the same symmetry elements as the crystal as a whole, since in fact they make up the crystal. In particular, the operation of any symmetry element present must bring a given atom, A for example, into coincidence with another atom of the same kind, namely A.

Consider the structures of a few common crystals in light of the above requirements. Figure 21 illustrates the unit cells of two ionic compounds, CsCl and NaCl. These structures, both cubic, are common to many other crystals and, wherever they

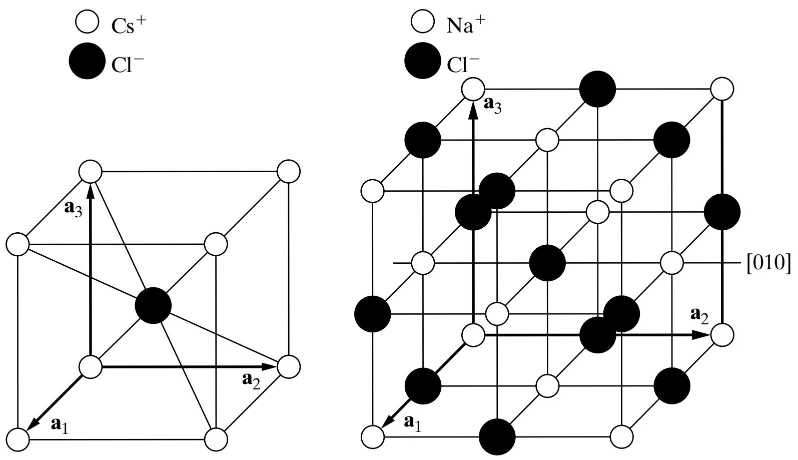

(a) CsCl (b) NaCl

Figure 21 The structures of (a) CsCl (common to CsBr, NiAl, ordered β-brass, ordered CuPd, etc.) and (b) NaCl (common to KCl, CaSe, PbTe, etc.).

occur, are referred to as the "CsCl structure" and the "NaCl structure." In considering a crystal structure, one of the most important things to determine is its Bravais lattice, since that is the basic framework on which the crystal is built and because it has a profound effect on the way in which that crystal diffracts x-rays.

What is the Bravais lattice of CsCl? Figure 21 (a) shows that the unit cell contains two atoms, ions really, since this compound is completely ionized even in the solid state: a cesium ion at 000 and a chlorine ion at $\frac{1}{2}\frac{1}{2}\frac{1}{2}$. The Bravais lattice is obviously not face-centered, but the body-centering translation $\frac{1}{2}\frac{1}{2}\frac{1}{2}$ connects two atoms. However, these are unlike atoms and the lattice is therefore *not* body-centered. It is, by elimination, simple cubic. If one wishes, one may think of both ions, the cesium at 000 and the chlorine at $\frac{1}{2}\frac{1}{2}\frac{1}{2}$, as being associated with the lattice point at 0 0 0. It is not possible, however, to associate any one cesium ion with any particular chlorine ion and refer to them as a CsCl molecule; the term "molecule" therefore has no real physical significance in such a crystal, and the same is true of most inorganic compounds and alloys.

Close inspection of Fig. 21(b) will show that the unit cell of NaCl contains 8 ions, located as follows:

4 Na^+ at	0 0 0,	$\frac{1}{2}$ $\frac{1}{2}$ 0,	$\frac{1}{2}$ 0 $\frac{1}{2}$,	and	0 $\frac{1}{2}$ $\frac{1}{2}$;
4 Cl^- at	$\frac{1}{2}$ $\frac{1}{2}$ $\frac{1}{2}$,	0 0 $\frac{1}{2}$,	0 $\frac{1}{2}$ 0,	and	$\frac{1}{2}$ 0 0

The sodium ions are clearly face-centered, and the face-centering translations [000] and $\langle\frac{1}{2}\frac{1}{2}0\rangle$, when applied to the chlorine ion at $\frac{1}{2}\frac{1}{2}\frac{1}{2}$, will reproduce all the chlorine-ion positions. The Bravais lattice of NaCl is therefore face-centered cubic. The ion positions, incidentally, may be written in summary form as:

$$4 \quad Na^+ \quad \text{at} \quad 0\ 0\ 0 \quad + \quad \text{face–centering translations.}$$

$$4 \quad Cl^- \quad \text{at} \quad \tfrac{1}{2}\ \tfrac{1}{2}\ \tfrac{1}{2} \quad + \quad \text{face–centering translations.}$$

Note also that in these, as in all other structures, the operation of any symmetry element possessed by the lattice must bring similar atoms or ions into coincidence. For example, in Fig. 21(b), 90° rotation about the 4-fold [010] rotation axis shown brings the chlorine ion at $0\,1\,\tfrac{1}{2}$ into coincidence with the chlorine ion at $\tfrac{1}{2}\,1\,1$, the sodium ion at 0 1 1 with the sodium ion at 1 1 1, etc

Elements and compounds often have closely similar structures. Figure 22 shows the unit cells of diamond and the zinc-blende form of ZnS. Both are face-centered cubic. Diamond has 8 atoms per unit cell, located at

$$0\ 0\ 0 \quad + \quad \text{face–centering translations.}$$

$$\tfrac{1}{4}\ \tfrac{1}{4}\ \tfrac{1}{4} \quad + \quad \text{face–centering translations.}$$

In other words, a "molecule" of two atoms is associated with each of the face-centered lattice points. The atom positions in zinc blende are identical with these, but the first set of positions is now occupied by one kind of atom (S) and the other by a different kind (Zn).

Note that diamond and a metal like copper have quite dissimilar structures, although both are based on a face-centered cubic Bravais lattice. To distinguish between these two, the terms "diamond cubic" and "face-centered cubic" are usually used. The industrially important semiconductor, silicon has the diamond cubic structure.

Instead of referring to a structure by name, such as the "NaCl structure," one can use the designations introduced years ago in *Strukturbericht* [G.8]. These consist of

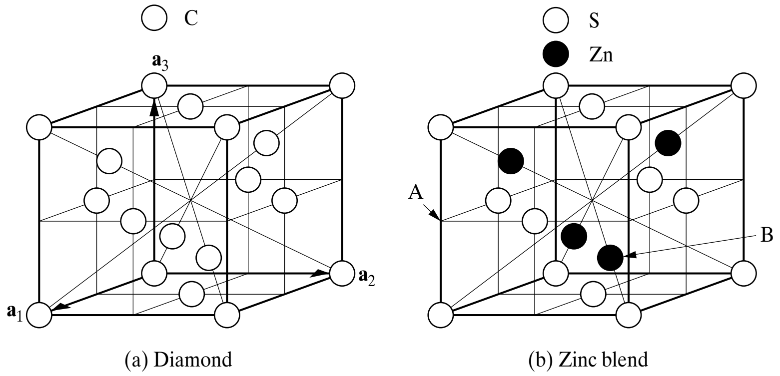

(a) Diamond (b) Zinc blend

Figure 22 The structures of (a) diamond (common to Si, Ge, and gray Sn) and (b) the zinc-blende form of ZnS (common to HgS, CuI, AlSb, BeSe, etc.).

a letter and a number: the letter A indicates an element, B an AB compound, C an AB_2 compound, etc. The structure of copper, for example, is called the A1 structure, α–Fe is A2, zinc is A3, diamond is A4, NaCl is B1, etc. A full list is given by Pearson [G.9, Vol. 1, p. 85].

Some rather complex crystals can be built on a cubic lattice. For example, the ferrites, which are magnetic and are used in recording tapes, computer floppy disks and in hard drives, have the formula $MO \cdot Fe_2O_3$, where M is a divalent metal ion like Mn, Ni, Fe, Co, etc. Their structure is related to that of the mineral spinel. The Bravais lattice of the ferrites is face-centered cubic, and the unit cell contains 8 "molecules" or a total of $8 \times 7 = 56$ ions. There are therefore 56/4 or 14 ions associated with each lattice point.

The number of atoms per unit cell in any crystal is partially dependent on its Bravais lattice. For example, the number of atoms per unit cell in a crystal based on a body-centered lattice must be a multiple of 2, since there must be, for any atom in the cell, a corresponding atom of the same kind at a translation of $\frac{1}{2}\,\frac{1}{2}\,\frac{1}{2}$ from the first. The number of atoms per cell in a base-centered lattice must also be a multiple of 2, as a result of the base-centering translations. Similarly, the number of atoms per cell in a face-centered lattice must be a multiple of 4.

The reverse of these propositions is not true. It would be a mistake to assume, for example, that if the number of atoms per cell is a multiple of 4, then the lattice is necessarily face-centered. The unit cell of the intermediate phase AuBe, for example (Fig. 23), contains 8 atoms and yet it is based on a simple cubic Bravais lattice. The atoms are located as follows:

4 Au at

$$u \quad u \quad u, \quad (\tfrac{1}{2} + u)(\tfrac{1}{2} - u)\overline{u}, \qquad \overline{u}(\tfrac{1}{2} + u)(\tfrac{1}{2} - u), \quad (\tfrac{1}{2} - u)\overline{u}(\tfrac{1}{2} + u),$$

4 Be at

$$w \quad w \quad w, \quad (\tfrac{1}{2} + w)(\tfrac{1}{2} - w)\overline{w}, \qquad \overline{w}(\tfrac{1}{2} + w)(\tfrac{1}{2} - w), \quad (\tfrac{1}{2} - w)\overline{w}(\tfrac{1}{2} + w),$$

where $u = 0.100$ and $w = 0.406$, each ± 0.005. If the parameter u is put equal to zero, the atomic coordinates of the gold atoms become those of a face-centered cubic cell. The structure of AuBe may therefore be regarded as distorted face-centered cubic, in which the presence of the beryllium atoms has forced the gold atoms out of their original positions by a distance $\pm u$, $\pm u$, $\pm u$. These translations are all in directions of the form <111>, i.e., parallel to body diagonals of the cube, and are shown as dotted lines in Fig. 23. The three-fold axes characteristic of cubic Bravais lattices remain, but four-fold axes are not present due to the distortion. Thus, this structure is an example of a cubic crystal system without set of three perpendicular four-fold axes.

It should now be apparent that the term "simple," when applied to a Bravais lattice, is used in a very special, technical sense and that some very complex structures can be built up on a "simple" lattice. In fact, they may contain more than a hundred atoms per unit cell. The only workable definition of a simple lattice is a negative

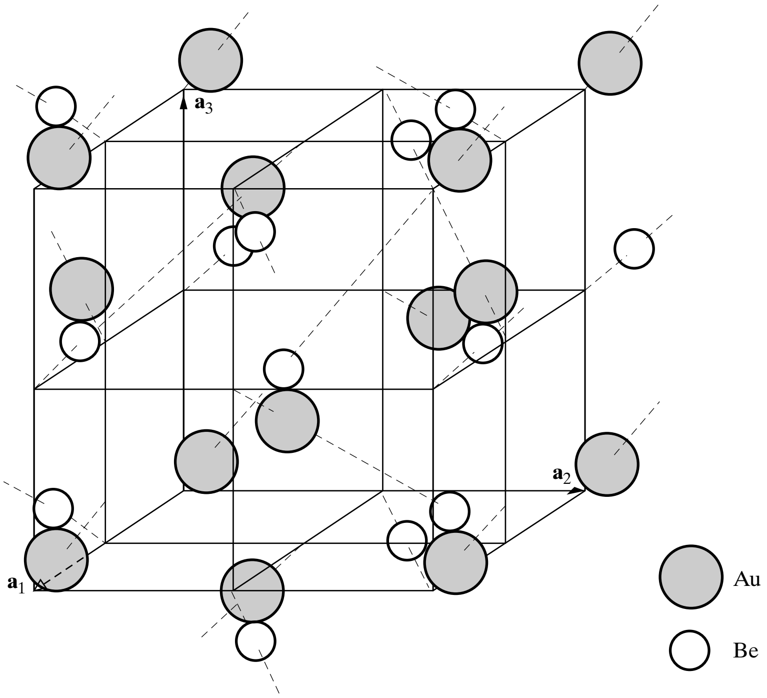

Figure 23 The structure of AuBe, shared by FeSi, NiSi, CoSi, MnSi, etc. It is known as the FeSi structure [7].

one: a given lattice is simple if it is neither body-, base-, nor face-centered; these latter possibilities can be ruled out by showing that the set of atomic positions does not contain the body-, base-, or face-centering translations. There is no rule governing the allowable number of atoms per cell in a simple lattice: this number may take on any one of the values 1, 2, 3, 4, 5, etc., although not in every crystal system and not every higher integer is permitted. Incidentally, not every theoretical possibility known to mathematical crystallography is realized in nature; for example, no known element crystallizes with a simple hexagonal lattice containing one atom per unit cell.

There is another way of arranging unlike atoms on a point lattice besides those considered so far and that is exemplified by the structure of *solid solutions*. These solutions are of two types, substitutional and interstitial; in the former, solute atoms substitute for, or replace, solvent atoms on the lattice of the solvent, while in the latter, solute atoms fit into the interstices of the solvent lattice. The interesting feature of these structures is that the solute atoms are distributed more or less at random. For example, consider a 10 atomic percent solution of molybdenum in chromium, which has a BCC structure. The molybdenum atoms can occupy either the corner or body-centered positions of the cube in a random, irregular manner, and a small portion of the crystal might have the appearance of Fig. 24(a). Five adjoining unit

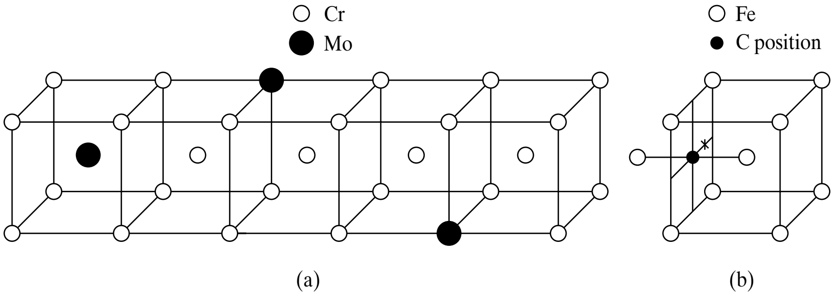

Figure 24 Structure of solid solutions: (a) Mo in Cr (substitutional); (b) C in α-Fe (interstitial).

cells are shown there, with a total of 29 atoms, 3 of which are molybdenum. This section of the crystal therefore contains somewhat more than 10 atomic percent molybdenum, but the next five cells would probably contain somewhat less. Such a structure does not obey the ordinary rules of crystallography: for example, the right-hand cell of the group shown does not have cubic symmetry, and one finds throughout the structure that the translation given by one of the unit cell vectors may begin on an atom of one kind and end on an atom of another kind. All that can be said of this structure is that it is BCC *on the average*, and experimentally it displays the x-ray diffraction effects proper to a BCC lattice. This is not surprising since the x-ray beam used to examine the crystal is so large compared to the size of a unit cell that it observes, so to speak, millions of unit cells at the same time and so obtains only an average "picture" of the structure.

The above remarks apply equally well to interstitial solid solutions. These form whenever the solute atom is small enough to fit into the solvent lattice without causing too much distortion. Ferrite, the solid solution of carbon in α–iron, is a good example.[6] In the unit cell shown in Fig. 24(b), there are two kinds of "holes" in the lattice: one at $\frac{1}{2}\,0\,\frac{1}{2}$ (marked ●)and equivalent positions in the centers of the cube faces and edges, and one at $\frac{1}{4}\,0\,\frac{1}{2}$ (marked ×) and equivalent positions. All the evidence at hand points to the fact that the carbon atoms in ferrite are located in the holes at $\frac{1}{2}0\frac{1}{2}$ and equivalent positions. On the average, however, no more than about 1 of these positions in 500 unit cells is occupied, since the maximum solubility of carbon in ferrite is only about 0.1 atomic percent.

Still another type of structure worth noting is that of *ordered solid solutions*. As described above, a typical substitutional solid solution has solute atoms distributed more or less at random on the lattice points of the solvent.[7] On the other hand, there are solutions in which this is true only at elevated temperatures; when cooled

---

[6] Note the double meaning of the word *ferrite*: (1) metallurgical, for the metallic solid solution mentioned above, and (2) ceramic or mineralogical, for the oxide $MO \cdot Fe_2O_3$ previously described.

[7] Of course, when the solution becomes concentrated, there is no real distinction between "solvent" and "solute." There is only one lattice, with two or more kinds of atoms distributed on it.

to lower temperatures, the solute atoms take up an orderly, periodic arrangement while still remaining on the lattice points of the solvent. The solid solution is then said to be *ordered* and to possess a *superlattice*. The alloy $AuCu_3$ is a classic example: at high temperatures the copper and gold atoms are located more or less at random on face-centered cubic lattice sites, while at low temperature the gold atoms occupy only the cube corner positions and the copper atoms only the face-centered positions. In its temperature range of stability then, an ordered solid solution resembles a chemical compound, with atoms of one kind on one set of lattice sites and atoms of a different kind on another set. But an ordered solid solution is a "half-hearted compound" because, when heated, it disorders before it melts; a real compound, like NaCl, remains ordered right up to the melting point. Crystallographically, the structures of the disordered and ordered solid solutions are quite different; disordered $AuCu_3$ is, on the average, face-centered cubic while the ordered form is simple cubic.

10 ATOM SIZES AND COORDINATION

When two or more unlike atoms unite to form a chemical compound, intermediate phase, or solid solution, the kind of structure formed is dependent, in part, on the relative sizes of the atoms involved. But what is meant by the size of an atom? To regard an atom as something like a billiard ball with a sharply defined bounding surface is surely an oversimplification, since electron density decreases gradually at the "surface" of the atom and that there is a small but finite probability of finding an electron at quite large distances from the nucleus. One, not entirely satisfactory, way of defining atomic size lies in considering a crystal as a collection of rigid spheres in contact. The size of an atom, then, is given by the distance of closest approach of atom centers in a crystal of the element, and this distance can be calculated from the lattice parameters.

For example, the lattice parameter a of α–iron is 2.87 Å, and in a BCC lattice the atoms are in contact only along the diagonals of the unit cube. The diameter of an iron atom is therefore equal to one half the length of the cube diagonal, or $(\sqrt{3}/2)a = 2.48$Å. The following formulas give the distance of closest approach in the three common structures:

$$\text{BCC} = \frac{\sqrt{3}}{2}a,$$

$$\text{FCC} = \frac{\sqrt{2}}{2}\text{a},$$

$$\text{HCP} = a \quad \text{(between atoms in basal plane)},$$

$$= \sqrt{\frac{a^2}{3} + \frac{c^2}{4}} \left(\begin{array}{c} \text{between atom in basal plan} \\ \text{and neighbors above or below} \end{array} \right) \tag{12}$$

To a first approximation, the size of an atom is a constant. In other words, an iron atom has about the same size whether it occurs in pure iron, an intermediate phase, or a solid solution. This is a very useful fact to remember when investigating unknown crystal structures, for it enables prediction of roughly how large a hole is necessary in a proposed structure to accommodate a given atom. More precisely, it is known that the size of an atom has a slight dependence on its *coordination number*, which is the number of nearest neighbors of the given atom and which depends on crystal structure. The coordination number of an atom in the FCC or HCP structures is 12, in BCC 8, and diamond cubic 4. The smaller the coordination number, the smaller the volume occupied by a given atom, and the approximate amount of contraction to be expected with decrease in coordination number is found to be:

Change in coordination	Size contraction, percent
12→8	3
12→6	3
12→4	12

This means, for example, that the diameter of an iron atom is greater if the iron is dissolved in FCC copper than if it exists in a crystal of BCC α–iron or is dissolved in BCC vanadium. If it were dissolved in copper, its diameter would be approximately 2.48/0.97, or 2.56 Å.

The size of an atom in a crystal also depends on whether its binding is ionic, covalent, metallic, or van der Waals, and on its state of ionization. The more electrons are removed from a neutral atom the smaller it becomes, as shown strikingly for iron, whose atoms and ions Fe, Fe^{++}, Fe^{+++} have diameters of 2.48, 1.66, and 1.34 Å, respectively.

The spatial arrangement of atoms about a given point is often described by words such as *octahedral* and *tetrahedral*. For example, in the NaCl structure of Fig. 21(b) the central Cl^- ion at $\frac{1}{2}\frac{1}{2}\frac{1}{2}$ is said to be octahedrally surrounded by Na^+ ions, because the six Na^+ ions in the face-centered positions lie on the corners of an octahedron, a solid bounded by eight triangular sides. In the zinc blende structure of Fig. 22(b) the empty position marked *A* is octahedrally surrounded by sulphur atoms, of which only four are in the cell shown, and would be referred to as an octahedral hole in the structure. This group of atoms is shown separately in Fig. 25. In the same structure the Zn atom at $\frac{1}{4}\frac{1}{4}\frac{1}{4}$, marked *B* in Fig. 22(b), is surrounded by four S atoms at the corners of a tetrahedron, a solid bounded by four triangular sides (Fig. 25). In fact, all four of the Zn atoms in the unit cell have tetrahedral S surroundings. Also in the ZnS structure the reader can demonstrate, by sketching three cells adjacent to the one shown, that the hole at *A* is tetrahedrally surrounded by Zn atoms. Thus, the hole at *A* has both octahedral (s) and tetrahedral (Zn) surroundings, an unusual circumstance.

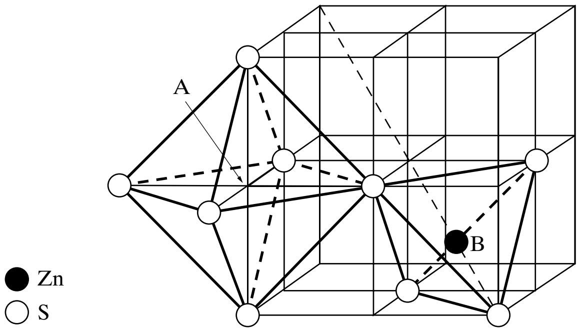

Figure 25 Portion of the zinc blend structure. Compare Figure 22(b). The hole at *A* has octahedral surroundings. The Zn atom at *B* has tetrahedral surroundings.

11 CRYSTAL SHAPE

The shape of crystals has been ignored thus far so that their internal structure could be emphasized. However, the shape of crystals is, to the layman, perhaps their most characteristic property, and nearly everyone is familiar with the beautifully developed flat faces exhibited by natural minerals or crystals artificially grown from a supersaturated salt solution. In fact, it was with a study of these faces and the angles between them that the science of crystallography began.

Nevertheless, the shape of crystals is really a secondary characteristic, since it depends on, and is a consequence of, the interior arrangement of atoms. Sometimes the external shape of a crystal is rather obviously related to its smallest building block, the unit cell, as in the little cubic grains of ordinary table salt (NaCl has a cubic lattice) or the six-sided prisms of natural quartz crystals (hexagonal lattice). In many other cases, however, the crystal and its unit cell have quite different shapes; gold, for example, has a cubic lattice, but natural gold crystals are octahedral in form, i.e., bounded by eight planes of the form {111}.

An important fact about crystal faces was known long before there was any knowledge of crystal interiors. It is expressed as the *law of rational indices*, which states that the indices of naturally developed crystal faces are always composed of small whole numbers, rarely exceeding 3 or 4. Thus, faces of the form {100}, {111}, $\{1\bar{1}00\}$, {210}, etc., are observed but not such faces as {510}, {719}, etc. Earlier discussion in this chapter concluded that planes of low indices have the largest density of lattice points, and it is a law of crystal growth that such planes develop at the expense of planes with high indices and few lattice points.

In materials work, however, crystals with well-developed faces are in the category of things heard of but rarely seen. They occur occasionally on the free surface of castings, in some electrodeposits, or under other conditions of no external constraint. Instead, a crystal is most usually a “grain,” seen through a microscope in the company of many other grains on a polished section. If an isolated single crystal is encountered it will have been artificially grown either from the melt, and thus have the shape of the crucible in which it solidified, or by recrystallization, and thus have the shape of the starting material, whether sheet, rod, or wire.

The shapes of the grains in a polycrystalline mass are the result of several kinds of forces, all of which are strong enough to counteract the natural tendency of each grain to grow with well-developed flat faces. The result is a grain roughly polygonal in shape with no obvious aspect of crystallinity. Nevertheless, that grain is a crystal and just as “crystalline” as, for example, a well-developed prism of natural quartz, since the essence of crystallinity is a periodicity of inner atomic arrangement and not any regularity of outward form.

12 CRYSTAL DEFECTS

There are a number of types of imperfections in the periodic structure of the individual grains of crystalline solids. These crystallographic defects are broadly classified as point, line and planar defects and can have important consequences in the mechanical, electrical, optical, etc. properties of a material. A large part of materials science and engineering concerns itself with the control and/or characterization of the different defects. Point defects such as substitutional or interstitial impurities were briefly discussed in Sec. 10. Edge and screw dislocations and dislocations with character intermediate between the two are linear defects in the periodic array of atoms within a crystal. In metals, multiplication and motion of dislocations occur at relatively low stress, and the relatively easy plastic deformation and high ductility of metals is the product of this. Large strains and very high dislocation densities can be introduced by operations such as forging, rolling, machining, shot peening or ball milling. There are a variety of planar defects including stacking faults and twins; these are described below.

In Sec. 9 the stacking sequence of close packed planes of the fcc and hcp structures was discussed. Stacking faults occur when the normal stacking sequence is interrupted. In the fcc structure, the normal stacking sequence $\ldots \mathrm{ABCABCABC} \ldots$can become $\ldots \mathrm{ABCAB}^{*}\mathrm{ABC} \ldots$ or $\ldots \mathrm{ABCA}^{*}\mathrm{CABCA} \ldots$, for example, by the removal of a C-layer or a B-layer, respectively. The asterisk in the previous sentence is used to indicate the position of the stacking fault. In the hcp system, the stacking sequence $\ldots \mathrm{ABABABAB} \ldots$ can become $\ldots \mathrm{ABABA}^{*}\mathrm{CBCBCB} \ldots$ Faults producing AA, BB or CC neighboring layers have a very high energy of formation, would require extraordinary circumstances to appear and would probably rapidly split into a set of closely-spaced, lower energy faults. In writing sequences such as those shown above, each letter represents a layer of atoms. Each layer extends to the end of the fault, and such planar faults must extend to the edge of the crystal or grain or must terminate at one or more dislocations [8, 9].

Some crystals have two parts symmetrically related to one another. These, called twinned crystals, are fairly common both in minerals and in metals and alloys. For a detailed discussion of twinning, see Barrett and Massalski [G.10].

The relationship between the two parts of a twinned crystal is described by the symmetry operation which will bring one part into coincidence with the other or with an extension of the other. Two main kinds of twinning are distinguished, depending on whether the symmetry operation is 180° rotation about an axis, called the twin axis, or reflection across a plane, called the twin plane. The plane on which the two parts of a twinned crystal are united is called the composition plane. In the case of a reflection twin, the composition plane may or may not coincide with the twin plane.

Of most interest to those who deal mainly with FCC, BCC, and HCP structures, are the following kinds of twins:

1. Annealing twins, such as occur in FCC metals and alloys (Cu, Ni, α–brass, Al, etc.), which have been cold-worked and then annealed to cause recrystallization.
2. Deformation twins, such as occur in deformed HCP metals (Zn, Mg, Be, etc.) and BCC metals (α–Fe, W, etc.).

Annealing Twins

Annealing twins in FCC metals are rotation twins, in which the two parts are related by a 180° rotation about a twin axis of the form <111>. Because of the high symmetry of the cubic lattice, this orientation relationship is also given by a 60° rotation about the twin axis or by reflection across the {111} plane normal to the twin axis. In other words, FCC annealing twins may also be classified as reflection twins. The twin plane is also the composition plane.

Occasionally, annealing twins appear under the microscope as in Fig. 26(a), with one part of a grain (B) twinned with respect to the other part (A). The two parts are in contact on the composition plane (111) which makes a straight-line trace on the plane of polish. More common, however, is the kind shown in Fig. 26(b). The grain shown consists of three parts: two parts (A_1 and A_2) of identical orientation separated by a third part (B) which is twinned with respect to A_1 and A_2. B is known as a twin band.

Figure 27 illustrates the structure of an FCC twin band. The plane of the main drawing is $(1\bar{1}0)$, the (111) twin plane is perpendicular to this plane, and the [111]

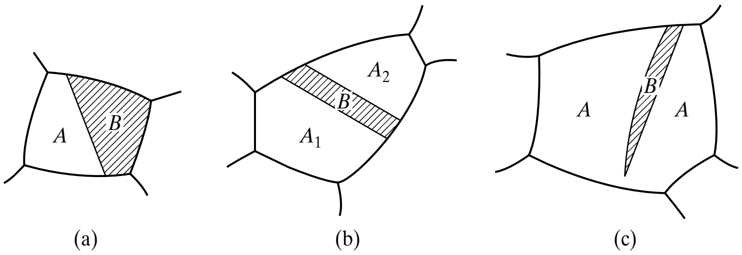

(a) (b) (c)

Figure 26 Twinned grains: (a) and (b) FCC annealing twins; (c) HCP deformation twin.

twin axis lies in it. Open circles represent atoms in the plane of the drawing and filled circles those in the layers immediately above or below. The reflection symmetry across the twin plane is suggested by the dashed lines connecting several pairs of atoms.

The statement that a rotation twin of this kind is related to the parent crystal by a 180° rotation about the twin axis is merely an expression of the orientation relationship between the two and is not meant to suggest that a twin is formed by a physical rotation of one part of the crystal with respect to another. Actually, FCC annealing twins are formed by a change in the normal growth mechanism. Suppose that, during normal grain growth following recrystallization, a grain boundary is roughly parallel to (111) and is advancing in a direction approximately normal to this boundary, namely [111]. To say that the boundary is advancing is to say that atoms are leaving the lattice of the consumed grain and joining that of the growing grain. The grain is therefore growing by the addition of layers of atoms parallel to (111), and these layers are piled up in the sequence *ABCABC* … in an FCC crystal. If, however, a mistake should occur and this sequence become altered to *CBACBA* … , the crystal so formed would still be FCC but it would be a twin of the former. If a similar mistake occurred later, a crystal of the original orientation would start growing and a twin band would be formed. With this symbolism, a twin band appears as follows:

A B C A B C B A C B A C A B C A B C

parent | twin | parent
crystal | band | crystal
⟶ | ⟷ | ⟵

In this terminology, the symbols themselves are imaged in the mirror *C*, the twin plane. At the left of Fig. 27 the positional symbols *A*, *B*, *C* are attached to various (111) planes to show the change in stacking which occurs at the boundaries of the twin band. Parenthetically, it should be remarked that twin bands visible under the light microscope are thousands of times thicker than the one shown in this drawing.

There is still another way of *describing* the orientation relationship between an FCC crystal and its twin: the (111) layers of the twin are in positions which would result from homogeneous shear in a $[11\bar{2}]$ direction, each layer moving by an amount proportional to its distance from the twin plane. In Fig. 27, this shear is indicated by the arrows going from initial positions *D, E, F* to final positions in the twin. Although it has been frequently suggested that such twins are *formed* by deformation, it is generally held that annealing twins are the result of the growth process described above. Nevertheless, this hypothetical shear is sometimes a useful way of describing the orientation relationship between a crystal and its twin.

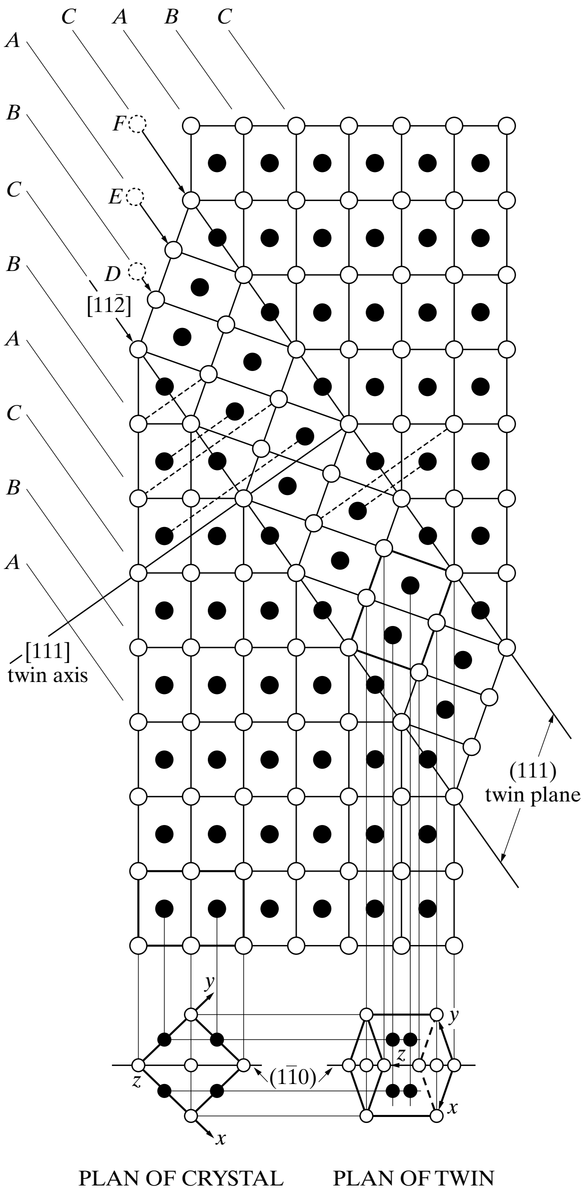

Figure 27. Twin band in FCC lattice. Plane of main drawing is (1$\bar{1}$0).

Deformation Twins

Deformation twins are found in both BCC and HCP lattices and are all that their name implies, since, in both cases, the cause of twinning is deformation. In each case, the orientation relationship between parent crystal and twin is that of reflection across a plane.

In BCC structures, the twin plane is (112) and the twinning shear is in the direction $[11\bar{1}]$. The only common example of such twins is in α–iron (ferrite) deformed by impact, where they occur as extremely narrow twin bands called Neumann bands. It should be noted that, in cubic lattices, both {112} and {111} reflection twinning produce the same orientation relationship; however, they differ in the interatomic distances produced, and an FCC lattice can twin by reflection on {111} with less distortion than on {112}, while for the same reason {112} is the preferred plane for BCC lattices.

In HCP metals, the twin plane is normally $(10\bar{1}2)$. The twinning shear is not well understood; in a gross sense, it takes place in the direction $[\bar{2}\bar{1}1]$ for metals with *c/a* ratios less than $\sqrt{3}$ (Be, Ti, Mg) and in the reverse direction $[21\bar{1}]$ for metals with *c/a* larger than $\sqrt{3}$ (Zn, Cd), but the direction of motion of individual atoms during shear is not definitely known. Figure 26(c) illustrates the usual form of a twin band in HCP metals, and it will be noted that the composition "plane," although probably parallel or nearly parallel to the twin plane, is not quite flat but often exhibits appreciable curvature.

General

Twins, in general, can form on different planes in the same crystal. For example, there are four {111} planes of different orientation on which twinning can take place in an FCC crystal. Accordingly, in the microstructure of recrystallized copper, for example, one often sees twin bands running in more than one direction in the same grain.

A crystal may also twin repeatedly, producing several new orientations. If crystal *A* twins to form *B*, which twins to form *C*, etc., then *B, C*, etc., are said to be first-order, second-order, etc., twins of the parent crystal *A*. Not all these orientations are new. In Fig. 26(b), for example, *B* may be regarded as the first-order twin of A_1, and A_2 as the first-order twin of *B*. A_2 is therefore the second-order twin of A_1 but has the same orientation as A_1.

13 THE STEREOGRAPHIC PROJECTION

Crystal drawings made in perspective or in the form of plan and elevation have their uses but are not suitable for displaying the angular relationship between lattice planes and directions. These angular relationships are often more interesting than any other aspect of the crystal, and a kind of drawing is needed on which the angles between planes can be accurately measured and which will permit graphical solution of problems involving such angles. The stereographic projection [10] fills this need. For details not given below, see Barrett and Massalski [G.10] and McKie and McKie [G.3].

The orientation of any plane in a crystal can be represented just as well by the inclination of the normal to that plane relative to some reference plane as by the inclination of the plane itself. All the planes in a crystal can thus be represented by a set of plane normals radiating from some one point within the crystal. If a refer-

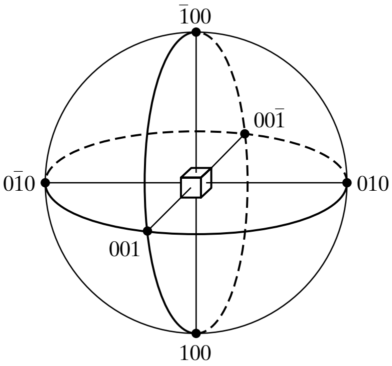

Figure 28 {100} poles of a cubic crystal.

ence sphere is now described about this point, the plane normals will intersect the surface of the sphere in a set of points called *poles*. This procedure is illustrated in Fig. 28, which is restricted to the {100} planes of a cubic crystal. The pole of a plane represents, by its position on the sphere, the orientation of that plane.

A plane may also be represented by the trace the extended plane makes in the surface of the sphere, as illustrated in Fig. 29, where the trace *ABCDA* represents the plane whose pole is P_1. This trace is a *great circle*, i.e., a circle of maximum diameter, if the plane passes through the center of the sphere. A plane not passing through the center will intersect the sphere in a *small circle*. On a ruled globe, for example, the longitude lines (meridians) are great circles, while the latitude lines, except the equator, are small circles.

The angle α between two planes is evidently equal to the angle between their great circles or to the angle between their normals (Fig. 29). But this angle, in degrees, can also be measured on the surface of the sphere along the great circle *KLMNK* connecting the poles P_1 and P_2 of the two planes, if this circle has been divided into 360 equal parts. The measurement of an angle has thus been transferred from the planes themselves to the surface of the reference sphere.

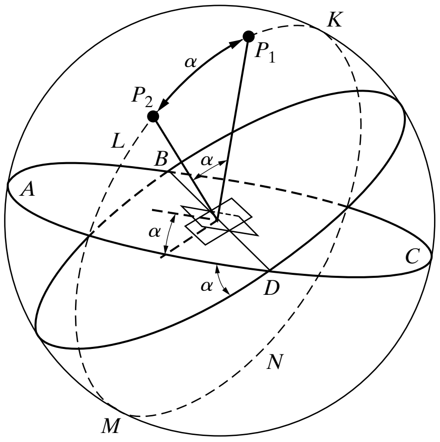

Figure 29 Angle between two planes.

Measuring angles on a flat sheet of paper rather than on the surface of a sphere, requires the same sort of transformation as used by the geographer who wants to transfer a map of the world from a globe to a page of an atlas. Of the many known kinds of projections, a map-maker usually chooses a more or less equal-area projection so that countries of equal area will be represented by equal areas on the map. In crystallography, however, an equiangular stereographic projection is most useful since it preserves angular relationships faithfully although distorting areas. It is made by placing a plane of projection normal to the end of any chosen diameter of the sphere and using the other end of that diameter as the point of projection. In Fig. 30 the projection plane is normal to the diameter AB, and the projection is made from the point B. If a plane has its pole at P, then the stereographic projection of P is at P', obtained by drawing the line BP and extending it until it meets

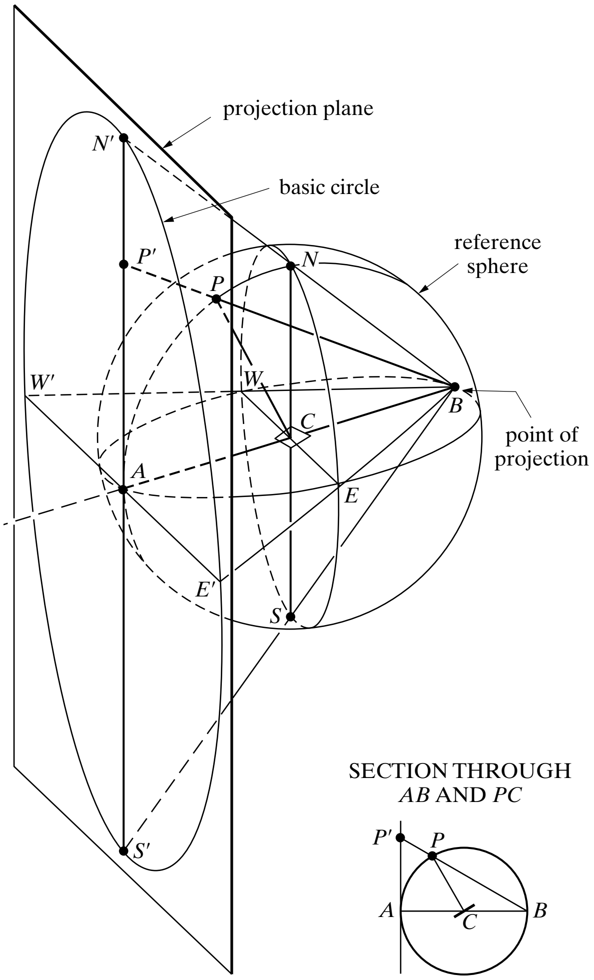

Figure 30 The stereographic projection

the projection plane. Alternately stated, the stereographic projection of the pole *P* is the shadow cast by *P* on the projection plane when a light source is placed at *B*. The observer, incidentally, views the projection from the side opposite the light source.

The plane *NESW* is normal to *AB* and passes through the center *C*. It therefore cuts the sphere in half and its trace in the sphere is a great circle. This great circle projects to form the *basic circle N′E′S′W′* on the projection, and all poles on the left-hand hemisphere will project within this basic circle. Poles on the right-hand hemisphere in Fig. 30 will project outside this basic circle, and those near *B* will have projections lying at very large distances from the center. In order to plot such poles, the point of projection must move to *A* and the projection plane to *B*; minus signs designate the new set of points while plus signs identify, the previous set (projected from *B*). Note that movement of the projection plane along *AB* or its extension merely alters the magnification; this plane is usually tangent to the sphere, as illustrated, but it can pass through the center of the sphere, for example, in which case the basic circle becomes identical with the great circle *NESW*.

A lattice plane in a crystal is several steps removed from its stereographic projection, and it may be worth-while at this stage to summarize these steps:

1. The plane *C* is represented by its normal *CP*.
2. The normal *CP* is represented by its pole *P*, which is its intersection with the reference sphere.
3. The pole *P* is represented by its stereographic projection *P′*.

After gaining some familiarity with the stereographic projection, the student will be able mentally to omit these intermediate steps and will then refer to the projected point *P′* as the pole of the plane *C* or, even more directly, as the plane *C* itself.

Great circles on the reference sphere project as circular arcs on the projection or, if they pass through the points *A* and *B* (Fig. 31), as straight lines through the center of the projection. Projected great circles always cut the basic circle in diametrically opposite points, since the locus of a great circle on the sphere is a set of diametrically opposite points. Thus the great circle *ANBS* in Fig. 31 projects as the straight line *N′S′* and *AWBE* as *W′E′*; the great circle *NGSH*, which is inclined to the plane of projection, projects as the circle are *N′G′S′*. If the half great circle *W AE* is divided into 18 equal parts and these points of division projected on *W′ AE′*, a graduated scale, at 10° intervals, is produced on the equator of the basic circle.

Small circles on the sphere also project as circles, but their projected center does not coincide with their center on the projection. For example, the circle *AJEK* whose center *P* lies on *AEBW* projects as *AJ′E′K′*. Its center *on the projection* is at *C*, located at equal distances from *A* and *E′*, but its *projected center* is at *P′*, located an equal number of degrees (45° in this case) from *A* and *E′*.

The device most useful in solving problems involving the stereographic projection is the *Wulff net* (named after its popularizer) [11] shown in Fig. 32. It is the projection of a sphere ruled with parallels of latitude and longitude on a plane par-

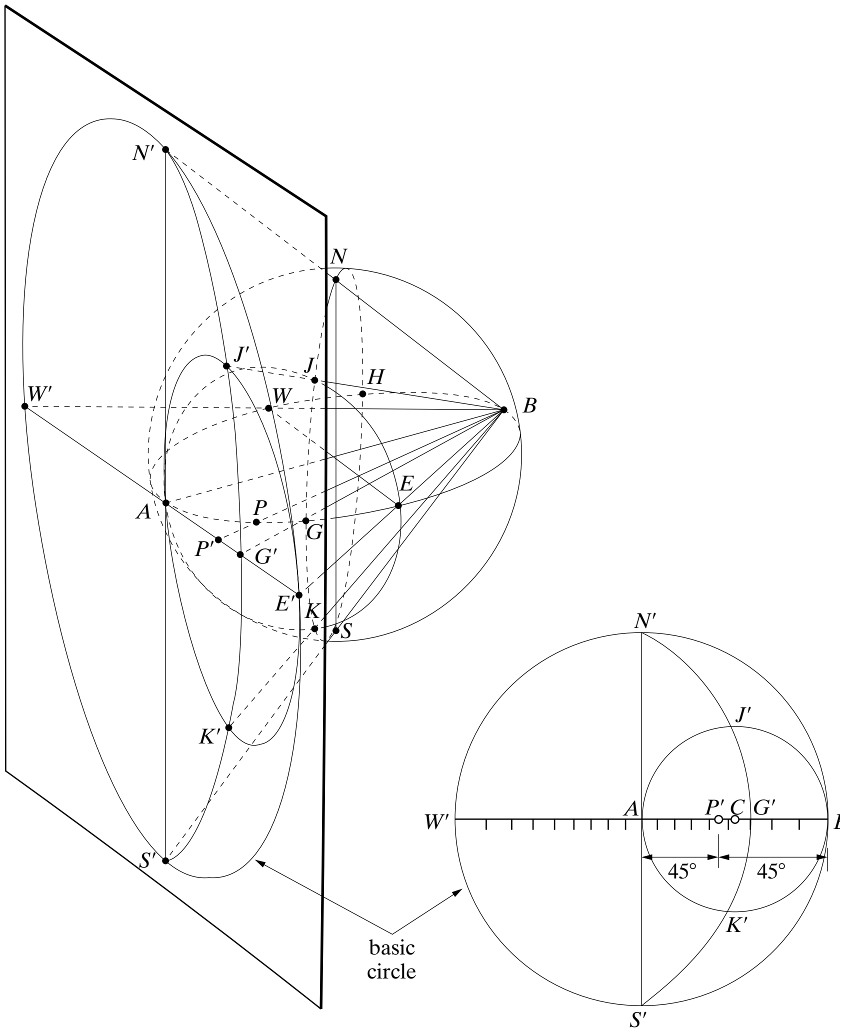

Figure 31 Stereographic projection of great and small circles.

allel to the north-south axis of the sphere. The latitude lines on a Wulff net are small circles extending from side to side and the longitude lines (meridians) are great circles connecting the north and south poles of the net. These nets are available in various sizes and can be plotted readily from equations available elsewhere [G.16], one of 18-cm diameter giving an accuracy of about one degree, which is satisfactory for most problems; to obtain greater precision, either a larger net or mathematical calculation must be used. Wulff nets are used by making the stereographic projection on tracing paper and with the basic circle of the same diameter as that of the Wulff

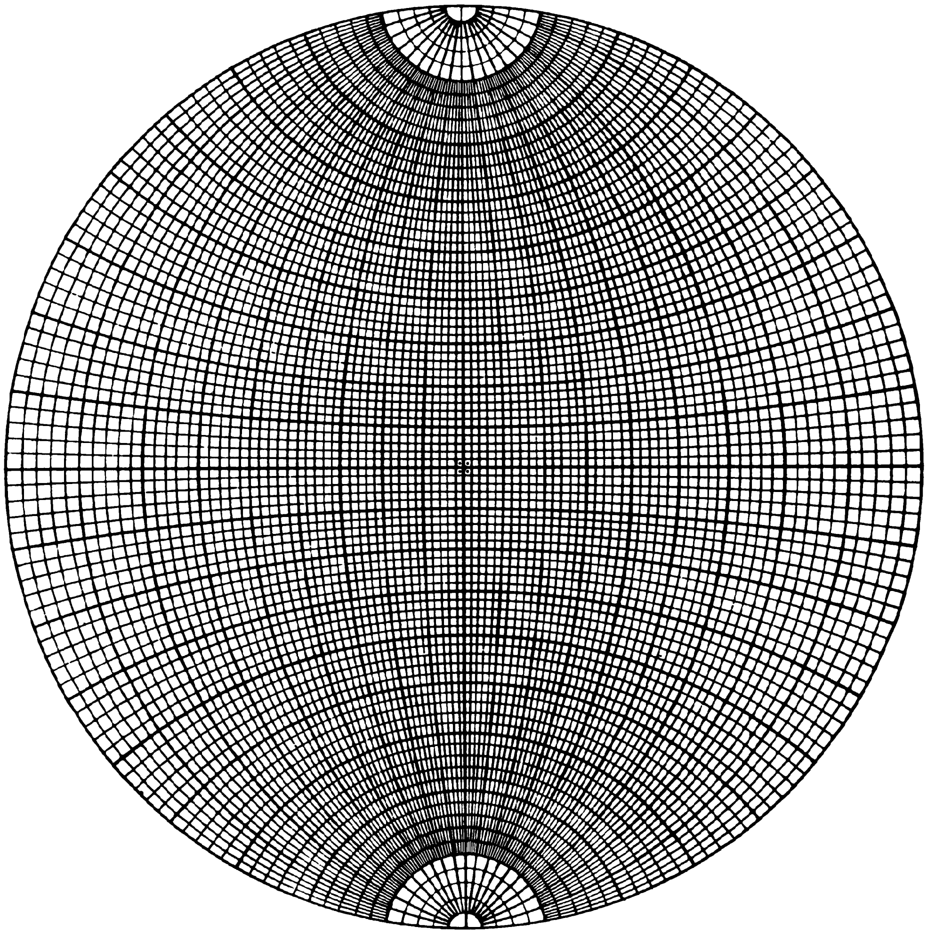

Figure 32 Wulff net drawn to 2° intervals.

net; the projection is then superimposed on the Wulff net, with the centers always coinciding.

Drawing the stereographic projection on tracing paper is not only more economical than drawing it directly on a Wulff net, but it also allows differentiation between the frame of reference of the crystal (represented by the stereographic projection on the paper) and the frame of reference of the laboratory, i.e., of the equipment on which the crystal is positioned for various measurements (the Wulff net). The sample and laboratory reference frames are not identical and both are needed. The sample may be mounted in a number of orientations on the equipment, and it may be necessary to realign the sample relative to the apparatus, e.g. with <001> in different orientations relative to vertical and to the incident beam direction S_0.

To return to the problem of the measuring the angle between two crystal planes, Fig. 29 showed that this angle could be measured on the surface of the sphere along the great circle connecting the poles of the two planes. This measurement can also be carried out on the stereographic projection *if, and only if, the projected poles lie on a great circle*. In Fig. 33, for example, the angle between the planes[8] A and B or C and D can be measured directly, simply by counting the number of degrees separating them along the great circle on which they lie. Note that the angle C-D equals the angle E-F, there being the same difference in latitude between C and D as between E and F.

If the two poles do not lie on a great circle, then the projection is rotated relative to the Wulff net until they do lie on a great circle, where the desired angle measurement can then be made. Figure 34(a) is a projection of the two poles P_1 and P_2 shown in perspective in Fig. 29, and the angle between them is found by the rotation illustrated in Fig. 34(b). This rotation of the projection is equivalent to rotation of the poles on latitude circles of a sphere whose north-south axis is perpendicular to the projection plane.

As shown in Fig. 29, a plane may be represented by its trace in the reference sphere. This trace becomes a great circle in the stereographic projection. Since every point on this great circle is 90° from the pole of the plane, the great circle may be found by rotating the projection until the pole falls on the equator of the underlying Wulff net and tracing that meridian which cuts the equator 90° from the pole, as illustrated in Fig. 35. If this is done for two poles, as in Fig. 36, the angle between the corresponding planes may also be found from the angle of intersection of the two great circles corresponding to these poles; it is in this sense that the stereographic projection is said to be angle-true. This method of angle measurement is not as accurate, however, as that shown in Fig. 34(b).

Often poles must be rotated around various axes. Rotation about an axis normal to the projection is accomplished simply by rotation of the projection around the center of the Wulff net. Rotation about an axis lying in the plane of the projection is performed by, first, rotating the *axis* about the center of the Wulff net until it coincides with the north-south axis if it does not already do so, and, second, moving the poles involved along their respective latitude circles the required number of degrees. Suppose it is required to rotate the poles A_1 and B_1 shown in Fig. 37 by 60° about the NS axis, the direction of motion being from W to E on the projection. Then A_1 moves to A_2 along its latitude circle as shown. B_1, however, can rotate only 40° before reaching the edge of the projection; then it moves 20° in from the edge to the point B'_1 on the other side of the projection, staying always on its own latitude circle. The final position of this pole on the positive side of the projection is at B_2 diametrically opposite B'_1.

(The student should carefully note that the angle between A_1 and A_2, for example, in Fig. 37 is *not* 60°. The pole A_2 is the position of A_1 after a 60° rotation about

---

[8] Here the planes are represented by their normals, as was discussed above.

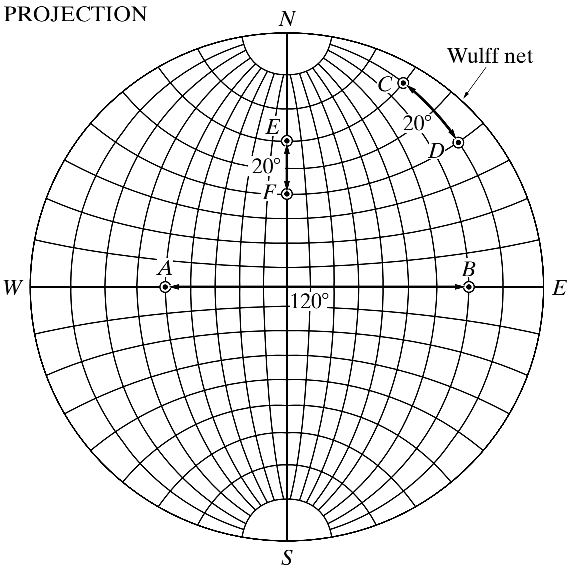

Figure 33 Stereographic projection superimposed on Wulff net for measurement of angle between poles. For illustrative purposes this net is graduated at 10° intervals..

NS, which is not the same thing. Consider the two great circles NA_1S and NA_2S; these are the traces of two planes between which there is a true dihedral angle of 60°. Any pole initially on NA_1S will be on NA_2S after a 60° rotation about *NS*, but the angle between the initial and final positions of the poles will be less than 60°, unless they lie on the equator, and will approach zero as the poles approach *N*.)

Rotation about an axis inclined to the plane of projection is accomplished by compounding rotations about axes lying in and perpendicular to the projection plane. In this case, the given axis must first be rotated into coincidence with one or the other of the two latter axes, the given rotation performed, and the axis then rotated back to its original position. Any movement of the given axis must be accompanied by a similar movement of all the poles on the projection.

For example, suppose A must be rotated about B_1 by 40° in a clockwise direction (Fig. 38). In (a) the pole to be rotated A_1 and the rotation axis B_1 are shown in their initial position. In (b) the projection has been rotated to bring B_1 to the equator of a Wulff net. A rotation of 48° about the *NS* axis of the net brings B_1 to the point B_2 at the center of the net; at the same time A_1 must go to A_2 along a parallel of latitude. The rotation axis is now perpendicular to the projection plane, and the required rotation of 40° brings A_2 to A_3 along a circular path centered on B_2. The operations which brought B_1 to B_2 must now be reversed in order to return B_2 to its original position. Accordingly, B_2 is brought to B_3 and A_3 to A_4, by a 48° reverse rotation about the *NS* axis of the net. In (c) the projection has been rotated back to its initial position, construction lines have been omitted, and only the initial and final positions of the rotated pole are shown. During its rotation about B_1, A_1 moves along the small circle shown. This circle is centered at *C* on the projection and not at its projected center B_1. To find *C*, use the fact that all points on the circle must lie

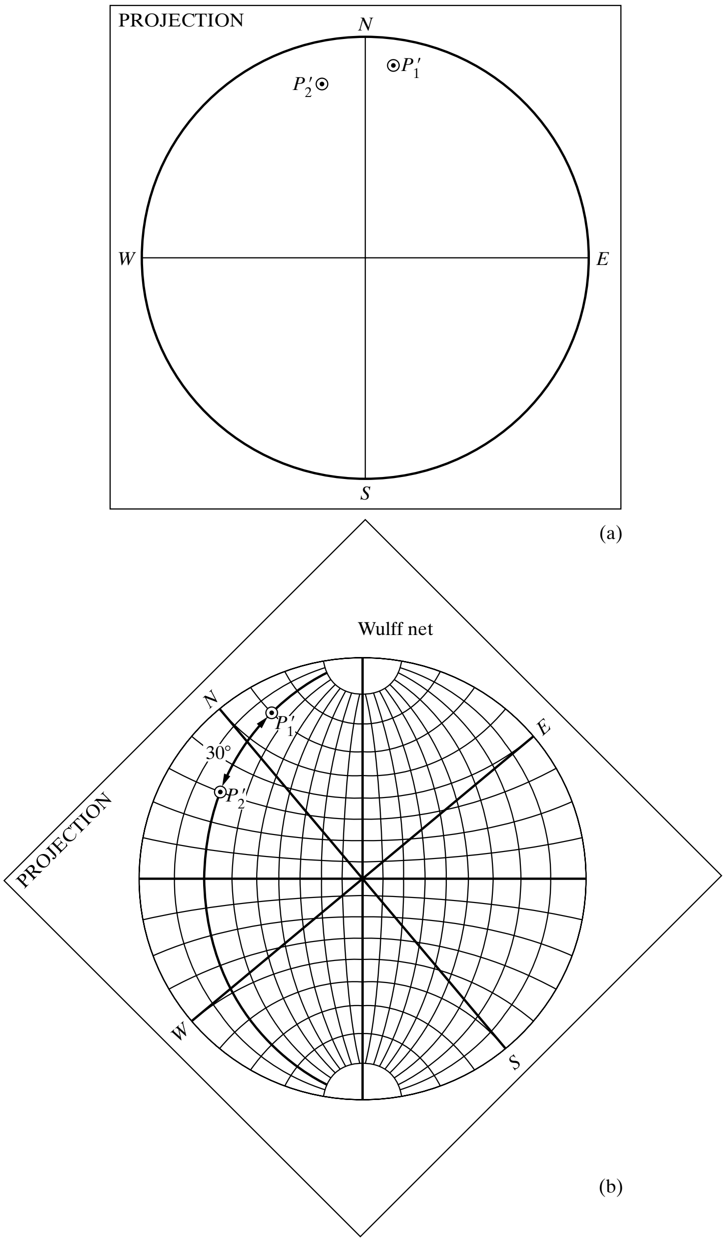

Figure 34 (a) Stereographic projection of poles P_1 and P_2 of Fig. 29. (b) Rotation of projection to put poles on same great circle of Wulff net. Angle between poles = 30°.

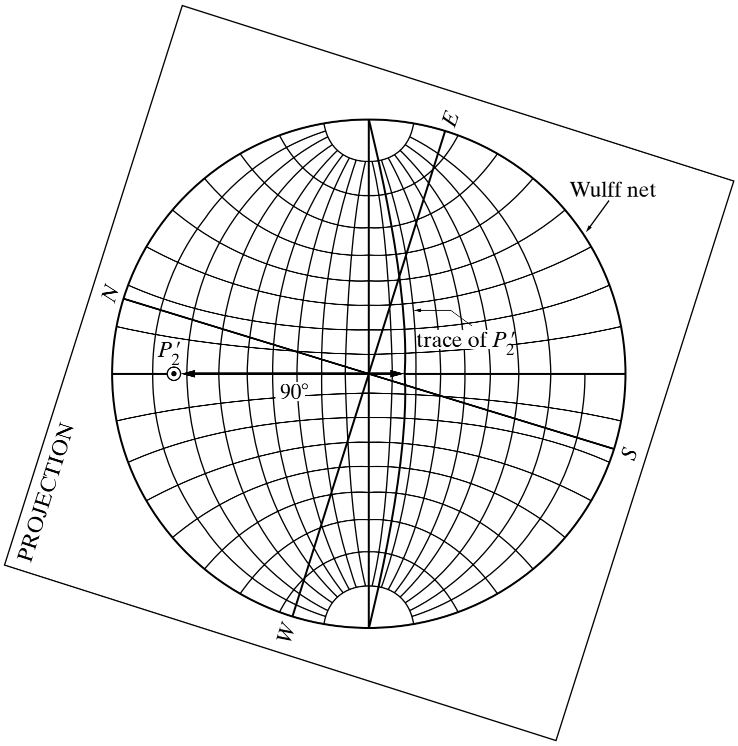

Figure 35 Method of finding the trace of a pole (the pole P'_2 in Fig. 34).

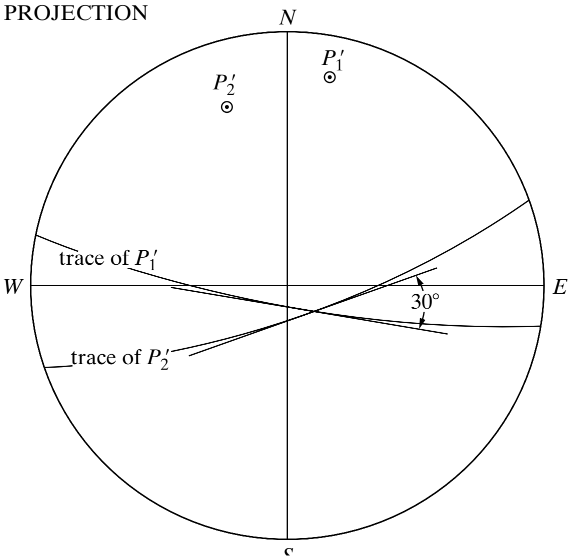

Figure 36 Measurement of an angle between two poles (P_1 and P_2 of Fig. 29) by measurement of the angle of intersection of the corresponding traces.

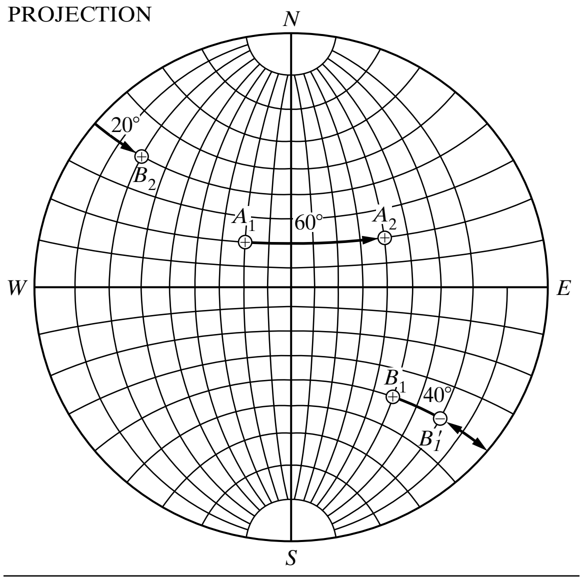

Figure 37 Rotation of poles about *NS* axis of projection.

at equal *angular* distances from B_1; in this case, measurement on a Wulff net shows that both A_1 and A_4 are 76° from B_1. Accordingly, locate other points, such as D, which are 76° from B_1, and, knowing three points on the required circle, its center C can be found by the methods of plane geometry.

In dealing with problems of crystal orientation a *standard projection* is of very great value, since it shows at a glance the relative orientation of all the important planes in the crystal. Such a projection is made by selecting some important crystal plane of low indices as the plane of projection [e.g., (100), (110), (111), or (0001)] and projecting the poles of various crystal planes onto the selected plane. The construction of a standard projection of a crystal requires a knowledge of the interplanar angles for all the principal planes of the crystal. A set of values applicable to all crystals in the cubic system is given in Table 4[TR 4]], but those for crystals of other systems depend on the particular axial ratios involved and must be calculated for each case by the equations given in Appendix: Lattice Geometry. A simple spreadsheet program suffices if interplanar angles are needed beyond those listed in Table 4 (for cubic crystals). Much time can be saved in making standard projections by making use of the zonal relation: the normals to all planes belonging to one zone are coplanar and at right angles to the zone axis. Consequently, the poles of planes of a zone will all lie on the same great circle on the projection, and the axis of the zone will be at 90° from this great circle. Furthermore, important planes usually belong to more than one zone and their poles are therefore located at the intersection of zone circles. It is also helpful to remember that important directions, which in the cubic system are normal to planes of the same indices, are usually the axes of important zones.

Figure 39(a) shows the principal poles of a cubic crystal projected on the (001) plane of the crystal or, in other words, a standard (001) projection. The location of

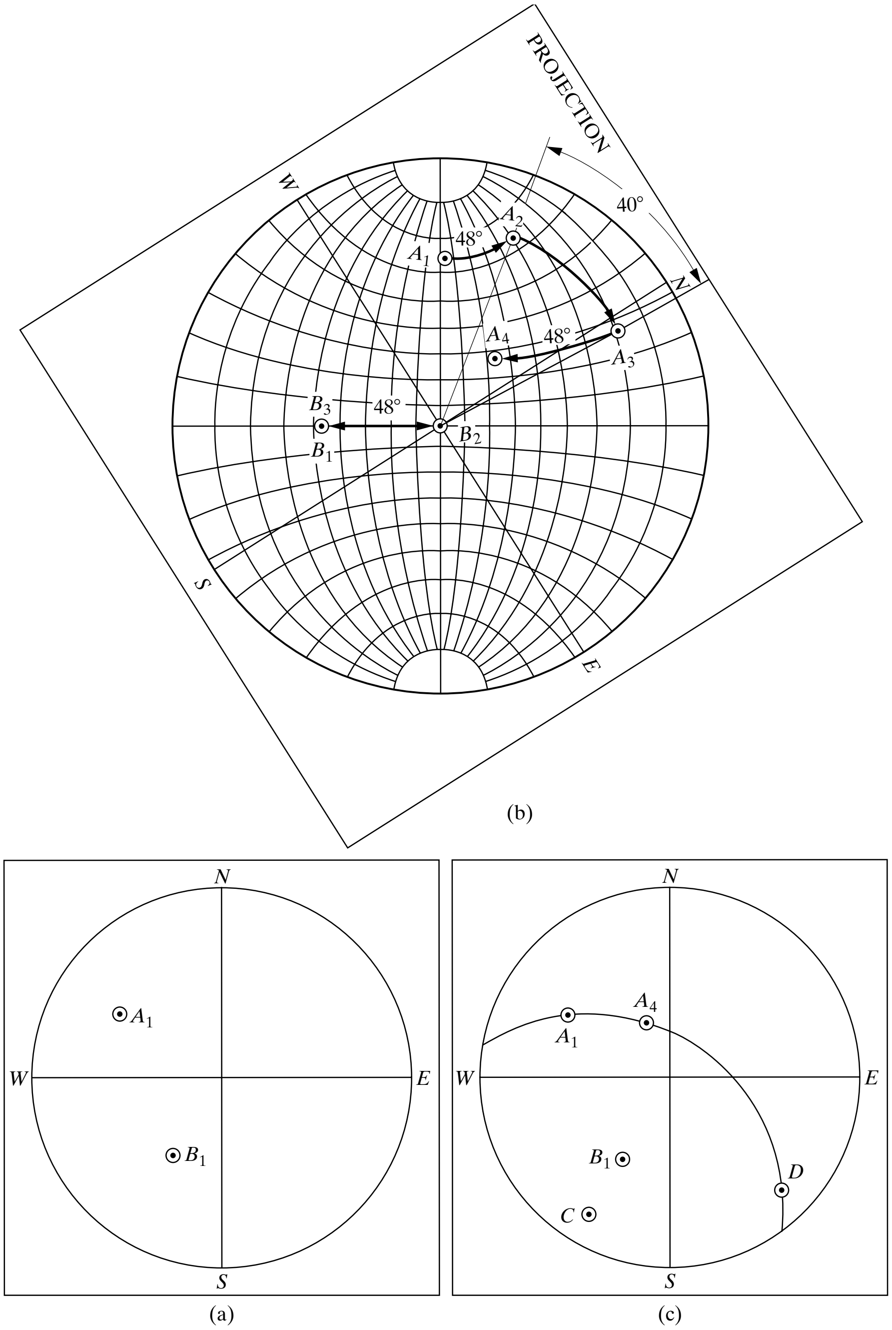

(b)

(a)

(c)

Figure 38 Rotation of a pole about an inclined axis.

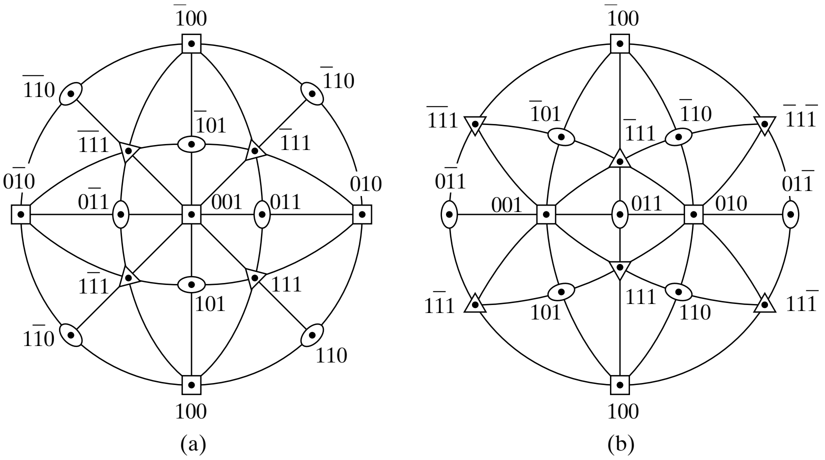

Figure 39 Standard projections of cubic crystals, (a) on (001) and (b) on (011).

the {100} cube poles follows immediately from Fig. 28. To locate the {110} poles first note from Table 4 that they must lie at 45° from {100} poles, which are themselves 90° apart. In this way (011) is found for example, on the great circle joining (001) and (010) and at 45° from each. After all the {110} poles are plotted, the {111} poles are found at the intersection of zone circles. Inspection of a crystal model or drawing or use of the zone relation given by Eq. (6) will show that (111), for example, belongs to both the zone $[\bar{1}01]$ and the zone $[0\bar{1}1]$. The pole of (111) is thus located at the intersection of the zone circle through $(0\bar{1}0)$, (101), and (010) and the zone circle through $(\bar{1}00)$, (011), and (100). This location may be checked by measurement of its angular distance from (010) or (100), which should be 54.7°. The (011) standard projection shown in Fig. 39(b) is plotted in the same manner. Alternatively, it may be constructed by rotating all the poles in the (001) projection 45° to the left about the *NS* axis of the projection, since this operation will bring the (011) pole to the center. In both of these projections symmetry symbols have been given each pole in conformity with Fig. 8(b), and it will be noted that the projection itself has the symmetry of the axis perpendicular to its plane, Figs. 39(a) and (b) having 4-fold and 2-fold symmetry, respectively.

Figure 40 is a standard (001) projection of a cubic crystal with considerably more detail and a few important zones indicated. A standard (0001) projection of a hexagonal crystal (zinc) is given in Fig. 41.

It is sometimes necessary to determine the *Miller indices of a given pole* on a crystal projection, for example the pole *A* in Fig. 42(a), which applies to a cubic crystal. If a detailed standard projection is available, the projection with the unknown pole can be superimposed on it and its indices will be disclosed by its coincidence with one of the known poles on the standard. Alternatively, the method illustrated in Fig. 42 may be used. The pole *A* defines a direction in space, normal to the plane (*hkl*) whose indices are required, and this direction makes angles

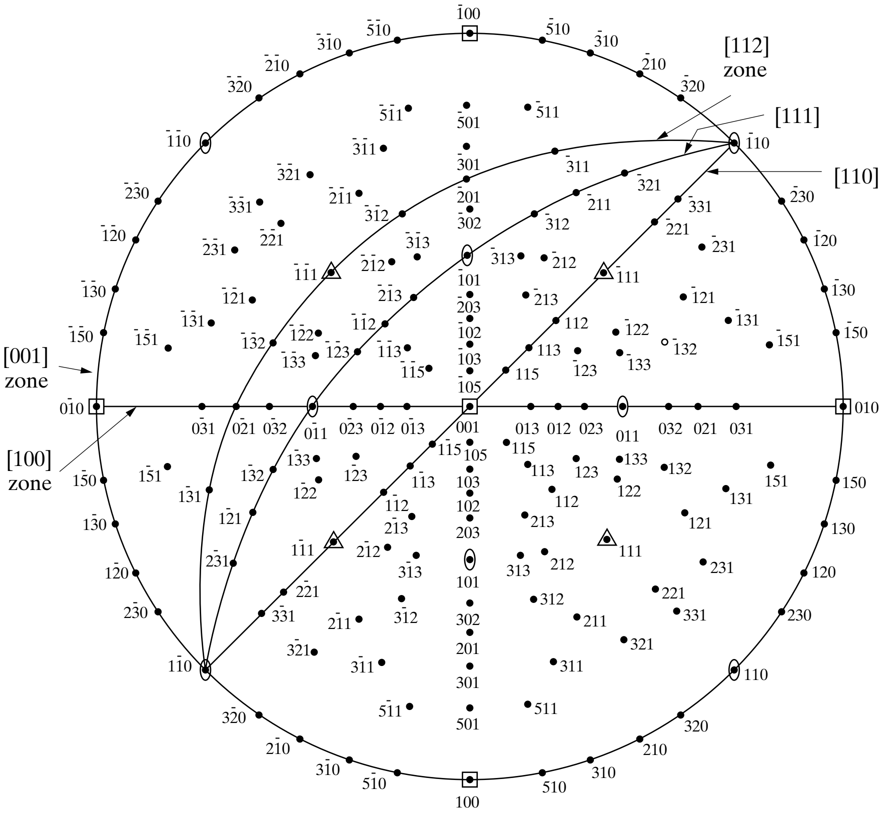

Figure 40 Standard (001) projection of a cubic crystal, after Barrett.

ρ, σ, τ with the coordinate axes **a**, **b**, **c**. These angles are measured on the projection as shown in (a). Let the perpendicular distance between the origin and the (hkl) plane nearest the origin be d [Fig. 42(b)], and let the direction cosines of the line A be $p, q\ r$. Therefore

$$p = \cos\rho = \frac{d}{a/h}, \qquad q = \cos\sigma = \frac{d}{b/k}, \qquad r = \cos\tau = \frac{d}{c/l},$$

$$h{:}k{:}l = pa{:}qb{:}rc. \tag{13}$$

For the cubic system the simple result is that the Miller indices required are in the same ratio as the direction cosines.

The lattice reorientation caused by *twinning* can be shown clearly on the stereographic projection. In Fig. 43 the open symbols are the {100} poles of a cubic crystal projected on the (001) plane. If this crystal is FCC, then one of its possible twin

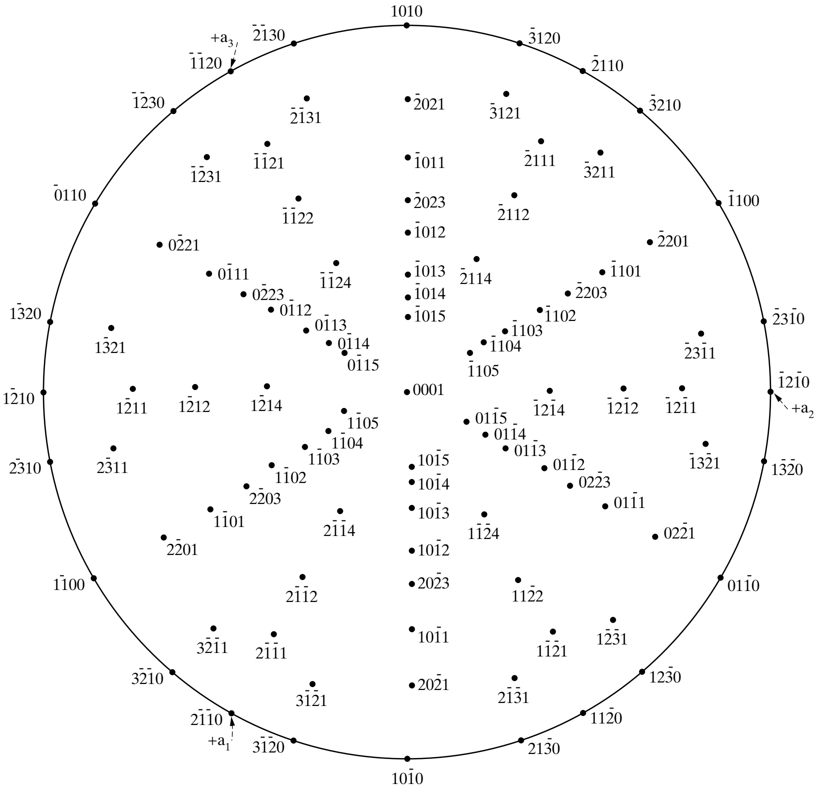

Figure 41 Standard (0001) projection for zinc (hexagonal, $c/a = 1.86$)

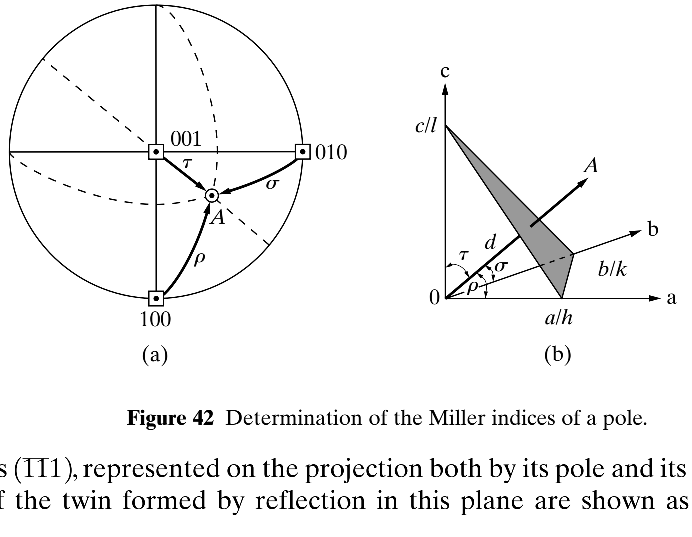

(a) (b)

Figure 42 Determination of the Miller indices of a pole.

planes is $(\bar{1}\bar{1}1)$, represented on the projection both by its pole and its trace. The cube poles of the twin formed by reflection in this plane are shown as solid symbols;

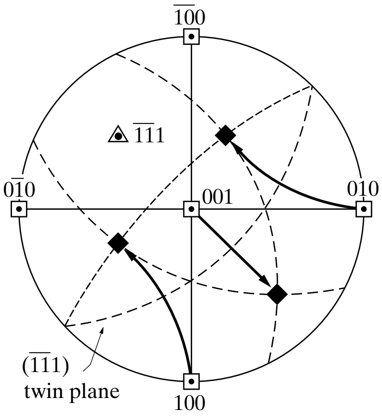

Figure 43 Stereographic projection of an FCC crystal and its twin.

these poles are located by rotating the projection on a Wulff net until the pole of the twin plane lies on the equator, after which the cube poles of the crystal can be moved along latitude circles of the net to their final position.

The main principles of the stereographic projection have now been presented and they will be used later in dealing with various practical problems in x-ray crystallography. Merely reading this section is not sufficient preparation for such problems. Practice with a Wulff net and tracing paper is required before the stereographic projection can be manipulated with facility and before three dimensions can be visualized from what is represented in two.

PROBLEMS

1 Draw the following planes and directions in a tetragonal unit cell: (001), (011), (113), [110], [201], $[\bar{1}01]$. Show cell axes.
2 Show by means of a $(1\bar{1}0)$ sectional drawing that [111] is perpendicular to (111) in the cubic system, but not, in general, in the tetragonal system.
3 In a drawing of a hexagonal prism, indicate the following planes and directions $(1\bar{2}10)$, $(10\bar{1}2)$, $(\bar{1}011)$, [110], $[11\bar{1}]$, [021]. Show cell axes.
4 Derive Eq. (2) of the text.
5 Show that the planes $(1\bar{1}0)$, $(1\bar{2}1)$, and $(\bar{3}12)$ belong to the zone [111].
6 Do the following planes all belong to the same zone: $(\bar{1}10)$, $(\bar{3}11)$, $(\bar{1}\bar{3}2)$? If so, what is the zone axis? Give the indices of any other plane belonging to this zone.
***7** Prepare a cross-sectional drawing of an HCP structure which will show that all atoms do not have identical surroundings and therefore do not lie on a point lattice.
8 Show that *c/a* for hexagonal close packing of spheres is 1.633.
9 Show that the HCP structure (with $c/a = 1.633$) and the FCC structure are equally close-packed, and that the BCC structure is less closely packed than either of the former.

10 The unit cells of several orthorhombic crystals are described below. What is the Bravais lattice of each and how do you know? Do not change axes. (In solving this kind of problem, examining the given atom positions for the existence or nonexistence of centering translations is generally more helpful than making a drawing of the structure.)

a) Two atoms of the same kind per unit cell located at $0\,\frac{1}{2}\,0$, $\frac{1}{2}\,0\,\frac{1}{2}$.

b) Four atoms of the same kind per unit cell located at
$0\,0\,z$, $0\,\frac{1}{2}\,z$, $0\,\frac{1}{2}\,(\frac{1}{2}+z)$, $0\,0\,(\frac{1}{2}+z)$.

c) Four atoms of the same kind per unit cell located at
$x\,y\,z$, $\bar{x}\,\bar{y}\,z$, $(\frac{1}{2}+x)(\frac{1}{2}-y)\bar{z}$, $(\frac{1}{2}-x)(\frac{1}{2}+y)\bar{z}$

d) Two atoms of one kind A located at $\frac{1}{2}\,0\,0$, $0\,\frac{1}{2}\,\frac{1}{2}$; and two atoms of another kind *B* located at $0\,0\,\frac{1}{2}$, $\frac{1}{2}\,\frac{1}{2}\,0$.

***11** Make a drawing, similar to Fig. 23, of a (112) twin in a BCC lattice and show the shear responsible for its formation. Obtain the magnitude of the shear strain graphically.

12 Construct a Wulff net, 18 cm in diameter and graduated at 30° intervals, by the use of compass, dividers, and straightedge only. Show all construction lines.

In some of the following problems, the coordinates of a point on a stereographic projection are given in terms of its latitude and longitude, measured from the center of the projection. Thus, the N pole is 90° N, 0° E, the E pole is 0° N, 90° E, etc.

13 Plane *A* is represented on a stereographic projection by a great circle passing through the N and S poles and the point 0°N, 70°W. The pole of plane *B* is located at 30°N, 50°W.

a) Find the angle between the two planes by measuring the angle between the poles of *A* and *B*.

b) Draw the great circle of plane *B* and demonstrate that the stereographic projection is angle-true by measuring with a protractor the angle between the great circles of *A* and *B*.

***14** Pole *A*, whose coordinates are 20°N, 50°E, is to be rotated about the axes described below. In each case, find the coordinates of the final position of pole *A* and show the path traced out during its rotation.

a) 100° rotation about the *NS* axis, counterclockwise looking from *N* to *S*.

b) 60° rotation about an axis normal to the plane of projection, clockwise to the observer.

c) 60° rotation about an inclined axis B, whose coordinates are 10°S, 30°W, clockwise to the observer.

15 Draw a standard (111) projection of a cubic crystal, showing all poles of the form {100}, {110}, {111} and the important zone circles between them. Compare with Figs. 39(a) and (b).

16 Draw a standard (001) projection of white tin (tetragonal, $c/a = 0.545$), showing all poles of the form {001}, {100}, {110}, {011}, {111} and the important zone circles between them. Compare with Fig. 39(a).

17 Draw a standard (0001) projection of beryllium (hexagonal, $c/a = 1.57$), showing all poles of the form $\{2\bar{1}\bar{1}0\}$, $\{10\bar{1}0\}$, $\{2\bar{1}\bar{1}1\}$, $\{10\bar{1}1\}$ and the important zone circles between them. Compare with Fig. 40.

18 On a standard (001) projection of a cubic crystal, in the orientation of Fig. 36(a), the pole of a certain plane has coordinates 53.3°S, 26.6°E. What are its Miller indices? Verify your answer by comparison of measured angles with those given in Table 4.

***19** Duplicate the operations shown in Fig. 43 and thus find the locations of the cube poles of a $(\bar{1}\bar{1}1)$ reflection twin in a cubic crystal. What are their coordinates?

20 Show that the twin orientation found in Prob. 19 can also be obtained by

- a) Reflection in a $\{112\}$ plane. Which one?
- b) 180° rotation about a $\langle 111 \rangle$ axis. Which one?
- c) 60° rotation about a $\langle 111 \rangle$ axis. Which one?

In (c), show the paths traced out by the cube poles during their rotation.

***21** Plot the great-circle route from Washington, D.C. (39°N, 77°W) to Moscow (56°N, 38°E).

- a) What is the distance between the two cities? (Radius of the earth = 6360 km.)
- b) What is the true bearing of an airplane flying from Washington to Moscow at the beginning, midpoint, and end of the trip? (The bearing is the angle measured clockwise from north to the flight direction. Thus east is 90° and west is 270°.)

22 Cellulose $(C_6H_{10}O_5)_x$ crystallizes as monoclinic crystals with lattice parameters $a = 7.87$ Å, $b = 10.31$ Å, $c = 10.13$ Å, and $\beta = 122°$.

- a) Plot the lattice points for ($h0l$), i.e., in direct space. Superimpose the lattice points of the adjacent ($h0l$) on the first plot.
- b) Plot the $h0l$ net of the reciprocal lattice (i.e., the reciprocal lattice plane containing reciprocal lattice points of the form $h0l$). Superimpose the points of the ($h1l$) reciprocal lattice net onto the first plot.

23 Lutetium has a hexagonal structure with lattice parameters $a = 3.516$ Å and $c = 5.570$ Å. Plot the $h0l$ plane of the reciprocal lattice of this material.

24 Aluminum silicate (mullite) $Al_6Si_2O_{13}$ has an orthorhombic Bravais lattice and lattice parameters $a = 7.5456$ Å, $b = 7.6898$ Å and $c = 2.8842$ Å. Assuming that the Bravais lattice is simple orthorhombic, in one diagram plot the $h0l$ net of the reciprocal lattice, and in a second diagram plot the $0kl$ net of the reciprocal lattice.

REFERENCES

The following books are listed more or less in the order they are encountered in the text

G.1 *International Tables for Crystallography*, Ed. A.J.C Wilson, Vol. A-C (Dordrecht Kluwer Academic Pub. for International Union of Crystallography, 1995). The reference ''book'' for crystallography and diffraction.

G.3 Duncan McKie and Chritine McKie. *Essentials of Crystallography* (Oxford: Blackwell Scientific Publications, 1986). In depth treatment of crystallography, general treatment of various diffraction techniques.

G.4 Watter Borcherdt-Ott. *Crystallography*, 2nd ed. (Berlin: Springer-Verlag, 1995). Focus is on crystallography.

G.5 Donald E, Sands. *Vectors and Tensors in Crystallography* (Reading, MA: Addison-Wesley Pub. Co., 1982). Quite abstract but very valuable to those focussing on vector/tensor mathematics.

G.6 Christopher Hammond. *The Basics of Crystallography and Diffraction,* International Union of Crystallography Text on Crystallography (Oxford: Oxford University Press, 1997). General coverage emphasizing crystallography and general principles of diffraction. Interesting Thumbnail biographical sketches of important workers are included.

G.7 L.H. Schwartz and J.B. Cohen. *Diffraction from Materials*, 2nd ed. (Berlin: Springer-Verlag). Wider ranging thorough coverage of crystallography, instruments and techniques and diffraction theory.

G.8 Strukturbericht (Leipzig: Akademische Verlagsgesellschaft, 1931-1943. Also available from Ann Arbor, MI.: Edwards Brothers, 1943). A series of seven volumes describing crystal structures whose solutions were published in the years 1913 to 1939, inclusive. Continued by: *Structure Reports* (Utrecdht. Oosthoek, 1951 to date). Sponsored by the International Union of Crystallography. The volume numbers begin with Vol. 8, where *Strukturbericht* left off. The results of structure determinations are usually given in sufficient detail that the reader has no need to consult the original paper.

G.10 Charles S. Barrett and T. B. Massalski. *Structure of Metals*, 3rd ed. (New York: McGraw-Hill, 1966). A classic book on the crystallographic aspects of physical metallurgy. Really two books in one, the first part dealing with the theory and methods of diffraction of x-rays, electrons, and neutrons; the second part with the structure of metals in the wider sense of the word. Very lucid account of stereographic projection. Stress measurement, phase transformations, preferred orientation.

G.16 Leonid V. Azaroff. *Elements of X-Ray Crystallography* (New York: McGraw-Hill, 1968). Crystallography, diffraction theory (kinematic and dynamic), structure analysis, single-crystal and powder methods.

ANSWERS TO SELECTED PROBLEMS

7. A section on $(\bar{1}2\bar{1}0)$ will show this

11. Shear strain = 0.707

14. a) 20°S, 30°W; b) 27°S, 48°E; c) 39°S, 61°E

19. 42°N, 26°E; 19°S, 45°W; 42°S, 63°E

21. a) 7890 km b) 34°, 68°, 135°.

This page intentionally left blank

Diffraction I: Geometry

1 INTRODUCTION

After the preliminary survey of the physics of x-rays and the geometry of crystals, this chapter will fit the two together and discuss the phenomenon of x-ray diffraction, which is an interaction of the two. Historically, this is exactly the way this field of science developed. For many years, mineralogists and crystallographers had accumulated knowledge about crystals, chiefly by measurement of interfacial angles, chemical analysis, and determination of physical properties. There was little knowledge of interior structure, however, although some very shrewd guesses had been made, namely, that crystals were built up by periodic repetition of some unit, probably an atom or molecule, and that these units were situated some 1 or 2 Å apart. On the other hand, there were indications, but only indications, that x-rays might be electromagnetic waves about 1 or 2 Å in wavelength. In addition, the phenomenon of diffraction was well understood, and it was known that diffraction, as of visible light by a ruled grating, occurred whenever wave motion encountered a set of regularly spaced scattering objects, provided that the wavelength of the wave motion was of the same order of magnitude as the repeat distance between the scattering centers.

Such was the state of knowledge in 1912 when the German physicist von Laue (1879-1960) took up the problem. Stimulated by a discussion with P. P. Ewald of Ewald's doctoral dissertation (scattering of electromagnetic waves by an array of harmonic oscillators [1]), von Laue reasoned that, *if* crystals were composed of regularly spaced atoms which might act as scattering centers for x-rays, and *if* x-rays were electromagnetic waves of wavelength about equal to the interatomic distance in crystals, then it should be possible to diffract x-rays by means of crystals. Under his direction, Friedrich and Knipping conducted experiments to test this hypothesis: A crystal of copper sulfate was set up in the path of a narrow beam of x-rays and a photographic plate was arranged to record the presence of diffracted beams, if any. The second attempt was successful and showed without doubt that x-rays *were* diffracted by the crystal out of the primary beam to form a pattern of spots on the photographic plate [2]. These experiments proved, at one and the same time, the

From Chapter 3 of *Elements of X-Ray Diffraction*, Third Edition. B.D. Cullity, S.R. Stock.

wave nature of x-rays and the periodicity of the arrangement of atoms within a crystal. Hindsight is always easy and these ideas appear quite simple now, when viewed from the vantage point of ninety years' development of the subject, but they were not at all obvious in 1912, and von Laue's hypothesis and its experimental verification must stand as a great intellectual achievement [G.11]

The account of these experiments was read with great interest by two English physicists, W. H. Bragg (1862-1942) and his son W. L. Bragg (1890-1971). The latter, although only a young student at the time-it was still the year 1912-successfully analyzed the Laue experiment and was able to express the necessary conditions for diffraction in a considerably simpler mathematical form than that used by von Laue [3]. He also attacked the problem of crystal structure with the new tool of x-ray diffraction and, in the following year, solved the structures of NaCl, KCl, KBr, and KI, all of which have the NaCl structure; these were the first complete crystal-structure determinations ever made [4]. The simpler structures of metals like iron and copper were not determined until later.

2 DIFFRACTION

Diffraction is due essentially to the existence of certain phase relations between two or more waves, and it is advisable, at the start, to get a clear notion of what is meant by phase relations. Consider a beam of x-rays, such as beam **1** in Fig. 1, proceeding from left to right. For convenience only, this beam is assumed to be plane-

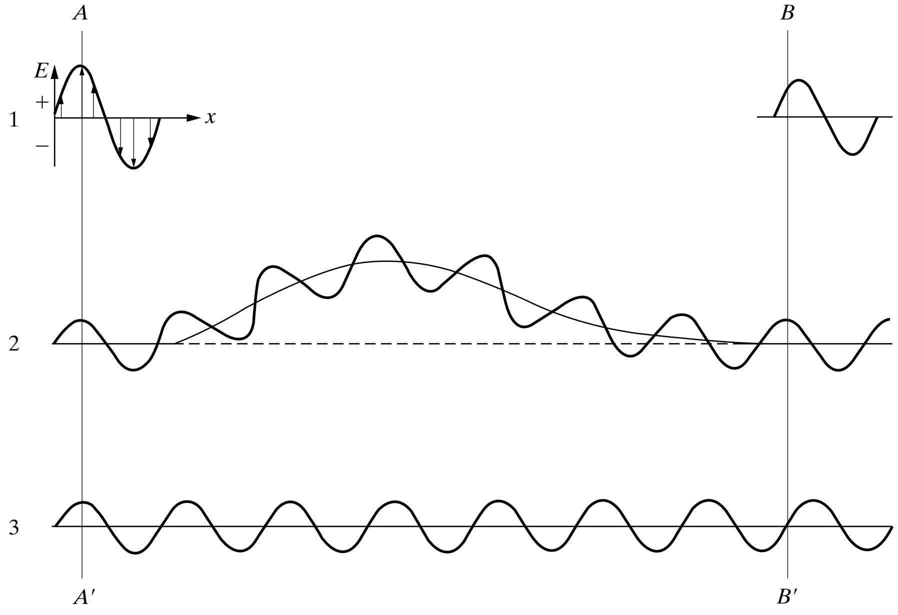

Figure 1 Effect of path difference on relative phase.

polarized so that the electric field vector **E** always lies in the plane of the drawing. Imagine this beam to be composed of two equal parts, ray **2** and ray **3**, each of half the amplitude of beam **1**. These two rays, on the wave front AA', are said to be completely *in phase* or in step; i.e., their electric-field vectors have the same magnitude and direction at the same instant at any point x measured along the direction of propagation of the wave. A *wave front* is a surface perpendicular to this direction of propagation.

Now consider an imaginary experiment, in which ray **3** is allowed to continue in a straight line but ray **2** is diverted by some means into a curved path before rejoining ray **3**. What is the situation on the wave front BB' where both rays are proceeding in the original direction? On this front, the electric vector of ray **2** has its maximum value at the instant shown, but that of ray **3** is zero. The two rays are therefore *out of phase*. Adding these two imaginary components of the beam together, produces the form of beam **1** shown in the upper right of the drawing. If the amplitudes of rays **2** and **3** are each 1 unit, then the amplitude of beam **1** at the left is 2 units and that of beam **1** at the right is 1.4 units, if a sinusoidal variation of **E** with x is assumed.

Two conclusions may be drawn from this illustration:

1. Differences in the length of the path traveled lead to differences in phase.
2. The introduction of phase differences produces a change in amplitude.

The greater the path difference, the greater the difference in phase, since the path difference, measured in wavelengths, exactly equals the phase difference, also measured in wavelengths. If the diverted path of ray **2** in Fig. 1 were a quarter wavelength longer than shown, the phase difference would be a half wavelength. The two rays would then be completely out of phase on the wave front BB' and beyond, and they would therefore annul each other, since at any point their electric vectors would be either both zero or of the same magnitude and opposite in direction. If the difference in path length were made three quarters of a wavelength greater than shown, the two rays would be one complete wavelength out of phase, a condition indistinguishable from being completely in phase since in both cases the two waves would combine to form a beam of amplitude 2 units, just like the original beam. Thus, two rays are completely in phase whenever their path lengths differ either by zero or by a whole number of wavelengths.

Differences in the path length of various rays arise quite naturally when considering how a crystal diffracts x-rays. Figure 2 shows a section of a crystal, its atoms arranged on a set of parallel planes $A, B, C, D, \ldots$, normal to the plane of the drawing and spaced a distance d' apart. Assume that a beam of perfectly parallel, perfectly monochromatic x-rays of wavelength λ is incident on this crystal at an angle θ, called the Bragg angle, where θ is measured between the incident beam and the particular crystal planes under consideration.

Whether this incident beam of x-rays will be diffracted by the crystal and, if so, under what conditions, are the questions central to this chapter. *A diffracted beam may be defined as a beam composed of a large number of scattered rays mutually reinforcing one another*. Diffraction is, therefore, essentially a scattering phenome-

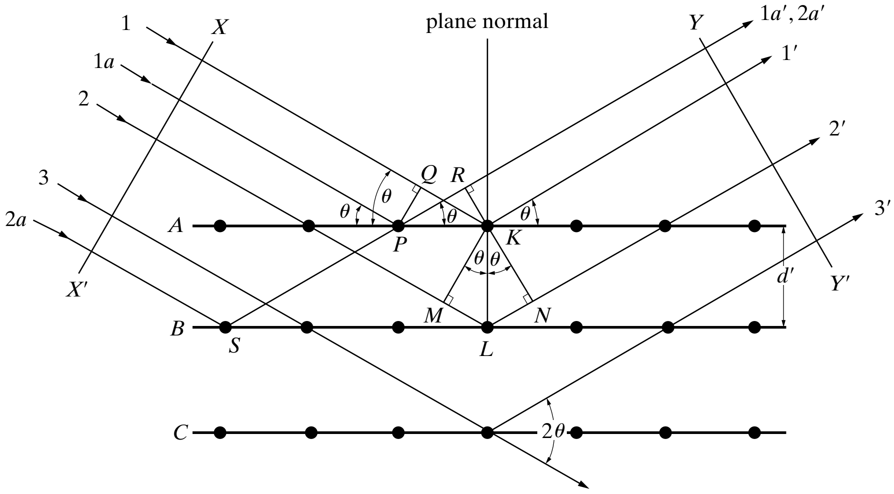

Figure 2 Diffraction of x-rays by a crystal.

non and not one involving any "new" kind of interaction between x-rays and atoms. Atoms scatter incident x-rays in all directions and the following paragraphs demonstrate that in some of these directions the scattered beams will be completely in phase and so reinforce each other to form diffracted beams.

For the particular conditions described by Fig. 2, the only diffracted beam formed is that shown, namely one making an exit angle θ with respect to the diffraction planes[1] equal to the angle θ of incidence. This will be shown, first, for one plane of atoms and, second, for all the atoms making up the crystal. Consider rays **1** and **1a** in the incident beam; they strike atoms K and P in the first plane of atoms and are scattered in all directions. Only in the directions 1′ and 1a′, however, are these scattered beams completely in phase and so capable of reinforcing one another; they do so because the difference in their length of path between the wave fronts XX' and YY' is equal to

$$QK - PR = PK\cos\theta - PK\cos\theta = 0.$$

Similarly, the rays scattered by all the atoms in the first plane in a direction parallel to 1′ are in phase and add their contributions to the diffracted beam. This will be true of all the planes separately, and it remains to find the condition for reinforcement of rays scattered by atoms in different planes. Rays **1** and **2**, for example, are scattered by atoms K and L, and the path difference for rays $\mathbf{1}K1'$ and $\mathbf{2}L2'$ is

$$ML + LN = d'\sin\theta + d'\sin\theta.$$

---

[1] Note that these angles are defined differently in x-ray diffraction and in general optics. In the latter, the angles of incidence and reflection are the angles which the incident and reflected beams make with the *normal* to the reflecting surface.

This is also the path difference for the overlapping rays scattered by S and P in the direction shown, since in this direction there is no path difference between rays scattered by S and L or P and K. Scattered rays $1'$ and $2'$ will be completely in phase if this path difference is equal to a whole number n of wavelengths, or if

$$n\lambda = 2d' \sin \theta. \tag{1}$$

This relation was first formulated by W. L. Bragg and is known as Bragg's law. It states the essential condition which must be met if diffraction is to occur. n is called the order of diffraction; it may take on any integral value consistent with $\sin\theta$ not exceeding unity and is equal to the number of wavelengths in the path difference between rays scattered by *adjacent* planes. Therefore, for fixed values of λ and d', there may be several angles of incidence $\theta_1, \theta_2, \theta_3, \ldots$ at which diffraction may occur, corresponding to $n = 1, 2, 3, \ldots$. In a first-order reflection ($n = 1$), the scattered rays $1'$ and $2'$ of Fig. 2 would differ in length of path (and in phase) by one wavelength, rays $1'$ and $3'$ by two wavelengths, rays $1'$ and $4'$ by three wavelengths, and so on throughout the crystal. The rays scattered by all the atoms in all the planes are therefore completely in phase and reinforce one another (constructive interference) to form a diffracted beam in the direction shown. In all other directions of space the scattered beams are out of phase and annul one another (destructive interference). The diffracted beam is rather strong compared to the sum of all the rays scattered in the same direction, simply because of the reinforcement which occurs,[2] but is extremely weak compared to the incident beam since the atoms of a crystal scatter only a small fraction of the energy incident on them.

It is helpful to distinguish three scattering modes:

1. By atoms arranged randomly in space, as in a monatomic gas. This scattering occurs in *all* directions and is weak. Intensities add.
2. By atoms arranged periodically in space, as in a perfect crystal:
    a) In a very few directions, those satisfying Bragg's law, the scattering is strong and is called diffraction. Amplitudes add.

---

[2] If the scattering atoms were not arranged in a regular, periodic fashion but in some independent manner, then the rays scattered by them would have a random phase relationship to one another. In other words, there would be an equal probability of the phase difference between any two scattered rays having any value between zero and one wavelength. Neither constructive nor destructive interference takes place under these conditions, and the intensity of the beam scattered in a particular direction is simply *the sum of the intensities* of all the rays scattered in that direction. If there are N scattered rays each of amplitude A and therefore of intensity A^2 in arbitrary units, then the intensity of the scattered beam is NA^2. On the other hand, if the rays are scattered by the atoms of a crystal in a direction satisfying Bragg's law, then they are all in phase and the amplitude of the scattered beam is *the sum of the amplitudes* of the scattered rays. The total amplitude is then N times the amplitude A of each scattered ray, or NA. The intensity of the scattered beam is therefore N^2A^2, or N times as large as if reinforcement had not occurred. Since N is very large for the scattering of x-rays from even a small bit of crystal, ($N = 1.1 \times 10^{19}$ atoms for 1 mg of iron), the role of reinforcement in producing a strong diffracted beam is considerable.

b) In most directions, those not satisfying Bragg's law, there is no scattering because the scattered rays cancel one another.

At first glance, the diffraction of x-rays by crystals and the reflection of visible light by mirrors appear very similar, since in both phenomena the angle of incidence is equal to the angle of reflection. It seems that the planes of atoms act as little mirrors which "reflect" the x-rays. Diffraction and reflection, however, differ fundamentally in at least three aspects:

1. The diffracted beam from a crystal is built up of rays scattered by all the atoms of the crystal which lie in the path of the incident beam. The reflection of visible light takes place in a thin surface layer only.
2. The diffraction of monochromatic x-rays takes place only at those particular angles of incidence which satisfy Bragg's law. The reflection of visible light takes place at any angle of incidence.
3. The reflection of visible light by a good mirror is almost 100 percent efficient. The intensity of a diffracted x-ray beam is extremely small compared to that of the incident beam.

Despite these differences, the terms "reflecting planes" and "reflected beams" are often used when diffracting planes and diffracted beams are described. This is common usage and, from now on, these terms will appear without quotation marks but with the tacit understanding that diffraction is meant and not reflection.[3] Also, always remember it is the constructive interference of scattering from the atoms which produces diffracted intensity. Lack of understanding of what the commonly used term "diffracting planes" represents, can lead to errors.

To sum up, diffraction is essentially a scattering phenomenon in which a large number of atoms cooperate. Since the atoms are arranged periodically on a lattice, the rays scattered by them have definite phase relations between them; these phase relations are such that destructive interference occurs in most directions of scattering, but in a few directions constructive interference takes place and diffracted beams are formed. Strictly speaking, for interference to occur, the interacting waves must be superimposed physically (i.e., waves $1a'$ and $2a'$ in Fig. 2), but given the cloud-like distribution of electrons around the nucleus of each scattering atom, the relatively large depth of penetration of the x-ray beam and the large number of scattering events which typically occur in a sample, the requirement for physical superposition is normally left implicit in treatments of diffraction. The two essentials are a wave motion capable of interference (x-rays) and a set of periodically arranged scattering centers (the atoms of a crystal).

---

[3] For the sake of completeness, it should be mentioned that x-rays *can* be totally reflected by a solid surface, just as visible light is by a mirror, but only at very small angles of incidence (below about one degree). X-ray reflectivity is a powerful technique for studying surfaces and internal interfaces which lie in the vicinity of the surface [5]. Commercial instrumentation ranging from high resolution diffractometers to dedicated x-ray reflectometers are available, and the theory and experimental methods are summarized elsewhere [6, 7].

3 BRAGG'S LAW

Two geometrical facts are worth remembering: (1) The incident beam, the normal to the diffraction plane, and the diffracted beam are always coplanar. (2) The angle between the diffracted beam and the transmitted beam is always 2θ. This is known as the diffraction angle, and it is this angle, rather than θ, which is usually measured experimentally.

As previously stated, diffraction in general occurs only when the wavelength of the wave motion is of the same order of magnitude as the repeat distance between scattering centers. This requirement follows from Bragg's law. Since $\sin\theta$ cannot exceed unity,

$$\frac{n\lambda}{2d'} = \sin\theta < 1. \tag{2}$$

Therefore, $n\lambda$ must be less than $2d'$. For diffraction, the smallest value of n is 1. ($n = 0$ corresponds to the beam diffracted in the same direction as the transmitted beam. It cannot be observed.) Therefore the condition for diffraction at any observable angle 2θ is

$$\lambda < 2d'. \tag{3}$$

For most sets of crystal planes d' is of the order of 3 Å or less, which means that λ cannot exceed about 6 Å. A crystal could not possibly diffract ultraviolet radiation, measuring for example, of wavelength about 500 Å. On the other hand, if λ is very small the diffraction angles requires very specialized equipment.

Bragg's law may be written in the form

$$\lambda = 2\frac{d'}{n}\sin\theta. \tag{4}$$

Since the coefficient of λ is now unity, a reflection of any order can be considered as a first-order reflection from planes, real or fictitious, spaced at a distance $1/n$ of the previous spacing. This turns out to be a real convenience, so that $d = d'/n$ and

$$\lambda = 2d\sin\theta. \tag{5}$$

This form will be used throughout this book.

This usage is illustrated by Fig. 3. Consider the second-order 100 reflection[4] shown in (a) for a simple cubic substance. Since it is second-order, the path difference ABC between rays scattered by adjacent (100), say i and $i + 1$ planes must be two whole wavelengths.

---

[4] This means the reflection from the (100) planes. Conventionally, the Miller indices of a diffraction plane *hkl*, written without parentheses, stand for the diffracted beam from the plane (*hkl*).

In the simple cubic structure all of the lattice points are on one of the (100) and are separated by $d = a/(1^2 + 0 + 0)^{0.5} = a$. If there were scatterers on the dotted plane midway between the *i*th and (*i*+1)th planes (Fig. 3b),[5] they would scatter one wavelength out of phase with the atoms on the *i*th and (*i*+1)th planes. The ith, (*i*+1/2)th and (*i*+1)th planes are, therefore, positions of equal phase in the diffracted beam. This periodicity, that for second order 100 diffraction, is *a*/2 and is indicated by d_{200}. Note that the formula for *d*-spacings using $h = 2$, $k = 0$ and $l = 0$ yields $d_{200} = a/2$. Similar considerations hold for diffraction of the third, fourth, etc., orders of (100), i.e., the, 300, 400, etc. reflections. In general, *n*th-order diffraction from (*hkl*) with spacing d' may be considered as a first-order diffraction from (*nh nk nl*) with spacing $d = d'/n$. Note that this convention accords with the definition of Miller indices since (*nh nk nl*) are the Miller indices of planes parallel to (*hkl*) but with 1/*n*th the spacing of the latter. The presence or absence of atoms at different positions within the unit cell, such as on the (*i*+1/2)th plane in Fig. 3, has a profound effect on the diffracted intensity observed for different reflections.

4 LAUE'S EQUATIONS

Bragg's equation describes diffraction in terms of a scalar equation. Crystals are, in general, three-dimensional entities, and, for greatest generality, equations developed to describe the diffracted beam directions need to be expressed in terms of vectors.

Consider a one-dimensional array of scatterers spaced *a* apart (Fig. 4). Let the incident beam direction be denoted $\mathbf{S}_0$ and make an angle α_o with the line of scatterers, and define the diffracted beam direction as $\mathbf{S}$. In order for the path difference to be an integral multiple of wavelengths $h\lambda$, the angle α which $\mathbf{S}$ makes with the line of scatterers must satisfy:

$$a(\cos\alpha - \cos\alpha_0) = h\lambda. \tag{6a}$$

This equation is satisfied for a series of cones with axes concentric with the row of scatterers and with semi-apex angle of α.

Next consider a two-dimensional network of scatterers with spacing *a* along one axis and *b* along the second axis. If the angles $\mathbf{S}_0$ and $\mathbf{S}$ make with the rows spaced *b* apart are β_0 and β, respectively, a second equation must simultaneously be satisfied in order for constructive interference to occur:

$$b(\cos\beta - \cos\beta_0) = k\lambda, \tag{6b}$$

where *k* is an integer. Similarly, a third condition arises when one considers a three-dimensional array of scatterers with spacing *c* in the third dimension:

---

[5] The dotted plane in Fig. 3 *is* occupied by atoms in the face-centered and body-centered Bravais lattices.

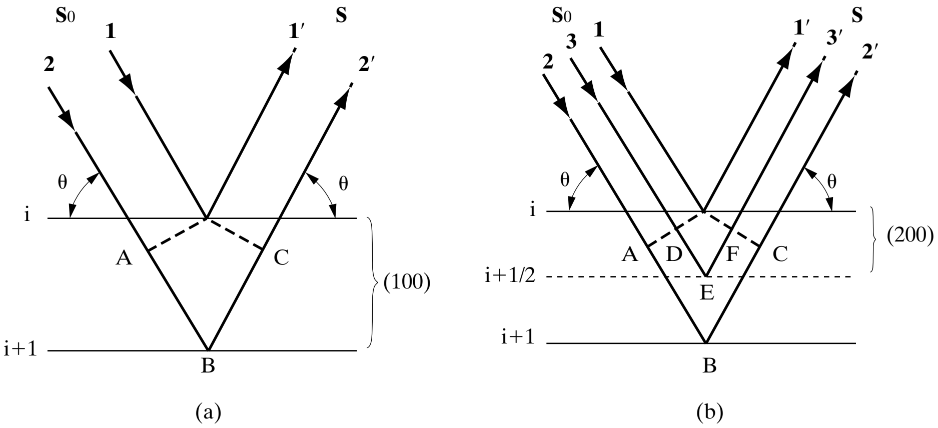

Figure 3 Equivalence of (a) a second-order 100 reflection and (b) a first-order 200 reflection. The incident and diffracted beam directions are $\mathbf{S}_0$ and $\mathbf{S}$, respectively, and the *i*th, (*i*+1/2)th and (*i*+1)th planes are labeled.

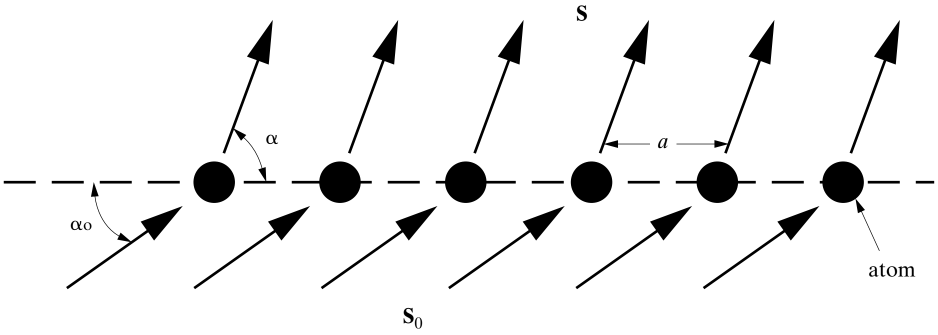

Figure 4 One-dimensional array of scatters with periodicity *a*, beam $\mathbf{S}_0$ incident at angle α_o and diffracted beam **S** at angle α.

$$c(\cos\gamma - \cos\gamma_0) = l\lambda, \tag{6c}$$

where *l* is an integer. The Eq. 6 are collectively known as Laue's Equations and emphasize the three-dimensional nature of diffraction. Generally, Bragg's law is more convenient to use for numerical purposes, and, as will be shown in the following section, the three-dimensionality of diffraction is more easily seen using the reciprocal lattice.

5 RECIPROCAL LATTICE AND DIFFRACTION

The reciprocal lattice can also be used to determine the geometric conditions for diffraction. First, in the direct space lattice consider the interference between scattering from two lattice points O and A (Fig. 5). Point O is at the origin of the lattice, and point A is located relative to O by vector **OA** = $p\mathbf{a}_1 + q\mathbf{a}_2 + r\mathbf{a}_3$, where *r, q,* and *p* are integers. Note that *p, q,* and *r* must be integers since both O and A are lattice points. For x-rays of wavelength λ, incident beam $\mathbf{S}_0$ and diffracted beam **S**, the path difference δ for x-rays scattered from O and A is

$$\begin{aligned}\delta &= \mathrm{uA} + \mathrm{Av} \\ &= \mathrm{Om} + \mathrm{On} \\ &= \mathrm{S}_0 \cdot \mathrm{OA} + (-\mathrm{S}) \cdot \mathrm{OA} \\ &= -\mathrm{OA} \cdot (\mathrm{S} - \mathrm{S}_0), \qquad (7)\end{aligned}$$

and the corresponding phase difference ϕ (in radians) is

$$\phi = 2\pi\delta/\lambda = -\frac{2\pi(\mathrm{S} - \mathrm{S}_0)\cdot \mathrm{OA}}{\lambda} = -2\pi \cdot \mathscr{S} \cdot \mathbf{OA} \qquad (8)$$

where **S** and $\mathbf{S}_0$ are unit vectors and $\mathscr{S} = (\mathrm{S} - \mathrm{S}_0/\lambda)$ and is termed the scattering vector. Note that $\mathscr{S}$ is in units of Å^{-1}. Implicit in this treatment is that vectors $\mathbf{a}_i$ are for a primitive unit cell for whatever crystal system is being considered. Giving the vectors $\mathbf{a}'_i$ in terms of a non-primitive unit cell has important consequences, however, which are beyond the scope of this chapter.

The link to the reciprocal latttice comes through defining $\mathscr{S}$ as a vector in that space, i.e., by letting

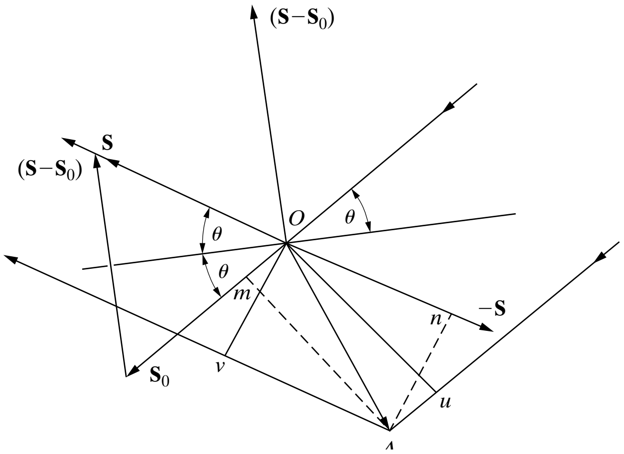

Figure 5 X-ray scattering by atoms at *O* and *A*. After Guinier [G.13].

$$\mathscr{S} = h'\mathbf{b_1} + k'\mathbf{b_2} + l'\mathbf{b_3}, \tag{9}$$

and noting that h', k' and l' have no special significance and are continuously variable. After substituting the vector expressions for $\mathscr{S}$ and **OA** in Eq. 8, the result is

$$\begin{aligned}\phi &= -2\pi(h'\mathbf{b_1} + k'\mathbf{b_2} + l'\mathbf{b_3})\cdot(p\mathbf{a_1} + q\mathbf{a_2} + r\mathbf{a_3}) \\ &= -2\pi(h'p + k'q + l'r).\end{aligned} \tag{10}$$

In order for diffraction to occur, ϕ must be an integral multiple of 2π; in order for this to be true simultaneously for many p, q, r (i.e., for many different scattering sites) h', k' and l' must be integers which will now be written h, k and l. Thus, $\mathscr{S}$ or $(S - S_0/\lambda)$ must start and end on points of the reciprocal lattice.

The conditions for diffraction can be represented graphically in reciprocal space using the Ewald sphere construction [2.3]. While the reciprocal lattice of a three dimensional crystal is also three dimensional, a convenient plane through reciprocal space normally is plotted; the reciprocal lattice plane perpendicular to $\mathbf{b}_3$ and through the origin of the reciprocal lattice is used to illustrate the Ewald sphere construction. The first step in plotting the Ewald sphere representation of diffraction is to construct the reciprocal lattice in question. Next one plots S_0/λ parallel to the incident beam direction, giving it length $1/\lambda$ Å^{-1} and terminating it at the origin of the reciprocal lattice. The sphere centered at the origin of vector S_0/λ and with radius $1/\lambda$ represents the locus of possible **S** for wavelength λ and is termed the Ewald sphere. In order for diffraction to be observed (i.e., for Bragg's law to be satisfied), **S** and, hence, $\mathscr{S}$ must end on a reciprocal lattice point. This means that $\mathscr{S}$ is parallel to the normal of (*hkl*)and has magnitude $1/d_{\text{hkl}}$, and Bragg's law (or the Laue equations) can be derived directly from the Ewald sphere construction. Perhaps the most important point to remember is that the Ewald sphere must intersect a reciprocal lattice point *hkl* for diffraction from (*hkl*) to be observed.

An important property of the transformation from the direct space lattice to the reciprocal lattice (and the reverse transformation) is that vectors in one lattice are physically parallel to their counterpart in the other lattice. For example, the direction from the Ewald sphere center to the reciprocal lattice point *hkl* on the sphere is **S** and defines the direction along which the diffracted beam $\mathbf{S}_{\text{hkl}}$ is observed. In direct space the parallel vector, also written as **S**, defines the diffracted beam direction. It is possible for certain $\mathbf{S}_0$ to produce two or more diffracted beams simultaneously, but, given the wavelengths of x-rays used in diffractometry and the lattice parameters of crystals, this possibility is unlikely. [6]

---

[6] In the case of electrons used in the transmission electron microscope, wavelengths are at least an order of magnitude smaller than those of x-rays used in diffractometry. The result, as will be seen in Sec. 9, is that multiple diffracted beams are the rule rather than the exception for electron diffraction.

There is another way of viewing the direct space to reciprocal space transformation. Note that the incident and diffracted beams $\mathbf{S}_0$ and $\mathbf{S}$ each consist of many parallel rays displaced from each other in space. Then the transformation to reciprocal space can be viewed as mapping all parallel rays to a single point, just as was seen for the periodic "planar" arrays of lattice point being mapped onto a single point in the reciprocal lattice. This aspect of the reciprocal lattice is covered in more detail in Sec. 9.

An example of the Ewald sphere construction is shown in Fig. 6 for a simple orthorhombic crystal with lattice parameters $a_1 = 2.0$ Å, $a_2 = 1.0$ Å and $a_3 = 3.0$ Å. The corresponding magnitudes of the reciprocal lattice vectors are $b_1 = 0.5$ Å^{-1}, $b_2 = 1.0$ Å^{-1} and $b_3 = 0.33$ Å^{-1}, and Fig. 6 shows the reciprocal lattice adjacent to the direct space lattice. If the orthorhombic crystal is oriented for 100 diffraction with Cu $K\alpha$ radiation ($\lambda = 1.54$ Å), $\mathbf{S}_0$ must make an angle of 22.6° with (100). This is shown for $\mathbf{S}_0$ in the plane of the paper, i.e., this $\mathbf{S}_0$ makes an angle of 22.6° with $\mathbf{a}_2$, and the resulting $\mathbf{S}$ makes the same angle with $-\mathbf{a}_2$.

Remember that the Bragg angle for 100 is not equal to that for 010 or 001 in the orthorhombic system. The lengths of S_0/λ and S/λ are $(1.54\ \text{Å})^{-1} = 0.649$ Å^{-1}, and S_0/λ and the corresponding Ewald sphere are shown to scale and in the correct orientation in the reciprocal lattice. The Ewald sphere intersects the reciprocal lattice point (1,0,0), and 100 diffraction will occur. Note that the direction of the diffracted beam in reciprocal space is parallel to that in direct space and that the angle between $\mathbf{S}_0$ and $\mathbf{S}$ in Fig. 6 is 2θ. One should also note that the symmetry present in the direct space lattice must also be reflected in the reciprocal lattice.

Rotation of $\mathbf{S}_0$ about $\mathbf{a}_3$ can be used to orient the crystal to diffract from other $<h00>$.[7] In order to orient the crystal shown in Fig. 6 for 200 diffraction, i.e., second order 100 diffraction, $\mathbf{S}_0$ must rotate 27.75° from its orientation in Fig. 6 toward $\mathbf{a}_1$. This rotation brings the Ewald sphere into contact with the 200 reciprocal lattice point. Similarly, $\mathbf{S}_0$ must rotate 45.2° counterclockwise from the orientation pictured in Fig. 6 in order to produce $\bar{1}00$ diffraction.

The possible diffraction beam directions for a given crystal can also be determined using the Ewald sphere construction. Consider the reciprocal lattice for the simple orthorhombic crystal shown in Fig. 6. Remembering that the condition for diffraction from (*hkl*) is that the Ewald sphere intersects the *hkl* reciprocal lattice point, the Ewald sphere can be rotated about the origin of the reciprocal lattice, through all possible orientations, to determine which *hkl* reflections are possible (Fig. 7). The result is the *limiting sphere* centered on the origin of the reciprocal lattice and with radius $2/\lambda$. All the diffracted beams corresponding to the reciprocal lattice points lying within or on the limiting sphere can be excited for the proper crystal orientation. One advantage of using the reciprocal lattice to determine

---

[7] Users of x-ray diffraction often speak of rotating the incident beam while keeping the crystal orientation fixed. For practical reasons, it is actually the crystal which is rotated and the incident x-ray beam which remains stationary.

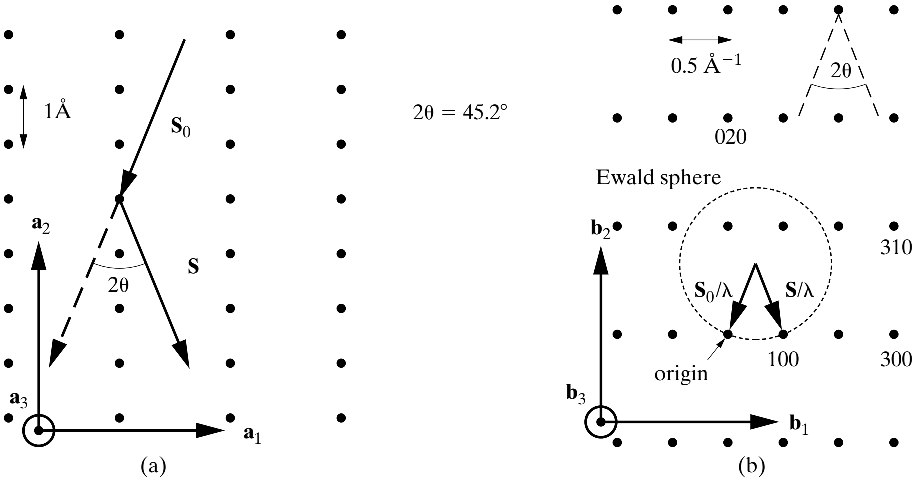

Figure 6 (a) Direct space lattice for a simple orthorhombic crystal and (b) the corresponding reciprocal space lattice and Ewald sphere for Cu $K\alpha$ radiation. The orientation of the incident beam $\mathbf{S}_0$ is such that 100 diffraction occurs, i.e., (100) are oriented to satisfy Bragg's law and the reciprocal lattice point 100 is on the Ewald sphere.

which diffracted beams are possible is that the directions of $\mathbf{S}$ and $\mathbf{S}_0$ are obvious; this is not the case for the numerical approach described in the previous paragraphs of this section. When numerical values of the Bragg angle are required, however, it is advantageous to use Bragg's law directly.

6 DIFFRACTION DIRECTIONS

What determines the possible directions, i.e., the possible angles 2θ, in which a given crystal can diffract a beam of monochromatic x-rays? Referring to Fig. 3, the various diffraction angles $2\theta_1, 2\theta_2, 2\theta_3, \ldots$ can be obtained from the (100) planes by using a beam incident at the correct angle $\theta_1, \theta_2, \theta_3, \ldots$ and producing first-, second-, third-, … order reflections. But diffraction can also be produced by the (110) planes, the (111) planes, the (213) planes, and so on. A general relation is needed which will predict the diffraction angle for *any* set of planes. This relation is obtained by combining Bragg's law and the plane-spacing equation applicable to the particular crystal involved.

For example, if the crystal is cubic, then

$$\lambda = 2d \sin \theta$$

and

$$\frac{1}{d^2} = \frac{(h^2 + k^2 + l^2)}{a^2}.$$

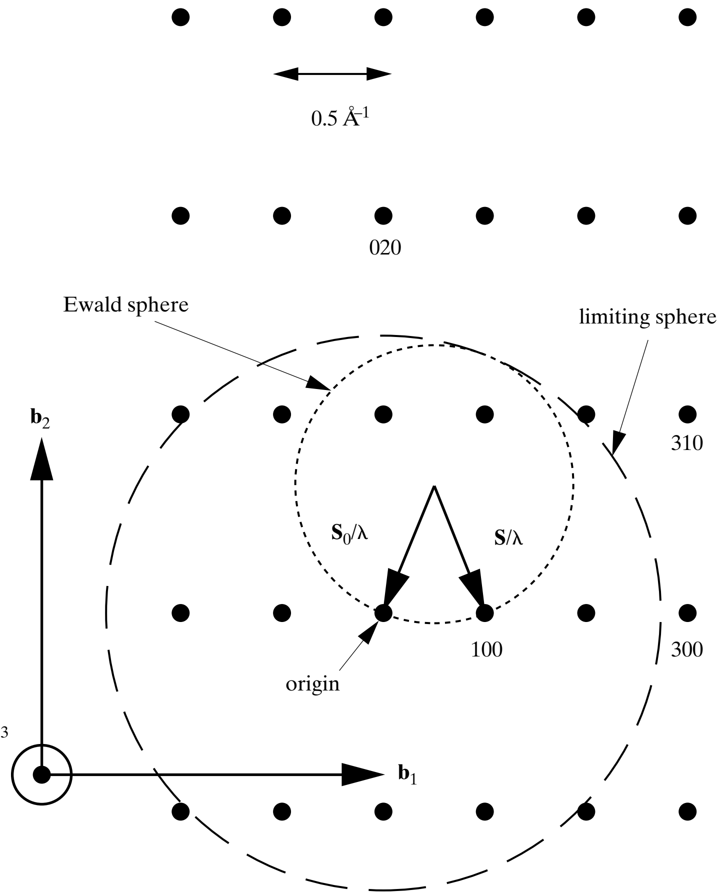

Figure 7 Illustration of the limiting sphere. The Ewald sphere and reciprocal lattice of Fig. 6 are shown for reference; $\mathbf{S}_0$ is shown oriented for 100 diffraction. Diffraction from 100, 200, 110, 010, etc. is possible for this crystal and x-ray wavelength; 300, 210, etc, diffraction cannot be observed.

Combining these equations rearranging terms produces

$$\sin^2\theta = \frac{\lambda^2}{4a^2}(h^2 + k^2 + l^2). \tag{11}$$

This equation predicts, for a particular incident wavelength λ and a particular cubic crystal of unit cell size a, all the possible Bragg angles at which diffraction can occur from the planes (hkl). For (110) planes, for example, Eq. (11) becomes

$$\sin^2\theta_{110} = \frac{\lambda^2}{2a^2}.$$

If the crystal is tetragonal, with axes *a* and *c*, then the corresponding general equation is

$$\sin^2\theta = \frac{\lambda^2}{4}\left(\frac{h^2 + k^2}{a^2} + \frac{l^2}{c^2}\right) \tag{12}$$

and similar equations can readily be obtained for the other crystal systems.

These examples show that the directions in which a beam of given wavelength is diffracted by a given set of lattice planes are determined by the crystal system to which the crystal belongs and its lattice parameters. In short, *diffraction directions are determined solely by the shape and size of the unit cell.* This is an important point and so is its converse: all that can be determined about an unknown crystal by measurements of the *directions* of diffracted beams are the shape and size of its unit cell. *Intensities* of diffracted beams are determined by the positions of the atoms within the unit cell, and it follows that intensities must be measured if any information at all is to be obtained about atom positions. For many crystals, there are particular atomic arrangements which reduce the intensities of some diffracted beams to zero. In such a case, there is simply no diffracted beam at the angle predicted by an equation of the type of Eqs. (11) and (12). It is in this sense that equations of this kind predict all *possible* iffracted beams.

7 X-RAY SPECTROSCOPY

Experimentally, Bragg's law can be applied in two ways. By using x-rays of known wavelength and measuring θ, the spacing d of various planes in a crystal are determined: this is *structure analysis* and is the subject, in one way or another, of the greater part of this book. Alternatively, a crystal with planes of known spacing d can be used to measure θ, and thus determine the wavelength λ of the radiation used: this is *x-ray spectroscopy*.

The essential features of an x-ray spectrometer [8] are shown in Fig. 8. X-rays from the tube T are incident on a crystal C which may be set at any desired angle to the incident beam by rotation about an axis through O, the center of the spectrometer circle. D is a detector which measures the intensity of the diffracted x-rays; it can also be rotated about O and set at any desired angular position. The crystal is usually cut or cleaved so that a particular set of diffracting planes of known spacing

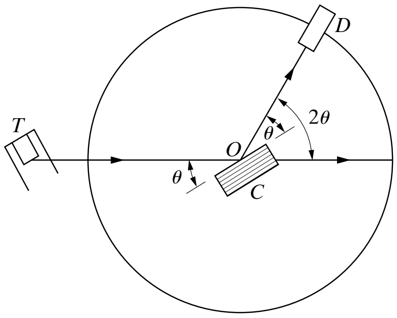

Figure 8 The x-ray spectrometer.

is parallel to its surface, as suggested by the drawing. In use, the crystal is positioned so that its diffracting planes make some particular angle θ with the incident beam, and D is set at the corresponding angle 2θ. The intensity of the diffracted beam is then measured and its wavelength calculated from Bragg's law, this procedure being repeated for various angles θ. W. H. Bragg designed and used the first x-ray spectrometer, and the Swedish physicist Siegbahn developed it into an instrument of very high precision.

X-ray spectroscopy is of concern only insofar as it concerns certain units of wavelength. Wavelength measurements made in the way just described are obviously relative, and their accuracy is no greater than the accuracy with which the plane spacing of the crystal is known.

Before considering how the first plane spacing was determined, first consider the subject of *x-ray density*. Normally the density of a solid is found by measuring the volume, usually of the order of a few cubic centimeters, and the weight of a particular specimen. But x-ray diffraction allows measurement of the lattice parameters of a crystal's unit cell, and therefore its volume, together with the number of atoms in the cell. Density determination can be based not on a few cubic centimeters but on the volume of a single unit cell, by defining the

$$\text{x–ray density} = \frac{\text{weight of atoms in unit cell}}{\text{volume of unit cell}}.$$

$$\rho = \frac{\sum A/N}{V}, \tag{13}$$

where ρ = density (g/cm^3), ΣA = sum of the atomic weights of all the atoms in the unit cell, N = Avogadro's number, and V = volume of unit cell (cm^3). Inserting the value of N produces

$$\rho = \frac{\sum A}{NV} = \frac{\sum A}{(6.02257 \times 10^{23})(V' \times 10^{-24})} = \frac{1.66042 \sum A}{V'}, \tag{14}$$

where ρ is in g/cm^3 and V' is the unit-cell volume in Å^3.

The macroscopic density of a particular specimen, determined from the weight and volume of that specimen, is usually less than, and cannot exceed, the x-ray density, because the macroscopic specimen will usually contain cracks and pores on the macroscopic scale and vacancies in the lattice on the atomic scale. The x-ray density is therefore a useful quantity to know. Comparing it to the macroscopic density of, for example, a pressed and sintered metal or ceramic compact, determines the percent porosity in the compact. X-ray densities are sometimes loosely called "theoretical densities"; they are not theoretical because they are determined experimentally.

To return to the problem of wavelength determination, it is an interesting and crucial fact that Bragg was able to solve the crystal structure of NaCl without knowing the wavelength of the x-rays being diffracted. All he knew—all he needed to know—was that there was one *single*, strong wavelength in the radiation from the x-ray tube, namely, the strong $K\alpha$ line of the tube target. Once the NaCl structure is known, it follows that there are four sodium and four chlorine atoms per unit cell, and that

$$\sum A = 4(\text{at. wt. Na}) + 4(\text{at. wt. Cl}).$$

If this value is inserted into Eq. (13) together with the macroscopic density ρ, the volume V' of the unit cell can be found. Because NaCl is cubic, the lattice parameter a is given simply by the cube root of V'. From this value of a and the cubic plane-spacing equation the spacing of any set of planes can be found.

In this way, Siegbahn obtained a value of 2.814 Å for the spacing of the (200) planes of rock salt (NaCl), which he could use as a basis for wavelength measurements [9]. This spacing was known to only four significant figures, because it was derived from a macroscopic density of that precision. However, Siegbahn was able to measure wavelengths in terms of this spacing much more accurately, namely, to six significant figures. Not wishing to throw away the high relative precision he could attain, he wisely decided to arbitrarily define a new unit in which relative wavelengths could be expressed. This was the X unit (XU), so called because its true value in absolute units (angstroms) was unknown. By defining the (200) spacing of rock salt to six significant figures as 2814.00 XU, the new unit was made as nearly as possible equal to 0.001 Å.

Once a particular wavelength was determined in terms of this spacing, the spacing of a given set of planes in any other crystal could be measured. Siegbahn thus measured the (211) spacing of calcite ($CaCO_3$), which he found more suitable as a standard crystal, and thereafter based all his wavelength measurements on this spacing. Its value is 3029.45 XU. Later on, the kilo X unit (kX) was introduced, a thousand times as large as the X unit and nearly equal to an angstrom. The kX unit is therefore *defined* by the relation

$$1 \text{ kX} = \frac{(211) \text{ plane spacing of calcite}}{3.02945}. \tag{15}$$

On this basis, Siegbahn and coworkers made very accurate measurements of wavelength in relative (kX) units and these measurements form the basis of most published wavelength tables.

It was found later that x-rays could be diffracted by a ruled grating such as is used in the spectroscopy of visible light, provided that the angle of incidence (the angle between the incident beam and the plane of the grating) is kept below the critical angle for total reflection. Gratings thus offer a means of making absolute wavelength measurements, independent of any knowledge of crystal structure. By a comparison of values so obtained with those found by Siegbahn from crystal diffraction, it was possible to calculate the following relation between the relative and absolute units:

$$1 \text{ kX} = 1.00202\text{Å}.$$

This conversion factor was adopted in 1946 by international agreement. Later work improved the accuracy of this factor, and the relation is now believed to be

$$1 \text{ kX} = 1.002056\text{Å}^*. \tag{16}$$

Note that this relation is stated in terms of still another unit, the Å* unit, which was introduced because of the still remaining uncertainty in the conversion factor. The difference between Å and Å* is only some five parts per million, and the distinction between the two units is negligible except in work of the very highest accuracy.

The present situation is not entirely clear, but the wavelength tables published by the International Union of Crystallography [Vol. C, G.1] are the best available value.

The distinction between kX and Å is unimportant if no more than about three significant figures are involved, because the kX unit is only about 0.2 percent larger than the angstrom. In precise work, on the other hand, units must be correctly stated, and on this point there has been considerable confusion in the past. Some wavelength values published prior to about 1946 are stated to be in angstrom units but are actually in kX units. Some crystallographers have used such a value as the basis for a precise measurement of the lattice parameter of a crystal, and the result has been stated, again incorrectly, in angstrom units. Many published parameters are therefore in error, and it is unfortunately not always easy to determine which ones are and which ones are not. The only safe rule to follow, in stating a precise parameter, is to give the wavelength of the radiation used in its determination. Similarly, any published table of wavelengths can be tested for the correctness of its units by noting the wavelength given for a particular characteristic line, Cu Kα_1 for example. The wavelength of this line is 1.540562 Å* (1974 value, 1.002056 as conversion factor), 1.54051 Å (1946 value, 1.00202 factor), or 1.53740 kX.

8 DIFFRACTION METHODS

Diffraction can occur whenever Bragg's law, $\lambda = 2d \sin \theta$, is satisfied. This equation puts very stringent conditions on λ and θ for any given crystal. With monochromatic radiation, an arbitrary setting of a single crystal in a beam of x-rays will not in general produce *any* diffracted beams. Some way of satisfying Bragg's law must be devised, and this can be done by continuously varying either λ or θ during the experiment. The ways in which these quantities are varied distinguish three main diffraction methods:

Method	λ	θ
Laue	Variable	Fixed
Rotating-crystal	Fixed	Variable (in part)
Powder	Fixed	Variable

Laue Method

The Laue method was the first diffraction method ever used, and it reproduces von Laue's original experiment. In this method, a beam of white radiation, the continuous spectrum from an x-ray tube, falls on a fixed single crystal. The Bragg angle θ is therefore fixed for every set of planes in the crystal, and each set selects and diffracts that particular wavelength which satisfies Bragg's law for the particular values of d and θ involved. Each diffracted beam thus has a different wavelength.

There are two variations of the Laue method, depending on the relative positions of source, crystal, and film (Fig. 9). In each, the film is flat and placed perpendicular to the incident beam. The film in the *transmission Laue method* (the original Laue method) is placed behind the crystal so as to record the beams diffracted in the forward direction. This method is so called because the diffracted beams are partially transmitted through the crystal. In the *back-reflection Laue method* the film is placed between the crystal and the x-ray source, the incident beam passing through a hole in the film, and the beams diffracted in a backward direction are recorded.

In either method, the diffracted beams form an array of spots on the film as shown in Fig. 10. This array of spots is commonly called a *pattern*, but the term is not used in any strict sense and does not imply any periodic arrangement of the spots. On the contrary, the spots are seen to lie on certain curves, as shown by the lines drawn on the photographs. These curves are generally ellipses or hyperbolas for transmission patterns [Fig. 10(a)] and hyperbolas for back-reflection patterns [Fig. 10(b)].

The spots lying on any one curve are reflections from planes belonging to one

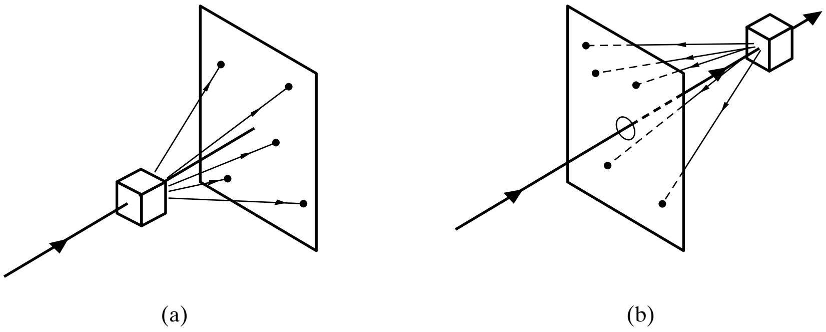

Figure 9 (a) Transmission and (b) back-reflection Laue methods.

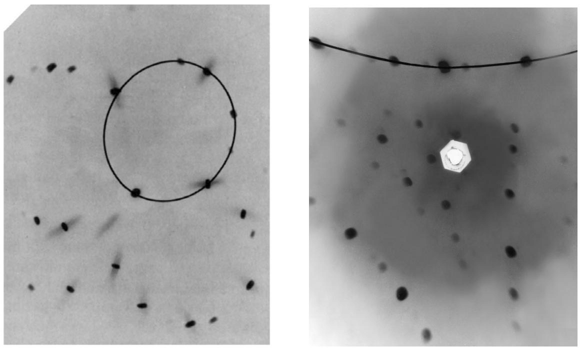

(a) (b)

Figure 10 (a) Transmission and (b) back-reflection Laue patterns of an aluminum crystal (cubic). Tungsten radiation, 30 kV, 19 mA.

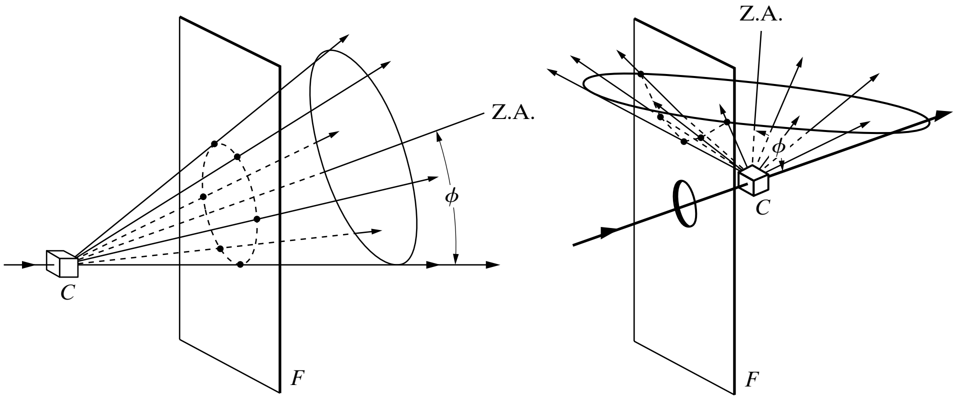

(a) (b)

Figure 11 Location of Laue spots (a) on ellipses in transmission method and (b) on hyperbolas in back-reflection method. (C = crystal, F = film, Z.A. = zone axis.)

zone. This is due to the fact that the Laue reflections from planes of a zone all lie on the surface of an imaginary cone whose axis is the zone axis. As shown in Fig. 11(a), one side of the cone is tangent to the transmitted beam, and the angle of inclination ϕ of the zone axis (Z.A.) to the transmitted beam is equal to the semi-apex angle of the cone. A film placed as shown intersects the cone in an imaginary ellipse passing through the center of the film, the diffraction spots from planes of a zone being arranged on this ellipse. When the angle ϕ exceeds 45°, a film placed between the crystal and the x-ray source to record the back-reflection pattern will intersect the cone in a hyperbola, as shown in Fig. 11(b).

The fact that the Laue reflections from planes of a zone lie on the surface of a cone can be demonstrated nicely with the stereographic projection. In Fig. 12, the crystal is at the center of the reference sphere, the incident beam I enters at the left, and the transmitted beam T leaves at the right. The point representing the zone axis

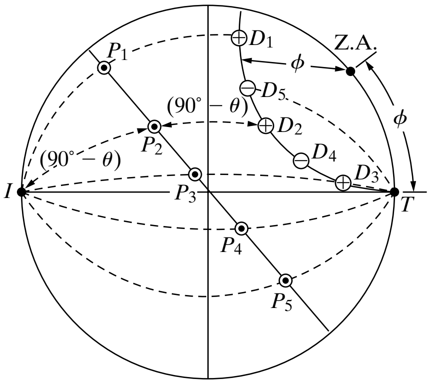

Figure 12 Stereographic projection of transmission Laue method.

lies on the circumference of the basic circle and the poles of five planes belonging to this zone, P_1 to P_5, lie on the great circle shown. The direction of the beam diffracted by any one of these planes, for example the plane P_2, can be found as follows. I, P_2, D_2 (the diffraction direction required), and T are all co-planar. Therefore D_2 lies on the great circle through I, P_2, and T. The angle between I and P_2 is $(90^\circ - \theta)$, and D_2 must lie at an equal angular distance on the other side of P_2, as shown. The diffracted beams so found, D_1 to D_5, are seen to lie on a small circle, the intersection with the reference sphere of a cone whose axis is the zone axis.

The positions of the spots on the film, for both the transmission and the back-reflection method, depend on the orientation of the crystal relative to the incident beam, and the spots themselves become distorted and smeared if the crystal has been bent or twisted in any way. These facts account for the two main uses of the Laue methods: the determination of crystal orientation and the assessment of crystal quality.

The Ewald sphere treatment of diffraction of a single wavelength λ from a crystal can be readily extended to the Laue method where multiple λ are incident. The range of wavelengths used is represented by a series of parallel incident beams, each with a different length proportional to $1/\lambda_i$. Note that each of these vectors terminates at the origin of the reciprocal lattice, and each has a different origin (Fig. 13). Thus, each incident beam S_o/λ_i has a corresponding Ewald sphere touching the origin of the reciprocal lattice and having radius $1/\lambda_i$. All of the different S_o/λ_i pass through the origin of the reciprocal lattice, and the corresponding Ewald spheres have centers lying on the line **OACDB** of Fig. 13, i.e., the incident beam direction. The range of wavelengths present in the incident beam is of course not infinite. It has a sharp lower limit at λ_{SWL}, the short-wavelength limit of the continuous spectrum; the upper limit is less definite and depends on experimental factors such as whether the transmission or back-reflection geometry is being used. In the example of the Ewald sphere construction shown in Fig. 13, the upper wavelength limit is taken as the wavelength of the K absorption edge of the silver in the emulsion (0.48 Å), because the effective photographic intensity of the continuous spectrum drops abruptly at that wavelength. This choice is most appropriate for trans-

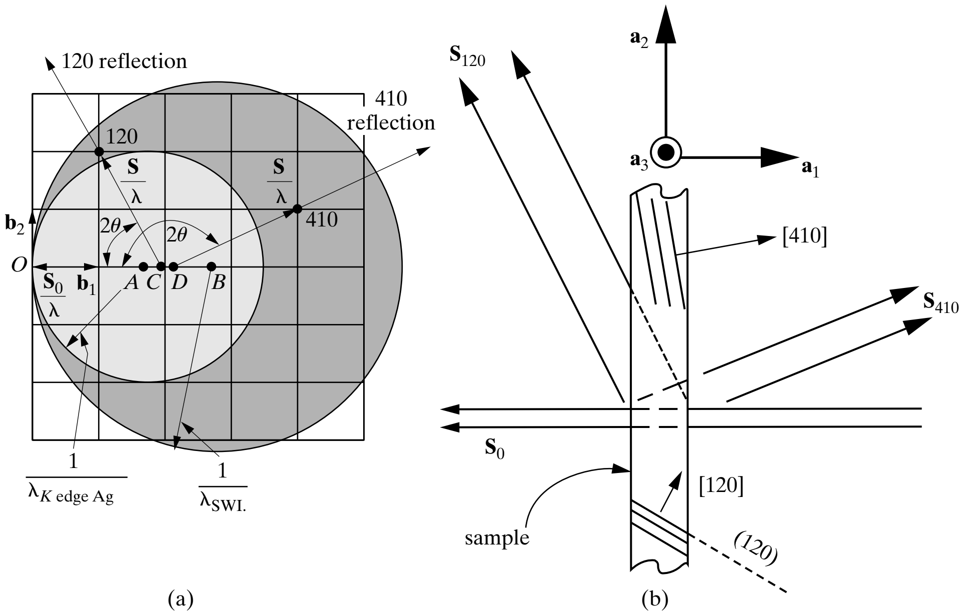

(a) (b)

Figure 13 Reciprocal lattice (a) and corresponding schematic of the crystal in direct space (b) for the Laue method. $(\mathbf{S} - \mathbf{S}_o)/\lambda = \mathrm{H}$.

mission Laue patterns of crystals which are quite absorbing since the value of the linear attenuation coefficient (of an element in a sample) rises rapidly with increasing wavelength. For back-reflection Laue patterns considerable darkening of the film wll occur for wavelengths above the silver edge and below the bromine K-edge as well as for somewhat longer wavelengths.

To these two extreme wavelengths correspond two extreme Ewald spheres, as shown in Fig. 13, which is a section through these spheres and the $l = 0$ layer of the reciprocal lattice. The incident beam is along the $\mathbf{b}_1$ vector, i.e., perpendicular to the (h00) planes of the crystal. The larger sphere shown is centered at B and has a radius equal to the reciprocal of λ_{SWL}, while the smaller sphere is centered at A and has a radius equal to the reciprocal of the wavelength of the silver K absorption edge. A whole series of spheres lie between these two, and any reciprocal-lattice point lying in the shaded region of the diagram is on the surface of one of these spheres and corresponds to a set of crystal planes oriented to diffract one of the incident wavelengths. In the forward direction, for example, a 120 reflection will be produced. To find its direction, locate a point C on AB which is equidistant from the origin O and the reciprocal-lattice point 120; C is therefore the center of the Ewald sphere passing through the point 120. Joining C to 120 gives the diffracted-beam vector S/λ for this reflection. The direction of the 410 reflection, one of the many backward-diffracted beams, is found in similar fashion; here the reciprocal-lattice point in question is situated on a Ewald sphere centered at D.

Rotating-Crystal Method

In the rotating-crystal method a single crystal is mounted with one of its axes, or some important crystallographic direction, normal to a monochromatic x-ray beam. A cylindrical film is placed around it and the crystal is rotated about the chosen direction, the axis of the film coinciding with the axis of rotation of the crystal (Fig. 14). As the crystal rotates, a particular set of lattice planes will, for an instant, make the correct Bragg angle for diffraction of the monochromatic incident beam, and at that instant a diffracted beam will be formed. The diffracted beams are again located on imaginary cones but now the cone axes coincide with the rotation axis. The result is that the spots on the film, when the film is laid flat, lie on imaginary horizontal "layer" lines, as shown in Fig. 15. Since the crystal is rotated about only one axis, the Bragg angle does not take on all possible values between 0° and 90° for every set of planes. Not every set, therefore, is able to produce a diffracted beam; sets perpendicular or almost perpendicular to the rotation axis are examples.

The Ewald sphere construction for monochromatic radiation can be used to illustrate why beams diffracted from a single crystal rotated about one of its axes lie on the surface of cones coaxial with the rotation axis. This interpretation of the patterns of diffraction spots was emphasized by Bernal [10]. Suppose a simple cubic crystal is rotated about the axis [001]. This is equivalent to rotation of the reciprocal lattice about the $\mathbf{b}_3$ axis. Figure 16 shows a portion of the reciprocal lattice oriented in this manner, together with the adjacent Ewald sphere.

All crystal planes having indices ($hk1$) are represented by points lying on a plane (called the "$l = 1$ layer") in the reciprocal lattice, normal to $\mathbf{b}_3$. When the reciprocal lattice rotates, this plane cuts the Ewald sphere in the small circle shown, and any

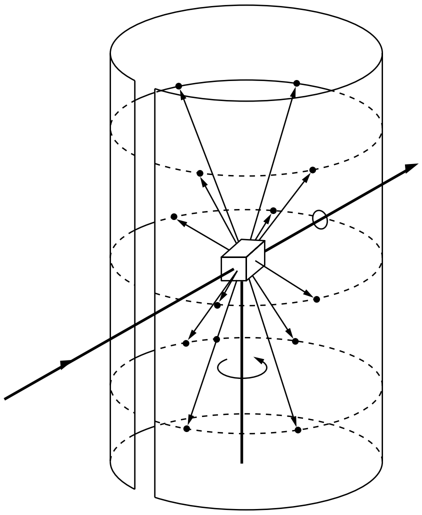

Figure 14 Rotating-crystal method.

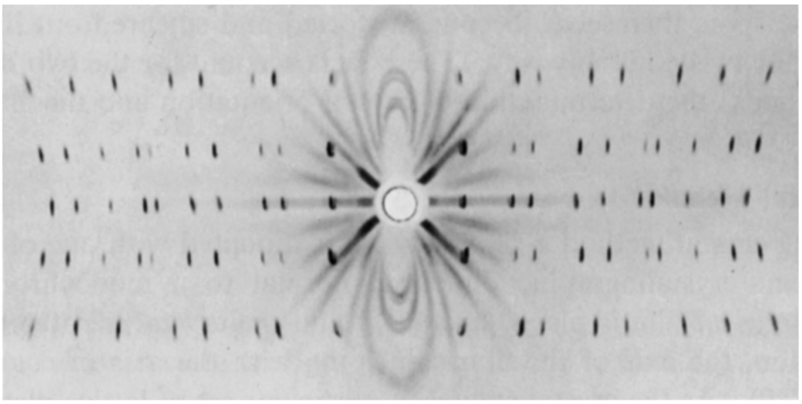

Figure 15 Rotating-crystal pattern of a quartz crystal (hexagonal) rotated about its c axis. Filtered copper radiation. (The streaks are due to the white radiation not removed by the filter.) (Courtesy of B. E. Warren.)

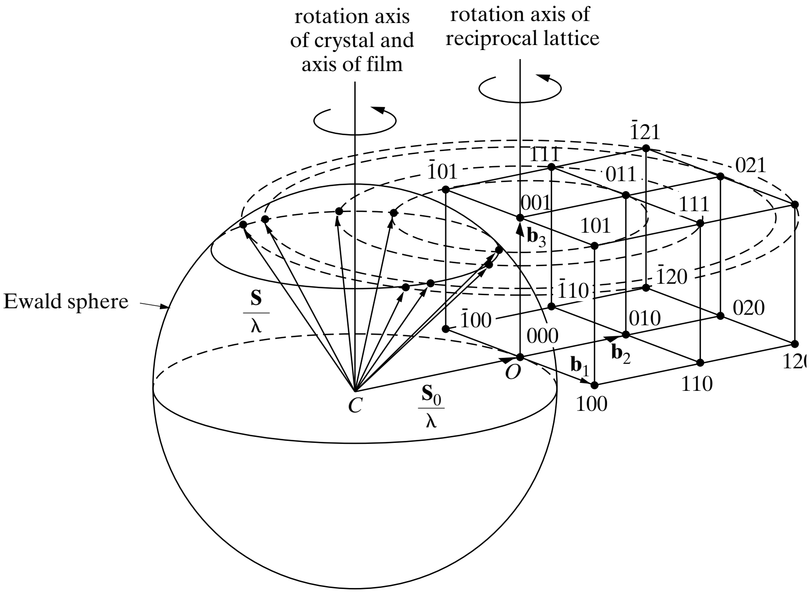

Figure 16 Reciprocal-lattice treatment of rotating-crystal method.

points on the $l = 1$ layer which touch the sphere surface must touch it on this circle. Therefore all diffracted-beam vectors S/λ must end on this circle, which is equivalent to saying that the diffracted beams must lie on the surface of a cone. In this particular case, all the *hk*1 points shown intersect the surface of the sphere sometime during their rotation about the $\mathbf{b}_3$ axis, producing the diffracted beams shown in Fig. 16. In addition many *hk0* and *hk*1 reflections would be produced, but these have been omitted from the drawing for the sake of clarity.

The chief use of the rotating-crystal method and its variations were in the determination of unknown crystal structures, but the complete determination of complex crystal structures is a subject beyond the scope of this book and outside the province of the average materials scientist/engineer who uses x-ray diffraction as a laboratory tool. Analyzing patterns consisting of layer lines of diffraction spots remains important however, for polymers and is beyond the scope of this chapter.

Powder Method

In the powder method, the crystal to be examined is reduced to a very fine powder or already is in the form of loose or consolidated microscopic grains. The sample in a suitable holder is placed in a beam of monochromatic x-rays. Each particle of the powder is a tiny crystal, or assemblage of smaller crystals, oriented at random with respect to the incident beam. Just by chance, some of the crystals will be correctly oriented so that their (100) planes, for example, can diffract the incident beam. Other crystals will be correctly oriented for 110 reflections, and so on. The result is that every set of lattice planes will be capable of diffraction. The mass of powder is equivalent, in fact, to a single crystal rotated, not about one axis, but about all possible axes.

Consider one particular *hkl* reflection, and remember that $\mathbf{S}$, $\mathbf{S}_0$ and $\mathbf{N}_{hkl}$, the normal to the diffraction planes (*hkl*), must be coplanar. One or more little crystals will, by chance, be so oriented that their (*hkl*) planes make the correct Bragg angle for diffraction; Fig. 17(a) shows one plane in this set and the diffracted beam formed. If this plane is now rotated about the incident beam in such a way that θ is kept constant, then the diffracted beam will travel over the surface of a cone as shown in Fig. 17 (b), the axis of the cone coinciding with the transmitted beam.

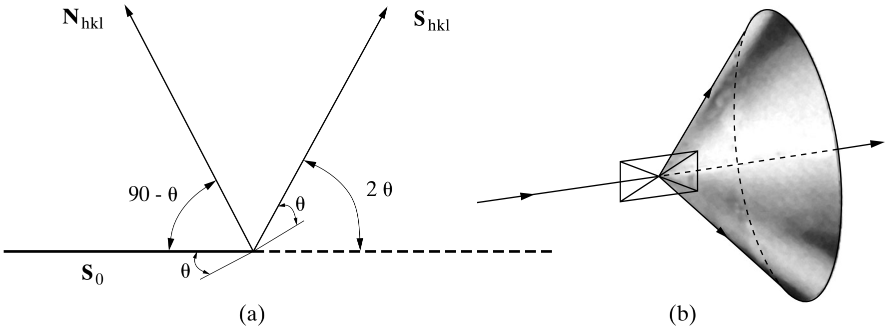

(a) (b)

Figure 17 Formation of a diffracted cone of radiation in the powder method.

Equivalently, one can imagine rotating $\mathrm{N}_{\mathrm{hkl}}$ about $\mathbf{S}_0$ while keeping the angle between them equal to $90° - \theta$ degrees.

This rotation does not actually occur, but the presence of a large number of crystal particles having all possible orientations is equivalent to this rotation, since among these particles there will be a certain fraction whose (*hkl*) planes make the correct Bragg angle with the incident beam and which at the same time lie in all possible rotational positions about the axis of the incident beam. The *hkl* reflection from a stationary mass of powder thus has the form of a conical sheet of diffracted radiation, and a separate cone is formed for each set of differently spaced lattice planes.

Figure 18 shows three such cones and also illustrates a common powder-diffraction method. In this, the Hull/Debye–Scherrer method [11, 12], a narrow strip of film is curved into a short cylinder with the specimen placed on its axis and the incident beam directed at right angles to this axis. [8] The cones of diffracted radiation intersect the cylindrical strip of film in lines, and when the strip is unrolled and laid flat, the resulting pattern appears as in Fig. 18(b). Actual patterns, produced by various metal powders, are shown in Fig. 19. Each diffraction line is made up of a large number of small spots, each from a separate crystal particle, the spots lying so close together that they appear as a continuous line. The lines are generally curved, unless they occur exactly at $2\theta = 90°$ when they will be straight. From the measured position of a given diffraction line on the film, θ can be determined, and from θ, knowing λ, the spacing d of the diffracting lattice planes which produced the line.

Conversely, if the shape and size of the unit cell of the crystal are known, the position of all possible diffraction lines on the film can be predicted. The line of lowest 2θ value is produced by diffraction from planes of the greatest spacing. In the cubic system, for example, d is a maximum when $(h^2 + k^2 + l^2)$ is a minimum, and the minimum value of this term is l, corresponding to (*hkl*) equal to (100). The 100 reflection is accordingly the one of lowest 2θ value. The next possible reflection will have indices *hkl* corresponding to the next higher value of $(h^2 + k^2 + l^2)$, namely 2, in which case (*hkl*) equals (110), and so on.

The reciprocal lattice of a randomly oriented powder sample consists of a series of reciprocal lattice (rel) shells centered on the origin of the reciprocal lattice. Remembering that all orientations are equally likely for a random powder sample, constructing the reciprocal lattice representing the powder is straight-forward: first draw the reciprocal lattice for a single grain and second rotate the reciprocal lattice points through all possible orientations. Each reciprocal lattice point *hkl* for the crystal becomes, therefore, a sphere of radius $1/d_{\mathrm{hkl}}$, centered on the reciprocal lattice origin (Fig. 20a). For an incident beam $\mathbf{S}_0$ and Bragg angles θ_{hkl}, a number of $\mathbf{S}_{\mathrm{hkl}}$

---

[8] Most authors term this technique the Debye–Scherrer method, but it seems reasonable to acknowledge the independent and more-or-less simultaneous development in the US and Germany during the First World War.

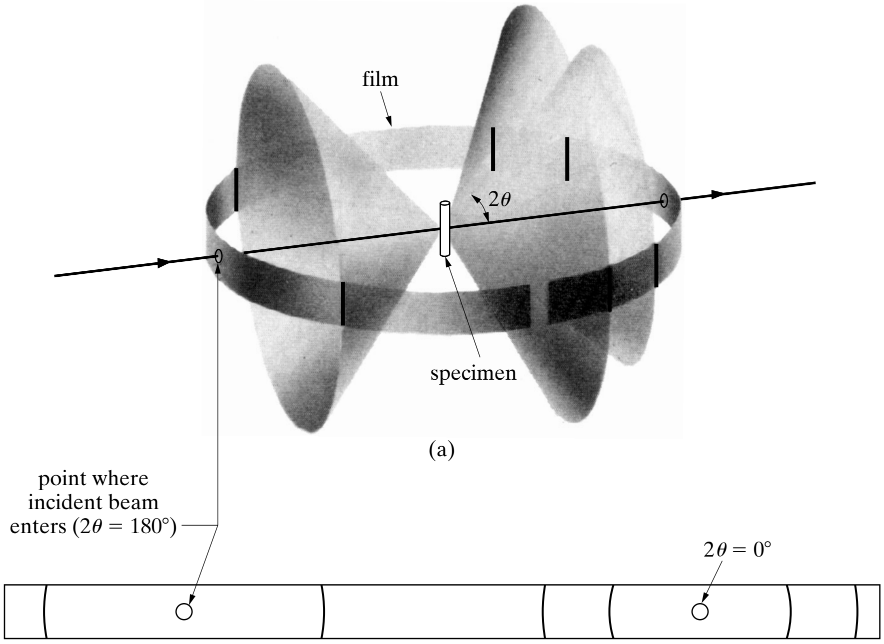

(b)

Figure 18 Hull/Debye–Scherrer powder method: (a) relation of film to specimen and incident beam; (b) appearance of film when laid flat.

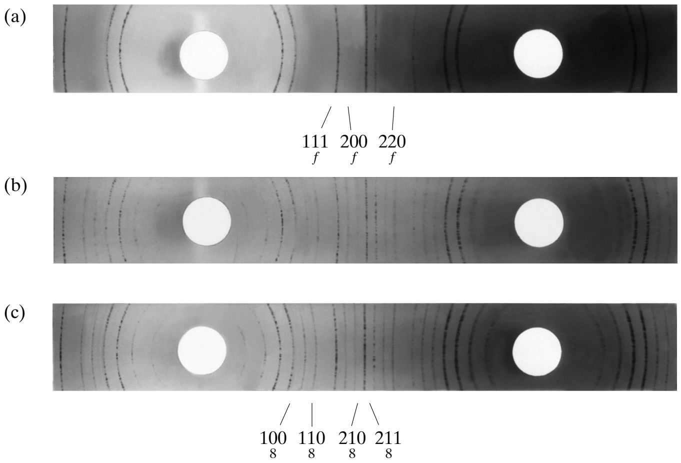

Figure 19 Hull/Debye–Scherrer powder patterns of copper (FCC), tungsten (BCC), and zinc (HCP). Filtered copper radiation, camera diameter = 5.73 cm.

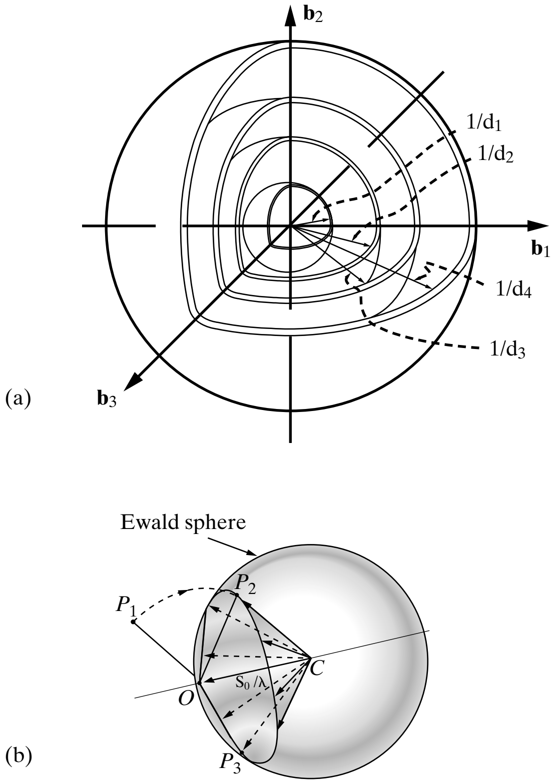

Figure 20 (a) Reciprocal lattice shells with radii 1/d_1, 1/d_2, 1/d_3 and 1/d_4, and (b) diffraction cones from the intersection of a reciprocal lattice shell and the Ewald sphere. When P_1 is rotated about the reciprocal lattice origin, it intersects the Ewald sphere at P_2, P_3 and other points of a circle.

simultaneously satisfy Bragg's law. The loci of $\mathbf{S}_{hkl}$ are determined by the intersection of the rel shells and the Ewald sphere and consist of a series of cones centered on $\mathbf{S}_0$ (diffraction in the forward direction) or on -$\mathbf{S}_0$ (diffraction in back-reflection). The formation of one such cone is illustrated in Fig. 20b, but for clarity the Ewald sphere is pictured and the reciprocal lattice shells are omitted. Instead, reciprocal lattice point P on one shell is rotated through all possible orientations. The resulting intersection of the shell and the Ewald sphere is a circle, and the locus of $\mathbf{S}_{hkl}$ is a cone.

The x-ray spectrometer can be used as a tool in diffraction analysis. This instrument is known as a *diffractometer* when it is used with x-rays of *known* wave-length to determine the *unknown* spacing of crystal planes [13], and as a spectrometer in the reverse case, when crystal planes of known spacing are used to determine

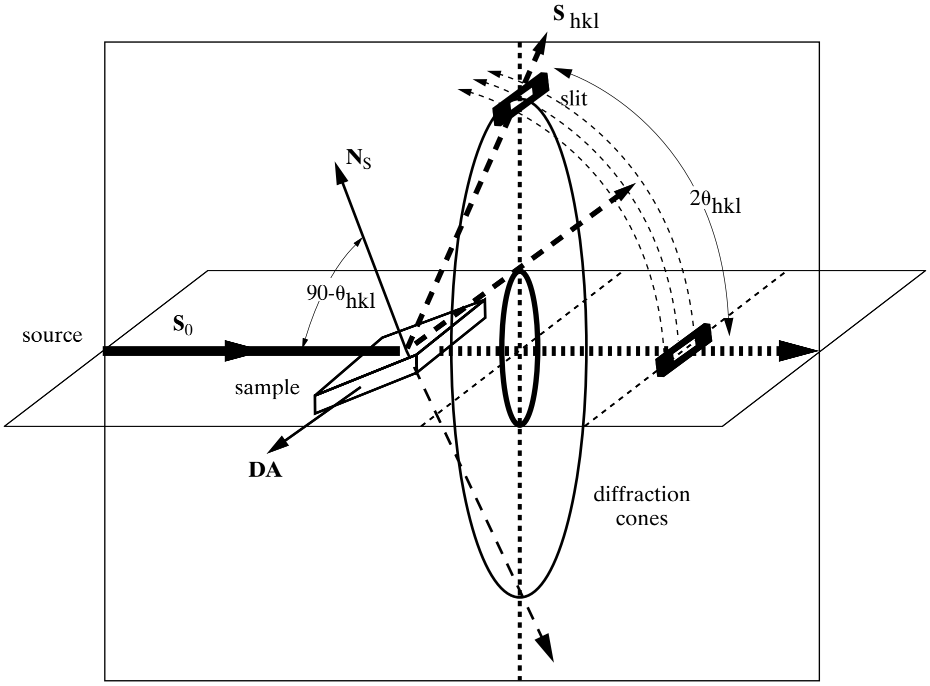

Figure 21 Illustration of the role of the slit on the detector in measuring diffraction peaks in powder diffractometry. Two diffraction cones are shown, $\mathbf{N_S}$ is the normal to the sample, **DA** is the diffractometer rotation axis; and $\mathbf{S}_0$, $\mathbf{N_S}$ and the portions of $\mathbf{S}_1$ and $\mathbf{S}_2$ (portions of the cones intersecting the slit) are coplanar.

unknown wavelengths. The diffractometer is always used with monochromatic radiation and measurements may be made on either single crystals or polycrystal line specimens (early developments are outline in [G.17 and G.18]), the detector intercepts and measures only a short arc of any one cone of diffracted rays (Fig. 21). Note that the diffractometer's receiving slit is essential to the observation of diffraction peaks of randomly-oriented, fine-grained powders. The diffraction cones are always present; in fact, cones for all possible *hkl* are present simultaneously. The receiving slit is necessary to eliminate all diffracted radiation except that passing through this very narrow angular window.

Different powder diffraction techniques sample different portions of reciprocal space, and a complete understanding of diffraction phenomena from a reciprocal space perspective requires rigorous definition of the reciprocal space sampling region for each technique. Developing such an understanding is beyond the scope of this book, and the reader is referred to more comprehensive treatments of reciprocal space [5].

The Hull/Debye–Scherrer and other camera methods and the diffractometer are very widely used. Powder diffraction is, of course, the only method that can be employed when a single-crystal specimen is not available, and this is the case more often than not in materials work. The method is especially suited for determining lattice parameters with high precision and for the identification of phases, whether they occur alone or in mixtures such as polyphase alloys, corrosion products, refractories, and rocks.

9 EXPERIMENTAL VISUALIZATION OF THE RECIPROCAL LATTICE

The preceding section discussed how the rotating crystal method allowed imaging of the distribution of reciprocal lattice points in space. Transmission electron microscopy (TEM) also images the reciprocal lattice directly: planes through the reciprocal lattice can be seen in certain TEM operating modes. In TEM there are a series of three or more lenses following the sample and providing the high magnifications which make the TEM so useful for materials characterization. The wave-like properties of electrons allow them to diffract from crystalline samples. Typically in TEM, electrons are accelerated to 100 keV or higher and have wavelengths of 0.037 Å or lower. This acceleration allows the electrons to be transmitted through samples whose thicknesses are on the order of 1000 Å. Because electrons carry a charge, magnetic lenses are effective at focusing electrons (unlike the case of x-rays where lenses can deflect the photons only a minescule fraction of a degree.) It is important to note that most materials' TEM imaging of materials relies on diffracted electrons to provide image contrast.

The very small wavelength of the electrons means that the radius of the corresponding Ewald sphere is very large compared to the spacing between reciprocal lattice points or compared to the Ewald sphere diameter for x-rays. For 0.037 Å radiation, the Ewald sphere radius is 25 Å^{-1} compared to ~1 Å^{-1} for x-rays and to ~0.5 Å^{-1} for the reciprocal lattice spacing. This means that the curvature of the Ewald sphere is gradual compared to the reciprocal lattice spacings, and that, in the vicinity of the origin of the reciprocal lattice, the Ewald sphere is essentially a plane cutting through the reciprocal lattice (Fig. 22). As will be seen in Ch. 4, the sample's thinness produces reciprocal lattice points which are elongated along the thin axis of the sample, i.e., rel rods or <u>re</u>ciprocal <u>l</u>attice rods, and the rods intersect the Ewald sphere over quite a large range of 1/d. This section of the reciprocal lattice

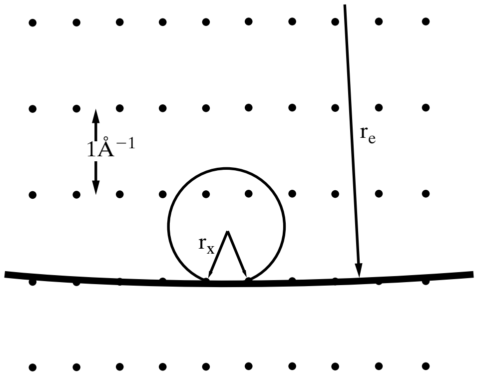

Figure 22 Reciprocal lattice of the orthorhombic crystal shown in Fig. 6 with the Ewald spheres and radii r_x for Cu *Kα* x-rays and r_e for 100 keV electrons.

imaged by the TEM is termed a diffraction pattern and is normally identified by the direction of incidence of the electrons, i.e., by the normal to the reciprocal lattice plane.

The TEM ray diagram pictured in Fig. 23 shows how an image of the sample or an image of the sample's diffraction pattern is obtained. The incident electrons are indicated by the arrows at the top of the figure, and one diffracted beam **G** and the transmitted beam **O** originating from each of three points (A, B and C) in the sample illustrate the electron-sample interactions of interest here. The diffracted and transmitted beams pass through the objective lens whose optic axis is **BB´**. Parallel rays are brought to a focus in the diffraction plane, and rays diverging from a point are recombined in the image plane. In other words, the three rays **G** from A, B and C are combined at G in the diffraction plane, and the rays **G** and **O** from A recombine at A´ in the image plane. If the other lenses of the TEM are focussed on the diffraction plane, the essentially planar section of the reciprocal lattice is imaged. If focussing is on the image plane, an image of the sample results. In other words, parallel directions are mapped onto a single point in the diffraction plane in just as all (*hkl*) in direct space were mapped onto point *hkl* in reciprocal space.

Figure 24 shows a diffraction pattern recorded from a grain of NiAl with the electron beam parallel to [100]. The four-fold symmetry expected along <100> in the CsCl structure is clearly seen. Multiple orders of each diffraction vector are seen simultaneously, an apparent contradiction of Bragg's law: for a single wavelength Bragg's law predicts that first and second order diffraction (*hkl* and 2*h* 2*k* 2*l*) occur at angles θ_{hkl} and θ_{2h2k2l} given, for cubic axial systems, by

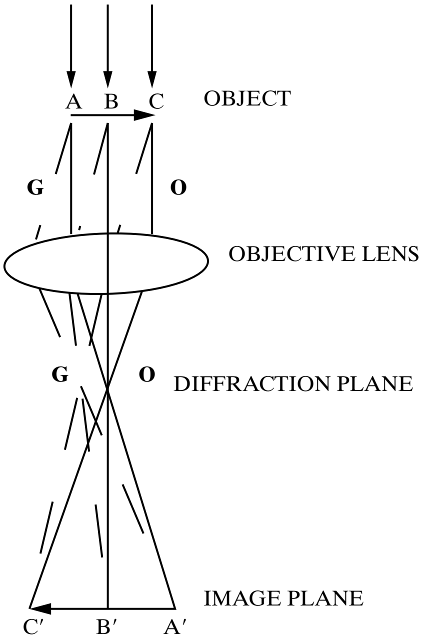

Figure 23 TEM ray diagram showing the diffraction plane and image plane.

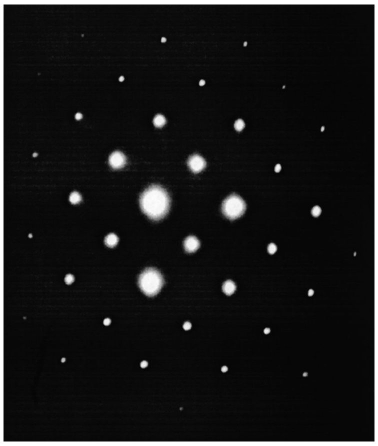

Figure 24 001 diffraction pattern from a grain of NiAl.

$$\sqrt{2}\sin\theta_{\mathrm{hkl}} = \sin\theta_{\mathrm{2h2k2l}}.$$

The question is how first and second order diffraction can occur simultaneously for the same angle of incidence of $\mathbf{S}_0$ if small rotations from the Bragg angle destroy constructive interference. Stated in other terms, the derivation of Bragg's law implicitly assumed that the diffraction peaks are delta functions, i.e., that the crystal has an infinitely narrow range of reflection.

The resolution to this apparent contradiction lies in the fact that *Bragg's law describes diffraction incompletely*. Very small crystal or grain dimensions have very wide diffraction ranges as a direct consequence of their small size. In other words, significant diffracted intensity occurs at angles off the exact Bragg condition, but development of an understanding of the factors governing diffracted intensity must precede discussion of how far a crystal must rotate before diffracted intensity drops to zero.

10 DIFFRACTION UNDER NONIDEAL CONDITIONS

In Sec 9, the discussion of diffraction patterns illustrated one consequence of deviation for "ideality". Before going any further, it is important to consider other aspects of the derivation of Bragg's law given in Sec. 2 in order to understand precisely under what conditions it is strictly valid. In the derivation certain ideal conditions were assumed, namely a perfect crystal and an incident beam composed of perfectly parallel and strictly monochromatic radiation. These conditions never actually exist. For example, the incident x-ray beam in most powder diffractometers is divergent and the characteristic lines from x-ray tubes have finite spectral widths. Also implicit is that once x-ray photons are diffracted they will not be re-directed; this assumption, the basis of kinematical diffraction theory, holds except for diffraction from thick, highly perfect crystals.

Imperfections in the crystal(s) making up a sample can broaden the diffraction peaks. Only the infinite crystal is really perfect and small size alone, of an otherwise perfect crystal, can be considered a crystal imperfection, and can lead to peak broadening. The presence of large numbers of dislocations (i.e., strain) in the grains of a sample can produce significant peak broadening. The inference of sample strain or crystallite size from peak widths (or shapes) is an important part of diffraction analysis of materials.

PROBLEMS

1 A transmission Laue pattern is made of a cubic crystal having a lattice parameter of 4.00 Å. The x-ray beam is horizontal. The $[0\bar{1}0]$ axis of the crystal points along the beam towards the x-ray tube, the $[\bar{1}00]$ axis points vertically upward, and the [001] axis is horizontal and parallel to the photographic film. The film is 5.00 cm from the crystal.

a) What is the wavelength of the radiation diffracted from the $(\bar{3}\bar{1}0)$ planes?
b) Where will the $\bar{3}\bar{1}0$ reflection strike the film?

***2** A transmission Laue pattern is made of a cubic crystal in the orientation of Prob. 1. By means of a stereographic projection similar to Fig. 12, show that the beams diffracted by the planes $(\bar{2}\bar{1}0)$, $(\bar{2}\bar{1}3)$, and (211), all of which belong to the zone $[\bar{1}20]$, lie on the surface of a cone whose axis is the zone axis. What is the angle ϕ between the zone axis and the transmitted beam?

3 Determine, and list in order of increasing angle, the values of 2θ and (hkl) for the first three lines (those of lowest 2θ values) on the powder patterns of substances with the following structures, the incident radiation being Cu $K\alpha$:

a) simple cubic (a = 3.00 Å),
b) simple tetragonal (a = 2.00 Å, c = 3.00 Å),
c) simple tetragonal (a = 3.00 Å, c = 2.00 Å),
d) simple rhombohedral (a = 3.00 Å, α = 80°).

4 Plot the reciprocal lattice for a polycrystalline sample of a material with a simple tetragonal structure and lattice parameters a = 4.0 Å and c = 5.0 Å. (Use a two-dimensional section through the three-dimensional space).

5 Sketch the Ewald sphere construction for 200 diffraction with Mo $K\alpha$ radiation and a polycrystalline specimen of a simple cubic substance with a = 3.30 Å. Graphically determine the angular rotation required to orient the sample for 300 diffraction if a $\theta - 2\theta$ diffractometer is being used.

6 Diffractometers typically can scan up to, but not beyond, 165° 2θ. For the sample in Problem 4, what are the indices (i.e., hkl) of the highest angle reflection if (a) Ag $K\alpha$ radiation is used, (b) Cu $K\alpha$ radiation is used and c) Cr $K\alpha$ radiation is used?

REFERENCES

The following books are listed more or less in the order they are encountered in the text

G.1 *International Tables for Crystallography*, Ed. A.J.C Wilson, Vol. A-C (Dordrecht Kluwer Academic Pub. for International Union of Crystallography, 1995). The reference ''book" for crystallography and diffraction.

G.11 P. P. Ewald, ed. *Fifty Years of X-Ray Diffraction* (Utrecht: International Union of Crystallography, 1962.) See pp. 31-56 and 293-294 for accounts of the von laue experiment. The early work of the Braggs is described on pp. 57-73 120-123, and 532-533. This interesting volume also contains the personal reminiscences of many eminent x-ray crystallographers.

G.13 André Guinier. *X-Ray Crystallographic Technology* (London: Hilger and Watts, 1952). Excellent treatment of the theory and practice of x-ray diffraction. The title is not fair to the book, which includes a considerable body of theory and detailed experimental technique. The theory and applications of the reciprocal lattice are very well described. Includes treatments of focusing monochromators, small-angle scattering, and diffraction by amorphous substances.

G.17 Harold P. Klug and Leroy E. Alexander. *X-Ray Diffraction Procedures*, 2nd ed. (New York: Wiley, 1974). Contains a great deal of useful detail on the theory and operation of powder cameras and diffractometers. Covers the following topics in depth: chemical analysis by diffraction, parameter measurement, line-broadening analysis, texture determination, stress measurement, and studies of amorphous materials. Single-crystal methods are not included.

G.18 W. Parrish, ed. *Advances in X-ray diffractometry and X-ray Spectrography* (Eindhoven: Centrex Pub. Co., 1962).

ANSWERS TO SELECTED PROBLEMS

2. 26.6°

Diffraction II: Intensities of Diffracted Beams

1 INTRODUCTION

As stated earlier, the positions of the atoms in the unit cell affect the intensities but not the directions of the diffracted beams. That this must be so may be seen by considering the two structures shown in Fig. 1. Both are orthorhombic with two atoms of the same kind per unit cell, but the one on the left is base-centered and the one on the right body-centered. Either is derivable from the other by a simple shift of one atom by the vector $\frac{1}{2}\mathbf{c}$.

Consider 001 diffraction with the aid of Fig. 2 which shows the (001) planes in profile. For the base-centered lattice shown in (a), suppose that Bragg's law is satisfied for the particular values of λ and θ employed. This means that the path difference ABC between rays **1´** and **2´** is one wavelength, so that rays **1´** and **2´** are in phase and diffraction occurs in the direction shown. Similarly, in the body-centered lattice shown in (b), rays **1´** and **2´** are in phase, since their path difference ABC is one wavelength. However, in this case, there is another plane of atoms midway between the (001) planes, and the path difference DEF between rays **1´** and **3´** is exactly half of ABC, or one-half wavelength. Thus rays **1´** and **3´** are completely out of phase and annul each other. Similarly, ray **4´** from the next plane of scatterers down (not shown) annuls ray **2´**, and so on throughout the crystal. There is no 001 reflection from the body-centered lattice.

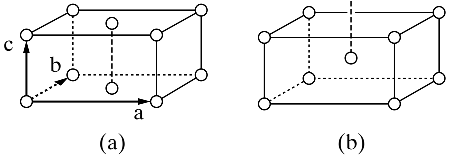

(a) (b)

Figure 1 (a) Base-centered and (b) body-centered orthorhombic unit cells.

From Chapter 4 of *Elements of X-Ray Diffraction*, Third Edition. B.D. Cullity, S.R. Stock.

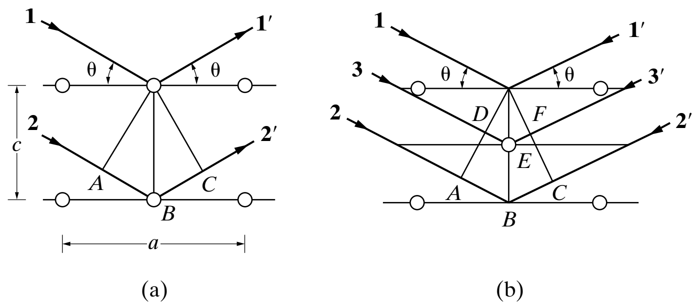

Figure 2 Diffraction from the (001) planes of scatterers in (a) base-centered and (b) body-centered orthorhombic lattices.

This example shows how a simple rearrangement of atoms within the unit cell can eliminate a reflection completely. More generally, the intensity of a diffracted beam is changed, not necessarily to zero, by any change in atomic positions, and, conversely, atomic positions can be determined only by observations of diffracted intensities. To establish an exact relation between atom position and intensity is the main purpose of this chapter. The problem is complex because of the many variables involved, and the relationship must be developed step by step: first by considering how x-rays are scattered by a single electron, then by an atom, and finally by all the atoms in the unit cell. These results are applied next to the powder method of x-ray diffraction and, to obtain an expression for the intensity of a powder pattern line, a number of other factors which affect the way in which a crystalline powder diffracts x-rays must be included.

2 SCATTERING BY AN ELECTRON

An x-ray beam can be described as an electromagnetic wave characterized by an electric field whose strength varies sinusoidally with time at any one point in the beam. Since an electric field exerts a force on a charged particle such as an electron, the oscillating electric field of an x-ray beam will set any electron it encounters into oscillatory motion about its mean position.

Now an accelerating or decelerating electron emits an electromagnetic wave. An example of this phenomenon appeared in the discussion of the x-ray tube, where x-rays are emitted because of the rapid deceleration of the electrons striking the target. Similarly, an electron which has been set into oscillation by an x-ray beam is continuously accelerating and decelerating during its motion and therefore emits an electromagnetic wave. In this sense, an electron is said to *scatter* x-rays, the scattered beam being simply the beam radiated by the electron under the action of the incident beam. The scattered beam has the same wavelength and frequency as the incident beam and is said to be *coherent* with it, since there is a definite relationship between the phase of the scattered beam and that of the incident beam which produced it. (The phase change on scattering from an electron is $\pi/2$. Because it is exactly the same for all the electrons in a crystal, it cancels in any consideration of phase differences between rays scattered by different atoms, and so does not affect the derivation of Bragg's law.)

Although x-rays are scattered in all directions by an electron, the intensity of the scattered beam depends on the angle of scattering, in a way which was first demonstrated by J. J. Thomson [1]. He found that the intensity I of the beam scattered by a single electron of charge e coulombs (C) and mass m kg, at a distance r meters from the electron, is given by

$$I = I_O\left(\frac{\mu_O}{4\pi}\right)^2\left(\frac{e^4}{m^2r^2}\right)\sin^2\alpha = I_O\frac{K}{r^2}\sin^2\alpha, \qquad (1)$$

where I_o = intensity of the incident beam, $\mu_0 = 4\pi \times 10^{-7}$ m kg C^{-2}, K = constant, and α = angle between the scattering direction and the direction of acceleration of the electron. Suppose the incident beam is traveling in the direction Ox (Fig. 3) and encounters an electron at O. The scattered intensity at P in the xz plane, where OP is inclined at a scattering angle of 2θ to the incident beam, is what must be determined. An unpolarized incident beam, such as that issuing from an x-ray tube, has its electric vector E in a random direction in the yz plane. This beam may be resolved into two plane-polarized components, having electric vectors $\mathbf{E}_y$ and $\mathbf{E}_z$ where

$$\mathrm{E}^2 = \mathrm{E}_y^2 + \mathrm{E}_z^2.$$

On the average, $\mathbf{E}_y$ will be equal to $\mathbf{E}_x$, since the direction of $\mathbf{E}$ is perfectly random. Therefore

$$\mathrm{E}_y^2 = \mathrm{E}_z^2 = \tfrac{1}{2}\mathrm{E}^2.$$

The intensity of these two components of the incident beam is proportional to the square of their electric vectors, since $\mathbf{E}$ measures the amplitude of the wave and the intensity of a wave is proportional to the square of its amplitude. Therefore

$$I_{Oy} = I_{Oz} = \tfrac{1}{2}I_O.$$

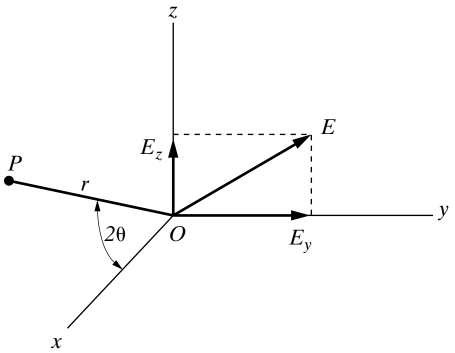

Figure 3 Coherent scattering of x-rays by a single electron.

The y component of the incident beam accelerates the electron in the direction Oy. It therefore gives rise to a scattered beam whose intensity at P is found from Eq. (1) to be

$$I_{Py} = I_{Oy}\frac{K}{r^2}.$$

since $\alpha = \measuredangle yOP = \pi/2$. Similarly, the intensity of the scattered z component is given by

$$I_{Pz} = I_{Oz}\frac{K}{r^2}\cos^2 2\theta,$$

since $\alpha = \pi/2 - 2\theta$. The total scattered intensity at P is obtained by summing the intensities of these two scattered components:

$$\begin{aligned} I_P &= I_{Py} + I_{Pz} \\ &= \frac{K}{r^2}(I_{Oy} + I_{Oz}\cos^2 2\theta) \\ &= \frac{K}{r^2}\left(\frac{I_O}{2} + \frac{I_O}{2}\cos^2 2\theta\right) \\ &= I_O\frac{K}{r^2}\left(\frac{1 + \cos^2 2\theta}{2}\right). \end{aligned} \tag{2}$$

This is the Thomson equation for the scattering of an x-ray beam by a single electron. The intensity of the scattered beam is only a minute fraction of the intensity of the incident beam; the value of K is $7.94 \times 10^{-30}\,\text{m}^2$, so that I_r/I_o is only 7.94×10^{-26} in the forward direction at 1 cm from the electron. The equation also shows that the scattered intensity decreases as the inverse square of the distance from the scattering electron, as one would expect, and that the scattered beam is stronger in forward or backward directions than in a direction at right angles to the incident beam.

The Thomson equation gives the absolute intensity (in ergs/sq cm/sec) of the scattered beam in terms of the absolute intensity of the incident beam. These absolute intensities are both difficult to measure and difficult to calculate, so it is fortunate that relative values are sufficient for practically all diffraction problems. In most cases, all factors in Eq. (2) except the last are constant during the experiment and can be omitted. This last factor, $\frac{1}{2}(1 + \cos^2 2\theta)$, is called the *polarization factor*; this is a rather unfortunate term because this factor enters the equation simply because the incident beam is unpolarized. The polarization factor is common to all intensity calculations, and it appears later in the equation for the intensity of a beam diffracted by a crystalline powder. If a monochromator is used, for example with a diffractometer, the polarization factor must include an additional term depending on θ_M, the Bragg angle for the monochromator, and it is $1/2(1 + \cos^2 2\theta \cos^2 2\theta_M)$.

There is another and quite different way in which an electron can scatter x-rays, and that is manifested in the *Compton effect*. This effect, discovered by A. H. Compton in 1923 [2], occurs whenever x-rays encounter loosely bound or free electrons and can be understood only by considering the incident beam not as a wave but as a stream of x-ray quanta or photons, each of energy $h\nu_1$. When such a photon strikes a loosely bound electron, the collision is an elastic one like that of two billiard balls (Fig. 4). The electron is knocked aside and the photon deflects through an angle 2θ. Since some of the energy of the incident photon is used in providing kinetic energy for the electron, the energy $h\nu_2$ of the photon after impact is less than its energy $h\nu_1$ before impact. The wavelength λ_2 of the scattered radiation is thus slightly greater than the wavelength λ_1 of the incident beam, the magnitude of the change being given by the equation

$$\Delta\lambda(\text{Å}) = \lambda_2 - \lambda_1 = 0.0486 \sin^2\theta. \tag{3}$$

The increase in wavelength depends only on the scattering angle, and it varies from zero in the forward direction ($2\theta = 0$) to 0.05 Å in the extreme backward direction ($2\theta = 180°$).

Radiation so scattered is called *Compton modified radiation*, and, besides having its wavelength increased, it has the important characteristic that *its phase has no fixed relation to the phase of the incident beam*. For this reason it is also known as incoherent radiation. It cannot take part in diffraction because its phase is only randomly related to that of the incident beam and cannot therefore produce any interference effects. Compton modified scattering cannot be prevented, however, and it has the undesirable effect of increasing the background in diffraction patterns.

(It should be noted that quantum theory can account for both the coherent and the incoherent scattering, whereas the wave theory is applicable only to the former. In terms of quantum theory, coherent scattering occurs when an incident photon bounces off an electron which is so tightly bound that the electron receives no momentum from the impact. The scattered photon therefore has the same energy, and hence wavelength, as it had before.)

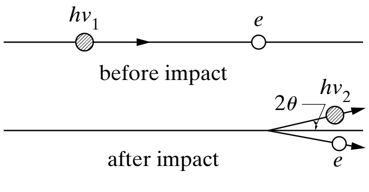

Figure 4 Elastic collision of photon and electron (Compton effect).

3 SCATTERING BY AN ATOM

When an x-ray beam encounters an atom, each electron in it scatters part of the radiation coherently in accordance with the Thomson equation. One might also expect the nucleus to take part in the coherent scattering, since it also bears a charge and should be capable of oscillating under the influence of the incident beam. However, the nucleus has an extremely large mass relative to that of the electron and cannot be made to oscillate to any appreciable extent; in fact, the Thomson equation shows that the intensity of coherent scattering is inversely proportional to the square of the mass of the scattering particle. The net effect is that coherent scattering by an atom is due only to the electrons contained in that atom.

The following question then arises: is the wave scattered by an atom simply the sum of the waves scattered by its component electrons? More precisely, does an atom of atomic number Z, i.e., an atom containing Z electrons, scatter a wave whose amplitude is Z times the amplitude of the wave scattered by a single electron? The answer is yes, if the scattering is in the forward direction ($2\theta = 0$), because the waves scattered by all the electrons of the atom are then in phase and the amplitudes of all the scattered waves can be added directly.

This is not true for other directions of scattering. The fact that the electrons of an atom are situated at different points in space introduces differences in phase between the waves scattered by different electrons. Consider Fig. 5, in which, for simplicity, the electrons are shown as points arranged around the central nucleus. The waves scattered in the forward direction by electrons A and B are exactly in phase on a wave front such as XX', because each wave has traveled the same distance before and after scattering. The other scattered waves shown in the figure, however, have a path difference equal to $(CB - AD)$ and are thus somewhat out of phase along a wave front such as YY', the path difference being less than one wave-

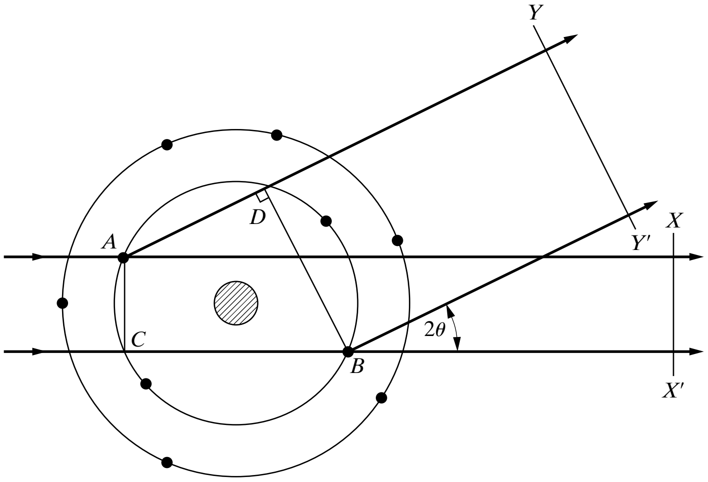

Figure 5 X-ray scattering by an atom.

length. Partial interference occurs between the waves scattered by A and B, with the result that the net amplitude of the wave scattered in this direction is less than that of the wave scattered by the same electrons in the forward direction.

A quantity f, *the atomic scattering factor*, is used to describe the "efficiency" of scattering of a given atom in a given direction. It is defined as a ratio of amplitudes:

$$f = \frac{\text{amplitude of the wave scattered by an atom}}{\text{amplitude of the wave scattered by one electron}}.$$

From what has been said already, it is clear that $f = Z$ for any atom scattering in the forward direction. As θ increases, however, the waves scattered by individual electrons become more and more out of phase and f decreases. The atomic scattering factor depends also on the wavelength of the incident beam: at a fixed value of θ, f will be smaller the shorter the wavelength, since the path differences will be larger relative to the wavelength, leading to greater interference between the scattered beams. The actual calculation of f involves $\sin\theta$ rather than θ, so that the net effect is that f decreases as the quantity $(\sin\theta)/\lambda$ increases. The scattering factor f is sometimes called the *form factor*, because it depends on the way in which the electrons are distributed around the nucleus.

Calculated values of f for various atoms and various values of $(\sin\theta)/\lambda$ are tabulated in Appendix: Lorentz-Polarization Factor, and a curve showing the typical variation of f, in this case for copper, is given in Fig. 6. Note again that the curve begins at the atomic number of copper, 29, and decreases to very low values for scattering in the backward direction (θ near 90°) or for very short wavelengths. Since the intensity of a wave is proportional to the square of its amplitude, a curve of scattered intensity from an atom can be obtained simply by squaring the ordinates of a curve such as Fig. 6.

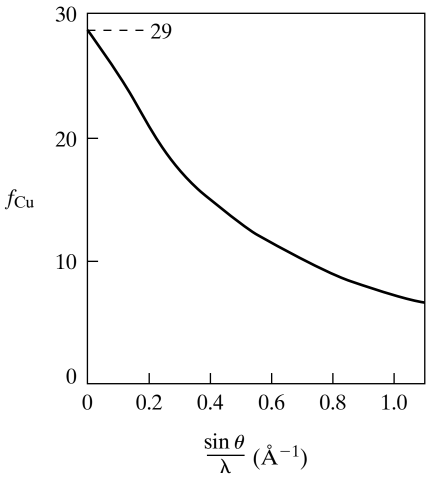

Figure 6 The atomic scattering factor of copper.

Strictly, the scattering factors f tabulated in Appendix: Lorentz-Polarization Factor apply only when the scattered radiation has a wavelength much shorter than that of an absorption edge of the scattering atom. When these two wavelengths are nearly the same, a small correction to f must be applied in precise work. Ordinarily, this effect, called *anomalous dispersion*, is neglected.

The scattering just discussed, whose amplitude is expressed in terms of the atomic scattering factor, is coherent, or unmodified, scattering, which is the only kind capable of being diffracted. On the other hand, incoherent, or Compton modified, scattering is occurring at the same time. Since the latter is due to collisions of quanta with loosely bound electrons, its intensity relative to that of the unmodified radiation increases as the proportion of loosely bound electrons increases. The intensity of Compton modified radiation thus increases as the atomic number Z decreases. It is for this reason that it is sometimes difficult to obtain good diffraction patterns of organic materials, which contain light elements such as carbon, oxygen, and hydrogen, since the strong Compton modified scattering from these substances increases the background and makes it difficult to observe the diffraction lines formed by the unmodified radiation. It is also found that the intensity of the modified radiation increases as the quantity $(\sin\theta)/\lambda$ increases. The intensities of modified scattering and of unmodified scattering therefore vary in opposite ways with Z and with $(\sin\theta)/\lambda$.

To summarize, when a monochromatic beam of x-rays strikes an atom, two scattering processes occur. Tightly bound electrons are set into oscillation and radiate x-rays of the same wavelength as that of the incident beam. More loosely bound electrons scatter part of the incident beam and slightly increase its wavelength in the process, the exact amount of increase depending on the scattering angle. The former is called coherent or unmodified scattering and the latter incoherent or modified; both kinds occur simultaneously and in all directions. If the atom is a part of a large group of atoms arranged in space in a regular periodic fashion as in a crystal, then another phenomenon occurs. The coherently scattered radiation from all the atoms undergoes reinforcement in certain directions and cancellation in other directions, thus producing diffracted beams. Diffraction is, essentially, reinforced coherent scattering.

The chief effects associated with the passage of x-rays through matter are summarized schematically in Fig. 7. The incident x-rays are assumed to be of high enough energy, i.e., of short enough wavelength, to cause the emission of photoelectrons and characteristic fluorescent radiation. The Compton recoil electrons shown in the diagram are the loosely bound electrons knocked out of the atom by x-ray quanta, the interaction giving rise to Compton modified radiation. Auger electrons are those ejected from an atom by characteristic x-rays produced within the atom.

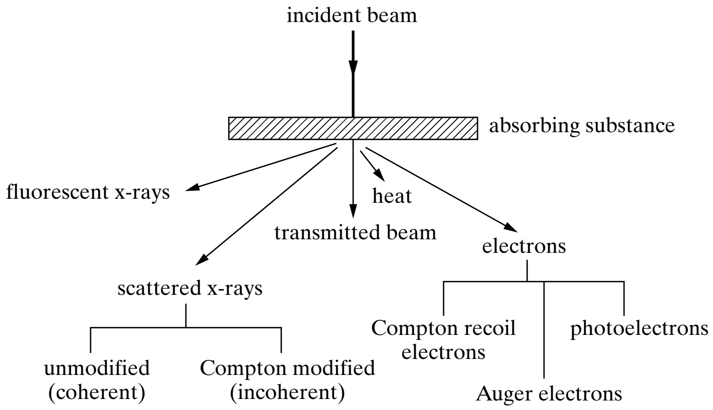

Figure 7 Effects produced by the passage of x-rays through matter, after Henry, Lipson, and Wooster [G.15].

4 SCATTERING BY A UNIT CELL

To arrive at an expression for the intensity of a diffracted beam, the coherent scattering must be considered, not from an isolated atom but from all the atoms making up the crystal. The mere fact that the atoms are arranged in a periodic fashion in space means that the scattered radiation is now severely limited to certain definite directions and is now referred to as a set of diffracted beams. The directions of these beams are fixed by Bragg's law, which is, in a sense, a negative law. If Bragg's law is not satisfied, no diffracted beam can occur; however, Bragg's law may be satisfied for a certain set of atomic planes and yet no diffraction may occur, as in the example given at the beginning of this chapter, because of a particular arrangement of atoms within the unit cell [Fig. 2(b)].

Assuming that Bragg's law is satisfied, the goal is to find the intensity of the beam diffracted by a crystal as a function of atom position. Since the crystal is merely a repetition of the fundamental unit cell, it is enough to consider the way in which the arrangement of atoms within a single unit cell affects the diffracted intensity.

Qualitatively, the effect is similar to the scattering from an atom, discussed in the previous section. Phase differences are found for the waves scattered by the individual electrons, for any direction of scattering except the extreme forward direction. Similarly, the waves scattered by the individual atoms of a unit cell are not necessarily in phase except in the forward direction, and determining how the phase difference depends on the arrangement of the atoms is the problem at hand.

This problem is most simply approached by finding the phase difference between waves scattered by an atom at the origin and another atom whose position is variable in the x direction only. For convenience, consider an orthogonal unit cell, a section of which is shown in Fig. 8. Take atom A as the origin and orient the incident beam $\mathbf{S}_0$ so that $h00$ diffractions occurs. The planes through the array of scatterers are shown as heavy lines in the drawing. This means that Bragg's law is satis-

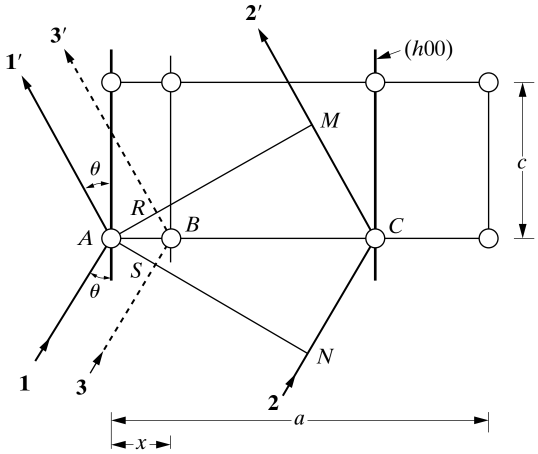

Figure 8 The effect of atom position on the phase difference between diffracted rays..

fied for this reflection and that $\delta_{2'1'}$ the path difference between ray **2´** and ray **1´**, is given by

$$\delta_{2'1'} = MCN = 2d_{h00} \sin\theta = \lambda.$$

From the definition of Miller indices,

$$d_{h00} = AC = \frac{a}{h}.$$

How is this reflection affected by x-rays scattered in the same direction by atom B, located at a distance x from A? Note that only this direction need be considered since only in this direction is Bragg's law satisfied for the h00 reflection. Clearly, the path difference between ray **3´** and ray **1´**, $\delta_{3'1'}$ will be less than λ; by simple proportion it is found to be

$$\delta_{3'1'} = RBS = \frac{AB}{AC}(\lambda) = \frac{x}{a/h}(\lambda).$$

Phase differences may be expressed in angular measure as well as in wavelength: two rays, differing in path length by one whole wavelength, are said to differ in phase by 360°, or 2π radians. If the path difference is δ, then the phase difference ϕ in radians is given by

$$\phi = \frac{\delta}{\lambda}(2\pi).$$

The use of angular measure is convenient because it makes the expression of phase differences independent of wavelength, whereas the use of a path difference to describe a phase difference is meaningless unless the wavelength is specified.

The phase difference, then, between the wave scattered by atom B and that scattered by atom A at the origin is given by

$$\phi_{3'1'} = \frac{\delta_{3'1'}}{\lambda}(2\pi) = \frac{2\pi h x}{a}.$$

If the position of atom B is specified by its fractional coordinate $u = x/a$, then the phase difference becomes

$$\phi_{3'1'} = 2\pi hu.$$

This reasoning may be extended to three dimensions, as in Fig. 9, in which atom B has actual coordinates $x\ y\ z$ or fractional coordinates $\frac{x}{a}\,\frac{y}{b}\,\frac{z}{c}$ equal to $u\ v\ w$, respectively. The following important relationship then applies between the phase difference between the wave scattered by atom B and that scattered by atom A at the origin, for the hkl reflection:

$$\phi = 2\pi(hu + kv + lw). \tag{4}$$

This relation is general and applicable to a unit cell of any shape. Figure 9 shows the planes with Miller indices *hkl* but one should always remember that interference between x-rays scattered from the atoms produces the diffracted beams and not reflection from "planes."

These two waves may differ, not only in phase, but also in amplitude if atom B and the atom at the origin are of different kinds. In that case, the amplitudes of these waves are given, relative to the amplitude of the wave scattered by a single electron, by the appropriate values of f, the atomic scattering factor.

The problem of scattering from a unit cell resolves itself, therefore, into one of adding waves of different phase and amplitude in order to find the resultant wave. Waves scattered by all the atoms of the unit cell, including the one at the origin, must be added. The most convenient way of carrying out this summation is by expressing each wave as a complex exponential function.

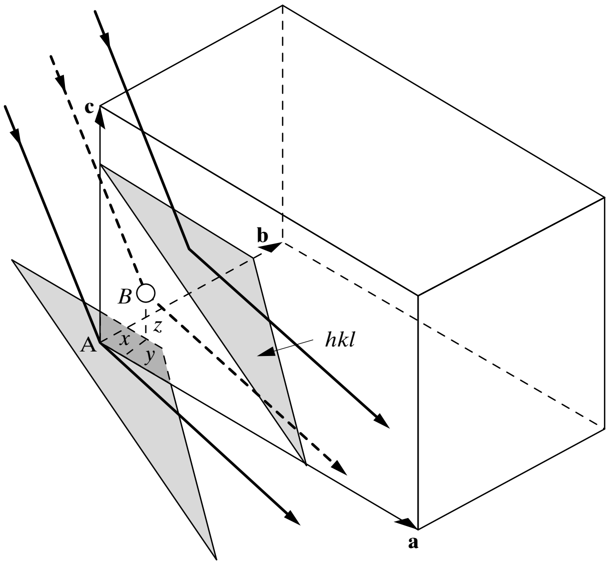

Figure 9 The three-dimensional analog of Fig. 8.

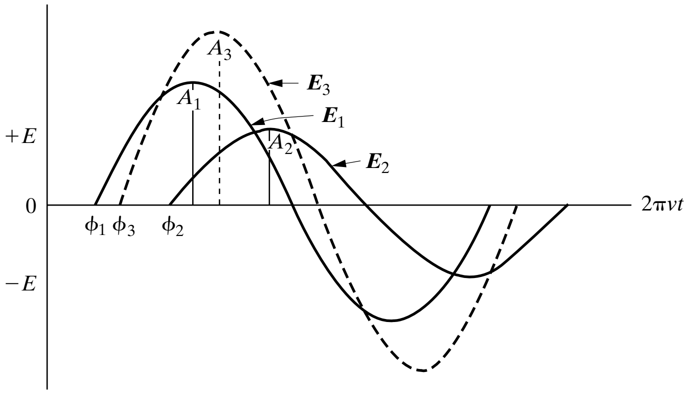

Figure 10 The addition of sine waves of different phase and amplitude.

The two waves shown as full lines in Fig. 10 represent the variations in electric field intensity **E** with time *t* of two rays on any given wave front in a diffracted x-ray beam. Their equations may be written

$$\mathbf{E}_1 = A_1 \sin(2\pi\nu t - \phi_1) \tag{5}$$

$$\mathbf{E}_2 = A_2 \sin(2\pi\nu t - \phi_2). \tag{6}$$

These waves are of the same frequency ν and therefore of the same wavelength λ, but differ in amplitude A and in phase ϕ. The dotted curve shows their sum $\mathbf{E}_3$, which is also a sine wave, but of different amplitude and phase.

Waves differing in amplitude and phase may also be added by representing them as vectors. In Fig. 11, each component wave is represented by a vector whose length is equal to the amplitude of the wave and which is inclined to the x-axis at an angle equal to the phase angle. The amplitude and phase of the resultant wave are then found simply by adding the vectors by the parallelogram law.

This geometrical construction may be avoided by use of the following analytical treatment, in which complex numbers are used to represent the vectors. A complex number is the sum of a real and an imaginary number, such as $(a + bi)$, where a and b are real and $i = \sqrt{-1}$ is imaginary. Such numbers may be plotted in the "complex plane," in which real numbers are plotted as abscissae and imaginary numbers as ordinates. Any point in this plane, or the vector drawn from the origin to this point, then represents a particular complex number $(a + bi)$.

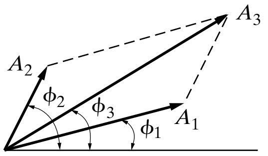

Figure 11 Vector addition of waves.

To find an analytical expression for a vector representing a wave, draw the wave vector in the complex plane as in Fig. 12. Here again the amplitude and phase of the wave are given by A, the length of the vector, and ϕ, the angle between the vector and the axis of real numbers. The analytical expression for the wave is now the complex number $(A\cos\phi + iA\sin\phi)$, since these two terms are the horizontal and vertical components OM and ON of the vector. Note that multiplication of a vector by i rotates it counterclockwise by 90°; thus multiplication by i converts the horizontal vector 2 into the vertical vector $2i$. Multiplication twice by i, that is, by $i^2=-1$, rotates a vector through 180° or reverses its sense; thus multiplication twice by i converts the horizontal vector 2 into the horizontal vector -2 pointing in the opposite direction.

Comparing the power-series expansions of e^{ix}, $\cos x$, and $\sin x$ and yields

$$e^{ix} = \cos x + i \sin x \tag{7}$$

or

$$Ae^{i\phi} = A\cos\phi + Ai\sin\phi. \tag{8}$$

Thus the wave vector may be expressed analytically by either side of Eq. (8). The expression on the left is called a complex exponential function.

Since the intensity of a wave is proportional to the square of its amplitude, an expression is needed for A^2, the square of the absolute value of the wave vector. When a wave is expressed in complex form, this quantity is obtained by multiplying the complex expression for the wave by its complex conjugate, which is obtained simply by replacing i by $-i$. Thus, the complex conjugate of $Ae^{i\phi}$ is $Ae^{-i\phi}$. Thus,

$$|Ae^{i\phi}|^2 = Ae^{i\phi}Ae^{-i\phi} = A^2, \tag{9}$$

which is the quantity desired. Or, using the other form given by Eq. (8),

$$A(\cos\phi + i\sin\phi)\,A(\cos\phi - i\sin\phi) = A^2(\cos^2\phi + \sin^2\phi) = A^2.$$

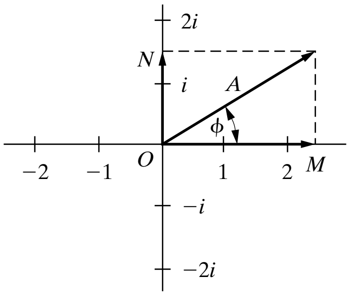

Figure 12 A wave vector in the complex plane.

Adding the scattered waves from each of the atoms in the unit cell requires addition of the complex numbers representing the amplitude and phase of each wave. The amplitude of each wave is given by the appropriate value of f for the scattering atom considered and the value of $(\sin\theta)/\lambda$ involved in the reflection. The phase of each wave is given by Eq. (4) in terms of the *hkl* reflection considered and the *uvw* coordinates of the atom. Using the previous relations, any scattered wave can be expressed in the complex exponential form:

$$Ae^{i\phi} = fe^{2\pi i(hu+kv+lw)}. \tag{10}$$

The resultant wave scattered by all the atoms of the unit cell is called the *structure factor*, because it describes how the atom arrangement, given by *uvw* for each atom, affects the scattered beam [3]. The structure factor, designated by the symbol F, is obtained by simply adding together all the waves scattered by the individual atoms. If a unit cell contains atoms $1, 2, 3, \ldots, N$, with fractional coordinates $u_1 v_1 w_1, u_2 v_2 w_2, u_3 v_3 w_3, \ldots$ then the structure factor for the *hkl* reflection is given by

$$F = f_1e^{2\pi i(hu_1+kv_1+lw_1)} + f_2e^{2\pi i(hu_2+kv_2+lw_2)} + f_3e^{2\pi i(hu_3+kv_3+lw_3)} + \cdots$$

This equation may be written more compactly as

$$F_{hkl} = \sum_{1}^{N} f_n e^{2\pi i(hu_n+kv_n+lw_n)}, \tag{11}$$

where the summation extends over all N atoms of the unit cell.

F is, in general, a complex number, and it expresses both the amplitude and phase of the resultant wave. Its absolute value $|F|$ gives the amplitude of the resultant wave in terms of the amplitude of the wave scattered by a single electron. Like the atomic scattering factor f, $|F|$ is defined as a ratio of amplitudes:

$$|F| = \frac{\text{amplitude of the wave scattered by all the atoms of a unit cell}}{\text{amplitude of the wave scattered by one electron}}.$$

The intensity of the beam diffracted by all atoms of the unit cell in a direction predicted by Bragg's law is proportional simply to $|F|^2$, the square of the amplitude of the resultant beam, and $|F|^2$ is obtained by multiplying the expression given for F in Eq. (11) by its complex conjugate F^*. Equation (11) is therefore a very important relation in x-ray crystallography, since it permits a calculation of the intensity of any *hkl* reflection from a knowledge of the atomic positions.

The result in Eg. 11 describes the wave scattered from the unit cell by adding together waves, differing in phase, scattered by individual atoms in the unit cell. Note that the phase difference between rays scattered by any two atoms, such as A and B in Fig. 8, is *constant* for every unit cell. In the direction predicted by Bragg's law, the rays scattered by all the atoms A in the crystal are exactly in phase and so are the rays scattered by all the atoms B, but between these two sets of rays there is a definite phase difference which depends on the relative positions of atoms A and B in the unit cell and which is given by Eq. (4).

Although it is more unwieldy, the following trigonometric equation may be used instead of Eq. (11):

$$F = \sum_{1}^{N} f_n[\cos 2\pi(hu_n + kv_n + lw_n) + i \sin 2\pi(hu_n + kv_n + lw_n)]. \quad (12)$$

One such term must be written down for each atom in the unit cell. In general, the summation will be a complex number of the form

$$F = a + ib,$$

where

$$a = \sum_{1}^{N} f_n \cos 2\pi(hu_n + kv_n + lw_n),$$

$$b = \sum_{1}^{N} f_n \sin 2\pi(hu_n + kv_n + lw_n)$$

and

$$|F|^2 = (a + ib)(a - ib) = a^2 + b^2. \quad (13)$$

Substitution for a and b gives the final form of the equation:

$$|F|^2 = [f_1 \cos 2\pi(hu_1 + kv_1 + lw_1) + f_2 \cos 2\pi(hu_2 + kv_2 + lw_2) + \cdots)^2$$

$$+ [f_1 \sin 2\pi(hu_1 + kv_1 + lw_1) + f_2 \sin 2\pi(hu_2 + kv_2 + lw_2) + \cdots)^2. \quad (14)$$

Equation (11) is much easier to manipulate, compared to this trigonometric from, particularly if the structure is at all complicated, since the exponential form is more compact.

5 SOME USEFUL RELATIONS

In calculating structure factors by complex exponential functions, many particular relations occur often enough to be worthwhile stating here. They may be verified by means of Eq. (7).

a) $e^{\pi i} = e^{3\pi i} = e^{5\pi i} = -1,$

b) $e^{2\pi i} = e^{4\pi i} = e^{6\pi i} = +1,$

c) *In general*, $e^{n\pi i} = (-1)^{n}$, where n is any integer,

d) $e^{n\pi i} = e^{-n\pi i}$, where n is any integer,

e) $e^{i\pi} + e^{-i\pi} = 2\cos x$.

6 STRUCTURE-FACTOR CALCULATIONS

Facility in the use of Eq. (11) can be gained only by working actual examples, such as those found here.

a) The simplest case is that of a unit cell containing only one atom at the origin, i.e., having fractional coordinates 0 0 0. Its structure factor is

$$F = fe^{2\pi i(0)} = f$$

and

$$F^2 = f^2.$$

F^2 is thus independent of h, k, and l and is the same for all reflections.

b) Consider now the base-centered cell discussed at the beginning of this chapter and shown in Fig. 1(a). It has two atoms of the same kind per unit cell located at 0 0 0 and $\frac{1}{2}\,\frac{1}{2}\,0$.

$$F = fe^{2\pi i(0)} + fe^{2\pi i(h/2 + k/2)}$$

$$= f\left[1 + e^{\pi i(h+k)}\right].$$

This expression may be evaluated without multiplication by the complex conjugate, since $(h + k)$ is always integral, and the expression for F is thus real and not complex. If h and k are both even or both odd, i.e., "unmixed," then their sum is always even and $e^{\pi i(h+k)}$ has the value 1. Therefore

$$F = 2f \text{ for } h \text{ and } k \text{ unmixed;}$$

$$F^2 = 4f^2.$$

On the other hand, if h and k are one even and one odd, i.e., "mixed," then their sum is odd and $e^{\pi i(h+k)}$ has the value -1. Therefore

$$F = 0 \text{ for } h \text{ and } k \text{ mixed;}$$

$$F^2 = 0.$$

Note that, in either case, the value of the l index has no effect on the structure factor. For example, the reflections 111, 112, 113, and 021, 022, 023 all have the same value of F, namely $2f$. Similarly, the reflections 011, 012, 013, and 101, 102, 103 all have a zero structure factor and are *systematically absent* [4].

c) The structure factor of the body-centered cell shown in Fig. 1(b) may also be calculated. This cell has two atoms of the same kind located at 0 0 0 and $\frac{1}{2}\,\frac{1}{2}\,\frac{1}{2}$.

$$F = fe^{2\pi i(0)} + fe^{2\pi i(h/2 + k/2 + l/2)}$$

$$= f[1 + e^{\pi i(h + k + l)}].$$

$$F = 2f \qquad \text{when } (h + k + l) \text{ is even;}$$

$$F = 4f^2.$$

$$F = 0 \qquad \text{when } (h + k + l) \text{ is odd;}$$

$$F^2 = 0.$$

The earlier geometrical conclusion that the base-centered cell would produce a 001 reflection but that the body-centered cell would not agrees with the structure-factor equations for these two cells. A detailed examination of the geometry of all possible reflections, however, would be a very laborious process compared to the straightforward calculation of the structure factor, a calculation that yields a set of rules governing the value of F^2 for all possible values of indices h, k and l.

d) A face-centered cubic cell may now be considered. Assume it contains four atoms of the same kind, located at 0 0 0, $\frac{1}{2}\,\frac{1}{2}$ 0, $\frac{1}{2}$ 0 $\frac{1}{2}$, and 0 $\frac{1}{2}\,\frac{1}{2}$.

$$F = fe^{2\pi i(0)} + fe^{2\pi i(h/2 + k/2)} + fe^{2\pi i(k/2 + l/2)} + fe^{2\pi i(h/2 + l/2)}$$

$$= f[1 + e^{\pi i(h + k)} + e^{\pi i(k + l)} + e^{\pi i(h + l)}].$$

If h, k, and l are unmixed, then all three sums $(h + k)$, $(h + l)$, and $(k + l)$ are even integers, and each term in the above equation has the value 1.

$$F = 4f \text{ for unmixed indices;}$$

$$F^2 = 16f^2.$$

If h, k, and l are mixed, then the sum of the three exponentials is -1, whether two of the indices are odd and one even, or two even and one odd. Suppose, for example, that h and l are even and k is odd, e.g., 012. Then $F = f(1 - 1 + 1 - 1) = 0$, and no reflection occurs.

$$F = 0 \text{ for mixed indices;}$$

$$F^2 = 0$$

Thus, reflections may occur for such planes as (111), (200), and (220) but not for the planes (100), (210), (112), etc.

TABLE 1

Bravais lattice	Reflections possibly present	Reflections necessarily absent
Simple	all	none
Base-centered	h and k unmixed*	h and k mixed*
Body-centered	$(h + k + l)$ even	$(h + k + l)$ odd
Face-centered	h, k, and l unmixed	h, k, and l mixed

* These relations apply to a cell centered on the C face. If reflections are present only when h and l ar unmixed, or when k and l are unmixed, then the cell is centered on the B or A face, respectively.

The reader may have noticed in the previous examples that some of the information given was not used in the calculations. In (a), for example, the cell was said to contain only one atom, but the shape of the cell was not specified; in (b) and (c), the cells were described as orthorhombic and in (d) as cubic, but this information did not enter into the structure-factor calculations. This illustrates the important point that *the structure factor is independent of the shape and size of the unit cell.* For example, *any* body-centered cell will have missing reflections for those planes which have $(h + k + l)$ equal to an odd number, whether the cell is cubic, tetragonal, or orthorhombic. The rules derived in the above examples are therefore of wider applicability than would at first appear and demonstrate the close connection between the Bravais lattice of a substance and its diffraction pattern. They are summarized in Table 1. These rules are subject to some qualification, since some cells may contain more atoms than the ones given in examples (a) through (d), and these atoms may be in such positions that reflections normally present are now missing. For example, diamond has a face-centered cubic lattice, but it contains eight carbon atoms per unit cell. All the reflections present have unmixed indices, but reflections such as 200, 222, 420, etc., are missing. The fact that the only reflections *present* have unmixed indices proves that the lattice is face-centered, while the extra missing reflections are a clue to the actual atom arrangement in this crystal.

e)This point may be further illustrated by the structure of NaCl. This crystal has a cubic lattice with 4 Na and 4 Cl atoms per unit cell, located as follows:

$$\begin{array}{lcccc} \text{Na} & 0\,0\,0 & \frac{1}{2}\,\frac{1}{2}\,0 & \frac{1}{2}\,0\,\frac{1}{2} & 0\,\frac{1}{2}\,\frac{1}{2} \\[1em] \text{Cl} & \frac{1}{2}\,\frac{1}{2}\,\frac{1}{2} & 0\,0\,\frac{1}{2} & 0\,\frac{1}{2}\,0 & \frac{1}{2}\,0\,0 \end{array}$$

In this case, the proper atomic scattering factors for each atom[1] must be inserted in the structure-factor equation, which will have eight terms:

$$F = f_{\text{Na}}e^{2\pi i(0)} + f_{\text{Na}}e^{2\pi i(h/2 + k/2)} + f_{\text{Na}}e^{2\pi i(h/2 + l/2)} + f_{\text{Na}}e^{2\pi i(k/2 + l/2)}$$

---

[1] Strictly, and if the calculation of F is to be made to the highest accuracy, scattering factors f for the ions Na^+ and Cl^- must be used, rather than the f values for the neutral atoms Na and Cl, because NaCl is ionized.

$$+f_{\mathrm{Cl}}\mathrm{e}^{2\pi i(h/2+k/2+l/2)} + \mathrm{f}_{\mathrm{Cl}}\mathrm{e}^{2\pi i(l/2)} + \mathrm{f}_{\mathrm{Cl}}\mathrm{e}^{2\pi i(k/2)} + \mathrm{f}_{\mathrm{Cl}}\mathrm{e}^{2\pi i(h/2)},$$

$$F = f_{\mathrm{Na}}[1 + e^{\pi i(h+k)} + e^{\pi i(h+l)} + e^{\pi i(k+l)}]$$

$$+f_{\mathrm{Cl}}[\mathrm{e}^{\pi \mathrm{i}(h+k+l)} + e^{\pi il} + e^{\pi ik} + e^{\pi ih}].$$

The sodium-atom positions are related by the face-centering translations and so are the chlorine-atom positions. *Whenever a lattice contains common translations, the corresponding terms in the structure-factor equation can always be factored out*, leading to considerable simplification. In this case:

$$F = f_{\mathrm{Na}}[1 + e^{\pi i(h+k)} + e^{\pi i(h+l)} + e^{\pi i(k+l)}]$$

$$+ f_{\mathrm{Cl}}e^{\pi i(h+k+l)}[1 + e^{\pi i(-h-k)} + e^{\pi i(-h-l)} + e^{\pi i(-k-l)}].$$

The signs of the exponents in the second bracket may be changed, by relation (d) of Sec. 5. Therefore

$$F = [1 + e^{\pi i(h+k)} + e^{\pi i(h+l)} + e^{\pi i(k+l)}][f_{\mathrm{Na}} + f_{\mathrm{Cl}}e^{\pi i(h+k+l)}].$$

Here the terms corresponding to the face-centering translations appear in the first factor; the second factor contains the terms that describe the “basis” of the unit cell, namely, the Na atom at 0 0 0 and the Cl atom at $\frac{1}{2}\,\frac{1}{2}\,\frac{1}{2}$. The terms in the first bracket, describing the face-centering translations, have already appeared in example (d), and they were found to have a total value of zero for mixed indices and 4 for unmixed indices. This shows at once that NaCl has a face-centered lattice and that

$$F = 0 \qquad \text{for mixed indices;}$$

$$F^2 = 0.$$

For unmixed indices,

$$F = 4[f_{\mathrm{Na}} + f_{\mathrm{Cl}}e^{\pi i(h+k+l)}].$$

$$F = 4(f_{\mathrm{Na}} + f_{\mathrm{Cl}}) \qquad \text{if } (h + k + l) \text{ is even;}$$

$$F^2 = 16(f_{\mathrm{Na}} - f_{\mathrm{Cl}})^2.$$

$$F = 4(f_{\mathrm{Na}} - f_{\mathrm{Cl}}) \qquad \text{if } (h + k + l) \text{ is odd;}$$

$$F^2 = 16(f_{\mathrm{Na}} - f_{\mathrm{Cl}})^2.$$

In this case, there are more than four atoms per unit cell, but the lattice is still face-centered. The introduction of additional atoms has not eliminated any reflections present in the case of the four-atom cell, but it has decreased some in intensity. For example, the 111 reflection now involves the difference, rather than the sum, of the scattering powers of the two atoms.

The student should carefully note that a lot of algebra can be eliminated, whenever a lattice is known to be centered in any way, by factoring common translations out of the structure-factor equation and inserting immediately the known values of the terms representing these translations. This shortcut procedure is illustrated for NaCl:

1. Write down the atom positions in abbreviated form:

   4 Na at 0 0 0 + face–centering translations,

   4 Cl at $\frac{1}{2}\frac{1}{2}\frac{1}{2}$ + face–centering translations.

2. Write down the equation for F as a product of two factors. The first is the value of the terms representing the common translations; the second has terms corresponding to the "basis" atoms of the cell. The equation is

$$F = \begin{bmatrix} 4 \\ 0 \end{bmatrix} [f_{Na} + f_{Cl}e^{\pi i(h+k+l)}] \quad \begin{matrix} \text{unmixed indices} \\ \text{mixed indices.} \end{matrix}$$

3. Simplify further, as necessary. In all structure-factor calculations the aim is to obtain a set of *general* equations that will give the value of F for *any* value of *hkl*.

This shortcut procedure is illustrated again, for the ZnS structure, in Sec. 13.

Before proceeding to the final example of this section, the effect of a specific basis on the non-systematically absent reflections will be illustrated using vector addition in the complex plane and the diamond structure discussed in example (d). The carbon atom positions are:

4 C at 0 0 0 + face–centering translations,

4 C at $\frac{1}{4}\frac{1}{4}\frac{1}{4}$ + face–centering translations.

Therefore,

$$F = \begin{bmatrix} 4 \\ 0 \end{bmatrix} f_c \{1 + e^{\pi i(h+k+l)/2}\} \quad \begin{matrix} \text{unmixed indices} \\ \text{mixed indicies.} \end{matrix}$$

Three types of interference result for the non-systematically absent reflections (h, k, l unmixed), depending on whether (i) h, k and l are odd, (ii) $h + k + l$ is an even multiple of two or (iii) $h + k + l$ is an odd multiple of two, and the results for a single basis are plotted in the complex plane for (i) - (iii) in Fig. 13 (left, middle and right), respectively. Multiplying the basis resultant by four (there are four bases per unit cell) yields the structure factor. Thus the fcc-allowed reflections 200 and 222 produce no diffracted intensity for the diamond cubic structure, and the structure factor for *hkl*-odd reflections differs by a factor of $\sqrt{2}$ from those with *hkl*-even-multiple of 2.

f) One other example of structure factor calculation will be given here. A close-packed hexagonal cell has two atoms of the same kind located at 0 0 0 and $\frac{1}{3}\,\frac{2}{3}\,\frac{1}{2}$.

$$F = fe^{2\pi i(0)} + fe^{2\pi i(h/3 + 2k/3 + l/2)}$$

$$= f[1 + e^{2\pi l((h + 2k)/3 + l/2)}].$$

For convenience, put $[(h + 2k)/3 + l/2) = g$.

$$F = f(1 + e^{2\pi ig}).$$

Since g may have fractional values, such as $\frac{1}{3}\,\frac{2}{3}\,\frac{5}{6}$, etc., this expression is still complex. Multiplication by the complex conjugate, however, will give the square of the absolute value of the resultant wave amplitude F.

$$|F|^2 = f^2(1 + e^{2\pi ig})(1 + e^{-2\pi ig})$$

$$= f^2(2 + e^{2\pi ig} + e^{-2\pi ig}).$$

By relation (e) of Sec. 5, this becomes

$$|F|^2 = f^2(2 + 2 \cos 2\pi g)$$

$$= f^2[2 + 2(2 \cos^2 \pi g - 1)]$$

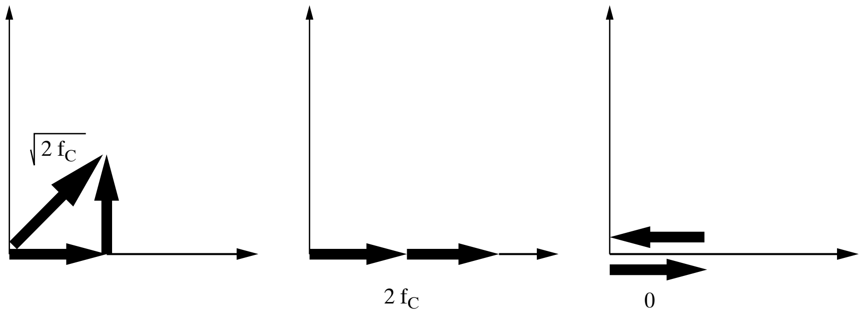

Figure 13 Complex plane representation of the interference between the carbon atoms of the basis of diamond for (left) *h*, *k*, *l* unmixed and odd; (middle) *h*, *k*, *l* unmixed and *h*+*k*+*l* equalling an even multiple of two and (right) *h*, *k*, *l* unmixed and *h*+*k*+*l* equalling an odd multiple of two. The resulting vector multiplied by four gives the structure factor F for each type of reflection. Note that in the right-hand drawing the vectors are displayed slightly from the real axis for better visibility.

$$= f^2(4\cos^2 \pi g)$$

$$= 4f^2 \cos^2 \pi\left(\frac{h + 2k}{3} + \frac{l}{2}\right)$$

$$= 0 \text{ when } (h + 2k) \text{ is a multiple of 3 and } l \text{ is odd.}$$

It is by these missing reflections, such as 11.1, 11.3, 22.1, 22.3, that a hexagonal structure is recognized as being close-packed. Not all the reflections present have the same structure factor. For example, if $(h + 2k)$ is a multiple of 3 and l is even, then

$$\left(\frac{h + 2k}{3} + \frac{l}{2}\right) = n, \text{ where } n \text{ is an integer;}$$

$$\cos \pi n = \pm 1,$$

$$\cos^2 \pi n = 1,$$

$$|F|^2 = 4f^2.$$

When all possible values of h, k, and l are considered, the results may be summarized as follows, where m is an integer:

$h + 2k$	l	$\|F\|^2$
3 m	odd	0
3 m	even	$4f^2$
3 m ± 1	odd	$3f^2$
3 m ± 1	even	f^2

7 APPLICATION TO POLYCRYSTAL DIFFRACTION

Any calculation of the intensity of a diffracted beam must always begin with the structure factor. The remainder of the calculation, however, varies with the particular diffraction method involved. For the Laue method, intensity calculations are so difficult that they are rarely made, since each diffracted beam has a different wavelength and blackens the film by a variable amount, depending on both the intensity and the film sensitivity for that particular wavelength. The factors governing diffracted intensity in the rotating-crystal and powder methods are somewhat similar, in that monochromatic radiation is used in each, but they differ in detail. The remainder of this chapter will be devoted to polycrystal diffraction, since it is of most general utility in materials work.

Six factors affect the relative intensity of the diffraction lines on a powder pattern:

1. polarization factor,
2. structure factor,

3. multiplicity factor,
4. Lorentz factor,
5. absorption factor,
6. temperature factor.

The first two of these have already been described, and the others will be discussed in the following sections.

8 MULTIPLICITY FACTOR

Consider the 100 reflection from a cubic lattice. In the powder specimen, some of the crystals will be so oriented that 100 diffraction occurs. Other crystals of different orientation may be in such a position that 010 or 001 diffraction can occur. Since $d_{100} = d_{010} = d_{001}$ the diffracted beams form part of the same diffraction cone. Now consider the 111 reflection. There are four sets of planes of the form {111} which have the same spacing but different orientation, namely, (111), $(11\bar{1})$, $(1\bar{1}\bar{1})$, and $(1\bar{1}1)$, whereas there are only three sets of the form {100}. Therefore, the probability that {111} will be correctly oriented for diffraction is 4/3 the probability that {100} will be correctly oriented. It follows that the intensity of the 111 reflection will be 4/3 that of the 100 reflection, other things being equal.

This relative proportion of *hkl* planes contributing to the same reflection enters the intensity equation as the quantity *p*, the *multiplicity factor*, which may be defined as the number of permutations of position and sign of $\pm h, \pm k, \pm l$ for planes having the same *d* and F^2. Parallel planes with different Miller indices, such as (100) and $(\bar{1}00)$, are counted separately as different planes, yielding numbers which are double those given in the preceding paragraph. Thus the multiplicity factor for the {100} planes of a cubic crystal is 6 and for the {111} planes 8.

The value of *p* depends on the crystal system: in a tetragonal crystal, the (100) and (001) planes do not have the same spacing, so that the value of *p* for {100} planes is reduced to 4 and the value for {001} planes to 2. Values of the multiplicity factor as a function of *hkl* and crystal system are given in “Appendix: Data for Calculation of the Temperature Factor.”

9 LORENTZ FACTOR

Next consider certain trigonometrical factors which influence the intensity of the diffracted beam. Suppose a narrow beam of parallel monochromatic rays is incident on a crystal [Fig. 14(a)], and let the crystal be rotated at a uniform angular velocity about an axis through *O* and normal to the drawing, so that a particular set of planes assumed for convenience to be parallel to the crystal surface, passes through the angle θ_B, at which Bragg’s law is exactly satisfied. The diffracted intensity is greatest at the exact Bragg angle but still appreciable at angles deviating slightly from the Bragg angle, so that a curve of intensity vs. 2θ is of the form shown in Fig. 14(b). If all the diffracted beams sent out by the crystal as it rotates through the Bragg angle are received on a photographic film or in a detector, the total energy of the diffracted beam can be measured. This energy

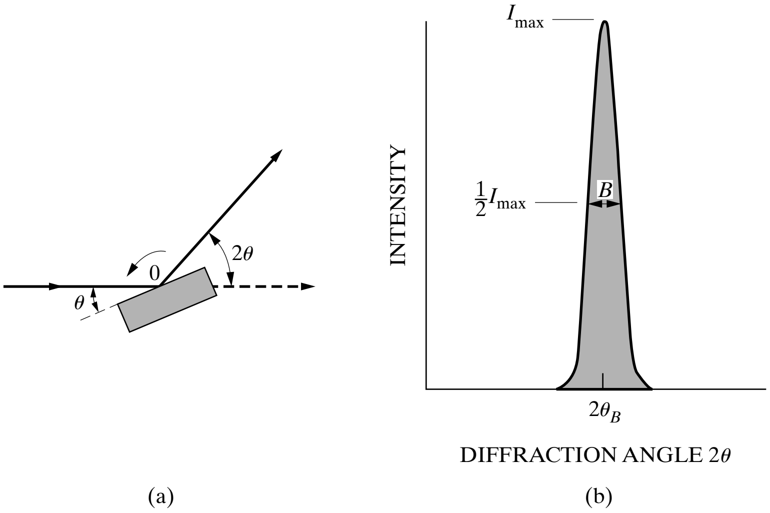

Figure 14 Diffraction by a crystal rotated through the Bragg angle.

is called the *integrated intensity* of the reflection and is given by the area under the curve of Fig. 14(b). The integrated intensity is of much more interest than the maximum intensity, since the former is characteristic of the specimen while the latter is influenced by slight adjustments of the experimental apparatus.

The integrated intensity of a reflection depends on the particular value of θ_B involved, even though all other variables are held constant. Finding this dependence requires separate consideration of two aspects of the diffraction curve: the maximum intensity and the breadth. When the planes of scatterers make an angle θ_B with the incident beam, Bragg's law is exactly satisfied and the intensity diffracted in the direction $2\theta_B$ is a maximum. But some energy is still diffracted in this direction when the angle of incidence differs slightly from θ_B, and the total energy diffracted in the direction $2\theta_B$ as the crystal is rotated through the Bragg angle is given by the value of $I_{\max}$ of the curve of Fig. 14(b). The value of $I_{\max}$ therefore depends on the angular range of crystal rotation over which the energy diffracted in the direction $2\theta_B$ is appreciable. In Fig. 15(a), the dashed lines show the position of the crystal after rotation through a small angle $\Delta\theta$ from the Bragg position. The incident beam and the diffracted beam under consideration now make unequal angles with the planes of scatterers, the former making an angle $\theta_1 = \theta_B + \Delta\theta$ and the latter an angle $\theta_2 = \theta_B - \Delta\theta$. The situation on an atomic scale is shown in Fig. 15(b). Consider only a single plane of atoms, since the rays scattered by all other planes are in phase with the corresponding rays scattered by the first plane. Let *a*

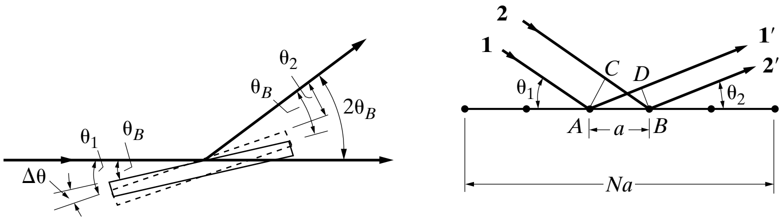

(a) (b)

Figure 15 Scattering in a fixed direction during crystal rotation.

equal the atom spacing in the plane and *Na* the total length[2] of the plane. The difference in path length for rays **1′** and **2′** scattered by adjacent atoms is given by

$$\begin{aligned}\delta_{1'2'} &= AD - CB\\ &= a\cos\theta_2 - a\cos\theta_1\\ &= a[\cos(\theta_B - \Delta\theta) - \cos(\theta_B + \Delta\theta)].\end{aligned}$$

By expanding the cosine terms and setting sin $\Delta\theta$ equal to $\Delta\theta$, since the latter is small:

$$\delta_{1'2'} = 2a\Delta\theta\sin\theta_{B,}$$

and the path difference between the rays scattered by atoms at either end of the plane is simply *N* times this quantity. When the rays scattered by the two end atoms are one wavelength out of phase, the diffracted intensity will be zero. (The proof of this is beyond the scope of this chapter.) The condition for zero diffracted intensity is therefore

$$2Na\,\Delta\theta\sin\theta_B = \lambda,$$

or

$$\Delta\theta = \frac{\lambda}{2\,Na\sin\theta_B}.$$

This equation gives the maximum angular range of crystal rotation over which appreciable energy will be diffracted in the direction $2\theta_B$. Since $I_{\max}$ depends on this range, $I_{\max}$ is proportional to $1/\sin\theta_B$. Other things being equal, $I_{\max}$ is therefore large at low scattering angles and small in the back-reflection region.

The breadth of the diffraction curve varies in the opposite way, being larger at large values of $2\theta_B$, as will be shown the half-maximum breadth *B* is proportional to $1/\cos\theta_B$. The integrated intensity of the reflection is given by the area under the diffraction curve and is therefore proportional to the product $I_{\max}B$, which is in turn proportional to $(1/\sin\theta_B)(1/\cos\theta_B)$ or to $1/\sin 2\theta_B$. Thus, as a crystal is rotated

---

[2] If the crystal is larger than the incident beam, then *Na* is the irradiated length of the plane; if it is smaller, Na is the actual length of the plane.

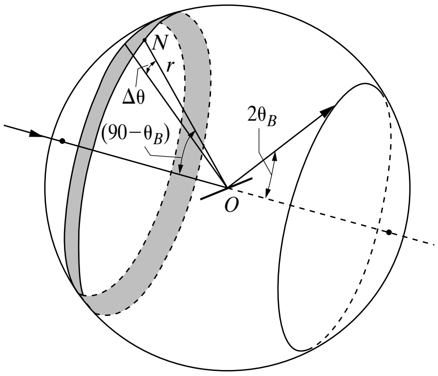

Figure 16 The distribution of plane normals for a particular cone of diffracted rays.

through the Bragg angle, the integrated intensity of a reflection, which is the quantity of most experimental interest, turns out to be greater for large and small values of $2\theta_B$ than for intermediate values, other things being equal.

The preceding remarks apply just as well to the powder diffraction as they do to the case of a rotating crystal, since the range of orientations available among the powder particles, some satisfying Bragg's law exactly, some not so exactly, are the equivalent of single-crystal rotation.

However, in polycrystal diffraction, a second geometrical factor arises because the integrated intensity of a reflection at any particular Bragg angle depends on the number of crystals oriented at or near that angle. This number is not constant even though the crystals are oriented completely at random. In Fig. 16 a reference sphere of radius r is drawn around the powder specimen located at O. For the particular hkl reflection shown, ON is the normal to this set of planes in one crystal of the powder. Suppose that the range of angles near the Bragg angle over which diffraction is appreciable is $\Delta\theta$. Then, for this particular reflection, only those crystals will be in a diffracting position which have the ends of their plane normals lying in a band of width $r\,\Delta\theta$ on the surface of the sphere. Since the crystals are assumed to be oriented at random, the ends of their plane normals will be uniformly distributed over the surface of the sphere; the fraction favorably oriented for a reflection will be given by the ratio of the area of the strip to that of the whole sphere. If ΔN is the number of such crystals and N the total number, then

$$\frac{\Delta N}{N} = \frac{r\Delta\theta \cdot 2\pi r \sin(90^\circ - \theta_B)}{4\pi r^2} = \frac{\Delta\theta \cos\theta_B}{2}.$$

The number of crystals favorably oriented for diffraction is thus proportional to $\cos\theta_{\mathrm{B}}$ and is quite small for reflections in the backward direction.

In assessing relative intensities, the total diffracted energy in one cone of rays is not compared with that in another but rather the integrated intensity per unit length of one diffraction line with that of another. For example, in one common arrangement of specimen and film, the Hull/Debye–Scherrer method, shown in

Fig. 17, the film obviously receives a greater proportion of a diffraction cone when the reflection is in the forward or backward direction than it does near $2\theta = 90^\circ$. The same is true of a diffractometer; in this case the height of the cylinder pictured in Fig. 17 represents the height of the receiving slit in front of the detector. Inclusion of this effect thus leads to a third geometrical factor affecting the intensity of a reflection. The length of any diffraction line being $2\pi R \sin 2\theta_B$, where R is the radius of the camera, the relative intensity per unit length of line is proportional to $1/\sin 2\theta_B$.

In intensity calculations, the three factors just discussed are combined into one and called the Lorentz factor [5]. Dropping the subscript on the Bragg angle, the result is:

$$\text{Lorentz factor} = \left(\frac{1}{\sin 2\theta}\right)(\cos \theta)\left(\frac{1}{\sin 2\theta}\right) = \frac{\cos \theta}{\sin^2 2\theta} = \frac{1}{4 \sin^2 \theta \cos \theta}.$$

This in turn is combined with the polarization factor $\frac{1}{2}(1 + \cos^2 2\theta)$ of Sec. 2 to give the combined Lorentz-polarization factor which, with a constant factor of $\frac{1}{8}$ omitted, is given by

$$\text{Lorentz–polarization factor} = \frac{1 + \cos^2 2\theta}{\sin^2 \theta \cos \theta}.$$

Values of this factor are plotted in Fig. 18 as a function of θ. The overall effect of these geometrical factors is to decrease the intensity of reflections at intermediate angles compared to those in forward or backward directions.

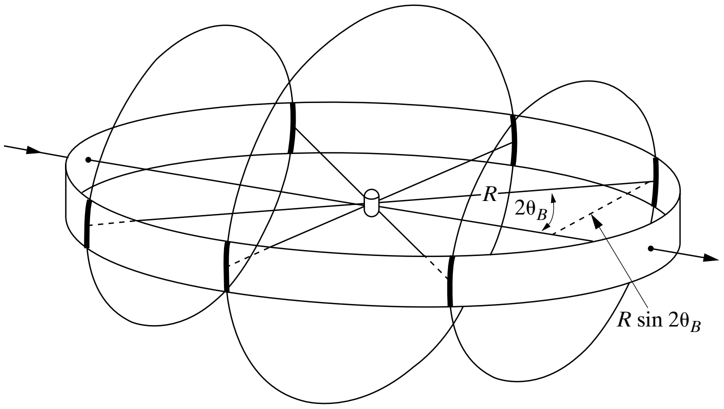

Figure 17 Intersection of cones of diffracted rays with Hull/Debye–Scherrer film.

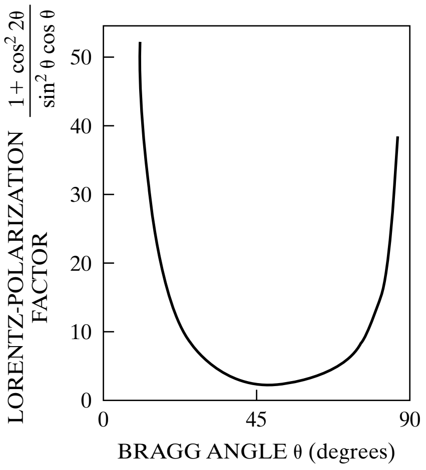

Figure 18 Lorentz-polarization factor.

10 ABSORPTION FACTOR

Still another factor affecting the intensities of the diffracted rays must be considered, and that is the absorption which takes place in the specimen itself. Introduction of the *absorption factor A* allows for this effect in intensity calculations; it is a number by which the calculated intensity is to be multiplied to allow for absorption. The calculation of A depends on the geometry of the diffraction method involved, and two geometries are considered below.

Hull/Debye–Scherrer Camera

The specimen in the Hull/Debye–Scherrer method has the form of a very thin cylinder of powder placed on the camera axis, and Fig. 19(a) shows the cross section of such a specimen. For the low-angle reflection shown, absorption of a particular ray

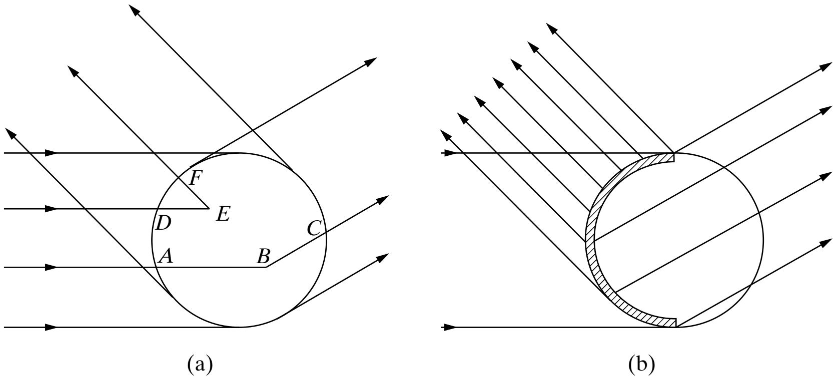

(a) (b)

Figure 19 Absorption in Hull/Debye–Scherrer specimens: (a) general case, (b) highly absorbing specimen.

in the incident beam occurs along a path such as AB; at B a small fraction of the incident energy is diffracted by a powder particle, and absorption of this diffracted beam occurs along the path BC. Similarly, for a high-angle reflection, absorption of both the incident and diffracted beams occurs along a path such as $(DE + EF)$. The net result is that the diffracted beam is of lower intensity than one would expect for a specimen of no absorption.

A calculation of this effect shows that the relative absorption increases as θ decreases, for any given cylindrical specimen. That this must be so can be seen from Fig. 19(b) which applies to a specimen (for example, tungsten) of very high absorption. The incident beam is very rapidly absorbed, and most of the diffracted beams originate in the thin surface layer on the left side of the specimen; backward-diffracted beams then undergo very little absorption, but forward-diffracted beams have to pass through the whole specimen and are greatly absorbed. Actually, the forward-diffracted beams in this case come almost entirely from the top and bottom edges of the specimen.[3] This difference in absorption between high-θ and low-θ reflections decreases as the linear absorption coefficient decreases, but the absorption is always greater for the low-θ reflections. The Hull/Debye–Scherrer absorption factor is written as $A(\theta)$ to emphasize the fact that it varies with θ. Qualitatively, therefore, $A(\theta)$ for any specimen increases as 2θ increases.

The calculation of $A(\theta)$ for a cylindrical specimen proceeds as follows. In Fig. 19(a) the path length $(AB + BC)$, for a given value of θ, is expressed as a function of the position x, y of the point B relative to coordinate axes fixed relative to the specimen. The absorption factor $A(\theta)$ is then given by the function $e^{-\mu(AB+BC)}$ integrated over the entire cross-sectional area of the specimen. This integration can only be performed numerically. The result is a table of values of $A(\theta)$ as a function of θ and of the product μr, where μ is the linear absorption coefficient of the specimen and r is its radius. The specimen is usually a powder compact, with an absorption coefficient given by

$$\mu_{\text{compact}} = \mu_{\text{solid}}\left(\frac{\rho_{\text{compact}}}{\rho_{\text{solid}}}\right), \tag{12}$$

where ρ is density.

Values of $A(\theta)$ have been calculated and tabulated by Bradley [6]. Tables of values can also be found in [G.1, Vol C pp 520-521]

Exact calculation of the absorption factor for a cylindrical specimen is often difficult, so it is fortunate that this effect can usually be neglected in the calculation of diffracted intensities, when the Hull/Debye–Scherrer method is used. Justification of this omission will be found in Sec. 11.

---

[3] The powder patterns show this effect, at least on the original films. The lowest-angle line in each pattern is split in two, because the beam diffracted through the center of the specimen is so highly absorbed. It is important to keep the possibility of this phenomenon in mind when examining Hull/Debye–Scherrer photographs, or split low-angle lines may be incorrectly interpreted as separate diffraction lines from two different reflections.

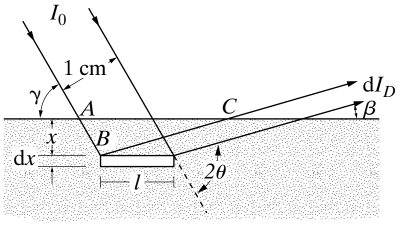

Figure 20 Diffraction from a flat plate: incident and diffracted beams have a thickness of 1 cm in a direction normal to the plane of the drawing.

Diffractometer

A diffractometer specimen usually has the form of a flat plate making equal angles with the incident and diffracted beams. As shown below, the absorption factor A equals $1/2\mu$, *independent of* θ. This independence of θ is due to the exact balancing of two opposing effects. When θ is small, the specimen area irradiated by an incident beam of fixed cross section is large, but the effective depth of x-ray penetration is small; when θ is large, the irradiated area is small, but the penetration depth is relatively large. The net effect is that the effective irradiated volume is constant and independent of θ.[4] Absorption occurs in any case, however, and the larger the absorption coefficient of the specimen, the lower the intensity of the diffracted beams, other things being equal. The important fact to note is that absorption decreases the intensities of all diffracted beams by the same factor and therefore does not enter into the calculation of *relative* intensities.

The calculation of A proceeds as follows, and, since this effect will come up again in later parts of this book, the calculation will be quite general. The incident beam in the diffractometer is actually divergent, but assume here that the beam is composed of parallel rays, because the divergence angle is very small (3°*or less*). In Fig. 20, the incident beam has intensity I_o (ergs/cm^2/sec), is 1cm square in cross section, and is incident on the powder plate at an angle y. Consider the energy diffracted from this beam by a layer of the powder of length l and thickness dx, located at a depth x below the surface. Since the incident beam undergoes absorption by the specimen over the path length AB, the energy incident per second on the layer considered is $I_0e^{-\mu(AB)}$ (ergs/sec), where μ is the linear absorption coefficient of the powder compact, given by Eq. (12). Let a be the volume fraction of the specimen containing particles having the correct orientation for diffraction of the incident beam, and b the fraction of the incident energy which is diffracted by one unit volume. Then the energy diffracted per second by the layer considered, which has a volume l dx, is given by $abl\, I_0e^{-\mu(AB)}\, dx$. But this diffracted energy is also decreased by absorption, by a factor of $e^{-\mu(BC)}$, since the diffracted rays have a path length of

---

[4] This only true if the incident beam has a constant angular divergence; some diffractometers utilize a variable divergence slit and A would no longer be constant and would vary with θ.

BC in the specimen. The energy flux per second in the diffracted beam outside the specimen, i.e., the integrated intensity, is therefore given by

$$\mathrm{d}I_D = ablI_O e^{-\mu(AB+BC)}\mathrm{d}x(\text{ergs/sec}). \tag{13}$$

But

$$\ell = \frac{1}{\sin\gamma}, \qquad AB = \frac{x}{\sin\gamma}, \qquad BC = \frac{x}{\sin\beta}.$$

Therefore,

$$\mathrm{d}I_D = \frac{I_O ab}{\sin\gamma} e^{-\mu x(1/\sin\gamma + 1/\sin\beta)}\mathrm{d}x. \tag{14}$$

(The reader might note that the analogous absorption effect in transmission, rather than reflection, is given later as Eq. (14-10).

For the particular specimen arrangement used in the parafocusing diffractometer, $\gamma = \beta = \theta$, and the above equation becomes

$$\mathrm{d}I_D = \frac{I_O ab}{\sin\theta} e^{-2\mu x/\sin\theta}\mathrm{d}x. \tag{15}$$

The total diffracted intensity is obtained by integrating over an infinitely thick specimen:

$$I_D = \int_{x=0}^{x=\infty} \mathrm{d}I_D = \frac{I_O ab}{2\mu}. \tag{16}$$

Here I_o, b, and μ are constant for all reflections (independent of θ, and a may also be regarded as constant. Actually, a varies with θ, but this variation is already corrected by the cos θ portion of the Lorentz factor (see Sec. 9) and need not be included here. Therefore, the absorption factor $1/2\mu$ is independent of θ for a flat specimen making equal angles with the incident and diffracted beams, provided the specimen fills the incident beam at all angles and is effectively of infinite thickness.

The criterion adopted for "infinite thickness" depends on the sensitivity of the intensity measurements or on what is regarded as negligible diffracted intensity. For example, it is arbitrary but quite reasonable to define infinite thickness as that thickness t which a specimen must have in order that the intensity diffracted by a thin layer on the back side be $\frac{1}{1000}$ of the intensity diffracted by a thin layer on the front side. Then, from Eq. (15),

$$\frac{\mathrm{d}I_D \ (\text{at } x = 0)}{\mathrm{d}I_D \ (\text{at } x = t)} = e^{2\mu/\sin\theta} = 1000,$$

from which

$$t = \frac{3.45\sin\theta}{\mu}.$$

This expression shows that "infinite thickness," for a metal specimen, is very small indeed. For example, suppose a specimen of nickel powder is being examined with Cu $K\alpha$ radiation at θ values approaching 90°. The density of the powder compact may be taken as about 0.6 the density of bulk nickel, which is 8.9 g/cm^3, leading to a value of μ for the compact of 261 cm^{-1}. The value of t is therefore 1.32×10^{-2} cm, or about five thousandths of an inch.

11 TEMPERATURE FACTOR

So far a crystal has been considered as a collection of atoms located at fixed points in the lattice. Actually, the atoms undergo thermal vibration about their mean positions even at the absolute zero of temperature, and the amplitude of this vibration increases as the temperature increases. In aluminum at room temperature, the average displacement of an atom from its mean position is about 0.17 Å, which is by no means negligible, being about 6 percent of the distance of closest approach of the mean atom positions in this crystal. This average displacement is on the order of the separation between electrons within an atom and should have the same effect on scattering; namely, destructive interference increases with increasing scattering angle 2θ. In fact, prior to Laue's experiment, one of the arguments advanced against the possibility of crystals diffracting was that thermal vibration at room temperature would destroy periodicity to the extent that peaks would never be observable [G11, p42].

Increased thermal vibration of the atoms, as the result of an increase in temperature, has three main effects:

1. The unit cell expands, causing changes in periodicity d and therefore in the 2θ positions of the diffraction lines. If the positions of one or more lines are measured as a function of temperature, the thermal expansion coefficient of the specimen can be determined by x-ray diffraction.
2. The intensities of the diffraction lines decrease.
3. The intensity of the background scattering between lines increases.

The second and third effects are described below. Here the interest is primarily in variations in intensity with 2θ at constant temperature (usually room temperature) and not in intensity changes with temperature.

Thermal agitation decreases the intensity of a diffracted beam because it degrades the periodicity of the lattice; at any instant there is a symmetric, random distribution of atom displacements about their equilibrium positions. Thus the reinforcement of waves scattered at the Bragg angle, the reinforcement which is called a diffracted beam, is not as perfect as it is for a crystal with fixed atoms. This reinforcement requires that the path difference, between waves scattered by adjacent layers of atoms in the crystal (lying parallel to (hkl)) be an integral number of wavelengths. If u is the average displacement of an atom from its mean position, reinforcement becomes more imperfect as the ratio u/d increases, i.e., as the temperature increases since that increases u, or as θ increases, since high–θ reflections correspond to low d values [7]. Thus the intensity of a diffracted beam decreases as the temperature is raised, and, for a constant temperature, thermal vibration causes a greater decrease in the diffracted intensity at high angles than at low angles. In intensity calculations this effect is included by introducing the *temperature factor* e^{-2M}, which is a number by which the calculated intensity is to be multiplied to allow for thermal vibration of the atoms [8]. Qualitatively, e^{-2M} decreases as 2θ increases. A method of calculating e^{-2M} when it is needed is outlined later, and Fig. 21 shows the result of such a calculation for iron.

The temperature effect and the previously discussed absorption effect in cylindrical specimens depend on angle in opposite ways and, to a first approximation, cancel each other in the Hull/Debye–Scherrer method. In back reflection, for example, absorption decreases the intensity of a diffracted beam very little but thermal agitation decreases it greatly, while in the forward direction the reverse is true. The two effects do not exactly cancel one another at all angles; however, if the comparison of line intensities is restricted to lines not differing too greatly in θ values, the absorption and temperature effects can be safely ignored in the Hull/Debye–Scherrer method. This is a fortunate circumstance, since both of these effects are rather difficult to calculate exactly.

Theoretically, thermal vibration of the atoms causes a very slight increase in the breadth B, measured at half-maximum intensity, of the diffraction lines, but diffraction lines are observed to be sharp right up to the melting point, and their maximum intensity gradually decreases.

It is also worth noting that the mean amplitude of atomic vibration is not a function of the temperature alone but depends also on the elastic constants of the crystal. At any given temperature, the less "stiff" the crystal, the greater the vibration amplitude u. This means that u is much greater at any one temperature for a soft, low-melting-point metal like lead than it is for, say, tungsten. Substances with low melting points have quite large values of u even at room temperature and therefore yield rather poor back-reflection photographs. For example, thermal atomic vibration in lead at $20^\circ C$ reduces the intensity of the highest-angle line observed with Cu $K\alpha$ radiation (at about 161° 2θ) to only 18 percent ($e^{-2M} = 0.18$) of the value for atoms at rest.

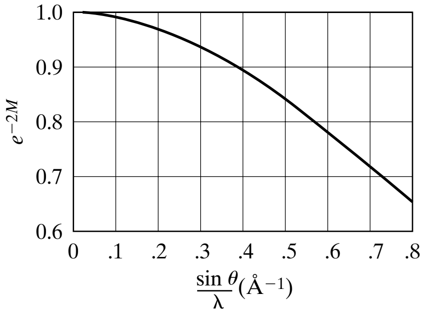

Figure 21 Temperature factor e^{-2M} of iron at $20^\circ C$ as a function of $(\sin\theta)/\lambda$.

In only one application described in this book will any quantitative information be needed about the temperature factor e^{-2M}, but it is convenient to describe the calculation here before considering other thermal effects. Formally, this effect is included by defining f as the atomic scattering factor of an atom undergoing thermal vibration, f_o as the same quantity for an atom at rest, and relating the two by

$$f = f_0 e^{-M}.$$

(The quantity f_o is then the scattering factor as usually tabulated.) Because the intensity of any line depends on f^2, calculated intensities must be multiplied by e^{-2M} to allow for thermal vibration. The quantity M depends on both the amplitude u of thermal vibration and the scattering angle 2θ:

$$M = 2\pi^2\left(\frac{\overline{u^2}}{\mathrm{d}^2}\right) = 8\pi^2\,\overline{u^2}\left(\frac{\sin\theta}{\lambda}\right)^2 = B\left(\frac{\sin\theta}{\lambda}\right)^2, \tag{17}$$

where $\overline{u^2}$ is the mean square displacement of the atom in a direction normal to the diffracting planes. The exact calculation of $\overline{u^2}$as a function of temperature is extremely difficult, which means that M or B is hard to determine accurately. Debye [8] has given the following expression:

$$M = \frac{6h^2T}{mk\Theta^2}\left[\phi(x) + \frac{x}{4}\right]\left(\frac{\sin\theta}{\lambda}\right)^2, \tag{18}$$

where h is Planck's constant, T the absolute temperature, m the mass of the vibrating atom, k Boltzmann's constant, Θ the Debye characteristic temperature of the substance in K, $x = \Theta/T$, and $\phi(x)$ is a function tabulated, along with values of Θ. Because $m = A/N$, where A = atomic weight and N = Avogadro's number, the coefficient of the bracketed terms above becomes

$$\frac{6h^2T}{mk\Theta^2} = \frac{(6)(6.02 \times 10^{26})(6.63 \times 10^{-34})^2T}{A\Theta^2(1.38 \times 10^{-23})(10^{-20})} = \frac{1.15 \times 10^4T}{A\Theta^2}$$

if λ is in angstroms. Equation (18) is approximate and applies only to elements with cubic crystal structure. For thorough treatments of the effect of thermal vibration on the diffraction pattern, see James [G.19] and Warren [G.20].

The thermal vibration of atoms has another effect on diffraction patterns. Besides decreasing the intensity of diffraction lines, it causes some general coherent scattering in all directions. This is called *temperature-diffuse scattering*; it contributes only to the general background of the pattern and its intensity gradually increases with 2θ. Contrast between lines and background naturally suffers, so this effect is a very undesirable one, leading in extreme cases to diffraction lines in the back-reflection region scarcely distinguishable from the background. Figure 22 illustrates this effect. In (a) is shown an extremely hypothetical pattern (only three lines, equally spaced, equally strong, with no background whatever) for atoms at rest; in (b) the lines, decreased in intensity by the factor e^{-2M}, are super-

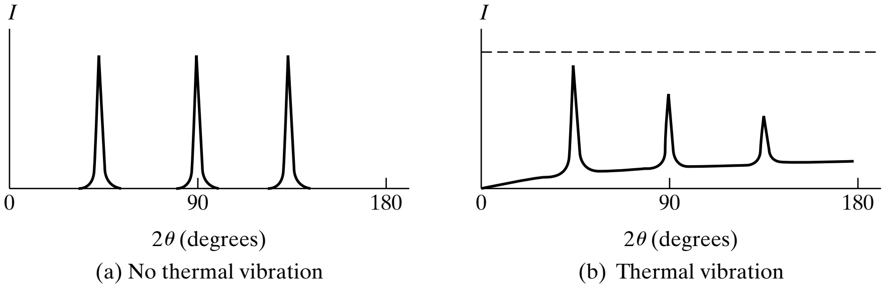

(a) No thermal vibration

(b) Thermal vibration

Figure 22 Effect of thermal vibration of the atoms on a powder pattern. Very schematic, see text.

imposed on a background of thermal diffuse scattering. At low temperatures there is very little background scattering due to thermal agitation and the diffraction lines are relatively intense; if the specimen is now heated to a high temperature, the lines become quite weak and temperature-diffuse scattering becomes an important part of the pattern.

The phenomenon of temperature-diffuse scattering is another example of scattering at non-Bragg angles. It is not surprising that such scattering should occur, since the displacement of atoms from their mean positions constitutes a kind of crystal imperfection and leads to a partial breakdown of the conditions necessary for perfect destructive interference between rays scattered at non-Bragg angles.

12 INTENSITIES OF DIFFRACTION PEAKS FROM POLYCRYSTALLINE SAMPLES

It is now possible to gather together the factors discussed in preceding sections into an equation for the relative intensity of powder pattern lines.

Hull/Debye–Scherrer Camera

$$\text{(Approximate)} \qquad I = |F|^2 p \left(\frac{1 + \cos^2 2\theta}{\sin^2\theta \cos\theta} \right), \tag{19}$$

where I = relative integrated intensity (arbitrary units), F = structure factor, p = multiplicity factor, and θ = Bragg angle. The trigonometric terms in parentheses are the Lorentz-polarization factor. In arriving at this equation, factors are omitted which are constant for all lines of the pattern. For example, all that is retained of the Thomson equation (Eq. 2) is the polarization factor $(1 + \cos^2 2\theta)$, with constant factors, such as the intensity of the incident beam and the charge and mass of the electron, omitted. The intensity of a diffraction line is also directly proportional to the irradiated volume of the specimen and inversely proportional to the camera radius, but these factors are again constant for all diffraction lines and may be neglected. Omission of the temperature and absorption factors means that Eq. (19) is valid only for lines fairly close together on the pattern; this latter restriction is not as serious as it may sound. Finally, it should be remembered that this equation gives the relative *integrated* intensity, i.e., the relative area under the curve of intensity vs. 2θ. If an exact expression is required, the absorption factor $A(\theta)$ and the temperature factor e^{-2M} must be inserted:

$$\text{(Extract)} \qquad I = |F|^2 p \left(\frac{1 + \cos^2 2\theta}{\sin^2 \theta \cos \theta} \right) A(\theta) e^{-2M}. \tag{20}$$

Diffractometer

Here the absorption factor is independent of θ and so does not enter into the calculation of relative intensities. Equation (19) becomes still less precise, because there is no longer any approximate cancellation of the absorption and temperature factors. Equation (19) may still be used, for adjacent lines on the pattern, but the calculated intensity of the higher-angle line, relative to that of the lower-angle line, will always be somewhat too large because of the omission of the temperature factor. The exact equation for the diffractometer is

$$\text{(Extract)} \qquad I = |F|^2 p \left(\frac{1 + \cos^2 2\theta}{\sin^2 \theta \cos \theta} \right) e^{-2M}. \tag{21}$$

Qualifications

The two following effects can make the above intensity equations invalid:

1) *Preferred orientation*. From the way in which the $\cos\theta$ portion of the Lorentz factor was determined in Sec. 9, it follows that Eqs. (19) through (21) are valid only when the crystals making up the specimen are randomly oriented in space. Preferred orientation of the crystal grains causes radical disagreement between calculated and observed intensities and, when such disagreement exists, preferred orientation should be the first possible cause to be suspected. It is relatively easy to prepare powder-compact specimens from ground powders or metal filings so that the ideal of perfect randomness of orientation is closely approached, but virtually all polycrystalline specimens of metal wire, metal sheet, manufactured ceramics, and even natural rocks or minerals will exhibit more or less preferential orientation of the grains. The presence of large grains within the sample can also lead to very different calculated and observed intensities. The method by which large grain and preferred orientation effects may be differentiated is discussed in Sec 9-8.
2) *Extinction* [G.19, G.20]. Equations (19) through (21) are derived on the basis of the so-called "ideally imperfect" crystal, one consisting of quite small mosaic blocks (of the order of 10^{-4}cm to 10^{-5}cm in thickness) which are so disoriented that they are all essentially nonparallel. Such a crystal

> has maximum diffracting power. A crystal made up of large mosaic blocks, some or all of which are accurately parallel to one another, is more nearly perfect and has a lower diffracting power. This *decrease* in the integrated intensity of the diffracted beam as the crystal becomes more nearly perfect is called *extinction*. Extinction is absent for the ideally imperfect crystal, and the mathematical treatment of diffraction used to derive Eqs. (19) through (21) is termed kinematical theory. The presence of extinction invalidates Eqs. (19) through (21) and requires use of dynamical diffraction theory. Any treatment that will make a crystal more imperfect will reduce extinction and, for this reason alone, powder specimens should be ground as fine as possible. Grinding not only reduces the crystal size and populates the diffraction cones more fully but also tends to decrease the mosaic block size, disorient the mosaic blocks, and strain them nonuniformly.

The extinction effect can operate, not only in single-crystal specimens, but also in the individual grains of polycrystalline specimens. Extinction may be assumed to be absent in ground or filed powders and is usually negligible in fine-grained polycrystalline specimens. If its presence is suspected in the latter, the specimen can always be reduced to powder by grinding or filing.

13 EXAMPLES OF INTENSITY CALCULATIONS

The use of Eq. (19) will be illustrated by the calculation of the position and relative intensities of the diffraction lines on a Hull/Debye–Scherrer pattern of copper made with Cu $K\alpha$ radiation: The calculations are most readily done on a computer using a spreadsheet program and the tabular form of Table 2 is convenient for comparison of observed and calculated peak intensities.

Remarks

Column 2: Since copper is face-centered cubic, F is equal to $4f_{\mathrm{Cu}}$ for lines of unmixed indices and zero for lines of mixed indices. The plane indices, all unmixed, are listed in this column in order of increasing values of $(h^2 + k^2 + l^2)$.
Column 4: For a cubic crystal, values of $\sin^2\theta$ are given

$$\sin^2\theta = \frac{\lambda^2}{4a^2}(h^2 + k^2 + l^2).$$

In this case, $\lambda = 1.542$ Å (Cu $K\alpha$) and $a = 3.615$ Å (lattice parameter of copper). Therefore, multiplication of the integers in column 3 by $\lambda^2/4a^2 = 0.0455$ gives the values of $\sin^2\theta$ listed in column 4. In this and similar calculations, three-figure accuracy is ample.
Column 6: Needed to determine the Lorentz-polarization factor and $(\sin\theta)/\lambda$.
Column 7: Obtained from Appendix: Multiplicity Factors for the Powder Method. Needed to determine f_{Cu}.

TABLE 2

1	2	3	4	5	6	7	8
Line	hkl	$h^2+k^2+l^2$	$\sin^2\theta$	$\sin\theta$	θ	$\frac{\sin\theta}{\lambda}(A^{-1})$	f_{Cu}
1	111	3	0.1365	0.369	21.7	0.24	22.1
2	200	4	0.1820	0.427	25.3	0.27	20.9
3	220	8	0.364	0.603	37.1	0.39	16.8
4	311	11	0.500	0.707	45.0	0.46	14.8
5	222	12	0.546	0.739	47.6	0.48	14.2
6	400	16	0.728	0.853	58.5	0.55	12.5
7	331	19	0.865	0.930	68.4	0.60	11.5
8	420	20	0.910	0.954	72.6	0.62	11.1

1	9	10	11	12	13	14
Line	F^2	p	$\frac{1+\cos^2 2\theta}{\sin^2\theta\cos\theta}$	Relative integrated intensity		
				Calc.	Calc.	Obs.
1	7810	8	12.03	7.52×10^5	10.0	vs
2	6990	6	8.50	3.56	4.7	s
3	4520	12	3.70	2.01	2.7	s
4	3500	24	2.83	2.38	3.2	s
5	3230	8	2.74	0.71	0.9	m
6	2500	6	3.18	0.48	0.6	w
7	2120	24	4.81	2.45	3.3	s
8	1970	24	6.15	2.91	3.9	s

Column 8: Obtained from Appendix: Lorentz-Polarization Factor.
Column 9: Obtained from the relation $F^2 = 16f^2_{Cu}$.
Column 10: Obtained from "Appendix: Data for Calculation of the Temperature Factor.
Column 11: Obtained from Appendix: Atomic Weights.
Column 12: These values are the product of the values in columns 9, 10, and 11, according to Eq. (19).
Column 13: Values from column 12 recalculated to give the first line an arbitrary intensity of 10, i.e., "normalized" to 10 for the first line.
Column 14: These entries give the observed intensities, visually estimated according to the following simple scale, from the original film for copper (vs = very strong, s = strong, m = medium, w = weak).

The agreement obtained here between observed and calculated intensities is satisfactory. Note how the value of the multiplicity p exerts a strong control over the line intensity. The values of $|F|^2$ and of the Lorentz-polarization factor vary smoothly with θ, but the values of p, and therefore of I, vary quite irregularly.

A more complicated structure may now be considered, namely that of the zinc-blende form of ZnS. This form of ZnS is cubic and has a lattice parameter of 5.41 Å. Here the relative intensities will be calculated for the first six lines on a Hull/Debye–Scherrer pattern made with Cu $K\alpha$ radiation.

As always, the first step is to work out the structure factor. ZnS has four zinc and four sulfur atoms per unit cell, located in the following positions:

$$\text{Zn:}\quad \tfrac{1}{4}\tfrac{1}{4}\tfrac{1}{4} \qquad + \qquad \text{face–centering translations,}$$

$$\text{S:}\quad 0\,0\,0 \qquad + \qquad \text{face–centering translations.}$$

Since the structure is face-centered, the structure factor will be zero for planes of mixed indices. From example (e) of Sec. 6, the terms in the structure-factor equation corresponding to the face-centering translations can be factored out and the equation for unmixed indices written down at once:

$$F = 4[f_S \quad + \quad f_{Zn}e^{(\pi i/2)(h+k+l)}].$$

$|F|^2$ is obtained by multiplication of the above by its complex conjugate:

$$|F|^2 = 16[f_S + f_{Zn}e^{(\pi i/2)(h+k+l)}][f_S + f_{Zn}e^{-(\pi i/2(h+k+l)}].$$

This equation reduces to the following form:

$$|F|^2 = 16\left[f_S^2 + f_{Zn}^2 + 2f_s f_{Zn}\cos\frac{x}{2}(h + k + l)\right]$$

Further simplification is possible for various special cases:

$$|F|^2 = 16(f_S^2 + f_{Zn}^2) \qquad \text{when } (h + k + l) \text{ is odd;} \tag{22}$$

$$|F|^2 = 16(f_S - f_{Zn})^2 \qquad \text{when } (h + k + l) \text{ is an odd multiple of 2;} \tag{23}$$

$$|F|^2 = 16(f_S + f_{Zn})^2 \qquad \text{when } (h + k + l) \text{ is an even multiple of 2.} \tag{24}$$

The intensity calculations are carried out in Table 3, with some columns omitted for the sake of brevity.

Remarks

Columns 5 and 6: These values are read from scattering-factor curves plotted from the data of Appendix: Lorentz-Polarization Factor.
Columns 7: $|F|^2$ is obtained by the use of Eq. (22), (23), or (24), depending on the particular values of *hkl* involved. Thus, Eq. (22) is used for the 111 reflection and Eq. (24) for the 220 reflection.

TABLE 3

1	2	3	4	5	6
Line	*hkl*	θ	$\frac{\sin\theta}{\lambda}(A^{-1})$	*f*S	*f*Zn
1	111	14.3	0.16	12.3	25.8
2	200	16.6	0.19	11.4	24.6
3	220	23.8	0.26	9.7	22.1
4	311	28.2	0.30	9.0	20.7
5	222	29.6	0.32	8.8	20.0
6	400	34.8	0.37	8.2	18.4

1	7	8	9	10	11
Line	$\|F\|^2$	*p*	$\frac{1+\cos^2 2\theta}{\sin^2\theta\cos\theta}$	Relative intensity Calc.	 Obs.
1	13070	8	30.0	10.0	vs
2	2790	6	21.7	1.2	w
3	16180	12	9.76	6.1	vs
4	8150	24	6.64	4.1	vs
5	2010	8	5.95	0.3	vw
6	11320	6	4.19	0.9	w

Columns 10 and 11: The agreement obtained here between calculated and observed intensities is again satisfactory. In this case, both the values of $|F|^2$ and of p vary irregularly with θ, leading to an irregular variation of I.

One further remark on intensity calculations is necessary. In the powder method, two sets of planes with different Miller indices can diffract to the same point on the film: for example, the planes (411) and (330) in the cubic system, since they have the same value of $(h^2 + k^2 + l^2)$ and hence the same spacing and 2θ or the planes (501) and (431) of the tetragonal system, since they have the same values of $(h^2 + k^2)$ and l^2. In such a case, the intensity of each reflection must be calculated separately, since in general the two will have different multiplicity and structure factors, and then added to find the total intensity of the line. This conclusion holds for diffractometry as well.

14 RECIPROCAL SPACE AND DIFFRACTED INTENSITIES

Reciprocal lattice can be seen as equally valid representation of the crystal as the direct space lattice; while the basis for the mapping is different, lattice vectors and Miller planes can be represented in both. The reciprocal lattice and the Ewald sphere construction can be used to determine diffracted beam directions. In this section, the reciprocal space treatment of diffraction will be further developed by associating the intensity diffracted by a given *hkl* (i.e., reciprocal lattice point) with its position in reciprocal space. Actually, each position within reciprocal space can be associated with a diffracted or scattered intensity, but this point is beyond the scope of this chapter.

Each *hkl* reflection has an intensity proportional to the structure factor squared, F^2_{hkl}. Suppose the value of F^2_{hkl} were assigned to each *hkl* in the reciprocal space lattice for a crystal. When the crystal were oriented so that the Ewald sphere went through point *hkl* the value of the intensity diffracted would be given by that F^2_{hkl} (ignoring the terms other than F^2_{hkl} in Eq. 20 and 21). Consider the 110 reciprocal lattice plane for NaCl plotted in Fig. 2(a): it is a rectangular net with [002] along one axis and [$\bar{1}10$] along the second orthogonal axis in the plane. Three values of F^2 are possible:

$F^2 = 0$	*h*, *k*, *l* mixed
$16(f_{\mathrm{Na}} + f_{\mathrm{Cl}})^2$	*h*, *k*, *l* unmixed, (*h*+*k*+*l*) is even
$16(f_{\mathrm{Na}} - f_{\mathrm{Cl}})^2$	*h*, *k*, *l* unmixed, (*h*+*k*+*l*) is odd.

The 110 reciprocal lattice plane of NaCl contains *hkl* of all three types, and these are indicated in Fig. 23(a).

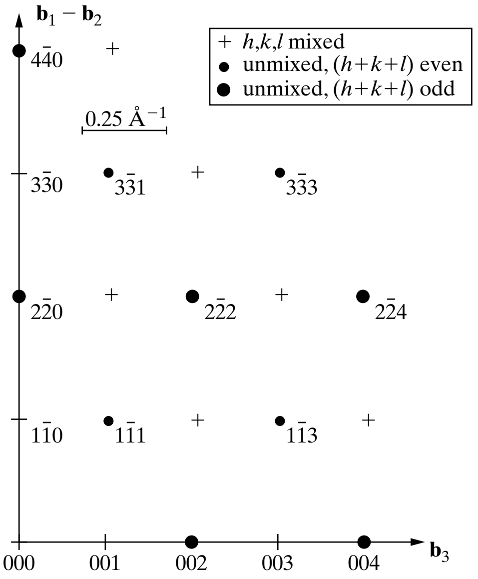

Figure 23 (a) Reciprocal lattice plane 110 for a crystal of NaCl showing the three F^2 values for this structure (see the legend for the meanings of the symbol). The dimensions of the rel points indicate intensity and not physical extent in reciprocal space.

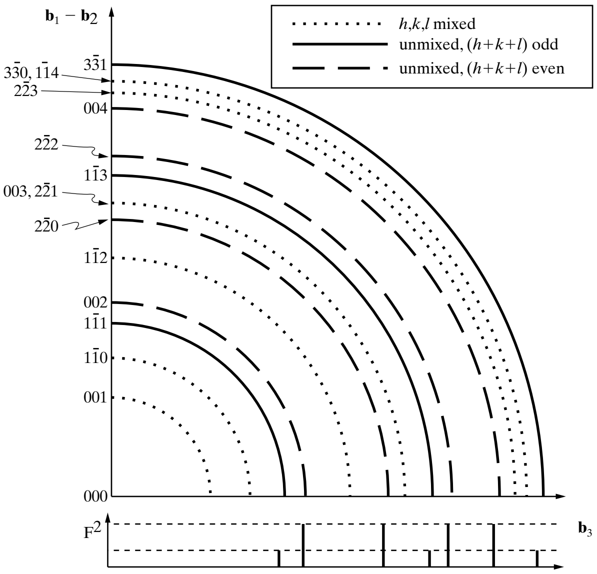

Figure 23 (b) Relshells intersecting one quadrant of reciprocal lattice plane 110 for polycrystalline, randomly-oriented NaCl. The axes refer to directions in one of the grains having the same orientation as that shown in (a). Only the rel shells for the points on the plane shown in (a), are included. The plot below the quadrant shows how F^2 would vary in a diffractometer scan (note that the horizontal axis is not 2θ nor is the vertical axis measured intensity).

It is somewhat more difficult to show the reciprocal lattice shells (rel shells) for polycrystalline NaCl. For a random powder, the one quadrant of the intersections of different rel shells with the 110 reciprocal lattice plane are shown in Fig. 23(b). Once again there are three types of shells, one of which is systematically absent. Note that only the relshells corresponding with the reciprocal lattice points on the 110 reciprocal lattice plane are shown: the systematically absent 210 and 310 shells are omitted for clarity. The diffraction pattern would have the appearance of the curve shown below Fig. 23(b). For fcc phases such as Cu, all non-zero fcc reflections would have equal F^2, but here, due to the presence of Na and Cl ions F^2 is modulated for non-systematically absent reflections.

15 MEASUREMENT OF X-RAY INTENSITY

In the examples just given, the observed intensity was estimated simply by visual comparison of one line with another. Although this simple procedure is satisfactory in a surprisingly large number of cases, there are problems in which a more precise measurement of diffracted intensity is necessary. Two methods are available for making such measurements, one dependent on the effect of x-rays on photographic emulsions or image plates and the other on the ability of x-rays to activate an electronic detector.

PROBLEMS

*__1__ Derive an expression for the absorption factor of a diffractometer specimen in the form of a flat plate of finite thickness t. (Note that the absorption factor now depends on θ). Index these lines (i.e., determine the Miller indices of each reflection) and calculate their relative integrated intensities.

*__2__ Consider the highest-angle on the diffraction pattern of Cu and of Pb, measured at 20° C with Cu $K\alpha$ radiation. By what percentage is the intensity of each of these lines reduced by thermal vibration of the atoms?

3 Consider a hypothetical element whose structure can be based on either of the following:

a) Cell A, base-centered tetragonal containing two atoms per cell, at $0\ 0\ 0$ and $\frac{1}{2}\,\frac{1}{2}\,0$, for which $a = 2\text{Å}$ and $c = 3\text{Å}$;

b) Cell B; simple tetragonal with one atom per cell at $0\ 0\ 0$.

Determine simplified structure-factor equations for each cell and the positions (2θ values) of the first four lines that would be *observed* ($F^2 \neq 0$) on a powder pattern made with Cu $K\alpha$ radiation. Plot the 2θ values of these lines in the manner of Fig 10-2, and label each line with its indices relative to Cell A and Cell B. Draw the two cells in the proper relation to one another, and show that the indices of any one observed line, other than obvious ones of the form $0\ 0\ l$, refer to the same plane of atoms.

[This problem illustrates several points: (1) we can choose any unit cell we wish, (2) the Miller indices of any given plane of atoms depend on the choice of cell, and (3) the diffraction pattern of the material is independent of the choice of cell.]

*__4__ Derive simplified expressions for F^2 for diamond, including the rules governing observed reflections. This crystal is cubic and contains 8 carbon atoms per unit cell, located in the following positions:

$$\begin{array}{cccc} 0\,0\,0 & \frac{1}{2}\,\frac{1}{2}\,0 & \frac{1}{2}\,0\,\frac{1}{2} & 0\,\frac{1}{2}\,\frac{1}{2} \\ \frac{1}{4}\,\frac{1}{4}\,\frac{1}{4} & \frac{3}{4}\,\frac{3}{4}\,\frac{1}{4} & \frac{3}{4}\,\frac{1}{4}\,\frac{3}{4} & \frac{1}{4}\,\frac{3}{4}\,\frac{3}{4} \end{array}$$

5 A certain tetragonal crystal has four atoms of the same kind per unit cell, located at $0\,\frac{1}{2}\,\frac{1}{4}$, $\frac{1}{2}\,0\,\frac{1}{4}$, $\frac{1}{2}\,0\,\frac{3}{4}$, $0\,\frac{1}{2}\,\frac{3}{4}$. (Do not change axes.)

a) Derive simplified expressions for F^2.

b) What is the Bravais lattice of this crystals?

c) What are the values of F^2 for the 100, 002, 111, and 011 reflections?

*__6__ Derive simplified expressions for F^2 for the wurtzite form of ZnS, including the rules governing observed reflections. This crystal is hexagonal and contains 2 ZnS per unit cell, located in the following positions:

$$\begin{array}{lll} \text{Zn:} & 0\,0\,0, & \frac{1}{3}\,\frac{2}{3}\,\frac{1}{2}, \\ \text{S:} & 0\,0\,\frac{3}{8}, & \frac{1}{3}\,\frac{2}{3}\,\frac{7}{8} \end{array}$$

Note that these positions involve a common translation, which may be factored out of the structure-factor equation.

Ignore the absorption and temperature factors in all of the following problems.

*__7__ A Debye–Scherrer pattern of tungsten (BCC) is made with Cu $K\alpha$ radiation. The first four lines on this pattern were observed to have the following θ values:

Line	θ
1	20.3°
2	29.2
3	36.7
4	43.6

8 A Hull/Debye–Scherrer pattern is made of silicon, which has the same structure as diamond, with Cu $K\alpha$ radiation. What are the indices of the first two lines on the pattern, and what is the ratio of the integrated intensity of the first to that of the second?

*__9__ A Hull/Debye–Scherrer pattern is made of the intermediate phase InSb with Cu $K\alpha$ radiation. This phase has the zinc-blende structure and a lattice parameter of 6.46 Å. What are the indices of the first two lines on the pattern, and what is the ratio of the integrated intensity of the first to the second?

10 Calculate the relative integrated intensities of the first six lines of the Hull/Debye–Scherrer pattern of zinc, made with Cu $K\alpha$ radiation. The indices and observed θ values of these lines are:

Line	*hkl*	θ
1	00.2	18.8°
2	10.0	20.2
3	10.1	22.3
4	10.2	27.9
5	11.0, 10.3	36.0
6	00.4	39.4

(Line 5 is made up of two unresolved lines from planes of very nearly the same spacing.) Compare your results with the intensities observed in the pattern.

REFERENCES

The following books are listed more or less in the order they are encountered in the text

G.1 *International Tables for Crystallography*, Ed. A.J.C Wilson, Vol. A-C (Dordrecht Kluwer Academic Pub. for International Union of Crystallography, 1995). The reference ‘’book” for crystallography and diffraction.

G.15 N. F. M. Henry, H. Lipson, and W. A. Wooster. *The Interpretation of X-Ray Diffraction Photographs* (London: Macmillan, 1951). Rotating and oscillating crystal methods, as well as powder methods, are described. Good section on analytical methods of indexing powder photographs.

G.19 R. W. James. *The Optical Principles of the Diffraction of X-Rays* (Woodbridge; CT: Ox Bow Press, 1982). Excellent book on advanced theory of x-ray diffraction. Includes thorough treatments of diffuse scattering (due to thermal agitation, small particle size, crystal imperfections, etc.), the use of Fourier series in structure analysis, and scattering by gases, liquids, and amorphous solids.

G.20 B. E. Warren. *X-Ray Diffraction* (Reading, MA: Addison-Wesley, 1969). Excellent advanced treatment, in which the author takes pains to connect theoretically derived results with experimentally observable quantities. Stresses diffraction effects due to thermal vibration, order-disorder, imperfect crystals, and amorphous materials. Includes a treatment of the dynamical theory of diffraction by a perfect crystal.

ANSWERS TO SELECTED PROBLEMS

1. $A = A(\theta) = (1/2\mu)[1 - \exp(-2\mu t/\sin\theta)]$

2. 34 percent reduction for copper, 82 percent for lead

4. $F^2 = 0$ for mixed indices; $F^2 = 0$ for $(h + k + l)$ an odd multiple of 2; $F^2 = 64\,f_C^2$ for $(h + k + l)$ an even multiple of 2; $F^2 = 32\,f_C^2$ for $(h + k + l)$ odd.

6.

$h + 2k$	l	F^2
$3n$	$2p + 1$ (as 1, 3, 5, 7 …)	0
$3n$	$8p$ (as 8, 16, 24 …)	$4(f_{Zn} + f_s)^2$
$3n$	$4(2p + 1)$ (as 4, 12, 20, 28 …)	$4(f_{Zn} - f_s)^2$
$3n$	$2(2p + 1)$ (as 2, 6, 10, 14 …)	$4(f_{Zn}^2 + f_s^2)$
$3n \pm 1$	$8p \pm 1$ (as 1, 7, 9, 15, 17 …)	$3(f_{Zn}^2 + f_s^2 - \sqrt{2}\,f_{Zn}f_s)$
$3n \pm 1$	$4(2p + 1) \pm 1$ (as 3, 5, 11, 13, 19, 21 …)	$3(f_{Zn}^2 + f_s^2 + \sqrt{2}\,f_{Zn}f_s)$
$3n \pm 1$	$8p$	$(f_{Zn} + f_s)^2$
$3n \pm 1$	$4(2p + 1)$	$(f_{Zn} - f_s)^2$
$3n \pm 1$	$2(2p + 1)$	$(f_{Zn}^2 + f_s^2)$

n and *p* are any integers, including zero.

7.

Line	*hkl*	Calc. Int.
1	110	10.0
2	200	1.7
3	211	3.5
4	220	1.1

9. 111 and 200. The ratio is 2400 to 1.

Diffraction III: Real Samples

1 INTRODUCTION

Before turning to the practical aspects of diffraction from materials, it is valuable to consider how diffraction peaks are altered by the presence of various types of defects. Indeed, knowledge of how diffraction peaks are changed by defects underlies many of the analyses described in the third section of the book. Defects can be small numbers of dislocations in crystals with dimensions of millimeters. At the other extreme, the dislocation density may be so high that it is difficult to imagine the existence of discrete dislocations. Small crystal or grain size can be thought of as another kind of defect and can alter diffraction peak widths. In the limit of 'grain' size approaching that of an atom, as in gases, liquids and amorphous solids such as glasses and many polymers, sharp diffraction peaks no longer exist, and important information about these materials can be gleaned from how they scatter x-rays. At the other limit, that of defect-free crystals with millimeter or greater dimensions, diffracted intensity must be treated in a fashion quite different from the approach you may already know.

2 CRYSTALLITE SIZE

Consider that *destructive interference is just as much a consequence of the periodicity of atom arrangement as is constructive interference*. If the path difference between x-rays photons scattered by the first two planes of atoms differs only slightly from an integral number of wavelengths, then the plane of atoms scattering x-rays exactly out of phase with the photons from the first plane will lie deep within the crystal. If the crystal is so small that this plane of atoms does not exist, then complete cancellation of all the scattered x-rays will not result. It follows that there is a connection between the amount of "out-of-phaseness" that can be tolerated and the size of the crystal. The result is that very small crystals cause broadening (a small angular divergence) of the diffracted beam, i.e., dif-

From Chapter 5 of *Elements of X-Ray Diffraction*, Third Edition. B.D. Cullity, S.R. Stock.

fraction (scattering) at angles near to but not equal to, the exact Bragg angle. Therefore consider the scattering of x-rays incident on the crystal at angles deviating slightly from the exact Bragg angle.

Suppose, for example, that the crystal has a thickness t measured in a direction perpendicular to a particular set of Bragg plane (Fig. 1). Let there be $(m + 1)$ planes in this set. Define the Bragg angle θ as a variable and let θ_B be the angle which exactly satisfies Bragg's law for the particular values of λ and d involved, or

$$\lambda = 2d \sin \theta_B.$$

In Fig. 1, rays **A**, **D**,..., **M** make exactly this angle θ_B with the diffraction planes. Ray **D´**, scattered by the atoms of the first lattice plane below the surface, is therefore one wavelength out of phase with **A´**; and ray **M´**, scattered by the mth plane of atoms below the surface, is m wavelengths out of phase with **A´**. Thus, at a diffraction angle $2\theta_B$, rays **A´**, **D´**,..., **M´** are completely in phase and unite to form a diffracted beam of maximum amplitude, i.e., a beam of maximum intensity, since the intensity is proportional to the square of the amplitude.

Incident x-rays that make angles only slightly different from θ_B, produce incomplete destructive interference. Ray **B**, for example, makes a slightly larger angle θ_1, such that ray **L´** from the mth plane below the surface is $(m + 1)$ wavelengths out of phase with **B´**, the ray from the surface plane. This means that midway in the crystal there is a plane populated by atoms scattering x-rays which are one-half (actually, an integer plus one-half) wavelength out of phase with ray **B´** from the atoms of the surface plane. These rays cancel one another, and so do the other rays from similar pairs of planes throughout the crystal, the net effect being that rays scattered by the top half of the crystal annul those scattered by the bottom half. The intensity of the beam diffracted at an angle $2\theta_1$ is therefore zero. It is also zero at an angle $2\theta_2$ where θ_2 is such that ray **N´** from the mth plane below the surface is

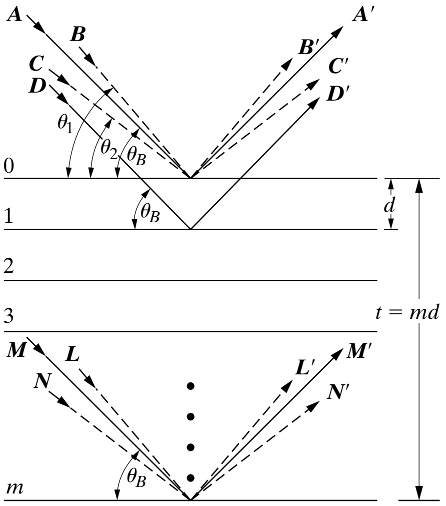

Figure 1 Effect of crystal size on diffraction.

$(m - 1)$ wavelengths out of phase with ray **C**′ from the surface plane. This defines, therefore, the two limiting angles, $2\theta_1$ and $2\theta_2$, at which the diffracted intensity must drop to zero. It follows that the diffracted intensities at angles near $2\theta_B$, but not greater than $2\theta_1$ or less than $2\theta_2$, are *not zero* but have values intermediate between zero and the maximum intensity of the beam diffracted at an angle $2\theta_B$. The curve of diffracted intensity vs. 2θ will thus have the form of Fig. 2(a) in contrast to Fig. 2(b), which illustrates the hypothetical case of diffraction occurring only at the exact Bragg angle.

The width of the diffraction curve of Fig. 2(a) increases as the thickness of the crystal decreases, because the angular range $(2\theta_1 - 2\theta_2)$ increases as m decreases. The width B is usually measured, in radians, at an intensity equal to half the maximum intensity, and this measure of width is termed the full-width at half maximum of FWHM. [Note that B is an angular width, in terms of 2θ (not θ), and not a linear width.] A rough measure of B, is one-half the difference between the two extreme angles at which the intensity is zero, which amounts to assuming that the diffraction line is triangular in shape. Therefore,

$$B = \frac{1}{2}(2\theta_1 - 2\theta_2) = \theta_1 - \theta_2.$$

The path-difference equations for these two angles are similar but related to the entire thickness of the crystal rather than to the distance between adjacent planes:

$$2t \sin \theta_1 = (m + 1)\lambda,$$

$$2t \sin \theta_2 = (m - 1)\lambda.$$

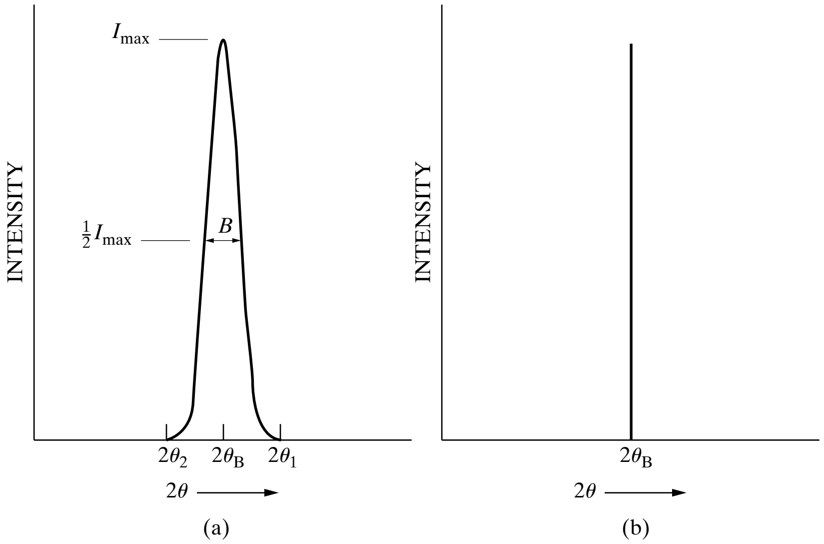

Figure 2 Effect of fine crystallite size on diffraction curves (schematic).

By subtraction,

$$t(\sin\theta_1 - \sin\theta_2) = \lambda,$$

$$2t\cos\left(\frac{\theta_1+\theta_2}{2}\right)\sin\left(\frac{\theta_1-\theta_2}{2}\right) = \lambda.$$

But θ_1 and θ_2 are both very nearly equal to θ_B, so that

$$\theta_1 + \theta_2 = 2\theta_B\,(\text{approx.})$$

and

$$\sin\left(\frac{\theta_1-\theta_2}{2}\right) = \left(\frac{\theta_1-\theta_2}{2}\right)(\text{approx.}).$$

Therefore

$$2t\left(\frac{\theta_1-\theta_2}{2}\right)\cos\theta_B = \lambda,$$

$$t = \frac{\lambda}{B\cos\theta_B}. \tag{1}$$

A more exact treatment of the problem gives

$$t = \frac{0.9\lambda}{B\cos\theta_B}, \tag{2}$$

which is known as Scherrer's formula [5.1]. It is used to estimate the *size* of very small crystals from the measured width of their diffraction curves. Note that whether a value of 0.9 or 1 is used depends on the shape(s) of the crystallites assumed to be in the sample. A detailed discussion appears elsewhere [G.17]. What is the order of magnitude of this effect? Suppose $\lambda = 1.5$ Å, $d = 1.0$ Å, and $\theta = 49^o$. Then for a crystal 1 mm in diameter the breadth B, due to the small crystal effect alone, would be about 2×10^{-7} radian (10^{-5} degree), or too small to be observable. Such a crystal would contain some 10^7 parallel lattice planes of the spacing assumed above. However, if the crystal were only 500 Å thick, it would contain only 500 planes, and the diffraction curve would be relatively broad, namely about 4×10^{-3} radian (0.2°), which is easily measurable.

Nonparallel incident rays, such as **B** and **C** in Fig. 1, actually exist in any real diffraction experiment, since the "perfectly parallel beam" assumed an idealization. Any actual beam of x-rays contains divergent and convergent rays as well as parallel rays, so that the phenomenon of diffraction at angles not exactly satisfying Bragg's law actually takes place.

Neither is any real beam ever strictly monochromatic. The usual "monochromatic" beam is simply one containing the strong $K\alpha$ component superimposed on the continuous spectrum. But the $K\alpha$ line itself has a width of about 0.001 Å and this narrow range of wavelengths in the nominally monochromatic beam is a further cause of line broadening, i.e., of measurable diffraction at angles close, but not equal, to $2\theta_B$, since for each value of λ there is a corresponding value of θ. (Translated into terms of diffraction line width, a range of wavelengths extending over 0.001 Å leads to an increase in line width, for $\lambda = 1.5$ Å and $\theta = 45^o$, of about 0.08^o over the width one would expect if the incident beam were strictly monochromatic.) Line broadening due to this natural "spectral width" is proportional to $\tan\theta$ and becomes quite noticeable as θ approaches 90^o.

3 INTERFERENCE FUNCTION

The calculation of the intensity of diffraction peaks in Ch. 4 was for diffraction at the exact Bragg angle θ_B. At this angle, and in the absence of any defects producing displacement of the unit cells of the crystal, the total amplitude diffracted by the N unit cells of the crystal is the sum of the amplitude F_n scattered by each unit cell:

$$A_{TOTAL} = NF_n. \tag{3}$$

At deviations from the exact Bragg angle, the individual unit cells will scatter slightly out of phase. Also, the vector $(\mathbf{S} - \mathbf{S_0})/\lambda$ no longer extends from the origin of the reciprocal lattice to a reciprocal lattice point. As was shown in the preceding section, x-rays scattered from an effectively infinite crystal at $\theta \neq \theta_B$ will be out of phase and the diffracted intensity will equal zero. If the crystal is small enough, however, the intensity will not go to zero off the exact Bragg condition, and the calculation which follows shows how diffracted intensity varies with angle as a function of the number of unit cells along the direction of the diffraction vector $(\mathbf{S} - \mathbf{S_0})$, i.e., along the direction *normal* to the Bragg planes.

Figure 3 shows the direct space and reciprocal space diagrams, respectively, for diffraction from a crystal at $\theta(1) > \theta_B(1)$ for 001 and at $\theta(2) > \theta_B(2)$ for 002, where "1" and "2" in parenthesis indicate the angle for the first and second order diffraction. If a θ–2θ diffractmeter is used, the portion of the reciprocal lattice sampled during a scan is indicated by the horizontal line from the origin in Fig. 3b (i.e., along $\mathbf{b}_3$ in this example). If $\mathbf{H}_{hkl}$ (or $\mathbf{H}$ for short) is the reciprocal lattice vector from the origin of the reciprocal lattice to the reciprocal lattice point hhe, the diffraction off the exact Bragg condition means that $(\mathbf{S} - \mathbf{S_0})/\lambda \neq \mathbf{H}$. The difference between these two vectors *along* the direction of $(\mathbf{S} - \mathbf{S}_0)/\lambda$ will be written as $\mathscr{s}$ is often termed the deviation parameter and is shown in Fig. 3. In order to calculate the intensity diffracted from the crystal at $\theta \neq \theta_B$, the phase differences for scattering from different unit cells must be included. For the three unit vectors of the crystal $\mathbf{a}_1$, $\mathbf{a}_2$, and $\mathbf{a}_3$:

$$A_{TOTAL} = \sum_{n_1=0}^{N_1-1}\sum_{n_2=0}^{N_2-1}\sum_{n_3=0}^{N_3-1} F \exp \frac{2\pi i}{\lambda}[(\mathbf{S} - \mathbf{S}_0) \cdot (n_1\mathbf{a}_1 + n_2\mathbf{a}_2 + n_3\mathbf{a}_3)], \tag{4}$$

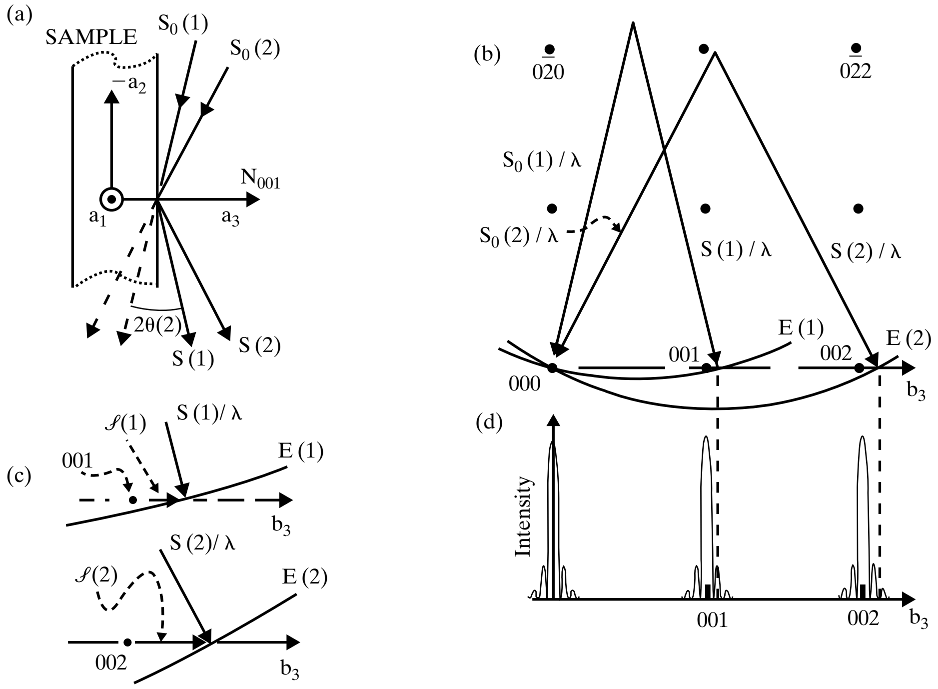

Figure 3 (a) Incident and diffracted beam directions for 001 and for 002 diffraction in direct space. (b) Ewald sphere construction for incident beam directions shown in (a). (c) Deviation parameter $\mathscr{s}$ for the geometries in (a) and (b). (d) Diffracted intensity verses orientation given by the intereference function as a function of deviation parameter, i.e., of Ewald sphere orientation. "E" denotes the Ewald sphere, and the number in parentheses ("1" or "2") indicates whether the quantities apply to 001 or 002 diffraction, respectively.

the integers n_i define the particular unit cells for which the phase difference is being calculated, and N_i are the total number of unit cells along $\mathbf{a}_i$. From the definition for the reciprocal lattice vector expressing the deviation from the exact Bragg condition (Fig. 3), i.e.,

$$(\mathbf{S} - \mathbf{S}_0)/\lambda = \mathbf{H} + \mathscr{s} = (h\mathbf{b}_1 + k\mathbf{b}_2 + l\mathbf{b}_3) + \mathscr{s}$$

$$A_{TOTAL} = F\sum_{n_1}\sum_{n_2}\sum_{n_3} exp[2\pi i(\mathbf{H} + \mathscr{s})\cdot(n_1\mathbf{a}_1 + n_2\mathbf{a}_2 + n_3\mathbf{a}_3)]$$

$$= F\sum_{n_1}\sum_{n_2}\sum_{n_3} \exp[\mathbf{2}\pi i(h\mathbf{b_1} + k\mathbf{b_2} + l\mathbf{b_3} + \mathscr{s})\cdot(n_1\mathbf{a}_1 + n_2\mathbf{a}_2 + n_3\mathbf{a}_3)] \quad (5)$$

Applying the orthonormality conditions for reciprocal and direct space vectors

$\mathbf{b}_j \cdot \mathbf{a_i} = \delta_{\mathrm{i}j}$, where is Kronecker's delta produces

$$A_{TOTAL} = F\sum_{n_1} \exp(2\pi i\mathscr{S}\cdot n_1\mathbf{a_1}) \sum_{\mathrm{n_3}} \exp(2\pi\ i\mathscr{S}\cdot n_2\mathbf{a_2}) \sum_{\mathrm{n_2}} \exp(2\pi i\mathscr{S}\cdot n_3\mathbf{a_3}) \qquad (6)$$

Each sum is independent and may be evaluated separately. Converting from exp form to sines, yields

$$\mathrm{A_{TOTAL}} = \mathrm{F}\left[\prod_{\mathrm{i}=1}^{3} \frac{\sin\ \pi\lambda\mathscr{S}\ \cdot\ \mathrm{N_i}\mathbf{a_i}}{\sin\ \pi\lambda\mathscr{S}\cdot\ \mathbf{a_i}}\right]\exp\{\pi[(\mathrm{N_1}-1)\mathbf{a}_1+(\mathrm{N_2}-1)\mathbf{a}_2+(\mathrm{N_3}-1)\mathbf{a}_3]\}, \qquad (7)$$

where II denotes the product of three terms shown in Eq. 6. Note that the last term is the phase factor relating $|\mathrm{A_T}|$ to $\mathrm{A_T}$, and this term is eliminated when the intensity is calculated:

$$\mathbf{I} = \mathrm{A_{TOTAL}} \quad \mathbf{A_{TOTAL}} = \mathbf{F^2}\prod_{\mathbf{i}} \frac{\sin^2\pi\ \mathscr{S}\cdot \mathrm{N_i a_i}}{\sin^2\pi\ \mathscr{S}\cdot \mathbf{a_i}} \qquad (8)$$

Equation 8 is known as the interference function.

By use of L'Hopital's rule, the maximum intensity at the Bragg peak can be shown to equal $\mathrm{F^2N^2}$ and, to a reasonable approximation, the width of the Bragg peak can be calculated to be proportional to 1/N, where N is the number of unit cells along $(\mathbf{S} - \mathbf{S}_0)$. Thus, the integrated intensity increases linearly with N.

Intensity, therefore, is a periodic function around each Bragg peak, a function which depends on the number of unit cells. The vector $\mathscr{S}$ is a three-dimensional vector so that the intensity for a certain deviation *along a specific direction* in reciprocal space depends on the *number of unit cells lying along that direction*. Another way of thinking about this is to think of the reciprocal lattice points lengthening into reciprocal lattice rods, i.e., rel rods, along the direction with the small number of unit cells. A simple way of showing this is to plot a constant contour of intensity, in reciprocal space, say one-half of the maximum. Figure 4(c) and (d) show such plots for the thin crystallite dimensions shown in a) and b). Vectors $\mathbf{S}_0$, $\mathbf{S}$, and $(\mathbf{S_0} - \mathbf{S})/\lambda$ are shown for $\theta < \theta_\mathrm{B}$. In the case where the rel rod is elongated parallel to the reciprocal space sampling region for the θ–2θ diffractometer, i.e., where the thin dimension of the crystal is parallel to the sample normal, a wider diffraction peak is observed. When the rel rod is perpendicular to the reciprocal space sampling region, the effective of the small crystal dimension is not seen in the scan.

This result, obtained from a reciprocal space perspective, is the same as that of Scherrer's equation. Both results highlight an important property of direct and reciprocal spaces. If a feature's dimension along a certain direct space direction is *large*, the feature's size along the corresponding direction in reciprocal space is *small*. The converse is true as well.

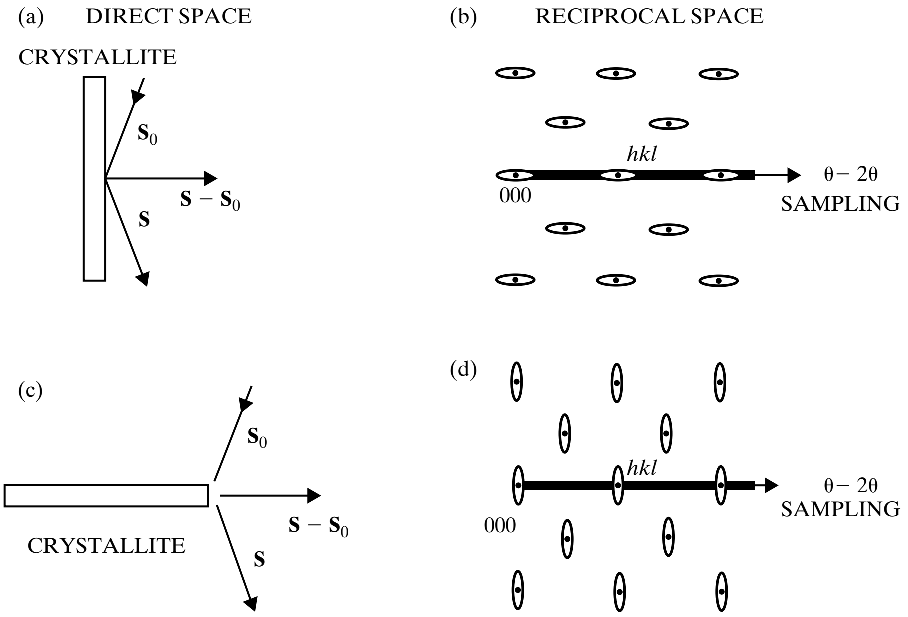

Figure 4 Illustration of detectability of diffraction peak broadening for a θ–2θ diffractometer for two crystallite orientations. (a) and (c) show direct space and reciprocal space, respectively, for one crystallite orientation relative to $\mathbf{S} - \mathbf{S}_0$ and (b) and (d) show the two spaces for a second crystallite orientation. The ellipses surrounding the reciprocal lattice points show the eleongation of the rel points into rel rods (due to small crystallite dimensions) and represent contours of constant diffracted intensity. The horizontal, solid bar represents the reciprocal space sampling region (RSSR).

4 STRAIN

In the preceeding sections crystal size was seen as a type of defect, i.e., a deviation from the crystal of infinite extent and perfect atomic periodicty assumed in the derivation 21. Dislocations and subgrains are another type of defect which have important consequences in diffraction. Before the existence of dislocations was established experimentally, considerable indirect evidence had been gathered showing that all real crystals possess, to a greater or lesser degree, a *mosaic structure* such as is illustrated in a greatly exaggerated fashion in Fig. 5.

A crystal with mosaic structure does not have its atoms arranged on a perfectly regular lattice extending from one side of the crystal to the other; instead, the lattice is broken up into a number of tiny blocks, each slightly disoriented one from another. The size of these blocks is of the order of 1000 Å, while the maximum angle of disorientation between them may vary from a very small value to as much as one degree, depending on the crystal. If this angle is ε, then diffraction of a parallel monochromatic beam from a "single" crystal will occur not only at an angle of incidence θ_B but at all angles between θ_B and $\theta_B + \varepsilon$. Another effect of mosaic struc-

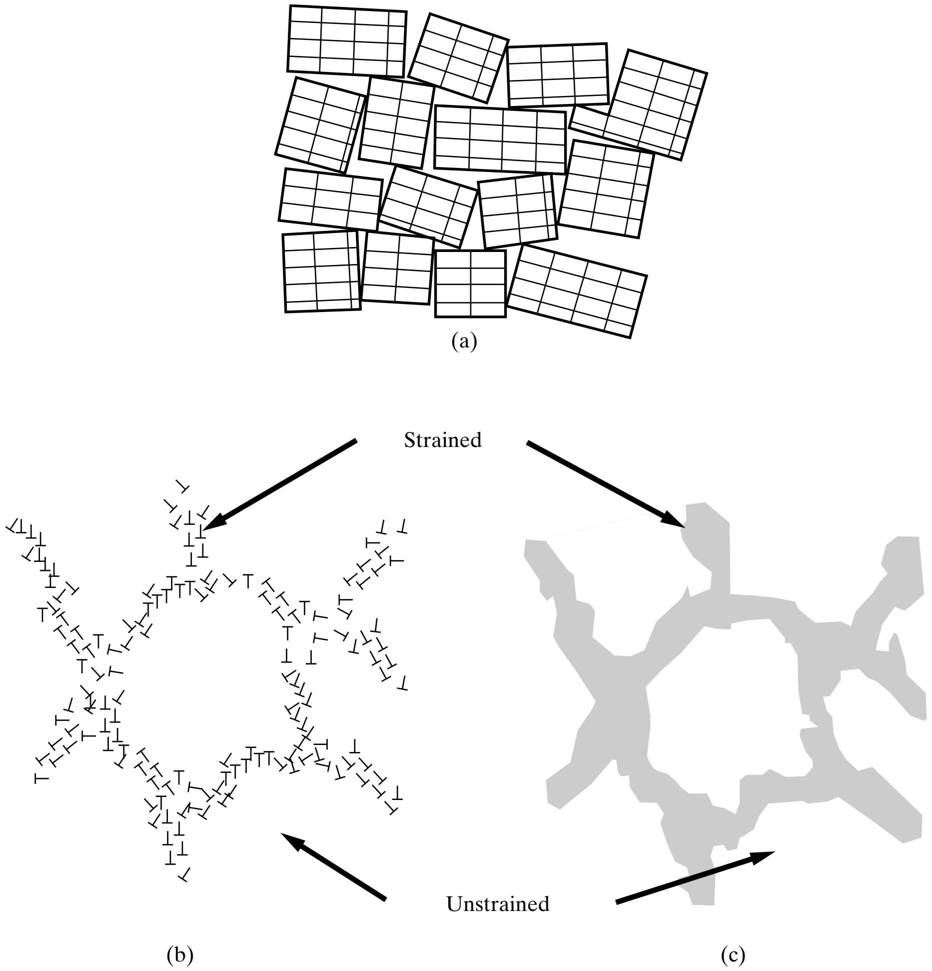

Figure 5 Mosaic structure of a real crystal. (a) Rotations between adjacent domains (left), (b) dislocations walls separating different mosaic blocks (middle) and (c) regions corresponding to high dislocation densities in (b) where microstrain is significant. In (b) the symbol $\perp$ shows the positions of dislocation lines running through the plane of the drawing.

ture is to increase the integrated intensity of the diffracted beam relative to that theoretically calculated for an ideally perfect crystal (Sec. 5).

In the 1960s the TEM provided direct evidence of mosaic structure. It showed that real crystals, whether single crystals or individual grains in a polycrystalline aggregate, had a substructure defined by the dislocations present. The density of these dislocations is not uniform; they tend to group themselves into walls (subgrain boundaries) surrounding small volumes having a low dislocation density (subgrains or cells). Today the term "mosaic structure" is seldom used, but the little blocks of Fig. 5 are identical with sub-grains and the regions between the blocks are the dislocation walls. It is the strains and strain gradients associated with the groups of dislocations that is responsible for the increase in integrated intensity of diffraction not the fact that there are rotated domains.

It is useful at this juncture to consider the effects of strain on diffraction peaks. Two types of stresses can be identified, *microstresses* and *macrostresses*. Microstresses and the corresponding microstrains vary from one grain to another, or from one part of a grain to another part, on a microscopic scale. On the other hand, the stress may be quite uniform over large distances; it is then referred to as *macrostress*.

The effect of strain, both uniform and nonuniform, on the direction of x-ray reflection is illustrated in Fig. 6. A portion of an unstrained grain appears in (a) on the left, and the set of transverse diffraction planes shown has everywhere its equilibrium spacing d_0. The diffraction line from these planes appears on the right. If the grain is then given a uniform tensile strain at right angles to the diffraction planes, their spacing becomes larger than d_0, and the corresponding diffraction line shifts to lower angles but does not otherwise change, as shown in (b). This line shift

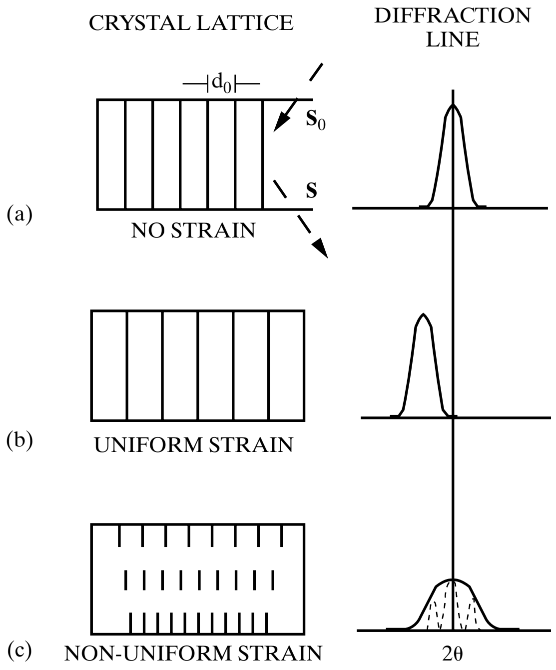

Figure 6 Effect of uniform and non-uniform strains (left side of the figure) on diffraction peak position and width (right side of the figure). (a) shows the unstrained sample, (b) shows uniform strain and (c) shows non-uniform strain within the volume sampled by the x-ray beam.

is the basis of the x-ray method for the measurement of macrostress. In (c) the grain is bent and the strain is nonuniform; on the top (tension) side the Bragg plane spacing exceeds d_0, on the bottom (compression) side it is less than d_0, and somewhere in between it equals d_0. Thus, a single grain can be thought of as composed of a number of small regions in each of which the plane spacing is substantially constant but different from the spacing in adjoining regions. These regions cause the various sharp diffraction lines indicated on the right of (c) by the dotted curves. The sum of these sharp lines, each slightly displaced from the other, is the broadened diffraction line shown by the full curve and, of course, the broadened line would normally be the only one experimentally observable. Differentiating Bragg's law yields the relation between the broadening produced and the nonuniformity of the strain:

$$b = \Delta 2\theta = -2\frac{\Delta d}{d}\tan\theta, \tag{9}$$

where b is the extra broadening, over and above the instrumental breadth of the line, due to a fractional variation in Bragg plane spacing $\Delta d/d$. This equation allows the variation in strain, $\Delta d/d$, to be calculated from the observed broadening. This value of $\Delta d/d$ however, includes both tensile and compressive microstrain and must be divided by two to obtain the maximum tensile strain alone, or maximum compressive strain alone, if these two are assumed equal. The maximum strain so found can then be multiplied by the elastic modulus E to give the maximum microstress present.

5 PERFECT CRYSTALS

Within a few years of the discovery of the diffraction of x-rays by crystals, it was apparent that the approach used to calculate diffracted intensities was inadequate to describe diffraction from highly perfect crystals [2, 3]. Diffracted intensities from perfect crystals were substantially less than those from deformed crystals, i.e., ideally imperfect crystals, and the variation of diffracted intensity with increasing levels of deformation was demonstrated [4]. Crystals with greater perfection exhibited diffraction peak widths which were smaller than those of less perfect crystals, but there appeared to be a minimum width of a diffraction peak which depended on the material, the wavelength of x-rays, the reflection and other factors. The assumptions behind the derivation of the *kinematical* diffraction equations did not apply to the case of highly perfect crystals with dimensions greater than ~ 1–5 μm.

Explaining the effects described above requires development of *dynamical* diffraction theory, but the origin of the decreased diffracting power of perfect crystals is easy to illustrate (Fig. 7). In the discussion which follows it is important to remember that every time a ray is diffracted it undergoes a phase shift of $\pi/2$ relative to the incident beam. If the incident beam with wave vector $\mathbf{K}_0$ enters a crystal at the correct angle θ for hkl diffraction, diffracted rays $\mathbf{K}_1$ are produced at angle 2θ

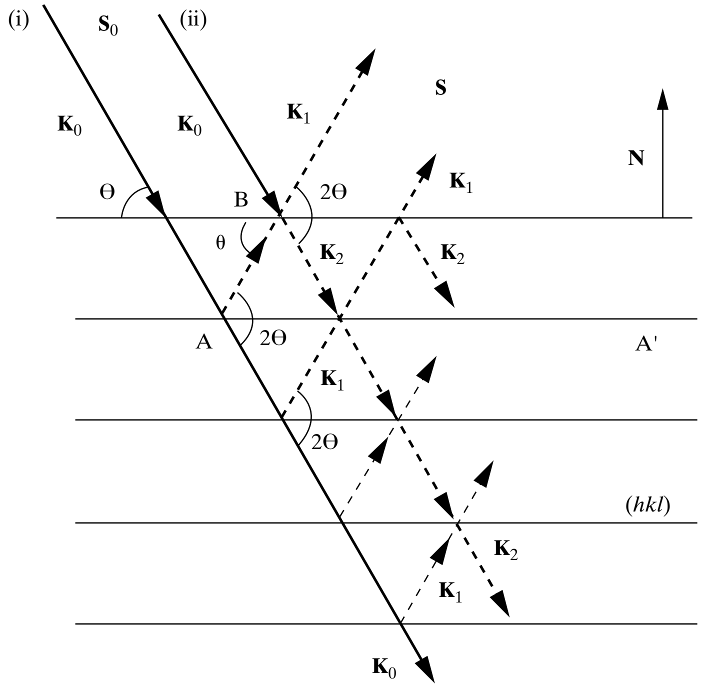

Figure 7 Illustration of the origin of primary extinction during *hkl* diffraction. **N** is the normal to (*hkl*), θ is the Bragg angle, and $\mathbf{K}_i$, i = 0, 1 and 2 are the wavevectors for the incident beam, the beam through 2θ from the incident beam and the beam diffracted through -2θ from the diffracted beam $\mathbf{K}_1$, respectively.

from $\mathbf{K}_0$. The probability of diffraction occurring at any particular plane of atoms is, of course, quite low, but in highly perfect crystals (with thicknesses greater than 1 μm) much of the incident intensity is eventually transferred to the diffracted beam.

Suppose diffraction occurs at A, producing an x-ray beam with wave vector $\mathbf{K}_1$ and a phase shift of $\pi/2$ with respect to $\mathbf{K}_0$. The beam $\mathbf{K}_1$ is incident, however, on another array of scatterers (atoms) at angle θ. At point B, therefore, there is a finite probability that $\mathbf{K}_1$ will be re-diffracted through angle -2θ, so that the diffracted ray has wave vector $\mathbf{K}_2$ parallel to but shifted in phase by $\pi/2 + \pi/2 = \pi$ with respect to $\mathbf{K}_0$. Thus $\mathbf{K}_2$ will interfere destructively with $\mathbf{K}_0$, and because intensity is being removed from the incident beam before it has a chance to diffract from depths below A-A´, the diffracted intensity will be lower than for an ideally imperfect crystal. This process is known as *primary extinction*.

In ideally imperfect crystals consisting of small coherent domains, primary extinction is not present but there is another type of extinction effect. When the crystal is oriented for diffraction the outermost domains remove a considerable portion of the primary beam's intensity by diffraction. This is in addition to the usual beam attenuation. Domains deeper in the sample with the same orientation of diffraction planes as those in the outer layer will, therefore, receive greatly reduced intensity, and *secondary extinction* is said to have occurred.

Dynamical diffraction theory describes the transfer of energy from the incident beam or forward direction to the diffracted beam direction and back again [5, 6]. Two differential equations are required to describe the energy transfer: one to partition the forward beam energy between the forward and diffracted beam directions and one to partition the diffracted beam energy between the diffracted and forward beam directions. The essential physical result is that two x-ray wavefields (termed Bloch waves) are excited in the forward direction and two wavefields are excited in the diffracted beam direction. These wavefields have wave vectors which are slightly different from $\mathbf{K}_0$ and $\mathbf{K}_1$, respectively, and the interaction of these wavefields produces interesting diffraction effects. Note that these wavefields actually exist [7] and are not merely a mathematical artifice. The method for obtaining a solution to this pair of coupled differential equations for the reflection geometry can be found in numerous works [e.g., G.7, G.19-G.24]. The integrated intensity for Bragg reflection from a thick crystal with negligible absorption is given by

$$I = \frac{8}{3\pi}\left(\frac{e^2}{mc^2}\right)\frac{N\lambda^2|F|}{\sin 2\theta}\left(\frac{1 + |\cos 2\theta|}{2}\right) \tag{10}$$

where N is the number of unit cells per unit volume.

The shape of the diffraction peak, i.e., intensity as a function of rotation of the sample crystal, is termed the crystal's rocking curve. For an incident plane wave and the reflection setting, dynamical theory predicts a flat-topped rocking curve; the simulation shown in Fig. 8 includes the effect of absorption which slightly changes the shape of the top of the curve. The flat-topped curve is known as the Darwin curve, and the width of the flat-top portion of the curve is termed the Darwin curve width $2s$. It is interesting to note that the peak reflectivity ($I_{\text{diffracted}}/I_{\text{incident}}$ at $\theta = \theta_B$) is 100% for the Darwin curve over the angular range $2s$ where

$$s = \left(\frac{e^2}{mc^2}\right)\frac{N\lambda^2|F|}{\pi \sin 2\theta}\left(\frac{1 + |\cos 2\theta|}{2}\right). \tag{11}$$

Allowing for the tails of the Darwin curve, the FWHM $\Delta\theta_0$ equals $2.12s$. For first order reflections, 5 arc sec $< \boldsymbol{\Delta}\theta_0 <$ 20 arc sec. Higher order reflections have considerably narrower rocking curves, and inclination of the diffraction planes relative to the sample surface, i.e., asymmetrically oriented diffraction planes, can also alter the Darwin curve width substantially. As noted in Fig. 8, absorption changes the shape of the Darwin curve, but discussion of this topic is beyond the scope of this book.

To illustrate the width of a perfect reflection, consider 211 (in terms of the rhombohedral axes) diffraction from calcite ($CaCO_3$), i.e., from the cleavage face. Following Warren [pp. 329-330 of G.20], $d_{211} = 3.035$ Å and $F_{211} = f_{ca} + f_c + f_o$ per

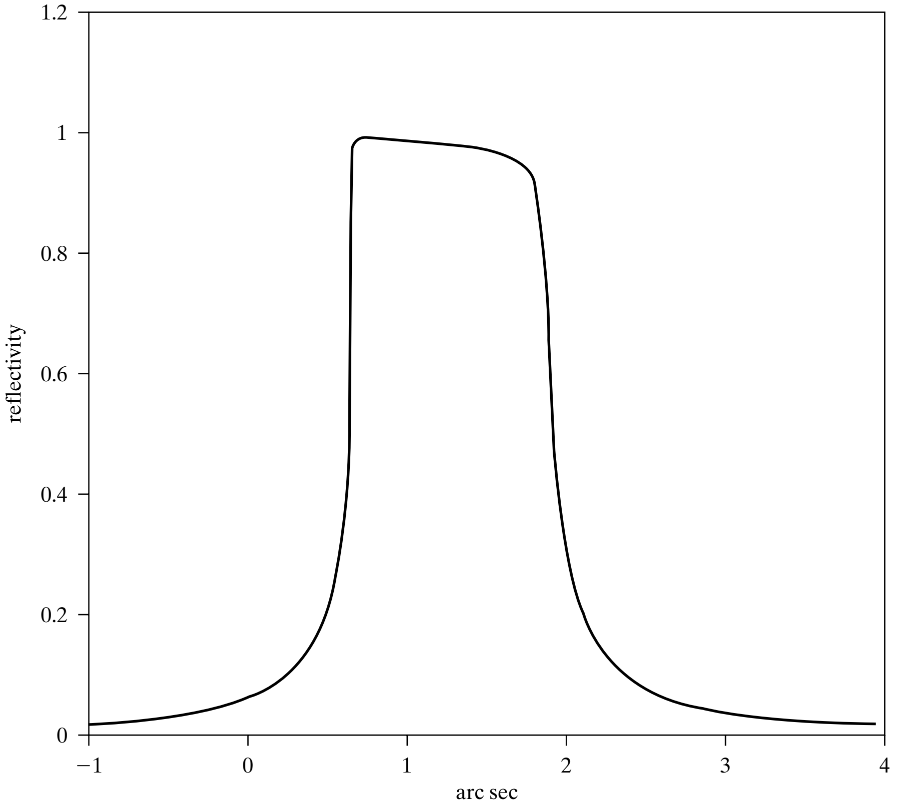

Figure 8 Simulated rocking curve for 004 silicon with Mo Kα_1 radiation and x-ray absorption. If x-ray absorption were absent, the top of the curve would be flat and the curve would be symmetrical. (Simulation with RADS Software, Bede Scientific.)

$CaCO_3$ molecule. For Cu Kα radiation, $\lambda = 1.542$, $F_{211} = 26.2$ per $CaCO_3$, and the number of $CaCO_3$ per cm^3 is $N = 1.64 \times 10^{22}$. For an unpolarized beam

$$S = \frac{(2.82 \times 10^{-13})(1.64 \times 10^{22})(1.54 \times 10^{-8})^2(26.2)^{0.936}}{\pi(0.491)}$$

$$= 17.4 \times 10^{-6}\text{rad} = 3.6 \text{ arc sec}$$

Therefore one expects $\Delta\theta_0 = 2.12\ s = 7.6$ arc sec.

Peak reflectivities (ratio of diffracted and incident monochromatic intensities) approaching 100% have been measured for incident plane waves [8], but it is important to realize that reflectivity drops precipitously if defects are present in the crystal. The FWHM of the Darwin curve represents a limit for a given geometry which can be approached but never exceeded. Just as the presence of linear and planar lattice faults decreases reflectivity, these defects increase the width of the crystal's rocking curve. Measurement of rocking curves is, therefore, an important method for assessing the perfection of crystals and epilayers, particularly those for micro electronic and optical applications.

The x-ray wavefield interactions described by dynamical theory occur within the Borrmann triangle ABC (Fig. 9). In the transmission setting the shape of the rocking curve is different from that of the reflection geometry and is a complex function of the thickness of the sample, even in the absence of significant absorption. All positions D on the exit surface of the crystal receive a greater or lesser intensity of x-rays due to the interference of the wavefields within the Borrmann triangle (the Pendellösung effect), and both the diffracted and transmitted beams project from the entire base of the triangle BC in their respective directions [9]. In the transmission or Laue geometry these wavefield interactions can be visualized through a technique called section topography.

Perhaps the most surprising dynamical diffraction effect is that of anomalous transmission in thick, perfect crystals (first observed by Borrmann in 1943 [10]). If $\mu t = 10$ or a similar large value, no intensity would be expected to be transmitted through a crystal since the intensity transmitted is given normally by $I = I_0 \exp(-\mu t)$. This result also holds for a perfect crystal (when it is thick), except at the exact Bragg angle. At the Bragg angle, however, significant intensity is observed in both the transmitted and diffracted beams. Dynamical diffraction theory demonstrates that one of the two wavefields is localized on the Bragg planes, i.e., on the rows of atoms comprising these planes, and the other is localized midway between the Bragg planes. Attenuation of the latter wavefield is quite low since the x-ray photons encounter relatively few electrons while the converse is true for the wavefield concentrated on the Bragg planes. Thus, attenuation of one of the wavefields is extremely low, but only at the exact Bragg angle, and intensity is transmitted for

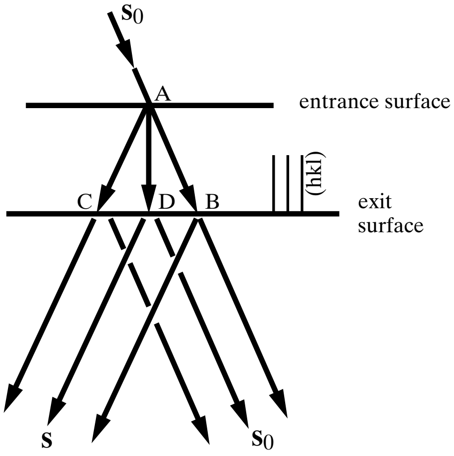

Figure 9 Borrmann triangle ABC in which x-ray wavefields interact.

$\mu t > 10$. The same effect is seen in electron diffraction in the TEM, where, due to the effect on images, it is termed anomalous absorption.

6 AMORPHOUS AND PARTIALLY CRYSTALLINE SAMPLES

In Sec. 2 through 4 examples were discussed of diffraction under nonideal conditions. In Sec. 5 diffraction from highly perfect crystals was discussed. These results are not deviations from Bragg's law because it was derived for certain ideal conditions and diffraction is only a special kind of scattering. This latter point cannot be too strongly emphasized. A single atom scatters an incident beam of x-rays in all directions in space, but a large number of atoms arranged in a perfectly periodic array in three dimensions to form a crystal scatters (diffracts) x-rays in relatively few directions. It does so precisely because the periodic arrangement of atoms causes destructive interference of the scattered rays in all directions *except* those predicted by Bragg's law, and in these directions constructive interference (reinforcement) occurs. It is not surprising, therefore, that measurable diffraction (scattering) occurs at non-Bragg angles whenever any crystal imperfection results in the partial absence of one or more of the necessary conditions for perfect destructive interference at these angles. These imperfections are generally slight compared to the overall regularity of the lattice, with the result that diffracted beams are confined to very narrow angular ranges centered on the angles predicted by Bragg's law for ideal conditions.

This relation between destructive interference and structural periodicity can be further illustrated by a comparison of x-ray scattering by solids, liquids, and gases (Fig. 10). The curve of scattered intensity vs. 2θ for a crystalline solid is almost zero everywhere except at certain angles where high sharp maxima occur: these are the diffracted beams. Both amorphous solids and liquids have structures characterized by an almost complete lack of periodicity and a tendency to "order" only in the sense that the atoms are fairly tightly packed together and show a statistical preference for a particular interatomic distance; the result is an x-ray scattering curve showing nothing more than one or two broad maxima. Finally, there are the monatomic gases, which have no structural periodicity whatever; in such gases, the atoms are arranged perfectly at random and their relative positions change constantly with time. The corresponding scattering curve shows no maxima, merely a regular decrease of intensity with increase in scattering angle. This curve would be entirely featureless, i.e., horizontal, if it were not for the fact that isolated atoms scatter x-rays more intensely at low 2θ angles than at high.

Information from the data such as that in the lower two curves of Fig. 10 can provide important clues to the structure of amorphous and semicrystalline samples.

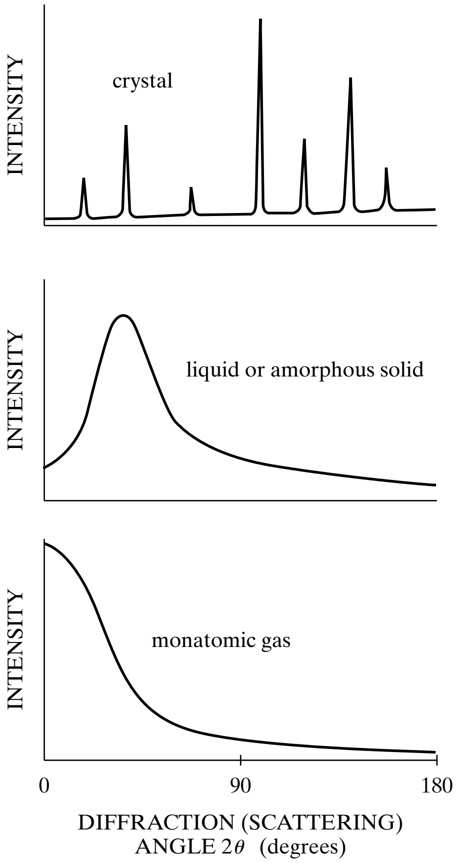

Figure 10 Comparative x-ray scattering by crystalline solids, amorphous solids, liquids, and monatomic gases (schematic). The three vertical scales are not equal.

PROBLEMS

1 In Fig. 1, put $m = 10$. (a) Write down a complete list of the path differences, in wavelengths λ, between the ray scattered by each plane below the surface and the ray scattered by the surface plane, for a scattering angle of $2\theta_1$. What plane scatters a ray exactly out of phase with the ray scattered by the third plane below the surface? What is the path difference for these two rays? (b) Write down a similar list of path differences for rays scattered at an angle halfway between $2\theta_B$ and $2\theta_1$ in order to convince yourself that these rays do *not* cancel one another.

***2** In Fig. 1, assume that the incident beam is perfectly parallel, instead of convergent, and incident at the angle θ_B. Does broadening of the diffracted beam still occur? If so, derive the relation between t and B.

***3** Calculate the breadth B (in degrees of 2θ), due to the small crystal effect alone, of the powder pattern lines of particles of diameter 1000, 750, 500, and 250 Å. Assume $\theta = 45^o$ and $\lambda = 1.5$ Å. For particles 250 Å in diameter, calculate the breadth B for $\theta = 10, 45$, and 80^o.

4 Check the value given in Sec. 2 for the increase in breadth of a diffraction line due to the natural width of the $K\alpha$ emission line. [*Hint:* Differentiate Bragg's law and find an expression for the rate of change of 2θ with λ.]
5 What strain is required to produce the same broadening as a crystallite size of 50 Å?
6 Show that the interference function's main maximum equals F^2N^2. What is the ratio of the heights of the main and first subsidary maxima of the interference function?
7 Calculate the Darwin curve width for Si 004 with (a) Cu $K\alpha$ radiation and (b) Ag $K\alpha$ radiation.
8 For calcite and for a parallel incident x-ray beam, at what number of unit cells does the FWHM of the interference function equal the Darwin curve width? (See Sec. 5.)

REFERENCES

The following books are listed more or less in the order they are encountered in the text

G.7 L.H. Schwartz and J.B. Cohen. *Diffraction from Materials*, 2nd ed. (Berlin: Springer-Verlag). Wider ranging thorough coverage of crystallography, instruments and techniques and diffraction theory.

G.17 Harold P. Klug and Leroy E. Alexander. *X-Ray Diffraction Procedures*, 2nd ed. (New York: Wiley, 1974). Contains a great deal of useful detail on the theory and operation of powder cameras and diffractometers. Covers the following topics in depth: chemical analysis by diffraction, parameter measurement, line-broadening analysis, texture determination, stress measurement, and studies of amorphous materials. Single-crystal methods are not included.

G.19 R. W. James. *The Optical Principles of the Diffraction of X-Rays* (Woodbridge; CT: Ox Bow Press, 1982). Excellent book on advanced theory of x-ray diffraction. Includes thorough treatments of diffuse scattering (due to thermal agitation, small particle size, crystal imperfections, etc.), the use of Fourier series in structure analysis, and scattering by gases, liquids, and amorphous solids.

G.20 B. E. Warren. *X-Ray Diffraction* (Reading, MA: Addison-Wesley, 1969). Excellent advanced treatment, in which the author takes pains to connect theoretically derived results with experimentally observable quantities. Stresses diffraction effects due to thermal vibration, order-disorder, imperfect crystals, and amorphous materials. Includes a treatment of the dynamical theory of diffraction by a perfect crystal.

ANSWERS TO SELECTED PROBLEMS

2 $\pm = 2\lambda/(B\cos\theta)$

3.

t	B	θ	B
1000 Å	0.11°	10°	0.31°
750	0.14	45	0.43
500	0.22	80	1.76
250	0.43		

This page intentionally left blank

Diffractometer Measurements

1 INTRODUCTION

The method of x-ray powder diffraction was devised independently in 1915 by Debye and Scherrer in Germany, and in 1916 by Hull in the United States, and initially relied on photographic film to record the angles and intensities of the diffracted beams. After the early work of W. H. and W. L. Bragg on x-ray spectra and crystal structure, diffractometry passed into a long period of relative disuse during which photographic recording in cameras was the most popular method of observing diffraction effects. The few diffractometers in use were all homemade and confined largely to the laboratories of research physicists. In the late 1940s, however, commercially made instruments became available; they rapidly became popular because they offered certain particular advantages over film techniques.

When properly employed, powder diffraction can yield a great deal of structural information about the material under investigation. Basically, this method involves the diffraction of monochromatic x-rays by a powder specimen. In this connection, "monochromatic" usually means the strong $K\alpha$ characteristic component of the α radiation from an x-ray tube operated above the K excitation potential of the target materials. In the case of diffractometry, a crystal monochromator is normally used to eliminate all wavelengths but the $K\alpha$ while in the photographic methods a filter is frequently used to enhance the ratio of the $K\alpha$ to other radiation. "Powder" can mean either an actual, physical powder held together with a suitable binder or any specimen in polycrystalline form. The method is thus eminently suited for materials work, since single crystals are not always available and such materials as polycrystalline wire, sheet, rod, polymeric fibers, etc., may be examined nondestructively without any special preparation.

From Chapter 6 of *Elements of X-Ray Diffraction*, Third Edition. B.D. Cullity, S.R. Stock.

Depending solely on the way it is used, the basic x-ray diffractometer/spectrometer is really two instruments:

1. An instrument for measuring x-ray spectra by means of a crystal of known structure.
2. An instrument for studying crystalline (and noncrystalline) materials by measurements of the way in which they diffract (scatter) x-rays of known wavelength.

The term *spectrometer* was originally used to describe both instruments, but, properly, it should be applied only to the first. The second instrument is aptly called a *diffractometer*: this name serves well to emphasize the particular use to which the instrument is being put, namely, diffraction analysis rather than spectrometry.

In this chapter, the design and operation of diffractometers will be described with particular, emphasis on the configurations most often encountered in materials work. Detailed information on diffractometer techniques appears in the books by Klug and Alexander [G.17] and by Jenkins and Snyder [G.25], and on the geometry of diffractometers appears in the monograph by Wilson [G.26].

Just as the emphasis in the present book is on diffraction rather than spectroscopy, the emphasis in this chapter is on the diffractometer. However, some experimental techniques used only, or mainly, in spectrometry are also described here, because they merge quite naturally with diffractometer techniques.

2 GENERAL FEATURES

In a diffraction camera, the intensity of a diffracted beam is measured through the amount of blackening it produces on a photographic film, a microphotometer measurement of the film being required to convert "amount of blackening" into x-ray intensity. In the diffractometer, the intensity of a diffracted beam is measured directly by an electronic x-ray detector. There are many types of x-ray detectors, but they all convert incoming x-rays into surges or pulses of electric current which are fed into various electronic components, including computers, for processing. The electronics counts the number of current pulses per unit of time, and this number is directly proportional to the intensity of the x-ray beam entering the detector.

Basically, a diffractometer is designed somewhat like the Hull/Debye–Scherrer camera except that a movable detector replaces the strip of film. In both instruments, essentially monochromatic radiation is used and the x-ray detector or film is placed on the circumference of a circle centered on the powder specimen. The essential features of a diffractometer are shown in Fig. 1. A powder specimen C, in the form of a flat plate, is supported on a table H, which can be rotated about an axis O perpendicular to the plane of the drawing. The x-ray source is S, the line focal spot on the target T of the x-ray tube; S is also normal to the plane of the drawing and therefore parallel to the diffractometer axis O. X-rays diverge from this source and are diffracted by the specimen to form a convergent diffract-

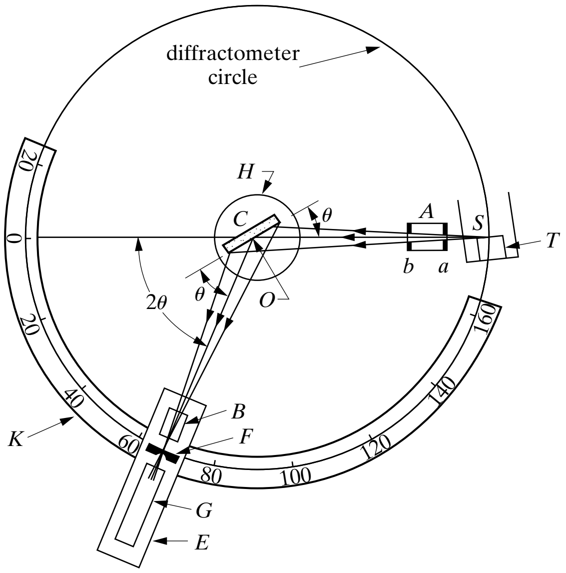

Figure 1 X-ray diffractometer (schematic).

ed beam which comes to a focus at the slit *F* and then enters the detector *G*. *A* and *B* are special slits which define and collimate the incident and diffracted beams. The monochromator or filter is usually placed in a special holder (not shown) in the diffracted, rather than the incident, beam; a monochromator or filter in the diffracted beam not only serves its primary function (suppression of $K\beta$ radiation) but also decreases background radiation originating in the specimen.

The receiving slits and detector are supported on the carriage *E*, which may be rotated about the axis *O* and whose angular position 2θ may be read on the graduated scale *K*. The supports *E* and *H* are mechanically coupled so that a rotation of the detector through $2x$ degrees is automatically accompanied by rotation of the specimen through x degrees. This coupling ensures that the angle of incidence on the flat specimen always equal the angle another, and both equal to half the total angle of diffraction, an arrangement necessary to preserve focusing conditions. In older instruments the detector may be power-driven at a constant angular velocity about the diffractometer axis or moved by hand to any desired angular position. Modern automated diffractometers generally collect data with the detector and sample set at a large number of fixed angles spaced by an angular increment on the order of 0.01°; the length of time counted and the size of the angular increment are controlled through software.

Figures 2 and 3 show two quite different configurations of a commercial instrument. Both configurations adhere to the design principles described above, but the positioning and details differ. The image in the lower right of Fig. 2 shows the diffractometer's radiation enclosure, and the PC next to the enclosure gives a sense of scale. In Fig. 2 the diffractometer axis is horizontal, and the detector moves in a vertical plane. In Fig. 3 the diffractometer axis is vertical, and the

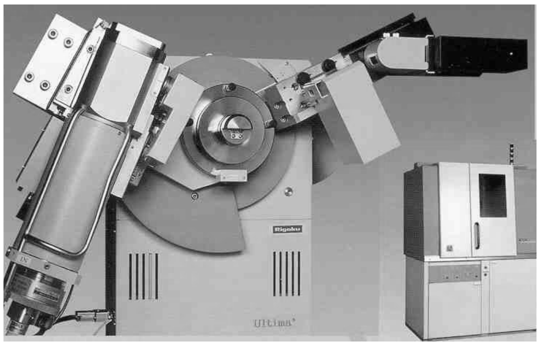

Figure 2 Rigaku diffractometer. The x-ray tube is at the left, and the inset phtograph shows the radiation enclosure and PC controlling the diffractometer motions (Courtesy Rigaku).

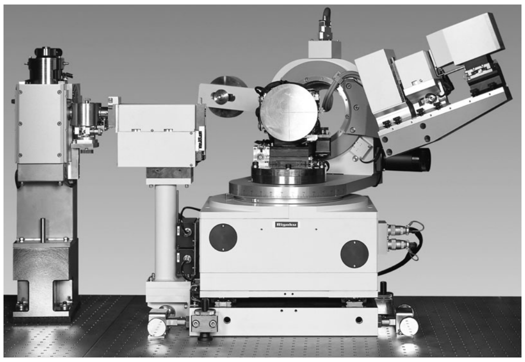

Figure 3 A second configuration of the Rigaku diffractometer shown in Fig. 2. Here additional sample rotations are possible. (Courtesy Rigaku... .)

detector moves in the horizontal plane. The configuration in Fig. 3 provides more sample rotation axes than in Fig. 2.

The way in which a diffractometer is used to mesure a diffraction pattern depends on the kind of circuit used to measure the rate of production of pulses in the detector. The pulse rate may be measured in two different ways:

1. The succession of current pulses is converted into a steady current, which is measured on a meter called *rate meter*, calibrated in such units as counts (pulses) per second (c/s or cps). Such a circuit gives a continuous indication of x-ray intensity.
2. The pulses of current are counted electronically in a circuit called *scaler,* and the average counting rate is obtained simply by dividing the number of pulses counted by the time spent in counting. This operation is essentially discontinuous because of the time spent in counting, and a scaling circuit is often quite inconvenient for following continuous changes in x-ray intensity.

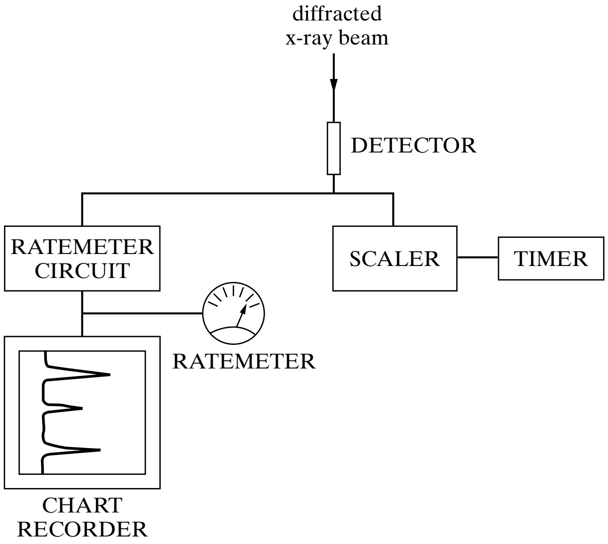

Figure 4 Block diagram of detector circuits for a diffractometer. The ratemeter circuit actuates a meter, for a visual indication of the counting rate, and a chart recorder. The scaler and timer operate together.

Corresponding to these two kinds of measuring circuits, there are two ways in which the diffraction pattern of an unknown substance may be obtained with a diffractometer (Fig. 4):

1. *Continuous Scan.* The detector is set near $2\theta = 0°$ and connected to a rate meter. The output of this circuit is fed to a strip-chart recorder. The detector is then driven at a constant angular velocity through increasing values of 2θ until the whole angular range is "scanned." At the same time, the paper chart on the recorder moves at a constant speed, so that distances along the length of the chart are proportional to 2θ. The result is a chart, such as Fig. 5, which gives a record of counts per second (proportional to diffracted intensity) vs. diffraction angle 2θ. A "high" scanning speed is typically 2° of 2θ per minute; at this rate a complete scan extending from, say, 10° to 160° 2θ, requires $150/2 = 75$ minutes. (The upper limit of detector motion, determined by contact between detector and x-ray tube, is about 160° 2θ.) This mode of operation has been superceded by computerized methods.
2. *Step Scan.* The detector is connected to a scaler and set at a fixed value of 2θ for a time sufficient to make an accurate count of the pulses obtained from the detector. The detector is then moved to a new angular position and the operation repeated. The range of 2θ of interest is covered in this fashion, and the curve of intensity vs. 2θ consists of the series of discrete measurements. With current computer-controlled diffractometers this is

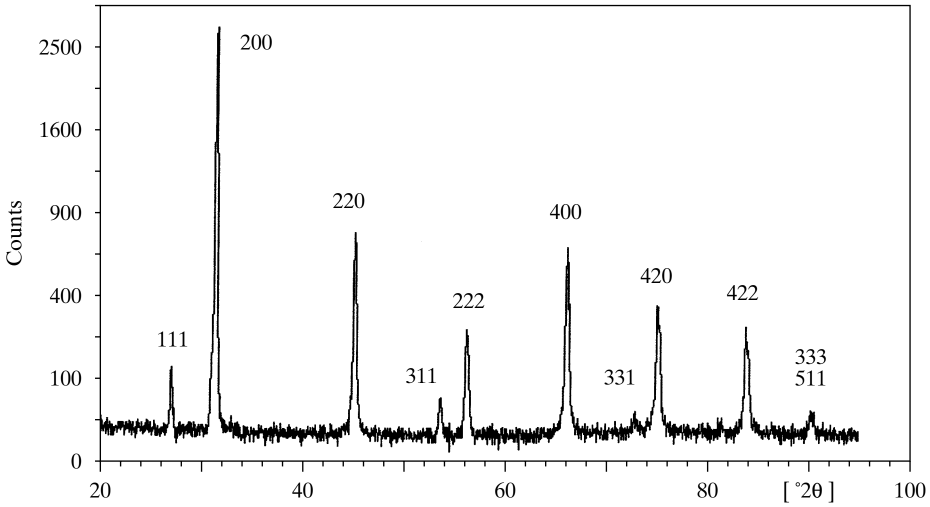

Figure 5 Diffraction pattern of NaCl powder. Copper Kα radiation, monochromator, variable divergence slit diffractometer. About one-half of the entire range of 2θ is shown here. The vertical axis shows the square root of the number of counts.

> the normal mode of operation and is no slower than continuous scanning. The digital diffraction pattern resulting from step scanning or computerized continuous scanning offers much greater convenience/power compared to strip chart recording since the data is ready for analysis with standard commercial or custom-written software. The time savings in measuring peak positions and intensities automatically is enormous. Accompanying this convenience is the very real danger that the incautious will no longer carefully examine the diffraction pattern itself, i.e., the shape of the different peaks, the changing background levels, etc., and thereby ignore potentially useful information, or worse, interpret artefacts such as electonic noise as diffraction peaks. Using software packages without understanding the algorithms employed can lead to serious errors.

There is a fundamental difference between the operation of a powder camera and a diffractometer. In a camera, all diffraction lines are recorded simultaneously, and variations in the intensity of the incident x-ray beam during the exposure can have no effect on relative line intensities. On the other hand, with a diffractometer, diffraction lines are recorded one after the other, and it is therefore imperative to keep the incident-beam intensity constant when relative line intensities must be measured accurately. Since the usual variations in line voltage are quite appreciable, the x-ray tube circuit of a diffractometer must include a voltage stabilizer and a tube-current stabilizer.

The kind of specimen used depends on the kind of material available. Flat metal sheet or plate may be examined directly; however, such materials almost always exhibit preferred orientation and this fact must be kept in mind in assessing relative intensities. This is also true of wires, which are best examined by cementing a number of lengths side by side on a glass plate. This plate is then inserted in the specimen holder so that the wire axes are at right angles to the diffractometer axis. Powder specimens are best prepared by lightly brushing the powder through a suitably-sized sieve into a recess in a glass, metal or plastic plate set on a slightly rough surface (the frosted end of a glass microscope slide or a matte cardboard surface) and compacting it from the back under just enough pressure to cause cohesion without use of a binder (Fig. 6 illustrates one successful method). Too much pressure causes preferred orientation of the powder particles. It is important to avoid motions which shear the assembly of particles, otherwise preferred orientation and unexpected peak intensities can result. A number of other successful powder "packing" have been compared [3] and discussed in detail [G.28,G.29]. In one important alternative to using a holder to contain the powder, the powder may be mixed with a binder and smeared on the surface of a glass slide.

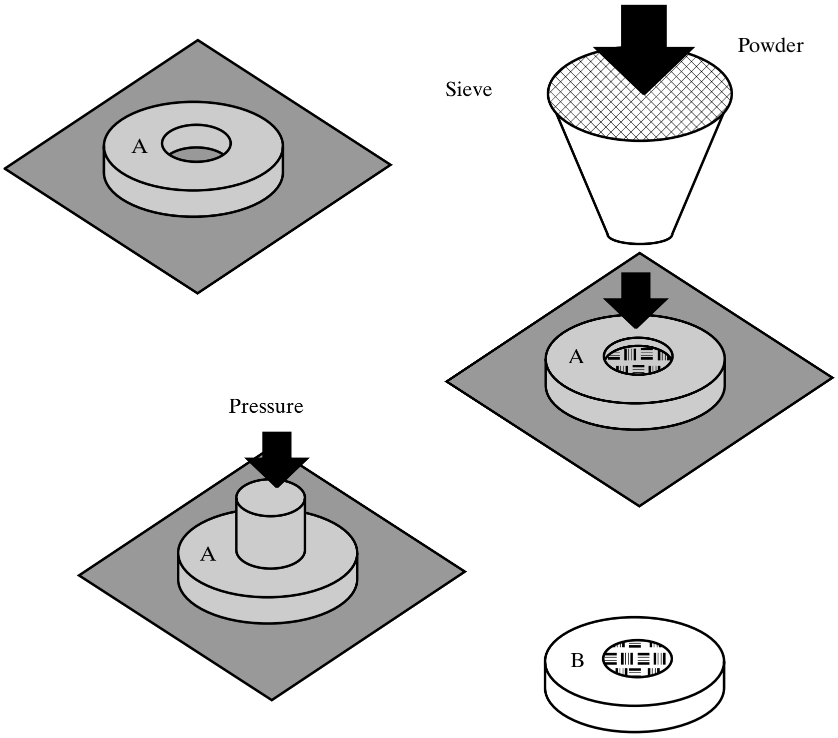

Figure 6 Steps in one method of diffractometer sample preparation: place holder face down on a slightly rough surface (frosted end of a glass microscope slide, matte cardboard, etc.) pour powder into sample holder from behind, press until powder is self-supporting in the holder, lift holder from surface and flip so that face B (the front of the sample holder) is exposed.

Any powder should be ground extremely fine, to a size of 10 μm or less, if relative line intensities are to be accurately reproducible; since the flat specimen is not rotated as a Hull/Debye–Scherrer, specimen is, the only way of obtaining an adequate number of particles having the correct orientation for diffraction is to reduce their average size. (Specimen "spinners" are available to rotate the specimen continuously in its own plane. But this kind of rotation is not nearly as effective in bringing new orientations into the beam as the kind that takes place in a Hull/Debye–Scherrer camera. Sample "rockers" which oscillate the sample about the diffractometer axis by an adjustable amount, on the order of 5°, are more effective than sample spinners.) Surface roughness also has a marked effect on relative line intensities. If the surface is rough, as in the case of a coarse powder compact, and the linear absorption coefficient high, the intensities of low-angle reflections will be abnormally low because of the absorption of the diffracted rays in each projecting portion of the surface. The only way to avoid this effect is to use a flat-surfaced compact of very fine powders or a specimen with a polished surface.

Single-crystal specimens may also be examined in a diffractometer by mounting the crystal on a goniometer allowing independent sample rotations about three orthogonal axes through the center of the volume irradiated by the x-ray beam. (Incidentally, independent rotation of the specimen about the diffractometer axis is often called an ω, rather than a θ, rotation.) In fact, special *single-crystal diffractometers* are available, designed solely for the determination of complex crystal structures. (Fig. 7(a) or for extremely high resolution measurement of diffraction peak widths of nearly perfect crystals, epilayers or superlattices (Fig. 7(b)).[1]

A diffractometer may be used for measurements at high or low temperatures by surrounding the specimen with the appropriate heating or cooling unit. Such an adaptation of the instrument is much easier with the diffractometer than with a camera because of the generally larger amount of free working space around the specimen in the former. An additional advantage is that dynamic measurements may be made. For example, the detector may be set to receive a prominent line of a phase stable only at room temperature; as the temperature is continuously increased, the ratemeter will continuously indicate and record the disappearance of that phase, in the form of a curve of line intensity vs. temperature.

Automated sample changers are available. Coupled with computer data acquisition and control, this kind of automation can result in continuous, unattended, day-and-night operation of a diffractometer. In the 1990's, diffractometers appeared whose modular optics could be changed very easily; the robust components allow rapid reconfiguration, sometimes within fifteen minutes. High resolution, parallel

---

[1] Epilayers are thin layers grown on single crystal substrates which generally have the same or closely matched lattice parameters. Superlattices, in the sense used here, are periodically alternating layers with, for example, different lattice parameters. The layer periodicity which is many times that of the crystal lattice gives rise to the term "superlattice." While a layer consisting of one-hundred periods of a superlattice might be considered very thick by a crystal grower, this number of periods in a crystal lattice would be considered quite small by a diffractionist and the term "superlattice" is a bit of a misnomer.

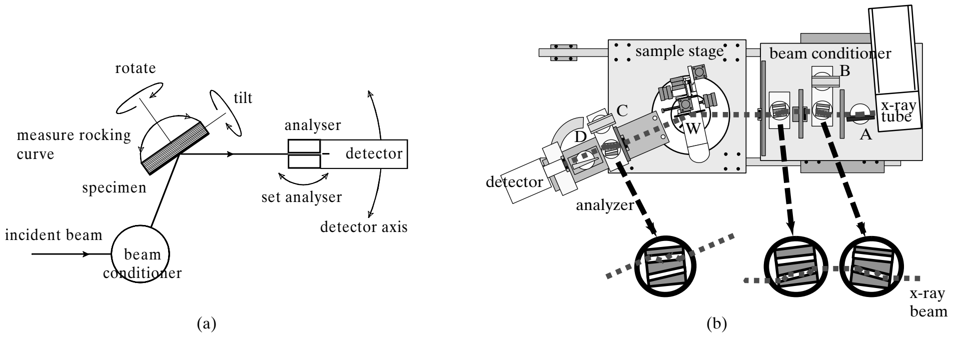

Figure 7 High resolution difractometers for single crystal samples, (a) schematic of a double axis diffractometer used for recording rocking curves and (b) diagram of a Bede Scientific triple axis diffractometer for recording rocking curves and for high resolution reciprocal space mapping.

beam or parafocusing beam conditioners can be interchanged, for example. Limited resources inevitably constrain the number of diffractometers available in one laboratory, and such modern instruments greatly improve the quality of data which it is practical to obtain.

In the succeeding sections, the various parts of the diffractometer will be described in greater detail. This summary of the general features of the instrument is enough to show its principal advantage over the powder camera: the quantitative measurement of line position and intensity is made in one operation with a diffractometer, whereas the same measurement with film technique requires at least two steps (recording the pattern on film and making a microphotometer record of the film) and leads to an over-all result which is generally of lower accuracy, and which includes a much smaller range of intensity values.[2]

This superiority of the diffractometer is reflected in the much higher cost of the instrument, a cost due not only to the precision machining necessary in its mechanical parts but also to the circuits needed to measure the intensity of diffracted beams and to the data acquisition and analysis software.

The diffractometer is a superb instrument for dealing with many problems. But it is not without its faults. A detector "sees" only the radiation to which it is exposed and is blind to all diffracted and scattered rays not lying in the plane of the diffractometer circle. A photographic film, with an area of several square inches, will intercept and record a great many rays, disclosing at a glance such conditions as coarse grains and preferred orientation; a diffractometer does not immediately

---

[2] Photographic emulsions have a much smaller dynamic range and require longer data collection times than do electronic detectors. Image storage plates, however, a newly developed re-usable x-ray "film", have a range comparable to that of electronic detectors and require very short exposure times; provided that an image plate reader is available, the ability to see entire diffraction cones can be preserved without the drawbacks of photographic emulsions.

see these things. As Guinier [G.30] puts it, "The photographic method is admirably suited to the *qualitative exploration of an unknown pattern*, since one can then find totally unexpected phenomena: The counter [i.e., the detector] is necessary for *quantitative measurements* on a pattern which is already known qualitatively."

3 X-RAY OPTICS

The chief reason for using a flat specimen is to take advantage of the focusing action described below and so increase the intensity of weak diffracted beams to a point where they can be accurately measured. The basis for this focusing is the geometrical theorem (Fig. 8): all angles inscribed in a circle and based on the same arc *SF* are equal to one another and equal to half the angle subtended at the center by the same arc. Suppose that x-rays proceeding in the directions *SA* and *SB* encounter a powder specimen located on the arc *AB*. Then the rays diffracted by the same (*hkl*) planes at points *A* and *B* will deviated through the same angle 2θ. But these deviation angles 2θ are each equal to $(180^\circ - \alpha)$, which means that the diffracted rays must proceed along *AF* and *BF*, and come to a focus at *F*.

Figure 9 shows how the geometry of Fig. 8 applies to the flat specimens used in θ–2θ, also termed Bragg–Brentano, diffractometers. For any position of the detector, the receiving slit *F* and the x-ray source *S* are always located on the diffractometer circle, which means that the face of the specimen, because of its mechanical coupling with the detector, is always tangent to a focusing circle centered on the normal to the specimen and passing through *F* and *S*. The focusing circle is not of constant size but increases in radius as the angle 2θ decreases, as

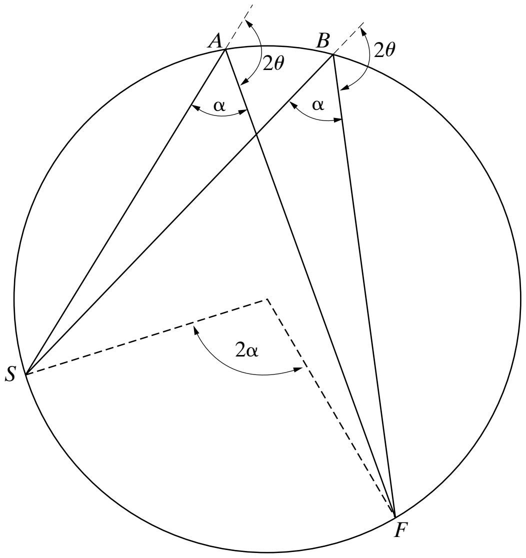

Figure 8 Focusing–geometry.

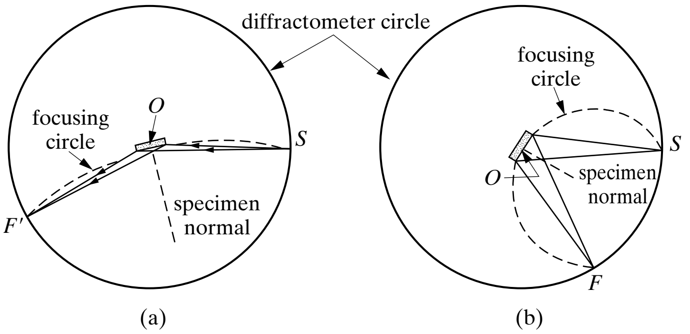

Figure 9 Focusing geometry for flat specimens in (a) forward reflection and (b) back reflection.

indicated in Fig. 9. Perfect focusing at *F* requires that the specimen be curved to fit the focusing circle. Use of a flat specimen causes some broadening of the diffracted beam at *F* and a small shift in line position toward smaller angles, particularly at 2θ angles less than about 60°; both effects can be lessened by decreasing the divergence of the incident beam, at the expense of decreased intensity. (Neither focusing nor intensity has to be sacrificed if the specimen surface always conforms to the focusing circle. A device to do this has been produced [4]. The powder specimen is mounted on a thin flexible strip, which is automatically bent to the proper curvature at each angle 2θ.)

The line source *S* extends considerably above and below the plane of the drawing of Fig. 9 and emits radiation in all directions, but the focusing described above requires that all rays in the incident beam be parallel to the plane of the drawing. This condition is realized as closely as possible experimentally by passing the incident beam through a *Soller slit* (Fig. 10), slit *A* in Fig. 1, which contains a set of closely spaced, thin metal plates parallel to the plane of the diffractometer circle. These plates remove a large proportion of rays inclined to the plane of the diffractometer circle and still allow the use of a line source of considerable length. Typical dimensions of a Soller slit are: length of plates 32 mm, thickness of plates 0.05 mm, clear distance between plates 0.43 mm. At either end of the slit assembly are rectangular slits *a* and *b*, the entrance slit *a* next to the source being narrower than the exit slit *b*. The combination of slits and plates splits the incident beam into a set of triangular wedges of radiation, whose apices are small sections of the line source as indicated in Fig. 10. There are, of course, some rays, not shown in the drawing, which diverge in planes perpendicular to the plane of the plates, and these rays cause the wedges of radiation to merge into one another a short distance away from the exit slit. However, the long, closely spaced plates do restrict this unwanted divergence to an angle of about 1.5°. Slits *a* and *b* define the divergence of the incident beam in the plane of the diffractometer circle. The slits commonly available have divergence angles ranging from very small values up to about 4°. In the forward-reflection region, a divergence angle of 1° is sufficient because of the low

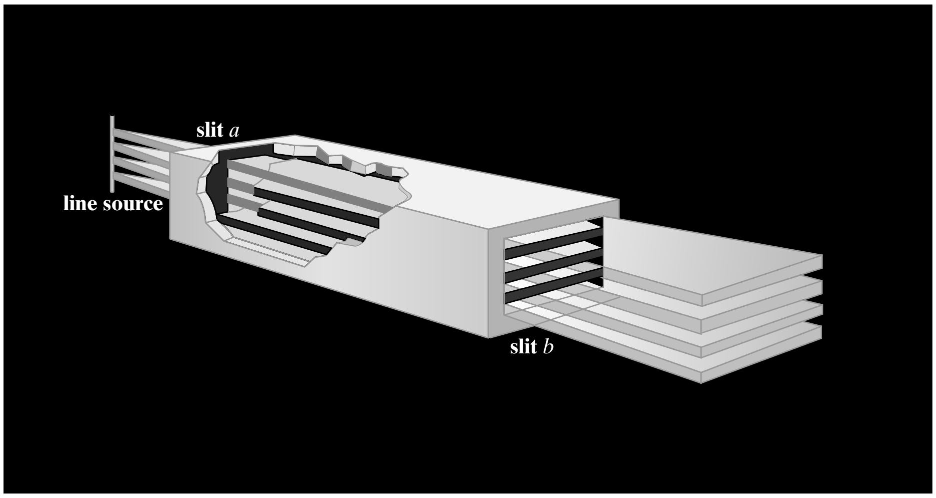

Figure 10 Soller slit (schematic). For simplicity, only three metal plates are shown; actual Soller slits contain about a dozen.

inclination of the specimen surface to the incident beam, but in back reflection an increase in divergence angle to 3 or 4° will increase the area irradiated and the diffracted intensity. But if line intensities are to be compared over the whole range of 2θ, the same divergence must be used throughout and the specimen must be wider than the beam at all angles. Some diffractometers, however, are equipped with automatically varying divergence slits which allow a constant area of the sample to be irradiated regardless of 2θ; this increases the intensity of higher 2θ peaks relative to those at lower 2θ and compensates for the rapidly falling diffracted peak intensities with increasing 2θ. Before results from this type of diffractometer can be compared to those of a conventional fixed-slit-width system, the intensities must be converted analytically to compensate for the larger volumes irradiated with variable slits.

The beam diffracted by the specimen passes through another Soller slit and the receiving slit F before entering the detector (Fig. 11). Since the receiving slit defines the width of the beam admitted to the detector, an increase in its width will increase the maximum intensity of any diffraction line being measured but at the expense of some loss of resolution. On the other hand, the relative *integrated intensity* of a diffraction line is independent of slit width, which is one reason for its greater fundamental importance.[3]

---

[3] A number of things besides slit width (e.g., x-ray tube current) will change the integrated intensity of a single diffraction line. The important thing to note, however, is that a change in any one of the operating variables changes the integrated intensities of all diffraction lines in the same ratio but can produce very unequal effects on maximum intensities. Thus, if I_1/I_2 is the ratio of the integrated intensities of two lines measured with a certain slit width and M_1/M_2 the ratio of their maximum intensities, then another measurement with a different slit width will result in the same ratio I_1/I_2 for the integrated intensities, but the ratio of the maximum intensities will now, in general, differ from M_1/M_2.

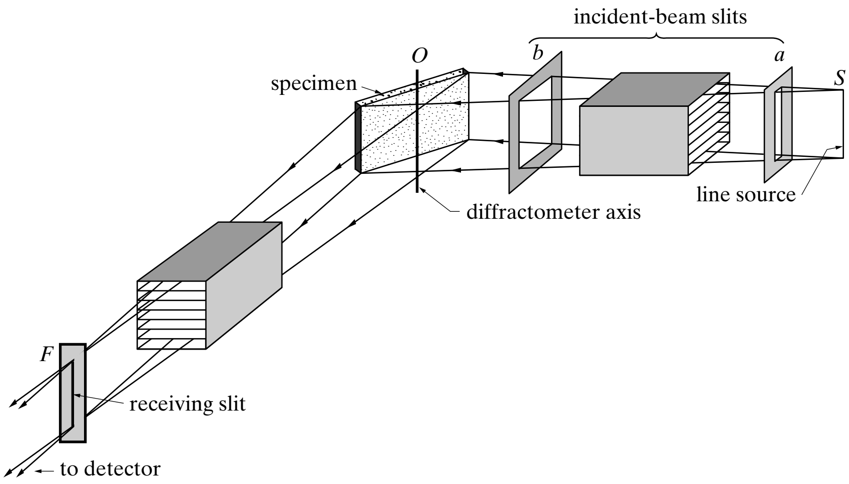

Figure 11 Arrangement of slits in diffractometer.

Because of the focusing of the diffracted rays and the relatively large radius of the diffractometer circle, about 15 cm in commercial instruments, a diffractometer can resolve very closely spaced diffraction lines. Indicative of this is the fact that resolution of the Cu $K\alpha$ doublet can be obtained at 2θ angles as low as about 40°. Such resolution can only be achieved with a correctly adjusted instrument, and it is necessary to so align the component parts that the following conditions are satisfied for all diffraction angles:

1. line source, specimen surface, and receiving-slit axis are all parallel,
2. the specimen surface coincides with the diffractometer axis, and
3. the line source and receiving slit both lie on the diffractometer circle.

At this point it is worth briefly mentioning capillary optics which condense the x-ray beam using perfect external reflection from the smooth, tapered surface of the inside of glass capillary tubes. Arrays of tubes have been fabricated so that significant sample areas can be covered, and the reader is referred to recent volumes of [G] where details of this evolving technology can be found.

The θ–2θ diffractometer is not the only type of powder diffractometer that may be encountered. One Bragg-Brentano variant is the θ–θ diffractometer where the sample remains stationary and the detector and x-ray source rotate. The focussing optics used in the θ–2θ diffractometer are also applied in the Seeman-Bohlin diffractometer whose geometry is similar to that of the Seemann–Bohlin camera the chief difference is that the detector slit traces the path NM in Fig. 7. The angle of incidence of the x-ray beam in the Seeman-Bohlin diffractometer can be very low, and this makes the instrument valuable for thin film studies.

4 DETECTORS (GENERAL)

Without exception all electronic detectors were developed by nuclear physicists for studies of radioactivity. They can detect not only x- and γ-radiation, but also charged particles such as electrons and α-particles, and the design of the detectors and associated circuits depends to some extent on what is to be detected. Here discussion is limited to x-rays of the wavelengths commonly encountered in diffraction.

Four types of detectors are currently in use: proportional, Geiger, scintillation, and semiconductor. All depend on the power of x-rays to ionize atoms, whether they are atoms of a gas (proportional and Geiger counters) or atoms of a solid (scintillation and semiconductor detectors). A general treatment of the first three types has been given by Parrish [5] and of all four by Knoll [6]. Often detectors are called "counters" even through this usage is not strictly correct. It persists, however, in usages such as "Geiger counter" which will undoubtedly continue because they are embedded in popular culture. Patterns of usage are similar for "proportional counters" (Sec. 5) and this nomenclature will be continued.

Three aspects of detector behavior are of concern here: losses, efficiency, and energy resolution. These are defined below and made more specific in later sections on particular detectors.

Counting Losses

The absorption of a quantum (photon) of x-rays in the active volume of a detector causes a voltage pulse in the detector output. Pulses from the detector then enter some very complex electronic circuitry, consisting of one or more pulse amplifiers, pulse shapers, etc. and, at the end, a scaler or ratemeter and, possibly, a pulse-height analyzer (Sec. 9). For the purposes of this section, all the circuitry beyond the detector will be termed the "electronics," and the behavior of the whole system namely, the detector-electronics combination is of interest.

If the x-ray beam to be measured is strong, the rate of pulse production in the detector will be high, and the counting rate given by the ratemeter will be high. (Roughly speaking, several thousand counts per second is a "high" rate in powder diffractometry, and less than a hundred cps a "low" rate.) As the counting rate increases, the time interval between pulses decreases and may become so small that adjacent pulses merge with one another and are no longer resolved or counted, as separate pulses. At this point counting loss has begun. The quantity that determines this point is the *resolving time* t_s of the detector electronics system, defined as the minimum time between two resolvable pulses.

The arrival of x-ray quanta at the detector is random in time. Therefore pulse production in the detector is random in time, and a curve showing the change in voltage of the detector output would look like Fig. 12. If the arrival and absorp-

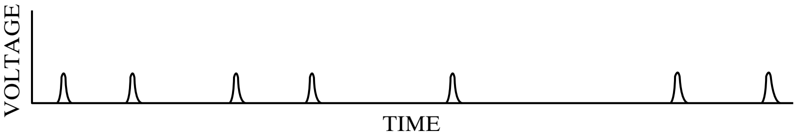

Figure 12 Randomly spaced voltage pulses produced by a detector.

tion of entering quanta were absolutely periodic in time, the maximum counting rate without losses would be given simply by $1/t_s$. But even if their average rate of arrival is no greater than $1/t_s$, some successive quanta may be spaced less than $1/t_s$ apart because of their randomness in time. It follows that counting losses will occur at rates less than t_s and that losses will increase as the rate increases, as shown in Fig. 13. Here quanta absorbed per second are directly proportional to the x-ray intensity, so that this curve has an important bearing on diffractometer measurements, because it shows the point at which the observed counting rate is no longer proportional to the x-ray intensity. The straight line shows the ideal response that can be obtained with a proportional counter at the rates shown. This linear, no-loss behavior is fortunately typical of most detectors used today in diffractometry; otherwise one would have the tedious task of correcting some observed counting rates for losses.

If the resolving time t_s of the detector-electronics is known, the point at which losses begin can be calculated by an easily remembered rule; a loss of one percent occurs at a rate of about one percent of $1/t_s$. Thus, if t_s is one microsecond, the counting rate should be linear to within one percent up to a rate of about 10,000 cps.

Ordinarily, the resolving time is unknown. But if nonlinear counting behavior is suspected, the counting rate at which losses begin can be determined experimentally by the following procedure. Position the detector to receive a strong diffracted beam, and insert in this beam a sufficient number of metal foils of uniform thickness to reduce the counting rate almost to the cosmic background. (Cosmic rays, because of their high penerating power, pass right through the walls of the detector

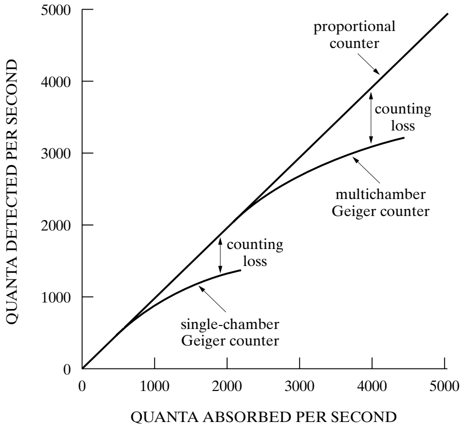

Figure 13 The effect of counting rate on counting losses for three kinds of detectors (schematic).

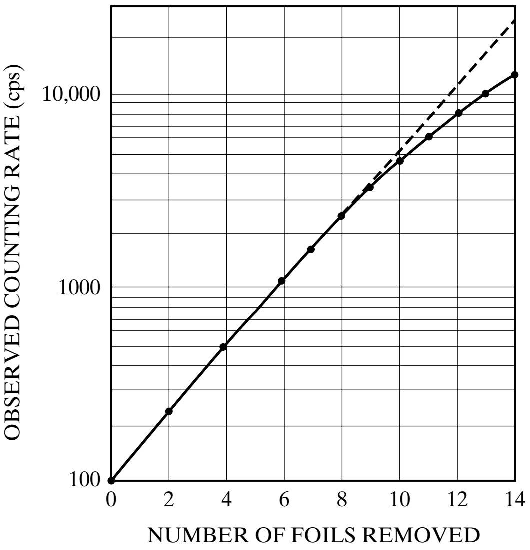

Figure 14 Calibration curve of a multichamber Geiger counter. Cu $K\alpha$ radiation. Nickel foils, each 0.01 mm thick, used as absorbers.

and continually produce a few counts per second.) Measure the counting rate, remove one foil, measure the counting rate, and continue in this manner until all the foils have been removed. Because each foil produces the same fractional absorption of the energy incident on it, a plot of observed counting rate (on a logarithmic scale) vs. number of foils removed from the beam (on a linear scale) will be linear up to the point where losses begin and will in fact resemble Fig. 13. A curve of this kind is shown in Fig. 14.

Counting Efficiency

The overall efficiency E of the detector-electronics system in detecing incident x-ray quanta as resolved pulses is the product of the absorption efficiency E_{abs} and the detection efficency E_{del}.

All detectors have a thin "window," usually of mica or beryllium, through which the x-rays must pass before reaching the active volume of the detector. The fraction of the incident radiation absorbed by the window $f_{\text{abs, w}}$ should be as small as possible, and the fraction absorbed by the detector itself $f_{\text{abs, d}}$ as large as possible. The absorption efficiency E_{abs} expressed as a fraction, is given by $(1 - f_{\text{abs, w}})(f_{\text{abs, d}})$. The detection efficiency E_{det} is simply $(1 - f_{\text{losses}})$, where f_{losses} represents the fractional counting losses described above. The overall efficiency is then

$$E = E_{\text{abs}}E_{\text{det}} = [(1 - f_{\text{abs, w}})(\text{f}_{\text{abs, d}})][1 - \text{f}_{\text{losses}}]. \tag{1}$$

As previously mentioned E_{det} is essentially 100 percent for most detectors used in diffractometry. Therefore E is determined by E_{abs} which can be calculated from the dimensions and absorption coefficients of the window and detector, and Fig. 15

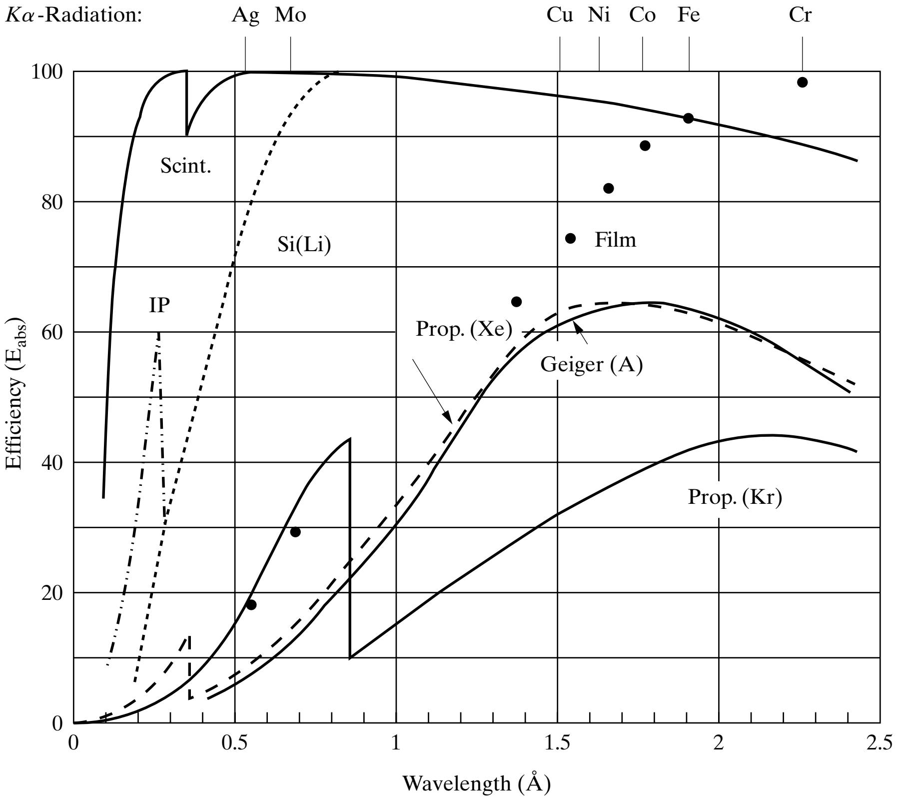

Figure 15 Calculated values of absorption efficiency E_{abs} (in percent) of various kinds of detectors, photographic x-ray film (black dots). After Parrish [5] and pp. 538-555 of Vol. C, of [G.1].

shows the result. Note particularly the dependence of E_{abs} on wavelength, due to the dependence of absorption coefficients on wavelength. Efficiency as a function of wavelength is also shown for film and for image storage plates. The efficiency of any detector is low for very short wavelengths, because most of these hard x-rays pass right through window and detector and are absorbed by neither; at long wavelengths E_{abs} decreases because of increasing absorption of soft x-rays by the window.

Energy Resolution

In most detectors the sizes of the voltage pulses produced by the detectors are proportional to the energy of the x-ray quantum absorbed. Thus, if absorption of a Cu $K\alpha$ quantum produces a pulse of V volts, then absorption of a Mo $K\alpha$ quantum will produce a pulse of $(20/9)V = 2.2\ V$.

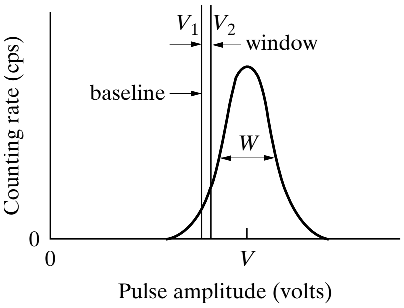

Figure 16 Distribution curve of pulse size. (The "window" and "baseline" are explained in Sec. 10.)

However, the size of a pulse is not sharply defined, even when the incident radiation is strictly monochromatic or, in energy terms, "monoenergetic." Instead of all pulses having exactly the same size V as suggested, for example, by Fig. 12, they have sizes distributed around V roughly as indicated in Fig. 16. Here the ordinate, "counting rate," is equivalent to the number of pulses having a particular size, so that this curve is a pulse-size distribution curve. If the width of the curve at half its maximum height is W and if V is the mean pulse size, then the resolution R of the detector is

$$\mathrm{R} = \frac{W}{V}. \tag{2}$$

The smaller R, the better the resolution.

Next consider the operation and performance of various detectors.

5 PROPORTIONAL COUNTERS

Consider the device shown in Fig. 17, consisting of a cylindrical metal shell (the cathode), about 10 cm long and 2 cm in diameter, filled with a gas and containing a fine metal wire (the anode) running along its axis. Note that the wire is electrically isolated from the shell, and suppose there is a constant potential difference of about 200 volts between anode and cathode. One end of the cylinder is covered with a window of high transparency to x-rays. Of the x-rays which enter the cylinder, a small fraction passes right through, but the larger part is absorbed by the gas; and this absorption is accompanied by the ejection of photoelectrons and Compton recoil electrons from the atoms of the gas. The net result is ionization of the gas, producing electrons, which move under the influence of the electric field toward the wire anode, and positive gas ions, which move toward the cathode shell. At a potential difference of about 200 volts, all these electrons and ions will be collected on the electrodes, and, if the x-ray intensity is constant, there will be a small constant current of the order of 10^{-12} amp or less through the resistance R_1. This current is a measure of the x-ray intensity. When operated in this manner, this device is called an *ionization chamber*. It was used in the original Bragg spectrometer but is now used mainly to measure the intensity of incident beams at synchrotron radiation

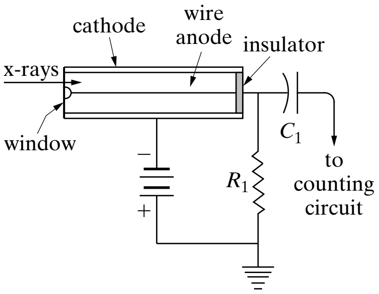

Figure 17 Gas counter (proportional or Geiger) and basic circuit connections.

sources. In this case the low sensitivity of ionization chambers is an advantage. Ionization chambers are also still used in some radiation survey meters.

The same instrument, however, can be made to act as a *proportional counter* if the voltage is raised to the neighborhood of 1000 volts. A new phenomenon now occurs, namely, multiple ionization or "gas amplification." The electric-field intensity is now so high that the electrons produced by the primary ionization are rapidly accelerated toward the wire anode and at an ever-increasing rate of acceleration, since the field intensity increases as the wire is approached. The electrons thus acquire enough energy to knock electrons out of other gas atoms, and these in turn cause further ionization and so on, until the number of atoms ionized by the absorption of a single x-ray quantum is some 10^3 to 10^5 times as large as the number ionized in an ionization chamber. As a result of this amplification a veritable avalanche of electrons hits the wire and causes an easily detectable pulse of current in the external circuit. This pulse leaks away through the large resistance R_1 but not before the charge momentarily added to the capacitor C_1 has been detected by the ratemeter or scaling circuit connected to C_1. At the same time the positive gas ions move to the cathode but at a much lower rate because of their larger mass. This whole process, which is extremely fast, is triggered by the absorption of one x-ray quantum.

A gas amplification factor A can be defined as follows: if n is the number of atoms ionized by one x-ray quantum, then An is the total number ionized by the cumulative process described above. (For example, if the gas in the counter is argon, energy of about 26 eV is required to produce an ion pair, i.e., a positive ion and an electron. If the incident radiation is Cu $K\alpha$ of energy 8040 eV, then the number n of ion pairs formed is 8040/26 or 310.) Figure 18 shows schematically how the gas amplification factor varies with the applied voltage. At the voltages used in ionization chambers, $A = 1$; i.e., there is no gas amplification, since the electrons produced by the primary ionization do not acquire enough energy to ionize other atoms. But when the voltage is raised into the proportional counter region, A becomes of the order of 10^3 to 10^5, and a pulse of the order of a few millivolts is produced. Moreover, the size of this pulse is proportional to the energy of the x-ray quantum absorbed, which accounts for the name of this counter. This proportionality is important, because it allows x-ray quanta of different energies (wavelengths) to be distinguished. (Sec. 9) (Historically, this counter was the first kind to exhibit such

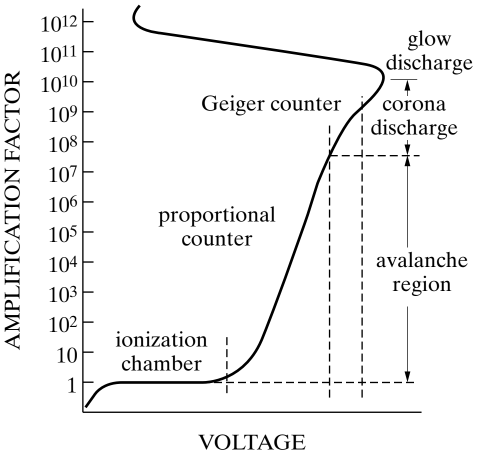

Figure 18 Effect of voltage on the gas amplification factor. Friedman [7].

proportionality. There are now others.) Pulses from the counter go to a preamplifier, mounted immediately adjacent to the counter; here they are amplified enough to be transmitted, without too much attenuation, along several feet of cable to the main amplifier and the rest of the electronics.

The correct voltage at which to operate the counter is found as follows. Position the counter to receive an x-ray beam of constant intensity. Measure the counting rate with a ratemeter or scaler while slowly increasing the voltage applied to the counter from a low value. Figure 19 shows how the counting rate will vary with voltage. Below the starting voltage the pulse size is less than the input sensitivity of the counting circuit and no counts are observed. The pulse size and observed counting rate then increase rapidly with voltage up to the threshold of the plateau, where the counting rate is almost independent of voltage. The voltage is then fixed at about 100 volts above threshold. (Note that x-rays of longer wavelength require a higher counter voltage. This means that the counter voltage should be reset when the x-ray tube in the diffractometer is changed for one with a different target.)

The proportional counter is essentially a very fast detector and has a linear counting curve up to about 10,000 cps. This ability to separate closely spaced puls-

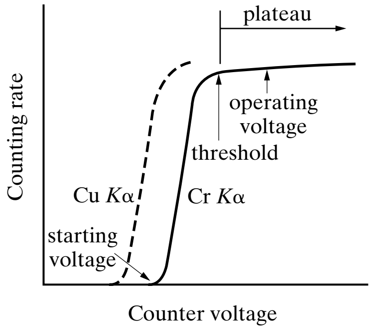

Figure 19 Effect of voltage applied to proportional counter on observed counting rate at constant x-ray intensity (schematic).

es is due to the fact that the avalanche triggered by the absorption of an x-ray quantum is confined to an extremely narrow region of the counter, 0.1 mm or less, and does not spread along the counter tube (Fig. 20). The rest of the counter volume is still sensitive to incoming x-rays.

The electric field near the end of the anode wire is not uniform. Proportional counters made with a side window, rather than the end window shown in Fig. 20 allow x-ray absorption to take place in a region of uniform field.

The gas in the counter is usually xenon, argon, or krypton at a pressure somewhat less than atmospheric. Figure 15 shows that a krypton counter has about the same sensitivity for all the characteristic radiations normally used in diffraction. But an argon or xenon counter is much less sensitive to short wavelengths, an advantage in most cases. Thus, if a diffraction pattern is made with filtered radiation from a copper target, use of an argon counter will produce semi-monochromatic conditions, in that the counter will be highly sensitive to Cu $K\alpha$ radiation and relatively insensitive to the short wavelength radiation that forms the most intense part of the continuous spectrum. The diffraction background will therefore be lower than if a krypton counter had been used. (The student may wish to record the spectrum of the copper-target x-ray tube in a diffractometer. This can be done by operating it as a spectrometer, with a single crystal, such as quartz or rock salt, in the specimen holder and recording the intensity diffracted from the crystal as a function of angle. With an argon-filled counter, the resulting spectrum will not look at all like what is expected. Instead, only the Cu $K\alpha$ and Cu $K\beta$ lines will be visible on a linear scale plot of intensity as a function of diffraction angle because the counter is insensitive to short wavelengths. The continuous spectrum can be observed only by effecting an opposite distortion: put several thicknesses of aluminum foil in the diffracted beam so as to absorb the Cu K lines more than the short wavelengths; at the same time, expand the ratemeter scale to allow for the decreased intensity of all wavelengths. With sufficiently heavy filtration by aluminum, the spectrum can be so distorted that the maximum in the continuous spectrum will be more intense, as recorded, than the characteristic lines. It is an instructive experiment.)

In x-ray spectroscopy but not in diffraction, there is a need to measure soft x-rays of wavelength about 5-20 Å. Because ordinary windows would almost totally absorb such radiation, thin sheet plastic is used as a window, so thin that it leaks. To allow for this, a stream of counter gas is continuously passed through the counter, which is then called a *gas-flow proportional counter*.

Another special type, the *position-sensitive proportional counter* has become important for certain applications. The diffracted x-ray beam enters the counter through a side window, striking the anode wire, which lies in the plane of the diffractometer circle, approximately at right angles. Because the electron avalanche is sharply localized (Fig. 20), the point where the electrons hit the wire can be determined by one of two methods, (Sec 10). Thus the angular position 2θ of a diffracted beam is found, not in the usual way by moving a detector with a narrow entrance slit to the position of the beam (Fig. 1), but by finding where the beam strikes the wire of a *fixed* wide-window counter. The counting circuit must include a multichannel analyzer (Sec. 9) in order to determine the profile of the diffraction line.

6 GEIGER COUNTERS

If the voltage on a proportional counter is increased to the neighborhood of 1500 volts, it will act as a Geiger counter. Historically, this was the first electronic counter; it is also called a Geiger-Müller or G-M counter.

The applied voltage is now so high that not only are some atoms ionized but others are raised to excited states and caused to emit ultraviolet radiation. These ultraviolet photons travel throughout the counter at high speed (light travels 10 cm in a third of a nanosecond), knocking electrons out of other gas atoms and out of the cathode shell. All the electrons so produced trigger other avalanches, and the net result is that one tremendous avalanche of electrons hits the whole length of the anode wire whenever an x-ray quantum is absorbed anywhere in the tube (Fig. 20). As a result the gas amplification factor A is now much larger, about 10^8 to 10^9, than in a proportional counter, and so is the size of the pulse produced, now some 1 to 10 volts. This means that no preamplifier is needed at the counter. On the debit side, all pulses have the same size, whatever the energy of the x-ray quanta.

The Geiger counter is also slow. Any one avalanche of electrons hits the anode wire in less than a microsecond, but the slowly moving positive ions require about 200 microseconds to reach the cathode. Thus the electron avalanche leaves behind it a cylindrical sheath of positive ions around the anode wire. The presence of this ion sheath reduces the electric field between it and the wire below the threshold value necessary to produce a Geiger pulse. Until this ion sheath has moved far enough away from the wire, the counter is insensitive to entering x-ray quanta. If these quanta are arriving at a very rapid rate, it follows that not every one will cause a separate pulse and the counter will become "choked." The resolving time is only about 10^{-4} sec, so that counting losses begin at a few hundred cps. Even the multichamber counter is not much better (Fig. 13); this counter has a number of chambers side by side, each with its own anode wire, and one chamber can therefore register a count while another one is in its insensitive period.

Because it cannot count at high rates without losses, the Geiger counter is now obsolete in diffractometry. It is still used in some radiation survey meters.

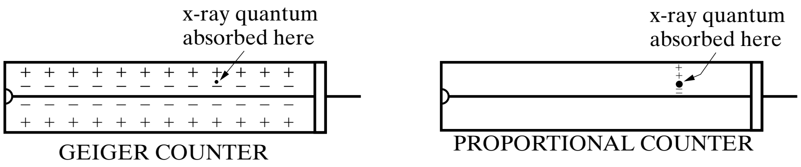

Figure 20 Differences in the extent of ionization between proportional and Geiger counters. Each plus (or minus) symbol represents a large number of positive ions (or electrons).

7 SCINTILLATION DETECTORS

This type of detector exploits the ability of x-rays to cause certain substances to fluoresce visible light, as in fluorescent screens.. The amount of light emitted is proportional to the x-ray intensity and can be measured by means of a phototube. Since the amount of light emitted is small, a special kind of phototube called a *photomultiplier* has to be used in order to obtain a measurable current output.

The substance generally used to detect x-rays is a sodium iodide crystal activated with a small amount of thallium. It emits violet light under x-ray bombardment. (The details of this emission are roughly as follows. Absorbed x-rays ionize some atoms, i.e., raise some electrons from the valence to the conduction band of NaI. These electrons then transfer some of their energy to the Tl^+ ion. When the excited ion returns to its ground state, light is emitted.) The light-emitting crystal is cemented to the face of a photomultiplier tube, as indicated in Fig. 21, and shielded from external light by means of aluminum foil. A flash of light (scintillation) is produced in the crystal for every x-ray quantum absorbed, and this light passes into the photomultiplier tube and ejects a number of electrons from the photocathode, which is a photosensitive material generally made of a cesium-antimony intermetallic compound. (For simplicity, only one of these electrons is shown in Fig. 21.) The emitted electrons are then drawn to the first of several metal *dynodes*, each maintained at a potential about 100 volts more positive than the preceding one, the last one being connected to the measuring circuit. On reaching the first dynode, each electron from the photocathode knocks two electrons, say, out of the metal surface, as indicated in the drawing. These are drawn to the second dynode where each knocks out two more electrons and so on. Actually, the gain at each dynode may be 4 or 5 and there are usually at least 10 dynodes. If the gain per dynode is 5 and there are 10 dynodes, then the multiplication factor is $5^{10} = 10^7$. Thus the absorption of one x-ray quantum in the crystal results in the collection of a very large number of elec-

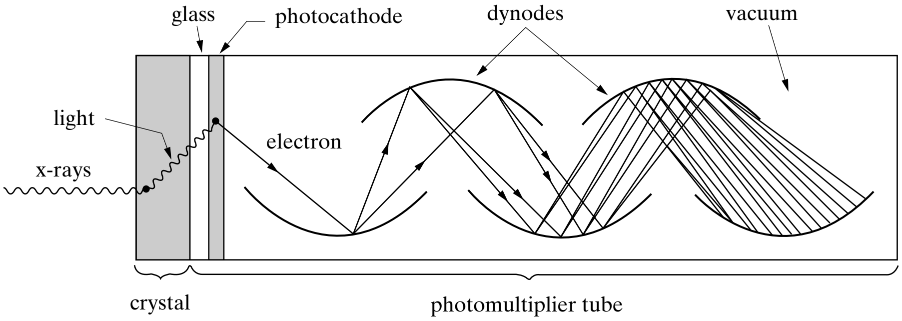

Figure 21 Scintillation detector (schematic). Electrical connections not shown.

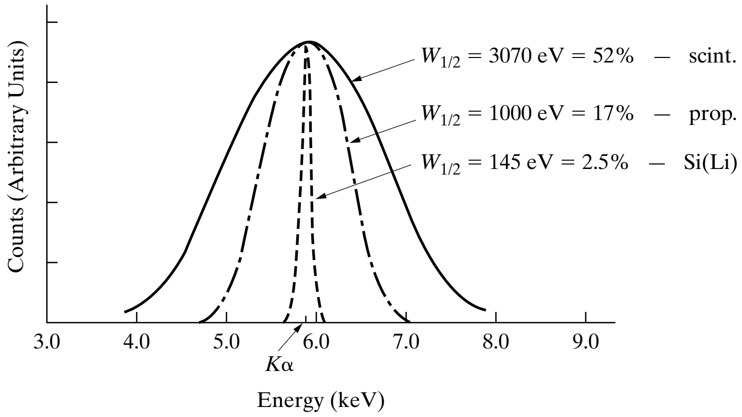

Figure 22 Pulse-height distribution curves for three kinds of detector. Incident radiation is Mn $K\alpha$ ($\lambda = 2.10$ Å, $h\nu = 5.90$ keV) from a radiative ^{55}Fe source. Data from Frankel and Adams [G.8] and [p. 540, Vol. C of G.1].

trons at the final dynode, producing a pulse about as large as a Geiger pulse, i.e., of the order of volts. Furthermore, the whole process requires less than a microsecond, so that a scintillation detector can operate at rates as high as 10^5 counts per second without losses. The correct detector voltage is found by the method used for the proportional counter, by plotting counting rate vs. voltage (Fig. 19).

As in the proportional counter, the pulses produced in a scintillation detector have sizes proportional to the energy of the x-ray quanta absorbed. But the pulse size corresponding to a certain quantum energy is much less sharply defined, as shown in Fig. 22 for typical proportional counters and scintillation (NaI·Tl) detectors. As a result, it is more difficult to discriminate, with a scintillation detector, between x-ray quanta of different wavelengths (energies) on the basis of pulse size.

The efficiency of a scintillation detector approaches 100 percent over the usual range of wavelengths (Fig. 15), because virtually all incident quanta are absorbed, even in a relatively thin crystal.

8 SEMICONDUCTOR DETECTORS

Developed in the 1960s, semiconductor detectors produce pulses proportional to the absorbed x-ray energy with better energy resolution than any other detector; this characteristic has made them of great importance in spectroscopy. For a variety of reasons, including expense and convenience of use, semiconductor detectors have not been used as widely in diffraction, as proportional or scintillation detectors.

Both silicon and germanium are used, germanium as a detector for gamma rays, and "harder" x-rays because it is heavier and therefore a better absorber, and silicon for x-rays. Originally both contained a small amount of lithium and were designated Si(Li) and Ge(Li), inevitably referred to as "silly" and "jelly." Their properties have been reviewed elsewhere [G.1, 9-12]. The Ge(Li) detectors have now been superceded by high purity germanium detectors (HPGe) which do not require Li drifting nor storage at low temperatures (even at ambient temperatures the mobility of lithium is high enough in germanium to degrade the lithium gradient).

Pure silicon is an intrinsic semiconductor. It has very high electrical resistivity, especially at low temperatures, because few electrons are thermally excited across the energy gap into the conduction band. However, incident x-rays can cause excitation and thereby create a free electron in the conduction band and a free hole in the valence band. As shown later, the absorption of one x-ray quantum creates about a thousand electron-hole pairs. If a high voltage is maintained across opposite faces of the silicon crystal, the electrons and holes will be swept to these faces, creating a small pulse in the external circuit.

It is essential that the silicon be intrinsic (*i*). It must neither be *n*-type, containing free electrons from donor impurities, nor *p*-type, containing free holes from acceptor impurities; in either type, the free charge carriers, at their usual concentrations, would overwhelm the few carriers produced by x-rays. Production of a reasonably large intrinsic crystal, which is not easy, requires two operations.

1. The starting material is a cylindrical crystal, some 3-5 mm thick and 5-15 mm in diameter. It is *p*-type, having been lightly doped with boron. Lithium is applied to one face and diffused into the crystal at an elevated temperature, producing a gradient of lithium concentration from high to low through the thickness. The lithium exists as Li^+ ions, and the free electrons it provides convert the crystal into *n*-type on one side, where the lithium concentration is high, leaving the other side *p*-type.
2. A voltage is then applied, also at an elevated temperature, to opposite faces, positive on the *n* side and negative on the *p* side (called "reverse bias"). This causes the Li^+ ions to "drift" toward the *p* side, resulting in a wide central region of constant lithium concentration; this region is now intrinsic because it has equal lithium and boron concentrations.

The result is the lithium-drifted silicon detector sketched in Fig. 23. The crystal is virtually all intrinsic, with the *p* and *n* portions confined to thin surface layers, which are exaggerated in the drawing. The very small pulses from the detector are amplified to the millivolt level by a field-effect transistor, abbreviated FET. (There is no charge amplification, such as occurs in a gas counter. The pulse from the detector contains only the charge liberated by the absorbed x-rays.)

Putting aside all of the above details of semiconductor physics, a Si(Li) detector simply is a solid-state ionization chamber, with one difference. X-rays incident on a gas ionization chamber produce a *constant* current (Sec. 5). In a Si(Li) detector the current flows in discrete *pulses*, because the voltage is high enough to sweep the detector free of charge carriers (the electrons and holes are highly mobile) before the next incident photon creates new carriers.

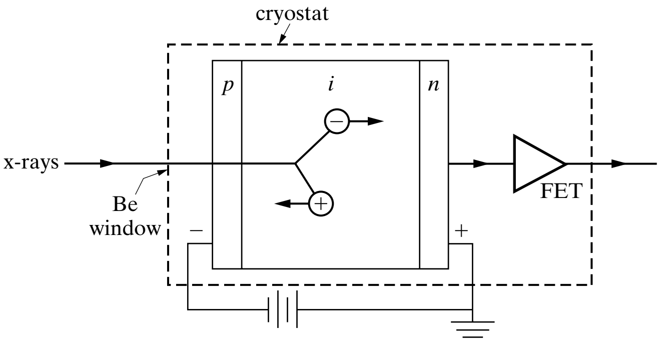

Figure 23 Si(Li) detector and FET preamplifier, very schematic. Both are in a cooled evacuated space, and x-rays enter through a beryllium window. The detector is operated at about 1000 volts. ⊖ = electron, ⊕ = hole.

A major disadvantage of the Si(Li) detector is that it must be operated at the temperature of liquid nitrogen (77 K = -196ºC) in order to minimize a constant current through the detector, even in the absence of x-rays, due to thermal excitation of electrons in the intrinsic region. Electronic "noise" in the FET increases with temperature and degrades the resolution. Thus both the detector and the FET have to be cooled, necessitating a bulky cryostat to hold several liters of liquid nitrogen or a Peltier solid state cooling circuit.

The efficiency of a Si(Li) detector resembles that of the other solid-state detector (scintillation), very high for intermediate wavelengths (Fig. 15). Very long wavelengths are partially absorbed by the detector window before they can reach the sensitive intrinsic layer. Very short wavelengths are partially transmitted by the entire detector.

The counting rate varies linearly with x-ray intensity up to rates of about 5,000-10,000 cps. Counting losses in the electronics system occur in the electronics rather than the detector. The electronics are more complex than usual and include, besides the usual pulse amplifiers and shapers, a multichannel pulse-height analyzer (Sec. 10).

The excellent energy resolution of a Si(Li) detector is shown in Fig. 22. The width W of the pulse distribution is so small that the Si(Li) detector can resolve the $K\alpha$ and $K\beta$ lines of manganese, which the other two detectors cannot do. Put another way, the resolution $R = W/V$ of the Si(Li) detector is 2.7 percent or some six times better than that of the proportional counter. For any kind of detector both W and W/V vary with V, i.e., with the energy $h\nu$ of the incident x-rays. Therefore any description of detector performance must specify the x-ray energy at which it is measured; the 5.90 keV energy of the Mn $K\alpha$ line is the usual standard reference. The width W, incidentally, is often written as FWHM (full width at half maximum) in the literature of this subject.

To create an electron-hole pair in silicon at 77 K requires an average energy of 3.8 eV. The absorption of a Mn $K\alpha$ quantum should therefore create 5900/3.8 =

1550 pairs. However, the actual number created by successive quanta might be 1540, 1560, 1555, … leading to a corresponding variation in the size of the output pulse. This statistical variation in the number of charge carriers created by x-ray absorption is the basic reason for the finite width W of the pulse distribution, and the same is true of proportional counters and scintillation detectors. In the Si(Li)-FET detector, there is an even larger contribution to W, namely, electronic noise in the FET preamplifier. At the energy of Mn $K\alpha$, more than half of the observed value of W is due to noise in the FET. Beyond a certain counting rate, the resolution of the system worsens (W becomes larger) as the count rate increases.

In any detector except the Geiger counter the average number n of ion pairs or electron-hole pairs produced is proportional to the energy E of the absorbed quantum. The actual number has a Gaussian (normal) distribution about the mean, and the width at half maximum of this distribution is proportional to the standard deviation σ, which is equal to $\sqrt{n}$. Therefore the resolution R is

$$R = \frac{W}{V} = \frac{k_1\sqrt{n}}{k_2 n} = \frac{k_3}{\sqrt{n}}, \tag{3}$$

where k_i are constants. The superior resolution of a Si(Li) detector is simply due to the large value of n, which is 1550 for Mn $K\alpha$. By comparison, n is only 5600/26 = 230 for an argon proportional counter and the same radiation, because 26 eV are needed to create an ion pair in argon. Actually, the inherent resolution of a Si(Li) detector (the resolution in the absence of preamplifier noise) is even better, for complex reasons, than the above statistical argument suggests.

Because n is proportional to E, Eq. (3) leads to the following energy or wavelength dependence of the resolution:

$$R = \frac{k_3}{\sqrt{n}} = \frac{k_4}{\sqrt{E}} = \frac{k_4}{\sqrt{h\nu}} = k_5\sqrt{\lambda}. \tag{4}$$

Although Eqs. (3) and (4) are useful for rough qualitative arguments, they do not include the substantial effect of electronic noise in Si(Li)-FET detectors. A better estimate of resolution in such detectors, is given by

$$R = \frac{W}{V} = \frac{[(100)^2 + 2.62E]^{1/2}}{E}. \tag{5}$$

where E is the x-ray energy in eV and the term 100 eV in the numerator is the present level of the electronic noise. This relation is important in spectroscopy.

9 PULSE-HEIGHT ANALYSIS

All the electronic detectors in use today (proportional, scintillation, and semiconductor) are "proportional" in the sense that they produce pulses having a size (amplitude) that is proportional to the energy of the incident x-rays. Electrical circuits that can distinguish between pulses of different size can therefore distinguish between x-rays of different energies (wavelengths), and this ability is of great value in many experimental techniques. These circuits, in order of increasing complexity, are:

1. Pulse-height discriminator.
2. Single-channel pulse-height analyzer.
3. Multichannel pulse-height analyzer.

Circuits (1) and (2) are invariably used with modern diffractometers to increase the peak/background ratio of diffraction line, and they are by no means necessary; quite adequate diffraction patterns can be obtained from a wide variety of specimens with no other "discriminator" than a $K\beta$ filter. Circuit (3) is required only in x-ray spectroscopy, in a very special kind of diffractometry (Sec. 10), and with a position-sensitive detector. Any one of these circuits is more effective, the better the resolution of the detector with which it operates.

Pulse-Height Discriminator

Suppose that x-rays of three wavelengths $a > b > c$ are incident on a detector. Then the detector will produce pulses A, B, C of different size, C being the largest (Fig. 24). If a circuit is inserted, just ahead of the scaler or ratemeter, that will allow only pulses larger than a certain selected size (V_1 volts) to pass and discriminate against smaller ones, then the A pulses will not be counted and the system will be blind to wavelength a. Such a circuit is called a pulse-height discriminator. It may be of some value in decreasing diffractometer background due to the specimen's fluorescent radiation, when that radiation has a wavelength much longer than that

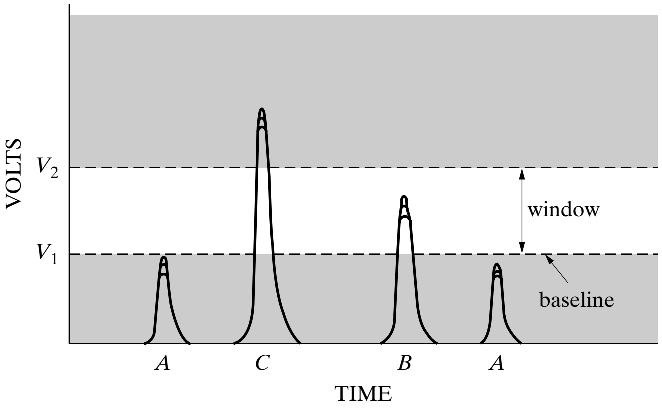

Figure 24 Pulse-height discrimination and analysis. The statistical spread in pulse size, measured by the width W of Fig. 16, is suggested above by the variable heights of each pulse.

which forms the diffraction lines, but it cannot weaken the short-wavelength components of the continuous spectrum.

Single-Channel Pulse-Height Analyzer

This instrument discriminates against any pulses smaller than V_1 volts (Fig. 24). In addition, it contains an *anti-coincidence circuit* that rejects any pulse larger than V_2, because such a pulse will simultaneously trigger both the V_1 and V_2 levels. The net result is that only pulses having sizes between V_1 and V_2 volts are passed. Out of the mixture of A, B, and C pulses entering the analyzer, only B pulses are passed to the counting circuit. The level V_1 is called the *baseline*, and the range from V_1 to V_2 is the *window* or *channel*. (Here, then, is another sense of the word "window." It is not a physical window, as at the entrance to a detector, but a voltage window.)

Both V_1 and V_2 are adjustable. If the window $(V_2 - V_1)$ is made quite small, say 0.5 volt, and the baseline V_1 continuously varied from low values to high values, with $(V_2 - V_1)$ constant, then a narrow window can be traversed across the voltage range of pulse heights; if the counting rate is measured at each setting of V_1, the result is an analysis of the distribution of pulse heights. It is in this way that curves like that of Fig. 16 are measured.

An analyzer can markedly reduce the background of a diffraction pattern, chiefly by excluding short-wavelength white radiation. For example, examining the 111 line from silicon powder with copper radiation and a xenon-filled proportional counter, Parrish [5] found the peak/background ratio to be 57 without an analyzer and 146 with one. To achieve this almost three-fold improvement, the analyzer window was centered on the center V (Fig. 16) of the Cu $K\alpha$ distribution and made wide enough to accept about 90 percent of it.

This method works best when the wavelength to be passed and the wavelength to be rejected are far apart. If they are close together, or if the detector has poor resolution, it will be hard to pass one and reject the other. There will then be two pulse distributions like that of Fig. 16 side by side and partially overlapping. A window set to pass a reasonable proportion of one set of pulses will also pass some of the other set.

Problems of window settings can arise even when the incident x-rays are monochromatic, because pulses of *two* different sizes can be produced. This can occur when the incident radiation is energetic enough to cause x-ray fluorescence in the detector. The fluorescent radiation may escape from the detector without causing any ionization, carrying with it some of the energy that would normally be absorbed. An *escape peak* of smaller-than-normal pulses is then formed, corresponding to this less-than-normal energy absorption.

As a specific example, consider the absorption of Mo $K\alpha$ radiation ($\lambda = 0.71$ Å, energy $E_1 = 17.4$ keV) in a krypton-filled proportional counter. The K absorption edge of krypton is at 0.87 Å ($W_K = 14.3$ keV), so that Mo $K\alpha$ radiation can cause the emission of Kr $K\alpha$ radiation ($\lambda = 0.98$ Å, energy $E_2 = 12.6$ keV). Some of the Mo $K\alpha$ quanta are absorbed with a total loss of energy, causing normal pulses of average size $V_a = kE_1 = 17.4\ k$ volts, where k is a constant. Absorption of other Mo $K\alpha$ quanta will involve an energy loss in the counter of only $(E_1 - E_2)$, because of the escaping Kr $K\alpha$, causing escape-peak pulses of average size $V_{ep} = k(E_1 - E_2) = k(17.4 - 12.6) = 4.8\ k$ volts. These two processes are illustrated in Fig. 25(a), where k is evidently about 1.9. (The term *escape peak* may be misleading to some. Note that the size of escape-peak pulses corresponds *not* to the escaping energy, but to the difference between the normal and escaping energies.) Shown in (b) are the normal and escape peaks for Cu $K\alpha$ radiation incident on a xenon counter; here the fluorescent radiation is the $L\alpha_1$ line.

The situation shown in Fig. 25(a) is unusual, in that there are more pulses in the escape peak than in the normal peak. If the window of a pulse-height analyzer is set to pass only the normal Mo $K\alpha$ pulses, then the observed counting rate (=observed x-ray intensity) would be less than half the value observed with no analyzer at all because without an analyzer all pulses would be counted. The number of pulses in the escape peak will be larger, relative to that in the normal peak, the greater the fluorescence yield of the counter material and the lower the absorption coefficient of the counter material for its own fluorescent radiation.

Escape pulses can occur in any "proportional" counter. In a NaI(Tl) scintillation detector they are caused by fluorescent iodine K radiation; in a Si(Li) detector by fluorescent silicon K radiation.

Escape peaks can be troublesome in x-ray spectroscopy. When several wavelengths are incident on the detector, the escape peak for wavelength λ_1 may fall on or near the normal peak for wavelength λ_2, causing uncertainty in the identification of λ_2.

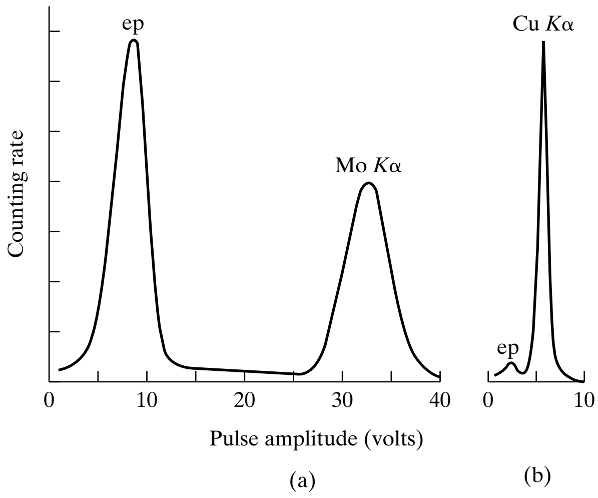

Figure 25 Pulse-height distribution curves showing escape peaks (ep) in proportional counters for (a) Mo $K\alpha$ radiation incident on a krypton counter and (b) Cu $K\alpha$ radiation incident on a xenon counter, Parrish [5].

Multichannel Pulse-Height Analyzer

This remarkable instrument, called MCA for short, usually has not one but upward of a thousand channels. It is designed to separate pulses from a detector that is receiving incident radiation of many wavelengths, by sorting pulses according to their size (amplitude).

An MCA is actually a special-purpose microprocessor with three functions [12]:

1. *Digitizing*. An analog-to-digital converter (ADC) converts the analog information contained in each pulse (amplitude in volts) into digital form, suitable for computer processing.
2. *Sorting and storage*. These operations are performed in the memory of the MCA. If the x-ray energy range to be examined extends from, say, 0 to 20 keV and the MCA has 1000 channels, then each channel spans an energy range of 20 eV. Channel number 295 would receive from the ADC information about any pulse activity in the range 5880-5900 eV. This channel would therefore get information (number of counts) about a vertical slice near the center of the Mn $K\alpha$ pulse distribution shown in Fig. 22. For the Si(Li) detector shown in Fig. 22, the base of the pulse distribution appears to be about 300 eV wide; information about Mn $K\alpha$ pulses would therefore be spread over 15 channels of the MCA.
3. *Display*. The contents of the MCA memory (total counts in each channel) may be displayed visually as counts vs. channel number (= counts vs. x-ray energy) on a CRT, plotted in hardcopy or stored digitally.

The operation of multichannel and single-channel instruments in performing pulse-height analysis may be contrasted as follows. In a single-channel instrument the entire energy range is scanned serially in time by one moving channel, as suggested by Fig. 15. In the MCA, a large number of fixed channels covers the energy range and all channels simultaneously receive the count-rate information appropriate to each channel.

Applications of the MCA to specific diffraction problems appear in the next section.

10 SPECIAL KINDS OF DIFFRACTOMETRY

The ability of the MCA to sort signals of various magnitudes has permitted the development of new kinds of diffractometers, radically different from the conventional, moving detector instrument to which this chapter is mainly devoted.

Energy-Dispersive Diffractometry

In the standard diffractometer, the various periodicities d of the arrays of atoms in a polycrystalline specimen diffract a single wavelength in various directions 2θ; the diffraction pattern is observed by moving a detector to the position of each diffracted beam in turn. On the other hand, if the incident beam consists of white radiation and the angle θ is fixed for all planes, the different sets of planes will diffract a set of different wavelengths into a detector set at a fixed position 2θ. If the detector is "proportional" and connected to a multichannel analyzer, the diffracted wavelengths can be sorted on the basis of their energies. This procedure, called *energy-dispersive diffractometry*, was first developed by Giessen, and Gordon and Buras *et al.* [13-15].

It is now appropriate to write Bragg's law in terms of photon energy E rather than wavelength λ:

$$E = h\nu = \frac{hc}{\lambda} = \frac{hc}{2d \sin \theta}. \tag{6}$$

For E in keV and d in Å, this becomes

$$E = \frac{6.20}{d \sin \theta}. \tag{7}$$

At constant θ, measurement of E will give the spacing d of each set of planes, and their indices (hkl) are found by methods that are beyond the scope of this chapter. The experimental arrangement and an example of the results obtained, from a plot of the contents of the various channels of the MCA, are shown in Fig. 26. The specimen was a sheet of polycrystalline platinum.

The fluorescent L lines of platinum appear at the left of Fig. 26(b). The energies of these lines are independent of 2θ The diffraction lines, on the other hand, have energies that depend on 2θ according to Eq. (7). Therefore the whole diffraction pattern can be shifted to higher or lower energies by changing 2θ, if it is necessary to prevent an overlap of fluorescent and diffraction lines. (If the nature of the specimen is entirely unknown, the presence of the fluorescence lines can be advantageous. The fluorescence lines disclose the chemical elements present in the specimen, while the diffraction lines disclose its crystal structure.

Compared to the conventional method (single wavelength, moving detector), energy-dispersive diffractometry is much faster, because the diffraction pattern is acquired simultaneously rather than serially. Typically, the entire pattern can be recorded in 1 to 5 minutes, whereas the conventional technique requires over an hour. However, the resolution of closely spaced diffraction lines is inferior to that of the conventional technique. Also on the debit side are the added cost of an MCA and the inconvenience of cooling the Si (Li) detector.

Some specimens, notably steels, give diffraction patterns composed of rather widely separated lines. For such materials high resolution is not needed. Voskamp

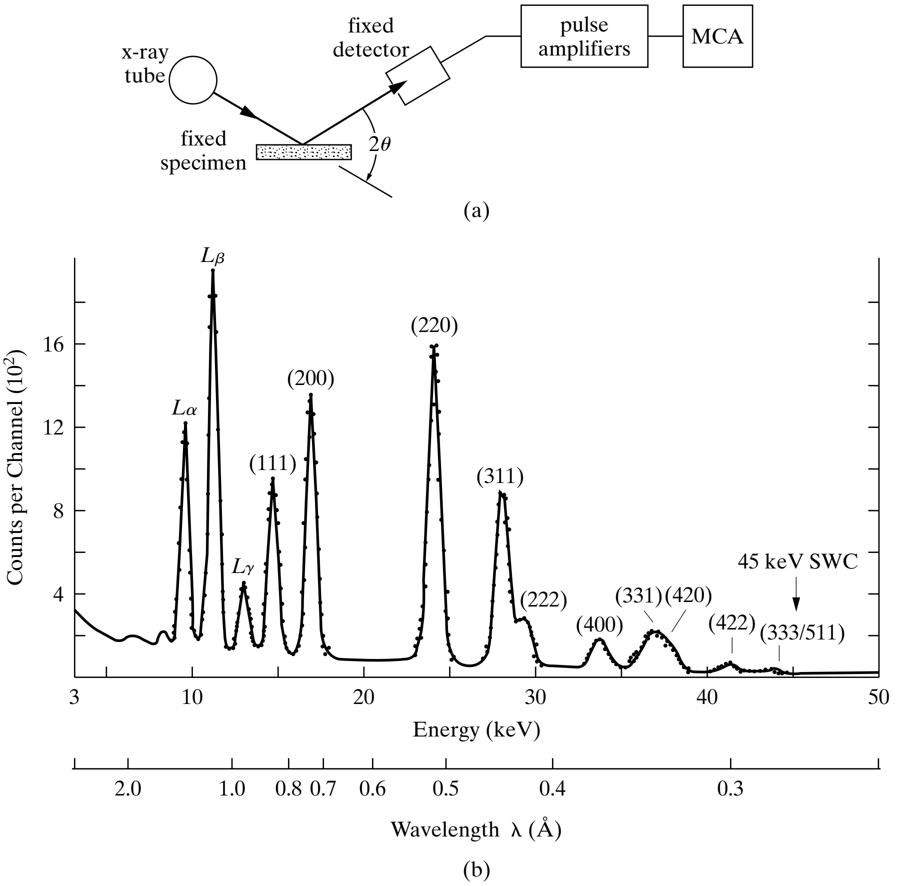

Figure 26 Energy-dispersive diffractometry. (a) Experimental arrangement. The x-ray tube is seen end on. Diffracted beam collimator not shown. (b) Diffraction pattern of polycrystalline platinum at $2\theta = 21.4°$ obtained with a Si(Li) detector and an iron-target x-ray tube operated at 45 kV and 8 mA. SWC = short wave cutoff = short-wavelength limit of incident beam. Giessen and Gordon [14].

[16] has described the use of energy-dispersive diffractometry for the examination of steels and gives references to other applications. Energy dispersive diffractometry has found increasing application at synchrotron radiation sources.

Position-Sensitive Diffractometry

A variety of one- and two-dimensional detectors can be used for diffractometry, detectors which allow the angular positions of many diffraction lines or even entire diffraction cones to be measured simultaneously. Some types of one- and two-dimensional detectors involved a side-window position-sensitive proportional counter (Sec. 5), a multichannel analyzer, and the measurement of the angular positions of many diffraction lines simultaneously. The anode wire of the counter, which is long and *curved*, coincides with a segment of the diffractometer circle and is connected, through appropriate circuits, to an MCA. The powder specimen is in the form of a thin rod centered on the diffractometer axis. The geometry of the apparatus therefore resembles that of a Hull/Debye–Scherrer camera, except that the curved film strip is replaced by a curved counter.

When "monochromatic" radiation is incident on the specimen, it sends out diffracted beams at particular 2θ angles. These beams enter the side window of the counter at particular points, causing pulse formation at those points. The pulse then travels to the two ends of the wire, and the position at which the pulse originates may be determined by digitally comparing the amplitude or the arrival time of the pulses at the ends of the anode. The pulse arrival times or the amplitudes are sorted by the MCA. The contents of the MCA memory are therefore number of pulses (counts) as a function of the position on the anode wire where the pulses originated (angle 2θ). A display of the contents of the MCA resembles the pattern recorded by a conventional diffractometer (Fig. 5).

This method is fast, because all diffracted beams incident on the detector are measured simultaneously. Commercially available position sensitive detectors subtend 2θ angles up to 120°, and in many cases this angular range is enough to record the entire portion of the diffraction pattern of interest. If the whole pattern is to be examined from near 0° to near 180°, the measurements is made in two overlapping steps. One manufacturer's detector spans 120° 2θ and is divided into 4096 channels corresponding to a 2θ step size of approximately 0.03° 2θ. Before using such a system the detector characteristics should be carefully characterized: variation of detector channel angular width of $\pm 1.5\%$ has been reported [17].

Two-dimensional detectors, also called area detectors, are widely used in crystallography and more recently in materials diffraction. Multi-wire proportional chambers and charge-coupled device (CCD) plus fluorescent screen detectors are popular as are image plates. The operation of multi-wire proportional chambers is basically the same as that of linear position sensitive detectors described above, and additional details may be found elsewhere [18]. Strong opinions exist, however, on the part of users concerning the relative merits of different commercial area detectors; a comparison of four such systems indicated that all four detectors produced acceptable data [19].

11 SCALERS

A scaler is an electronic device which counts each pulse produced by the detector. Once the number of pulses over a measured period of time is known, the average counting rate is obtained by simple division.

A scaler consists of a number of identical *stages* connected in series. Each stage is a circuit that divides, or scales down, the entering pulses by a constant factor before transmitting them to the next stage. This factor is 10 in a *decade scaler* and 2 in a *binary scaler*.

The first stage of a decade scaler transmits one pulse to the second stage for every ten pulses that enter the first stage. In a five-stage scaler the fifth stage will have transmitted one pulse when 10^5 pulses have entered the scaler, and the *scaling factor* is said to be 10^5. If, say, 12,327 pulses have entered the scaler when it is turned off, that count will be displayed as a decimal number on the front of the scaler, an LED (light emitting diode) or liquid crystal display. More often the count is shipped directly to a memory buffer in the computer controlling data acquisition.

A binary scaler operates in a similar way, but now the scaling factor is 2^n, where n is the number of stages. Some binary scalers do not appear to be binary to the user, because the contents of the individual stages are not displayed; only the total count, in decimal form, appears at the front of the scaler.

A scaler can be operated in two ways to obtain the average counting rate:

1. *Counting for a fixed time*. The desired time t is selected and the timer automatically stops the scaler after t seconds. The average counting rate is then N/t, where N is the displayed number of pulses (counts).
2. *Counting a fixed number of pulses*. The desired number of counts N is selected. If N is to be, say, 10,000 counts, the switch will connect the timer to the output of the fourth stage of a decade scaler. When 10,000 pulses have entered the scaler, the fourth stage will transmit its first pulse and that pulse will stop the timer and cause the time required to accumulate the N counts to be recorded.

In the fixed time counting mode, either counts per unit time or total counts can be plotted as a a function of 2θ. In the fixed counts mode, counts per unit time is plotted as a function of 2θ. Software in many commercial diffraction systems will allow operation in fixed time or fixed counts mode.

Because the arrival of x-ray quanta in the detector is random in time, the accuracy of a counting rate measurement is governed by the laws of probability. Two counts of the same x-ray beam for identical periods of time will not be precisely the same because of the random spacing between pulses, even though the detector and scaler are functioning perfectly. Clearly, the accuracy of a rate measurement of this kind improves as the time of counting is prolonged, and it is therefore important to know how long to count in order to attain a specified degree of accuracy. The number of pulses N counted for a fixed time in repeated measurements of a constant x-ray intensity will have a Gaussian (normal) distribution about the true value N_t obtained by averaging many measurements, with a standard deviation σ of $\sqrt{N}$. The relative standard deviation to be expected in a single count of N pulses is then

$$\text{Relative } \sigma = \frac{\sqrt{N}}{N}(100) = \frac{100}{\sqrt{N}} \text{ percent.} \tag{8}$$

The probable error[4] in a single count is

$$\text{Probable error} = 0.67\,(\text{relative } \sigma) = \frac{67}{\sqrt{N}} \text{ percent.} \tag{9}$$

These expressions give the following errors:

Number of pulses counted	Relative standard deviation (percent)	Probable error (percent)
1,000	3.2	2.1
10,000	1.0	0.7
100,000	0.3	0.2

Note that the error depends only on the number of pulses counted and not on their rate, which means that high rates and low rates can be measured with the same accuracy, if the counting times are chosen to produce the same total number of counts in each measurement. In principle, when highest precision is required, the second scaling method outlined above, in which the time is measured for a fixed number of counts, is preferable to the first, since it permits intensity measurements of the same accuracy of both high- and low-intensity beams. In most cases, however, fixed time counting provides adequate accuracy.

The probable error[5] in the measured intensity of a diffraction line *above* background increases as the background intensity increases. If N_P and N_B are the numbers of counts obtained in the same time at the peak of the diffraction line and in the background adjacent to the line, respectively, then the error in $(N_P - N_B)$ is of more interest than in the error in N_P. Assuming that N_P and N_B are normally distributed and combining the two quantities yields a variance equal to the sum of the variances of the quantities involved. (Variance $= \sigma^2$, where σ = standard deviation.) In this case,

$$\sigma^2_{P-B} = \sigma^2_P + \sigma^2_B = N_P + N_B;$$

$$\sigma_{P-B} = (N_P + N_B)^{1/2},$$

$$\text{Relative} \qquad \sigma_{P-B} = \frac{(N_P + N_B)^{1/2}}{(N_P - N_B)}. \tag{10}$$

---

[4] The probable error is that which is just as likely to be exceeded as not. Three times the probable error is a somewhat more useful figure, as the probability that this will be exceeded is only 0.04. Thus, if a single measurement gives 1000 counts, then the probable error is $67/\sqrt{1000} = 2.1$ percent or 21 counts. Then the probability is 0.5 that this count lies in the range $N_t \pm 21$, where N_t is the true number of counts, while the probability is 0.96 that the measured value lies in the range $N_t \pm 63$.

[5] The probable error is that which is just as likely to be exceeded as not. Three times the probable error is a somewhat more useful figure, as the probability that this will be exceeded is only 0.04. Thus, if a single measurement gives 1000 counts, then the probable error is $67/\sqrt{1000} = 2.1$ percent or 21 counts. Then the probability is 0.5 that this count lies in the range $N_t \pm 21$, where N_t is the true number of counts, while the probability is 0.96 that the measured value lies in the range $N_t \pm 63$.

As indicated in Sec. 2, the integrated intensity of a diffraction line is typically determined by measuring the counts at a number of angular positions of the sample and detector. The line profile is then integrated numerically (many manufacturers' powder diffraction software include this feature; otherwise the data can be exported to a personal computer or workstation). To obtain the same relative accuracy of both the line profile and the adjacent background, all measurements should be made by counting a fixed number of pulses.

A largely superseded method of measuring integrated intensity (from the period before digital data acquisition was common) exploits the integrating property of the scaler. In Fig. 27 the shaded area P is the integrated intensity of the diffraction line shown. Select two detector positions $2\theta_1$ and $2\theta_2$, well into the background on either side of the line. Scan from $2\theta_1$ to $2\theta_2$, the scaler being started at the beginning of the scan and stopped at the end. Let the time required for this scan be t and the number of counts accumulated be N_{PB}; this number is proportional to the sum of the areas P and B. Then count for a time $t/2$ at $2\theta_1$ and for a time $t/2$ at $2\theta_2$. Let the total count accumulated in these two fixed-position measurements be N_B. This number is proportional to the area B, because it is the count that would have been obtained in a scan for time t from $2\theta_1$ to $2\theta_2$ if the diffraction peak were absent. The integrated intensity of the peak is then

$$N_P = N_{PB} - N_B. \tag{11}$$

When the integrated intensities of two diffraction lines are to be compared, both lines must be scanned with the same detector slit (receiving slit) at the same speed. Because this method involves counting for a fixed time, the background and low-intensity portions of the diffraction time are measured with less accuracy than the high-intensity portions. The counting time should be chosen so that the low intensities are measured to the accuracy required by the particular problem involved; it will then follow that the high intensities are measured with unnecessarily high accuracy, but that is unavoidable in a fixed-time method.

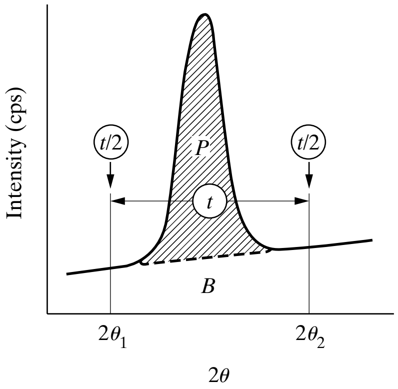

Figure 27 Determination of integrated intensity by scanning and measuring counts with a scaler. The encircled symbols are the times spent in counting.

12 RATEMETERS

The rate meter, as its name implies, is a device which indicates the average counting rate directly without requiring, as in the scaler-timer combination separate measurements of the number of counts and the time. It does this by a circuit which, in effect, smooths out the succession of randomly spaced pulses from the detector into a steady current, whose magnitude is proportional to the average rate of pulse production in the detector.

The heart of a ratemeter circuit is a series arrangement of a capacitor and resistor. To understand the action of a ratemeter, some of the properties of such a circuit must be reviewed, notably the way in which the current and voltage vary with time. Consider the circuit shown in Fig. 28(a), in which the switch S can be used either to connect a to c and thus apply a voltage to the capacitor, or to connect b to c and thus short-circuit the capacitor and resistor. When a is suddenly connected to c, the voltage across the capacitor reaches its final value V not instantaneously but only over a period of time, and at a rate which depends on the resistance R and the capacitance C, as shown in Fig. 28(b). The product of R and C has the dimensions of time (seconds, in fact, if R is in megohms and C in microfarads), and it may be shown that the voltage across the capacitor reaches 63 percent of its final value in a time given by RC, known as the *time constant* of the circuit. The time required to reach 99 percent of its final value is $4.6RC$. Conversely, if the fully charged capacitor, bearing a charge $Q = CV$, is suddenly shorted through the resistor by connecting b to c, the charge does not immediately disappear but leaks away at a rate dependent on the time constant. The charge drops to 37 percent of its initial value in a time equal to RC and to 1 percent in a time equal to $4.6RC$.

A complete ratemeter circuit consists of two parts. The first is a pulse-amplifying and pulse-shaping portion which electronically converts the detector pulses, which vary in amplitude and shape from detector to detector, into rectangular pulses of fixed dimensions in voltage and time. These pulses are then fed into the second por-

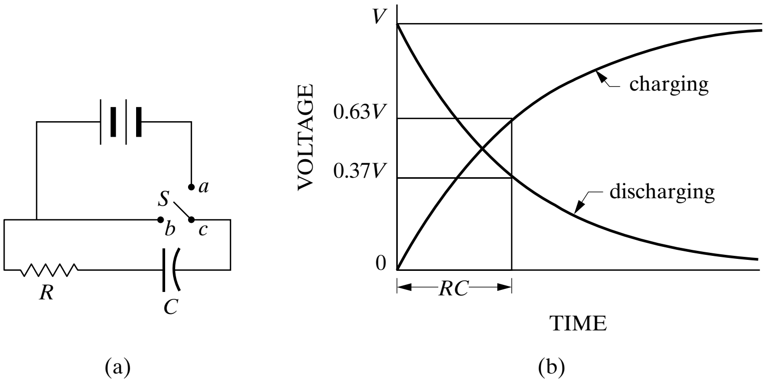

(a) (b)

Figure 28 The capacitor-resistor circuit.

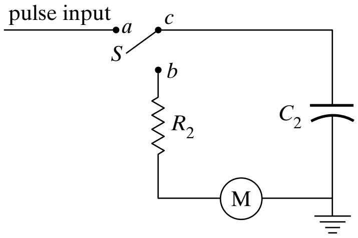

Figure 29 Measuring portion of ratemeter circuit.

tion, which is the measuring circuit shown in Fig. 29, a circuit basically similar to that of Fig. 28(a) and having a time constant R_2C_2. S_1, shown as a simple switch, is actually an electronic circuit which connects *a* to *c* each time a pulse arrives and then connects *b* to *c* immediately afterwards. A constant charge is thus added to the capacitor for each pulse received and this charge leaks away through the resistor until, at equilibrium, the rate of addition of charge is just balanced by the rate of leakage. The rate of charge leakage is simply the current through the microammeter *M*, which therefore indicates the rate of pulse production in the detector and, in turn, the x-ray intensity. In the past, diffractometer systems would include in addition to the indicating meter, a chart recorder which produce a continuous record of the intensity. With the advent of inexpensive computers, chart recorders have been supplanted by software data acquisition; it is still possible to find chart recorders in operation with diffractometers.

Even when the x-ray intensity is constant (constant average counting rate), the spacing of the detector pulses is random in time, which means that the counting rate actually varies with time over short periods. The ratemeter responds to these statistical fluctuations in the counting rate, and its response speed is greater the smaller the time constant. This follows from the discussion of the capacitor-resistor circuit: any change in the pulse rate causes a change in the current through the circuit, but the latter change always lags behind the former; the amount of lag is less for a small time constant than for a large one. Random fluctuations in the counting rate are therefore more evident with a small time constant, because the current in the circuit then follows the changes in counting rate more closely. This feature is illustrated in Fig. 30, which shows the automatically recorded output of a ratemeter when the detector is receiving a constant-intensity x-ray beam. The large fluctuations at the left have been reduced in magnitude by successive increases in the time constant, effected by changing the value of C_2. Evidently, a *single* reading of the position of the indicating meter needle or the recorder pen of a ratemeter may be seriously in error, and more so at low time constants than at high. In Sec. 11, the error in a counting-rate measurement was demonstrated to decrease as the number of counts increased. Now it may be shown that a ratemeter acts as if in counted for a time $2R_2C_2$, in the sense that the accuracy of any single reading is equivalent to a count made with a scaler for a time $2R_2C_2$. Therefore, the relative probable error in any single ratemeter reading is given by the counterpart of Eq. (9), namely by

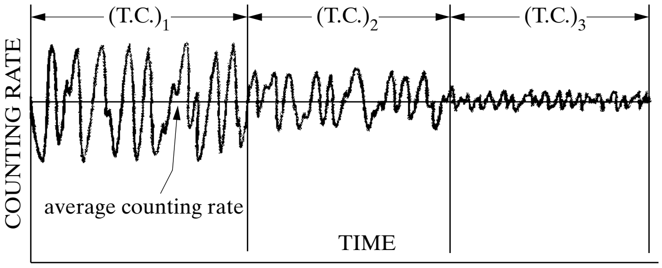

Figure 30 Effect of time constant (T.C.) on recorded fluctuations in counting rate at constant x-ray intensity (schematic). Time constants changed abruptly at times shown. (T.C.)$_1$ $<$ (T.C.)$_2$ $<$ (T.C.)$_3$.

$$\text{Probable error} = \frac{67}{\sqrt{2\pi R_2 C_2}}\ \text{percent}, \tag{12}$$

where n is the average counting rate. This equation also shows that the probable error is less for high counting rates than for low, when the time constant remains the same; this effect is evident in plots (fixed time) of any diffraction line, where the fluctuations are smaller at the top of the line than in the background.

The most useful feature of a ratemeter is its ability to follow *changes* in the average counting rate, a function for which the scaler unsuited since a change in the average counting rate occurring during the time a count is being made with a scaler will go entirely undetected. It is this feature of a ratemeter which is so useful in diffractometry. A diffraction pattern can be scanned over the angular range expected to contain a diffraction peak, and the moving detector automatically transmits, through the ratemeter, a continuous record of the intensity it observes as the diffraction angle is changed. This allows very quick positioning of the detector at the of the peak's maxima. On the other hand, the ratemeter is less accurate than the scaler, both because of the unavoidable statistical fluctuations in its output and because of the errors inherent in its indicating or recording instruments.

As mentioned earlier, a large time constant smooths out fluctuations in the average counting rate by increasing the response time to changes in rate. But when a sharp diffraction line is being scanned, the average counting rate is changing rapidly, and the ratemeter ought to indicate this change as accurately as possible. From this point of view, a short response time, produced by a small time constant, is required. A ratemeter must therefore be designed with these two conflicting factors in mind, and the time constant should be chosen large enough to smooth out most of the statistical fluctuations and yet small enough to give a reasonably short response time.

Most commercial ratemeters have several scales available to cover various ranges of x-ray intensity (100, 1000, and 10,000 cps for full-scale deflection of the ratemeter's needle and linear or logarithmic scales, for example). A logarithmic scale is useful when looking for weak lines or when exploring an unknown pattern: weak lines will be emphasized and the strong lines will not go off-scale. Smaller time constants are used with the higher scales, just as short counting times are used with a scaler when the counting rate is high. In some instruments, the time constant appropriate to each scale is fixed by the manufacturer, and in others the operator can select any one of several time constants, ranging from about 0.5 to 15 sec, manually by switches or electronically under software control, which insert the proper capacitance in the circuit. The proper time constant to use is, of course, not unrelated to the scanning speed, for a fast scan demands a fast response from the ratemeter and therefore a short time constant. A time constant which is too large for the scanning speed used will slightly shift the peaks of diffraction lines in the direction of the scan and lower their maximum intensity and, because of its excessive smoothing action, may actually obliterate weak diffraction lines and cause them to go unnoticed. In choosing a time constant, it is therefore better to err on the short side. A good rule to follow is to make the time constant less than half the *time width* of the receiving slit, where the time width is defined as the time required for the slit to travel its own width. For example, if a 0.2° slit is used at a scanning speed of 2°/min, then the time width of the slit is (0.2/2)(60) = 6 sec, and the time constant should therefore be less than 3 sec. The same rule can be used to find the proper slit width for a given scanning speed when the time constant is fixed.

13 MONOCHROMATIC OPERATION

The background of a diffraction pattern obtained with a diffractometer may be reduced by means of a single-channel pulse-height analyzer, as mentioned in Sec. 9. An even better method is to use a crystal monochromator in the diffracted beam. Balanced filters present still another option.

Monochromating Crystal

The purest kind of radiation to use in a diffraction experiment is radiation which has itself been diffracted, since it is entirely monochromatic.[6] With a diffractometer one has the option, which does not exist with a powder camera, of placing a crystal

---

[6] This statement requires some qualification. When a crystal monochromator is set to diffract radiation of wavelength λ from a particular set of planes, then these same planes will also diffract radiation of wavelength $\lambda/2$ and $\lambda/3$ in the second and third order, respectively, and at exactly the same angle 2θ. These components of submultiple wavelength are of relatively low intensity when the main component is $K\alpha$ characteristic radiation but, even so, their presence is undesirable whenever precise calculations of the intensity diffracted by the *specimen* must be made. The submultiple components may be eliminated from the beam from the monochromator by reducing the tube voltage to the point where these wavelengths are not produced. If the main component is Cu $K\alpha$ radiation, this procedure is usually impractical because of the decrease in intensity attendant on a reduction in tube voltage to 16 kV (necessary to eliminate the $\lambda/2$ and $\lambda/3$ components). Usually, a compromise is made by operating at a voltage just insufficient to generate the $\lambda/3$ component (24 kV for copper radiation) and by using a crystal which has, for a certain set of planes, a negligible diffracting power for the $\lambda/2$ component. Fluorite (CaF_2) is such a crystal, the structure factor for the 222 reflection being much less than for the 111. The diamond cubic crystals, silicon and germanium, are even better, since their structure factors for the 222 reflection are actually zero.

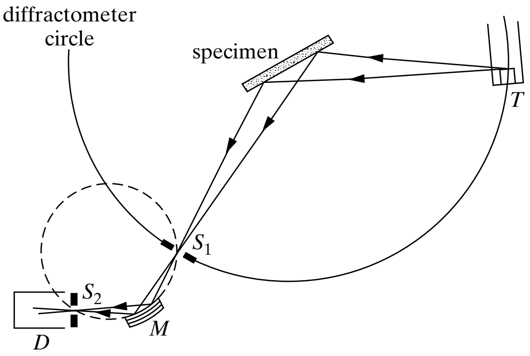

Figure 31 Diffractometer with monochromating crystal M in diffracted beam. detector T = x-ray tube.

monochromator in the diffracted, rather than the incident, beam. Figure 31 shows such an arrangement. The diffracted beam from the specimen comes to a focus at the receiving slit S_1, diverges to the focusing monochromator M, and comes to a focus again at the detector slit S_2. Detector, crystal, and slits are mounted on one support and rotate as a unit about the diffractometer axis.

Even though intensity is decreased during diffraction by a monochromator, a $K\beta$ filter is not needed because the monochromator is set to diffract only $K\alpha$ radiation. As a result, and because of the focusing action of the monochromator, the intensity of a diffraction line at the detector can actually be higher with a monochromator than without, particularly if the monochromating crystal is graphite.

Placement of the monochromator in the diffracted beam has the advantage of suppressing background radiation originating in the *specimen*, such as fluorescent radiation and incoherent (Compton modified) scattered radiation. For example, if a steel specimen or any iron-rich material is examined with copper radiation in an ordinary diffractometer, the background due to fluorescent Fe K radiation will be unacceptably high. But if a monochromator is added and oriented to diffract only Cu $K\alpha$, the background is reduced practically to zero, because the fluoresced Fe $K\alpha$ and Fe $K\beta$ do not enter the detector. A monochromator may therefore eliminate the need for an extra tube, such as a Cr-target tube, for the examination of steel specimens.

The diffractometer in Fig. 2 is equipped with a diffracted beam monochromator. There are two kinds of monochromators in use, depending on whether the crystal is unbent or bent and cut.

An unbent crystal is not a very efficient reflector, as can be seen from Fig. 32. This is because the beam from an x-ray tube is never composed only of parallel rays, even when defined by a slit or collimator, but contains a large proportion of convergent and divergent radiation. When the crystal is set at the correct Bragg angle for the parallel component of the incident beam, it can diffract only that component and none of the other rays, with the result that the diffracted beam is of very low intensity although it is itself perfectly parallel, at least in the plane of the drawing. In a plane at right angles, the diffracted beam may contain both convergent and divergent radiation.

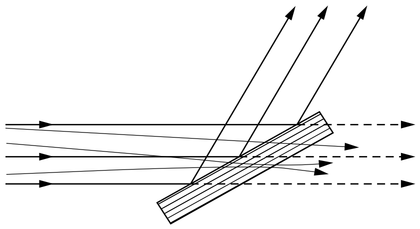

Figure 32 Monochromatic reflection when the incident beam is nonparallel.

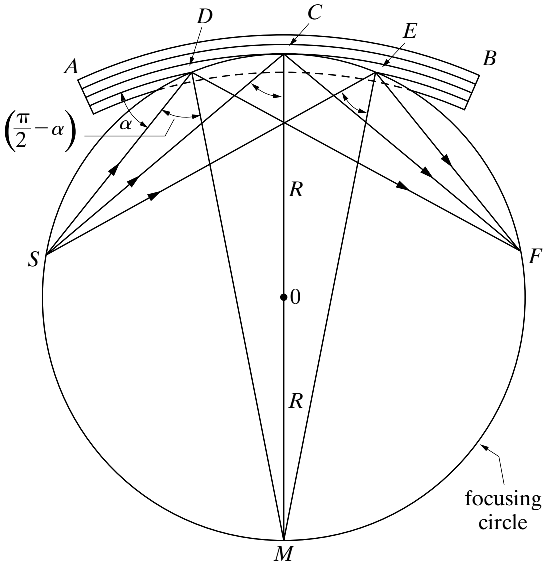

Figure 33 Focusing monochromator (cut and bent).

A large gain in intensity may be obtained by using a bent and cut crystal, which operates on the focusing principle illustrated in Fig. 33. A line source of x-rays, the focal line on the tube target or the focused diffracted beam from the sample, is located at S perpendicular to the plane of the drawing. The crystal AB is in the form of a rectangular plate and has a set of diffracting planes parallel to its surface. It is elastically bent into a circular form so that the radius of curvature of the plane through C is $2R = CM$; in this way, all the plane normals are made to pass through M, which is located on the same circle, of radius R, as the source S. If the face of the crystal is then cut away behind the dotted line to a radius of R, then all rays diverging from the source S will encounter the lattice planes at the same Bragg angle α, since the angles SDM, SCM, and SEM are all equal to one another, being inscribed on the same arc SM, and have the value $(\pi/2 - \alpha)$.[7]

---

[7] The symbol α is used in place of θ in order to keep the diffraction angles from sample and monochromator distinct.

When the Bragg angle is adjusted to that required for diffraction of the $K\alpha$ component of the incident beam, then a strong monochromatic beam will be diffracted by the crystal. Moreover, since the diffracted rays all originate on a circle passing through the source S, they will converge to a focus at F, located on the same circle as S and at the same distance from C, in much the same way as previously discussed for parafocusing diffractometers. This kind of monochromator is called the Johansson type.

In practice the crystal is not bent and then cut as described above, but the unbent crystal, usually of quartz, is first cut to a radius of $2R$ and then bent against a circular form of radius R. This procedure will produce the same net result. The value of α required for the diffraction of a particular wavelength λ from planes of spacing d is given by Bragg's law:

$$\lambda = 2d \sin \alpha. \tag{13}$$

The source-to-crystal distance SC, which equals the crystal-to-focus distance CF, is given by

$$SC = 2R \cos\left(\frac{\pi}{2} - \alpha\right). \tag{14}$$

Combining Eqs. (13) and (14) results in

$$SC = R\frac{\lambda}{d}. \tag{15}$$

For diffraction of Cu $K\alpha$ radiation from the planes of quartz, the distance SC is 14.2 cm for a value of R of 30 cm.

The chief value of the focusing monochromator lies in the fact that all the monochromatic rays in the incident beam are utilized and the diffracted rays from a considerable area of the crystal surface are all brought to a focus. This leads to a large concentration of energy and a considerable reduction in counting time (required to obtain a set number of counts) compared to the unbent-crystal monochromator first described. However, the latter does produce a semiparallel beam of radiation, and, even though it is of very low intensity, such a beam is required in some experiments. If the monochromating crystal is bent but not cut, some concentration of energy will be achieved inasmuch as the diffracted beam will be convergent, but it will not converge to a perfect focus.

Many crystals have been used as monochromators: NaCl, LiF, SiO_2 (quartz), Al, Si, Ge, graphite, InSb, etc. For discussion of their relative merits and details of design and use, see Guinier [G.13, G.30], chap. 2 of Vol. C of [G.1], Klug and Alexander [G.17] or Jekins and Snyder [G.25]. Graphite gives the strongest diffracted beam.

New types of monochromators are under development for diffractometry; examples include crystals of an in situ composite $TaSi_2$-Si [20, 21], Si-Ge gradient crystals [22] and metallic multilayers. The $TaSi_2$-Si composite consists of 10^6 cm^{-2} single-crystal rods of Ta_2Si in a single crystal Si matrix; the spacing of the parallel, 1 μm diameter rods is quite uniform as is the distribution of strain in the Si matrix and the crystals have very large peak and integrated reflectivities over the energy range from 4 to 160 keV. Multilayers also have a larger angular acceptance range than crystals such as Si; this is the result of their periodic structure alternating high and low atomic number layers. A typical, commercially-available multilayer for powder diffractometry using Cu $K\alpha$ radiation consists of 50 periods of W/Si linearly graded between 15 and 100 Å [23].

The use of a monochromator between the x-ray tube and the sample produces a change in the relative intensities of the beams diffracted by the specimen. Equation (4-2), for example, was derived for the completely unpolarized incident beam obtained from the x-ray tube. Any beam diffracted by a crystal, however, becomes partially polarized by the diffraction process itself, which means that the beam from a crystal monochromator is partially polarized before it reaches the specimen. Under these circumstances the usual polarization factor $(1 + \cos^2 2\theta)/2$, which is included must be replaced by the factor $(1 + \cos^2 2\alpha \cos^2 2\theta)/(1 + \cos^2 2\alpha)$, where 2α is the diffraction angle in the monochromator (Fig. 33) and 2θ is the diffraction angle of the sample. Since the denominator in this expression is independent of θ, it may be omitted; the combined Lorentz-polarization factor for crystal-monochromated radiation is therefore $(1 + \cos^2 2\alpha \cos^2 2\theta)/\sin^2\theta \cos\theta$. This factor should be substituted when a monochromator is used with a diffractometer.

Balanced Filters

Another method of operating under essentially monochromatic conditions, a method peculiar to the diffractometer, employs *Ross filters*, also called balanced filters [G.17, G.25]. This method depends on the fact that the absorption coefficients of all substances vary in the same way with wavelength; i.e., they are proportional to λ^3. If filters are made of two substances differing in atomic number by one, and their thicknesses adjusted so that they produce the same absorption for a particular wavelength, then they will have the same absorption for all wavelengths *except* those lying in the narrow wavelength region between the K absorption edges of the two substances. This region defines the *pass band* of the filter combination. If these filters are placed alternately in a heterochromatic x-ray beam. i.e., a beam containing rays of different wavelengths, then the difference between the intensities transmitted in each case is due only to wavelengths lying in the pass band. When the pass band is chosen to include a strong characteristic component of the spectrum, then the net effect is that of a strong monochromatic beam.

The isolation of Cu $K\alpha$ radiation may be taken as an example. Its wavelength is 1.542 Å, which means that cobalt and nickel can be used as filter materials since their K absorption edges (1,608 and 1.488 Å, respectively) effectively bracket the Cu $K\alpha$ line. Their linear absorption coefficients μ are plotted in Fig. 34, which shows that balancing can be obtained by making the nickel filter somewhat thinner than the cobalt one. When their thicknesses x are adjusted to the correct ratio, then $\mu_{\text{Ni}} x_{\text{Ni}} = \mu_{\text{Co}} x_{\text{Co}}$ except in the pass band, and a plot of μx versus λ has the appearance of Fig. 34(b). Since $\mu x = -\ln I_x/I_o$, the transmission factors I_x/I_o (ratio of transmitted to incident intensity) of the two filters are now equal for all wavelengths except those in the pass band, which is only 0.12 Å wide. At each angle 2θ at which the intensity is to be measured with the diffractometer, first one filter and then the other is placed in the diffracted beam before it enters the detector. The intensity of the diffracted beam passing through each filter is measured, and the difference in the measurements gives the diffracted intensity of only the Cu $K\alpha$ line and the relatively weak wavelengths immediately adjacent to it in the pass band.

It should be emphasized that the beam entering the detector is never physically monochromatic, as it is when a crystal monochromator is used. Radiation with a great many wavelengths enters the detector when either filter is in place, but every wavelength transmitted by one filter has the same intensity as that transmitted by the other filter, except those wavelengths lying in the pass band and these are transmitted quite unequally by the two filters. Therefore, when the intensity measured

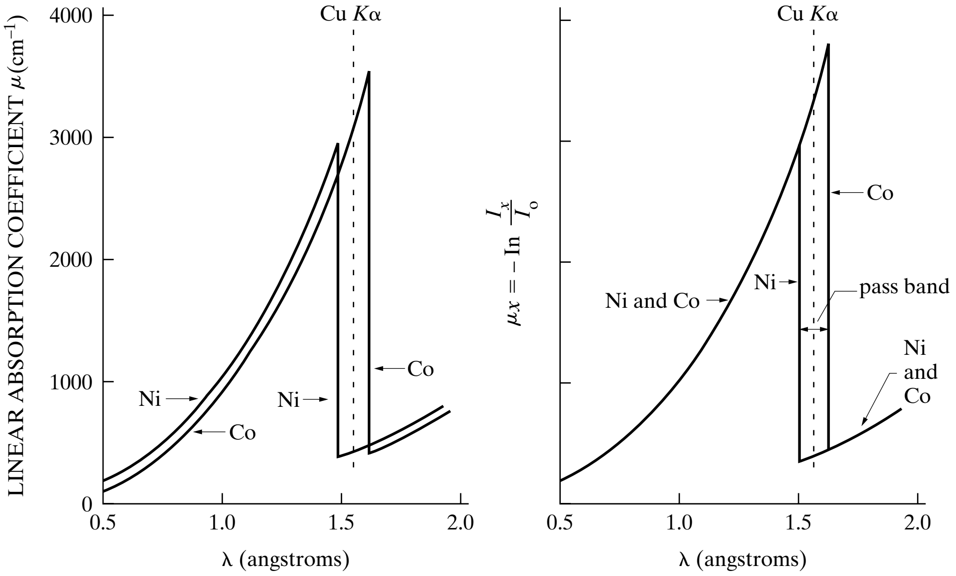

(a) (b)

Figure 34 Ross filters for Cu $K\alpha$ radiation: (a) absorption coefficients of filter materials; (b) μx values after balancing.

with one filter is subtracted from that measured with the other filter, the difference is zero for every wavelength except those in the pass band.

In practice, balancing of the filters is carried out by inserting two foils of approximately the same thickness into suitable holders which can be slipped into place in the beam entering the detector. One foil is always perpendicular to the x-ray beam, while the other may be rotated about an axis at right angles to the beam; in this way the second foil may be inclined to the beam at such an angle that its effective thickness x equals the thickness required for balancing. Perfect balancing at all wavelengths outside the pass band is not possible, although it may be approached quite closely, because μ does not vary exactly as λ^3 and because the magnitude of the K absorption jump (ratio of absorption coefficients for wavelengths just shorter and just longer than the K edge) is not exactly the same for all elements.

Note also that balanced filters will not exclude Compton scattering, which differs in wavelength by only 0.05 Å or less from the wavelength of the diffracted beam and which will therefore generally fall inside the pass band. And if the radiation forming the diffracted beam is, for example, Cu $K\alpha$, then neither a monochromating crystal nor balanced filters will exclude diffusely scattered Cu $K\alpha$ caused, for example, by thermal vibration of the atoms.

14 Determination of Diffraction Peak Positions

There are many ways of systematically assigning 2θ positions to the peaks in a diffraction pattern, and Fig. 35 illustrates the methods described below. The particular method used depends on the application and on the computing power available. It is useful to distinguish two situations: the first when many peaks are to be recorded and the second when only a few points spanning a specific part of a single peak are to be measured. In general, peaks will be smoothed by modern diffractometer

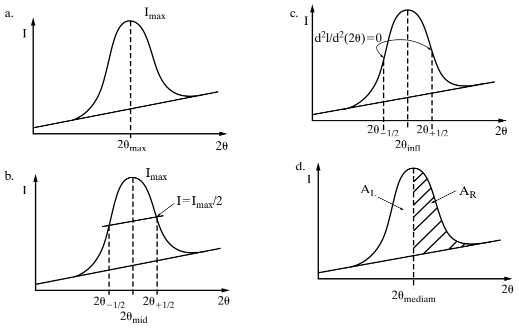

$$2\theta_{max}=d[I_{top}(2\theta)-I_{back}(2\theta)]/d(2\theta)$$

$$2\theta_{mid}=1/2[2\theta_{-1/2}+2\theta_{+1/2}]$$

$$2\theta_{infl}=1/2[2\theta'_{-1/2}+2\theta'_{+1/2}]$$

$$<2\theta>=\frac{\int 2\theta\cdot I(2\theta)\cdot d(2\theta)}{\int I(2\theta)\cdot d(2\theta)}$$

Figure 35 Different methods of defining peak position. a) peak maximum $2\theta_{max}$, b) mid-point of half-maximum intensities $2\theta_{mid}$, c) average of the points of inflection $2\theta_{infl}$, d) peak median $2\theta_{median}$ and (not shown graphically) peak centroid $< 2\theta >$. Equations for a) - c) are shown below the plots; note that $K\alpha_2$ and background stripping is assumed in all calculations except $2\theta_{max}$ where it is indicated explicitly.

software prior to stripping the $K\alpha_2$ peaks from the data via the Rachinger alogrithm [24, 25], and details can be found elsewhere [G.17, G.25].

In diffraction patterns spanning many peaks, the intuitively simplest definition is the position of the peak maximum $2\theta_{\text{max}}$ (mathematically termed the mode of the peak). This can provide sufficient precision for routine scans whose purpose is to confirm the identity of a phase or mixture of phases. For numerical data, this position is obtained when $dI/d(2\theta) = 0$. In analysis of chart recordings or other analog output such as figures in published reports, there may be little practical alternative to selecting this angle by inspection. Another alternative is to use the midpoint of the two half-maximum intensities of each peak $2\theta_{\text{mid}}$ or the midpoint of the points of inflection of the peak $2\theta_{\text{infl}}$. An alternative is to calculate the median angle $2\theta_{\text{median}}$ of the peak, i.e., the angular position where the area under the peak A_L to the left of $2\theta_{\text{median}}$ equals the area A_R to the right. The position of the centroid or center of gravity of a peak $< 2\theta >$ corresponds to the mathematical mean of the peak: it is calculated from the equation given at the bottom of Fig. 35. Of the methods mentioned above, the centroid method provides the most robust measure of peak position. Because the computation required is transparent to the user of modern software, the centroid method should be used in all work but that requiring the highest precision, and most users of x-ray diffraction, except those measuring residual stresses, should find this adequate.

Yet another approach is to fit the peaks with Gaussian, Lorentizian, combined Gaussian-Lorentzian or other functions and to use the function's maximum as the peak position. This has proved to be very valuable in a variety of applications such as structure determination from polycrystalline samples. Using the whole pattern, including background, can be very valuable, and this approach minimizes the principal drawback of the centroid method, the sensitivity of $< 2\theta >$ to the level of background chosen. Fitting the top 15% of the intensity of a diffraction peak to a parabola, for example, is used routinely in residual stress analysis and has been demonstrated to be more robust than the centroid method [26]. In the following paragraphs the parabolic-fit, top 15% method is described as an example of the peak fitting approach. The axis of the parabola is assumed to be the peak center (Fig. 36), and this method [27] is widely used in macrostress measurements.

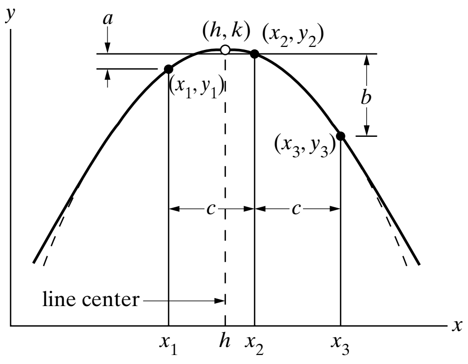

Figure 36 Three-point method for fitting a parabola. $x = 2\theta$, $y = I$.

The equation of a parabola with its axis parallel to the y axis and vertex at (h, k) is

$$(x - h)^2 = p(y - k). \tag{16}$$

If $x = 2\theta$ and $y = I$, this equation represents the shape of the diffraction line near its peak. Substitute several pairs of $2\theta, I$ values into the equation and solve for h by the method of least squares. Then the value of h equals the 2θ position of the line center. Only two or three points on either side of the peak near its maximum are sufficient to locate the parabola with surprising accuracy. The positions of diffraction lines as broad as 8° 2θ at half-maximum intensity can be reproducibly determined to within 0.02° by this method.

A simpler method, much used, for locating the parabola axis was suggested by Koistinen and Marburger [28]. Only three points on the line profile need be measured but they must be separated by the same angular interval c, as shown in Fig. 36. The central point should be near the maximum and the other two have intensities of about 85 percent of the maximum. Once the intensity differences $a = y_2 - y_1$ and $b = y_2 - y_3$ are found, the center of the line is given by

$$h = x_1 + \frac{c}{2}\left(\frac{3a + b}{a + b}\right). \tag{17}$$

The y coordinate may be intensity I in counts/sec, counts n for a fixed time, or reciprocal times $1/t$ for a fixed count.

When the lines are broad, certain corrections should be applied to the intensity data *before* finding the line center, as pointed out by Koistinen and Marburger. In calculating the relative intensities of the various lines on a powder pattern, it can be demonstrated that one factor controlling these intensities was the Lorentz-polarization (L-P) factor $(1 + \cos^2 2\theta)/(\sin^2\theta \cos\theta)$. This factor can vary considerably over the width of a single line, when the line is broad and in the high-angle region. However, the L-P factor applies to integrated intensities. To obtain an expression governing intensities at particular values of 2θ within a single line, drop the $(1/\cos\theta)$ term, which relates to line breadth in order to obtain the modified L-P factor $(1 + \cos^2 2\theta)/\sin^2\theta$. The variation of this factor with 2θ makes a high-angle line asymmetrical about its center. Absorption in the specimen has a similar effect when ψ, the angle of the diffraction plane normal relative to the sample normal, is not zero, because the absorption factor is then $(1 - \tan\psi \cot\theta)$. Combining these two factors into one and calling it the LPA factor, yields

$$\begin{aligned} LPA &= (\text{modified L} - \text{P factor})(\text{absorption factor}) \\ &= \left(\frac{1 + \cos^2 2\theta}{\sin^2\theta}\right)(1 - \tan\psi\ \cot\theta). \end{aligned} \tag{18}$$

Measured intensities are to be divided by *LPA* in order to make the lines more nearly symmetrical, before determining the line center by the least-squares or three-point method. Finally, if the background is high, because of fluorescence by the specimen, better accuracy is attainable by subtracting the background, assumed linear across the line, before applying the *LPA* correction and finding the line center.

PROBLEMS

1 A powder specimen in the form of a rectangular plate has a width of 0.5 in., measured in the plane of the diffractometer circle, which has a radius of 5.73 in. If it is required that the specimen entirely fill the incident beam at all angles and that measurements must be made to angles as low as $2\theta = 10°$, what is the maximum divergence angle (measured in the plane of the diffractometer circle) that the incident beam may have?

***2** Even the weather can affect the long-term stability of the measured intensity of x-rays from a well-stabilized tube, because a change in barometric pressure or humidity changes the absorption of x-rays by air. What is the percent change in the measured intensity of Cr $K\alpha$ resulting from a 3-percent drop in pressure over a 12-hour period, a not uncommon event? (Assume a path length in air of 27 cm and take μ of air for Cr $K\alpha = 3.48 \times 10^{-2}\,\text{cm}^{-1}$.)

3 Cu $K\alpha$ radiation is incident on a xenon-filled proportional counter. Calculate the ratio of the average pulse size in the escape peak to that in the normal peak. Compare your result with that of Fig. 25(b).

***4** If a count N_P of 30,000 is obtained at the peak of a diffraction line and, in the same time, a count N_B of 10,000 in the background adjacent to the line, calculate the percent probable error in (a) N_P and (b) $(N_P - N_B)$.

5 A diffraction pattern of polycrystalline platinum is obtained by energy-dispersive diffractometry at $\theta = 10.7°$: Calculate the energy (in keV) at which the 220 line will appear and compare your result with Fig. 26(b).

***6** a) Calculate the ratio of the effective thicknesses of cobalt and nickel filters when they are balanced for all wavelengths except Cu $K\alpha$. (Obtain an average value applicable to a wavelength range extending from about 0.5 Å to about 2 Å.)
b) When the filters are balanced, calculate the ratio of the intensity of Cu $K\alpha$ radiation transmitted by the nickel filter to that transmitted by the cobalt filter, assuming the same incident intensity in each case. The effective thickness of the nickel filter is 0.00035 in.

REFERENCES

The following books are listed more or less in the order they are encountered in the text

G.1 *International Tables for Crystallography*, Ed. A.J.C Wilson, Vol. A-C (Dordrecht Kluwer Academic Pub. for International Union of Crystallography, 1995). The reference ''book'' for crystallography and diffraction.

G.8 Strukturbericht (Leipzig: Akademische Verlagsgesellschaft, 1931-1943. Also available from Ann Arbor, MI.: Edwards Brothers, 1943). A series of seven volumes describing crystal structures whose solutions were published in the years 1913 to 1939, inclusive. Continued by: *Structure Reports* (Utrecdht. Oosthoek, 1951 to date). Sponsored by the International Union of Crystallography. The volume numbers begin with Vol. 8, where *Strukturbericht* left off. The results of structure determinations are usually given in sufficient detail that the reader has no need to consult the original paper.

G.13 André Guinier. *X-Ray Crystallographic Technology* (London: Hilger and Watts, 1952). Excellent treatment of the theory and practice of x-ray diffraction. The title is not fair to the book, which includes a considerable body of theory and detailed experimental technique. The theory and applications of the reciprocal lattice are very well described. Includes treatments of focusing monochromators, small-angle scattering, and diffraction by amorphous substances.

G.17 Harold P. Klug and Leroy E. Alexander. *X-Ray Diffraction Procedures*, 2nd ed. (New York: Wiley, 1974). Contains a great deal of useful detail on the theory and operation of powder cameras and diffractometers. Covers the following topics in depth: chemical analysis by diffraction, parameter measurement, line-broadening analysis, texture determination, stress measurement, and studies of amorphous materials. Single-crystal methods are not included.

G.25 Ron Jenkins and Robert L. Snyder. *Introduction to X-ray Powder Diffractometry* (New York, John Wiley & Sons, Inc, 1996).

G.26 A. J. C. Wilson. *Mathematical Theory of X-ray Powder Diffractometry*, (Gordon & Breech, New York, 1963), 128 pp.

G.28 Victor E. Buhrke, Ron Jenkins and Deane K. Smith. *A Practical Guide for the Preparation of Specimens for X-ray Fluorescence and X-ray Diffraction Analysis*. (New York: Wiley-VCH, 1998).

G.29 L. S. Zevin and G. Kimmel. *Quantitative X-ray Diffractometry*, edited by I. Mureinik, Springer, 1995, New York.

G.30 A. Guinier. *X-Ray Diffraction in Crystals, Imperfect Crystals, and Amorphous Bodies* (San Francisco: W. H. Freeman, 1963 and reprinted by Dover 1994). Largely theoretical and more advanced than [G.13].

ANSWERS TO SELECTED PROBLEMS

1. 0.44° **2**. 2.8 percent

4. a) 0.39 percent; b) 0.67 percent

6. a) 1.14 (Co) to 1 (Ni); b) 10.5

Powder Photographs

1 INTRODUCTION

Any device designed to hold a specimen and photographic film to record diffracted beams is called an x-ray *camera*, but most such cameras bear little resemblance to cameras used for photography by visible light. In many cases, photographic film has been replaced by image storage plates of by electronic area detectors, but the apparatus are still termed cameras and the methods are still known, collectively, as photographic methods.

There are three main photographic powder methods in use, differentiated by the relative position of the specimen and film:

1. *Hull/Debye–Scherrer method*. The film is placed on the surface of a cylinder and the specimen on the axis of the cylinder.
2. *Focusing method*. The film, specimen, and x-ray source are all placed on the surface of a cylinder.
3. *Pinhole method*. The film is flat, perpendicular to the incident x-ray beam, and located at any convenient distance from the specimen.

In all these methods, the diffracted beams lie on the surfaces of cones whose axes lie along the incident beam or its extension; each cone of rays consists of diffracted beams from particular *hkl*. In the Hull/Debye–Scherrer and focusing methods, only a narrow strip of film is used and the recorded diffraction pattern consists of short arcs, normally termed lines, formed by the intersections of the cones of radiation with the film. In the pinhole method, the whole cone intersects the film to form a circular diffraction ring.

The various powder cameras are in many respects complementary with the diffractometer. The diffractometer has the great advantage of being able to measure the positions *and* intensities of diffraction lines simultaneously and quickly. Cameras are very much cheaper than a diffractometer, but photographic methods are generally slow (except for Polaroid film and image plates for flat plate cameras and for specially built curved image plate systems, (e.g., [1]), and the

From Chapter 7 of *Elements of X-Ray Diffraction*, Third Edition. B.D. Cullity, S.R. Stock.

measurement of line intensities requires an additional operation. However, exact line intensities are by no means needed in many investigations, and there are at least three circumstances when a powder camera is definitely superior to a diffractometer:

1. When only a very small amount of specimen is available. (Specimens weighing as little as one milligram, or even less, can be successfully examined in a powder camera; the diffractometer ordinarily requires a specimen of the order of half a gram or more.)
2. When an entire diffraction ring must be recorded, as in the rapid estimation of grain size and preferred orientation.
3. When the specimen is so large, heavy, or immovable that the diffraction-recording equipment must be brought to the specimen rather than vice versa.

Powder photographic methods are described in great and useful detail by Klug and Alexander [G.17].

2 HULL/DEBYE–SCHERRER METHOD

A typical Hull/Debye–Scherrer camera is shown in Fig. 1. It consists essentially of a cylindrical chamber with a light-tight cover, a collimator to admit and define the incident beam, a beam stop to confine and stop the transmitted beam, a means for holding the film tightly against the inside circumference of the camera, and a spec-

Figure 1 Hull/Debye–Scherrer camera, with cover plate removed. (Courtesy of Philips Electronic Instruments, Inc.)

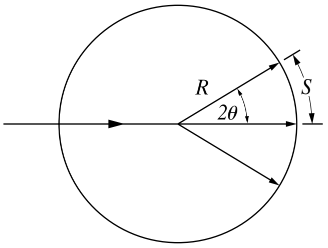

Figure 2 Geometry of the Hull/Debye–Scherrer method. Section through film and one diffraction cone.

imen holder that can be rotated. The collimator is important not only to define the area of the sample irradiated but also to produce a beam consisting of rays as nearly parallel as possible.

Camera diameters vary from about 5 to about 20 cm. The greater the diameter, the greater the resolution or separation of a particular pair of lines on the film. In spectroscopy, resolving power is the power of distinguishing between two components of radiation which have wavelengths very close together and is given by $\lambda/\Delta\lambda$, where $\Delta\lambda$ is the difference between the two wavelengths and λ is their mean value; in crystal-structure analysis, resolving power is the ability to separate diffraction lines from sets of planes of very nearly the same spacing, or as the value of $d/\Delta d$.[1] Thus, if S is the distance measured on the film from a particular diffraction line to the point where the transmitted beam would strike the film (Fig. 2), then

$$S = 2\theta R$$

and

$$\Delta S = R\Delta 2\theta, \tag{1}$$

where R is the radius of the camera. Two sets of planes of very nearly the same spacing will give rise to two diffracted beams separated by a small angle $\Delta 2\theta$; for a given value of $\Delta 2\theta$, Eq. (1) shows that ΔS, the separation of the lines on the film, increases with R. The resolving power may be obtained by differentiating
Bragg's law:

$$\lambda = 2d \sin \theta$$

$$\frac{\mathrm{d}\theta}{\mathrm{d}d} = \frac{-1}{d} \tan \theta. \tag{2}$$

But

$$\mathrm{d}\theta = \frac{\mathrm{d}S}{2R}.$$

---

[1] Resolving power is often defined by the quantity $\Delta\lambda/\lambda$, which is the reciprocal of that given above. However, the *power* of resolving two wavelengths which are nearly alike is a quantity which should logically *increase* as $\Delta\lambda$, the difference between the two wavelengths to be separated, decreases. This is the reason for the definition given in the text. The same argument applies to interplanar spacings d.

Therefore

$$\frac{dS}{dd} = \frac{-2R}{d} \tan \theta$$

$$\text{Resolving power} = \frac{d}{\Delta d} = \frac{-2R}{\Delta S} \tan \theta, \qquad (3)$$

where d is the mean spacing of the two sets of planes, Δd the difference in their spacings, and ΔS the separation of two diffraction lines which appear just resolved on the film. Equation (3) shows that the resolving power increases with the size of the camera; this increased resolution is obtained, however, at the cost of increased exposure time, and the smaller cameras are usually preferred for all but the most complicated patterns. A camera diameter of 5.73 cm is often used and will be found suitable for most work. This particular diameter, equal to 1/10 the number of degrees in a radian, facilitates calculation, since θ (in degrees) is obtained simply by multiplication of S (in cm) by 10, except for certain corrections necessary in precise work. Equation (3) also shows that the resolving power of a given camera increases with θ, being directly proportional to $\tan \theta$.

The increased exposure time required by an increase in camera diameter is due not only to the decrease in intensity of the diffracted beam with increased distance from the specimen, but also to the partial absorption of both the incident and diffracted beams by the air in the camera. For example, the curves of Fig. 3 show that, in a camera of 19 cm diameter (about the largest in common use), the decrease in intensity due to air absorption is about 18 percent for Cu $K\alpha$ radiation and about 48 percent for Cr $K\alpha$ radiation. This decrease in intensity may be avoided by evacuating the camera or by filling it with a light gas such as hydrogen or helium during the exposure.

Correct design of the pinhole system which collimates the incident beam is important, especially when weak diffracted beams must be recorded. The exit pinhole scatters x-rays in all directions, and these scattered rays, if not prevented from striking the film, can seriously increase the intensity of the background. A "guard-

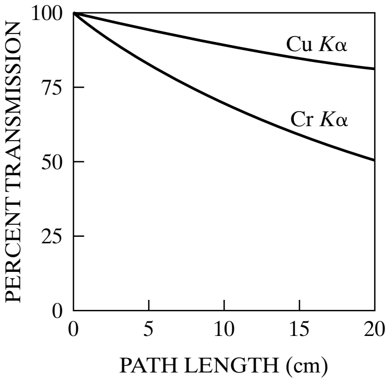

Figure 3 Absorption of Cu $K\alpha$ and Cr $K\alpha$ radiation by air.

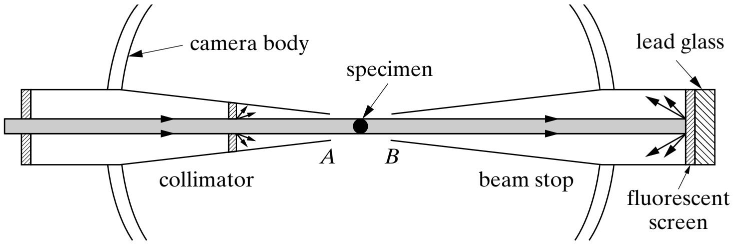

Figure 4 Design of collimator and beam stop (schematic).

ed-pinhole" assembly which practically eliminates this effect is shown in Fig. 4, where the divergent and convergent rays in the incident beam are ignored and only the parallel component is shown. The collimator tube is extended a considerable distance beyond the exit pinhole and constricted so that the end *A* is close enough to the main beam to confine the radiation scattered by the exit pinhole to a very narrow angular range and yet not close enough to touch the main beam and be itself a cause of further scattering. The beam stop is usually a thick piece of lead glass placed behind a fluorescent screen, the combination allowing the transmitted beam to be viewed with safety when adjusting the camera in front of the x-ray tube. Back scatter from the stop is minimized by extending the beam-stop tube backward and constricting its end *B*. Another reason for extending the collimator and beam-stop tubes as close to the specimen as possible is to minimize the extent to which rays scattered by air from the primary beam can reach the film. Both tubes are tapered to interfere as little as possible with low-angle and high-angle diffracted beams.

Some cameras have rectangular slits rather than pinholes to define the beam, the long edges of the slits being parallel to the axis of the specimen. The use of slits instead of pinholes decreases exposure time by increasing the irradiated volume of the specimen, but requires more accurate positioning of the camera relative to the source and produces diffraction lines which are sharp only along the median line of the film.

3 SPECIMEN PREPARATION

Metals and alloys may be converted to powder by filing or, if they are sufficiently brittle, by grinding in a small agate mortar. In either case, the powder should be filed or ground as fine as possible, preferably to pass a 325-mesh screen, in order to produce smooth, continuous diffraction lines. The screened powder is usually annealed in evacuated glass or quartz capsules in order to relieve the strains due to filing or grinding. These strains are so low in extremely brittle solids (most minerals and ceramics) that annealing may be omitted.

Special precautions are necessary in screening two-phase alloys. If a small, representative sample is selected from an ingot for x-ray analysis, then that entire sample must be ground or filed to pass through the screen. The common method of grinding until an amount sufficient for the x-ray specimen has passed the screen, the oversize being rejected, may lead to very erroneous results. One phase of the alloy is usually more brittle than the other, and that phase will more easily be ground into fine particles; if the grinding and screening are interrupted at any point, then the material remaining on the screen will contain less of the more brittle phase than the original sample while the undersize will contain more, and neither will be representative.

The final specimen for the Hull/Debye–Scherrer camera should be in the form of a thin rod, 0.5 mm or less in diameter and about 1 cm long. There are various ways of preparing such a specimen, one of the simplest being to coat the powder on the surface of a fine glass fiber with a small amount of glue or petroleum jelly. Other methods consist in packing the powder into a thin-walled capillary tube made of a weakly absorbing substance such as cellophane or lithium borate glass, or in extruding a mixture of powder and binder through a small hole. Polycrystalline wires or polymer fibers may be used directly, but since they usually exhibit some preferred orientation, the resulting diffraction pattern must be interpreted with that fact in mind. Strongly absorbing substances may produce split low-angle lines; if this effect becomes troublesome, it may be eliminated by diluting the substance involved with some weakly absorbing substance, so that the absorption coefficient of the composite specimen is low. Both flour and cornstarch have been used for this purpose. The diluent chosen should not produce any strong diffraction lines of its own and too much of it should not be used, or the lines from the substance being examined will become spotty. These and other details of specimen preparation are described elsewhere [G.28].

After the specimen rod is prepared, it is mounted in its holder so that it will lie accurately along the rotation axis of the camera when the specimen holder is rotated. This adjustment is made by viewing the specimen through a short-focus lens or low-power microscope temporarily inserted into the camera in place of the beam-stop tube; the specimen holder is then adjusted so that the specimen does not appear to wobble when the holder is rotated. Rotation of the specimen during the exposure is common practice but not an intrinsic part of the powder method; its only purpose is to produce continuous, rather than spotty, diffraction lines by increasing the number of powder particles in diffracting positions.

4 FILM AND OTHER DETECTION MEDIA

Fluorescent Screens

Fluorescent screens are made of a thin layer of zinc sulfide, containing a trace of nickel, mounted on a cardboard backing. Under the action of x-rays, this compound fluoresces in the visible region, i.e., emits visible light, in this case yellow light. Other phosphors are also used. Although most diffracted beams are too weak to be detected by this method, fluorescent screens are widely used in diffraction work to locate the position of the primary beam when adjusting apparatus. In cameras such screens often find use as intensifiers for photographic emulsions.

Photographic Film

Photographic film is affected by x-rays in much the same way as by visible light. However, the emulsion on ordinary film is too thin to absorb much of the incident x-radiation, and only absorbed x-rays can be effective in blackening the film. For this reason, x-ray films are made with rather thick layers of emulsion on both sides in order to increase the total absorption. (Division of the total emulsion thickness into two layers permits easier penetration of the film-processing solutions.) The grain size is also made large for the same purpose: this has the unfortunate consequence that x-ray films are grainy, do not resolve fine detail, and cannot stand much enlargement.

Because the mass absorption coefficient of any substance varies with wavelength, it follows that film sensitivity, i.e., the amount of blackening caused by x-ray beams of the same intensity, depends on their wavelength. This should be borne in mind whenever white radiation is recorded photographically; for one thing, this sensitivity variation alters the effective shape of the continuous spectrum. Figure 5(a) shows the intensity of the continuous spectrum as a function of wavelength and (b) the variation of film sensitivity. This latter curve is merely a plot of the mass absorption coefficient of silver bromide, the active ingredient of the emulsion, and is marked by discontinuities at the *K* absorption edges of silver and bromine. (Note, incidentally, how much more sensitive the film is to the *K* radiation from copper than to the *K* radiation from molybdenum, other things being equal.) Curve (c) of Fig. 5 shows the net result, namely the amount of film blackening caused by the various wavelength components of the continuous spectrum, or what might be called the “effective photographic intensity” of the continuous spectrum. These curves are only approximate, however, and in practice it is almost impossible to measure photographically the relative intensities of two beams of different wavelength. On the other hand, the relative intensities of beams of the *same* wavelength can be accurately measured by photographic means, and such measurements are described in Sec. 16.

The Polaroid Land rapid-process system of photography has been adapted to some kinds of diffraction equipment. The Polaroid film is backed by an intensifying screen which converts x-rays to visible light that can darken the film. X-ray exposures are about one tenth of those required by x-ray film, and finished prints are available about ten seconds after the x-ray exposure.

Image Plates

Originally developed for medical radiology, image plates consist of a thick x-ray sensitive phosphor (typically 150 μm of BaFBr:Eu^{2+} or more recently BaF(Br,I):Eu^{2+}) on a flexible plastic backing. X-rays incident on the 5 μm diameter

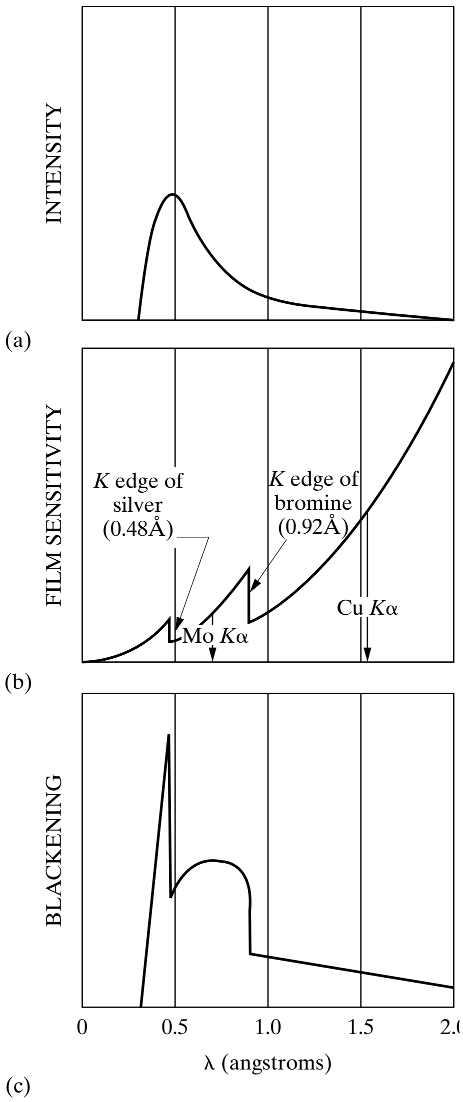

Figure 5 Relation between film sensitivity and effective shape of continuous spectrum (schematic): (a) continuous spectrum from a tungsten target at 40kV; (b) film sensitivity; (c) blackening curve for spectrum shown in (a).

grains of the phosphor ionize a fraction of the Eu^{2+} ions to Eu^{3+}, and the liberated electrons are trapped at F-centers.[2] During nondestructive reading of the exposed plate, illumination by visible light (typically a very small diameter He-Ne laser

---

[2] F centers are point defects and are also called color centers: in NaCl, for example, a vacancy in the Cl sub-lattice is one type of F center and can capture electrons and absorb light photons.

beam with 632.8 nm wavelength) liberates the trapped electrons to the conduction band. The electrons then recombine with Eu^{3+} ions, converting them to Eu^{2+} and producing light characteristic of the transition, i.e., with 398 nm wavelength. The wavelength of this photostimulated emission is far enough from that of the stimulating light that a conventional photomultiplier tube can be used to collect the light emitted from picture elements (pixels) down to 25 μm × 25 μm in size. Any residual image can be erased simply by exposing the image plate to a large dose of visible light. This reusable x-ray "film" has a dynamic range of five orders of magnitude, which is comparable to that of electronic detectors. Image plates are also much faster than x-ray film, typically 35 times faster than Polaroid Type 57 film and 500 times faster than Kodak SR-5 x-ray film [2], and have very high efficiencies. More information can be found elsewhere [3, 4].

5 FILM LOADING

The film for Hull/Debye–Scherrer is a narrow strip punched with one or two holes. Normally x-ray film for Hull/Debye–Scherrer cameras comes in rolls of the correct width and must be punched and cut to the right length.

Figure 6 illustrates three methods of arranging the film strip. The small sketches on the right show the loaded film in relation to the incident beam, while the films laid out flat are indicated on the left. In (a), a hole is punched in the center of the film so that the film may be slipped over the beam stop; the transmitted beam thus *leaves* through the hole in the film. The pattern is symmetrical about the center, and the θ value of a particular reflection is obtained by measuring U, the distance apart of two diffraction lines formed by the same cone of radiation, and using the relation

$$4\theta R = U. \tag{4}$$

Photographic film always shrinks slightly during processing and drying, and this shrinkage effectively changes the camera radius. The film-shrinkage error may be minimized by slipping the ends of the film under metal knife-edges which cast a sharp shadow near each end of the film. In this way, a standard distance is impressed on the film which will shrink in the same proportion as the distance between a given pair of diffraction lines. If the angular separation $4\theta K$ of the knife-edges in the camera is known, either by direct measurement or by calibration with a substance of known lattice parameter, then the value of θ for a particular reflection may be obtained by simple proportion:

$$\frac{\theta}{\theta_K} = \frac{U}{U_K}, \tag{5}$$

where U_K is the distance apart of the knife-edge shadows on the film.

Figure 6(b) illustrates a method of loading the film which is just the reverse of the previous one. Here the incident beam *enters* through the hole in the film, and θ is obtained from the relation

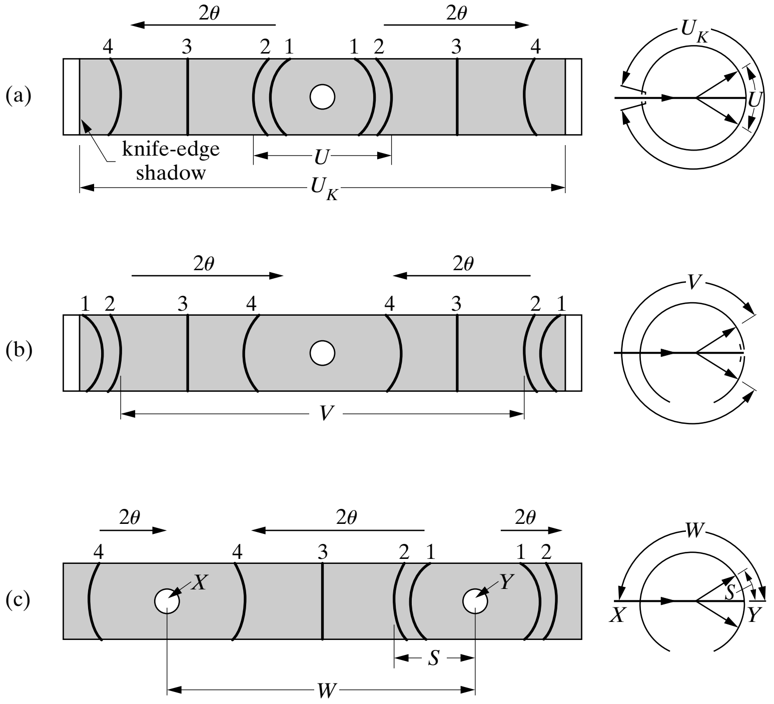

Figure 6 Methods of film loading in Hull/Debye–Scherrer cameras. Coresponding lines have the same numbers in all films.

$$(2\pi - 4\theta)R = V. \tag{6}$$

Knife-edges may also be used in this case as a basis for film-shrinkage corrections.

The unsymmetrical, or Straumanis, method of film loading is shown in Fig. 6(c). Two holes are punched in the film so that it may be slipped over both the entrance collimator and the beam stop. Since it is possible to determine from measurements on the film where the incident beam entered the film circle and where the transmitted beam left it, no knife-edges are required to make the film-shrinkage correction. The point $X(2\theta = 180°)$, where the incident beam entered, is halfway between the measured positions of lines 4,4; similarly, the point $Y(2\theta = 0°)$, where the transmitted beam left, is halfway between lines 1,1. The difference between the positions of X and Y gives W, and θ is found by proportion:

$$\frac{2\theta}{\pi} = \frac{S}{W}. \tag{7}$$

Unsymmetrical loading thus provides for the film-shrinkage correction without calibration of the camera or knowledge of any camera dimension. It is the most popular film arrangement.

The shapes of the diffraction lines in Fig. 6 should be noted. The low-angle lines are strongly curved because they are formed by cones of radiation which have a small apex angle 4θ. The same is true of the high-angle lines, although naturally they are curved in the opposite direction. Lines for which 4θ is nearly equal to 180° are practically straight. This change of line shape with change in θ may also be seen in the powder photographs.

6 CAMERAS FOR SPECIAL CONDITIONS

Various kinds of special cameras have been devised for obtaining diffraction patterns from specimens subjected to unusual conditions of temperature or pressure. These cameras, usually of the Hull/Debye–Scherrer or flat plate types and usually custom-built, have designs that vary from laboratory to laboratory.

High-Temperature Cameras

Materials investigations frequently require that the crystal structure of a phase stable only at high temperature be determined. In many cases, this can be accomplished by quenching the specimen at a high enough rate to suppress the decomposition of the high-temperature phase and then examining the specimen in an ordinary camera at room temperature. In other cases, the transformation into the phases stable at room temperature cannot be suppressed, and a high-temperature camera is necessary in order that the specimen may be examined at the temperature at which the phase in question is stable. Such a camera may also be used to determine coefficients of thermal expansion from measurements of lattice parameters as a function of temperature.

High-temperature cameras all involve a small furnace, usually of the electric-resistance type, to heat the specimen and a thermocouple to measure its temperature. The main design problem is to keep the film cool without too great an increase in the camera diameter; this requires water-cooling of the body of the camera and/or the careful placing of radiation shields between the furnace and the film, shields so designed that they will not interfere with the diffracted x-ray beams. The furnace which surrounds the specimen must also be provided with a slot of some kind to permit the passage of the incident and diffracted beams. If the specimen is susceptible to oxidation at high temperatures, means of evacuating the camera or of filling it with an inert gas must be provided; or the powder specimen may be sealed in an evacuated thin-walled silica tube. Because of the small size of the furnace in a high-temperature camera, the temperature gradients in it are usually quite steep, and special care must be taken to ensure that the temperature recorded by the thermocouple is actually that of the specimen itself. Specimen temperatures as high as 3000ºC have been attained. Since the intensity of any reflection is decreased by an increase in temperature, the exposure time required for a high-temperature diffraction pattern is normally rather long.

Low-Temperature Cameras

These cameras are usually designed for specimen temperatures down to about –150°C. Diffraction studies at still lower temperatures can be more easily made with the diffractometer.

The simplest cooling method is to run a thin stream of coolant, such as liquid air, over the specimen throughout the x-ray exposure. The diffraction pattern of the coolant will also be recorded but this is easily distinguished from that of a crystalline solid, because the typical pattern of a liquid contains only one or two very diffuse maxima in contrast to the sharp diffraction lines from a solid. Scattering from the liquid will, however, increase the background blackening of the photograph.

A better method is to cool the specimen with a stream of cold gas. Liquid nitrogen, for example, boils at 77°K (= –196°C) and can easily produce nitrogen gas at the specimen at about –150°C. Gas produces much less background scattering than a liquid coolant.

High-Pressure Cameras

Many substances have quite different crystal structures at high pressure. Usually these structures exist only under pressure, and their study necessarily requires high-pressure cameras. Maximum pressures reached in such cameras are of the order of 500 kilobars (1 bar = 10^5 MPa^2 = 14.5 lb/in^2 $\approx$ 1 atmosphere).

Camera design involves the difficult problem of applying large forces to the specimen and simultaneously getting x-ray beams into and out of it. Hydrostatic pressures up to about 5 kbars have been achieved in cameras operated under gas pressure. Higher pressures are obtained by compressing the specimen between anvils, either uniaxially or tetrahedrally (along directions, in cubic notation, of the form {111}).

7 SEEMANN–BOHLIN CAMERA

The geometrical focusing used in the Bragg–Bretano (θ-2θ) and Seemann-Bohlin diffractometers is exploited in the Seemann–Bohlin camera shown in Fig. 7. The slit S acts as a virtual line source of x-rays, the actual source being the extended focal spot on the target T of the x-ray tube. Only converging rays from the target can enter this slit and, after passing it, they diverge to the specimen AB. For a particular *hkl* reflection, each ray is then diffracted through the same angle 2θ, with the result that all diffracted rays from various parts of the specimen converge to a focus at F. As in any powder method, the diffracted beams lie on the surfaces of cones whose axes are coincident with the incident beam; in this case, a number of incident beams contribute to each reflection, and a diffraction line is formed by the intersection of a number of cones with the film.

The ends of the film strip are covered by knife-edges M and N, which cast reference shadows on the film. The value of θ for any diffraction line may be found from the distance U, measured on the film, from the line to the shadow of the low-angle knife-edge N, by use of the relation

$$4\theta R = U + \text{arc } SABN. \tag{8}$$

In practice, θ is found by calibrating the camera with an internal standard of known lattice parameter, such as NaCl, rather than by the use of Eq. (8). Differentiation of Eq. (8), yields

$$\mathrm{d}\theta = \frac{\mathrm{d}U}{4R}. \tag{9}$$

This relation may be combined with Eq. (2) to give

$$\frac{\mathrm{d}U}{\mathrm{d}d} = -\frac{4R}{d}\tan\theta.$$

$$\text{Resolving power} = \frac{d}{\Delta d} = -\frac{4\mathrm{R}}{\Delta \mathrm{U}}\tan\theta. \tag{10}$$

The resolving power, or ability to separate diffraction lines from planes of almost the same spacing, is therefore twice that of a Hull/Debye–Scherrer camera of the same radius. In addition, the exposure time is much shorter, because a much larger specimen is used (the arc AB of Fig. 7 is of the order of 1 cm) and diffracted rays from a considerable volume of material are all brought to one focus. The Seemann–Bohlin camera is, therefore, useful in studying complex diffraction patterns, whether they are due to a single phase or to a mixture of phases such as occur in alloy systems.

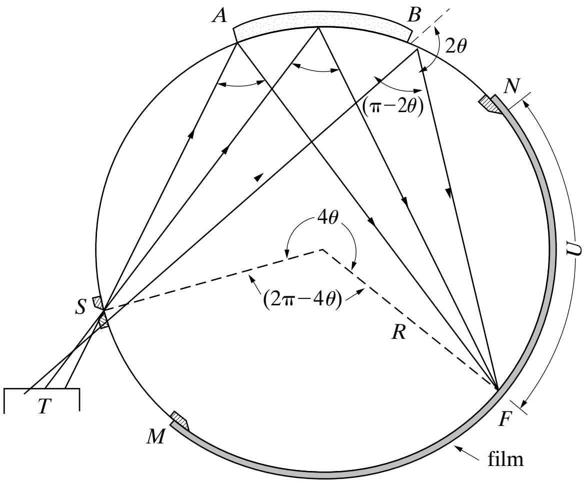

Figure 7 Seemann-Bohlin focusing camera. Only one *hkl* reflection is shown.

On the debit side, the Seemann–Bohlin camera has the disadvantage that the lines registered on the film cover only a limited range of 2θ values, particularly on the low-angle side. The Seemann–Bohlin camera, in itself, is now virtually obsolete (the diffractometer has greater resolution), except in combination with a monochromator. The combination is then called a Guinier camera (Sec. 14).

8 BACK-REFLECTION FOCUSING CAMERAS

The most precise measurement of lattice parameter is made in the back-reflection region. The most suitable camera for such measurements is the symmetrical back-reflection focusing camera illustrated in Fig. 8.

It employs the same focusing principle as the Seemann-Bohlin camera, but the film straddles the slit and the specimen is placed diametrically opposite the slit. Means are usually provided for slowly oscillating the specimen through a few degrees about the camera axis in order to produce smooth diffraction lines. A typical film, punched in the center to allow the passage of the incident beam, is shown in Fig. 8. The value of θ for any diffraction line may be calculated from the relation

$$(4\pi - 8\theta)R = V, \tag{11}$$

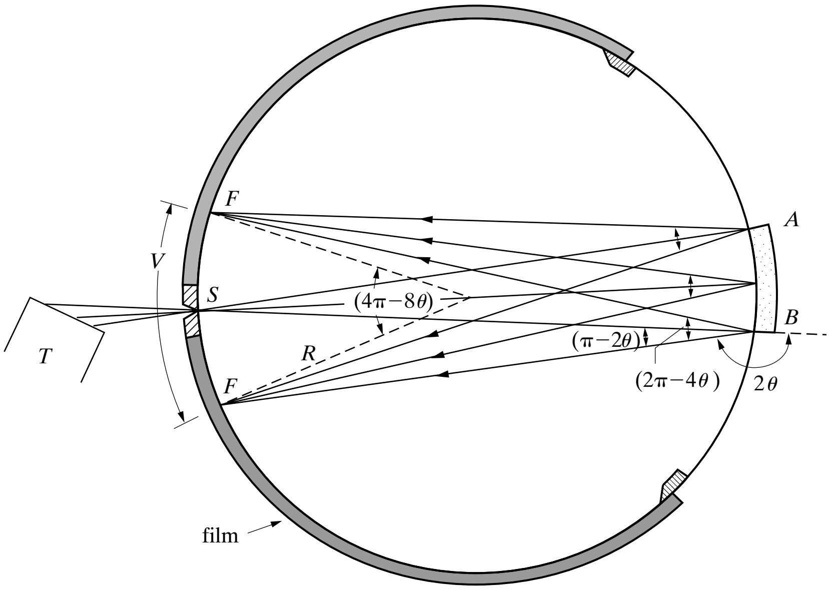

Figure 8 Symmetrical back-reflection focusing camera. Only one *hkl* reflection is shown.

where V is the distance on the film between corresponding diffraction lines on either side of the entrance slit.

Differentiation of Eq. (11) gives

$$\Delta\theta = \frac{-1}{4R}\,\Delta\left(\frac{V}{2}\right), \tag{12}$$

where $\Delta(V/2)$ is the separation on the film of two reflections differing in Bragg angle by $\Delta\theta$. Combination of this equation with Eq. (2) shows that

$$\text{Resolving power} = \frac{d}{\Delta d} = \frac{4\text{R}}{\Delta(\text{V}/2)}\tan\theta. \tag{13}$$

The resolving power of this camera is therefore the same as that of a Seemann–Bohlin camera of the same diameter.

In the pattern shown in Fig. 9, two pairs of closely spaced lines can be seen, lines 1 and 2 and lines 4 and 5. Each pair is a doublet formed by reflection from one set of planes of the two components, $K\alpha_1$ and $K\alpha_2$, which make up $K\alpha$ radiation. These component lines are commonly found to be resolved, or separated, in the back-reflection region. (The β lines in this photograph are not resolved since $K\beta_1$ radiation consists only of a single wavelength.) To determine the conditions under which a given camera can separate two components of radiation which have almost the same wavelength, the spectroscopic definition of resolving power must be employed namely $\lambda/\Delta\lambda$, where $\Delta\lambda$ is the difference between the two wavelengths and λ is their mean value. For Cu $K\alpha$ radiation, these wavelengths are:

$$\lambda(\text{Cu } K\alpha_2) = 1.54439 \text{ Å*}$$

$$\lambda(\text{Cu } K\alpha_1) = \underline{1.54056}$$

$$\Delta\lambda = 0.00383$$

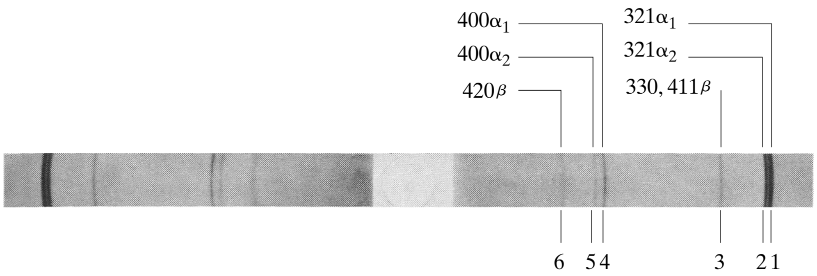

Figure 9 Powder photograph of tungsten made in a symmetrical back-reflection focusing camera, 4.00 in. (10.16 cm) in diameter. Unfiltered copper radiation.

Therefore

$$\frac{\lambda}{\Delta\lambda} = \frac{1.542}{0.00383} = 403.$$

The resolving power of the camera must exceed this value, for the particular reflection considered, if the component lines are to be separated on the film.

Differentiating Bragg's law, yields

$$\lambda = 2d \sin \theta$$

$$\frac{d\theta}{d\lambda} = \frac{1}{2d \cos \theta} = \frac{\tan \theta}{2d \sin \theta} = \frac{\tan \theta}{\lambda}$$

$$\frac{\lambda}{\Delta\lambda} = \frac{\tan \theta}{\Delta\theta}. \tag{14}$$

Substitution of Eq. (12) gives

$$\text{Resolving power} = \frac{\lambda}{\Delta\lambda} = \frac{-4R\tan \theta}{\Delta(V/2)}. \tag{15}$$

The negative sign here can be disregarded; it merely means that an increase in λ causes a decrease in $V/2$, since the latter is measured from the center of the film. Equation (15) demonstrates that the resolving power increases with the camera radius and with θ, becoming very large near 90°. This latter point is clearly evident in Fig. 9, which shows a greater separation of the higher-angle 400 reflections as compared to the 321 reflections.

By use of Eq. (15), the resolving power can be calculated for the 321 reflections, and the camera used to obtain Fig. 9. The camera radius is 2.00 in. (5.08 cm), and the mean θ value for these reflections is about 65.7°. The line breadth at half maximum intensity is about 0.04 cm. The two component lines of the doublet will be clearly resolved on the film if their separation is twice their breadth (Fig. 10). Therefore

$$\Delta\left(\frac{V}{2}\right) = 2(0.04) = 0.08\text{cm}$$

$$\frac{\lambda}{\Delta\lambda} = \frac{(4)(2.00)(2.54)(\tan 65.7^{\circ})}{(0.08)} = 563.$$

Since this value exceeds the resolving power of 403, found above to be necessary for resolution of the Cu $K\alpha$ doublet, this doublet should be resolved for the 321 reflection, and such is seen to be the case in Fig. 9. At some lower angle, this would not be true and the two components would merge into a single, unresolved line. The fact that resolution of the $K\alpha$ doublet normally occurs only in the back-reflection region can be seen from the Hull/Debye–Scherrer photographs.

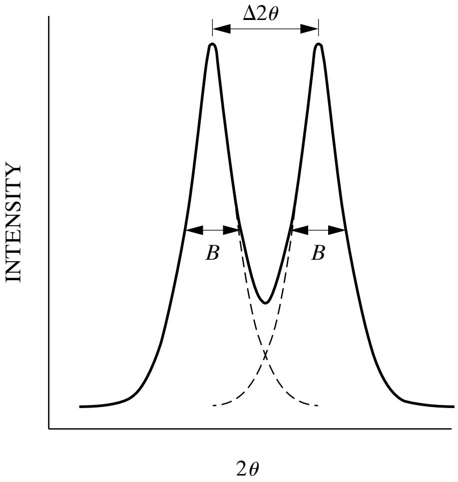

Figure 10 Resolution of closely spaced lines. The lines shown have $\Delta 2\theta = 2B$. Any smaller separation might make the two lines appear as one.

9 PINHOLE PHOTOGRAPHS

When "monochromatic" radiation is used to examine a "powder" specimen in a Laue (flat-film) camera, the result is often called, for no particularly good reason, a pinhole photograph. It is also called a flat-plate photograph. (There is no general agreement on the name of this method. Klug and Alexander [G.17], for example, call it the "monochromatic-pinhole technique.") Either a transmission or a back-reflection camera may be used. A typical transmission photograph recorded on standard x-ray film is shown in Fig. 11 for a sample of fine-grained aluminum sheet. This geometry is used in commercially available diffraction apparatus using two-dimensional detectors such as CCD's or multiwire proportional counters. Output from a multiwire detector system is shown in Fig. 12; note that the detector was not perpendicular to the incident x-ray beam when this pattern was recorded. This method is also becoming increasing popular with image plates at synchrotron radiation sources; monochromatic radiation is normally used. Polychromatic synchrotron radiation, however, can be used profitably for highly textured samples: a filter possessing an absorption edge at an appropriate wavelength can help in the identification of which features in the pattern are formed by a given diffraction plane [5]. One such pattern recorded in the transmission geometry appears in Fig. 13.

The pinhole method has the advantage that an entire Debye ring, and not just a part of it, is recorded on the film. On the other hand, the range of θ values which are recorded is rather limited: either low-angle or high-angle reflections may be obtained, but not those in the median range of θ (see Fig. 14). One can, of course, rotate the flat sheet of film from the orientations shown, but only partial cones will be recorded. It is also possible to make a cylinder of film whose axis is the incident beam (Fig. 15); cameras with this design are commercially available. In the transmission method, the value of θ for a particular reflection is found from the relation

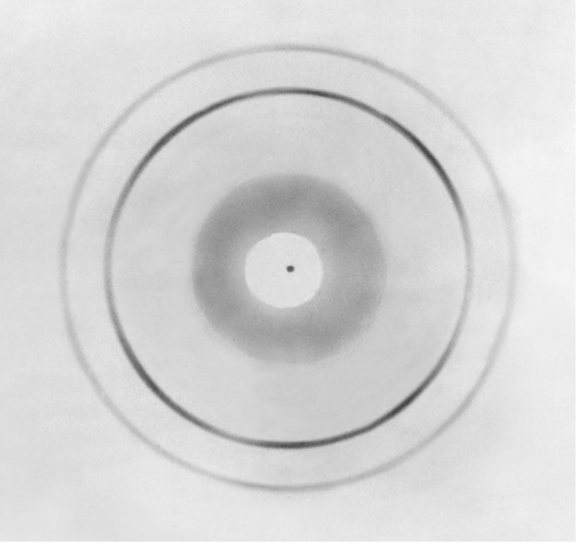

Figure 11 Transmission pinhole photograph of an aluminum sheet specimen. Filtered copper radiation. (The diffuse circular band near the center is caused by white radiation. The nonuniform blackening of the Debye rings is due to preferred orientation in the specimen.)

$$\tan 2\theta = \frac{U}{2D}, \tag{16}$$

where U = diameter of the Debye ring and D = specimen-to-film distance. The corresponding relation for the back-reflection method is

$$\tan(\pi - 2\theta) = \frac{V}{2D}, \tag{17}$$

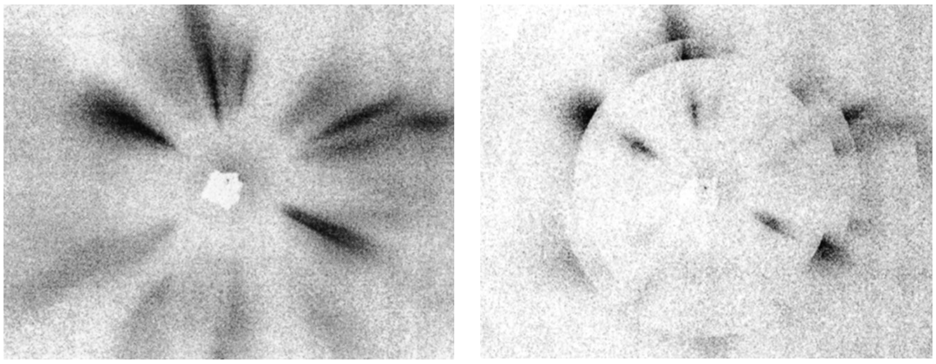

Figure 12 Diffraction patterns collected with a two-dimensional multiwire detector of random (left) and oriented (right) thin film samples of yttrium barium copper oxide. (Data courtesy of T.A. Polley, D.W. Stollberg and Microcoating Technologies.)

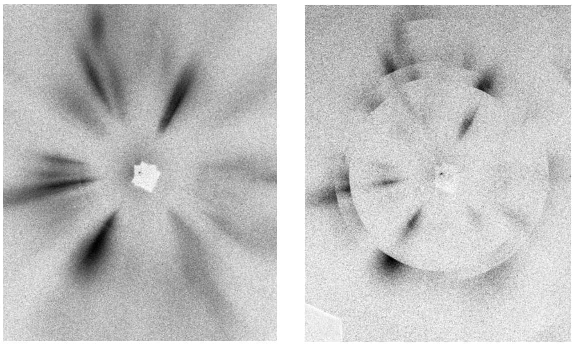

Figure 13 Transmission pinhole diffraction pattern using synchrotron white radiation of an aluminum sample deformed in torsion. The pattern at the left was recorded without and pattern at the right with a palladium filter inserted in the beam; the two sharp changes in contrast in the right-hand pattern show the positions (angles) at which grains are oriented for 111 and 200 diffraction of the Pd K-edge wavelength (0.509 Å). [7.6]

where V = diameter of the Debye ring. The distance D is usually of the order of 3 to 5 cm.

Powder specimens may be prepared simply by spreading a bit of the powder mixed with a binder on any convenient support. For a transmission photograph a piece of paper or cellophane will do. If there is any doubt about diffraction from the support material, a control pattern without the specimen can be prepared.

However, the greatest utility of the pinhole method in materials work lies in the fact that polycrystalline specimens can be examined directly. In back reflection, a specimen, mounted in the usual 1-in. (25-mm) diameter plastic mount for microscopic examination, can be positioned so that the primary beam falls on any selected area: the advantage of being able to examine the same area of the specimen both with the microscope and with x-rays is obvious; it is worth noting also that both methods of examination, the optical and the x-ray, provide information only about the surface layer of the specimen. The transmission method is restricted to wire and sheet specimens which are not too highly absorbing.

There is an optimum specimen thickness for the transmission method, because the diffracted beams will be very weak or entirely absent if the specimen is either too thin (insufficient volume of diffracting material) or too thick (excessive absorp-

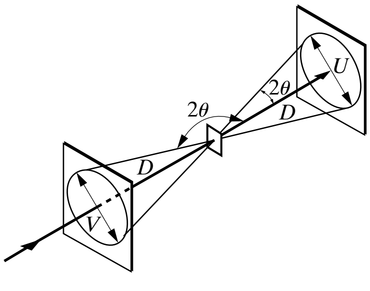

Figure 14 Angular relationships in the pinhole method.

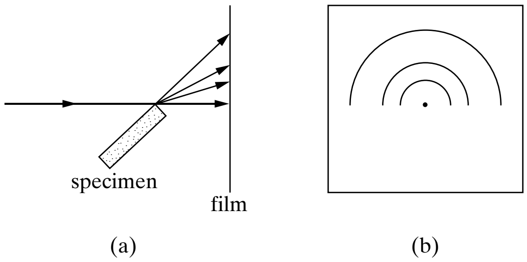

Figure 15 Transmission pinhole method for thick specimens: (a) section through incident beam: (b) partial pattern obtained.

tion). The specimen thickness which produces the maximum diffracted intensity is given by $1/\mu$, where μ is the linear absorption coefficient of the specimen. Inspection shows that this condition can also be stated as follows: a transmission specimen is of optimum thickness when the intensity of the beam transmitted through the specimen is $1/e$, or about 1/3, of the intensity of the incident beam. Normally this optimum thickness is of the order of a few thousandths of an inch (0.1 mm). There is one way, however, in which a partial transmission pattern can be obtained from a thick specimen and that is by diffraction from an edge (Fig. 15). Only the upper half of the pattern is recorded on the film, but that is all that is necessary in many applications. The same technique has also been used in some Hull/Debye–Scherrer cameras.

The pinhole method is used in studies of preferred orientation, grain size, and crystal quality. With a back-reflection camera, fairly precise lattice parameter measurements can be made by this method. Precise knowledge of the specimen-to-film distance D is not necessary, provided the proper extrapolation equation is used or the camera is calibrated. The calibration is usually performed for each exposure, simply by smearing a thin layer of the calibrating powder over the surface of the specimen; in this way, reference lines of known θ value are formed on each film.

When the pinhole method is used for lattice parameter measurements, the film or specimen, or both, is moved during the exposure to produce smooth, continuous diffraction lines. By rotating or oscillating the film about the axis of the incident beam, the reflections from each reflecting particle or grain are smeared along the Debye ring. The specimen itself may be rotated about the incident beam axis or about any axis parallel to the incident beam, or translated back and forth in any direction in a plane parallel to the specimen surface. Such movements increase the number of grains in diffracting positions and allow a greater proportion of the total specimen surface to take part in diffraction, thus ensuring that the information recorded on the film is representative of the surface as a whole. Any camera in which the specimen can be so moved during the exposure that the incident beam traverses a large part of its surface is called an *integrating camera*.

The camera has a motor to rotate the specimen for such integration. The sectored disc on the cassette of this camera is designed for recording two or more partial patterns on one film for comparative purposes. After the first pattern is made, the specimen is changed, the disc is rotated about the collimator by an amount sufficient to cover the previously exposed portion of film and uncover an unexposed portion, and the second exposure is made. Or the disc may be removed, in order to record complete Debye rings from a single specimen.

10 MICROBEAMS AND MICROCAMERAS

Sometimes one has only a minute amount of material from which a diffraction pattern has to be obtained. Or one may wish to obtain a pattern from only a very small region of a large specimen. In either case, a very small incident beam, called a *microbeam*, is needed, of the order of 100 μm ($= 0.1$ mm $= 4 \times 10^{-3}$ in.) or less in diameter. Beams with diameters on the order of 10 μm are routinely used with synchrotron radiation [7, 8], and beams smaller than 1 μm in diameter have beam obtained [9].

The central problem is the design and construction of the collimator and its placement relative to the focal spot of the x-ray tube. Hirsch [7.10] has discussed these matters. Collimators are often made of glass capillary tubing. If such collimators are used with ordinary x-ray tubes, the collimated beam will be weak and exposure times very long, because most of the x-rays coming from the tube are wasted. The proper procedure is to employ a microfocus tube. Use of perfect external reflection from the inner surface of glass capillary tubes with variable taper greatly increases the intensity of the microbeam compared to a pinhole collimator, and use of multiple capillaries to increase x-ray intensity still further appears very attractive [11]. The price that is paid for the smaller diameter, higher intensity beam is increased divergence.

While it may be possible to adapt an ordinary pinhole camera to some microbeam work simply by changing the collimator, better results will be obtained with a specially designed *microcamera* [10, G.17]. Such a camera will usually have a small specimen-to-focal-spot distance (to increase intensity and improve collimation), a small specimen-to-film distance (to reduce exposure time), and some arrangement for accurately positioning the specimen in the beam. Diffraction patterns of specimens amounting to as little as 10 micrograms have been obtained in such cameras.

11 CHOICE OF RADIATION

With any of the powder methods described above, the investigator must choose the radiation best suited to the problem at hand. In making this choice, the two most important considerations are:

1. The characteristic wavelength used should not be shorter than the K absorption edge of the specimen, or the fluorescent radiation produced will badly fog the film. In the case of alloys or compounds, it may be difficult or impossible to satisfy this condition for every element in the specimen.

2. Bragg's law shows that the shorter the wavelength, the smaller the Bragg angle for planes of a given spacing. Decreasing the wavelength will therefore shift every diffraction line to lower Bragg angles and increase the total number of lines on the film, while increasing the wavelength will have the opposite effect. The choice of a short or a long wavelength depends on the particular problem involved.

Whatever the radiation, the appropriate filter is used to suppress the $K\beta$ component of the radiation. All in all, Cu $K\alpha$ radiation is generally the most useful. It cannot be employed with ferrous materials, however, since it will cause fluorescent radiation from the iron in the specimen; instead, Co $K\alpha$, Fe $K\alpha$, or Cr $K\alpha$ radiation should be used.

Precise lattice-parameter measurements require that there be a number of lines in the back-reflection region, while some specimens may yield only one or two. This difficulty may be avoided by using unfiltered radiation, in order to have $K\beta$ as well as $K\alpha$ lines present.

12 BACKGROUND RADIATION

A good powder photograph has sharp intense lines superimposed on a background of minimum intensity. However, the diffraction lines themselves vary in intensity, because of the structure of the crystal itself, and an appreciable background intensity may exist, due to a number of causes. The two effects together may cause the weakest diffraction line to be almost invisible in relation to the background.

This background intensity is due to the following causes:

1. *Fluorescent radiation emitted by the specimen*. It cannot be too strongly emphasized that the characteristic wavelength used should be longer than the K absorption edge of the specimen, in order to prevent the emission of fluorescent radiation. Incident radiation so chosen, however, will not completely eliminate fluorescence, since the short-wavelength components of the continuous spectrum will also excite K radiation in the specimen. For example, suppose a copper specimen is being examined with Cu $K\alpha$ radiation of wavelength 1.542 Å from a tube operated at 30 kV. Under these conditions the short-wavelength limit is 0.413 Å. The K absorption edge of copper is at 1.380 Å. The $K\alpha$ component of the incident radiation will not cause fluorescence, but all wavelengths between 0.413 and 1.380 Å will. If a nickel filter is used to suppress the $K\beta$ component of the incident beam, it will also have the desirable effect of reducing the intensity of some of the short wavelengths which cause fluorescence, but it will not eliminate them completely, particularly in the wavelength region near 0.6 Å, where the intensity of the continuous spectrum is high and the absorption coefficient of nickel rather low.

It is sometimes possible to filter part of the fluorescent radiation from the specimen by placing the proper filter over the *film*. For example, if a steel specimen is examined with copper radiation, which is not generally advisable, the situation may be improved by covering the film with aluminum foil, because aluminum has a greater absorption for the fluorescent Fe $K\alpha$ radiation contributing to the background than for the Cu $K\alpha$ radiation forming the diffraction lines. In fact, the following is a good general rule to follow: if it is impossible to use a wavelength longer than the K absorption edge of the specimen, choose one which is considerably shorter and cover the film with a filter. Sometimes the air itself will provide sufficient filtration. Thus excellent patterns of aluminum can be obtained with Cu $K\alpha$ radiation, even though this wavelength (1.54 Å) is much shorter than the K absorption edge of aluminum (6.74 Å), simply because the Al $K\alpha$ radiation excited has such a long wavelength (8.34 Å) that it is almost completely absorbed in a few centimeters of air.

2. *Diffraction of the continuous spectrum*. Each crystal in a powder specimen forms a weak Laue pattern, because of the continuous radiation component of the incident beam. This is true whether or not that particular crystal has the correct orientation to diffract the characteristic component into the Debye ring. Many crystals in the specimen are therefore contributing only to the background of the photograph and not to the diffraction ring, and the totality of the Laue patterns from all the crystals is a continuous distribution of background radiation. If the incident radiation has been so chosen that very little fluorescent radiation is emitted, then diffraction of the continuous spectrum is the largest single cause of high background intensity in powder photographs.
3. *Diffuse scattering from the specimen itself*.
    a) Incoherent (Compton modified) scattering. This kind of scattering becomes more intense as the atomic number of the specimen decreases.
    b) Coherent scattering.
        (i) Temperature-diffuse scattering. This form is more intense with soft materials of low melting point.
        (ii) Diffuse scattering due to various kinds of imperfection in the crystals. Any kind of randomness or strain will cause such scattering.
4. *Diffraction and scattering from other than the specimen material*.
    a) Collimator and beam stop. This kind of scattering can be minimized by correct camera design, as discussed in Sec. 2.
    b) Specimen binder, support, or enclosure. The glue or other adhesive used to compact the powder specimen, the glass fiber to which the powder is attached, or the glass or fused-quartz tube in which it is enclosed all contribute to the background of the photograph, since these are all amorphous substances. The amount of these materials should be kept to the absolute minimum.

c) Air. Diffuse scattering from the air may be avoided by evacuating the camera or filling it with a light gas such as hydrogen or helium.

13 CRYSTAL MONOCHROMATORS

If a single crystal is set to diffract the strong $K\alpha$ component of the general radiation from an x-ray tube and this diffracted beam is used as the incident beam in a camera, then the causes of background radiation listed under (1) and (2) above can be completely eliminated. Since the other causes of background scattering are less serious, the use of crystal-monochromated radiation produces diffraction photographs of remarkable clarity. There are two kinds of monochromators in use, depending on whether the reflecting crystal is unbent or bent and cut.

As discussed in Sec 6-13, an unbent crystal is not a very efficient reflector, and a large gain in intensity may be obtained by using a bent and cut crystal, which operates on the focusing principle. The reduction in exposure time can be considerable. Note that the use of a monochromator produces a change in the relative intensities of the beams diffracted by the specimen. the usual polarization factor $(1 + \cos^2 2\theta)/2$, which is included, must be replaced by the factor $(1 + \cos^2 2\alpha \ \cos^2 2\theta)/(1 + \cos^2 2\alpha)$, where 2α is the diffraction angle in the monochromator (see Fig. 16).

14 GUINIER CAMERAS [G.13, G.17]

The focusing monochromator is best used with powder cameras especially designed to take advantage of the particular property of the diffracted beam, namely its focusing action. A cylindrical camera (Fig. 16) is used with the specimen and film arranged on the surface of the cylinder. Low-angle reflections are registered with the camera placed in position C, in which case the specimen D must be thin enough to be examined in transmission. High-angle reflections are obtained by back reflection with the camera in position C', shown dashed, and the specimen at D'; the geometry of the camera is then exactly similar to that of the Seemann-Bohlin camera, the focal point F of the monochromatic beam acting as a virtual source of divergent radiation. In either case, the diffracted rays from the specimen are focused on the film for all hkl reflections; the only requirement is that the film be located on a circle passing through the specimen and the point F.

The combination of a focusing monochromator and a focusing camera is known as a Guinier camera, pioneered by Guinier in the late 1930s. Later investigators produced variants known by hyphenated names. Thus, the Guinier-de Wolff "cam-

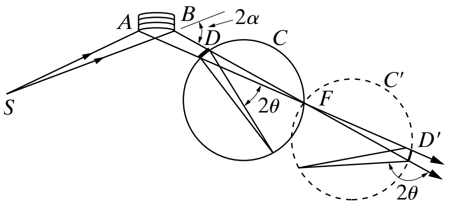

Figure 16 Cameras used with focusing monochromators. Only one diffracted beam is shown in each case. After Guinier [G.13].

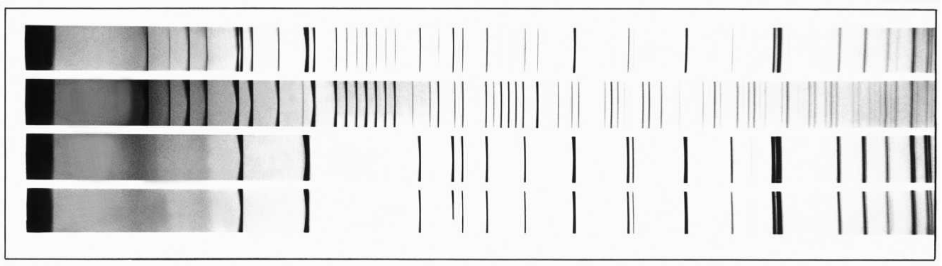

Figure 17 Single film with four powder patterns, made with Guinier-de Wolff camera. The two bottom patterns are of quartz, the third from the bottom is of ammonium alum, and the top one is of a mixture of quartz and ammonium alum. The range of 2θ angles is 4° to 82°. (Courtesy of Enraf-Nonius Inc., Delft.)

era" [12] is a set of two, or four, Guinier cameras stacked one above the other and separated by baffles; patterns from two or four different specimens are registered simultaneously on one piece of film (Fig. 17): this arrangement is possible because the beam from the monochromator in Fig. 16 is physically wide enough normal to the plane of the drawing to be split into two or four beams. The Guinier-Jagodzinski "camera" [13] has two cameras on one support, arranged as in Fig. 16 but symmetrically with respect to the incident beam, one for transmission and one for back reflection: three specimens can be examined simultaneously in each camera.

Compared to a Hull/Debye-Scherrer camera of the same size, operated directly from the x-ray tube, a Guinier camera provides a much clearer pattern with twice the resolution and about the same exposure time, but any one Guinier camera covers only a limited range of 2θ. It is best suited to the examination of particular parts of complex patterns.

15 MEASUREMENT OF LINE POSITION

The solution of any powder photograph begins with the measurement of the positions of the diffraction lines on the film. Measurements are made using a light box with an opal-glass plate on top, illuminated from below, on which the film to be measured is placed. On top of the glass plate is a graduated scale carrying a slider equipped with a vernier and cross-hair; the cross-hair is moved over the illuminated film from one diffraction line to another and their positions noted. The film is usually measured without magnification. A low-power hand lens may be of occasional use, but magnification greater than 2 or 3 diameters usually causes the line to merge into the background and become invisible, because of the extreme graininess of x-ray film.

After the line positions are measured, their θ values are calculated from the appropriate equation for the camera involved; this can be done without great effort using various math software packages or spread sheets. But if no great precision is needed and many patterns are to be evaluated rapidly, both of these steps can be avoided in routine work by making a cardboard scale marked with θ values; this scale is placed next to the film and the θ value of each line read off. A separate scale will be needed for each size and type of camera. Scales giving directly the spacing d of the reflecting planes causing each line may also be made for any particular wavelength, such as Cu $K\alpha$.

16 MEASUREMENT OF LINE INTENSITY

Many diffraction problems require an accurate measurement of the integrated intensity, or the breadth at half maximum intensity, of a diffraction line on a powder photograph. For this purpose it is necessary to obtain a curve of intensity vs. 2θ for the line in question.

The intensity of an x-ray beam may be measured by the amount of blackening it causes on a photographic film. The photographic density (blackening) of a film is in turn measured by the amount of visible light the film will transmit, with an instrument called a *microphotometer* or microdensitometer. A photometer is an instrument that measures light intensity with some kind of photocell, and a microphotometer is one that operates with an extremely thin light beam, about 0.1 mm wide, defined by narrow slits. The x-ray film to be measured is slowly traversed across this beam, and the intensity of the light passing through the film is continuously measured with a photocell connected to a recording galvanometer. The result is a plot like that of Fig. 18.

The microphotometer is little used today because the detector of a diffractometer is faster, more accurate, and more sensitive. However, when only a camera is available or when circumstances are such that a camera is required (Sec. 1) then a microphotometer is the only means of measuring diffracted intensities quantitatively. Two-dimensional microdensitometers are also commercially available and are capable of digitizing film with pixel (picture element) sizes down to 25 μm. These are useful for flat-plate photographs. More information can be found in sources such as [G.17].

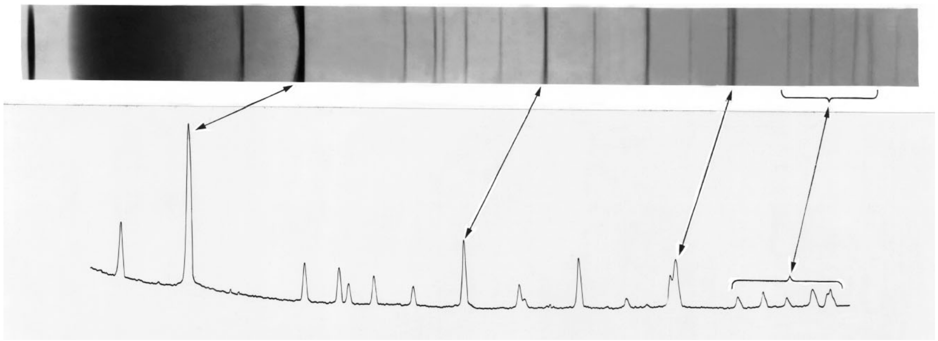

Figure 18 Powder pattern of quartz (above) and corresponding microphotometer trace (below). (Courtesy of U.S. Bureau of Mines.) [14]

PROBLEMS

***1** Plot a curve similar to that of Fig. 3 showing the absorption of Fe $K\alpha$ radiation by air. Take the composition and density of air. If a 1-hr exposure in air is required to produce a certain diffraction line intensity in a 19-cm-diameter camera with Fe $K\alpha$ radiation, what exposure is required to obtain the same line intensity with the camera evacuated, other conditions being equal?

***2** Derive an equation for the resolving power of a Hull/Debye–Scherrer camera for two wavelengths of nearly the same value, in terms of ΔS, where S is defined by Fig. 2.

3 For a Hull/Debye–Scherrer pattern made in a 5.73-cm-diameter camera with Cu $K\alpha$ radiation, calculate the separation of the components of the $K\alpha$ doublet in degrees and in centimeters for θ=10, 35, 60, and 85° .

***4** What is the smallest value of θ at which the Cr $K\alpha$ doublet will be resolved in a 5.73-cm-diameter Hull/Debye–Scherrer camera? Assume that the line width is 0.03 cm and that the separation must be twice the width for resolution.

5 A powder pattern of zinc is made in a Hull/Debye–Scherrer camera 5.73 cm in diameter with Cu $K\alpha$ radiation.

a) Calculate the resolving power necessary to separate the 11.0 and 10.3 diffraction lines.
b) Calculate the resolving power of the camera used, for these lines. Assume that the line width is 0.03 cm.
c) What minimum camera diameter is required to produce resolution of these lines?

REFERENCES

The following books are listed more or less in the order they are encountered in the text

G.13 André Guinier. *X-Ray Crystallographic Technology* (London: Hilger and Watts, 1952). Excellent treatment of the theory and practice of x-ray diffraction. The title is not fair to the book, which includes a considerable body of theory and detailed experimental technique. The theory and applications of the reciprocal lattice are very well described. Includes treatments of focusing monochromators, small-angle scattering, and diffraction by amorphous substances.

G.17 Harold P. Klug and Leroy E. Alexander. *X-Ray Diffraction Procedures*, 2nd ed. (New York: Wiley, 1974). Contains a great deal of useful detail on the

theory and operation of powder cameras and diffractometers. Covers the following topics in depth: chemical analysis by diffraction, parameter measurement, line-broadening analysis, texture determination, stress measurement, and studies of amorphous materials. Single-crystal methods are not included.

G.28 Victor E. Buhrke, Ron Jenkins and Deane K. Smith. *A Practical Guide for the Preparation of Specimens for X-ray Fluorescence and X-ray Diffraction Analysis*. (New York: Wiley-VCH, 1998).

ANSWERS TO SELECTED PROBLEMS

1. 41 minutes **2**. $\lambda/\Delta\lambda = 2\,R\,\tan\,\theta/\Delta S$

4. 81° **6**. 4.2 cm

Laue Photographs

1 INTRODUCTION

The present chapter deals with the Laue method only from the experimental side. Both aspects are described in a book by Amoros et al. [G.31].

Laue photographs are the easiest kind of diffraction pattern to make and require only the simplest kind of apparatus. White radiation is necessary, and the best source is a tube with a heavy-metal target, such as tungsten, since the intensity of the continuous spectrum is proportional to the atomic number of the target metal. Good patterns can also be obtained with radiation from other metals, such as molybdenum or copper. Ordinarily, the presence of strong characteristic components, such as W $L\alpha_1$, Cu $K\alpha$, Mo $K\alpha$ etc., in the radiation used, does not complicate the diffraction pattern in any way or introduce difficulties in its interpretation. Such a component will be diffracted only if the crystal happens to be oriented in just such a way that Bragg's law is satisfied for that component, and then the only effect will be the formation of a Laue spot of exceptionally high intensity.

The specimen used in the Laue method is a single crystal. This may mean an isolated single crystal or one particular crystal grain, not too small, in a polycrystalline aggregate. The only restriction on the size of a crystal in a polycrystalline mass is that it must be no smaller than the incident x-ray beam, if the pattern obtained is to correspond to that crystal alone.

Each diffracted beam in the Laue method has a different wavelength, selected from the incident polychromatic beam by the d spacing and θ value of the (hkl) planes producing the reflection. If x-rays were visible like light, each diffracted beam would be a different color. Although these colors cannot be seen by the unaided eye, colored Laue patterns can be made by special photographic procedures. Blum [1] made such patterns by preparing a special film, in which the three color-producing layers of emulsion in color film were separated by layers containing metal atoms that acted as filters for the incident x-rays. Ting et al. [G.2] achieved the same result with commercially available materials, and it is also possible to

From Chapter 8 of *Elements of X-Ray Diffraction*, Third Edition. B.D. Cullity, S.R. Stock.

achieve this effect by recording the Laue pattern multiple times, each time with a different absorption filter.

The position of any Laue spot is unaltered by a change in plane spacing, since the only effect of such a change is to alter the wavelength of the diffracted beam. It follows that two crystals of the same orientation and crystal structure, but of different lattice parameter, will produce identical Laue patterns.

2 CAMERAS

Laue cameras are so simple to construct that homemade models are not uncommon.

Transmission Camera

Figure 1 shows a transmission camera, in this case a dual-purpose instrument, and Fig. 2 illustrates its essential parts. A is the collimator, a device used to produce a narrow incident beam made up of rays as nearly parallel as possible; it usually consists of two pinholes in line, one in each of two lead disks set into the ends of the collimator tube. C is the single-crystal specimen supported on the holder B. F is the light-tight film holder, or *cassette*, made of a frame, a removable metal back, and a sheet of opaque paper; the film, usually 4 × 5 in. (10 × 13 cm) in size, is sandwiched between the metal back and the paper. S is the beam stop, designed to prevent the transmitted beam from striking the film and causing excessive blackening. A small copper disk, about 0.5 mm thick, cemented on the paper film cover serves very well for this purpose: it stops all but a small fraction of the beam transmitted through the crystal, while this small fraction serves to record the position of this beam on the film. The shadow of a beam stop of this kind.

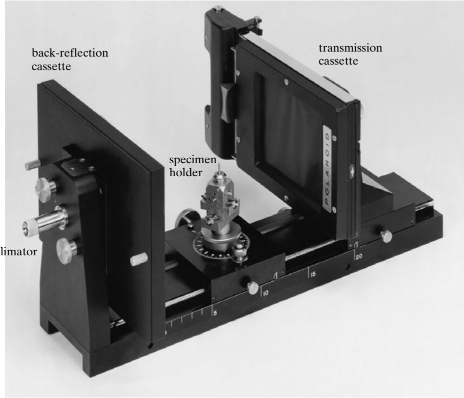

Figure 1 Combination transmission and back-reflection Laue camera. In this camera the Polaroid cassette (at right) and the cassette for ordinary film (at left) are interchangeable; either can be used for transmission or for back reflection. (Courtesy of Blake Industries, Inc.)

The Bragg angle θ corresponding to any transmission Laue spot is found very simply from the relation

$$\tan 2\theta = \frac{r_1}{D}, \tag{1}$$

where r_1 = distance of spot from center of film (point of incidence of transmitted beam) and D = specimen-to-film distance (usually 5 cm). Adjustment of the specimen-to-film distance is best made by using a feeler gauge of the correct length.

The voltage applied to the x-ray tube has a decided effect on the appearance of a transmission Laue pattern. It is of course true that the higher the tube voltage, the more intense the spots, other variables, such as tube current and exposure time, being held constant. But there is still another effect due to the fact that the continuous spectrum is cut off sharply on the short-wavelength side at a value of the wavelength which varies inversely as the tube voltage. Laue spots near the center of a transmission pattern are caused by first-order reflections from planes inclined at very small angles to the incident beam. In this circumstance, only short-wavelength radiation can satisfy Bragg's law, but, if the tube voltage is too low to produce the wavelength required, the corresponding Laue spot will not appear on the pattern. It therefore follows that there is a region near the center of the pattern which is devoid of Laue spots and that the size of this region increases as the tube voltage decreases. The tube voltage therefore affects not only the intensity of each spot, but also the number of spots. This is true also of spots far removed from the center of the pattern: some of these are due to (hkl) so oriented and of such a spacing that they diffract radiation of wavelength close to the short-wavelength limit, and such spots will be eliminated by a decrease in tube voltage no matter how long the exposure.

Back-Reflection Camera

A back-reflection camera is illustrated in Figs. 3 and 4 and at the left of Fig. 1.

The Bragg angle θ for any spot on a back-reflection pattern may be found from the relation

$$\tan(180^\circ - 2\theta) = \frac{r_2}{D}, \tag{2}$$

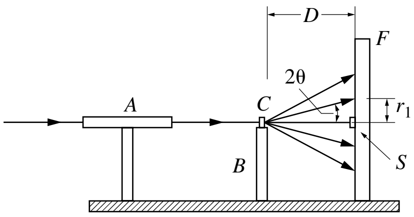

Figure 2 Transmission Laue camera.

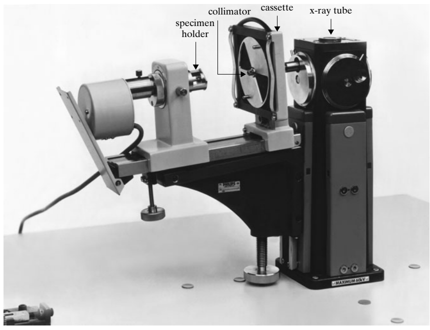

Figure 3 Back-reflection Laue camera. The sectored disc on the front of the cassette would be removed for a Laue photograph. (Courtesy of Philips Electronic Instruments, Inc.)

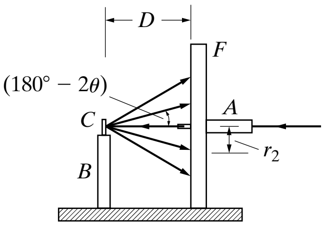

Figure 4 Back-reflection Laue camera (schematic).

where r_2 = distance of spot from center of film and D = specimen-to-film distance (usually 3 cm). In contrast to transmission patterns, back-reflection patterns may have spots as close to the center of the film as the size of the collimator permits. Such spots are caused by high-order overlapping reflections from (hkl) almost perpendicular to the incident beam. Since each diffracted beam is formed of a number of wavelengths, the only effect of a decrease in tube voltage is to remove one or more short-wavelength components from some of the diffracted beams. The longer wavelengths will still be diffracted, and the decrease in voltage will not, in general, remove any spots from the pattern.

General

To obtain a diffraction pattern a Laue camera must be correctly oriented with respect to the x-ray tube. This alignment requires that the collimator axis point directly at the focal spot on the tube target and make an angle of about 6° with the face of the target. Normally a spot focus (as opposed to a line focus) is used. The camera is moved relative to the tube until the primary beam, observed on a small fluorescent screen held near the collimator exit, is of maximum intensity and circular, not elliptical, in section.

Transmission patterns can usually be obtained with much shorter exposures than back-reflection patterns. For example, with a tungsten-target tube operating at

30 kV and 20 mA and an aluminum crystal about 1 mm thick, the required exposure is about 5 min in transmission and +30 min in back reflection. This difference is due to the fact that the atomic scattering factor f decreases as the quantity $(\sin\theta)/\lambda$ increases, and $(\sin\theta)/\lambda$ is much larger in back reflection than in transmission. Transmission patterns are also clearer, in the sense of having greater contrast between the diffraction spots and the background, since the coherent scattering, which forms the spots, and the incoherent (Compton modified) scattering, which contributes to the background, vary in opposite ways with $(\sin\theta)/\lambda$. The incoherent scattering reaches its maximum value in the back-reflection region; it is in this region also that the temperature-diffuse scattering is most intense. In both Laue methods, the short-wavelength radiation in the incident beam will cause most specimens to emit K fluorescent radiation. If this becomes troublesome in back reflection, it may be minimized by placing a filter of aluminum sheet 0.01 in. (0.25 mm) thick in front of the film.

If necessary, the intensity of a Laue spot may be increased by means of an *intensifying screen*, as used in radiography. This resembles a fluorescent screen in having an active material coated on an inert backing such as cardboard, the active material having the ability to fluoresce in the visible region under the action of x-rays. When such a screen is placed with its active face in contact with the film (Fig. 5), the film is blackened not only by the incident x-ray beam but also by the visible light which the screen emits under the action of the beam. Whereas fluorescent screens emit yellow light, intensifying screens are designed to emit blue light, which is more effective than yellow in blackening the film. Calcium tungstate intensifying screens are used at short x-ray wavelengths (about 0.5 Å or less), while zinc sulfide with a trace of silver can be used at longer wavelengths.

An intensifying screen should not be used if it is important to record fine detail in the Laue spots, as in some studies of crystal distortion, since the presence of the screen will cause the spots to become more diffuse than they would ordinarily be. Each particle of the screen which is struck by x-rays emits light in *all* directions and therefore blackens the film outside the region blackened by the diffracted beam itself, as suggested in Fig. 5. This effect is aggravated by the fact that most x-ray film is double-coated, the two layers of emulsion being separated by an appreciable thickness of film base. Even when an intensifying screen is not used, double-coated film causes the size of a diffraction spot formed by an obliquely incident beam to be larger than the cross section of the beam itself; in extreme cases, an apparent doubling of the diffraction spot results, as shown in Fig. 6.

Intensifying screens of one kind or another are routinely used for x-ray radiography but not for diffraction. Most film manufacturers make one or more kinds of film designed for radiography and another kind for diffraction, whether for the Laue or powder method. Diffraction films are faster and have coarser grain. They are designed for use without an intensifying screen and are often named “no screen” to emphasize this fact.

It is likely that most Laue patterns recorded since the mid 1970’s have been on high speed Polaroid film in a camera incorporating an intensifier screen. This film,

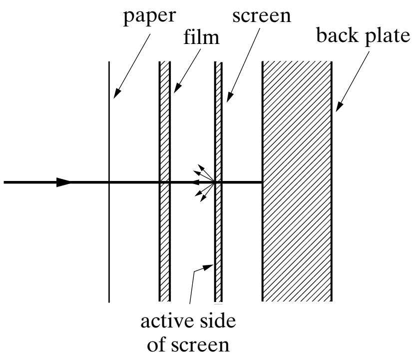

Figure 5 Arrangement of film and intensifying screen (exploded view).

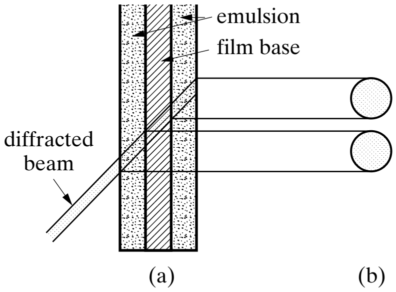

Figure 6 Effect of double-coated film on appearance of Laue spot: (a) section through diffracted beam and film; (b) front view of doubled spot on film.

designed for optical microscopy, requires no development or fixation tanks, is very rapid and can include negatives as well as positive images. Multiwire x-ray detectors, image storage plates or CCD (charge coupled device) detectors have also been used to record Laue patterns rapidly and in digital form; systems based on these technologies have found a place in the production environment.

3 SPECIMENS AND HOLDERS

Obviously, a specimen for the transmission method must have low enough absorption to transmit the diffracted beams; in practice, this means that relatively thick specimens of a light element like aluminum may be used but that the thickness of a fairly heavy element like copper must be reduced, by etching, for example, to a few thousandths of an inch. On the other hand, the specimen must not be too thin or the diffracted intensity will be too low, since the intensity of a diffracted beam is proportional to the volume of diffracting material. In the back-reflection method, there is no restriction on the specimen thickness and quite massive specimens may be examined, since the diffracted beams originate in only a thin surface layer of the specimen. This difference between the two methods may be stated in another way and one which is well worth remembering: any information about a thick specimen obtained by the back-reflection method applies only to a thin surface layer of that specimen, whereas information recorded on a transmission pattern is representative of the complete thickness of the specimen, simply because the transmission specimen must necessarily be thin enough to transmit diffracted beams from all parts of its cross section.

There is a large variety of specimen holders in use, each suited to some particular purpose. The simplest consists of a fixed post to which the specimen is attached with wax, plasticine or epoxy. A more elaborate holder is required when it is necessary to set a crystal in some particular orientation relative to the x-ray beam. In this case, a three-circle goniometer is used (Fig. 7); it has three mutually perpendicular axes of rotation, two in the horizontal plane and one in the vertical, and is so constructed that the crystal, cemented to the tip of the short metal rod at the top, is not displaced in space by any of the three possible rotations.

After the orientation of a crystal has been determined by the Laue method, it is sometimes necessary to cut the crystal along some selected plane. A more massive goniometer-holder than that of Fig. 7 is then required; such a holder can be removed from the track of the Laue camera and transferred to a similar track on the cutting device without disturbing the orientation of the crystal.

In the examination of sheet specimens, it is frequently necessary to obtain diffraction patterns from various points on the surface, and this requires movement of the specimen, between exposures, in two directions at right angles in the plane of the specimen surface, this surface being perpendicular to the incident x-ray beam. The mechanical stage from a microscope can be easily converted to this purpose as are components for laser optics.

It is often necessary to know exactly where the incident x-ray beam strikes the specimen, as, for example, when one wants to obtain a pattern from a particular grain, or a particular part of a grain, in a polycrystalline mass. This is sometimes a rather difficult matter in a back-reflection camera because of the short distance between the film and the specimen. One method is to project a light beam through the collimator and observe its point of incidence on the specimen with a mirror or prism held near the collimator. An even simpler method is to push a stiff straight wire through the collimator and observe where it touches the specimen with a small mirror, of the kind used by dentists, fixed at an angle to the end of a rod.

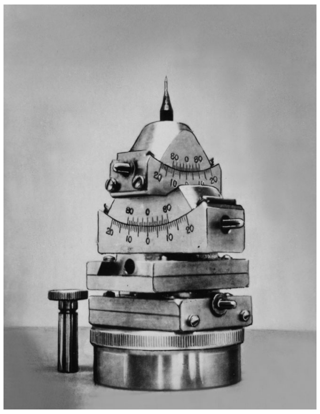

Figure 7 Goniometer with three rotation axes. (Courtesy of Charles Supper Co.)

4 COLLIMATORS

Collimators of one kind or another are used in all varieties of x-ray cameras, and it is therefore important to understand their function and to know what they can and cannot do. To "collimate" means, literally, to "render parallel," and the perfect collimator would produce a beam composed of perfectly parallel rays. Such a collimator does not exist, and the reason, essentially, lies in the source of the radiation, since every tube emits radiation in all possible directions and even synchrotron radiation possesses save divergence.

Consider the simplest kind of collimator (Fig. 8), consisting of two circular apertures of diameter d separated by a distance u, where u is large compared to d. If there is a point source of radiation at S, then all the rays in the beam from the collimator are nonparallel, and the beam is conical in shape with a maximum angle of divergence β_1 given by the equation

$$\tan\frac{\beta_1}{2} = \frac{\mathrm{d}/2}{\mathrm{v}}, \tag{3}$$

where v is the distance of the exit pinhole from the source. Since β_1 is always very small, this relation can be closely approximated by the equation

$$\beta_1 = \frac{d}{v} \text{ radian.} \tag{4}$$

Whatever is done to decrease β_1 and therefore to render the beam more nearly parallel will at the same time decrease the intensity of the beam. Note also that the entrance pinhole serves no function when the source is very small, and may be omitted.

No actual source is a mathematical point, and, in practice, x-ray tubes are encountered which have focal spots of finite size, usually rectangular in shape. The projected shape of such a spot, at a small target-to-beam angle, is either a small square or a very narrow line, depending on the direction of projection. These are termed spot-focus and line focus sources, respectively. Such sources produce beams having parallel, divergent, and convergent rays.

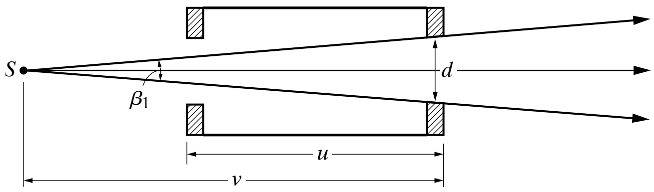

Figure 8 Pinhole collimator and small source.

Figure 9 illustrates the case when the projected source shape is square and of such a height h that convergent rays from the edges of the source cross at the center of the collimator and then diverge. The maximum divergence angle is now given by

$$\beta_2 = \frac{2d}{u} \text{ radian,} \tag{5}$$

and the center of the collimator may be considered as the virtual source of these divergent rays. The beam issuing from the collimator contains not only parallel and divergent rays but also convergent ones, the maximum angle of convergence being given by

$$\alpha = \frac{d}{u + w} \text{ radian,} \tag{6}$$

where w is the distance of the crystal from the exit pinhole. The size of the source shown in Fig. 9 is given by

$$h = d\left(\frac{2v}{u} - 1\right). \tag{7}$$

In practice, v is very often about twice as large as u, which means that the conditions illustrated in Fig. 9 are achieved when the pinholes are about one-third the size of the projected source. If the value of h is smaller than that given by Eq. (7), then conditions will be intermediate between those shown in Figs. 8 and 9; as h approaches zero, the maximum divergence angle decreases from the value given by Eq. (5) to that given by Eq. (4) and the proportion of parallel rays in the beam and the maximum convergence angle both approach zero. When h exceeds the value given by Eq. (7), none of the conditions depicted in Fig. 9 is changed, and the increase in the size of the source merely represents wasted energy.

When the shape of the projected source is a fine line, the geometry of the beam varies between two extremes in two mutually perpendicular planes. In a plane at right angles to the line source, the shape is given by Fig. 8 and in a plane parallel to the source by Fig. 9. Aside from the component which diverges in the plane of the

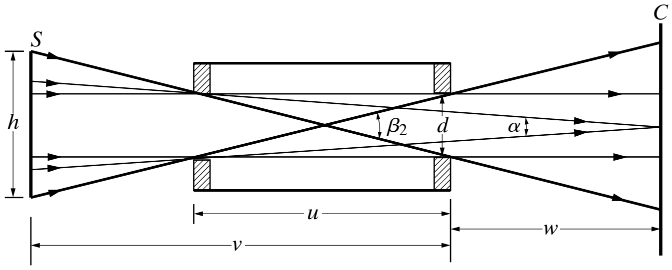

Figure 9 Pinhole collimator and large source. S = source, C = crystal.

source, the resulting beam is shaped somewhat like a wedge. Since the length of the line source greatly exceeds the value given by Eq. (7), a large fraction of the x-ray energy is wasted with this arrangement of source and collimator.

The extent of the nonparallelism of actual x-ray beams may be illustrated by taking, as typical values, $d = 0.5$ mm, $u = 5$ cm, and $w = 3$ cm. Then Eq. (5) gives $\beta_2 = 1.15°$ and Eq. (6) gives $\alpha = 0.36°$. These values may of course be reduced by decreasing the size of the pinholes, for example, but this reduction will be obtained at the expense of decreased beam intensity and increased exposure time.

The collimators of most cameras, both for Laue and powder photographs, produce beams about 1 mm in diameter. Much smaller beams are used in *microcameras* for special purposes.

5 THE SHAPES OF LAUE SPOTS

As will be seen later, Laue spots become smeared if the diffracting crystal is distorted. Here, however, the concern is with the shapes of spots obtained from perfect, undistorted crystals. These shapes are greatly influenced by the nature of the incident beam, i.e., by its convergence or divergence, and it is important to realize this fact, or Laue spots of "unusual" shape may be erroneously taken as evidence of crystal distortion.

Consider the transmission case first, and assume that the crystal is thin and larger than the cross section of the primary beam at the point of incidence. If this beam is mainly divergent, which is the usual case in practice (Fig. 8 or 9), then a focusing action takes place on diffraction. Figure 10 is a section through the incident beam and any diffracted beam; the incident beam, whose cross section at any point is circular, is shown issuing from a small source, real or virtual. Each ray of the incident beam which lies in the plane of the drawing diffracts at a slightly different Bragg angle, this angle being a maximum at A and decreasing progressively toward B. The lowermost rays, deviate therefore through a greater angle 2θ than the upper ones, with the result that the diffracted beam converges to a focus at F. This is true only of the rays in the plane of the drawing; those in a plane at right angles

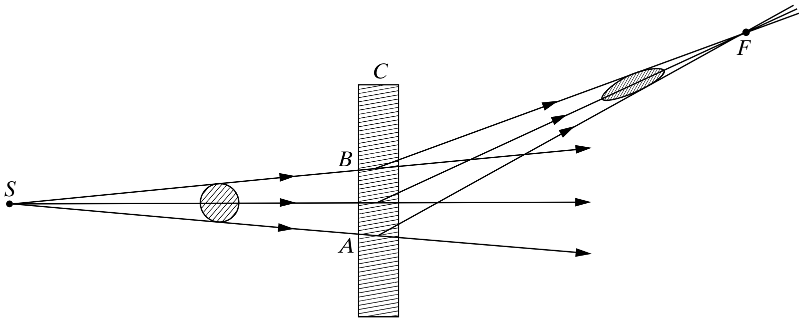

Figure 10 Focusing of diffracted beam in the transmission Laue method. S = source, C = crystal, F = focal point.

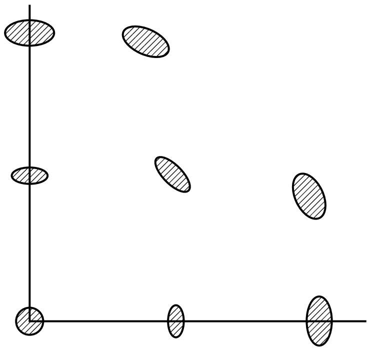

Figure 11 Shape of transmission Laue spots as a function of position.

continue to diverge after diffraction, with the result that the diffracted beam is elliptical in cross section. The film intersects different diffracted beams at different distances from the crystal, so elliptical spots of various sizes are observed, as shown in Fig. 11. This is not a sketch of a Laue pattern but an illustration of spot size and shape as a function of spot position in one quadrant of the film. Note that the spots are all elliptical with their minor axes aligned in a radial direction and that spots near the center and edge of the pattern are thicker than those in intermediate positions, the latter being formed by beams near their focal point. Spots having the shapes illustrated are fairly common.

In back reflection, no focusing occurs and a divergent incident beam continues to diverge in all directions after diffraction. Back-reflection Laue spots are therefore more or less circular near the center of the pattern, and they become increasingly elliptical toward the edge, due to the oblique incidence of the rays on the film, the major axes of the ellipses being approximately radial.

PROBLEMS

***1** A transmission Laue pattern is made of an aluminum crystal with 40-kV tungsten radiation. The film is 5 cm from the crystal. How close to the center of the pattern can Laue spots be formed by diffraction planes of maximum spacing, namely (111), and those of next largest spacing, namely (200)?

2 A transmission Laue pattern is made of an aluminum crystal with a specimen-to-film distance of 5 cm. The (111) planes of the crystal make an angle of 3° with the incident beam. What minimum tube voltage is required to produce a 111 reflection?

***3** (a) A back-reflection Laue pattern is made of an aluminum crystal at 50 kV. The (111) planes make an angle of 88° with the incident beam. What orders of reflection are present in the beam diffracted by these planes? (Assume that wavelengths larger than 2.0 Å are too weak and too easily absorbed by air to register on the film.) b)What orders of the 111 reflection are present if the tube voltage is reduced to 40 kV?

REFERENCES

The following books are listed more or less in the order they are encountered in the text

G.2 L.S. Birks. *X-Ray Spectrochemical Analysis*, 2nd ed. (New York: Interscience, 1969). Clear, brief treatment of wavelength and energy dispersive methods, with emphasis on the problems of quantitative analysis. Includes electron-probe microanalysis.

G.31 J. L. Amoros, M. J. Buerger, and M. L. Canut de Amoros. *The Laue Method* (New York: Academic Press, 1974). Describes the various projections used with the Laue method and the application of this method to studies of crystal symmetry and diffuse scattering.

ANSWERS TO SELECTED PROBLEMS

1. 0.67 cm for (111); 0.77 cm for (200)

3. a) 3rd to 18th; b) 3rd to 15th.

Phase Identification by X-Ray Diffraction

1 INTRODUCTION

A given substance always produces a characteristic diffraction pattern, whether that substance is present in the pure state or as one constituent of a mixture of substances. This fact is the basis for the diffraction method of chemical analysis. *Qualitative analysis* for a particular substance is accomplished by identification of the pattern of that substance. *Quantitative analysis* is also possible, because the intensities of the diffraction lines due to one phase of a mixture depend on the proportion of that phase in the specimen.

The particular advantage of diffraction analysis is that it discloses the presence of a substance *as that substance actually exists in the sample*, and not in terms of its constituent chemical elements. For example, if a sample contains the compound A_xB_y, the diffraction method will disclose the presence of A_xB_y as such, whereas ordinary chemical analysis would show only the presence of elements A and B. Furthermore, if the sample contained both A_xB_y and A_xB_{zy}, both of these compounds would be disclosed by the diffraction method, but chemical analysis would again indicate only the presence of A and B.[1] To consider another example, chemical analysis of a plain carbon steel reveals only the amounts of iron, carbon, manganese, etc., which the steel contains, but gives no information regarding the phases present. Is the steel in question wholly martensitic, does it contain both martensite and austenite, or is it composed only of ferrite and cementite? Questions such as these can be answered by the diffraction method. Another rather obvious appli-

---

[1] Of course, if the sample contains only A and B, and if it can be safely assumed that each of these elements is wholly in a combined form, then the presence of A_xB_y and A_xB_{zy} can be demonstrated by calculations based on the amounts of A and B in the sample. But this method is not generally applicable, and it usually involves a prior assumption as to the constitution of the sample. For example, a determination of the total amounts of A and B present in a sample composed of A, A_xB_y, and Bcannot, in itself, disclose the presence of A_xB_y, either qualitatively or quantitatively.

From Chapter 9 of *Elements of X-Ray Diffraction*, Third Edition. B.D. Cullity, S.R. Stock.

cation of diffraction analysis is in distinguishing between different allotropic modifications of the same substance: solid silica, for example, exists in one amorphous and six crystalline modifications, and the diffraction patterns of these seven forms are all different.

Diffraction analysis is therefore useful whenever it is necessary to know the state of chemical combination of the elements involved or the particular phases in which they are present. As a result, the diffraction method has been widely applied for the analysis of such materials as ores, clays, refractories, alloys, corrosion products, wear products, industrial dusts, etc. Compared with ordinary chemical analysis, the diffraction method has the additional advantages that it is usually much faster, requires only a very small sample, and is nondestructive. Detailed treatments of chemical analysis by x-ray diffraction are given by Klug and Alexander [G.17] and Jerkins and Snyder [G.25].

2 BASIC PRINCIPLES

The powder pattern of a substance is characteristic of that substance and forms a sort of fingerprint by which the substance may be identified. A collection of diffraction patterns for a great many substances, allows identification of an unknown by recording its diffraction pattern and then locating in the file of known patterns one which matches the pattern of the unknown exactly. The collection of known patterns has to be fairly large, if it is to be at all useful, and then pattern-by-pattern comparison in order to find a matching one becomes out of the question.

What is needed is a system of classifying the known patterns so that the one which matches the unknown can be located quickly. Such a system was devised by Hanawalt in 1936 [1]. Any one powder pattern is characterized by a set of *line positions* 2θ and a set of relative line *intensities* I/I_1 scaled relative to I_1, the peak in the pattern with maximum intensity. But the angular positions of the lines depend on the wavelength used, and a more fundamental quantity is the spacing d of the lattice planes forming each line. Hanawalt therefore decided to describe each pattern by listing the d and I values of its diffraction lines, and to arrange the known patterns in decreasing values of d for the strongest line in the pattern. This arrangement made possible a search procedure which would quickly locate the desired pattern. In addition, the problem of solving the pattern was avoided and the method could be used even when the crystal structure of the substance concerned was unknown.

3 POWDER DIFFRACTION FILE

The task of building up a collection of known patterns was initiated by Hanawalt, Rinn, and Frevel [1] at the Dow Chemical Company; they obtained and classified diffraction data on some 1000 different substances. It soon became apparent that these data were of great potential value to a wide range of industries and, beginning in 1941, several technical societies, including the American Society for Testing and Materials, began to cooperate in acquiring and disseminating diffraction data. From

1941 to 1969 the ASTM published and sold an increasing volume of data in the form of 3 × 5 in. file cards, one card for each pattern. Since 1969 this activity has been carried out by the Joint Committee on Powder Diffraction Standards(JCPDS) which in 1978 was renamed the International Centre for Diffraction Data (ICDD) [2]. Approximately three-hundred scientists from around the world participate in the Centre. In 1995 the Powder Diffraction File (PDF) contained nearly 62,000 diffraction patterns in 45 sets, with a new set of about 2000 patterns being added each year. The substances included are elements, alloys, inorganic compounds, minerals, organic compounds, and organometallic compounds.

Hanawalt Method

Since more than one substance can have the same, or nearly the same, d value for its strongest line and even its second strongest line, Hanawalt decided to characterize each substance by the d values of its *three* strongest lines, namely d_1, d_2, and d_3 for the strongest, second-strongest, and third-strongest line, respectively. The values of d_1, d_2, and d_3, together with relative intensities, are usually sufficient to characterize the pattern of an unknown and enable the corresponding pattern in the file to be located. Originally, in each section or set of the ASTM file, the cards were arranged in groups characterized by a certain range of d_1 spacings and identified by a set number and a card number within that set. Within each group, e.g., the group covering d_1 values from 2.29 to 2.25 Å, the cards were arranged in decreasing order of d_2 values, rather than d_1 values. When several substances in the same group had identical d_2 values, the order of decreasing d_3 values was followed. The groups themselves were arranged in decreasing order of their d_1 ranges. However, as the number of cards grew, the direct card search became unwieldy, and it was recognized that it would become more cumbersome as the file became larger. Accordingly, the JCPDS decided to number the cards randomly, or chronologically, in each set, rather than according to the value of d_1, and to use the Hanawalt Search Manual to replace the group-arranged card sets.

A typical card from the PDF is reproduced in Fig. 1. Note that new patterns have superceded older patterns in a number of cases when better data became available, and, for this reason, there are gaps in the older sets of cards. Individual 3 × 5 in. (8 × 13 cm) cards are no longer available. Instead, these cards, grouped in inorganic and organic sections, are found in the following forms:

Microfiche. Cards are photographically reduced and printed on 4 × 6 in. (10 × 15 cm) sheets of photographic film (microfiche), but this format is fading from use.

Books. Cards from Sets 1 to 45 are reproduced, three to a page, in book form. All cards from these sets, inorganic and organic, are included. The number of sets per volume has decreased as the rate of addition of new patterns have increased.

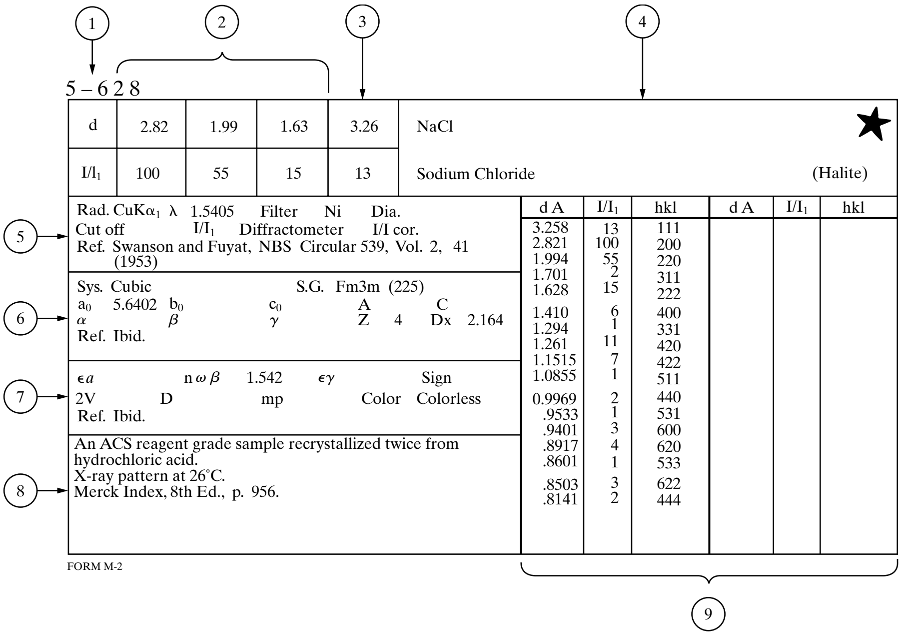

5 – 6 2 8

d	2.82	1.99	1.63	3.26	NaCl ★
I/I_1	100	55	15	13	Sodium Chloride (Halite)

Rad. $CuK\alpha_1$ λ 1.5405 Filter Ni Dia.
Cut off I/I_1 Diffractometer I/I cor.
Ref. Swanson and Fuyat, NBS Circular 539, Vol. 2, 41 (1953)

Sys. Cubic S.G. Fm3m (225)
a_0 5.6402 b_0 c_0 A C
α β γ Z 4 Dx 2.164
Ref. Ibid.

ϵa $n \omega \beta$ 1.542 $\epsilon\gamma$ Sign
2V D mp Color Colorless
Ref. Ibid.

An ACS reagent grade sample recrystallized twice from hydrochloric acid.
X-ray pattern at 26°C.
Merck Index, 8th Ed., p. 956.

d A	I/I_1	hkl	d A	I/I_1	hkl
3.258	13	111			
2.821	100	200			
1.994	55	220			
1.701	2	311			
1.628	15	222			
1.410	6	400			
1.294	1	331			
1.261	11	420			
1.1515	7	422			
1.0855	1	511			
0.9969	2	440			
.9533	1	531			
.9401	3	600			
.8917	4	620			
.8601	1	533			
.8503	3	622			
.8141	2	444			

FORM M-2

Figure 1 Standard 3 × 5 in. ICDD diffraction data card (card 628 from Set 5) for sodium chloride. Appearing on the card are 1 (file number), 2 (three strongest lines), 3 (lowest-angle line), 4 (chemical formula and name of substance), 5 (data on diffraction method used), 6 (crystallographic data), 7 (optical and other data), 8 (data on specimen), and 9 (diffraction pattern). Intensities are expressed as percentages of I_1, the intensity of the strongest line on the pattern. Most cards have a symbol in the upper right corner indicating the quality of the data: * (high quality), *i* (lines indexed, intensities fairly reliable), *c* (calculated pattern), and *o* (low reliability). (Courtesy of International Centre for Diffraction Data)

Magnetic Tape. Various formats are available for different tape drives and computer operating systems, but this media has become more or less obsolete since software began to be distributed via CDs.

CD-ROM. These are optical discs read with low-power laser light reflected from a pattern of pits written by the recording laser. Typically 680 Mbytes of data can be stored in a disc, and because the CD technology was originally was developed for consumer audio electronics, it is very cost-effective and provides good performance for databases such as the PDF.

Numerous vendors offer software for searching computer-based format of the PDF for a particular pattern, using numerical, alphabetical or other methods.

1. *Alphabetical.* Substances are listed alphabetically by name. After the name are given the chemical formula, the *d* values and relative intensities (as subscripts) of the three strongest lines and the file number of the card. All entries are fully cross-indexed: i.e., both “sodium chloride” and “chloride:

sodium" are listed. This manual is useful if the investigator has any knowledge of the chemical composition of the sample.

2. *Numerical*. Substances are listed in terms of the *d* spacings of their three strongest lines, and *d* spacings and intensities are given for a total of eight lines for each substance. Also included are the chemical formula and file number. Each substance is currently listed twice (d_1, d_2 and d_2, d_1) if $I_2/I_1 >$ 0.75 and $I_3/I_1 \leq 0.75$. If $I_3/I_1 > 0.75$ and $I_4/I_1 < 0.75$, the substance is listed three times (d_1, d_2; d_2, d_1; and d_3, d_1. The pattern appears four times when $I_4/I_1 > 0.75$ (d_1, d_2; d_2, d_1; d_3, d_1; and d_4, d_1). All entries are divided into groups according to the first spacing listed; the arrangement within each group is in decreasing order of the second spacing listed. The purpose of these additional listings (second-strongest line first and third-strongest line first) is to enable the user to match an unknown with an entry in the search manual even when complicating factors have altered the relative intensities of the three strongest lines of the unknown. These complications are usually due to the presence of more than one phase in the sample. This leads to additional lines and even superimposed lines. Use of the numerical search manual requires no knowledge of the chemical composition of the sample.

Fink Method

The Fink method [3] of numerical searching of the data file relies more on *d* spacings than on intensities. It was originally designed for use with electron diffraction patterns, where observed line intensities are not always directly related to structure and therefore not always a reliable guide to identification. It is sometimes helpful to use the Fink index when there is difficulty identifying an unknown phase using the Hanawalt index; the presence of large amounts of preferred orientation in solid samples is one instance in which intensities may not correspond to those expected from the powder diffraction file.

In the Fink-method search manual, which covers inorganic compounds only, *d* spacings and intensities are listed for the eight strongest lines of each substance. The order of listing is determined by the four strongest lines. Each substance is listed four times in Set 24 and later (six times in earlier sets), with one of the four strongest lines listed first and the others following in descending order of *d* values.

4 PROCEDURE

Identification of the unknown begins with recording its diffraction pattern. Sample preparation should result in fine grain size and in a minimum of preferred orientation, which can cause relative line intensities to differ markedly from their normal values. Note also that relative line intensities depend to some extent on wavelength; this should be kept in mind if the observed pattern is compared with one in the data file made with a different wavelength. Most of the patterns in the file were made with Cu $K\alpha$ radiation, except those for iron-bearing substances.

The pattern may be recorded with a Hull/Debye–Scherrer camera, Guinier camera, or diffractometer. Here again, line intensities depend on the apparatus. In particular, absorption effects cause high-angle lines on a Hull/Debye-Scherrer pattern to be stronger, relative to low-angle lines, than on a diffractometer recording.

After the pattern of the unknown is prepared, the *d*-spacing corresponding to each line on the pattern is calculated. If the diffraction pattern has been obtained on film, relative line intensities are usually estimated by eye, on a scale running from 100 for the strongest line down to 10 or 5 for the weakest. If a densitometer is available, it may be used to provide more accurate values of diffracted intensities. For data recorded with a diffractometer, the background must be subtracted from the peak intensity before computing I_1/I_1 for each peak. In general, the background for a given sample varies with diffraction angle. Modern, computer-integrated diffractometers generally have software to identify peaks positions (angles and *d*-spacings) and to calculate the relative intensities of peaks.

After the experimental values of d and I/I_1 are tabulated, the unknown can be identified by the following procedure:

1. Locate the proper d_1 group in the numerical search manual.
2. Read down the second column of d values to find the closest match to d_2. (In comparing experimental and tabulated d values, always allow for the possibility that either set of values may differ by ±0.01 Å.)
3. After the closest match has been found for d_1, d_2, and d_3, compare their relative intensities with the tabulated values.
4. When good agreement has been found for the lines listed in the search manual, locate the proper PDF card and compare the d and I/I_1 values of all the observed lines with those tabulated. When full agreement is obtained, identification is complete.

5 IDENTIFICATION OF SINGLE PHASE SAMPLES

When the unknown is a single phase, the search procedure is relatively straight-forward. Consider, for example, the pattern described in Table 1. It was obtained with Cu $K\alpha$ radiation and a Hull/Debye–Scherrer camera: line intensities were estimated. The experimental values of d_1, d_2, and d_3 are 2.82, 1.99, and 1.63 Å, respectively. By examining the numerical search manual, strongest line is found to fall is found to within the 2.84-2.80 Å group of d_1 values. Inspection of the listed d_2 values in this group discloses twenty-seven substances having d_2 = 1.99 Å, but only five of these have d_1 = 2.82 Å. The data on these five are shown in Table 2 in the form given in the manual. And of these five only NaCl has d_3 = 1.63 Å, Note that the intensities listed for the three strongest lines of this substance agree fairly well with the observed intensities; so do the data for the other five lines listed in the manual.

TABLE 1 PATTERN OF UNKNOWN

d(Å)	I/I_1	d(Å)	I/I_1
3.25	10	1.00	20
2.82	100	0.95	5
2.18	5	0.94	20
1.99	60	0.89	20
1.71	5	0.86	5
1.63	30	0.85	20
1.42	20	0.82	10
1.25	30	0.79	10
1.15	30	0.78	20
1.09	5		

Turn to PDF card 5-628, reproduced in Fig. 1 and compares the complete pattern given there with the observed one. In general the agreement is good, but there are some discrepancies, and these must be resolved before the identification as NaCl is accepted. These discrepancies are:

1. A very weak line with $d = 2.18$ Å, not listed on the file card is observed. Calculation shows that this line is a 220 reflection of Cu $K\beta$ radiation not removed by the filter. Note that the even stronger 200 reflection would also produce a $K\beta$ line, but this $K\beta$ line falls on the 111 $K\alpha$ line and is therefore not seen separately.

TABLE 2 PORTION OF THE ICDD HANAWALT SEARCH MANUAL*

QM	Strongest reflections								PSC	Chemical formula	Mineral name; common name	PDF #	I/I_c
*	**2.82_x**	**1.99_3**	**3.99_2**	1.63_2	1.41_1	1.26_1	1.07_1	1.78_1	cP5	$Ca_{0.6}Sr_{0.4}NbO_3$		47-35	7.05
	2.82_x	**1.99_9**	**3.26_8**	1.63_7	1.41_1	1.26_1	1.15_1	1.73_1	cF8	PdO		46-1211	
*	**2.82_9**	**1.99_x**	**2.30_6**	1.41_4	1.63_2	0.89_1	1.20_1	1.15_1	cP5	$KMgF_3$		18-1033	0.90
*	**2.82_x**	**1.99_6**	**1.63_2**	3.26_1	1.26_1	1.15_1	0.94_1	0.89_1	cF8	NaCl	Halite, syn	5-628	
C	**2.82_x**	**1.99_x**	**1.99_8**	1.26_3	1.63_2	1.15_2	0.94_1	1.41_1	cP2	BePd		18-428	

*Extracted from the numerical search manual (Inorganic Compounds, Hanawalt Search Manual, Sets 1-48, 1998). The different quality marks (QM) are explained in Fig. 1. The three strongest lines appear in bold-face type. Intensities (rounded) are shown by the suffix x = 100 and the subscripts 9, 8, 7 … = 90, 80, 70 … The PSC is composed of the Pearson Bravais lattice mnemonic followed by the number of atoms in the unit cell: C denotes cubic, F face-centered and P primitive. The ratio I/Ic gives the ratio of the intensity of the most intense peak of the phase's pattern to that of the most intense peak of corundum hexagonal reflection 113.

2. The 331 line ($d = 1.294$ Å) listed on the file card is not observed. However, its intensity is expected to be very low.
3. Two high-angle lines ($d = 0.79$ and 0.78 Å) are observed but are not listed on the PDF card. Often the file cards' data do not extend to highest-accessible 2θ values. However, these lines can be indexed as 711-551 and 640 lines, which are the next expected lines after 444 in the FCC sequence.
4. After the fifth observed line, observed intensities on the Hull/Debye–Scherrer pattern are all higher than those on the file pattern, which was obtained with a diffractometer. These differences are due to absorption effects, as mentioned in Sec. 4.

Because the discrepancies are now understood, the identification of the the specimen as NaCl is complete, or more precisely, the data is consistent with NaCl and not with any other phase in the file. However, not all identifications are as positive as this example. A few unexplained weak lines are often assumed to be due to an unknown impurity: the identification of the main constituent is then somewhat tentative, and its reliability depends on the judgement and experience of the investigator. See also Sec. 8.

Because small *d* spacings correspond to back-reflection lines, they are measurable with greater precision than large *d* spacings. Spacings smaller than about 1 Å should therefore be computed to the nearest 0.001 Å, rather than to 0.01 Å as in Table 1, in order to permit a better match with data in the file.

6 IDENTIFICATION OF PHASES IN MIXTURES

The analysis is now more complex, but not impossible. Consider the pattern in Table 3, obtained with Cu $K\alpha$ radiation and a diffractometer, for which $d_1 = 2.09$ Å, $d_2 = 2.47$ Å, and $d_3 = 1.80$ Å. Examination of the numerical index in the d_1 group 2.09 to 2.05 Å reveals several substances having d_2 values near 2.47 Å, but in no case do the three strongest lines, taken together, agree with those of the unknown. This impasse suggests that the unknown is actually a mixture of phases, and that it is incorrect to assume that the three strongest lines in the pattern of the unknown are all due to the same substance. Suppose the strongest line ($d = 2.09$ Å) and the sec-

TABLE 3 PATTERN OF UNKNOWN

d(Å)	I/I_1	d(Å)	I/I_1
3.01	5	1.22	4
2.47	72	1.08*	20
2.13	28	1.04*	3
2.09*	100	0.98	5
1.80*	52	0.91*	4
1.50	20	0.83*	8
1.29	9	0.81*	10
1.28*	18		

TABLE 4 PATTERN OF COPPER

d(Å)	I/I_1
2.088	100
1.808	46
1.278	20
1.0900	17
1.0436	5
0.9038	3
0.8293	9
0.8083	8

ond-strongest line (d = 2.47 Å) are formed by two different phases, and that the third-strongest line (d = 1.80 Å) is due to, say, the first phase. In other words, assume that d_1 = 2.09 Å and d_2 = 1.80 Å for one phase. A search of the same group of d_1 values, but now in the vicinity of d_2 = 1.80 Å, discloses agreement between the three strongest lines of the pattern of copper, PDF card 4-0836, and three lines in the pattern of our unknown. Turning to PDF card 4-0836, all lines of the copper pattern, described in Table 4, agree with the starred lines in Table 3, the pattern of the unknown.

One phase of the mixture is thus shown to be copper, providing that the remainder of the lines can be assigned to some other substance. These remaining lines are listed in Table 5. By multiplying all the observed intensities by a normalizing factor of 1.39, the intensity of the strongest line is increased to 100. Searching the index and PDF in the usual way reveals that these remaining lines agree with the pattern of cuprous oxide, Cu_2O, which is given at the right of Table 5. The unknown is thus shown to be a mixture of copper and cuprous oxide.

The analysis of mixtures becomes still more difficult when a line from one phase is superimposed on a line from another, and when this composite line is one of the three strongest lines in the pattern of the unknown. The usual procedure then leads only to a very tentative identification of one phase, in the sense that agreement is obtained for some d values but not for all the corresponding intensities. This in itself is evidence of line superposition. Such patterns can be untangled by separating lines which agree in d value with those of phase X, the observed intensity of any superimposed lines being divided into two parts. One part is assigned to phase X, and the balance, together with the remaining unidentified lines, is treated as in the previous example.

Analysis of patterns containing multiple overlapping peaks requires careful tracking of how much intensity is from each individual phase. This can be done using a spread sheet, for example, or by the graphical plot-replot method [4] which is outlined below. In this subtractive method, the steps are:

1. Make a “stick” plot of I/I_1 vs d for the unknown mixture. Perhaps the most useful plot is I/I_1 vs ln d which is easily made on semi-log paper; this allows

TABLE 5

Remainder of pattern of unknown			Pattern of Cu_2O	
	I/I_1			
d(Å)	Observed	Normalized	d(Å)	I/I_1
3.01	5	7	3.020	9
2.47	72	100	2.465	100
2.13	28	39	2.135	37
			1.743	1
1.50	20	28	1.510	27
1.29	9	13	1.287	17
1.22	4	6	1.233	4
			1.0674	2
0.98	5	7	0.9795	4
			0.9548	3
			0.8715	3
			0.8216	3

systematic peak shifts due to various diffractometer errors to be easily recognized. About 10 or 20 increments of I/I_1 are sufficient.

2. Select likely possibilities (“three strongest lines”, a priori knowledge, hunches) and make “stick” plots for these knowns based on PDF cards.
3. Solve the “jig-saw” puzzle, allowing for superposition of lines:
    a. Graphically subtract the relative intensities of the first identified phase of the mixture. Note that the normalization of the identified phase may need to be changed to match the pattern: the mixture’s most intense peak may not be the 100% peak of the identified phase.
    b. Replot the remaining lines (i.e. those with non-zero intensities), renormalizing the maximum peak to 100% intensity. This is done to allow easy comparison of the remainder with another phase from the PDF.
    c. Repeat a. and b. until all peaks are accounted for.
4. Every line in the pattern must be assigned to some material. *All* major lines of each component identified (i.e., of each card) must be present. All remainders from subtractions must be zero or higher since negative intensities do not exist. In practise, negative remainders I/I_1 less than 0.05 are acceptable. Preferred orientation is often the cause of less than perfect agreement of intensities.

Completing the steps listed above is sufficient for most analyses. For a complete analysis, however, the following should be done.

5. Prepare mixtures of the identified components until the original diffraction pattern is duplicated. This step adds considerable reliability to the identification.
6. Compare absolute intensities of the peaks in the unknown and duplicating mixtures to see if there is any noncrystalline material in the unknown.

The plot-replot algorithm was developed before the advent of personal computers, and in many cases the same steps, albeit without plotting, can be done using a spreadsheet. A spreadsheet allow rapid sorting of the phases present in a mixture, but the plot-replot or other graphical approaches provide a better over-all view of the hypothetical constituents of the experimental pattern.

The following example illustrates the use of the plot-replot method. Fig. 2 shows the diffraction pattern of the unknown mixture, recorded with Cu $K\alpha$ radiation, a step size of 0.02° 2θ and counting time of 1 sec. The diffractometer used to collect the data was equipped with a post-sample monochromator and with an incident beam slit whose width varied automatically with 2θ so as to irradiate a constant area of the sample. Thus, the measured peak intensities at high 2θ are greater than they would be for a diffractometer with a fixed-width divergence slit (i.e., the

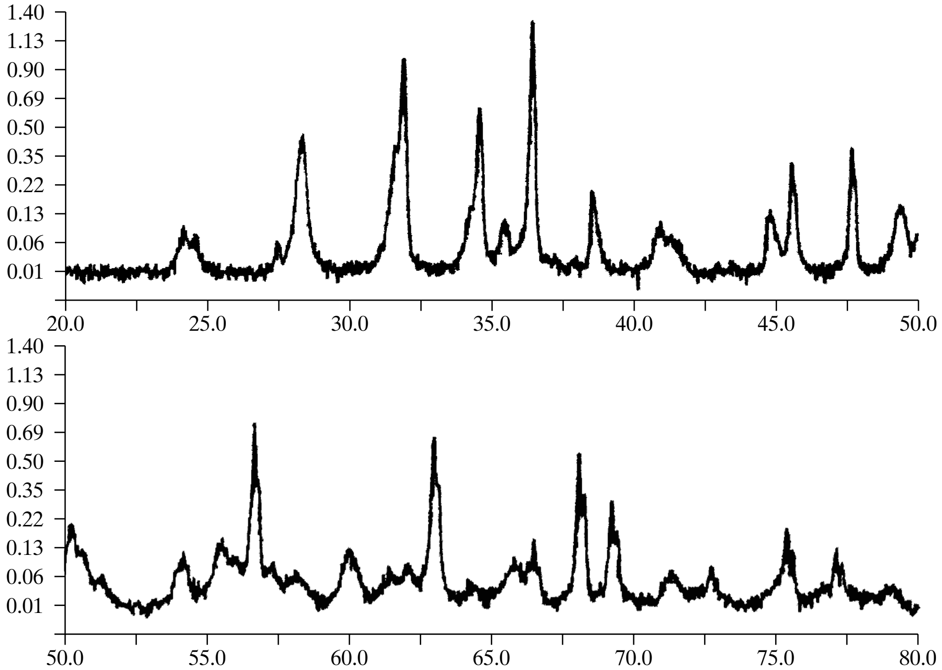

Figure 2 Diffraction pattern of a multi-phase sample recorded with a variable slit θ-2θ diffractometer. The pattern is plotted as the square root of the intensity (in thousands of counts) as a function of 2θ (degrees).

data which appears in the PDF). Note also that the vertical axis plots the square root of intensity in order to show the low intensity peaks more clearly.

Important clues sometimes can be gleaned by examining the entire diffraction pattern, peaks and background. Differences in peak shapes or widths, for example, can suggest which peaks belong to which phase. The pattern in Fig. 2 consists or many peaks of different shapes, and several peaks can be resolved from neighboring peaks (e.g., those at ~32°, 34°, 57°), suggesting that there may be additional peaks which cannot be resolved. The vertical bars on the plot indicate the peaks the diffractometer software has identified, but overmuch reliance on these types of routines is unwise, and their results should always be checked manually (i.e., by comparing the identified peak positions with the diffraction pattern itself). For example, peaks at ~63°, 68° and 74° in Fig. 2 appear to have been missed by the software, whereas similar appearing peaks in the same angular range (~57°, 69° and 76°) have been found.

Table 6 lists the average *d* and I/I_1 for the mixture obtained from scans of three repackings of the sample in a powder holder. The average intensities of the peaks identified by the software have been corrected to values which would have been observed were a one degree fixed divergence slit used. The ten most intense peaks appear in bold type in Table 6, numerical values of intensities for peaks above 5% are given in normal type and the remaining intensities are represented by "o". For the three repackings, the *d*-spacings of all peaks were reproducible within ±0.005 Å, and the relative intensities varied no more than ±3% compared to I_1.

Table 7 lists only the ten most intense peaks of the mixture, and the identification proceeds by checking triplets of peaks against the Hanawalt Index: lines 10, 6 and 8 match zincite (ZnO, card 36-1451) lines 2.48_x, 2.86_6, 2.60_4. The third column of the Table compares zincite's *d*-spacings and intensities with the experimental data, and Fig. 3(a) shows the corresponding I vs. ln d plots. Multiplying the remainder shown in column four by 2.5 yields the renormalized set of lines shown in column five. Lines 4 and 5 match the Index's entry for baddeleyite (ZrO_2, card 37-1484), and the remaining lines match halite (NaCl, card 5-628). The corresponding I vs. ln *d* plots appear in Fig. 3(b) and (c).

The largest remainder from the ten most intense peaks is 4% of the pattern's maximum intensity, and this is not surprising because this peak is primarily from halite, grains of which have a strong cubic morphology. All but three of the very smallest peaks (out of the 43 identified by the software) are from either ZnO, ZrO_2 or NaCl; examination of the three diffraction patterns recorded of the mixture, one of which is shown in Fig. 2, indicates that these three peaks are noise. As all of the expected peaks from the PDF cards are observed, and no major peaks in the experimental pattern have not been assigned to one of the three substances, this identification would be accepted with considerable confidence. In fact, these three phases were combined in the mixture for purposes of this example.

In Fig. 4 the diffractometer software is used to compare the experimental pattern with the PDF patterns of the phases identified in the analysis. This type of soft-

TABLE 6 LIST OF D-SPACING AND RELATIVE INTENSITIES FOR THE PEAKS IN FIG. 2, CONVERTED FROM THE VARIABLE INCIDENT BEAM SLIT DATA TO INTENSITIES WHICH WOULD HAVE BEEN OBSERVED WITH A 1° FIXED INCIDENT SLIT. PEAKS WITH INTENSITIES LESS THAN 5% ARE REPRESENTED BY “0” AND THE INTENSITIES AND D-SPACINGS ARE THE AVERAGE FROM THREE SAMPLE REPACKINGS.

line	d(Å)	I(%)	line	d(Å)	I(%)
1	3.68	7	26	1.66	6
2	3.62	5	27	1.62	31
3	3.24	0	28	1.60	0
4	3.15	40	29	1.58	0
5	2.84	27	30	1.54	0
6	2.80	83	31	1.51	0
7	2.62	8	32	1.49	0
8	2.60	46	33	1.48	31
9	2.53	6	34	1.45	0
10	2.47	100	35	1.42	0
11	2.40	0	36	1.40	0
12	2.37	0	37	1.38	22
13	2.34	10	38	1.36	12
14	2.21	0	39	1.32	0
15	2.20	5	40	1.30	0
16	2.17	0	41	1.26	6
17	2.08	0	42	1.23	0
18	2.02	6	43	1.21	0
19	1.99	20			
20	1.90	20			
21	1.84	8			
22	1.81	10			
23	1.80	0			
24	1.78	0			
25	1.69	0			

TABLE 7 NUMERICAL ILLUSTRATION OF THE GRAPHICAL SUBTRACTIONS IN FIG. 3*

Line	Unknown	36-1451	Remain.	Renorm.	37-1484	Remain.	Renorm.	5-628
10	2.47_x	2.476_x	0	–	–	–	–	–
6	2.80_{83}	2.814_{57}	26	2.80_{65}	–	65	2.80_x	2.82_x
8	2.60_{46}	2.603_{44}	2	2.60_{05}	–	5	2.50_{08}	–
4	3.15_{40}	–	–	3.15_x	3.16_x	0	–	–
27	1.62_{31}	1.625_{32}	−1	–	–	–	–	–
33	1.48_{29}	1.477_{29}	0	–	–	–	–	–
5	2.84_{27}	–	–	2.84_{68}	2.84_{68}	0	–	–
37	1.38_{22}	1.378_{22}	0	–	–	–	–	–
19	1.99_{20}	–	–	1.99_{50}	–	50	1.99_{77}	1.99_{55}
20	1.91_{20}	1.911_{23}	-3	–	–	–	–	–

* Instead of rounding each peak's intensity to the nearest 10% and using the most significant digit in the subscript to indicate intensity, as in the Hanawalt Index, a two digit subscript is used to indicate intensity to the nearest 1%. The peak intensity of 68% is indicated by the subscript "68" instead of "7".

ware is very useful for rapidly confirming the presence of phases suspected to be present but is less useful without this knowledge.

7 COMPUTERIZED SEARCH-MATCH

The procedure for searching the PDF for a pattern or patterns matching that of the unknown is essentially one of matching numbers. This task is ideally suited to the computer. As the number of phases in the unknown increases beyond two, manual searching becomes very difficult and time consuming; computer searching is then more efficient. This is especially true since the personal computer revolution of the 1980's has allowed automatic peak intensity and *d*-spacing measurement to be the rule rather than the exception: data files listing I and *d* values or even the entire diffraction pattern can be exported into search-match programs without inordinate effort.

At least 17 stand-alone phase identification programs are available in addition to those provided by hardware vendors with their instruments [5]. The goal of these programs is to scan the reference data base selecting the phase(s) with highest probability of comprising the unknown sample. Usually the best a program can do is to rank the possibilities based on some figure of merit calculated using a particular algorithm (for example, see Eq. 1 below). The different programs' procedures vary widely, and there are often many tricks to getting the best results, tricks which can be learned only from long experience with a specific program.

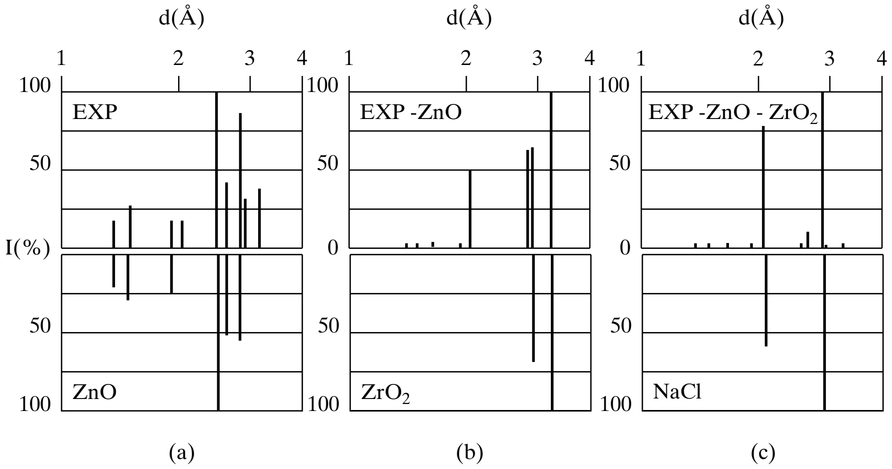

Figure 3 Illustration of the plot-replot method for identifying phases in mixtures. Only peaks with intensities greater than or equal to 20% in Fig. 2 and the corresponding Table 6 are shown. In (a) the top plot shows the experimental peak intensities as a function of ln *d* while the bottom plot shows the first phase identified ZnO, zincite, card 36-1451. The top plot of (b) shows the intensities remaining in the experimental pattern after subtracting the zincite peaks' intensities and renormalizing. The bottom plot of pattern (b) shows the peaks of the second phase ZrO_2, zirconia, card 37-1484. The plots in (c) show the same steps as in (b) and show that NaCl, halite, card 5-628, accounts for the remaining peaks of the pattern.

Computer searching is not immune to errors originating in the pattern of the unknown or in the data file. If the unknown contains only one phase, the software may produce from 10 to 50 matching patterns, depending on the width Δd of the "window" selected by the user; this window is the range of *d* values about a given experimental value within which a match is judged acceptable. The value(s) of *d*-spacing window(s) in software packages are sometimes not obvious, and considerable caution must be exercised when using search-match software with which one is unfamiliar. In many laboratories more than one researcher will use the search-match software, and the default settings must be checked at the start of every session. From the excessive number of possible matches provided by the computer, the user must select the most probable ones, usually on the basis of some knowledge of the unknown's chemical composition.

Search-match programs are very powerful: an early program successfully identified six phases in a mixture [6]. Automatic phase identification, however, is very sensitive to the quality of data in the PDF. In a study of 76 different phosphate minerals (common as well as rare species), 43% were unequivocally identified, 18% were identified with other (absent) phases also being identified, 15% were listed in the output file but were not identified and the remaining 24% did not appear in the output list; and inaccuracies in some of the 275 PDF reference patterns of phosphate minerals in sets 1-31 were found to be the principal origin of the failure of one-in-four identifications of this study [7].

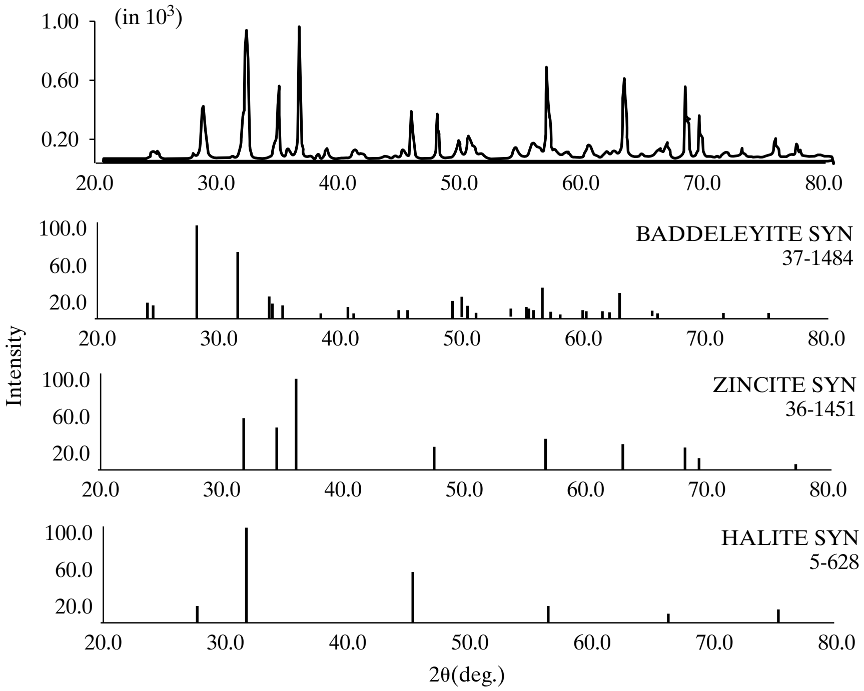

Figure 4 Comparison of the experimental diffraction pattern shown in Fig. 2 (note the linear intensity scale) with the cards of the phases identified in Fig. 3 and Table 7.

Fortunately standards are being raised for new additions to the PDF, and considerable effort has gone into replacing inaccurate cards. Routine use of an internal standard[2] in samples would help to minimize uncertainties in experimental peak positions. Full diffraction patterns and not merely lists of I and *d* are now being added to the PDF [8]; this should lead to major improvements in future phase identification.

One figure of merit which has gained acceptance as a measure of both the accuracy of the diffraction peak positions and the completeness of the pattern is

$$F_N = \frac{1}{|\overline{\Delta 2\theta}|}\frac{N}{N_{\text{poss}}}, \tag{1}$$

where N_{poss} is the number of independent diffraction lines possible up to the Nth observed line and $|\overline{\Delta 2\theta}|$ is the average absolute discrepancy between calculated and observed 2θ values [9 -10]. The units of F_N are reciprocal degrees, and the higher the accuracy or the more complete the pattern, the larger is F_N. Thus, F_N=100

---

[2] Addition to the unknown of a small amount of a phase with known *d*-spacings and with peaks which do not interfere with the principle peaks of the unknown. Systematic errors in the peak positions of the unknown(s) can be corrected by observing the shifts in the peaks of the internal standard.

means that the average 2θ difference was $\leq 0.01°$. In the study of phosphate minerals cited earlier in this section, computer identification was quite reliable for $F_{30} \geq 6.0$, and remeasurement of 34 of the 275 phosphate mineral PDF patterns improved the average F_{30} from 11.5 to 49.9 [7].

Before discussing the practical difficulties which might be encountered in phase identification work, it is instructive to compare the results of a search-match program on the mixture analyzed manually in Sec. 6. SANDMAN, the search-match program provided with the diffractometer used to record the pattern in question, grades the agreement between reference and experimental peaks using a Lorentzian probability distribution instead of relying on a window with definite limits for the "hit/miss" decision. This makes SANDMAN quite robust and allows it to score patterns primarily on the basis of relative line positions and to report the level of systematic errors explicitly for a given match.

The program performs a search through the entire PDF using the eight lines of the Hanawalt Index and checking multiple permutations. A second pass is used to match only the best candidates with the full pattern (generally those lines with $I/I_1 \geq 10\%$ or the 15 most intense lines [11]). SANDMAN adds the patterns of the phases identified and compares the result with the experimental pattern; most other search-match programs are subtractive rather than additive. For the mixture analyzed in the previous section, SANDMAN used 15 peaks down to $I/I_1 = 7.9\%$ in the search and matched 126 patterns to the experimental pattern. SANDMAN identified cards 37-1484 (baddeleyite, ZrO_2), 36-1451 (zincite, ZnO) and 17-469 (nadorite) explicitly, with very high match scores for the first two; however, it produced nearly as good a match for halite (NaCl, 5-628) as for nadorite.

8 PRACTICAL DIFFICULTIES

In theory, the Hanawalt method should lead to the positive identification of any substance whose diffraction pattern is included in the powder diffraction file. In practice, various difficulties arise, and these are usually due either to errors in the diffraction pattern of the unknown or to errors in the PDF.

Errors of the first kind, those affecting the observed positions and intensities of the diffraction lines, have been discussed in various parts of this text and need not be reexamined here. However, the possibility of abnormal intensities due to preferred orientation or graininess needs continuous emphasis. Preferred orientation is particularly common in surface deposits on metals, such as oxide or sulfide layers. If the deposit is very thin, its removal may not yield enough material for examination. The diffractometer is then an ideal instrument for examining the deposit *in situ*, because of the shallow penetration of x-rays. Very thin deposits can yield good diffraction lines, and the analyst can often make a positive identification, even in the presence of pronounced preferred orientation, if he or she has some knowledge of crystal morphology and of the chemical composition of the deposit. Thus, a very thin deposit on sheet steel was identified as graphite by a single strong basal-plane reflection and the knowledge that graphite crystals are normally oriented with their basal planes more or less parallel to the substrate on which they have grown.

Preferred orientation is also a problem with particulate samples which have well-defined, platey habits. It is easy to imagine that plate-like samples will tend to lie with their major face parallel to the sample surface. If large grains are present in a particulate sample, some diffraction lines will have abnormally large intensities. While graininess can be regarded as a type of preferred orientation, it is better to treat its effect separately. With a few large crystals present in an otherwise suitable sample, there is a chance that one of the large crystals is correctly oriented for *hkl* diffraction. In this case, the intensity of that particular *hkl* will be abnormally high. The difference between graininess and preferred orientation can be seen upon repacking the sample (with the same material as was used in the first packing). In a sample with preferred orientation, the peak intensities I_j/I_i will be reproduced from packing to packing. If large grains are present, the intensities will vary widely.

The data in Table 8 illustrates what might be observed from grainy samples. The sample was produced from shards of a 100 Si wafer mixed with 325 mesh Si powder. The first three columns of intensities are from three separate samples made by smearing petroleum jelly on a glass slide and sprinkling the sample material on the slide. The second group of three columns of intensities are from the same material packed into a powder holder. The final column gives the PDF intensity ratios. As would be expected, the intensity of the 400 line is abnormally high in one case. It is for this reason that it is always desirable to run at least three re-packings of a sample of an unknown.

These remarks on abnormal intensities are not meant to suggest that successful use of the Hanawalt method requires extremely accurate intensity measurements. If reasonable care has been taken to minimize preferred orientation, then it is often

TABLE 8

			I/I_i						$(I/I_i)_{PDF}$
hkl	*d*(Å)		Glass slide			Powder holder			
		Packing:	1	2	3	1	2	3	
111	3.11		100	100	100	69	100	100	100
220	1.91		51	59	52	31	44	46	55
311	1.63		37	26	23	20	25	30	30
400	1.35		7	7	5	100	7	3	6
331	1.24		5	11	10	8	10	13	11
422	1.11		5	7	8	8	11	14	12
511	1.04		5	-	4	5	6	4	6

enough to be able to list the diffraction lines in the correct *order* of decreasing intensity.

Errors in the PDF itself are generally more serious, because they may go undetected by the investigator and lead to mistaken identifications. Many such errors existed in the earlier editions of the file, but critical editing by members of the ICDD has resulted in the removal of incorrect data and in the labeling of doubtful data as being of low reliability. Moreover, the ICDD supports continuing work at the National Institute of Standards and Technology and elsewhere, in which the diffraction patterns of pure, well-characterized specimens are carefully prepared and the data added to the file. Most of the high-quality, "starred" patterns in the card file, such as that in Fig. 1, have been obtained at NIST.

Whenever any doubt exists in the investigator's mind as to the validity of a particular identification, he or she should prepare her or his, own standard pattern. Thus, if the unknown has been tentatively identified as substance X, the pattern of pure X should be prepared under exactly the same experimental conditions used for the pattern of the unknown. Comparison of the two patterns will furnish positive proof, or disproof, of identity.

The Hanawalt method fails completely, of course, when the unknown is a substance not listed, in the PDF, or when the unknown is a mixture and the component to be identified is not present in sufficient quantity to yield a good diffraction pattern. The latter effect can be quite troublesome and mixtures may be encountered which contain more than 50 percent of a particular component without the pattern of that component being visible in the pattern of the mixture.

PROBLEMS

The d and I/I_i values tabulated in Probs. 1 to 4 represent the diffraction patterns of various unknown substances. Identify the substances involved by reference to the ICDD powder diffraction file.

*1	d(Å)	I/I_1	d(Å)	I/I_1	d(Å)	I/I_1
	3.66	50	1.46	10	1.06	10
	3.17	100	1.42	50	1.01	10
	2.24	80	1.31	30	0.96	10
	1.91	40	1.23	10	0.85	10
	1.83	30	1.12	10		
	1.60	20	1.08	10		

2

d(Å)	I/I_1	d(Å)	I/I_1	d(Å)	I/I_1
5.85	60	2.08	10	1.47	20
3.05	30	1.95	20	1.42	10
2.53	100	1.80	60	1.14	20
2.32	10	1.73	20	1.04	10

***3**

d(Å)	I/I_1	d(Å)	I/I_1	d(Å)	I/I_1
2.40	50	1.25	20	0.85	10
2.09	50	1.20	10	0.81	20
2.03	100	1.06	20	0.79	20
1.75	40	1.02	10		
1.47	30	0.92	10		
1.26	10				

4

d(Å)	I/I_1	d(Å)	I/I_1	d(Å)	I/I_1
3.02	100	2.11	10	1.46	10
2.79	10	1.90	20	1.17	10
2.52	10	1.65	10		
2.31	30	1.62	10		

REFERENCES

The following books are listed more or less in the order they are encountered in the text

G.17 Harold P. Klug and Leroy E. Alexander. *X-Ray Diffraction Procedures*, 2nd ed. (New York: Wiley, 1974). Contains a great deal of useful detail on the theory and operation of powder cameras and diffractometers. Covers the following topics in depth: chemical analysis by diffraction, parameter measurement, line-broadening analysis, texture determination, stress measurement, and studies of amorphous materials. Single-crystal methods are not included.

G.25 Ron Jenkins and Robert L. Snyder. *Introduction to X-ray Powder Diffractometry* (New York, John Wiley & Sons, Inc, 1996).

ANSWERS TO SELECTED PROBLEMS

1. BaS **3**. Mixture of Ni and NiO

This page intentionally left blank

Determination of Crystal Structure

1 INTRODUCTION

Since 1913, when W. L. Bragg solved the structure of NaCl, the structures of many thousands of crystals, organic and inorganic, have been determined. This vast body of knowledge is of fundamental importance in such fields as crystal chemistry, solid-state physics, and the biological sciences because, to a large extent, structure determines properties and the properties of a substance are never fully understood until its structure is known. In metallurgy, a knowledge of crystal structure is a necessary prerequisite to any understanding of such phenomena as plastic deformation, alloy formation, or phase transformations. Crystal structure underlies technologically useful effects such as piezoelectricity, and knowledge of it is required for understanding the nature of point and other atomic-scale defects controlling many materials properties.

The work of structure determination goes on continuously since there is no dearth of unsolved structures. New substances are constantly being synthesized, and the structures of many old ones remain unknown. In themselves, crystal structures vary widely in complexity: the simplest can be solved in a few hours, while the more complex may require months or even years for their complete solution. (Proteins form a notable example of the latter kind; some protein structures are now known, but others still defy solution.) Complex structures require complex methods of solution, and structure determination in its entirety is more properly the subject of a series of books than of a single chapter. Therefore, only some of the principles and their application to the solution of fairly simple structures will be considered here. Because polycrystalline diffraction patterns are the kind most often encountered by the materials scientist/engineer, this chapter will treat only these methods.

The basic principles involved in structure determination may already be familiar to you. In brief, the crystal structure of a substance determines the diffraction pattern of that substance or, more specifically, the shape and size of

From Chapter 10 of *Elements of X-Ray Diffraction*, Third Edition. B.D. Cullity, S.R. Stock.

the unit cell determines the angular positions of the diffraction lines, and the arrangement of the atoms within the unit cell determines the relative intensities of the lines. It may be worthwhile to state this again in tabular form:

Crystal structure	Diffraction pattern
Unit cell	Line positions
Atom positions	Line intensities

Since structure determines the diffraction pattern, it should be possible to go in the other direction and deduce the structure from the pattern. It is possible *but not by any direct manner*. Given a structure, its diffraction pattern can be calculated in a very straightforward fashion; but the reverse problem, that of directly calculating the structure from the observed pattern, has not yet been solved for the general case (Sec. 7). The procedure adopted is essentially one of trial and error. On the basis of an educated guess, a structure is assumed, its diffraction pattern calculated, and the calculated pattern compared with the observed one. If the two agree in all detail, the assumed structure is correct; if not, the process is repeated as often as is necessary to find the correct solution. The problem is not unlike that of deciphering a code, and requires of the crystallographer the same qualities possessed by a good cryptanalyst, namely, knowledge, perseverance, and not a little intuition.

The determination of an unknown structure proceeds in three major steps:

1. The shape and size of the unit cell are deduced from the angular positions of the diffraction lines. An assumption is first made as to which of the seven crystal systems the unknown structure belongs and then, on the basis of this assumption, the correct Miller indices are assigned to each reflection. This step is called “indexing the pattern” and is possible only when the correct choice of crystal system has been made. Once this is done, the shape of the unit cell is known (from the crystal system), and its size is calculable from the positions and Miller indices of the diffraction lines.
2. The number of atoms per unit cell is then computed from the shape and size of the unit cell, the chemical composition of the specimen, and its measured density.
3. Finally, the positions of the atoms within the unit cell are deduced from the relative intensities of the diffraction lines.

Only when these three steps have been accomplished is the structure determination complete. The third step is generally the most difficult, and there are many structures which are known only incompletely, in the sense that this final step has not yet been made. Nevertheless, a knowledge of the shape and size of the unit cell, without any knowledge of atom positions, is in itself of very great value in many applications.

The average materials scientist/engineer is rarely, if ever, called upon to determine an unknown crystal structure. If the structure is at all complex, its determination is a job for a specialist in x-ray crystallography, who can bring special techniques, both experimental and mathematical, to bear on the problem. He or she should, however, know enough about structure determination to unravel any simple structures encountered and, what is more important, to index the powder patterns of substances of *known* structure, as this is a routine problem in almost all diffraction work. The procedures given below for indexing patterns are applicable whether the structure is known or not, but they are of course very much easier to apply if the structure is known beforehand.

Many crystal structures allow substitution of atoms of one element for another. Materials such as GaAs and InSb, both of which have the zinc blende structure, and have lattice parameters 5.653 Å and 6.479 Å, respectively, are isotypes. As such, it is not surprising that considerable In, for example, can replace Ga atoms in the GaAs lattice; this type of alloying, in which the minority atoms are in solid solution, can improve mechanical properties, i.e., resistance to dislocation generation, propagation and multiplication. Whenever there are two types of atoms occupying a lattice or a set of sub-lattice sites, it is possible that the different atoms take up a nonrandom or ordered arrangement. This ordering can be long range or short range, and examining ordering is an important subset of crystal structure determination in materials work. Accordingly, the last three sections of this chapter concern themselves with what can be learned about ordering from diffraction from polycrystalline samples.

2 PRELIMINARY TREATMENT OF DATA

The first step in determining the crystal structure of a polycrystalline sample is recording the diffraction pattern over as wide a range of 2θ as possible, normally with diffractometry. Specimen preparation must ensure random orientation of the individual particies of powder, if the observed relative intensities of the diffraction lines are to have any meaning in terms of crystal structure. After the pattern is obtained the value of $\sin^2\theta$ is calculated for each diffraction line; this set of $\sin^2\theta$ values is the raw material for the determination of cell size and shape. Or one can calculate the d value of each line and work from this set of numbers.

Since the problem of structure determination is one of finding a structure which will account for all the lines on the pattern, in both position and intensity, the investigator must make sure at the outset that the observed pattern does not contain any extraneous lines. The ideal pattern contains lines formed by x-rays of a single wavelength, diffracted only by the substance whose structure is to be determined. There are therefore two sources of extraneous lines:

1. *Diffraction of x-rays having wavelengths different from that of the principal component of the radiation.* If filtered radiation is used, then $K\alpha$ radiation is the principal component, and characteristic x-rays of any other wave-

length may produce extraneous lines. The chief offender is $K\beta$ radiation, which is never entirely removed by a filter and may be a source of extraneous lines for reflections with high diffracting power. A quick check for $K\beta$ radiation begins with identification of the most intense line of the pattern, presumably formed with $K\alpha$ radiation. Using $\lambda_{K\alpha}$, d_1 is calculated from $2\theta_\alpha$ via Bragg's law. If $K\beta$ radiation is present, a diffraction peak from d_1 results at a $2\theta_\beta$ different from $2\theta_\alpha$ and the relationship between diffraction angles and wavelengths is

$$\left(\frac{\lambda_{K\alpha}^2}{\lambda_{K\beta}^2}\right)\sin^2\theta_\beta = \sin^2\theta_\alpha, \tag{1}$$

where $\lambda_{K\alpha}^2/\lambda_{K\beta}^2$ has a value near 1.2 for most radiations. If it is suspected that a particular line is due to $K\beta$ radiation, multiplication of its $\sin^2\theta$ value by $\lambda_{K\alpha}^2/\lambda_{K\beta}^2$ will give a value equal, or nearly equal, to the value of $\sin^2\theta$ for some $K\alpha$ line on the pattern, unless the product exceeds unity. The $K\alpha$ line corresponding to a given $K\alpha$ line is always located at a smaller angle 2θ and has lower intensity. However, since $K\alpha$ and $K\beta$ lines (from different planes) may overlap on the pattern, Eq. (1) alone can establish only the possibility that a given line is due to $K\beta$ radiation, but it can never prove that it is. Another possible source of extraneous lines is L characteristic radiation from tungsten contamination on the target of the x-ray tube, particularly if the tube is old. If such contamination is suspected, equations such as (1) can be set up to test the possibility that certain lines are due to tungsten radiation.

2. *Diffraction by substances other than the unknown*. Such substances are usually impurities in the specimen but may also include the specimen mount or badly aligned slits. Careful specimen preparation and good experimental technique will eliminate extraneous lines due to these causes.

For reasons beyond the scope of this chapter, the observed values of $\sin^2\theta$ always contain small systematic errors. These errors are not large enough to cause any difficulty in indexing patterns of cubic crystals, but they can seriously interfere with the determination of some noncubic structures. The best method of removing such errors from the data is to calibrate the camera or diffractometer with a substance of known lattice parameter, mixed with the unknown, i.e., by adding an internal standard. The difference between the observed and calculated values of $\sin^2\theta$ for the standard substance gives the error in $\sin^2\theta$, and this error can be plotted as a function of the observed values of $\sin^2\theta$. Figure 1 shows a correction curve of this kind, obtained with a particular specimen and a particular Hull/Debye–Scherrer camera.[1] The errors represented by the ordinates of such a

---

[1] For the shape of this curve.

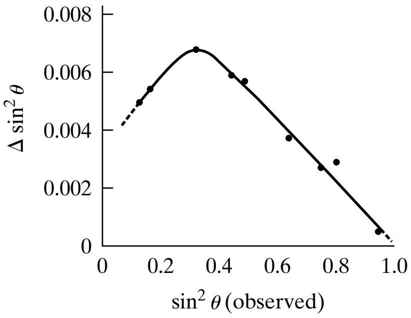

Figure 1 An example of a correction curve for $\sin^2\theta$ values.

curve can then be applied to each of the observed values of $\sin^2\theta$ for the diffraction lines of the unknown substance. For the particular determination represented by Fig. 1, the errors shown are to be subtracted from the observed values.

3 INDEXING PATTERNS OF CUBIC CRYSTALS

A cubic crystal gives diffraction lines whose $\sin^2\theta$ values satisfy the following equation, obtained by combining the Bragg's law with the plane-spacing equation for the cubic system, as in Eq. (3-11):

$$\frac{\sin^2\theta}{(h^2 + k^2 + l^2)} = \frac{\sin^2\theta}{s} = \frac{\lambda^2}{4a^2}. \tag{2}$$

Since the sum $s = (h^2 + k^2 + l^2)$ is always integral and $\lambda^2/4a^2$ is a constant for any one pattern, the problem of indexing the pattern of a cubic substance is one of finding a set of integers s which will yield a constant quotient when divided one by one into the observed $\sin^2\theta$ values. (Certain integers, such as 7, 15, 23, 28, 31, etc., are impossible because they cannot be formed by the sum of three squared integers.) Once the proper integers s are found, the indices *hkl* of each line can be written down by inspection or from the tabulation in "Appendix: Quadratic Forms of Miller Indices."

The proper set of integers s is not hard to find because there are only a few possible sets. Each of the four common cubic lattice types has a characteristic sequence of diffraction lines, described by their sequential s values:

Simple cubic:	1, 2, 3, 4, 5, 6, 8, 9, 10, 11, 12, 13, 14, 16, . . .
Body-centered cubic:	2, 4, 6, 8, 10, 12, 14, 16, . . .
Face-centered cubic:	3, 4, 8, 11, 12, 16, . . .
Diamond cubic:	3, 8, 11, 16, . . .

Each set can be tried in turn. If a set of integers satisfying Eq. (2) cannot be found, then the substance involved does not belong to the cubic system, and other possibilities (tetragonal, hexagonal, etc.) must be explored. Note that some s values from the lists shown above may be absent, even though the sample in question properly belongs to one of the three cubic Bravais lattices. Diamond cubic materials such as

Si are FCC, but symmetry, due to presence of two Si atoms per lattice site, dictates that $s = 4, 12$, etc. will be absent.

The following example will illustrate the steps involved in indexing the pattern of a cubic substance and finding its lattice parameter. In this particular example, Cu $K\alpha$ radiation was used and eight diffraction lines were observed. Their $\sin^2\theta$ values are listed in the second column of Table 1. Values of $(\sin^2\theta)/s$ for the three cubic Bravais lattices are given in columns 4, 8, and 10 for FCC, simple cubic and BCC, respectively. If the observed lines are from a particular lattice type, the $(\sin^2\theta)/s$ values should be constant. The data in Table 1 reveal the material to be fcc. The fifth column lists the lattice parameter calculated from each line position, and the sixth column gives the Miller indices of each line. The systematic error in $\sin^2\theta$ appears as a gradual decrease in the value of $\lambda^2/4a^2$, and a gradual increase in the value of a, as θ increases. The systematic error in a decreases as θ increases; therefore, the value of a for the highest-angle line, namely, 3.62 Å, is the most accurate of those listed. The analysis of line positions face-centered therefore leads to the conclusion that the substance involved, copper in this case, is cubic in structure with a lattice parameter of 3.62 Å. Certain information about the arrangement of atoms within the unit cell has been obtained, and use of observed line intensities was required in order to obtain this information. In this particular case, the observation consisted simply in noting which lines had zero intensity.

TABLE 1

1	2	3	4	5	6	7	8	9	10
			FCC			SC		BCC	
Line	$\sin^2\theta$	$s = (h^2+k^2+l^2)$	$\frac{\sin^2\theta}{s} = \frac{\lambda^2}{4a^2}$	a(Å)	hkl	s	$\frac{\sin^2\theta}{s}$	s	$\frac{\sin^2\theta}{s}$
1	0.140	3	0.0467	3.57	111	1	0.140	2	0.0700
2	0.185	4	0.0463	3.59	200	2	0.093	4	0.0463
3	0.369	8	0.0461	3.59	220	3	0.123	6	0.0615
4	0.503	11	0.0457	3.61	311	4	0.123	8	0.0629
5	0.548	12	0.0457	3.61	222	5	0.110	10	0.0548
6	0.726	16	0.0454	3.62	400	6	0.121	12	0.0605
7	0.861	19	0.0453	3.62	331	8	0.108	14	0.0615
8	0.905	20	0.0453	3.62	420	9	0.101	16	0.0566

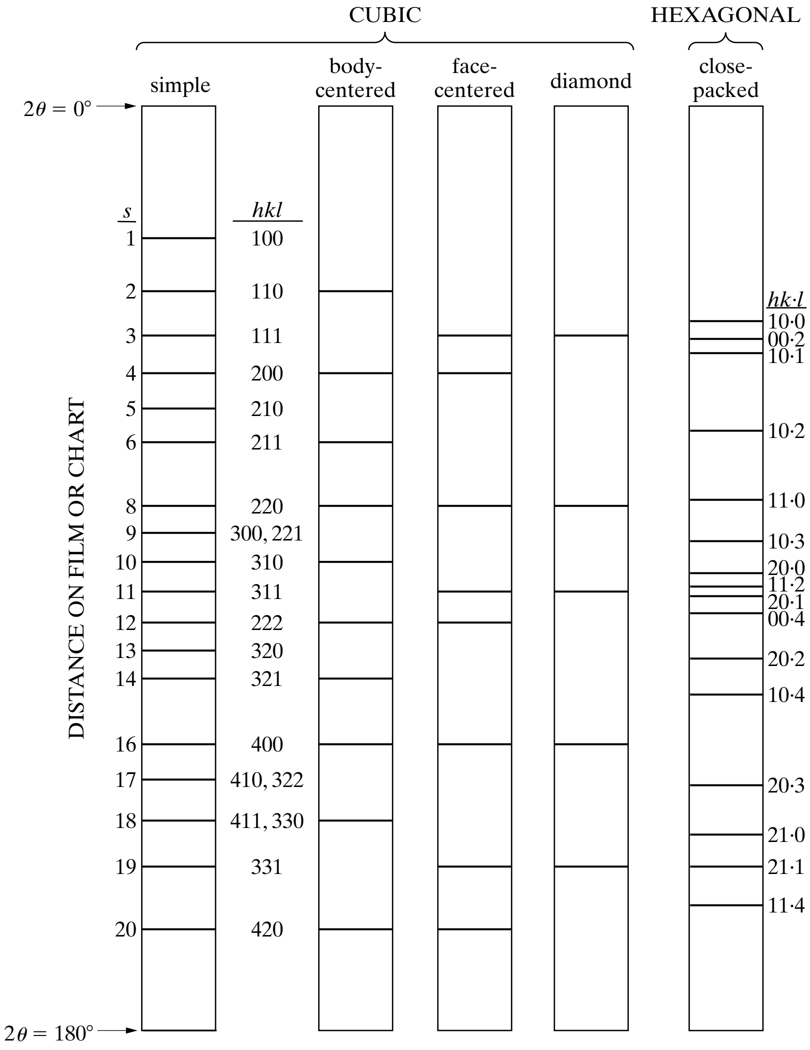

Figure 2 Calculated diffraction patterns for various lattices $s = (h^2 + k^2 + l^2)$

The characteristic line sequences for cubic lattices are shown graphically in Fig. 2, in the form of calculated diffraction patterns. The calculations are made for Cu $K\alpha$ radiation and a lattice parameter a of 3.50 Å. The positions of all the diffraction lines which would be formed under these conditions are indicated as they would appear on a film or chart of the length shown. (For comparative purposes, the pattern of a hexagonal close-packed structure is also illustrated, since this structure is frequently encountered. The line positions are calculated for Cu $K\alpha$ radiation, $a = 2.50$ Å, and $c/a = 1.633$, which corresponds to the close packing of spheres.)

Powder patterns of cubic substances can usually be distinguished at a glance from those of noncubic substances, since the latter patterns normally contain many more lines. In addition, the Bravais lattice can usually be identified by inspection: there is an almost regular sequence of lines in simple cubic and body-centered cubic patterns, but the former contains almost twice as many lines, while a face-centered cubic pattern is characterized by a pair of lines, followed by a single line, followed by a pair, another single line, etc.

The problem of indexing a cubic pattern is of course very much simplified if the substance involved is *known* to be cubic and if the lattice parameter is also known. The simplest procedure then is to calculate the value of $\lambda^2/4a^2$ and divide this value into the observed $\sin^2\theta$ values to obtain the value of s for each line.

There is one difficulty that may arise in the interpretation of cubic powder patterns, and that is due to a possible ambiguity between simple cubic and body-centered cubic patterns. There is a regular sequence of lines in both patterns up to the sixth line; the sequence then continues regularly in body-centered cubic patterns, but is interrupted in simple cubic patterns since $s = 7$ is impossible. Therefore, if λ is so large, or a so small, that six lines or less appear on the pattern, the two Bravais lattices are indistinguishable. For example, suppose that the substance involved is actually body-centered cubic but the investigator mistakenly indexes it as simple cubic, assigning the value $s = 1$ to the first lines, $s = 2$ to the second line, etc. He or she thus obtains a value of $\lambda^2/4a^2$ twice as large as the true one, and a value of a which is $1/\sqrt{2}$ times the true one. This mistake becomes apparent when the number of atoms per unit cell is calculated from the measured density of the specimen (Sec. 6); the wrong cell size will give a nonintegral value for the number of atoms per cell, and such a value is impossible. The ambiguity in the diffraction pattern itself can be avoided by choosing a wavelength short enough to produce at least seven lines on the pattern.

4 INDEXING PATTERNS OF NONCUBIC CRYSTALS

The problem of indexing powder patterns becomes more difficult as the number of unknown parameters increases. There is only one unknown parameter for cubic crystals, the cell edge a, but noncubic crystals have two or more, and special techniques have had to be devlsed in order to index the patterns of such crystals. Graphical methods were the primary method before computers became widespread; availability of spreadsheet programs, for example, allows rapid implementation of routines for indexing diffraction patterns from non-cubic phases. Analytical methods of indexing involve arithmetical manipulation of the observed $\sin^2\theta$ values in an attempt to find certain relationships among them. Since each crystal system is characterised by particular relationships between $\sin^2\theta$ values, recognition of these relationships identifies the crystal system and leads to a solution of the line indices. These analytical methods are due mainly to Hesse and Lipson [1, 2, G.15, G.32, G.33].

Tetragonal System

Here the $\sin^2\theta$ values must obey the relation:

$$\sin^2\theta = A(h^2 + k^2) + Cl^2, \tag{3}$$

where $A(= \lambda^2/4a^2)$ and $[C = \lambda^2/4c^2]$ are constants for any one pattern. The problem is to find these constants, since, once found, they will disclose the cell parameters a and c and enable the line indices to be calculated. The value of A is obtained from the $hk0$ lines. When $l = 0$, Eq. (3) becomes

$$\sin^2\theta = A(h^2 + k^2). \tag{4}$$

The permissible values of $(h^2 + k^2)$ are 1, 2, 4, 5, 8, etc. Therefore the $hk0$ lines must have $\sin^2\theta$ values in the ratio of these integers, and A will be some number which is $1, \frac{1}{2}, \frac{1}{4}, \frac{1}{5}, \frac{1}{8}$, etc., times the $\sin^2\theta$ values of these lines. C is obtained from the other lines on the pattern and the use of Eq. (3) in the form

$$\sin^2\theta - A(h^2 + k^2) = Cl^2. \tag{5}$$

Differences represented by the left-hand side of the equation are set up, for various assumed values of h and k, in an attempt to find a consistent set of Cl^2 values, which must be in the ratio 1, 4, 9, 16, etc. Once these values are found, C can be calculated.

Hexagonal System

For hexagonal crystals, an exactly similar procedure is used. In this case, $\sin^2\theta$ values are given by

$$\sin^2\theta = A(h^2 + hk + k^2) + Cl^2, \tag{6}$$

where $A = \lambda^2/3a^2$ and $C = \lambda^2/4c^2$. Permissible values of $(h^2 + hk + k^2)$ are tabulated in "Appendix: Quadratic Forms of Miller Indices" they are 1, 3, 4, 7, 9, etc. The indexing procedure is best illustrated by means of a specific example, namely, the powder pattern of zinc, whose observed $\sin^2\theta$ values are listed in Table 2. First divide the $\sin^2\theta$ values by the integers 1, 3, 4, etc., and tabulate the results, as shown by Table 3, which applies to the first six lines of the pattern. Then examine these numbers, looking for quotients which are equal to one another or equal to one of the observed $\sin^2\theta$ values. In this case, the two starred entries, 0.112 and 0.111, are the most nearly equal, so assume that lines 2 and 5 are $hk0$ lines. Then, tentatively put $A = 0.112$ which is equivalent to saying that line 2 is 100. Since the $\sin^2\theta$ value of line 5 is very nearly 3 times that of line 2, line 5 should be 110. To find the value of C, the equation

$$\sin^2\theta - A(h^2 + hk + k^2) = Cl^2 \tag{7}$$

TABLE 2

Line	Intensity	$\sin^2\theta$	*hkl*
1	s	0.097	00.2
2	s	0.112	10.0
3	vs	0.136	10.1
4	m	0.209	10.2
5	s	0.322	10.3, 11.0
6	vw	0.390	00.4
7	m	0.434	11.2
8	m	0.472	20.1
9	vw	0.547	20.2
10	w	0.668	20.3
11	m	0.722	11.4, 10.5
12	m	0.806	21.1
13	w	0.879	21.2

must be used. Now subtract from each $\sin^2\theta$ value the value of A (= 0.112), $3A$ (= 0.336), $4A$ (= 0.448), etc., and look for remainders (Cl^2) which are in the ratio of 1, 4, 9, 16, etc. These figures are given in Table 4. Here the five starred entries are of interest, because these numbers (0.024, 0.097, 0.221, and 0.390) are very nearly in the ratio 1, 4, 9, and 16. Therefore put $0.024 = C(1)^2$, $0.097 = C(2)^2$, $0.221 = C(3)^2$, and $0.390 = C(4)$. This gives $C = 0.024$ and immediately identifies line 1 as 002 and line 6 as 004. Since line 3 has a $\sin^2\theta$ value equal to the sum of A and C, its indices must

TABLE 3

Line	$\sin^2\theta$	$\frac{\sin^2\theta}{3}$	$\frac{\sin^2\theta}{4}$	$\frac{\sin^2\theta}{7}$	*hkl*
1	0.097	0.032	0.024	0.014	
2	0.112*	0.037	0.028	0.016	100
3	0.136	0.045	0.034	0.019	
4	0.209	0.070	0.052	0.030	
5	0.332	0.111*	0.083	0.047	110
6	0.390	0.130	0.098	0.056	

TABLE 4

Line	$\sin^2\theta$	$\sin^2\theta - A$	$\sin^2\theta - 3A$	*hkl*
1	0.097*			002
2	0.112	0.000		100
3	0.136	0.024*		101
4	0.209	0.097*		102
5	0.332	0.221*		110, 103
6	0.390*	0.278	0.054	004

be 101. Similarly, the indices of lines 4 and 5 are found to be 102 and 103, respectively. In this way, indices are assigned to all the lines on the pattern, and a final check on their correctness is made in the usual manner by a comparison of observed and calculated $\sin^2\theta$ values.

Orthorhombic System

The basic equation governing the $\sin^2\theta$ values is now

$$\sin^2\theta = Ah^2 + Bk^2 + Cl^2. \tag{8}$$

The indexing problem is considerably more difficult here, in that three unknown constants, A, B, and C, have to be determined. The general procedure, which is too lengthy to illustrate here, is to search for significant differences between various pairs of $\sin^2\theta$ values. For example, consider any two lines having indices *hk*0 and *hk*1, with *hk* the same for each, such as 120 and 121; the difference between their $\sin^2\theta$ values is C. Similarly, the difference between the $\sin^2\theta$ values of two lines such as 310 and 312 is $4C$, and so on. If the structure is such that there are many lines missing from the pattern, because of a zero structure factor for the corresponding planes, then the difficulties of indexing are considerably increased, inasmuch as the missing lines may be the very ones which would supply the most easily recognized clues if they were present. Despite such difficulties, this analytical method has been applied successfully to a number of orthorhombic patterns. One requisite for its success is fairly high accuracy in the $\sin^2\theta$ values (at least ± 0.0005), and the investigator should therefore correct all observations for systematic errors before attempting to index the pattern.

Monoclinic and Triclinic Systems

These crystal systems involve four and six independent constants, respectively. The corresponding powder patterns are of great complexity and may contain more than a hundred lines.

General

Analytical methods of indexing are search procedures designed to reveal certain numerical relationships among the observed $\sin^2\theta$ values. The digital computer is therefore a natural tool to use, and many computer programs have been written for the indexing of powder patterns. Spreadsheets can be used to great effect.

Computer indexing is not always successful. The computer may yield not one but many sets of indices that approximately conform to the input data; it is then up to the investigator's experience and judgment to select the correct set. Extraneous diffraction lines and inaccurate $\sin^2\theta$ values can mislead a computer as well as a human searcher.

The powder patterns of low-symmetry substances are so difficult to solve that the crystal structures of such substances are almost always determined by examining a single crystal, by either the rotating-crystal method, one of its variants, With these methods the x-ray crystallographer can, without much difficulty or by an other technique determine the shape and size of an unknown unit cell, no matter how low its symmetry. The single-crystal specimen need not be large: a crystal as small as 0.1 mm in any dimension can be successfully handled and will give a satisfactory diffraction pattern with tube-based x-radiation. With synchrotron x-radiation, samples with dimensions of micrometers have been studied. Many substances are very difficult to prepare in single-crystal form, and the development of the Rietveld method for polycrystalline single- and multi-phase samples has greatly extended the range of structures which can be determined [3-5].

5 THE EFFECT OF CELL DISTORTION ON THE POWDER PATTERN

At this point it is profitable to digress slightly from the main subject of this chapter and to examine some of the changes produced in a powder pattern when the unit cell of the substance involved is distorted in various ways. Because there are many more lines on the pattern of a substance of low symmetry, such as triclinic, than on the pattern of a substance of high symmetry, such as cubic, any distortion of the unit cell which decreases its symmetry, in the sense of introducing additional variable parameters, will increase the number of lines on the powder pattern.

Figure 3 graphically illustrates this point. On the left is the calculated diffraction pattern of the body-centered cubic substance whose unit cell is shown at the top. The line positions are computed for $a = 4.00$ Å and Cr $K\alpha$ radiation. If this cell is expanded or contracted uniformly but still remains cubic, the diffraction lines merely shift their positions but do not increase in number, since no change in cell symmetry is involved. However, if the cubic cell is distorted along only one axis, then it

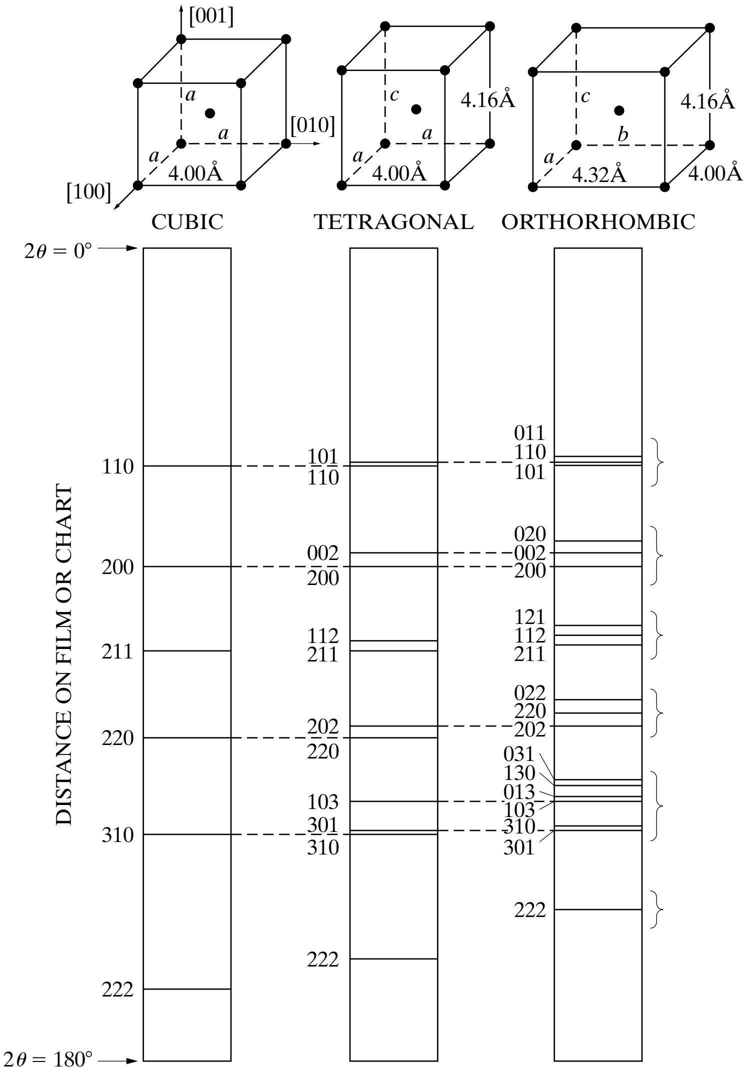

Figure 3. Effects of cell distortion on powder patterns. Lines unchanged in position are connected by dashed lines.

becomes tetragonal, its symmetry decreases, and more diffraction lines are formed. The center pattern shows the effect of stretching the cubic cell by 4 percent along its [001] axis, so that *c* is now 4.16 Å. Some lines are unchanged in position, some are shifted, and new lines have appeared. If the tetragonal cell is now stretched by 8 percent along its [010] axis, it becomes orthorhombic, with $a = 4.00$ Å, $b = 4.32$ Å, and $c = 4.16$ Å, as shown on the right. The result of this last distortion is to add still more lines to the pattern. The increase in the number of lines is due essentially to the introduction of new d spacings, caused by nonuniform distortion. Thus, in the cubic cell, d_{200}, d_{020}, d_{002} are the same and only one line is formed, called the 200 line, but this line splits into two when the cell becomes tetragonal, since now $d_{002} \neq d_{200} \neq d_{020}$. When the cell becomes orthorhombic, all three spacings are different and three lines are formed.

Changes of this nature are not uncommon among phase transformations and ordering reactions. For example, the powder pattern of slowly cooled plain carbon steel shows lines due to ferrite (body-centered cubic) and cementite (Fe_3C, orthorhombic). When the same steel is quenched from the austenite region, the phases present are martensite (body-centered tetragonal) and, possibly, some untransformed austenite (face-centered cubic). The a and c parameters of the martensite cell do not differ greatly from the a parameter of the ferrite cell. The result is that the diffraction pattern of a quenched steel shows pairs of martensite lines occurring at about the same 2θ positions as the individual lines of ferrite in the previous pattern. (These line pairs, however, are seldom resolved; martensite contains so much microstrain that each line of a pair is so broad that it merges with its neighbor.) If the quenched steel is now tempered, the martensite will ultimately decompose into ferrite and cementite, and each pair of martensite lines will coalesce into a single ferrite line. Somewhat similar effects can be produced in a copper-gold alloy having the composition represented by the formula AuCu. This alloy is cubic in the disordered state but becomes either tetragonal or orthorhombic when ordered, depending on the ordering temperature (see Sec. 10).

The changes produced in a powder pattern by cell distortion depend, in degree, on the amount of distortion. If the latter is small, the pattern retains the main features of the pattern of the original undistorted cell. Thus, in Fig. 3, the nineteen lines of the orthorhombic pattern fall into the six bracketed groups shown, each group corresponding to one of the single lines on the cubic pattern. In fact, an experienced crystallographer, if confronted with this orthorhombic pattern, might recognize this grouping and guess that the unit cell of the substance involved was not far from cubic in shape, and that the Bravais lattice was either simple or body-centered, since the groups of lines are spaced in a fairly regular manner. But if the distortion of the cubic cell had been much larger, each line of the original pattern would split into such widely separated lines that no features of the original pattern would remain.

6 DETERMINATION OF THE NUMBER OF ATOMS IN A UNIT CELL

To return to the subject of structure determination, the next step after establishing the shape and size of the unit cell is to find the number of atoms in that cell, because the number of atoms must be known before their positions can be determined. Because the volume of the unit cell, calculated from the lattice parameters by means of the equations given in "Appendix: Lattice Geometry," multiplied by the measured density of the substance equals the weight of all the atoms in the cell

$$\sum A = \frac{\rho V'}{1.66042}, \tag{3.14}$$

where ΣA is the sum of the atomic weights of the atoms in the unit cell, ρ is the density (g/cm^3), and V' is the volume of the unit cell (Å^3). If the substance is an element of atomic weight A, then

$$\sum A = n_1 A,$$

where n_1 is the number of atoms per unit cell. If the substance is a chemical compound, or an intermediate phase whose composition can be represented by a simple chemical formula, then

$$\sum A = n_2 M,$$

where n_2 is the number of "molecules" per unit cell and M the molecular weight. The number of atoms per cell can then be calculated from n_2 and the composition of the phase.

When determined in this way, the number of atoms per cell is always an integer, within experimental error, except for a very few substances which have "defect structures." In these substances, atoms are simply missing from a certain fraction of those lattice sites which they would be expected to occupy, and the result is a nonintegral number of atoms per cell. FeO and the β phase in the Ni-Al system are examples.

7 DETERMINATION OF ATOM POSITIONS

To find the positions of a known number of atoms in a unit cell of known shape and size, are required, the observed relative *intensities* of the diffracted beams, since these intensities are determined by atom positions. In finding the atom positions, however, the procedure is one of trial and error, because there is no known general method of directly calculating atom positions from observed intensities.

To see why this is so, consider the two basic equations involved, namely,

$$I = |F|^2 p\left(\frac{1 + \cos^2 2\theta}{\sin^2\theta \cos\theta}\right), \tag{4-19}$$

which gives the relative intensities of the diffracted beams, and

$$F = \sum_{i}^{N} f_n e^{2\pi i(hu_n + kv_n + lw_n)}, \tag{4-11}$$

which gives the value of the structure factor F for the hkl reflection in terms of the atom positions uvw. Since the relative intensity I, the multiplicity factor p and the Bragg angle θ are known for each line on the pattern, the value of $|F|$ for each reflection follows. But $|F|$ measures only the relative amplitude of each reflection, whereas requires measurement of both the amplitude and phase of one reflection relative to another, i.e., F and not merely $|F|$. This is the crux of the problem. Since intensity, the square of the diffracted amplitude is all that can be measured, amplitude but not phase is determined, not the structure factor but only its absolute value. This "phase problem," baffled crystallographers for years, but it has been addressed via direct methods of structure determination, applicable to some structures. No direct method has yet been found powerful enough to solve the structure of *any* crystal.

Atom positions, therefore, can be determined only by trial and error. A set of atom positions is assumed, the intensities corresponding to these positions are calculated, and the calculated intensities are compared with the observed ones, the process being repeated until satisfactory agreement is reached. The problem of selecting a structure for trial is not as hopelessly broad as it sounds, since the investigator has many aids for guidance. Foremost among these is the accumulated knowledge of previously solved structures. From these known structures a few likely candidates, may be selected as a starting point. Analysis proceeds on the assumption that this unknown structure is the same as, or very similar to, one of these known ones. A great many known structures may be classified into groups according to the kind of bonding (ionic, covalent, metallic, or mixtures of these) which holds the atoms together, and a selection among these groups is aided by a knowledge of the probable kind of atomic bonding in the unknown phase, as judged from the positions of its constituent elements in the periodic table. For example, suppose the phase of unknown structure has the chemical formula AB, where A is strongly electropositive and B strongly electronegative, and that its powder pattern is characteristic of a simple cubic lattice. Then the bonding is likely to be ionic, and the CsCl structure is strongly suggested. But the FeSi structure is also a possibility. In this particular case, one or the other can be excluded by a density measurement, since the CsCl cell contains one "molecule" and the FeSi cell four. If this were not possible, diffracted intensities would have to be calculated on the basis of each cell and compared with the observed ones. It is this simple kind of structure determination, illustrated by an example in the next section, that the materials scientist or engineer should be able to carry out unaided.

Needless to say, many structures are too complex to be solved by this simple approach and the crystallographer must turn to more powerful methods. Chief among these are space-group theory and Fourier series. Although any complete description of these subjects is beyond the scope of this text, a few general remarks may serve to show their utility in structure determination. The *theory of space groups*, one of the triumphs of mathematical crystallography, relates crystal symmetry, on the atomic scale, to the possible atomic arrangements which possess that symmetry. For example, if a given substance is known to be hexagonal and to have *n* atoms in its unit cell, then space-group theory lists all possible arrangements of *n* atoms which will have hexagonal symmetry. This listing of possible arrangements aids tremendously in the selection of trial structures. A further reduction in the number of possibilities can then be made by noting the indices of the reflections absent from the diffraction pattern. By such means alone, i.e., before any detailed consideration is given to relative diffracted intensities, space-group theory can often exclude all but two or three possible atomic arrangements. There are 230 different space groups, and the possible atomic arrangements in each group are listed in [G.1, Vol. A].

A *Fourier series* is a type of infinite trigonometric series by which any kind of periodic function may be expressed. Now the one essential property of a crystal is that its atoms are arranged in space in a periodic fashion. This means that the density of electrons is also a periodic function of position in the crystal, rising to a maximum at the point where an atom is located and dropping to a low value in the region between atoms. To regard a crystal in this manner, as a positional variation of electron density rather than as an arrangement of atoms, is particularly appropriate where diffraction is involved, in that x-rays are scattered by electrons and not by atoms as such. Since the electron density is a periodic function of position, a crystal may be described analytically by means of the Fourier series. This method of description is very useful in structure determination because it can be shown that the coefficients of the various terms in the series are related to the F values of the various x-ray reflections. But such a series is not of immediate use, since the structure factors are not usually known both in magnitude and phase. However, another kind of series has been devised, called the Patterson function, whose coefficients are related to the experimentally observable $|F|$ values and which gives, not electron density, but information regarding the various interatomic vectors in the unit cell. This information is frequently enough to determine the phase of the various structure factors; then the first kind of series can be used to map out the actual electron density throughout the cell and thus disclose the atom positions.

8 EXAMPLE OF STRUCTURE DETERMINATION

As a simple example, consider an intermediate phase which occurs in the cadmium-tellurium system. Chemical analysis of the specimen, which appeared essentially one phase under the microscope, showed it to contain 46.6 weight percent Cd and 53.4 weight percent Te. This is equivalent to 49.8 atomic percent Cd and can be represented by the formula CdTe. The specimen was reduced to powder and a diffraction pattern obtained with a Hull/Debye–Scherrer camera and Cu $K\alpha$ radiation.

The observed values of $\sin^2\theta$ for the first 16 lines are listed in Table 5, together with the visually estimated relative line intensities. This pattern can be indexed on the basis of a cubic unit cell, and the indices of the observed lines are given in the table. The lattice parameter, calculated from the $\sin^2\theta$ value for the highest-angle line, is 6.46 Å.

The density of the specimen, as determined by weighing a quantity of the powder in a pyknometer bottle, was 5.82 g/cm^3.

$$\sum A = \frac{(5.82)(6.46)^2}{1.66042} = 945.$$

TABLE 5

Line	Intensity	$\sin^2 \theta$	*hkl*
1	s	0.0462	111
2	vs	0.1198	220
3	vs	0.1615	311
4	vw	0.1790	222
5	m	0.234	400
6	m	0.275	331
7	s	0.346	422
8	m	0.391	511, 233
9	w	0.461	440
10	m	0.504	531
11	m	0.575	620
12	w	0.616	533
13	w	0.688	444
14	m	0.729	711, 551
15	vs	0.799	642
16	s	0.840	731, 553

Since the molecular weight of CdTe is 240.02, the number of "molecules" per unit cell is 945/240.02 = 3.94, or 4, within experimental error.

Knowing that the unit cell of CdTe is cubic and that it contains 4 "molecules" of CdTe, i.e., 4 atoms of cadmium and 4 atoms of tellurium possible arrangements of these atoms in the unit cell can be evaluated. Examination of the indices listed in Table 5 reveals that the indices of the observed lines are all unmixed and that the Bravais lattice must be face-centered. (Not all possible sets of unmixed indices are present, however: 200, 420, 600, 442, 622 and 640 are missing from the pattern. These reflections may be too weak to be observed, and the fact that they are missing does not invalidate the conclusion that the lattice is face-centered.) Now there are two common face-centered cubic structures of the AB type, i.e., containing two different atoms in equal proportions, and both contain four "molecules" per unit cell: these are the NaCl structure and the zinc-blende form of ZnS. Both of these are logical possibilities even though the bonding in NaCl is ionic and in ZnS covalent, since both kinds of bonding have been observed in telluride structures.

The next step is to calculate relative diffracted intensities for each structure and compare them with experiment, in order to determine whether or not one of these structures is the correct one. If CdTe has the NaCl structure, then its structure factor for unmixed indices is given by

$$F^2 = 16(f_{Cd} + f_{Te})^2, \text{ if } (h + k + l) \text{ is even,}$$

$$F^2 = 16(f_{Cd} - f_{Te})^2, \text{ if } (h + k + l) \text{ is odd.} \qquad (9)$$

On the other hand, if the ZnS structure is correct, then the structure factor for unmixed indices is given by

$$|F^2| = 16(f^2_{Cd} + f^2_{Te}), \text{ if } (h + k + l) \text{ is odd,}$$

$$|F^2| = 16(f_{Cd} - f_{Te})^2, \text{ if } (h + k + l) \text{ is an odd multiple of 2,}$$

$$|F^2| = 16(f_{Cd} + f_{Te})^2, \text{ if } (h + k + l) \text{ is an even multiple of 2.} \qquad (10)$$

Even before making a detailed calculation of relative diffracted intensities by means of the NaCl structure can almost be eliminated as a possibility simply by inspection of Eqs. (9). The atomic numbers of cadmium and tellurium are 48 and 52, respectively, so the value of $(f_{Cd} + f_{Te})^2$ is several hundred times greater than the value of $(f_{Cd} - f_{Te})^2$, for all values of $(\sin\theta)/\lambda$. Then, if CdTe has the NaCl structure, the 111 reflection should be very weak and the 200 reflection very strong, Actually, 111 is strong and 200 is not observed. Further evidence that the NaCl structure is incorrect is given in the fourth column of Table 6, where the calculated intensities of the first eight possible lines are listed: there is no agreement whatever between these values and the observed intensities.

On the other hand, if the ZnS structure is assumed, intensity calculations lead to the values listed in the fifth column. The agreement between these values and the observed intensities is excellent, except for a few minor inconsistences among the low-angle reflections, and these are due to neglect of the absorption factor. In particular, note that the ZnS structure satisfactorily accounts for all the missing reflections (200, 420, etc), since the calculated intensities of these reflections are all extremely low. Therefore this sample of CdTe has the structure of the zinc-blende form of ZnS.

After a given structure has been shown to be in accord with the diffraction data, it is advisable to calculate the interatomic distances involved in that structure. This calculation not only is of interest in itself but also to disclose any gross errors that may have been made, since there is obviously something wrong with a proposed structure if it brings certain atoms impossibly close together. In the present structure, the nearest neighbour to the Cd atom at 0 0 0 is the Te atom at $\frac{1}{4}\frac{1}{4}\frac{1}{4}$. The Cd-

TABLE 6

1	2	3	4	5
Line	*hkl*	Observed Intensity	Calculated Intensity*	
			NaCl structure	ZnS structure
1	111	s	0.05	12.4
	200	nil	13.2	0.03
2	220	vs	10.0	10.0
3	311	vs	0.02	6.2
4	222	vw	3.5	0.007
5	400	m	1.7	1.7
6	331	m	0.01	2.5
	420	nil	4.6	0.01
7	422	s	. . . . . .	3.4
8	511, 333	m	. . . . . .	1.8
9	440	w	. . . . . .	1.1
10	531	m	. . . . . .	2.0
	600, 442	nil	. . . . . .	0.005
11	620	m	. . . . . .	1.8
12	533	w	. . . . . .	0.9
	622	nil	. . . . . .	0.004
13	444	w	. . . . . .	0.6
14	711, 551	m	. . . . . .	1.8
	640	nil	. . . . . .	0.005
15	642	vs	. . . . . .	4.0
16	731, 652	s	. . . . . .	3.3

*Calculated Intensities have been adjusted so that the 220 line has an intensity of 10.0 for both structures.

Te Interatomic distance is therefore $a/4 = 2.80$ Å. For comparison a "theoretical" Cd-Te interatomic distance can be found simply by averaging the distances of closest approach in the pure elements. In doing this, the atoms are treated as rigid spheres in contact and ignore the effects of coordination number and type of bonding on atom size are ignored. These distances of closest approach are 2.98 Å in pure cadmium and 2.86 Å in pure tellurium, the average being 2.92 Å. The observed Cd-Te interatomic distance is 2.80 Å, or some 4.1 percent smaller than the calculated value; this difference is not unreasonable and can be largely ascribed to the covalent bonding which characterizes this structure. In fact, it is a general rule that the A-B interatomic distance in an intermediate phase A_xB_y is always somewhat smaller than the average distance of closest approach in pure A and pure B, because the mere existence of the phase shows that the attractive forces between unlike atoms is greater than that between like atoms. If this were not true, the phase would not form.

9 ORDER-DISORDER DETERMINATION

In most substitutional solid solutions, the two kinds of atoms A and B are arranged more or less at random on the atomic sites of the lattice. In solutions of this kind the only major effect of a change in temperature is to increase or decrease the amplitude of thermal vibration. But there are some solutions which have this random structure only at elevated temperatures. When these solutions are cooled below a certain critical temperature T_c, the A atoms arrange themselves in an orderly, periodic manner on one set of atomic sites, and the B atoms do likewise on another set. The solution is then said to be *ordered* or to possess a *superlattice*. When this periodic arrangement of A and B atoms persists over very large distances in the crystal, it is known as *long-range order*. If the ordered solution is heated above T_c, the atomic arrangement becomes more or less random again and the solution is said to be *disordered*.

The change in atom arrangement which occurs on ordering changes a large number of physical and chemical properties, and the existence of ordering may be inferred from some of these changes. However, the only conclusive evidence for a disorder-order transformation is a particular kind of change in the x-ray diffraction pattern of the substance. Evidence of this kind was first obtained by the American metallurgist Bain in 1923, for a gold-copper solid solution having the composition $AuCu_3$ [6]. Since that time, the same phenomenon has been discovered in many other alloy systems.

Data on the ordered structures found in particular alloys are given by Barrett and Massalski [G.10] and Pearson [G.9]. The theory of the diffraction phenomena involved is treated by Warren [G.10] and Guinier [G.30].

10 LONG-RANGE ORDER

The classic example of the order-disorder transformation appears in the copper-gold system. The gold and copper atoms of $AuCu_3$, above a critical temperature of

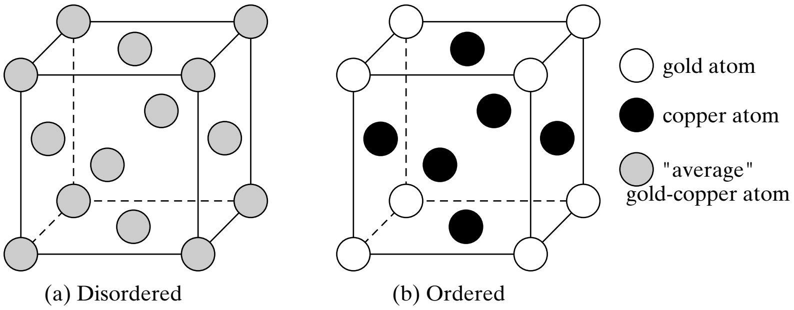

(a) Disordered (b) Ordered

Figure 4 Unit cells of the disordered and ordered forms of $AuCu_3$

about 390°C, are arranged more or less at random on the atomic sites of a face-centered cubic lattice, as illustrated in Fig. 4(a). If the disorder is complete, the probability that a particular site is occupied by a gold atom is simply $\frac{1}{4}$, the atomic fraction of gold in the alloy, and the probability that it is occupied by a copper atom is $\frac{1}{4}$, the atomic fraction of copper. These probabilities are the same for every site and, considering the structure as a whole, a statistically "average" gold-copper atom occupies each site. Below the critical temperature, the gold atoms in a perfectly ordered alloy occupy only the corner positions of the unit cube and the copper atoms the face-centered positions, as illustrated in Fig 4(b). Both structures are cubic and have practically the same lattice parameters. Figure 5 shows how the two atomic arrangements differ on a particular lattice plane. The same kind of ordering has been observed in $PtCu_3$, $FeNi_3$, $MnNi_3$, and $(MnFe)Ni_3$.

What differences will exist between the diffraction patterns of ordered and disordered $AuCu_3$? Since there is only a very slight change in the size of the unit cell on ordering, and none in its shape, there will be practically no change in the positions of the diffraction lines. But the change in the positions of the atoms must necessarily cause a change in line intensities. Calculating the structure factor F for each atom arrangement illustrates the nature of these charges.

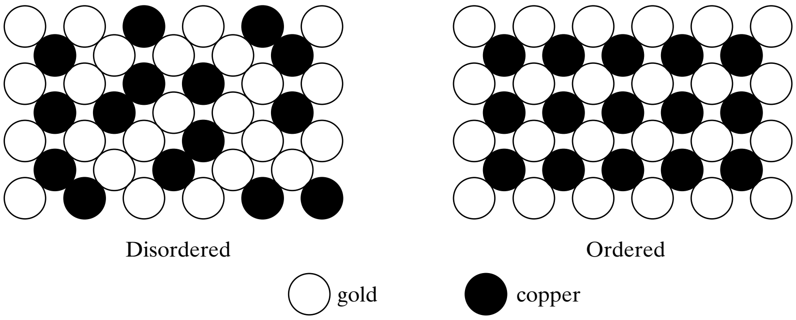

Figure 5 Atom arrangements on a (100) plane, disordered and ordered $AuCu_3$.

a) *Complete disorder*. The atomic scattering factor of the "average" gold–copper atom is given by

$$f_{av} = (\text{atomic fraction Au})f_{Au} + (\text{atomic fraction Cu})f_{Cu},$$

$$f_{av} = \frac{1}{4}f_{Au} + \frac{3}{4}f_{Cu}.$$

There are four "average" atoms per unit cell, at 0 0 0, $\frac{1}{2}, \frac{1}{2}, 0, \frac{1}{2}, 0, \frac{1}{2}$ and $0, \frac{1}{2}, \frac{1}{2}$. Therefore the structure factor is given by

$$F = \sum f e^{2\pi i(hv + kv + lw)}$$

$$F = f_{av}[1 + e^{\pi i(h+k)} + e^{\pi i(h+l)} + e^{\pi i(k+l)}]$$

By example (d), this becomes

$$F = 4f_{av} = (f_{Au} + 3f_{cu}), \text{ for } hkl \text{ unmixed,}$$

$$F = 0, \text{ for } hkl \text{ mixed} \tag{11}$$

Therefore, as might be expected, the disordered alloy produces a diffraction pattern similar to that of any face-centered cubic metal, say pure gold or pure copper. No reflections of mixed indices are present.

b) *Complete order*. Each unit cell now contains one gold atom, at 0 0 0, and three copper atoms, at $\frac{1}{2}, \frac{1}{2}, 0, \frac{1}{2}, 0, \frac{1}{2}$ and $0, \frac{1}{2}, \frac{1}{2}$.

$$F = f_{Au} + f_{Cu}[e^{\pi i(h+k)} + e^{\pi i(h+l)}e^{\pi i(k+l)}];$$

$$F = (f_{Au} + 3f_{Cu}), \qquad \text{for } hkl \text{ unmixed,}$$

$$F = (f_{Au} - f_{Cu}), \qquad \text{for } hkl \text{ mixed} \tag{12}$$

The ordered alloy thus produces diffraction lines for all values of *hkl*, and its diffraction pattern therefore resembles that of a simple cubic substance. In other words, there has been a change of Bravais lattice on ordering; the Bravais lattice of the disordered alloy is face-centered cubic and that of the ordered alloy simple cubic.

The diffraction lines from planes of unmixed indices are called *fundamental lines*, since they occur at the same positions and with the same intensities in the patterns of both ordered and disordered alloys. The extra lines which appear in the pattern of an ordered alloy, arising from planes of mixed indices, are called *superlattice lines*, and their presence is direct evidence that ordering has taken place. The physical reason for the formation of superlattice lines may be deduced from an examination of Fig. 4. Consider 100 diffraction from the disordered structure, i.e., a beam of wavelength λ incident at an angle θ which satisfies Bragg's law. The atoms at the top and bottom of the unit cell scatter in phase, therefore, and reinforcement occurs. Midway between the planes of constant phase, however, is a second set of atoms (i.e., a "plane") containing, on the average, exactly the same distribution of gold and copper atoms. These atoms scatter out of phase and exactly the same amplitude as the atoms at the top and bottom faces of the unit cell. Complete cancellation results and there is no 100 reflection. In the ordered alloy, on the other hand, the distribution of gold and copper atoms is no longer uniform: the occupancy at the top/bottom of the unit cell (both copper and gold atoms) differs from that in the middle (only copper atoms). As before the top/bottom layers scatter out of phase with the midsection of the unit cell, but now the amplitude scattered differs because of the difference in scattering power of the gold and copper atoms. The ordered structure therefore produces a weak 100 reflection. And, as Eqs. (12) show, all the superlattice lines are much weaker than the fundamental lines, since their structure factors involve the difference rather than the sum, of the atomic scattering factors of each atom. This effect is shown quite clearly in Fig. 6, where *f* and *s* are used to designate the fundamental and superlattice lines, respectively.

At low temperatures, the long-range order in $AuCu_3$ is virtually perfect but, as T_c is approached, some randomness sets in. This departure from perfect order can be described by means of the *long-range order parameter S*, defined as follows:

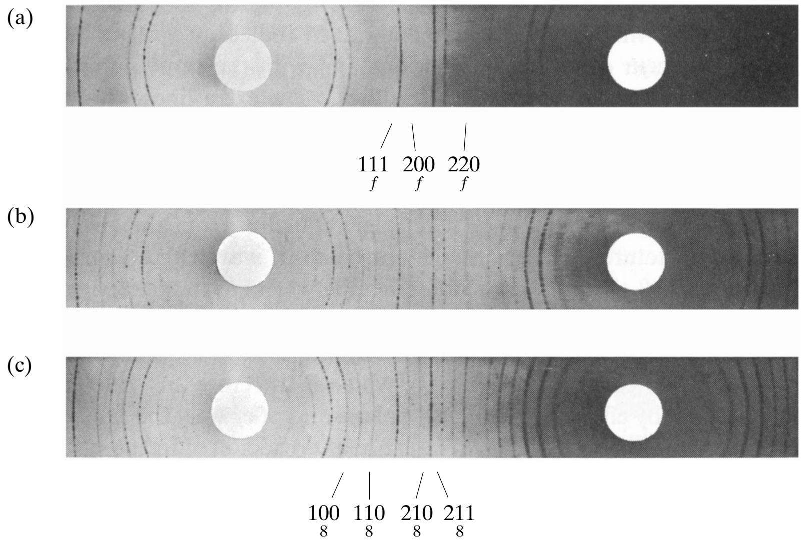

Figure 6 Powder patterns of $AuCu_3$ (very coarse-grained) made with filtered copper radiation: (a) quenched from 440°C (disordered): (b) held 30 min at 360°C and quenched (partially ordered): (c) slowly cooled from 360°C to room temperature (completely ordered).

$$S = \frac{r_A - F_A}{1 - F_A}, \tag{13}$$

where r_A = fraction of A sites occupied by the "right" atoms, i.e., A atoms, and F_A = fraction of A atoms in the alloy. When the long-range order is perfect, $r_A = 1$ by definition, and therefore $S = 1$. When the atomic arrangement is completely random, $r_A = F_A$ and $S = 0$. For example, consider 100 atoms of $AuCu_3$, i.e., 25 gold atoms and 75 copper atoms. Suppose the ordering is not perfect and only 22 of these gold atoms are on "gold sites," i.e., cube corner positions, the other 3 being on "copper sites." Then, considering the gold atom as the A atom in Eq. 13, $r_A = 22/25 = 0.88$ and $F_A = 25/100 = 0.25$. Therefore,

$$S = \frac{0.88 - 0.25}{1.00 - 0.25} = 0.84$$

describes the degree of long-range order present. The same result is obtained for the distribution of copper atoms.

Any departure from perfect long-range order in a superlattice causes the superlattice lines to become weaker. It may be shown [G.20] that the structure factors of partially ordered $AuCu_3$ are given by

$$F = (f_{Au} + 3f_{Cu}), \quad \text{for } hkl \text{ unmixed,}$$

$$F = S(f_{Au} - f_{Cu}), \quad \text{for } hkl \text{ mixed.} \tag{14}$$

Comparing these equations with Eqs. (12) shows that only the superlattice lines are affected. But the effect is a strong one, because the intensity of a superlattice line is proportional to $|F|^2$ and therefore to S^2. For example, a decrease in order from $S = 1.00$ to $S = 0.84$ decreases the intensity of a superlattice line by about 30 percent. The weakening of superlattice lines by partial disorder is illustrated in Fig. 6. Comparing the integrated intensity ratio of a superlattice and fundamental line, determines S experimentally.

Values of S obtained in this way are shown in Fig. 7 as a function of the absolute temperature T, expressed as a fraction of the critical temperature T_c. For $AuCu_3$ the value of S decreases gradually, with increasing temperature, to about 0.8 at T_c and then drops abruptly to zero. Above T_c the atomic distribution is random and there are no superlattice lines. One might expect that the energy lost from the superlattice lines should appear in some form in the pattern of a completely disordered alloy. As a matter of fact it does, in the form of a weak diffuse background extending over the whole range of 2θ. This diffuse scattering is due to randomness and illustrates any departure from perfect periodicity of atom arrangement results in some diffuse scattering at non-Bragg angles.

Von Laue showed that if two kinds of atoms A and B are distributed completely at random in a solid solution, then the intensity of the diffuse scattering produced is given by

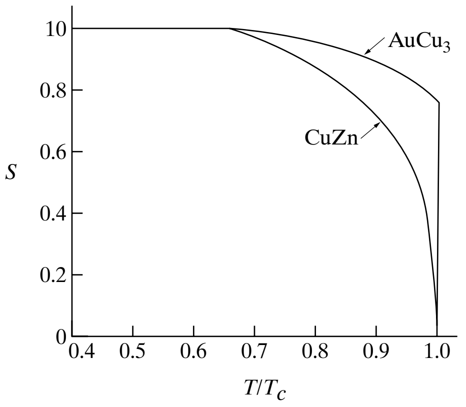

Figure 7 Variation of the long-range order parameter S with temperature, for $AuCu_3$ and CuZn. ($AuCu_3$ data from Keating and Warren [7]; CuZn data from Chipman and Warren [8].)

$$I_D = k(f_A - f_B)^2, \tag{15}$$

where k is a constant for any one composition, and f_A and f_B are atomic scattering factors [G.20]. Both f_A and f_B decrease as $(\sin\theta)/\lambda$ increases, and so does their difference; therefore I_D is a maximum at $2\theta = 0$ and decreases as 2θ increases. This diffuse scattering is very difficult to measure experimentally. It is weak to begin with and is superimposed on other forms of diffuse scattering that may also be present, namely, Compton modified scattering, temperature-diffuse scattering, etc. It is worth noting, however, that Eq. (15) is quite general and applies to any random solid solution, whether or not it is capable of undergoing ordering at low temperatures. This part will be revisited in Sec. 11.

Another aspect of long-range order that requires some mention is the effect of change in composition. Since the ratio of corner sites to face-centered sites in the $AuCu_3$ lattice is 1:3, it follows that perfect order can be attained only when the ratio of gold to copper atoms is also exactly 1:3. But ordering can also take place in alloys containing somewhat more, or somewhat less, than 25 atomic percent gold, as shown by the phase diagram of Fig. 8. In an ordered alloy containing somewhat more than 25 atomic percent gold, all the corner sites are occupied by gold atoms, and the remainder of the gold atoms occupy some of the face-centered sites normally occupied by copper atoms. Just the reverse is true for an alloy containing less than 25 atomic percent gold. But as the phase diagram shows, there are limits to the variation in composition which the ordered lattice will accept without becoming unstable. In fact, if the gold content is increased to about 50 atomic percent, an entirely different ordered alloy, AuCu, can be formed.

Before considering the ordering transformation in AuCu, which is rather complex, it is instructive to examine the behavior of β-brass. This alloy is stable at room temperature over a composition range of about 46 to almost 50 atomic percent zinc, and so may be represented fairly closely by the formula CuZn. At high temperatures its structure is, statistically, body-centered cubic, with the copper and zinc atoms distributed at random. Below a critical temperature of about 460°C, ordering

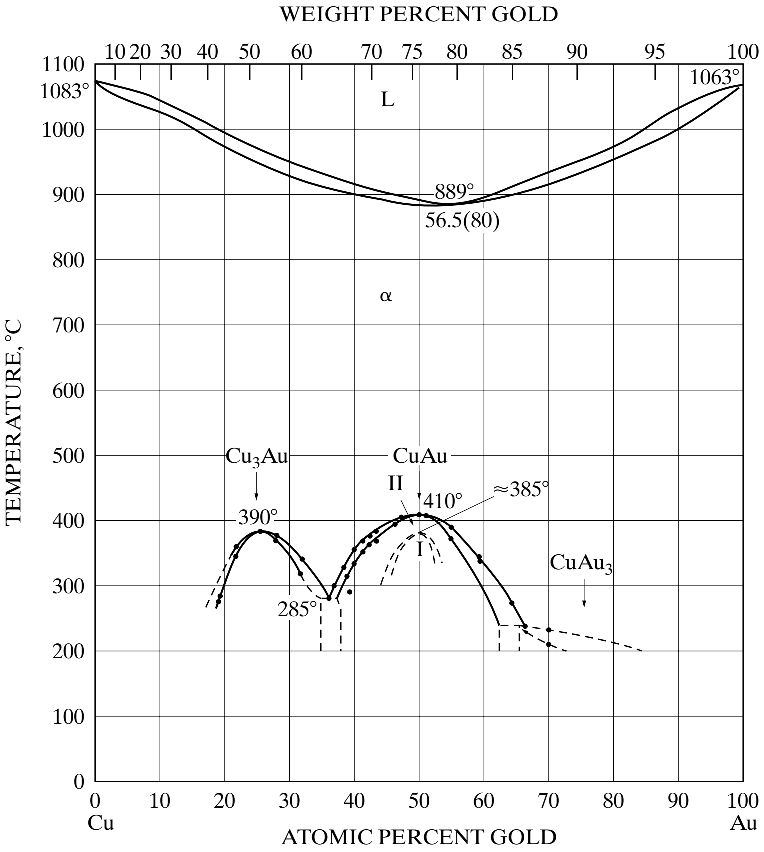

Figure 8 Phase diagram of the copper–gold system. Hansen and Anderko [9].

occurs; the cell corners are then occupied only by copper atoms and the cell centers only by zinc atoms, as indicated in Fig. 9. The ordered alloy therefore has the CsCl structure and its Bravais lattice is simple cubic. Other alloys which have the same ordered structure are CuBe, CuPd, and FeCo.

By calculations similar to those made in the previous section, the structure factors of β-brass, for the ideal composition CuZn, can be shown to be

$$F = (f_{\text{Cu}} + f_{\text{Zn}}), \quad \text{for } (h + k + l) \text{ even},$$

$$F = S(f_{\text{Cu}} - f_{\text{Zn}}), \quad \text{for } (h + k + l) \text{ odd}. \tag{16}$$

In other words, there are fundamental lines, those for which $(h + k + l)$ is even, which are unchanged in intensity whether the alloy is ordered or not. And there are superlattice lines, those for which $(h + k + l)$ is odd, which are present only in the

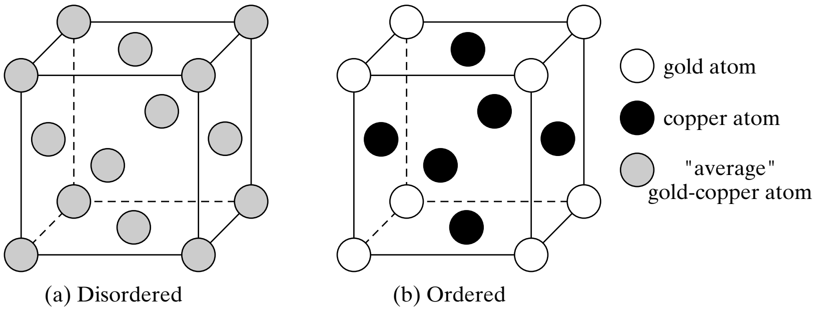

Figure 9 Unit cells of the disordered and ordered forms of CuZn.

pattern of an alloy exhibiting some degree of order, and then with an intensity which depends on the degree of order present.

Figure 7 indicates how the degree of long-range order in CuZn varies with the temperature. The order parameter for CuZn decreases continuously to zero as T approaches T_c, whereas for $AuCu_3$ it remains fairly high right up to T_c and then drops abruptly to zero. There is also a notable difference in the velocity of the disorder-order transformation in these two alloys. The transformation in $AuCu_3$ is relatively so sluggish that the structure of this alloy at any temperature can be retained by quenching to room temperature, as evidenced by the diffraction patterns in Fig. 6, which were made at room temperature. In CuZn, on the other hand, ordering is so rapid that disorder existing at an elevated temperature cannot be retained at room temperature, no matter how rapid the quench. Therefore, any specimen of CuZn at room temperature can be presumed to be almost completely ordered. (The S vs. T/T_c curve for CuZn, shown in Fig. 7, was necessarily based on measurements made *at* temperature with a high-temperature diffractometer.)

Not all order-disorder transformations are as simple crystallographically speaking, as those occurring in $AuCu_3$ and CuZn. Complexities are encountered, for example, in gold-copper alloys at or near the composition AuCu; these alloys become ordered below a critical temperature of about 410°C or lower, depending on the composition (see Fig. 8). Whereas the ratio of gold to copper atoms in $AuCu_3$ is 1:3, this ratio is 1:1 for AuCu, and the structure of ordered AuCu must therefore be such that the ratio of gold sites to copper sites is also 1:1. Two ordered forms are produced, depending on the ordering temperature, and these have different crystal structures:

a) Tetragonal AuCu, designated I, formed by slow cooling from high temperatures or by isothermal ordering below about 385°C. The unit cell is shown in Fig. 10(a). It is almost cubic in shape, since c/a equals about 0.93, and the gold and copper atoms occupy alternate (002) planes.
b) Orthorhombic AuCu, designated II, formed by isothermal ordering between about 410° and 385°C. Its very unusual unit cell, shown in

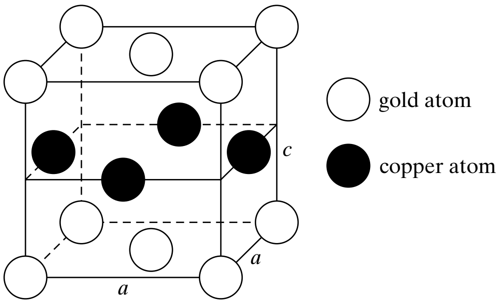

(a) I-tetragonal

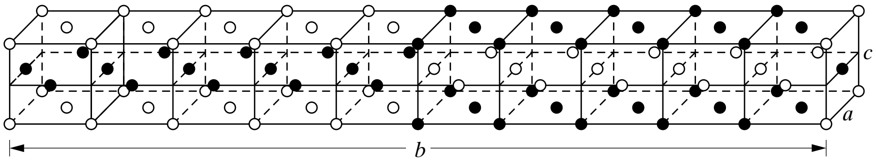

(b) II-orthorhombic

Figure 10 Unit cells of the two ordered forms of AuCu.

> Fig. 10 (b), is formed by placing ten tetragonal cells like that of I side by side and then translating five of them by the vectors c/2 and a/2 with respect to the other five. (Some distortion occurs, with the result that each of the ten component cells, which together make up the true unit cell, is not tetragonal but orthorhombic; i.e., *b* is not exactly ten times *a*, but equal to about 10.02*a*. The *c/a* ratio is about 0.92) The result is a structure in which the atoms in any one (002) plane are wholly gold for a distance of *b*/2, then wholly copper for a distance of *b*/2, and so on. It is called a long-period superlattice.

From a crystallographic viewpoint, there is a fundamental difference between the kind of ordering which occurs in $AuCu_3$ or CuZn, on the one hand, and that which occurs in AuCu, on the other. In $AuCu_3$ there is a change in Bravais lattice, but no change in crystal system, accompanying the disorder-order transformation: both the disordered and ordered forms are cubic. In AuCu, the ordering process changes both the Bravais lattice and the crystal system, the latter from cubic to tetragonal, AuCu(I), or orthorhombic, AuCu(II). These changes are due to changes in the symmetry of atom arrangement, because the crystal system to which a given structure belongs depends ultimately on the symmetry of that structure. In the gold–copper system, the disordered phase α is cubic, because the arrangement of gold and copper atoms on a face-centered lattice has cubic symmetry, in a statistical sense, at any composition. In $AuCu_3$, the ordering process puts the gold and copper atoms in definite positions in each cell (Fig. 4), but this arrangement still has cubic symmetry so the cell remains cubic. In ordered AuCu, on the other hand, to consider only the tetragonal modification, the atom arrangement is such that there is no longer three-fold rotational symmetry about directions of the form {111}. Inasmuch as this is the minimum symmetry requirement for the cubic system, this cell [Fig. 10 (a)] is not cubic. There is, however, four-fold rotational symmetry about [001], but not about [010] or [100]. The ordered form is accordingly tetragonal. The segregation of gold and copper atoms on alternate (002) planes causes c to differ from a, in this case in the direction of a small contraction of c relative to a, because of the difference in size between the gold and copper atoms. But even if c were equal to a, the cell shown in Fig. 10 (a) would still be classified as tetragonal on the basis of its symmetry.

Since the intensity of a superlattice line from an ordered solid solution is much lower than that of a fundamental line the following question is important to consider: Will it ever be so low that the line cannot be detected? Ignoring the variation in multiplicity factor and Lorentz-polarization factor from line to line, and assuming that the relative integrated intensities of a superlattice and fundamental line are given by their relative $|F|^2$ values, produces an approximate estimate. For fully ordered $\mathrm{AuCu_3}$, Eqs. (12) show that

$$\frac{\text{Intensity (superlattice line)}}{\text{Intensity (fundamental line)}} \approx \frac{|F|_s^2}{|F|_f^2} = \frac{(f_{\mathrm{Au}} - f_{\mathrm{Cu}})^2}{(f_{\mathrm{Au}} + 3f_{\mathrm{Cu}})^2} \tag{17}$$

At $(\sin\theta)/\lambda = 0$, we can put $f = Z$ and since the atomic numbers of gold and copper are 79 and 29, respectively, Eq. (17) becomes, for small scattering angles,

$$\frac{I_s}{I_f} \approx \frac{(79 - 29)^2}{[79 + 3(29)]^2} \approx 0.09$$

Superlattice lines are therefore only about one-tenth as strong as fundamental lines, but they can still be detected without difficulty, as shown by Fig. 6.

But in CuZn, even when fully ordered, the situation is much worse. The atomic numbers of copper and zinc are 29 and 30, respectively, and, making the same assumptions as before,

$$\frac{I_s}{I_f} \approx \frac{(f_{\mathrm{Cu}} - f_{\mathrm{Zn}})^2}{(f_{\mathrm{Cu}} + f_{\mathrm{Zn}})^2} \approx \frac{(29 - 30)^2}{(29 + 30)^2} \approx 0.0003$$

This ratio is so low that the superlattice lines of ordered CuZn can be detected by x-ray diffraction only under very special circumstances. (The powder pattern of this alloy, ordered or disordered, ordinarily appears to be that of a body-centered cubic substance.) The same is true of any superlattice of elements A and B which differ in atomic number by only one or two units, because the superlattice-line intensity is generally proportional to $(f_{\mathrm{A}} - f_{\mathrm{B}})^2$.

There is one way, however, of increasing the intensity of a superlattice line relative to that of a fundamental line, when the two atoms involved have almost the same atomic numbers, and that is by the proper choice of the incident wavelength.

The atomic scattering factor f of any element is usually considered to be independent of the wavelength of the scattered radiation, as long as the quantity $(\sin\theta)/\lambda$ is constant. This is not quite true. When the incident wavelength λ is nearly equal to the wavelength λ_K of the K absorption edge of the scattering element, then the atomic scattering factor of that element may be several units lower than it is when λ is very much shorter than λ_K. This change in f is *anomalous dispersion*. Physically, it can be regarded as a resonance effect in which the oscillations of the K electrons, which are the cause of the scattering, are disturbed when the radiation being scattered has a frequency near that at which K electrons can be actually ejected from the atom. If f_0 = atomic scattering factor for $\lambda \ll \lambda_K$ (this is the usual value as tabulated, for example, in "Appendix: Atomic Scattering Factors") and Δf = change in f_0 when λ is near λ_K, then the quantity $f = f_0 + \Delta f$ gives the value of the atomic scattering factor when λ is near λ_K. Figure 11 shows approximately how Δf varies with λ/λ_K, and this curve may be used to estimate the correction Δf which must be applied for any particular combination of wavelength and scattering element.

Strictly speaking, Δf depends also on the atomic number of the scattering element, which means that a different correction curve is required for every element. But the variation of Δf with Z is not very large, and Fig. 11, which is computed for an element of medium atomic number (about 50), can be used with fairly good accuracy as a master correction curve for any element. Figure 11 was calculated from data in James [G.19, p. 608]. Anomalous dispersion is also discussed by

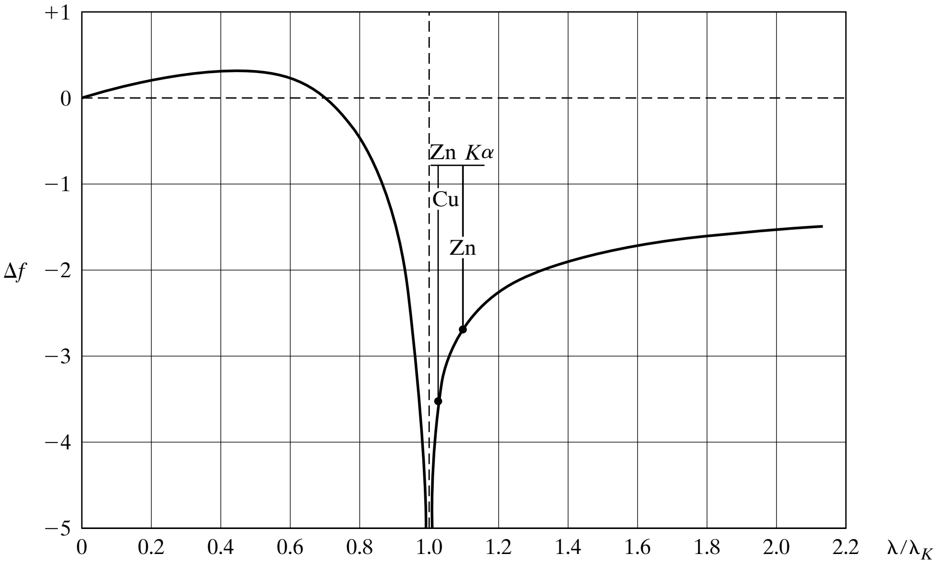

Figure 11 Variation of the scattering-factor correction Δf with λ/λ_K. See text for details. The two points on the curve show the corrections for the scattering of Zn $K\alpha$ radiation by copper and zinc atoms.

Guinier [G.30]. Values of Δf as a function of Z at constant λ, for five characteristic wavelengths, can be calculated from data in [G.1., Vol.C].

When λ/λ_K is less than about 0.8, the correction is practically negligible. When λ/λ_K exceeds about 1.6, the correction is practically constant and independent of small variations in λ_K. But when λ is near λ_K, the slope of the correction curve is quite steep, which means that the Δf correction can be quite different for two elements of nearly the same atomic number. By taking advantage of this fact, the intensity of a superlattice line can often be increased above its normal value.

For example, if ordered CuZn is examined with Mo $K\alpha$ radiation, λ/λ_K is 0.52 for the copper atom and 0.55 for the zinc atom. The value of Δf is then about +0.3 for either atom, and the intensity of a superlattice line would be proportional to $[(29 + 0.3) - (30 + 0.3)]^2 = 1$ at low values of 2θ. Under these circumstances the line would be invisible in the presence of the usual background. But if Zn $K\alpha$ radiation is used, λ/λ_K becomes 1.04 and 1.11 for the copper and zinc atoms, respectively, and Fig. 11 shows that the corrections are -3.6 and -2.7, respectively. The superlattice-line intensity is now proportional to $[(29 - 3.6) - (30 - 2.7)]^2 = 3.6$, which is large enough to permit detection of the line. It was by means of Zn $K\alpha$ radiation that Jones and Sykes [10] first detected ordering in CuZn. Cu $K\alpha$ radiation also offers some advantage over Mo $K\alpha$, but not so large an advantage as Zn $K\alpha$, and order in CuZn can be detected with Cu $K\alpha$ only if crystal-monochromated radiation is used or if the specimen is a single crystal.

To a very good approximation, the change in atomic scattering factor Δf is independent of scattering angle and therefore a constant for all lines on the diffraction pattern.

Taking advantage of this anomalous change in scattering factor near an absorption edge push the x-ray method about as far as it will go. A better tool for the detection of order in alloys of metals of nearly the same atomic number is neutron diffraction. Two elements may differ in atomic number by only one unit and yet their neutron scattering powers may be entirely different, a situation conducive to high superlattice-line intensity.

11 SHORT-RANGE ORDER AND CLUSTERING

Above the critical temperature T_c long-range order disappears and the atomic distribution becomes more or less random. This is indicated by the absence of superlattice lines from the powder pattern. But careful analysis of the diffuse scattering which forms the background of the pattern shows that perfect randomness is not attained. Instead, there is a greater than average tendency for *unlike* atoms to be nearest neighbors. This conditions is known as *short-range order*.

For example, when perfect long-range order exists in $AuCu_3$, a gold atom located at 0 0 0 is surrounded by 12 copper atoms at $\frac{1}{2}\frac{1}{2}0$ and equivalent positions (see Fig. 4), and any given copper atom is surrounded by 8 copper and 4 gold atoms. This kind of grouping is a direct result of the existing long-range order, which also requires that gold atoms be on corner sites and copper atoms on face-centered sites.

Above T_c this order breaks down and, if the atomic distribution became truly random, a given gold atom might be found on either a corner or face-centered site. It would then have only $\frac{3}{4}(12) = 9$ copper atoms as nearest neighbours, since on the average 3 out of 4 atoms in the solution are copper. Actually, it is observed that some short-range order exists above T_c: at 405°C, for example, which is 15°C above T_c, there are on the average about 11.0 copper atoms around any given gold atom [11].

This is a quite general effect. Any solid solution which exhibits long-range order below a certain temperature exhibits some short-range order above that temperature. Above T_c the degree of short-range order decreases as the temperature is raised; i.e., increasing thermal agitation tends to make the atomic distribution more and more random. One interesting fact about short-range order is that it has also been found to exist in solid solutions which do *not* undergo long-range ordering at low temperatures, such as gold-silver and gold-nickel solutions.

Another kind of departure from randomness in a solid solution is the tendency of *like* atoms to be close neighbors. This effect is known as *clustering*, and it has been observed in aluminum-silver and aluminum-zinc solutions. In fact, there is probably no such thing as a perfectly random solid solution. All real solutions probably exhibit either short-range ordering or clustering to a greater or lesser degree, simply because they are composed of unlike atoms with particular forces of attraction or repulsion operating between them. Short-range order, however, is far more common than clustering.

The degree of short-range order or clustering may be defined in terms of a suitable parameter, just as long-range order is, and the value of this parameter may be related to the diffraction effects produced. The general nature of these effects is illustrated in Fig. 12, where the intensity of the diffuse scattering is plotted, not against 2θ, but against a function of $\sin \theta$. (The fundamental lines are not included in Fig. 12 because their intensity is much too high compared with the diffuse scattering shown, but the positions of two of them, 111 and 200, are indicated on the abscissa.) If the atomic distribution is perfectly random, the scattered intensity decreases gradually as 2θ or $\sin \theta$ increases from zero, in accordance with Eq. (15). If short-range order exists, the scattering at small angles becomes less intense and low broad maxima occur in the scattering curve; these maxima are usually located at the same angular positions as the sharp superlattice lines formed by long-range ordering. Clustering causes strong scattering at low angles.

These effects, however, are all very weak and are masked by the other forms of diffuse scattering which are always present. As a result, the details shown in Fig. 12 are never observed in an ordinary powder pattern made with filtered radiation. To disclose these details and so learn something about the structure of the solid solution, it is necessary to use strictly monochromatic radiation and, preferably, single-crystal specimens, and to make allowances for the other forms of diffuse scattering, chiefly temperature-diffuse and Compton modified, that are always present.

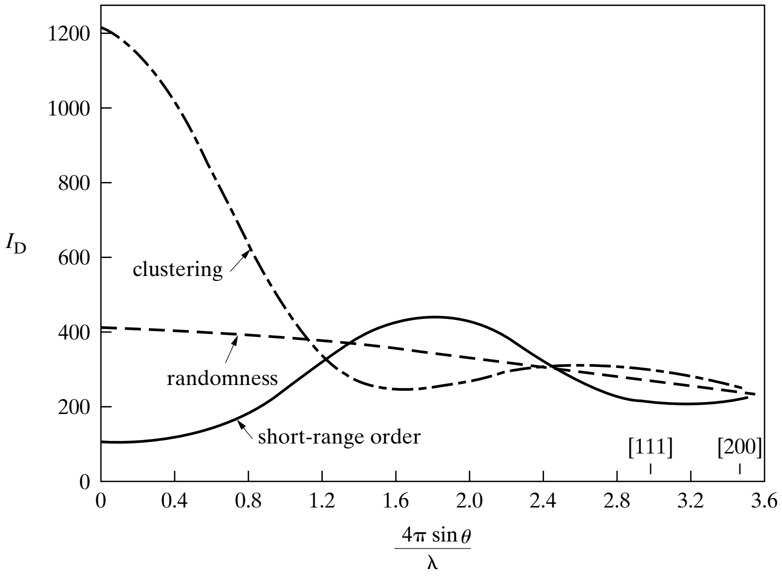

Figure 12 Calculated intensity I_D of diffuse scattering in powder patterns of solid solutions (here, the face-centered cubic alloy Ni_4Au) which exhibit complete randomness, short-range order, and clustering. The short-range order curve is calculated on the basis of one additional unlike neighbor over the random configuration, and the clustering curve on the basis of one less unlike neighbor. Warren and Averbach [12].

PROBLEMS

***1** The powder pattern of aluminum, made with Cu $K\alpha$ radiation, contains ten lines, whose $\sin^2\theta$ values are 0.1118, 0.1487, 0.294, 0.403, 0.439, 0.583, 0.691, 0.727, 0.872, and 0.981. Index these lines and calculate the lattice parameter.

2 A pattern is made of a cubic substance with unfiltered chromium radiation. The observed $\sin^2\theta$ values and intensities are 0.265(m), 0.321(vs), 0.528(w), 0.638(s), 0.793(s), and 0.958(vs). Index these lines and state which are due to $K\alpha$ and which to $K\beta$ radiation. Determine the Bravais lattice and lattice parameter. Identify the substance by reference to “Appendix: Crystal Structures of Some Elements”.

In each of the following problems th powder pattern of an element is represented by the observed $\sin^2\theta$ values of the first seven or eight lines on the pattern, made with Cu $K\alpha$ radiation. In each case, index the lines, find the crystal system, Bravais lattice, and approximate lattice parameter (or parameters), and identify the element from the tabulation given in “Appendix: Crystal Structures of Some Elements”.

*6	7	*8
0.0603	0.1202	0.0768
0.1610	0.238	0.0876
0.221	0.357	0.0913
0.322	0.475	0.1645
0.383	0.593	0.231
0.484	0.711	0.274
0.545	0.830	0.308
0.645		0.319

7 An Hull/Debye–Scherrer pattern is made with Cu $K\alpha$ radiation of $AuCu_2$ quenched from a temperature T_1. The ratio of the integrated intensity of the 420 line to that of the 421 line is found to be 4.38. Calculate the value of the long-range order parameter S at temperature T_1. (Take the lattice parameter of $AuCu_3$ as 3.75 Å. Ignore the small difference between the Lorentz-polarization factors for these two lines and the corrections to the atomic scattering factors mentioned in Sec. 10).

8 Calculate the ratio of the integrated intensity of the 100 superlattice line to that of the 110 fundamental line for fully ordered β-brass, if Cu $K\alpha$ radiation is used. Estimate the corrections to the atomic scattering factors from Fig. 11. The lattice parameter of β-brass (CuZn) is 2.95 Å.

9 a) What is the Bravais lattice of AuCu(I), the ordered tetragonal modification?

b) Calculate the structure factors for the disordered and ordered (tetragonal) forms of AuCu.

c) On the basis of the calculations made in (b) and a consideration of the change in the c/a ratio, describe the qualitative differences between the powder patterns of the ordered (tetragonal) and disordered forms of AuCu.

REFERENCES

The following books are listed more or less in the order they are encountered in the text

G.1 *International Tables for Crystallography*, Ed. A.J.C Wilson, Vol. A-C (Dordrecht Kluwer Academic Pub. for International Union of Crystallography, 1995). The reference ''book" for crystallography and diffraction.

G.9 W. B. Pearson. *A Handbook of Lattice Spacings and Structures of Metals and Alloys* (New York: Pergamon Press, 1958). A most useful source of information. Gives the crystal structures of intermediate phases, and the variation of lattice parameter with composition in solid solutions, of binary and ternary alloys. Also gives the crystal structures of metal borides, carbides, hydrides, nitrides, and binary oxides.

G.10 Charles S. Barrett and T. B. Massalski. *Structure of Metals*, 3rd ed. (New York: McGraw-Hill, 1966). A classic book on the crystallographic aspects of physical metallurgy. Really two books in one, the first part dealing with the theory and methods of diffraction of x-rays, electrons, and neutrons; the second part with the structure of metals in the wider sense of the word. Very lucid account of stereographic projection. Stress measurement, phase transformations, preferred orientation.

G.15 N. F. M. Henry, H. Lipson, and W. A. Wooster. *The Interpretation of X-Ray Diffraction Photographs* (London: Macmillan, 1951). Rotating and oscillating crystal methods, as well as powder methods, are described. Good section on analytical methods of indexing powder photographs.

G.19 R. W. James. *The Optical Principles of the Diffraction of X-Rays* (Woodbridge; CT: Ox Bow Press, 1982). Excellent book on advanced theory of x-ray diffraction. Includes thorough treatments of diffuse scattering (due to thermal agitation, small particle size, crystal imperfections, etc.), the use of Fourier series in structure analysis, and scattering by gases, liquids, and amorphous solids.

G.20 B. E. Warren. *X-Ray Diffraction* (Reading, MA: Addison-Wesley, 1969). Excellent advanced treatment, in which the author takes pains to connect theoretically derived results with experimentally observable quantities. Stresses diffraction effects due to thermal vibration, order-disorder, imperfect crystals, and amorphous materials. Includes a treatment of the dynamical theory of diffraction by a perfect crystal.

G.30 A. Guinier. *X-Ray Diffraction in Crystals, Imperfect Crystals, and Amorphous Bodies* (San Francisco: W. H. Freeman, 1963 and reprinted by Dover 1994). Largely theoretical and more advanced than [G.13].

G.32 H. Lipson and H. Steeple. *Interpretation of X-Ray Powder Diffraction Patterns* (London: Macmillan, 1970). An updating and expansion of that part of [G. 15] that dealt with powder methods.

G.33 Leonid V. Azaroff and Martin J. Buerger. *The Powder Method in X-Ray Crystallography* (New York: McGraw-Hill, 1958). The making and interpretation of Hull/Debye–Scherrer photographs, including precise parameter measurements.

ANSWERS TO SELECTED PROBLEMS

1. 111, 200, 220, 311, 222, 400, 331, 420, 422, and 511 (333); a = 4.05 Å

4. 111, 220, 311, 400, 331, 422, 511 (333), 440. Diamond cubic; a = 5.4 Å; silicon.

6. 100, 002, 101, 102, 110, 103, 200, 112. Hexagonal close-packed; a = 3.2 Å, c = 5.2 Å; magnesium.

8. 0.0010

This page intentionally left blank

Phase-Diagram Determination

1 INTRODUCTION

An alloy is a combination of two or more metals, of metals and nonmetals or of non-metals. It may consist of a single phase or of a mixture of phases, and these phases may be of different types, depending only on the composition of the alloy and the temperature,[1] provided the alloy is at equilibrium. The changes in the constitution of the alloy produced by given changes in composition or temperature may be conveniently shown by means of a *phase diagram* and also called an equilibrium diagram or constitution diagram. Normally, it is a plot of temperature vs. composition, divided into areas wherein a particular phase or mixture of phases is stable. As such it forms a sort of map of the alloy system involved. Phase diagrams are therefore of great importance in materials science and engineering, and much time and effort have been devoted to their determination. This chapter, therefore, covers how x-ray methods can be used in the study of phase diagrams of binary systems.

X-ray methods are, of course, not the only ones which can be used in investigations of this kind. The two classical methods are thermal analysis and microscopic examination, and many diagrams have been determined by these means alone. Diffraction-based methods however, supplement these older techniques in many useful ways and provide, in addition, the only means of determining the crystal structures of the various phases involved. Because x-ray diffraction is so widely available and requires relatively trivial sample preparation it is the technique most often used for phase identification. Of course, TEM is also useful for crystal structure studies, but it is best employed for miniscule volumes of material. Most phase diagrams today are therefore determined by a combination of all three methods. In

---

[1] The pressure on the alloy is another effective variable, but it is usually held constant at that of the atmosphere and may be neglected.

From Chapter 11 of *Elements of X-Ray Diffraction*, Third Edition. B.D. Cullity, S.R. Stock.

addition, measurements of other physical properties may be used to advantage in some alloy systems: among the most important of these subsidiary techniques are measurements of the change in length and of the change in electric resistance as a function of temperature.

In general, among the various experimental techniques differ in sensitivity, and therefore in usefulness, from one portion of the phase diagram to another. Thus, thermal analysis is the best method for determining the liquidus and solidus, including eutectic and peritectic horizontals, but it may fail to reveal the existence of eutectoid and peritectoid horizontals because of the sluggishness of some solid-state reactions or the small heat effects involved. Such features of the diagram are best determined by microscopic examination or x-ray diffraction, and the same applies to the determination of solvus (solid solubility) curves.

2 GENERAL PRINCIPLES

The key to the interpretation of the powder patterns of alloys is the fact that each phase produces its own pattern independently of the presence or absence of any other phase. Thus a single-phase alloy produces a single pattern while the pattern of a two-phase alloy consists of two superimposed patterns, one due to each phase.

Assume, for example, that two elements A and B are *completely soluble* in the solid state, as illustrated by the phase diagram of Fig. 1. The solid phase α, called a *continuous solid solution*, is of the substitutional type; it varies in composition, but not in crystal structure, from pure A to pure B, which must necessarily have the same structure. The lattice parameter of α also varies continuously from that of pure A to that of pure B. Since all alloys in a system of this kind consist of the same single phase, their powder patterns appear quite similar, the only effect of a change in composition being to shift the diffraction-line positions in accordance with the change in lattice parameter.

More commonly, the two elements A and B are only *partially soluble* in the solid state. The first additions of B to A go into solid solution in the A lattice, which may

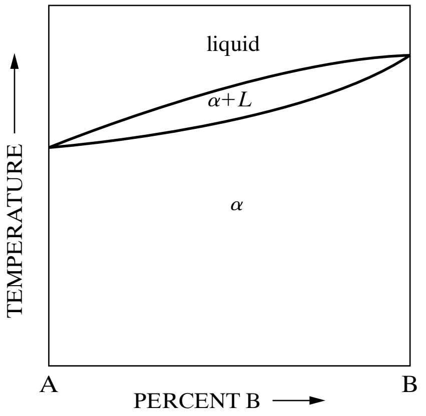

Figure 1 Phase diagram of two metals showing complete solid solubility.

expand or contract as a result, depending on the relative sizes of the A and B atoms and the type of solid solution formed (substitutional or interstitial). Ultimately the solubility limit of B in A is reached, and further additions of B cause the precipitation of a second phase. This second phase may be a B-rich solid solution with the same structure as B, as in the alloy system illustrated by Fig. 2(a). Here the solid solutions α and β are called *primary solid solutions* or *terminal solid solutions*. Or the second phase which appears may have no connection with the B-rich solid solution, as in the system shown in Fig. 2(b). Here the effect of supersaturating α with metal B is to precipitate the phase designated γ. This phase is called an *intermediate solid solution* or *intermediate phase*. It usually has a crystal structure entirely different from that of either α or β, and it is separated from each of these terminal solid solutions, on the phase diagram, by at least one two-phase region.

Phase diagrams much more complex than those just mentioned are often encountered in practice, but they are always reducible to a combination of fairly simple types. When an unknown phase diagram is being investigated, it is best to make a preliminary survey of the whole system by preparing a series of alloys at definite composition intervals, say 5 or 10 atomic percent, from pure A to pure B. The powder pattern of each alloy and each pure element is then prepared. These patterns may appear quite complex but, no matter what the complexities, the patterns may be unraveled and the proper sequence of phases across the diagram may be established, if proper attention is paid to the following principles:

1. *Equilibrium*. Each alloy must be at equilibrium at the temperature where the phase relations are being studied.
2. *Phase sequence*. A horizontal (constant temperature) line drawn across the diagram must pass through single-phase and two-phase regions alternately.

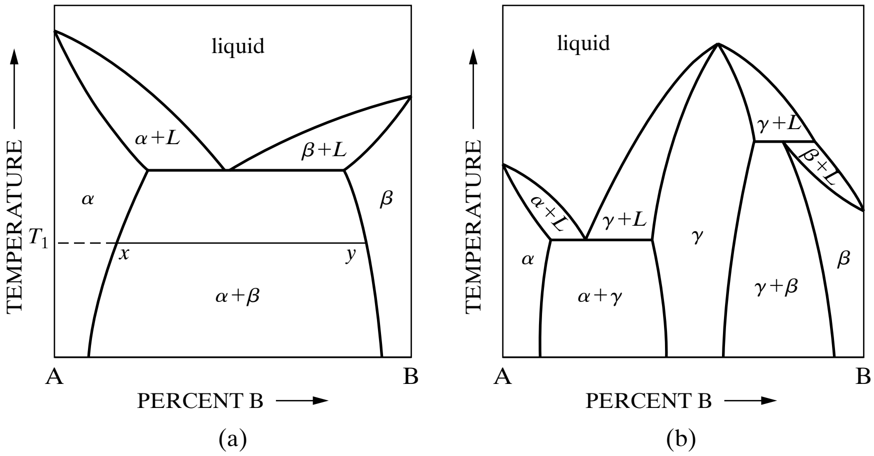

Figure 2 Phase diagrams showing (a) partial solid solubility, and (b) partial solid solubility together with the formation of an intermediate phase.

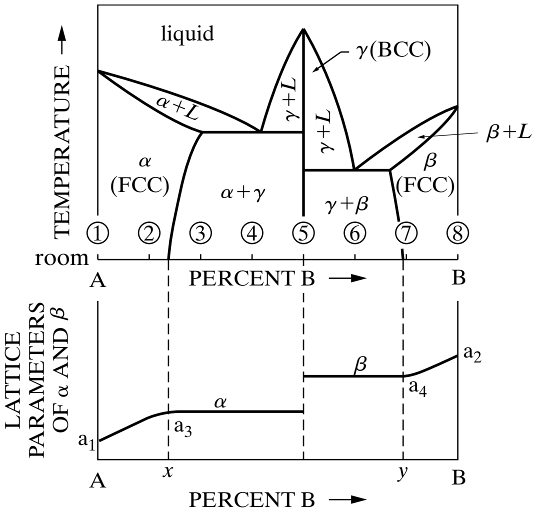

Figure 3 Phase diagram and lattice constants of a hypothetical alloy system.

3. *Single-phase regions*. In a single-phase region, a change in composition generally produces a change in lattice parameter and therefore a shift in the positions of the diffraction lines of that phase.
4. *Two-phase regions*. In a two-phase region, a change in composition of the alloy produces a change in the relative amounts of the two phases but no change in their compositions. These compositions are fixed at the intersections of a horizontal "tie line" with the boundaries of the two-phase field. Thus, in the system illustrated in Fig. 2(a), the tie line drawn at temperature T_1 shows that the compositions of α and β at equilibrium at this temperature are x and y respectively. The powder pattern of a two-phase alloy brought to equilibrium at temperature T_1 will therefore consist of the superimposed patterns of α of composition x and β of composition y. The patterns of a series of alloys in the xy range will all contain the same diffraction lines at the same positions, but the intensity of the lines of the α phase relative to the intensity of the lines of the β phase will decrease in a regular manner as the concentration of B in the alloy changes from x to y, since this change in total composition decreases the amount of α relative to the amount of β.

These principles are illustrated with reference to the hypothetical alloy system shown in Fig. 3. This system contains two substitutional terminal solid solutions α and β, both assumed to be face-centered cubic, and an intermediate phase γ, which is body-centered cubic. The solubility of either A or B in γ is assumed to be negligibly small: the lattice parameter of γ is therefore constant in all alloys in which this phase appears. On the other hand the parameters of α and β vary with composition in the manner shown by the lower part of Fig. 3. Since the B atom is assumed to be larger than the A atom, the addition of B expands the A lattice, and the parameter of α increases from a_1 for pure A to a_3 for a solution of composition x, which represents the limit of solubility of B in A at room temperature. In two-phase ($\alpha + \gamma$) alloys containing more than x percent B, the parameter of α remains constant at its saturated value a_3. Similarly, the addition of A to B causes the parameter of β to decrease from a_2 to a_4 at the solubility limit, and then remain constant in the two-phase ($\gamma + \beta$) field.

Calculated powder patterns, in a format similar to that which would be seen in film from a Hull/Debye–Scherrer camera, are shown in Fig. 4 for the eight alloys designated by number in the phase diagram of Fig. 3. It is assumed that the alloys have been brought to equilibrium at room temperature by slow cooling. Examination of these patterns reveals the following:

1. Pattern of pure A (face-centered cubic).
2. Pattern of α almost saturated with B. The expansion of the lattice causes the lines to shift to smaller angles 2θ.
3. Superimposed patterns of α and γ. The α phase is now saturated and has its maximum parameter a_3.

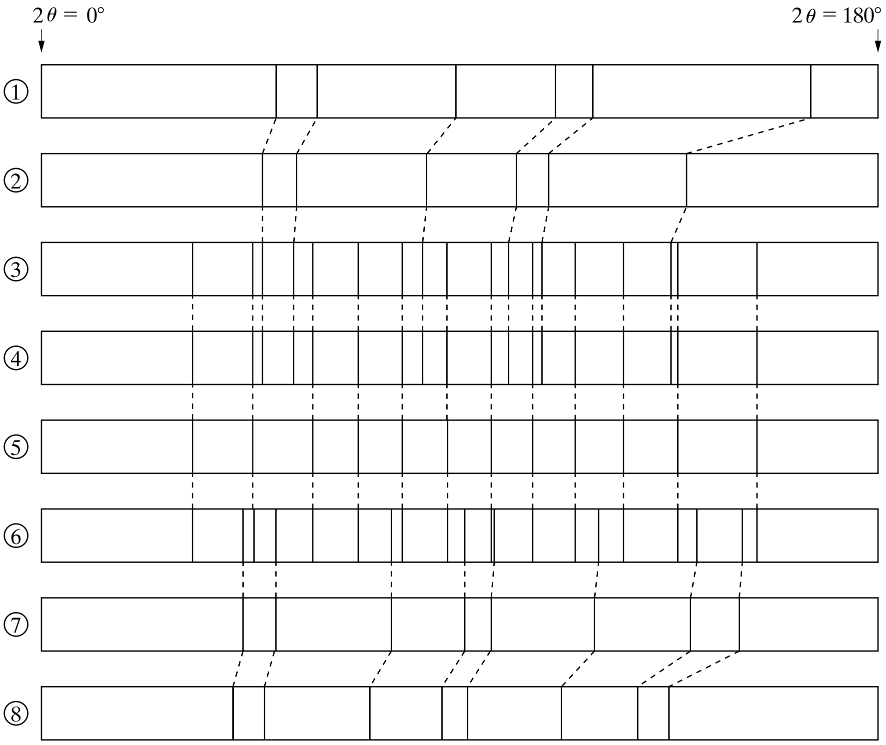

Figure 4 Calculated powder patterns of alloys 1 to 8 in the alloy system shown in Fig. 3.

4. Same as pattern 3, except for a change in the relative intensities of the two patterns which is not indicated on the drawing.
5. Pattern of pure γ (body-centered cubic).
6. Superimposed patterns of γ and of saturated β with a parameter of a_4.
7. Pattern of pure β with a parameter somewhat greater than a_4.
8. Pattern of pure B (face-centered cubic).

When an *unknown* phase diagram is being determined, the investigator must, of course, work in the reverse direction and deduce the sequence of phases across the diagram from the observed powder patterns. This is done by visual comparison of patterns prepared from alloys ranging in composition from pure A to pure B, and the previous example illustrates the nature of the changes which can be expected from one pattern to another. Corresponding lines in different patterns are identified by placing the patterns side by side as in Fig. 4 and noting which lines are common to the two patterns. [2] This may be difficult in some alloy systems where the phases involved have complex diffraction patterns, or where it is suspected that lines due to $K\beta$ radiation may be present in some patterns and not in others. It is important to remember that a diffraction pattern of a given phase is characterized not only by line positions but also by line intensities. This means that the presence of phase X in a mixture of phases cannot be proved merely by coincidence of the lines of phase X with a set of lines in the pattern of the mixture; the lines in the pattern of the mixture which coincide with the lines of phase X must also have the *same relative intensities* as the lines of phase X. The addition of one or more phases to a particular phase weakens the diffraction lines of that phase, simply by dilution, but it cannot change the intensities of those lines relative to one another. Finally, it should be noted that the crystal structure of a phase need not be known for the presence of that phase to be detected in a mixture: it is enough to know the positions and intensities of the diffraction lines of that phase.

Phase diagram determination by x-ray methods usually begins with a determination of the room-temperature equilibria. The first step is to prepare a series of alloys by melting and casting, or by melting and solidification. The resulting ingots are homogenized at a temperature just below the solidus to remove segregation, and very slowly cooled to room temperature.[3] Powder specimens are then prepared by grinding or filing, depending on whether the alloy is brittle or not. If the alloy is brittle enough to be ground into powder, the resulting powder is usually sufficiently stress-free to give sharp diffraction lines. Filed powders, however, must be re-

---

[2] When working with films, superposition of the two films is generally confusing and may make some of the weaker lines almost invisible. A better method of comparison consists of slitting each Hull/Debye–Scherrer film lengthwise down its center and placing the center of one film adjacent to the center or another. The curvature of the diffraction lines then does not interfere with the comparison of line positions..

[3] Slow cooling alone may not suffice to produce room-temperature equilibrium, which is often very difficult to achieve. It may be promoted by cold working and recrystallizing the cast alloy, in order to decrease its grain size and thus accelerate diffusion, prior to homogenizing and slow cooling.

annealed to remove the stresses produced by plastic deformation during filing before they are ready for x-ray examination. Only relatively low temperatures are needed to relieve stresses, but the filings should again be slowly cooled, after the stress-relief anneal, to ensure equilibrium at room temperature. Screening is usually necessary to obtain fine enough particles for x-ray examination, and when two-phase alloys are being screened, precautions should be observed.

After the room-temperature equilibria are known, a determination of the phases present at high temperatures can be undertaken. Powder specimens are sealed in small evacuated silica tubes, heated to the desired temperature long enough for equilibrium to be attained, and rapidly quenched. Diffraction patterns of the quenched powders are then made at room temperature. This method works very well in many alloy systems, in that the quenched powder retains the structure it had at the elevated temperature. In some alloys, however, phases stable at high temperature will decompose on cooling to room temperature, no matter how rapid the quench, and such phases can be studied only by means of a high-temperature camera or diffractometer.

The latter instrument is of particular value in work of this kind because it allows continuous observation of a diffraction line. For example, the temperature below which a high-temperature phase is unstable, such as a eutectoid temperature, can be determined by setting the diffractometer detector to receive a prominent diffracted beam of the high-temperature phase, and then measuring the intensity of this beam as a function of temperature as the specimen is slowly cooled. The temperature at which the intensity falls to that of the general background is the temperature required, and any hysteresis in the transformation can be detected by a similar measurement on heating.

3 SOLID SOLUTIONS

Inasmuch as solid solubility, to a greater or lesser extent, is so common, it is valuable to digress a little at this point to consider how the various kinds of solid solutions may be distinguished experimentally. Irrespective of its extent or its position on the phase diagram, any solid solution may be classified as one of the following types, solely on the basis of its crystallography:

1. Interstitial.
2. Substitutional.
   a) Random.
   b) Ordered. (Because of its special interest, this type is beyond the scope of this chapter)
   c) Defect. (A very rare type.)

Information on specific solid solutions, particularly on the variation of lattice

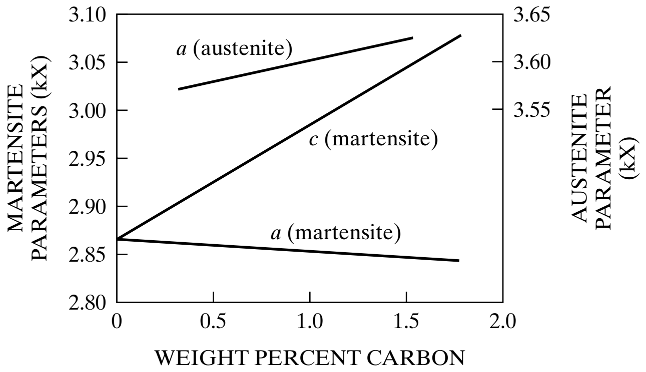

Figure 5 Variation of martensite and austenite lattice parameters with carbon content. After Roberts [1].

parameter with composition, is given by Pearson [G.8].

An *interstitial solid solution* of B in A is to be expected only when the B atom is so small compared to the A atom that it can enter the interstices of the A lattice without causing much distortion. As a consequence, about the only interstitial solid solutions of any importance in metallurgy are those formed between a metal and one of the elements, carbon, nitrogen, hydrogen, and boron, all of which have atoms less than 2 Å in diameter. The interstitial addition of B to A is always accompanied by an increase in the volume of the unit cell. If A is cubic, then the single lattice parameter *a* must increase. If A is not cubic, then one parameter may increase and the other decrease, as long as these changes result in an increase in cell volume. Thus, in austenite, which is an interstitial solid solution of carbon in face-centered cubic γ-iron, the addition of carbon increases the cell edge *a*. But in martensite, a metastable interstitial solid solution of carbon in α-iron, the *c* parameter of the body-centered tetragonal cell increases while the *a* parameter decreases, when carbon is added. These effects are illustrated in Fig. 5.

The density of an interstitial solid solution is given by the basic density equation

$$\rho = \frac{1.66042 \sum A}{V'}.$$

where

$$\sum A = n_s A_s + n_i A_i \tag{1}$$

n_s and n_i are numbers of solvent and interstitial atoms, respectively, per unit cell; and A_s and A_i are atomic weights of solvent and interstitial atoms, respectively. Note that the value of n_s is an integer and independent of the concentration of the interstitial element, and that n_i is normally a small fraction of unity.

The formation of a *random substitutional solid solution* of B and A may be accompanied by either an increase or a decrease in cell volume, depending on whether the B atom is larger or smaller than the A atom. In continuous solid solutions of ionic salts, such as KCl-KBr, the lattice parameter of the solution is directly proportional to the atomic percent solute present. This relationship, Vegard's law, is not strictly obeyed by metallic solid solutions and, in fact, there is no reason why it should be. However, it is often used as a sort of yardstick by which one solution may be compared with another, particularly in ternary III-V compounds such as AlGaAs or InGaAs used for microelectronics applications. Figure 6 shows both positive and negative deviations from Vegard's law among solutions of face-centered cubic metals, and even larger deviations have been found in hexagonal close-packed solutions. In terminal and intermediate solid solutions, the lattice parameter may or may not vary linearly with the atomic percent solute and, when the variation *is* linear, the parameter found by extrapolating to 100 percent solute does not usually correspond to the atom size deduced from the parameter of the pure solute, even when allowance is made for a possible change in coordination number.

The density of a random substitutional solid solution with the ΣA factor being given by

$$\sum A = n_{\text{solvent}} A_{\text{solvent}} + n_{\text{solute}} A_{\text{solute}}, \tag{2}$$

where n again refers to the number of atoms per cell and A to the atomic weight. But here $(n_{\text{solvent}} + n_{\text{solute}})$ is a constant integer, equal to the total number of atoms per cell. Whether a given solution is interstitial or substitutional may be decided by determining whether the x-ray density calculated according to Eq. (1) or that calculated according to Eq. (2) agrees with the directly measured density.

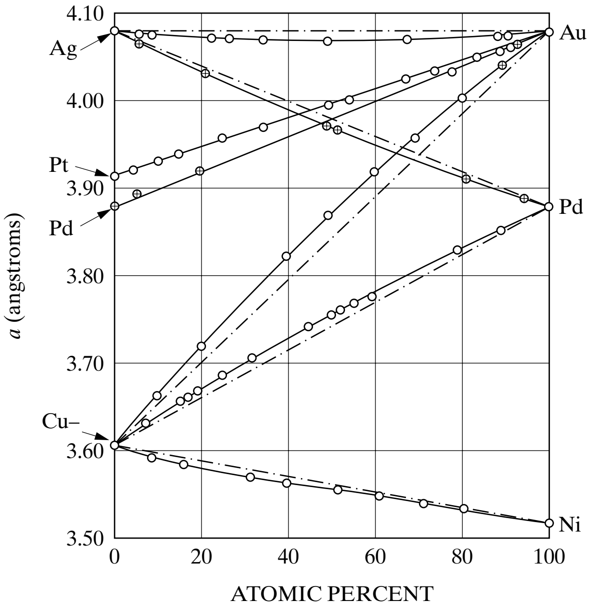

Figure 6 Lattice parameters of some continuous solid solutions. Dot-dash lines indicate Vegard's law. Barrett.

Defect substitutional solid solutions are ones in which some lattice sites, normally occupied by atoms at certain compositions, are simply vacant at other compositions. Solutions of this type are rare among metals; the best-known example is the intermediate β solution in the nickel-aluminum system [p. 387, G.8]. A defect solution is disclosed by anomalies in the curves of density and lattice parameter vs. composition. Suppose, for example, that the solid solution of B in A is perfectly normal up to x percent B, but beyond that point a defect lattice is formed; i.e., further increases in B content are obtained, not by further substitution of B for A, but by dropping A atoms from the lattice to leave vacant sites. Under these circumstances, the density and lattice parameter curves will show sudden changes in slope, or even maxima or minima, at the composition x. Furthermore, the x-ray density calculated according to Eq. (2) will no longer agree with the direct density simply because Eq. (2), as usually used, applies only to normal solutions where all lattice sites are occupied. The actual structure of a defect solid solution, including the proportion of vacant lattice sites at any given composition, can be determined by a comparison of the direct density with the x-ray density, calculated according to Eq. (2), and an analysis of the diffracted intensities.

4 DETERMINATION OF SOLVUS CURVES (DISAPPEARING-PHASE METHOD)

To return to the main subject of this chapter, consider the methods used for determining the position of a solvus curve (solid solubility curve) on a phase diagram. Such a curve forms the boundary between a single-phase solid region and a two-phase solid region, and the single-phase solid may be a primary or intermediate solid solution.

One method of locating such curves is based on the "lever rule." This rule, with reference to Fig. 7 for example, states that the relative proportions of α and β in an alloy of composition z in equilibrium at temperature T_1 is given by the relative lengths of the lines zy and zx, or that

$$W_\alpha(z - x) = W_\beta(y - z), \tag{3}$$

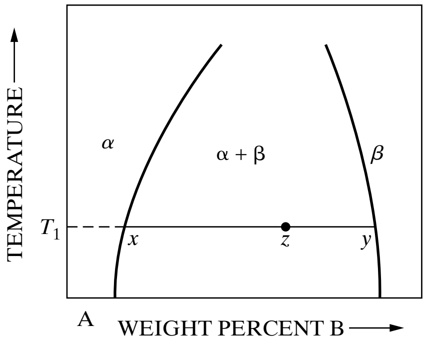

Figure 7 Lever-rule construction for finding the relative amounts of two phases in a two-phase field.

where W_α and W_β denote the relative weights of α and β if x, y, and z are expressed in weight percent. It follows from Eq. (3) that the weight fraction of β in the alloy varies linearly with composition from 0 at point x to 1 at point y. The intensity of any diffraction line from the β phase also varies from zero at x to a maximum at y, but the variation with weight percent B is not generally linear.[4] Nevertheless, this variation may be used to locate the point x. A series of alloys in the two-phase region is brought to equilibrium at temperature T_1 and quenched. From diffraction patterns made at room temperature, the ratio of the intensity I_β of a prominent line of the β phase to the intensity I_α of a prominent line of the α phase is plotted as a function of weight percent B. The composition at which the ratio I_β/I_α extrapolates to zero is taken as the point x. (Use of the ratio I_β/I_α rather than I_β alone eliminates the effect of any change which may occur in the intensity of the incident beam from one diffraction pattern to another. However, this ratio also varies nonlinearly with weight percent B.) Other points on the solvus curve are located by similar experiments on alloys quenched from other temperatures. This method is known, for obvious reasons, as the disappearing-phase method.

Since the curve of I_β/I_α vs. weight percent B is not linear, high accuracy in the extrapolation depends on having several experimental points close to the phase boundary which is being determined. The accuracy of the disappearing-phase method is therefore governed by the sensitivity of the x-ray method in detecting small amounts of a second phase in a mixture, and this sensitivity varies widely from one alloy system to another. The intensity of a diffraction line depends on, among other things, the atomic scattering factor f, which in turn is almost directly proportional to the atomic number Z. Therefore, if A and B have nearly the same atomic number, the α and β phases will consist of atoms having almost the same scattering powers, and the intensities of the α and β diffraction patterns will also be roughly equal when the two phases are present in equal amounts. Under favorable circumstances such as these, an x-ray pattern can reveal the presence of less than 1 percent of a second phase. On the other hand, if the atomic number of B is considerably less than that of A, the intensity of the β pattern may be so much lower than that of the α pattern that a relatively large amount of β in a two-phase mixture will go completely undetected. This amount may exceed 50 percent in extreme cases, where the atomic numbers of A and B differ by some 70 or 80 units. Under such circumstances, the disappearing-phase x-ray method is practically worthless. On the whole, the microscope is superior to x-rays when the disappearing-phase method is used, inasmuch as the sensitivity of the microscope in detecting the presence of a second phase is generally very high and independent of the atomic numbers of the elements involved. However, this sensitivity does depend on the particle size of the second phase, and if this is very small, as it often is at low temperatures, the second phase may not be detectable under the optical microscope. Hence the method of microscopic examination is not particularly accurate for the determination of solvus curves at low temperatures. In some cases, TEM is particularly valuable.

---

[4] The reasons for nonlinearity are beyond the scope of this chapter.

Whichever technique is used to detect the second phase, the accuracy of the disappearing-phase method increases as the width of the two-phase region decreases. If the $(\alpha + \beta)$ region is only a few percent wide, then the relative amounts of α and β will vary rapidly with slight changes in the total composition of the alloy, and this rapid variation of W_α/W_β will enable the phase boundary to be fixed quite precisely. This is true, for the x-ray method, even if the atomic numbers of A and B are widely different, because, if the $(\alpha + \beta)$ region is narrow, the compositions of α and β do not differ very much and neither do their x-ray scattering powers.

5 DETERMINATION OF SOLVUS CURVES (PARAMETRIC METHOD)

As was just seen, the disappearing-phase method of locating the boundary of the α field is based on a determination of the composition at which the β phase just disappears from a series of $(\alpha + \beta)$ alloys. The parametric method, on the other hand, is based on observations of the α solid solution itself. This method depends on the fact, previously mentioned, that the lattice parameter of a solid solution generally changes with composition up to the saturation limit, and then remains constant beyond that point.

Suppose the exact location of the solvus curve shown in Fig. 8(a) is to be determined. A series of alloys, 1 to 7, is brought to equilibrium at temperature T_1, where the α field is thought to have almost its maximum width, and quenched to room temperature. The lattice parameter of α is measured for each alloy and plotted against alloy composition, resulting in a curve such as that shown in Fig. 8(b). This curve has two branches: an inclined branch *bc*, which shows how the parameter of α varies with the composition of α, and a horizontal branch *de*, which shows that the α phase in alloys 6 and 7 is saturated, because its lattice parameter does not change with change in alloy composition. In fact, alloys 6 and 7 are in a two-phase region

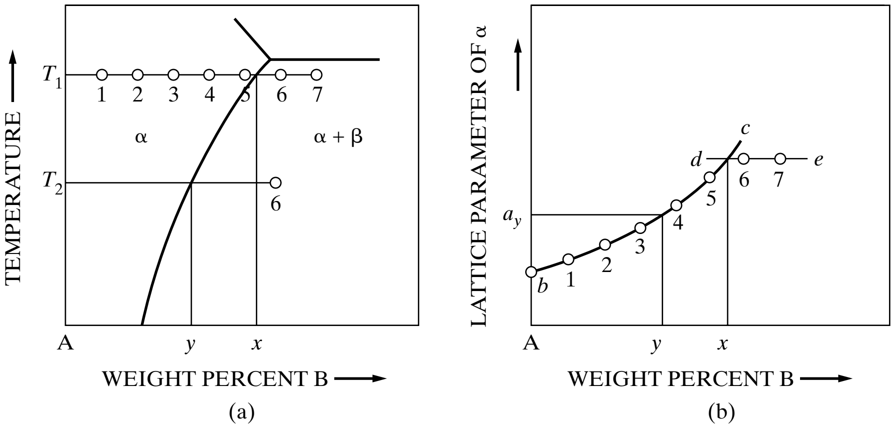

Figure 8 Parametric method for determining a solvus curve.

at temperature T_1, and the only difference between them is in the amounts of saturated α they contain. The limit of the α field at temperature T_1 is therefore given by the intersection of the two branches of the parameter curve. This locates one point on the solvus curve, namely x percent B at T_1.

Other points could be found in a similar manner. For example, if the same series of alloys were equilibrated at temperature T_2, a parameter curve similar to Fig. 8(b) would be obtained, but its inclined branch would be shorter and its horizontal branch lower. But heat treatments and parameter measurements on all these alloys are unnecessary, once the parameter-composition curve of the solid solution has been established. Only one two-phase alloy is needed to determine the rest of the solvus. Thus, if alloy 6 is equilibrated at T_2 and then quenched, it will contain α saturated at that temperature. Suppose the measured parameter of α in this alloy is a_y. Then, from the parameter-composition curve, parameter a_y, indicates that α contains y percent B. This fixes a point on the solvus at temperature T_2. Points on the solvus at other temperatures may be found by equilibrating the same alloy, alloy 6, at various temperatures, quenching, and measuring the lattice parameter of the contained α.

The parameter-composition curve, branch *bc* of Fig. 8(b), thus serves as a sort of master curve for the determination of the whole solvus. For a given precision of lattice parameter measurement, the accuracy with which the solvus can be located depends markedly on the slope of the parameter-composition curve. If this curve is nearly flat, i.e., if changes in the composition of the solid solution produce very small changes in parameter, then the composition, as determined from the parameter, will be subject to considerable error and so will the location of the solvus. However, if the curve is steep, just the opposite is true, and relatively crude parameter measurements may suffice to fix the location of the solvus quite accurately. In the parametric method, precision in parameter measurement is more important than accuracy.

Figure 9 illustrates the use of the parametric method in determining the solid solubility of antimony in copper as a function of temperature. The sloping curve in (a) was found from parameter measurements made on a series of alloys, containing from 0 to about 12 weight percent Sb, equilibrated at 630°C. The horizontal lines represent the parameters of two-phase alloys, containing about 12 weight percent Sb, equilibrated at the temperatures indicated. The solvus curve constructed from these data is given in (b), together with adjoining portions of the phase diagram.

In most cases, the parametric method is more accurate than the disappearing-phase method, whether based on x-ray measurements or microscopic examination, in the determination of solvus curves at low temperatures. As mentioned earlier, both x-ray diffraction and microscopic examination may fail to disclose the presence of small amounts of a second phase, although for different reasons. When this occurs, the disappearing-phase method always results in a measured extent of solubility *higher* than the actual extent. But the parametric method, since it is based on measurements made on the phase whose range of solubility is being determined (the α phase), is not influenced by any property of the second phase (the β phase).

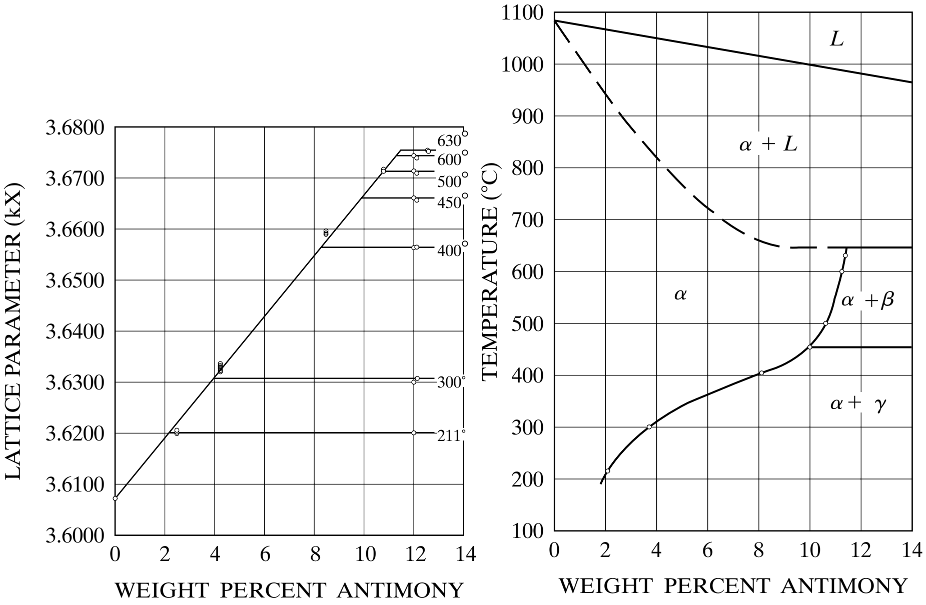

(a) (b)

Figure 9 Solvus curve determination in the copper-antimony system by the parametric method: (a) parameter versus composition curve; (b) solubility versus temperature curve. Mertz and Mathewson [2].

The β phase may have an x-ray scattering power much higher or lower than that of the α phase, and the β phase may precipitate in the form of large particles or small ones, without affecting the parameter measurements and do on the α phase.

Note that the parametric method is not confined to determining the extent of primary solid solutions, as in the examples given above. It may also be used to determine the solvus curves which bound an intermediate solid solution on the phase diagram. Note also that the parametric method may be employed even when the crystal structure of the α phase is so complex that its diffraction lines cannot be indexed. In this case, the plane spacing d corresponding to some high-angle line or, even more directly, the 2θ value of the line, is plotted against composition and the resulting curve used in exactly the same way as a parameter-composition curve. In fact, the "parametric" method could be based on the management of any property of the solid solution which changes with the composition of the solid solution, e.g., its electric resistivity.

PROBLEMS

***1** Metals A and B form a terminal solid solution α, cubic in structure. The variation of the lattice parameter of α with composition, determined by quenching single-phase alloys from an elevated temperature, is found to be linear, the parameter varying from 3.6060 Å for pure A to 3.6140 Å in α containing 4.0 weight percent B. The solvus curve is to be determined by quenching a two-phase alloy containing 5.0 weight percent B from a series of temperatures and measuring the parameter of the contained α. How precisely must the parameter be measured if the solvus curve is to be located within ± 0.1 weight percent B at any temperature?

2 The two-phase alloy mentioned in Prob. 1, after being quenched from a series of temperatures, contains α having the following measured parameters:

Temperature	Parameter
100°C	3.6082Å
200	3.6086
300	3.6091
400	3.6098
500	3.6106
600	3.6118

Plot the solvus curve over this temperature range. What is the solubility of B in A at 440°C?

REFERENCES

The following books are listed more or less in the order they are encountered in the text

G.8 Strukturbericht (Leipzig: Akademische Verlagsgesellschaft, 1931-1943. Also available from Ann Arbor, MI.: Edwards Brothers, 1943). A series of seven volumes describing crystal structures whose solutions were published in the years 1913 to 1939, inclusive. Continued by: *Structure Reports* (Utrecdht. Oosthoek, 1951 to date). Sponsored by the International Union of Crystallography. The volume numbers begin with Vol. 8, where *Strukturbericht* left off. The results of structure determinations are usually given in sufficient detail that the reader has no need to consult the original paper.

ANSWERS TO SELECTED PROBLEMS

1. ± 0.0002 Å

This page intentionally left blank

Quantitative Phase Analysis

1 INTRODUCTION

Within fifteen years of the discovery of diffraction of x-rays by crystals and ten years of the publication of diffraction patterns of polycrystalline materials, x-ray diffraction was being used for phase quantification [1]. By 1936, the internal standard method was in use [2]. Use of the various quantitative methods, however, requires impeccable technique and careful calibration, and this probably has limited the extent this technique has been applied [G.25]. Nonetheless, retained austenite content in steel [3] has been quantified by x-ray diffraction with an uncertainty better than 1%; in the same study point counting (optical microscopy) and magnetic susceptibility measurements yielded virtually identical compositions, with the uncertainty in the susceptibility method being comparable, with that of diffraction and that of the microscopy method being somewhat larger. Information beyond that appearing below can be found elsewhere [G.17, G.25, G.29].

2 CHEMICAL ANALYSIS BY PARAMETER MEASUREMENT

The lattice parameter of a binary solid solution of B in A depends only on the percentage of B in the alloy, as long as the solution is unsaturated. This fact can be made the basis for chemical analysis by parameter measurement. All that is needed is a parameter vs. composition curve, such as curve *bc*, which can be established by measuring the lattice parameter of a series of previously analyzed alloys. This method has been used in diffusion studies to measure the change in concentration of a solution with distance from the original interface. Its accuracy depends entirely on the slope of the parameter-composition curve. In alpha brasses, which can contain from 0 to about 40 percent zinc in copper, an accuracy of ±1 percent zinc can be achieved without difficulty. Methods for obtaining the highest precision in lattice parameter determination are beyond the scope of this chapter.

From Chapter 12 of *Elements of X-Ray Diffraction*, Third Edition. B.D. Cullity, S.R. Stock.

One source of data on lattice parameters is Pearson's compilation [G.9]. Applications of the parameter method are described by Zwell and Danko [4].

This method is applicable only to binary alloys. In ternary solid solutions, for example, the percentage of two components can be independently varied. The result is that two ternary solutions of quite different compositions can have the same lattice parameter.

3 BASIC PRINCIPLES OF MULTIPHASE QUANTITATIVE ANALYSIS

Quantitative analysis by diffraction is based on the fact that the intensity of the diffraction pattern of a particular phase in a mixture of phases depends on the concentration of that phase in the mixture. The relation between intensity and concentration is not generally linear, because the diffracted intensity depends markedly on the absorption coefficient of the mixture and this itself varies with the concentration.

To find the relation between diffracted intensity and concentration, the basic equation for the intensity diffracted by a powder specimen must be the starting point. The form of this equation depends on the kind of apparatus used, namely, camera or diffractometer; consider only the diffractometer here. The exact expression for the intensity diffracted by a single-phase powder specimen in a diffractometer is

$$I_{hkl} = \left(\frac{I_o A\lambda^3}{32\pi r}\right)\left[\left(\frac{\mu_o}{4\pi}\right)^2 \frac{e^4}{m^2}\right]\left(\frac{1}{v^2}\right)\left[|F(hkl)|^2 p\left(\frac{1+\cos^2 2\theta}{\sin^2\theta\cos\theta}\right)\right]\left(\frac{e^{-2M}}{2\mu}\right). \qquad (1)$$

Here I_{hkl} = integrated intensity per unit length of diffraction line (joules sec^{-1} m^{-1}), I_0 intensity of incident beam (joules sec^{-1} m^{-2}), A = cross-sectional area of incident beam (m^2), λ = wavelength of incident beam (m), r = radius of diffractometer circle (m), $\mu_0 = 4\pi \times 10^{-7}$m kg C^{-2}, e = charge on electron (C), m = mass of electron (kg), v = volume of unit cell (m^3), F_{hkl} = structure factor for reflection hkl, p = multiplicity factor, θ = Bragg angle, e^{-2M} = temperature factor, and μ = linear absorption coefficient (m^{-1}), which enters as the absorption factor $1/2\mu$.[1]

The derivation of this equation can be found in various advanced texts, for example, those of Warren [G.20] and James [G.19]. It applies to a polycrystalline specimen, made up of randomly oriented grains, in the form of a flat plate of effectively infinite thickness, making equal angles with the incident and diffracted beams and completely filling the incident beam at all angles θ. The second factor in square

---

[1] A digression on names and symbols is in order here. The quantity I_0 in Eq. (1) is a true intensity, i.e., energy per unit area per unit time (joules m^{-2} sec^{-1}), and I_0A is the *power* of the incident beam. This means that I is the power per unit length of diffraction line in the diffracted beam. If this beam is then incident on a film or detector for a certain time t, then the response of the film or detector is a measure of the *energy It* in unit length of the diffraction line. This is the quantity commonly called integrated intensity. A more descriptive term would be "total diffracted energy," but the term "integrated intensity," symbolized by I, has been too long entrenched in the vocabulary of x-ray diffraction to be changed now.

brackets, containing F, p, and θ, will be recognized, the approximate equation for relative line intensities in a Hull/Debye–Scherrer pattern.[2]

As Eq. (1) stands, it applies only to a pure substance. But suppose the goal is to analyze a mixture of two phases, α and β. Then Eq (1) can be rewritten in terms of one particular line of the α phase. $I(hkl)$ now becomes the intensity of the selected line of the α phase, and the right side of the equation $I_\alpha(hkl)$ must be multiplied by c_α, the volume fraction of α in the mixture, to allow for the fact that the diffracting volume of α in the mixture is less than it would be if the specimen were pure α. Finally, substitute μ_m for μ, where μ_m is the linear absorption coefficient of the mixture, and combine all factors that are constant and independent of the concentration of α, and this yields

$$I_\alpha = \frac{K_1 c_\alpha}{\mu_m}, \tag{2}$$

where K_1 is a constant. The value of K_1 is unknown, because I_0 is generally unknown, but this is unimportant if the ratio of I_α to the intensity of some standard reference line is formed. The concentration of α can then be found from this ratio.

The three main methods of analysis differ in what is used as a reference line: (1) *external standard method* (a line from pure α), (2) *direct comparison method* (a line from another phase in the mixture), and (3) *internal standard method* (a line from a foreign material mixed with the specimen).

In all methods, the absorption coefficient μ_m of the mixture is itself a function of c_α and can have a large effect on the measured intensity I_α. Alexander and Klug [5] were the first to clearly recognize this effect and to work out the equations needed in analysis.

4 EXTERNAL STANDARD METHOD

To put Eq. (2) in a useful form, μ_m needs to be expressed in terms of the concentration.

$$\frac{\mu_m}{\rho_m} = w_\alpha\left(\frac{\mu}{\rho_\alpha}\right) + w_\beta\left(\frac{\mu}{\rho_\beta}\right), \tag{3}$$

where w denotes the weight fraction and ρ the density. Consider a unit volume of the mixture. Its weight is ρ_m and the weight of contained α is $w_\alpha\rho_\mathrm{m}$. Therefore, the volume of α is $w_\alpha\rho_\mathrm{m}/\rho_\alpha$, which equals c_α and a similar expression holds for c_β. Equation (3) then becomes

$$\begin{aligned}\mu_m &= c_\alpha\mu_\alpha + c_\beta\mu_\beta = c_\alpha\mu_\alpha + (1 - c_\alpha)\mu_\beta \\ &= c_\alpha(\mu_\alpha - \mu_\beta) + \mu_\beta;\end{aligned}$$

---

[2] For the sake of brevity, the indices *hkl* will not be explicitly written after this point in the text, unless, they are required for clarity.

$$I_\alpha = \frac{K_1 c_\alpha}{c_\alpha(\mu_\alpha - \mu_\beta) + \mu_\beta}. \tag{4}$$

This equation relates the intensity of a diffraction line from one phase to the volume fraction of that phase and the linear absorption coefficients of both phases.

To put Eq. (4) on a weight basis, consider a unit mass of the mixture. The volume of the contained α is w_α/ρ_α and the volume of β is w_β/ρ_β. Therefore,

$$c_\alpha = \frac{W_\alpha/\rho_\alpha}{W_\alpha/\rho_\alpha + W_\beta/\rho_\beta} \tag{5}$$

$$= \frac{W_\alpha/\rho_\alpha}{W_\alpha(1/\rho_\alpha - 1/\rho_\beta) + 1/\rho_\beta}. \tag{6}$$

Combining Eqs. (4) and (6) and simplifying yields

$$I_\alpha = \frac{K_1 w_\alpha}{\rho_\alpha\{w_\alpha[(\mu/\rho)_\alpha - (\mu/\rho)_\beta] + (\mu/\rho)_\beta\}} \tag{7}$$

For the pure α phase, either Eq. (2) or (7) gives, for the same line,

$$I_{\alpha p} = \frac{K_1}{\mu_\alpha}, \tag{8}$$

where the subscript ρ denotes diffraction from the pure phase. Division of Eq. (7) by Eq. (8) eliminates the unknown constant K_1 and gives

$$\frac{I_\alpha}{I_{\alpha p}} = \frac{w_\alpha(\mu/\rho)_\alpha}{w_\alpha\{[(\mu/\rho)_\alpha - (\mu/\rho)_\beta] + (\mu/\rho)_\beta\}}. \tag{9}$$

This equation permits quantitative analysis of a two-phase mixture, provided that the mass absorption coefficients of each phase are known. If they are not known, a calibration curve can be prepared by using mixtures of known composition. In each case, a specimen of pure α must be available as a reference material, and the measurements of I_α and $I_{\alpha\rho}$ must be made under identical conditions.

In general, the variation of the intensity ratio $I_\alpha/I_{\alpha\rho}$ with w_α is not linear, as shown by the curves of Fig. 1. The experimental points were obtained by measurements on synthetic binary mixtures of powdered quartz, cristobalite, beryllium oxide, and potassium chloride; the curves were calculated by Eq. (9). The agreement is excellent. The line obtained for the quartz-cristobalite mixture is straight because these substances are two allotropic forms of silica and hence have identical mass absorption coefficients. When the mass absorption coefficients of the two phases are equal, Eq. (9) becomes simply

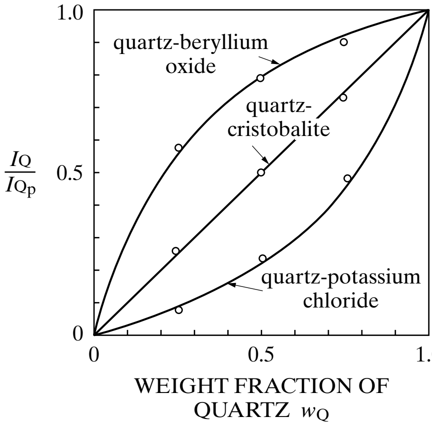

Figure 1 Diffractometer measurements made with Cu $K\alpha$ radiation on binary mixtures. I_Q is the intensity of the reflection from the $d = 3.34$ Å planes of quartz in a mixture. I_Q is the intensity of the same reflection from pure quartz. Alexander and Klug [5].

$$\frac{I_\alpha}{I_{\alpha p}} = w_\alpha.$$

Fig. 1 illustrates very clearly how the intensity of a particular diffraction line from one phase depends on the absorption coefficient of the other phase. For Cu $K\alpha$ radiation, the mass absorption coefficient of BeO is 8.6, of SiO_2 is 34.9, and of KCl is 124 cm^2/g.

5 DIRECT COMPARISON METHOD

This method does not require a sample of the pure phase whose composition is being determined because the required reference line comes from another phase in the mixture.

The direct comparison method is of great interest because it can be applied directly to polycrystalline aggregates. Since its development by Averbach and Cohen [6], it has been widely used for measuring the amount of retained austenite in hardened steel and will be described here in terms of that specific problem, although the method itself is quite general.

The hardening of steel requires two operations: (1) heating to a high temperature to form a homogeneous, face-centered-cubic solid solution called austenite, and (2) quenching the austenite to room temperature to transform it to a hard, metastable, body-centered-tetragonal solid solution called martensite. In practice, the quenched steel may contain some undissolved carbides and, because of incomplete transformation, some austenite is often retained at room temperature. The effect of this austenite on the service behavior of the steel is usually detrimental, but sometimes beneficial. At any rate there is considerable interest in methods of determining the exact amount of austenite present. Quantitative microscopic examination is fairly satisfactory as long as the austenite content is fairly high, but becomes unreliable below about 15 percent austenite in many steels. The x-ray method, on the other hand, is quite accurate in this low-austenite range, often the range of greatest practical interest.

Assume that a hardened steel contains only two phases, martensite and austenite. The problem is to determine the composition of the mixture, when the two phases have the same composition but different crystal structure. The external standard method cannot be used, because it is usually impossible to obtain a reference sample of pure austenite, or of known austenite content, of the same chemical composition as the austenite in the unknown. Instead, proceed as follows. In the basic intensity equation, Eq. (1), put

$$K_2 = \left(\frac{I_o A \lambda^3}{32\pi r}\right)\left[\left(\frac{\mu_o}{4\pi}\right)^2 \frac{e^4}{m^2}\right]$$

and

$$R = \left(\frac{1}{v^2}\right)\left[|F|^2 p\left(\frac{1 + \cos^2 2\theta}{\sin^2\theta\cos\theta}\right)\right](e^{-2M}). \tag{10}$$

The diffracted intensity is then given by

$$I = \frac{K_2 R}{2\mu}, \tag{11}$$

where K_2 is a constant, independent of the kind and amount of the diffracting substance, and R depends on θ, hkl, and the kind of substance. Designating austenite by the subscript γ and martensite by the subscript α, Eq. (11) for a particular diffraction line of each phase becomes:

$$I_\gamma = \frac{K_2 R_\gamma c_\gamma}{2\mu_m},$$

$$I_\alpha = \frac{K_2 R_\alpha c_\alpha}{2\mu_m}.$$

Division of these equations yields

$$\frac{I_\gamma}{I_\alpha} = \frac{R_\gamma c_\gamma}{R_\alpha c_\alpha}. \tag{12}$$

The value of c_γ/c_α can therefore be obtained from a measurement of I_γ/I_α and a calculation of R_γ and R_α (Note that the calculation of R values requires a knowledge of the crystal structures and lattice parameters of both phases.) Once c_γ/c_α is found, the value of c_γ can be obtained from the additional relationship:

$$c_\gamma + c_\alpha = 1.$$

Thus, an absolute measurement of the austenite content of the steel is obtained by direct comparison of the integrated intensity of an austenite line with the integrated intensity of a martensite line.[3] By comparing several pairs of austenite-

---

[3] Recalling the earlier discussion of the disappearing-phase x-ray method of locating a solvus line, the intensity ratio I_γ/I_α is not a linear function of the volume fraction c_γ, or, for that matter, of the weight fraction w_γ.

martensite lines, several independent determinations of the austenite content result.

If the steel contains a third phase, namely, Fe_3C (cementite), the cementite concentration can be determined either by quantitative microscopic examination or by diffraction. By measuring I_c, the integrated intensity of a particular cementite line, and calculating R_c, an equation similar of Eq. (12) allows c_γ/c_c to be obtained. The value of c_γ is then found from the relation

$$c_\gamma + c_\alpha + c_c = 1.$$

In choosing diffraction lines to measure, overlapping or closely adjacent lines from different phases must be avoided, while such lines can be deconvoluted, the uncertainties involved warrant choosing well-resolved lines. Figure 2 shows the calculated patterns of austenite and martensite in a 1.0 percent carbon steel, made with Cr $K\alpha$ radiation. Unfortunately, the strong 111 austenite line is too close to the 101-110 martensite line for separate measurement of its integrated intensity. Suitable austenite lines are the 200 and 220; these may be compared with the 002-200 and 12–11 martensite doublets. These "doublets," due to the tetragonality of the martensite unit cell are not usually resolved into separate lines because all lines are usually quite broad, both from the martensite and austenite, as shown by the pattern in Fig. 3. (The unresolved martensite lines are then indexed as a cubic line; for example, the 002-200 doublet is called the 200 line.) The line broadening is due to the nonuniform microstrain in both phases of the quenched steel and, very often, the fine grain size.

If substantial amounts of carbide are present, as in some tool steels, carbide lines may overlap α and γ lines and cause difficulties in measurement. Durnin and Ridal [3] list the α and γ lines that do or do not overlap the lines of Fe_3C and six alloy carbides.

While chromium radiation is the most popular, shorter wavelengths such as Fe $K\alpha$, Co $K\alpha$, and Mo $K\alpha$ will increase the number of lines on the pattern and thus provide more measurable pairs. The low resolution of energy-dispersive diffractometry is no hindrance here, because the diffraction lines of steel are well separated, and Voskamp has described the application of that technique to austenite measurement.

In calculating the value of R for a particular diffraction line, various factors should be kept in mind. The unit cell volume v is calculated from the measured lattice parameters, which are a function of carbon and alloy content. When the martensite doublets are unresolved, the structure factor and multiplicity of the martensite are calculated on the basis of a body-centered *cubic* cell; this procedure, in effect, adds together the integrated intensities of the two lines of the doublet, which is exactly what is done experimentally when the integrated intensity of an unresolved doublet is measured. For greatest accuracy in the calculation of F, the atomic scattering factor f should be corrected for anomalous scattering by an amount Δf, particularly when Co $K\alpha$ radiation is used. The value of the temperature factor e^{-2M} can be taken from the curve.

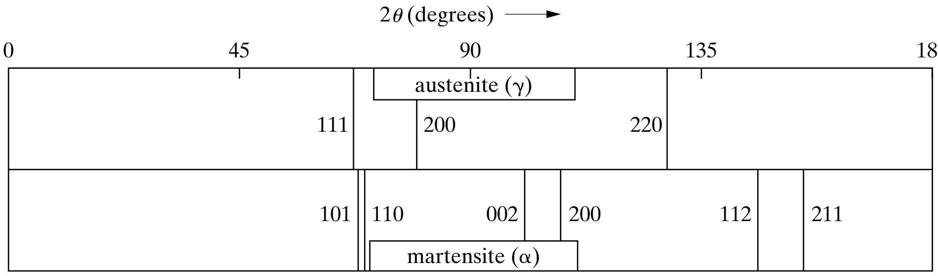

Figure 2 Calculated powder patterns of austenite and martensite, each containing 1.0 percent carbon in solution. Cr $K\alpha$ radiation.

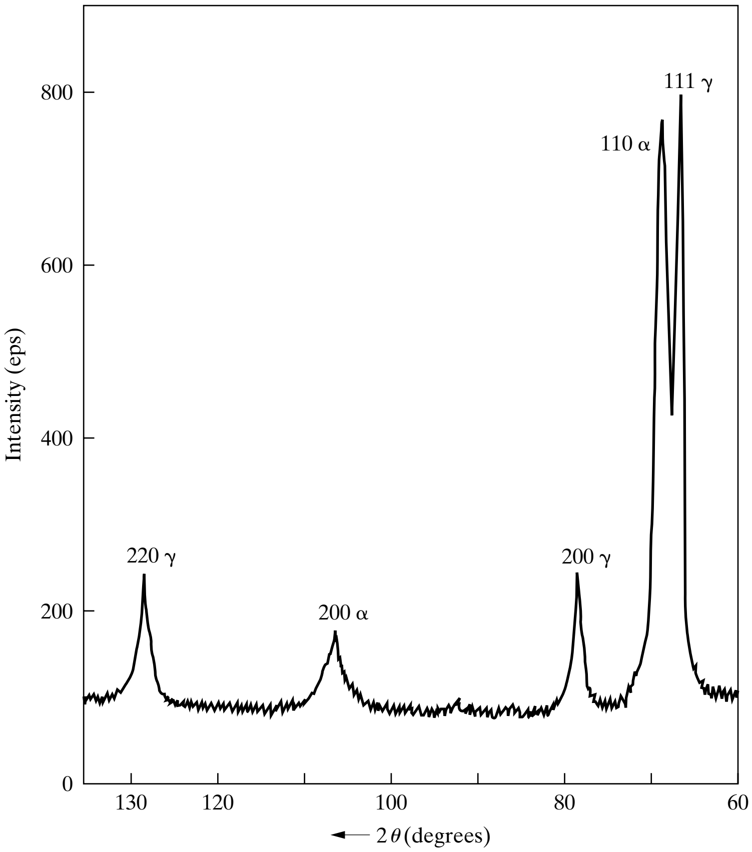

Figure 3 Partial diffractometer pattern of an oil-quenched Ni-V steel, containing about 30 volume percent austenite (γ). Chromium radiation, V filter.

Specimen preparation involves wet grinding to remove the surface layer, which may be decarburized or otherwise nonrepresentative of the bulk of the specimen, followed by standard metallographic polishing and etching. This procedure ensures a flat, reproducible surface for the x-ray examination, and allows a preliminary examination of the specimen to be made with the microscope. In grinding and polishing, care should be taken not to produce excessive heat or plastic deformation which would cause partial decomposition of both the martensite and austenite.

In the measurement of diffraction line intensity, it is essential that the *integrated intensity*, not the maximum intensity, be measured. Large variation in line shape can occur because of variations in microstrain and grain size. These variations in line shape will not affect the integrated intensity, but they can make the values of maximum intensity absolutely meaningless.

The sensitivity of the x-ray method in determining small amounts of retained austenite is limited chiefly by the intensity of the continuous background present. The lower the background, the easier it is to detect and measure weak austenite lines. With filtered radiation the minimum detectible amount is about 2 volume percent austenite, and with crystal-monochromated radiation probably about 0.2 percent. The error in the austenite content, originating in the calculation of R and the measurement of I, is probably about 5 percent of the amount present, in the absence of preferred orientation (Sec. 7).

In 1971 the National Bureau of Standards (NBS, now NIST) issued a standard reference material (SRM-485) containing a specified amount of austenite [7]. In 1987 NIST listed four ferrous x-ray diffraction standards (SRM 485a-488), and as recently as 1995 SRM 487 and 488 were still in NIST's catalog. Such standard materials are useful to the investigator who wishes to check his or her experimental and computational technique.

Other analytical problems to which the direct comparison method has been applied include the determination of mixed iron oxides in the oxide scale on steel [8], the beta phase in titanium alloys [9], and mixed uranium and plutonium carbides [10].

6 INTERNAL STANDARD METHOD

In this method a diffraction line from the phase being determined is compared with a line from a standard substance mixed with the sample in known proportions. The internal standard method is therefore restricted to samples in powder form.

Suppose the amount of phase A must be determined in a mixture of phases $A, B, C, \ldots$, where the relative amounts of the other phases present $(B, C, D, \ldots)$ may vary from sample to sample. With a known amount of original sample, mix a known amount of a standard substance S to form a new composite sample. Let c_A and c'_A be the volume fractions of phase A in the original and composite samples, respectively, and let c_s be the volume fraction of S in the composite sample. If a diffraction pattern is now prepared from the composite sample, then from Eq. (2) the intensity of a particular line from phase A is given by

$$I_{\mathrm{A}} = \frac{K_3 c'_A}{\mu_m},$$

and the intensity of a particular line from the standard S by

$$I_{\mathrm{S}} = \frac{K_4 c_{\mathrm{S}}}{\mu_m},$$

Division of one expression by the other gives

$$\frac{I_{\mathrm{A}}}{I_{\mathrm{S}}} = \frac{K_3 c'_A}{K_4 c_S}. \tag{13}$$

(Note that μ_{m} the linear absorption coefficient of the mixture and an unknown quantity, drops out. Physically, this means that variations in absorption, due to variations in the relative amounts of B, C, D, …, have no effect on the ratio $I_{\mathrm{A}}/I_{\mathrm{S}}$ since they affect I_{A} and I_{S} in the same proportion.)

By extending Eq. (5) to a number of components,

$$c'_A = \frac{w'_{\mathrm{A}}/\rho_{\mathrm{A}}}{w'_{\mathrm{A}}/\rho_{\mathrm{A}} + w'_{\mathrm{B}}/\rho_{\mathrm{B}} + w'_{\mathrm{C}}/\rho_{\mathrm{C}} + \cdots + w_{\mathrm{S}}/\rho_{\mathrm{S}}}$$

and a similar expression exists for c_{S}. Therefore,

$$\frac{c'_A}{c_{\mathrm{S}}} = \frac{w'_A \rho_{\mathrm{S}}}{\rho_A w_{\mathrm{S}}}.$$

Substitution of this relation into Eq. (13) gives

$$\frac{I_{\mathrm{A}}}{I_{\mathrm{S}}} = K_5 w'_A, \tag{14}$$

if w_s is kept constant in all the composite samples. The relation between the weight fractions of A in the original and composite samples is:

$$w'_A = w_{\mathrm{A}}(1 - w_{\mathrm{S}}). \tag{15}$$

Combination of Eqs. (14) and (15) gives

$$\frac{I_{\mathrm{A}}}{I_{\mathrm{S}}} = K_6 w_{\mathrm{A}}. \tag{16}$$

The intensity ratio of a line from phase A and a line from the standard S is therefore a linear function of W_{A}, the weight fraction of A in the original sample. A calibration curve can be prepared from measurements on a set of synthetic samples, containing known concentrations of A and a constant concentration of a suitable standard. Once the calibration curve is established, the concentration of A in an unknown sample is obtained simply by measuring the ratio I_A/I_S for a composite sample containing the unknown and the same proportion of standard as was used in the calibration.

The internal standard method has been widely used for the measurement of the quartz content of industrial dusts. In this analysis, fluorite (CaF_2) has been found to be a suitable internal standard. Figure 4 shows a calibration curve prepared from mixtures of quartz and calcium carbonate, of known composition, each mixed with enough fluorite to make the weight fraction of fluorite in each composite sample equal to 0.20. The curve is linear and through the origin as predicted by Eq. (16). Bumsted [11] describes the determination of quartz in dust by this method, with particular attention to the problems posed by very small samples. Note that systematic errors which vary with w_S would not be detected in a calibration employing Eq. 16. Both microabsorption and preferred orientation can be dependent on w_S [12] (see Sec. 8).

Strictly speaking, Eq. (16) is valid only for integrated intensities, and the same is true of all other intensity equations in this chapter. Yet it has been found possible to determine the quartz content of dusts with satisfactory accuracy by simply measuring maximum intensities. This short cut is permissible here only because the shape of the diffraction lines is found to be essentially constant from sample to sample. There is therefore a constant proportionality between maximum and integrated intensity and, as long as all patterns are made under identical experimental conditions, the measurement of maximum intensities gives satisfactory results. Quite erroneous results would be obtained by this procedure if the particle size of the samples were very small and variable, since then a variable amount of line broadening would occur, and this would cause a variation in maximum intensity independent of sample composition.

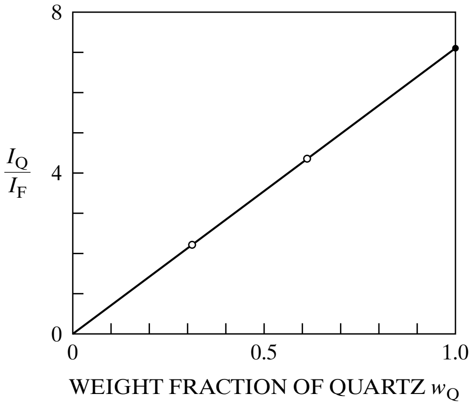

Figure 4 Calibration curve for quartz analysis, with fluorite as internal standard. I_o is the intensity of the d = 3.34 Å line of quartz, and I_F is the intensity of the d = 3.16 Å line of fluorite. Alexander and Klug [5].

Other applications of the internal standard method include the analysis of cement [13], the analysis of clay minerals [14], and the determination of chrysotile asbestos in airborne dust [15].

7 OTHER METHODS

The International Centre for Diffraction Data has generalized the internal standard method by comparing the strongest line on the pattern of a large number of substances with the strongest line from a single standard reference material. The material chosen was α–$\mathrm{Al_2O_3}$, a synthetic corundum commercially available as "Linde A" powder. Values of I/I_{cor}, where I is the maximum intensity of the strongest line from the compound, I_{cor} the same quantity for the corundum, and I/I_{cor} was determined from a mixture, of equal parts by weight, of the compound and corundum, are available in the Powder Diffraction File for many, although far from all, phases. The value of I/I_{cor}, which is reported to two significant figures, for any particular compound A establishes a single point on the calibration curve, like Fig. 4, of compound A; if an equi-weight mixture of corundum and the unknown is then made, the weight fraction of A in the unknown is given simply by one half the ratio of I_A/I_{cor} for the unknown-corundum mixture to the tabulated value I_A/I_{cor} for the A-corundum mixture. This method is fast, because the calibration has already been done, but its accuracy is probably low, in view of the use of maximum, rather than integrated, intensities. Variations in line broadening would be expected to introduce errors.

The ratio I/I_c provides one type of reference intensity for quantitative phase determinations. Reference phases other than corundum, reflections other than those with maximum intensity and arbitrary concentrations can be used, and this leads to a more general definition of Reference Intensity Ratio (RIR) for the phase of interest α and the reference phase β [12,16]:

$$\mathrm{RIR}_{\alpha\beta} = \frac{\mathrm{I}_\alpha(hkl)\ \ I_\beta^{\mathrm{rel}}(h'k'l')\,w_\beta}{\mathrm{I}_\beta(h'k'l')\ \ \mathrm{I}_\alpha^{\mathrm{rel}}(hkl)\ \ w_\alpha}, \tag{17}$$

where hkl and $h'k'l'$ represent specific reflections from α and β phases, respectively, and $I_j^{rel}(mno)$ denotes the intensity of phase j's mno peak relative to the 100% line of that phase. Rearranging this equation yields, for the internal standard method

$$\mathrm{w}_\alpha = \frac{\mathrm{I}_\alpha(hkl)\ \ I_\beta^{\mathrm{rel}}(h'k'l')\ \ \ w_\beta}{\mathrm{I}_\beta(h'k'l')\ \ \mathrm{I}_\alpha^{\mathrm{rel}}(hkl)\ \ \mathrm{RIR}_{\alpha,\beta}} \tag{18}$$

Careful calibration via the normal internal standards approach may be used to fix the RIR value, or derivation from other RIR's may be used, e.g.,

$$\mathrm{RIR}_{\alpha,\beta} = \frac{\mathrm{RIR}_{\alpha,\gamma}}{\mathrm{RIR}_{\beta,\gamma}} \tag{19}$$

Better accuracy and greater insulation from the effects of texture (as will be discussed in Sec. 8) can be obtained by using multiple peaks of each phase for the quantification process. It is necessary to normalize each peak relative to the other peaks in the mixture so that a meaningful average is obtained, and one way of properly weighting intensities of the different peaks is to normalize each peak's intensity by the relative intensities measured (by the investigator under the same conditions) in the pure phase. Generally, the data from the PDF card of that phase is not reliable enough for this purpose. For each peak n in the phase of interest *p in the unknown,* the ratio of the observed intensity (in counts) is made with the relative intensity of peak n in pure phase p, and the average ratio for the N peaks of phase p is:

$$\bar{\mathrm{I}}_{p}^{obs} = \frac{1}{\mathrm{N}} \sum_{n=1}^{N} \frac{I_p^{obs}(n)}{I_p^{rel}(n)} \tag{20}$$

Another approach to quantitative phase analysis involves fitting the entire pattern, not just selected peaks, or even all of the peak intensities, but the peak shapes and background between peaks [e.g., 17]. The Rietveld method is particularly well-suited to determining the amounts of different phases in complex mixtures.

8 PRACTICAL DIFFICULTIES

In any method involving powders, accurate sampling and homogeneous mixing can present problems. They are not trivial, and errors in these operations can produce large errors in the final result. Such matters are discussed by Klug and Alexander [G.17], Jenkins and Snyder [G.25] and Zevin and Vimmel [G.29].

Certain effects can cause great difficulty in quantitative analysis because they cause observed intensities to depart widely from the theoretical. The most important of these complicating factors are:

1. *Preferred orientation*. The basic intensity equation, Eq. (1), is derived on the premise of random orientation of the constituent crystals in the sample and is not valid if any preferred orientation exists. It follows that, in the preparation of powder samples for the diffractometer, every effort should be made to avoid preferred orientation. If the sample is a solid polycrystalline aggregate, the analyst has no control over the distribution of orientations in it, but he or she should at least be aware of the possibility of error due to preferred orientation (texture). The texture problem has probably received most attention in connection with determining austenite in steel by the direct comparison method. Here there is a direct check on texture, because the calculated R values for one phase are simply the theoretical line intensities, in arbitrary units, for that phase in the absence of texture. If the measured intensities of the various lines of a particular phase, say α, are not in the same ratio as their R values, then texture exists; the austenite

content determined from a particular pair of α and γ lines will then differ from the value found from another pair. Two approaches have been made to the problem of measuring austenite in the presence of texture:

a) *Averaging intensities* [18-22]. The basic idea here is simple. If certain lines from, say, austenite are abnormally weak because of texture, then other austenite lines will be abnormally strong. Only by measuring all the lines and averaging them in a particular way is valid data obtained This method, here crudely termed "intensity averaging," has had considerable success, at the cost of increased measurement and computation time. The number of diffraction lines required for the analysis increases with the degree of texture. For strongly textured materials Mo $K\alpha$ radiation is needed to provide enough lines.

b) *Averaging orientations* [23, 24]. Here the specimen is rotated in particular ways during the measurement of line intensity in order to present more crystal orientations to the incident beam.

2. *Microabsorption*. Consider diffraction from a given crystal of α in a mixture of α and β crystals. The incident beam passes through both α and β crystals on its way to a particular diffracting α crystal, and so does the diffracted beam on its way out of the sample. Both beams are decreased in intensity by absorption, and the decrease can be calculated from the total path length and μ_m, the linear absorption coefficient of the mixture. But a small part of the total path lies entirely within the diffracting α crystal, and for this portion μ_α is the applicable absorption coefficient. If μ_α is much larger than μ_β, or if the particle size of α is much larger than that of β, then the total intensity of the beam diffracted by the α crystals will be much less than that calculated, since the effect of microabsorption in each diffracting α crystal is not included in the basic intensity equation. Evidently, the microabsorption effect is negligible when $\mu_\alpha \approx \mu_\beta$ and both phases have the same particle size, or when the particle size of both phases is very small. Powder samples should therefore be finely ground before analysis.
3. *Extinction*. This effect produces a reduction in diffracted intensity as a crystal becomes more nearly perfect. Equation (1) is derived for the ideally imperfect crystal, one in which extinction is absent. Samples for chemical analysis should therefore be free of extinction, and this can be accomplished, for powder samples, by grinding or filing. If a solid aggregate must be analyzed directly, the possibility of some extinction in the individual grains of the aggregate should be kept in mind.

Microabsorption and extinction, if present, can seriously decrease the accuracy of the direct comparison method, because this is an absolute method. Fortunately, both effects are negligible in the case of hardened steel. Inasmuch as both the austenite and martensite have the same composition and only a 4 percent difference in density, their linear absorption coefficients are practically identical. Their average particle sizes are also roughly the same. Therefore, microabsorption does not occur. Extinction is absent because of the very nature of hardened steel. The change in specific volume accompanying the transformation of austenite to martensite sets up nonuniform strains in both phases so severe that both kinds of crystals can be considered highly imperfect. If these fortunate circumstances do not exist, and they do not in most other alloy systems, the direct comparison method should be used with caution and checked by some independent method.

On the other hand, the presence of microabsorption and extinction does not invalidate the internal standard method, provided these effects are constant from sample to sample, including the calibration samples. Microabsorption and extinction affect only the values of the constants K_3 and K_4 in Eq. (13), and therefore the constant K_6 in Eq. (16), and the latter constant determines only the slope of the calibration curve. Therefore, microabsorption and extinction, if present, will have no effect on the accuracy of the internal standard method as long as the crystals of the phase being determined, and those of the standard substance, do not vary in degree of perfection or particle size from one sample to another.

PROBLEMS

1 Microscopic examination of a hardened 1.0 percent carbon steel shows no undissolved carbides. X-ray examination of this steel in a diffractometer with filtered cobalt radiation shows that the integrated intensity of the 311 austenite line is 2.33 and the integrated intensity of the unresolved 112-211 martensite doublet is 16.32, both in arbitrary units. Calculate the volume percent austenite in the steel.

REFERENCES

The following books are listed more or less in the order they are encountered in the text

G.9 W. B. Pearson. *A Handbook of Lattice Spacings and Structures of Metals and Alloys* (New York: Pergamon Press, 1958). A most useful source of information. Gives the crystal structures of intermediate phases, and the variation of lattice parameter with composition in solid solutions, of binary and ternary alloys. Also gives the crystal structures of metal borides, carbides, hydrides, nitrides, and binary oxides.

G.17 Harold P. Klug and Leroy E. Alexander. *X-Ray Diffraction Procedures*, 2nd ed. (New York: Wiley, 1974). Contains a great deal of useful detail on the theory and operation of powder cameras and diffractometers. Covers the following topics in depth: chemical analysis by diffraction, parameter measurement, line-broadening analysis, texture determination, stress measurement, and studies of amorphous materials. Single-crystal methods are not included.

G.19 R. W. James. *The Optical Principles of the Diffraction of X-Rays* (Woodbridge; CT: Ox Bow Press, 1982). Excellent book on advanced theory of x-ray diffraction. Includes thorough treatments of diffuse scattering (due to thermal agitation, small particle size, crystal imperfections, etc.), the use of Fourier series in structure analysis, and scattering by gases, liquids, and amorphous solids.

G.20 B. E. Warren. *X-Ray Diffraction* (Reading, MA: Addison-Wesley, 1969). Excellent advanced treatment, in which the author takes pains to connect theoretically derived results with experimentally observable quantities. Stresses diffraction effects due to thermal vibration, order-disorder, imperfect crystals, and amorphous materials. Includes a treatment of the dynamical theory of diffraction by a perfect crystal.

G.25 Ron Jenkins and Robert L. Snyder. *Introduction to X-ray Powder Diffractometry* (New York, John Wiley & Sons, Inc, 1996).

G.29 L. S. Zevin and G. Kimmel. *Quantitative X-ray Diffractometry*, edited by I. Mureinik, Springer, 1995, New York.

ANSWERS TO SELECTED PROBLEMS

1. B volume percent.

Precise Parameter Measurements

1 INTRODUCTION

Many applications of x-ray diffraction require precise knowledge of the lattice parameter (or parameters) of the material under study. In the main, these applications involve solid solutions; since the lattice parameter of a solid solution varies with the concentration of the solute, the composition of a given solution can be determined from a measurement of its lattice parameter. Thermal expansion coefficients can also be determined, without a dilatometer, by measurements of lattice parameter as a function of temperature in a high-temperature camera or diffractometer. Since, in general, a change in solute concentration or temperature produces only a small change in lattice parameter, rather precise parameter measurements must be made in order to measure these quantities with any accuracy. This chapter concentrates on the methods used to obtain high precision with polycrystalline samples, leaving the various applications to be discussed elsewhere. Cubic substances will be covered first, because they are the simplest, but the general conclusions will also be valid for noncubic materials, which will be discussed in detail later.

The process of measuring a lattice parameter is a very indirect one, and is fortunately of such a nature that high precision is fairly easily obtained. The parameter a of a cubic substance is directly proportional to the spacing d of any particular set of Bragg planes. Measuring the Bragg angle θ for hkl and using Bragg's law to determine d allows calculation of a. But it is sin θ, not θ, which appears in Bragg's law. Precision in d, or a, therefore depends on precision in sin θ, a derived quantity, and not on precision in θ, the measured quantity. This is fortunate because the value of sin θ changes very slowly with θ in the neighborhood of 90°, as inspection of Fig. 1 or a table of sines will show. For this reason, a very accurate value of sin θ can be obtained from a measurement of θ which is itself not particularly precise, *provided that θ is near 90°*. For example, an error in θ of 1° leads to an error in sin θ of

From Chapter 13 of *Elements of X-Ray Diffraction*, Third Edition. B.D. Cullity, S.R. Stock.

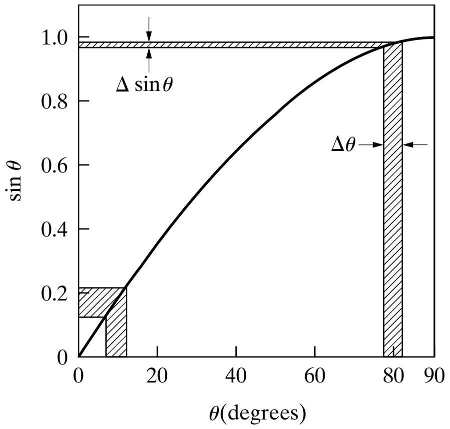

Figure 1 The variation of sin θ with θ. The error in sin θ caused by a given error in θ decreases as θ increases ($\Delta\theta$ exaggerated).

1.7 percent at $\theta = 45^o$ but only 0.15 percent at $\theta = 85^o$. Stated in another way, the angular position of a diffracted beam is much more sensitive to a given change in plane spacing when θ is large than when it is small.

The same result follows directly from differentiation of Bragg's law with respect to θ:

$$\frac{\Delta \mathrm{d}}{\mathrm{d}} = \frac{\Delta\lambda}{\lambda} - \cot\theta\Delta\theta. \tag{1}$$

Neglecting $\Delta\lambda$ yields

$$\frac{\Delta d}{d} = -\cot\theta\Delta\theta. \tag{2}$$

In the cubic system,

$$a = d\sqrt{h^2 + k^2 + l^2}.$$

Therefore

$$\frac{\Delta a}{a} = \frac{\Delta d}{d} = -\cot\theta\Delta\theta. \tag{3}$$

Since $\cot\theta$ approaches zero as θ approaches 90°, $\Delta a/a$, the fractional error in a caused by a given error in θ, also approaches zero as θ approaches 90°, or as 2θ approaches 180°. The key to precision in parameter measurements therefore lies in the use of back reflected beams having 2θ values as near to 180° as possible.

Although the parameter error disappears as 2θ approaches 180°, diffracted beams cannot be observed at this angle. Because the values of a calculated for the various lines on the pattern approach the true value more closely as 2θ increases, the true value of a should be found simply by plotting the measured values against 2θ and extrapolating to $2\theta = 180^o$. Unfortunately, this curve is not linear and the extrapolation of a nonlinear curve is not accurate. If the measured values of a are plotted against certain functions of θ, however, rather than against θ or 2θ directly, the resulting curve is a straight line which may be extrapolated with confidence. The bulk of this chapter is devoted to showing how these functions can be derived and used. Because the exact form of the function depends on the geometry of the apparatus used to record the diffraction pattern, the nature and functional dependence of systematic errors must be examined before extrapolation procedures can be discussed.

Prior to developing such a mathematical understanding, it is important to appreciate what sort of precision is possible. Without any extrapolation or any particular attention to good experimental technique, simply by selection of the parameter calculated for the highest-angle line on the pattern, a precision of 0.01 Å usually results. Since the lattice parameters of many engineering materials are in the neighborhood of 3 to 4 Å, this represents a precision of about 0.3 percent. With good experimental technique and the use of the proper extrapolation function, this precision can be increased to 0.001 Å, or 0.03 percent, without much difficulty. Finally, about the best precision that can be expected is 0.0001 Å, or 0.003 percent, but this can be obtained only by the expenditure of considerable effort, both experimental and computational.

In work of high precision it is imperative that the units in which the measured parameter is expressed, kX or Å, be correctly stated. In order to avoid confusion on this point, the reader is advised to review the discussion of these units "Diffraction I: Geometry." The actual *numerical value* of the wavelength or wavelengths used in the determination of the parameter should be explicitly stated.

Methods of determining lattice parameters with high precision are reviewed by Barrett and Massalski [G.10], Klug and Alexander [G.17], Parrish and Wilson [G.13], Azaroff and Buerger [G.33], and Jenkins and Snyder [G.25]

2 DIFFRACTOMETERS

The general approach in finding an extrapolation function is to consider the various effects which can lead to errors in the measured values of θ, and to find out how these errors in θ vary with the angle θ itself. The diffractometer is a complex apparatus and therefore subject to misalignment of its component parts. A further difficulty with most commercial diffractometers is the impossibility of observing the same back-reflected cone of radiation on both sides of the incident beam. Thus, the experimenter has no automatic check on the accuracy of the angular scale of the instrument or the precision of its alignment.

When a diffractometer is used to measure d-spacings, the more important sources of systematic error in d are the following:

1. Misalignment of the instrument. In particular, the center of the incident beam must intersect the diffractometer axis and the 0° position of the detector slit.

2. Use of a flat specimen instead of a specimen curved to conform to the focusing circle. This error is minimized, with loss of intensity, by decreasing the irradiated width of the specimen by means of an incident beam of small horizontal divergence.
3. Absorption in the specimen. Specimens of low absorption should be made as thin as possible.
4. Displacement of the specimen from the diffractometer axis (Fig. 2) This is usually the largest single source of error. It causes an error in d given by

$$\frac{\Delta d}{d} = -\frac{D \cos^2\theta}{R \sin\theta}, \tag{4}$$

where D is the specimen displacement parallel to the diffraction-plane normal (positive when the displacement is in front of the axis) and R is the diffractometer radius (Problem 6).

5. Vertical divergence of the incident beam. This error is minimized, with loss of intensity, by decreasing the vertical opening of the detector slit.

The functional forms of the various systematic errors in peak position are summarized elsewhere [G.26], but no single extrapolation function can be completely satisfactory, because $\Delta d/d$ varies as $\cos^2\theta$ for errors (2) and (3) but as $\cos^2\theta/\sin\theta$ for error (4). Often the effect of (5) is included in the extrapolation function so that $\Delta d/d$ varies as $[\cos^2\theta/\sin\theta + \cos^2\theta/\theta]$. The sum in the brackets is termed the Nelson-Riley function and is used primarily for data collected with Hull/Debye–Scherrer camera (Sec. 3). Extrapolation against $\cos^2\theta$ is often termed

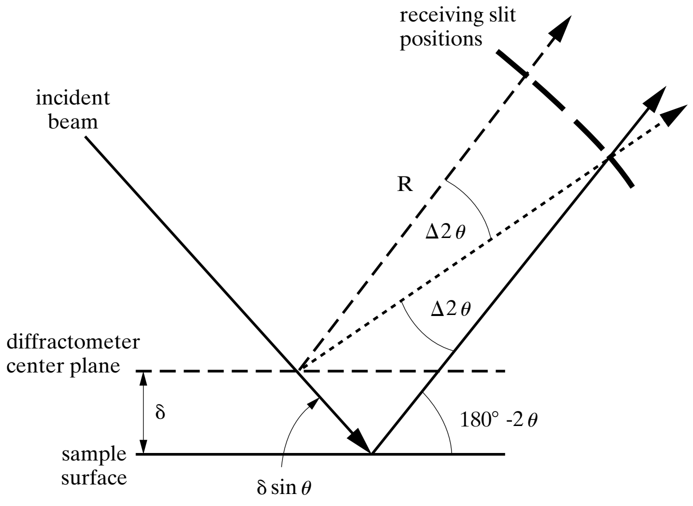

Figure 2. Illustration of shift of peak position Δ2θ as a function of sample displacement.

the Bradley-Jay method and is valid only for diffraction peaks with $\theta > 60^o$. Presumably the function that gives the better straight line will disclose what error is predominant.

The suggested procedure is therefore:

a) Carefully align the component parts of the instrument in accordance with the manufacturer's instructions.
b) Adjust the specimen surface to coincide as closely as possible with the diffractometer axis.
c) Extrapolate the calculated parameters against $\cos^2\theta/\sin\theta$ or $\cos^2\theta$ to a value of $\theta = 90^o$.

For a cubic crystal with a lattice parameter a_0 and an extrapolation based on displacement error,

$$\frac{\Delta d}{d} = \frac{\Delta a}{a_0} = \frac{a - a_0}{a_0} = k_1\frac{\cos^2\theta}{\sin\,\theta}, \tag{5}$$

and, after rearranging terms, the apparent lattice parameter a is

$$a = a_0 + a_0k_1\frac{\cos^2\theta}{\sin\,\theta}. \tag{6}$$

If a Nelson-Riley extrapolation function is appropriate,

$$\frac{a - a_0}{a} = k_2\left[\frac{\cos^2\theta}{\sin\,\theta} + \frac{cos^2\theta}{\theta}\right] \tag{7}$$

which converts to

$$a = a_0 - a_0k_2\left[\frac{\cos^2\theta}{\sin\,\theta} + \frac{cos^2\theta}{\theta}\right]. \tag{8}$$

A similar equation applies for the Bradley-Jay function. Note that all of these extrapolation functions yield $a = a_0$ at $\theta = 90^o$.

Every effort should, of course, be made to measure line positions precisely. To achieve a precision of 3 parts in 100,000, equivalent to ±0.0001 Å in the lattice parameter, Eq. (2) shows that the 2θ position of a line at $2\theta = 160^o$ must be measured to within 0.02° and lower angle lines even more closely. Recording peaks with ratemeter output and continuous scanning can be problematic, and step scanning should be used. Before computerized diffractometers were available it was customary to take the 2θ value of the peak's maximum intensity as the line position; now peak centroids or more sophisticated methods for establishing peak position (which are standard in the field of stress measurement are recommended.)

Noncubic crystals present additional difficulties, regardless of the particular extrapolation function chosen. Consider, for example, hexagonal and tetragonal crystals. The difficulty is simply this: the position of a line which has indices *hkl* is determined by two parameters, a and c, and it is impossible to calculate both of them from the observed $\sin^2\theta$ value of that line alone. One way of avoiding this difficulty is to ignore the *hkl* lines and divide the remainder into two groups, those with indices $hk0$ and those with indices $00l$. A value of a is calculated for each $hk0$ line and a value of c from each $00l$ line; two separate extrapolations are then made to find a_0 and c_0. Since there are usually very few $hk0$ and $00l$ lines in the back-reflection region, the extrapolations necessarily will be less accurate. Instead, it is better to use Cohen's analytical method (Sec. 7) for noncubic substances.

Extrapolation should be done with least squares fitting of the data and the extrapolation function chosen to represent the systematic errors. Use of least squares eliminates the variability in how different individuals assign a straight line through the same set of points, and most pocket calculators and computer spreadsheet programs have built-in routines for least squares fitting of data.

It should be noted that the least-squares fitting is not a way of finding the best curve to fit a given set of observations. The investigator must know at the outset, from an understanding of the phenomenon involved, the kind of relation (linear, parabolic, exponential, etc.) the two quantities x and y are supposed to obey. All the least-squares method can do is to give the best values of the constants in the equation selected, but it does this in a quite objective and unbiased manner.

To conclude this section, a few general remarks on the nature of errors may not be amiss. In the measurement of a lattice parameter, as in many other physical observations, two kinds of error are involved, *systematic* and *random*. A systematic error is one which varies in a regular manner with some particular parameter. Further, a systematic error is always of the same sign. Random errors, on the other hand, are the ordinary chance errors involved in any direct observation; they may be positive or negative and do not vary in any regular manner with the 2θ position of the diffraction line.

Systematic errors in a approach zero as θ approaches 90° and may be eliminated by use of the proper extrapolation function. The magnitude of these errors is proportional to the slope of the extrapolation line and, if these errors are small, the line will be quite flat. If the systematic errors were increased on purpose, say, by displacing the sample from the diffractometer axis, the slope of the line will increase but the extrapolated value of a_0 will remain the same. The random errors involved in measuring line positions show up as random errors in a, and are responsible for the deviation of the various points from the extrapolation line. The random errors in a also decrease in magnitude as θ increases, due essentially to the slow variation of $\sin\theta$ with θ at large angles.

These various effects are summarized graphically in Fig. 3. In (a) the calculated points conform quite closely to the line, indicating small random errors, but the line itself is quite steep because of large systematic errors. The opposite situation is shown in (b): here the systematic error is small, but the wide scatter of the points

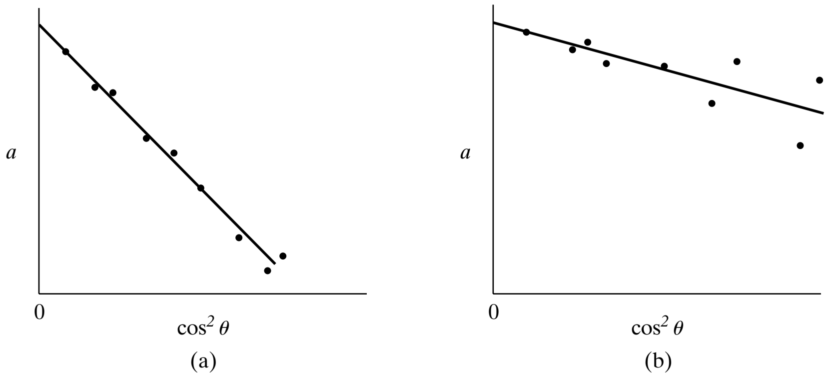

Figure 3 Extreme forms of extrapolation curves (schematic): (a) large systematic errors, small random errors; (b) small systematic errors, large random errors.

shows that large random errors have been made. Inasmuch as the uncertainty in a regression line increases with the degree of scatter, it is obvious that every possible effort should be made to minimize random errors at the start.

3 HULL/DEBYE–SCHERRER CAMERAS

Historically, extrapolation methods were developed for the Hull/Debye–Scherrer camera, and, even though this method normally would not be chosen today for lattice parameter measurements, it is instructive to go through some of the geometry leading to the extrapolation functions.

For a Hull/Debye–Scherrer camera, the chief sources of error in θ are the following:

1. Film shrinkage.
2. Incorrect camera radius.
3. Off-centering of specimen.
4. Absorption in specimen.

Since only the back-reflection region is suitable for precise measurements, consider these various errors in terms of the quantities S' and ϕ, defined in Fig. 4. S' is the distance on the film between two corresponding back-reflection lines; 2ϕ is the supplement of 2θ, i.e., $\phi = 90^o - \theta$. These quantities are related to the camera radius R by the equation

$$\phi = \frac{S'}{4R}. \tag{9}$$

Shrinkage of the film, caused by processing and drying, causes an error $\Delta S'$ in the quantity S'. The camera *radius* may also be in error by an amount ΔR. The effects

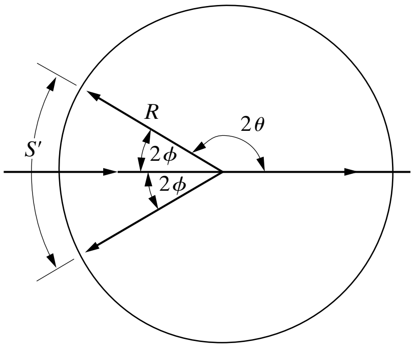

Figure 4

of these two errors on the value of ϕ may be found by writing Eq. (9) in logarithmic form:

$$\ln \phi = \ln S' - \ln 4 - \ln R. \tag{10}$$

Differentiation then gives

$$\frac{\Delta\phi}{\phi} = \frac{\Delta S'}{S'} - \frac{\Delta R}{R}. \tag{11}$$

The error in ϕ due to shrinkage and the radius error is therefore given by

$$\Delta\phi_{S',R} = \left(\frac{\Delta S'}{S'} - \frac{\Delta R}{R}\right)\phi. \tag{12}$$

The shrinkage error can be minimized by loading the film so that the incident beam enters through a hole in the film, since corresponding back-reflection lines are then only a short distance apart on the film, and their separation S' is little affected by film shrinkage. The method of film loading is not at all suitable for precise measurements. Instead, methods (b) or (c) should be used. Method (c), the unsymmetrical or Staumanis method of film loading, is particularly recommended since no knowledge of the camera radius is required.

An *off-center specimen* also leads to an error in ϕ. Whatever the displacement of the specimen from the camera center, this displacement can always be broken up into two components, one (Δx) parallel to the incident beam and the other (Δy) at right angles to the incident beam. The effect of the parallel displacement is illustrated in Fig. 5(a). Instead of being at the camera center C', the specimen is displaced a distance Δx to the point O. The diffraction lines are registered at D and C instead of at A and B, the line positions for a properly centered specimen. The error in S' is then $(AC + DB) = 2DB$, which is approximately equal to $2ON$, or

$$\Delta S' - 2ON = 2\Delta x \sin 2\phi. \tag{13}$$

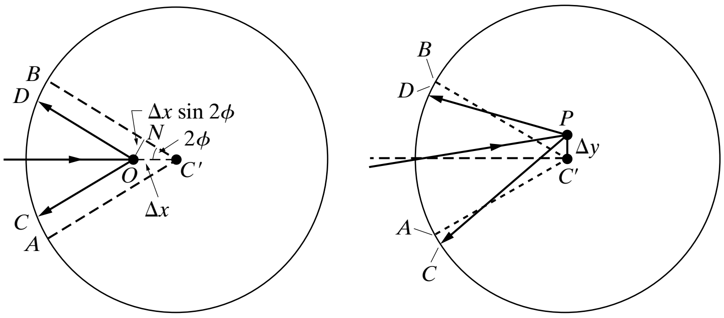

(a) (b)

Figure 5 Effect of specimen displacement on line positions.

The effect of a specimen displacement at right angles to the incident beam [Fig. 5(b)] is to shift the lines from A to C and from B to D. When Δy is small, AC is very nearly equal to BD and so, to a good approximation, no error in S' is introduced by a right-angle displacement.

The total error in S' due to specimen displacement in some direction inclined to the incident beam is therefore given by Eq. (13). This error in S' causes an error in the computed value of ϕ. Inasmuch as the various errors one at a time, are being considered the radius error ΔR can be set equal to zero, so that Eq. (11) becomes

$$\frac{\Delta\phi}{\phi} = \frac{\Delta S'}{S'}, \tag{14}$$

which shows how an error in S' alone affects the value of ϕ. By combining Eqs. (9), (13) and (14); the error in ϕ due to the fact that the specimen is off center is given by

$$\Delta\phi_C = \frac{\phi \Delta S'}{S'} = \frac{\phi(2\Delta x \sin 2\phi)}{4R\phi} = \frac{\Delta x}{R} \sin\phi \cos\phi. \tag{15}$$

It should not be assumed that the centering error is removed when the specimen is so adjusted, relative to the rotating shaft of the camera, that no perceptible wobble can be detected when the shaft is rotated. This sort of adjustment is taken for granted in this discussion. The off-center error refers to the possibility that the axis of rotation of the *shaft* is not located at the center of the camera, due to improper construction of the camera.

Absorption in the specimen also causes an error in ϕ. This effect, often the largest single cause of error in parameter measurements, is unfortunately very difficult to calculate with any accuracy. But back-reflected rays come almost entirely from that side of the specimen which faces the collimator. Therefore, to a rough approximation, the effect of a centered, highly absorbing specimen is the same as that of a non-absorbing specimen displaced from the camera center in the manner shown in Fig. 9(a). Consequently if is reasonable to assume that the error in ϕ due to absorption, $\Delta\phi_A$, is included in the centering error given by Eq. (13).

Thus, the overall error in ϕ due to film shrinkage, radius error, centering error, and absorption, is given by the sum of Eqs. (12) and (15):

$$\Delta\phi_{S',R,C,A} = \left(\frac{\Delta S'}{S'} - \frac{\Delta R}{R}\right)\phi + \frac{\Delta x}{R}\sin\phi\cos\phi. \tag{16}$$

But

$$\phi = 90^o - \theta,\ \Delta\phi = -\Delta\theta,\ \sin\phi = \cos\theta, \text{ and } \cos\phi = \sin\theta.$$

Therefore Eq. (3) becomes

$$\frac{\Delta d}{d} = -\frac{\cos\theta}{\sin\theta}\Delta\theta = \frac{\sin\phi}{\cos\phi}\Delta\phi \tag{17}$$

and

$$\frac{\Delta d}{d} = \frac{\sin\phi}{\cos\phi}\left[\left(\frac{\Delta S'}{S'} - \frac{\Delta R}{R}\right)\phi + \frac{\Delta x}{R}\sin\phi\cos\phi\right]. \tag{18}$$

In the back-reflection region, ϕ is small and may be replaced, in the first term of Eq. (18), by $\sin\phi\cos\phi$, since $\sin\phi \approx \phi$ and $\cos\phi \approx 1$, for small values of ϕ. Then,

$$\frac{\Delta d}{d} = \left(\frac{\Delta S'}{S'} - \frac{\Delta' R}{R} + \frac{\Delta x}{R}\right)\sin^2\phi. \tag{19}$$

The bracketed terms are constant for any one film, so that

$$\frac{\Delta d}{d} = K\sin^2\phi = K\cos^2\theta, \tag{20}$$

where K is a constant. Accordingly, the important result is that the fractional errors in d are directly proportional to $\cos^2\theta$, and therefore approach zero as $\cos^2\theta$ approaches zero or as θ approaches 90°. In the cubic system,

$$\frac{\Delta d}{d} = \frac{\Delta a}{a} = \frac{a - a_0}{a_0} = K\cos^2\theta, \tag{21}$$

and

$$a = a_0 + a_0 K\cos^2\theta. \tag{22}$$

Hence, for cubic substances, if the value of a computed for each line on the pattern is plotted against $\cos^2\theta$, a straight line should result, and a_0, the true value of a, can be found by extrapolating this line to $\cos^2\theta = 0$. (Or, since $\sin^2\theta = 1 - \cos^2\theta$, the various values of a may be plotted against $\sin^2\theta$, and the line extrapolated to $\sin^2\theta = 1$. As noted in the previous section, this extrapolation function is sometimes called the Bradley-Jay function.

From the various approximations involved in the derivation of Eq. (22), it is clear that this equation is true only for large values of θ (small values of ϕ). Therefore, only lines having θ values greater than about 60° should be used in the extrapolation, and the more lines there are with θ greater than 80°, the more precise is the value of a_0 obtained. To increase the number of lines in the back-reflection region, it is common practice to employ unfiltered radiation so that $K\beta$ as well as $K\alpha$ can be diffracted. If the x-ray tube is demountable, special alloy targets can also be used to increase the number of lines; or two exposures can be made on the same film with different characteristic radiations. In any case, it must never be assumed that the process of extrapolation can automatically produce a precise value of a_0 from careless measurements made on a film of poor quality. For high precision, the lines must be sharp and the $K\alpha$ doublets well resolved at high angles, which means in turn that the individual particles of the specimen must be strain-free and not too fine. The line positions must be determined carefully, and it is best to measure each one two or three times and average the results. In computing a for each line, the proper wavelength must be assigned to each component of the $K\alpha$ doublet when that line is resolved, and when it is not resolved, the weighted mean wavelength should be used.

Other functions of, besides $\sin^2\theta$ or $\cos^2\theta$, may be used as a basis for extrapolation. For example, replacing $\sin\phi\ \cos\phi$ in Eq. (18) by ϕ, instead of replacing ϕ by $\sin\phi\cos\phi$, yields

$$\frac{\Delta d}{d} = K\phi \tan \phi. \tag{23}$$

Therefore, a plot of a against $\phi\tan\phi$ will also be linear and will extrapolate to a_0 at $\phi\tan\phi = 0$. In practice, there is not much difference between an extrapolation against $\phi\tan\phi$ and one against $\cos^2\theta$ (or $\sin^2\theta$), and either will give satisfactory results. Nelson and Riley [2] and Taylor and Sinclair [3] analyzed the various sources of error, particularly absorption, more rigorously than is done above and showed that Eq. 7 and 8, the Nelson–Riley function, holds quite accurately down to very low values of θ and not just at high angles. The values of a_0 can be found by plotting a against the Nelson–Riley function, which approaches zero as θ approaches 90°. Although it is doubtful whether any advantage results from using the Nelson-Riley function instead of $\cos^2\theta$ in the back-reflection region, the greater range of linearity of the Nelson–Riley function is an advantage when there are only a few lines in the high-angle region.

4 BACK–REFLECTION FOCUSING CAMERAS

A camera of this kind is preferred over Hull/Debye–Scherrer cameras for work of the highest precision, since the position of a diffraction line on the film is twice as sensitive to small changes in plane spacing with this camera as it is with a Hull/Debye–Scherrer camera of the same diameter. It is, of course, not free from sources of systematic error. The most important of these are the following:

1. Film shrinkage.
2. Incorrect camera radius.
3. Displacement of specimen from camera circumference.
4. Absorption in specimen. (If the specimen has very low absorption, many of the diffracted rays will originate at points outside the camera circumference even though the specimen surface coincides with the circumference).

A detailed analysis of these various sources of error shows that they produce fractional errors in d which are very closely proportional to $\phi \tan \phi$, where ϕ is again equal to $(90^o - \theta)$. This function is therefore the one to use in extrapolating lattice parameters measured with this camera.

5 PINHOLE CAMERAS

The pinhole camera, used in back reflection, is not really an instrument of high precision in the measurement of lattice parameters, but it is mentioned here because of its very great utility in work on highly-textued on samples which cannot, for whatever reason, be reduced to powder. This method has became interestingly attractive as two-dimensional detectors have found increasing application. Since both the film and the specimen surface are flat, no focusing of the diffracted rays occurs, and the result is that the diffraction lines are much broader than is normally desirable for precise measurement of their positions. The chief sources of systematic error are the following:

1. Film shrinkage (when photographic emulsions are used)
2. Incorrect specimen-to-film distance.
3. Absorption in the specimen.

In this case it may be shown that the fractional error in d is proportional to $\sin 4\phi \tan \phi$, or to the equivalent expression $\cos^2\theta\,(2\cos^2\theta - 1)$, where $\phi = (90^o - \theta)$. With either of these extrapolation functions a fairly precise value of the lattice parameter can be obtained; in addition, the back-reflection pinhole camera has the particular advantage that mounted metallographic specimens may be examined directly. This means that a parameter determination can be made on the same part of a specimen as that examined under the microscope. A dual examination of this kind is quite valuable in many problems, especially in the determination of phase diagrams.

6 EXAMPLE

The example in this section illustrates how well extrapolation methods can compensate for systematic errors, even if they are substantial. This example provides a series of controlled (and known) errors and illustrates extrapolation procedures used with diffractometry. The reader should not regard extrapolation procedures as a quick fix for poor sample preparation, data collection or data analysis technique. Quality, precise measurement of lattice parameters follows the ancient adage: "Garbage in, garbage out."

Several diffraction patterns of a solid copper sample displaced from the correct position in a θ-2θ diffractometer serve to illustrate how well extrapolation methods can correct systematic errors. The sample used in this illustration was a copper disk formed by packing copper particles into a cylindrical mold, infiltrating with epoxy and metallographically polishing the end of the cylinder. Four diffraction patterns were recorded with the top of the sample displaced 0, 4, 8 or 16 thicknesses of household aluminum foil (nominally 25 μm thick) from the reference surface. Note that the reference surface presumably coincided with the exact center of the sample rotation axis and the center of the detector rotation axis, i.e., tangent to the focussing circle. Data for each of the four scans were recorded on a diffractometer equipped with a copper x-ray tube, a post-sample monochromator and a variable width divergence slit set to irradiate a constant 10 mm length of the sample surface. The diffraction patterns were recorded using a step size of 0.05^o 2θ, rather too coarse for this type of work, and a constant counting time of 1 sec per step. Software provided by the diffractometer's manufacturer determined peak positions using the centroid for intensities having a second derivative with respect to angle which were less than zero. For the peaks with an unresolved $K_{\alpha1}$ and $K_{\alpha2}$ doublet, the weighted average of the $K_{\alpha1}$ and $K_{\alpha2}$ wavelengths was used to calculate the d-spacing; when the doublet could be resolved the $K_{\alpha1}$ peak and its wavelength were used.

The columns of Table 1 show the 2θ and corresponding lattice parameters for all reflections measured from the diffraction patterns of the 0, 100, 200, and 400 μm displacements of the sample. The last column gives the value of the extrapolation function for the eight diffraction peaks of the undisplaced sample. The last two rows give the arithmetic mean of the measurements and the extrapolated value of the lattice parameter a_0, respectively. Clearly, simple averaging is inappropriate, and use of the value of the lattice parameter for the highest 2θ line is inadvisable. Extrapolation to $\theta = 90^o$ gives lattice parameters for the four scans which differ only in the fourth decimal place (Fig. 6). Before quoting four decimal places for a lattice parameter, it is important to realize the effect of uncontrolled temperature variation: thermal expansion will change the lattice parameter. For pure copper at 25°C, the linear thermal expansion coefficient is about $16.6 \times 10^{-6}{}^\circ C^{-1}$ [4], and this is large enough to cause a change in the fourth decimal place for temperature changes as small as 1°C. The diffractometer used for these measurements is in a small radiation shielding box which also surrounds the x-ray tube (which becomes warm to the touch during operation); the entire instrument, including electronics, is

TABLE 1

		$2\theta°$ a (Å)	displacements (μm)				$(\cos^2\theta)/(\sin\theta)$
Line	hkl		0	100	200	400	
1	111	2θ	43.39	43.28	43.24	43.08	2.335
		a	3.610	3.618	3.622	3.634	
2	200	2θ	50.50	50.41	50.37	50.21	1.918
		a	3.612	3.618	3.620	3.632	
3	220	2θ	74.14	74.06	74.02	73.87	1.056
		a	3.615	3.618	3.620	3.626	
4*	311	2θ	89.94	89.87	89.83	89.72	0.708
		a	3.615	3.618	3.618	3.622	
5*	222	2θ	95.16	95.08	95.05	94.93	0.616
		a	3.617	3.617	3.618	3.620	
6*	400	2θ	116.86	116.86	116.84	116.73	0.322
		a	3.616	3.616	3.617	3.619	
7*	331	2θ	136.49	136.44	136.44	136.38	0.148
		a	3.615	3.616	3.616	3.617	
8*	420	2θ	144.70	144.62	144.60	144.63	0.096
		a	3.615	3.616	3.616	3.616	
		$\bar{a}$	3.614	3.617	3.618	3.623	
		a_0	3.6150	3.6148	3.6148	3.6145	

* Measurements made for resolved $K_{\alpha 1}$ peaks.

in a cabinet surrounding the radiation shielding box. Gradual warming of several °C could be anticipated for these closely confined instruments; similar thermal drift in more open instruments, even in air conditioned rooms, should also be expected.

7 COHEN'S METHOD

In preceding sections the most accurate value of the lattice parameter of a cubic substance was found by plotting the value of a calculated for each reflection against a particular function, which depends on the apparatus used, and extrapolating to a value a_0 at $\theta = 90°$. Two different things are accomplished by this procedure: (a) systematic errors are eliminated by selection of the proper extrapolation function, and

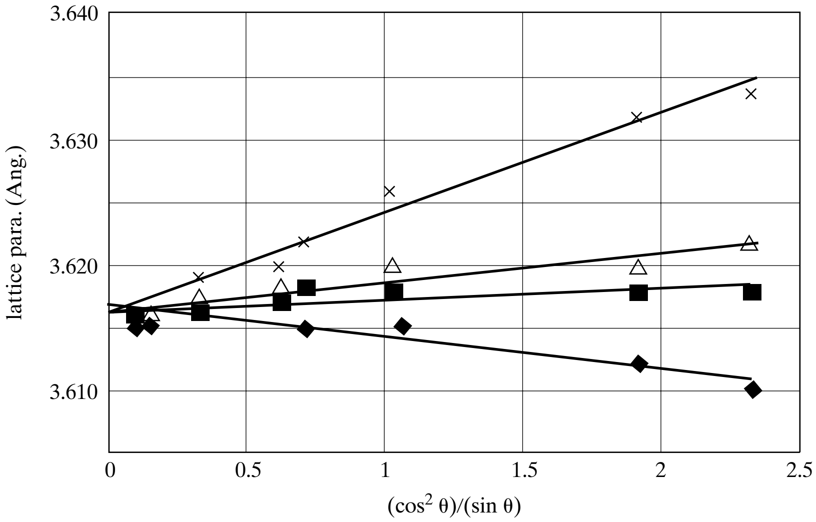

Figure 6 Plots of the apparent lattice parameter as a functional of the displacement extrapolation factor. The data is for a polycrystalline copper sample and was recorded with Cu Kα radiation. The diamonds, squares, triangles and x's show the data for 0, 100, 200 and 400 μm sample displacements, respectively.

(b) random errors are reduced using the least-squares method devised by Cohen [5].

Cubic system

Suppose a cubic substance is being examined in a Hull/Debye–Scherrer camera. Then Eq. (21), namely,

$$\frac{\Delta d}{d} = \frac{\Delta a}{a} = K \cos^2 \theta, \tag{21}$$

defines one possible extrapolation function. Instead of using the least-squares method to find the best straight line on a plot of $\bar{a}$ against $\cos^2 \theta$, Cohen applied the method to the observed $\sin^2 \theta$ values directly. Squaring Bragg's law and taking logarithms of each side produces

$$\ln \sin^2 \theta = \ln\left(\frac{\lambda^2}{4}\right) - 2 \ln d. \tag{24}$$

Differentiation then gives

$$\frac{\Delta \sin^2 \theta}{\sin^2 \theta} = -\frac{2\Delta d}{d}. \tag{25}$$

By substituting this into Eq. (20), the error in $\sin^2 \theta$ varies with θ as:

$$\Delta \sin^2\theta = -2K\sin^2\theta\cos^2\theta = D\sin^2 2\theta, \tag{26}$$

where D is a new constant. [This equation is valid only when the $\cos^2\theta$ extrapolation function is valid. If some other extrapolation function is used, Eq. (26) must be modified accordingly.] A plot of $\Delta \sin^2\theta$ vs $\sin^2\theta$ (observed). Now the true value of $\sin^2\theta$ for any diffraction line is given by

$$\sin^2\theta\,(\text{true}) = \frac{\lambda^2}{4a_0^2}(h^2 + k^2 + l^2), \tag{27}$$

where a_0, the true value of the lattice parameter, is the quantity sought. But

$$\sin^2\theta\,(\text{observed}) - \sin^2\theta\,(\text{true}) = \Delta\sin^2\theta,$$

$$\sin^2\theta - \frac{\lambda^2}{4a_0^2}(h^2 + k^2 + l^2) = D\sin^2 2\theta,$$

$$\sin^2\theta = C\alpha + A\delta, \tag{28}$$

where

$$C = \frac{\lambda^2}{4a_0^2},\ \alpha = (h^2 + k^2 + l^2),\ A = \frac{D}{10},\ \text{and}\ \delta = 10\sin^2 2\theta.$$

(The factor 10 is introduced into the definitions of the quantities A and δ solely to make the coefficients of the various terms in the normal equations of the same order of magnitude.)

The experimental values of $\sin^2\theta$, α, and δ are now substituted into Eq. (28) for each of the n back-reflection lines used in the determination. This gives n equations in the unknown constants C and A, and these equations can be solved for the most probable values of C and A by the method of least squares.[1] Once C is found, a_0 can be calculated directly from the relation given above; the constant A is related to the amount of systematic error involved and is constant for any one film, but varies slightly from one film to another.

If lines from three different wavelengths (Cu $K\alpha_1$, Cu $K\alpha_2$, and Cu $K\beta$) are to be used in the analysis, the data must be "normalized" to any one wavelength by use

---

[1] In linear regression, the variable y_i is assumed to be related approximately linearly to the variables x_{1j}, x_{2j}, … by coefficients β_0, β_1, β_2, … via

$$y_j = \beta_0 + \beta_j x_{1j} + \beta_2 x_{2j} + \ \ldots\ - \beta_h x_{hj} + \varepsilon_j,\ j = 1, 2, \ldots, n\ n \geq h + 1$$

where $\boldsymbol{\varepsilon}_j$ is the error in each measurement [6]. The general linear model is treated most conveniently using matrices $\underline{\mathbf{Y}} = \underline{\underline{\mathbf{X}}}\underline{\boldsymbol{\beta}} + \underline{\boldsymbol{\varepsilon}}$ where

$$\mathbf{y} = \begin{bmatrix} y_1 \\ y_2 \\ \vdots \\ y_n \end{bmatrix},\ \underline{\underline{\mathbf{X}}} = \begin{bmatrix} 1 & x_{11} & x_{21} & \cdots & x_{n1} \\ 1 & x_{12} & x_{22} & \cdots & x_{n2} \\ \vdots & & & & \\ 1 & x_{1n} & x_{2n} & \cdots & x_{nn} \end{bmatrix},\ \boldsymbol{\beta} = \begin{array}{c} \beta_0 \\ \beta_1 \\ \mathbf{E}\beta_2\mathbf{U} \\ \vdots \\ \beta_n\ . \end{array}$$

of the proper multiplying factor. For example suppose all lines were to be normalized to the $K\beta$ wavelength. Then for a particular, line formed by $K\alpha_1$ radiation, for instance,

$$\cos^2\phi_{K\alpha_1} = \frac{\lambda^2_{K\alpha_1}}{4a_0^2}\alpha + A\delta_{K\alpha_1}, \tag{29}$$

$$\left(\frac{\lambda^2_{K\beta}}{\lambda^2_{K\alpha_1}}\right)\cos^2\phi_{K\alpha_1} = \left(\frac{\lambda^2_{K\beta}}{\lambda^2_{K\alpha_1}}\right)\left(\frac{\lambda^2_{K\alpha_1}}{4a_0^2}\right)\alpha + \left(\frac{\lambda^2_{K\beta}}{\lambda^2_{K\alpha_1}}\right)A\delta_{K\alpha_1} \tag{30}$$

From Bragg's law,

$$\left(\frac{\lambda^2_{K\beta}}{\lambda^2_{K\alpha_1}}\right)\cos^2\phi_{K\alpha_1} = \cos^2\phi_{K\beta} \tag{31}$$

Therefore,

$$\cos^2\phi_{K\beta} = \left(\frac{\lambda^2_{K\beta}}{4a_0^2}\right)\alpha + A\left(\frac{\lambda^2_{K\beta}}{\lambda^2_{K\alpha_1}}\right)\delta_{K\alpha_1}, \tag{32}$$

where $(\lambda^2_{K\beta}/\lambda^2_{K\alpha_1})\delta_{K\alpha 1}$ is a normalized δ. Equation (32) now refers only to the $K\beta$ wavelength, i.e., it gives the position, in terms of $\cos^2\phi$, that a $K\alpha_1$ line would have if it were formed by $K\beta$ radiation. Lines due to $K\alpha_2$ radiation can be normalized in a similar manner. The values of the two normalizing factors, for copper radiation, are

$$\frac{\lambda^2_{K\beta}}{\lambda^2_{K\alpha_1}} = 0.816688 \quad \text{and} \quad \frac{\lambda^2_{K\beta}}{\lambda^2_{K\alpha_2}} = 0.812644. \tag{33}$$

Cohen's method of determining lattice parameters is even more valuable when applied to noncubic substances, since, there is more than one lattice parameter

---

and the errors are

$$\underline{\boldsymbol{\varepsilon}} = \begin{bmatrix} \boldsymbol{\varepsilon}_1 \\ \boldsymbol{\varepsilon}_2 \\ \vdots \\ \boldsymbol{\varepsilon}_n \end{bmatrix}.$$

The least squares estimator **b** for the regression coefficients β is that which satisfies and $\frac{\partial}{\partial \underline{\mathbf{b}}}[(\underline{\mathbf{y}} - \underline{\underline{X}}\,\underline{\mathbf{b}})^T(\underline{\mathbf{y}} - \underline{\underline{X}}\,\underline{\mathbf{b}})] = 0$ and $(\underline{\underline{\mathrm{x}}}^{\mathrm{T}}\underline{\underline{\mathrm{X}}})\underline{\mathbf{b}} = \underline{\underline{x}}^{\mathrm{T}}\underline{\mathrm{y}}$ $\quad \mathbf{b} = (\underline{\underline{\mathrm{x}}}^{\mathrm{T}}\underline{\underline{\mathrm{x}}})^{-1}\underline{\underline{\mathrm{x}}}^{\mathrm{T}}\underline{\mathrm{y}}$. Here the superscript "T" denotes the transpose of the matrix in question, a single underline a vector, a double underline a matrix and the superscript "-1" denotes the inverse matrix.

involved. Cohen's method, provides a direct means of determining these parameters, although the equations are naturally more complex than those needed for cubic substances. For example, suppose that the substance involved is hexagonal. Then

$$\sin^2\theta(\text{true}) = \frac{\lambda^2}{4}\cdot\frac{4}{3}\cdot\frac{h^2+hk+k^2}{a_0^2} + \frac{\lambda^2}{4}\cdot\frac{l^2}{c_0^2} \tag{34}$$

and

$$\sin^2\theta - \frac{\lambda^2}{3a_0^2}(h^2+hk+k^2) - \frac{\lambda^2}{4c_0^2}(l^2) = D\sin^2 2\theta, \tag{35}$$

if the pattern is made in a Hull/Debye–Scherrer camera. Rearranging this equation and introducing new symbols yields.

$$\sin^2\theta = C\alpha + B\gamma + A\delta, \tag{36}$$

where

$$C = \frac{\lambda^2}{3a_0^2},\quad \alpha = (h^2+hk+k^2),\quad B = \frac{\lambda^2}{4c_0^2},\quad \gamma = l^2,$$

$$A = \frac{D}{10},\quad \text{and } \delta = 10\sin^2 2\theta.$$

The values of C, B, and A, of which only the first two are really needed, are found from the three normal equations:

$$\Sigma\alpha\sin^2\theta = C\,\Sigma\alpha^2 + B\,\Sigma\alpha\gamma + A\,\Sigma\alpha\delta,$$

$$\Sigma\gamma\sin^2\theta = C\,\Sigma\alpha\gamma + B\,\Sigma\gamma^2 + A\,\Sigma\gamma\delta,$$

$$\Sigma\delta\sin^2\theta = C\,\Sigma\alpha\delta + B\,\Sigma\delta\gamma + A\,\Sigma\delta^2,$$

The solution for these equations comes from the matrix equation

$$\begin{bmatrix} \Sigma\alpha^2 & \Sigma\alpha\gamma & \Sigma\alpha\delta \\ \Sigma\alpha\gamma & \Sigma\gamma^2 & \Sigma\gamma\delta \\ \Sigma\alpha\delta & \Sigma\delta\gamma & \Sigma\delta^2 \end{bmatrix}^{-1} \begin{bmatrix} \Sigma\alpha\sin^2\theta \\ \Sigma\gamma\sin^2\theta \\ \Sigma\delta\sin^2\theta \end{bmatrix} = \begin{bmatrix} A \\ B \\ C \end{bmatrix}. \tag{37}$$

For diffractometer data, the equations need to be modified for the different extrapolation factor. Instead of Eq. (35), one has

$$\sin^2\theta - \frac{\lambda^2}{3a_0^2}(h^2+hk+k^2) - \frac{\lambda^2}{4c_0}(l^2) = \frac{2D}{R}\cos^2\theta\sin\theta \tag{38}$$

where R is the radius of the diffractometer and D is the sample displacement; α, C, B and γ have the same values as before and

$$\mathrm{A} = 2\mathrm{D}/(10\mathrm{R}) \text{ and } \delta = 10\cos^2\theta\sin\theta.$$

The normal equations are given in Eq. (36) above.

As an example consider the data obtained for titanium (PDF card 5-682 which lists $a_0 = 2.950$ Å and $c_0 = 4.686$ Å). A total of seven diffraction peaks were recorded using Cu Kα radiation, 40 kV and 30 mA, a variable slit diffractometer equipped with a post-sample monochromator, a step size of 0.04°2θ and counting time of 1 sec per point. Note that the step size is a bit larger than ideal. Table 2 lists the data used in this example; peak positions were determined using a centroid second derivative method. The resulting matrices yield

$$\begin{bmatrix} A \\ B \\ C \end{bmatrix} = \begin{bmatrix} 38 & 30 & 51.32 \\ 30 & 131 & 82.90 \\ 51.32 & 82.90 & 96.72 \end{bmatrix}^{-1} \begin{bmatrix} 4.280 \\ 6.319 \\ 6.946 \end{bmatrix} = \begin{bmatrix} 0.09 \\ 0.027 \\ 5.07 \times 10^{-4} \end{bmatrix} \tag{39}$$

and

$$a_0 = \sqrt{\left(\frac{1.5404}{3C}\right)^2} = 2.965 \text{ and } c_0 = \sqrt{\left(\frac{1.5404}{4\mathrm{B}}\right)^2} = 4.687$$

The differences from the values on the PDF card are

$$\frac{\Delta a}{a} = 0.5\% \text{ and } \frac{\Delta c}{c} = 0.02\%.$$

TABLE 2

peak	2θ°	d(Å)	hkl	α	γ	δ
1	35.368	2.536	111	1	0	2.756
2	38.695	2.325	002	0	4	2.949
3	40.365	2.233	101	1	1	3.039
4	53.728	1.705	102	1	4	3.596
5	63.050	1.473	110	3	0	3.799
6	71.095	1.325	103	1	9	3.849
7	76.202	1.248	112	3	4	3.821

8 GENERAL

This chapter has dealt with powder methods exclusively. But there is also interest in measuring the lattice parameters of single crystals. Bond devised a method capable of very high precision, provided the crystal specimen is of sufficiently high quality [7, 8]. With this method Baker *et al.* [9] were able to measure the thermal expansion coefficient of an MgO crystal over a temperature interval of only 1.0°C, and these investigators have attained a precision of one part in ten million in parameter measurements.

Multiple beam, multiple axis diffractometry allows lattice parameter changes to be detected down to one part per billion [10]. The variation of lattice parameters in the population of Si crystals serving as references was surveyed by NIST using this type of comparator; variations of $\delta a/a$ on the order of 10^{-8} were found [11]. Triple axis diffractometry with a reference crystal of known lattice parameter mounted next to the sample is being increasingly used for lattice parameter determinations. Recently a double axis procedure, also using a reference crystal, has produced $\Delta a/a$ values better than 5×10^{-5} [12, 13].

In work of the highest precision a small correction for refraction is sometimes applied (see, for example, [1]). The index of refraction for x-rays in matter differs very slightly from unity, so that an x-ray has slightly different wavelengths in air and in a crystal. The correction to a lattice parameter is less than 0.0001 Å. Again, in work of the highest precision, it is necessary to control and report the temperature of the specimen during the parameter determination (Problem 1).

Investigators who wish to check their measurement techniques against those of a standardizing laboratory can buy a sample of silicon powder from the U.S. Bureau of Standards. These samples, known as Standard Reference Material 640, were made available in 1974 [14]. The Bureau states the weighted average of the lattice parameter of this material to be 5.43088 Å, with an estimated standard error of 3.5×10^{-5} Å.

In 1983 a new batch of Si was certified [15] (SRM 640a), and other reference materials include SRM 675 fluorophlogopite, a synthetic mica with a significant peak below $10^{\circ}2\theta$; SRM 674, a series of five crystalline phases (Al_2O_3 corundum, ZnO, TiO_2 rutile, Cr_2O_3 and CeO_2) for intensity standardization; SRM 640b of Si; LaB_6, a line profile as well as a lattice parameter standard and others [16]. Recent work may lead to silver behenate being adopted as a low angle diffraction standard [17]; its lowest angle diffraction peak is at approximately $1.5^{\circ}2\theta$ for Cu $K\alpha$ radiation.

In the measurement of any physical quantity one should always be aware of the distinction between precision and accuracy:

a) *Precision* is reproducibility.
b) *Accuracy* is the approach to the "true" value.

It is therefore quite possible to make highly precise but inaccurate measurements through the use, for example, of improperly calibrated instruments or because of inadequate correction for systematic errors. Even careful investigators usually overestimate the accuracy of their measurements, probably misled by their high precision.

For example, in the late 1950s the International Union of Crystallography distributed samples of a single lot of silicon powder to fifteen laboratories interested in precision parameter measurements [18]. The mean of the reported parameter values was 5.43054 Å at 25°C, referred to the same wavelength scale and corrected for refraction. The average precision claimed by the participating laboratories was ±0.00011 Å (2 parts per 100,000), but the spread in reported parameters (highest minus lowest) was 0.00067 Å (12 parts per 100,000). If the mean value of the parameter is taken as the true value for this lot of material, then some laboratories are about three times as inaccurate as their precision might suggest.

This result is not an isolated example. Similar interlaboratory comparisons have been made with respect to other physical measurements, sometimes on the same specimen, with similar results. We all think we are better than we are.

PROBLEMS

***1** The lattice parameter of copper is to be determined to a precision of ±0.0001 Å at 20°C. Within what limits must the temperature of the specimen be controlled if errors due to thermal expansion are to be avoided? The linear coefficient of thermal expansion of copper is 16.6×10^{-6} per °C.

2 The following data were obtained from a Hull/Debye–Scherrer pattern of a simple cubic substance, made with copper radiation. The given $\sin^2\theta$ values are for the $K\alpha_1$ lines only.

Determine the lattice parameter α_o, accurate to four significant figures, by graphical extrapolation of α against $\cos^2\theta$.

***3** From the data given in Prob. 2, determine the lattice parameter to four significant figures by Cohen's method.

4 From the data given below, determine the lattice parameter of tungsten to five significant figures by graphical extrapolation of α against $\phi \tan \phi$.

Line	hkl	λ	α	ϕ	Observed		Normalized to K_β	
					$\cos^2\phi$	δ	$\cos^2\phi$	δ
1	321	$K\alpha_1$	14	24.518*	0.82779	3.2	0.67606	2.6
2	321	$K\alpha_2$	14	24.193	0.83205	3.2	0.67616	2.6
3	411, 330	$K\beta$	18	21.167	0.85962	2.5	0.86962	2.5
4	400	$K\alpha_1$	16	13.302	0.94706	1.0	0.77345	0.8
5	400	$K\alpha_2$	16	12.667	0.95191	1.0	0.77356	0.8
6	420	$K\beta$	20	10.454	0.96708	0.7	0.96708	0.7

***5** If the fractional error in the plane spacing d is accurately proportional to the function $(\cos^2\theta/\sin\theta + \cos^2\theta/\theta)$ over the whole range of θ, show that a plot of $\Delta\sin^2\theta$ against $\sin^2\theta$ has a maximum, as illustrated for a particular case. At approximately what value of θ does the maximum occur?

6 Derive Eq. (4).

REFERENCES

The following books are listed more or less in the order they are encountered in the text

G.10 Charles S. Barrett and T. B. Massalski. *Structure of Metals*, 3rd ed. (New York: McGraw-Hill, 1966). A classic book on the crystallographic aspects of physical metallurgy. Really two books in one, the first part dealing with the theory and methods of diffraction of x-rays, electrons, and neutrons; the second part with the structure of metals in the wider sense of the word. Very lucid account of stereographic projection. Stress measurement, phase transformations, preferred orientation.

G.13 André Guinier. *X-Ray Crystallographic Technology* (London: Hilger and Watts, 1952). Excellent treatment of the theory and practice of x-ray diffraction. The title is not fair to the book, which includes a considerable body of theory and detailed experimental technique. The theory and applications of the reciprocal lattice are very well described. Includes treatments of focusing monochromators, small-angle scattering, and diffraction by amorphous substances.

G.17 Harold P. Klug and Leroy E. Alexander. *X-Ray Diffraction Procedures*, 2nd ed. (New York: Wiley, 1974). Contains a great deal of useful detail on the theory and operation of powder cameras and diffractometers. Covers the following topics in depth: chemical analysis by diffraction, parameter measurement, line-broadening analysis, texture determination, stress measurement, and studies of amorphous materials. Single-crystal methods are not included.

G.25 Ron Jenkins and Robert L. Snyder. *Introduction to X-ray Powder Diffractometry* (New York, John Wiley & Sons, Inc, 1996).

G.26 A. J. C. Wilson. *Mathematical Theory of X-ray Powder Diffractometry*, (Gordon & Breech, New York, 1963), 128 pp.

G.33 Leonid V. Azaroff and Martin J. Buerger. *The Powder Method in X-Ray Crystallography* (New York: McGraw-Hill, 1958). The making and interpretation of Hull/Debye–Scherrer photographs, including precise parameter measurements.

ANSWERS TO SELECTED PROBLEMS

1. ± 1.7°C

3. 4.997 Å

5. Near $\theta = 34°$

This page intentionally left blank

Structure of Polycrystalline Aggregates

1 INTRODUCTION

The normal way in which metals ceramics and other crystalline materials are produced and used is in the form of polycrystalline aggregates, composed of a great many individual crystals usually of microscopic size. Because the properties of such aggregates are of great technological importance, they have been intensively studied in many ways. In such studies the two most useful techniques are microscopic examination and x-ray diffraction, and the wise investigator will use them both; one complements the other, and both together can provide a great deal of information about the structure of an aggregate.

The properties (mechanical, electrical, chemical, etc.) of a single-phase aggregate are determined by two factors:

1) the properties of a single crystal of the material, and
2) the way in which the single crystals are put together to form the composite mass.

In this chapter the focus in on the second factor, namely, the *structure* of the aggregate, using this term in its broadest sense to mean the relative size, quality, and orientation of the grains making up the aggregate. Whether these grains are large or small, strained or unstrained, oriented at random or in some particular way, frequently has very important effects on the properties of the material.

If the aggregate contains more than one phase, its properties naturally depend on the properties of each phase considered separately and on the way these phases occur in the aggregate. Such a material offers wide structural possibilities since,

From Chapter 14 of *Elements of X-Ray Diffraction*, Third Edition. B.D. Cullity, S.R. Stock.

in general, the size, quality, and orientation of the grains of one phase may differ from those of the other phase or phases.

This chapter is divided into two parts. The first covers crystal size and crystal quality and the techniques for separating these contributions to line broadening. The second part deals with the orientation of the crystals within solids, i.e., with texture; techniques for texture qualification are covered.

CRYSTAL SIZE AND QUALITY

2 GRAIN SIZE

The size of the grains in a polycrystalline material has pronounced effects on many of its properties, the best known being the increase in strength and hardness of a metal or alloy which accompanies a decrease in grain size. This dependence of properties on grain size makes the measurement of grain size a matter of some importance in the control of most metal forming operations.

The grain sizes encountered in engineering materials range from about 1000 to 1 μm. These limits are, of course, arbitrary and represent rather extreme values; typical values fall into a much narrower range, namely, about 100 to 10 μm. The most accurate method of measuring grain size in this range is by microscopic examination; the usual procedure is to determine the average number of grains per unit area of the polished section and report this in terms of an "index number" established by ASTM. The equation

$$n = 2^{N-1}$$

relates n, the number of grains per square inch when viewed at a magnification of 100 ×, and N, the ASTM "index number" or "grain-size number." Grain-size numbers of 4 and 8, for example, correspond to grain diameters of 90 and 22 μm, respectively.

Although x-ray diffraction is decidedly inferior to microscopic examination in the accurate measurement of grain size, one diffraction photograph[1] can yield semiquantitative information about grain size, *together with* information about crystal quality and orientation. A transmission or back-reflection pinhole photograph made with filtered radiation is often used, but a focussing monochromator placed between the x-ray tube and the sample can also be used. If the back-reflection method is used, the surface of the specimen (which need not be polished) should be etched to remove any disturbed surface layer which might be present, because most of the diffracted radiation originates in a thin surface layer (see Secs. 4 and 5).

---

[1] In this context "photograph" can mean a two-dimensional diffraction pattern recorded on a photographic emulsion, a two-dimensional wire detector, a CCD (charge-coupled device) camera or an image plate. The advantages and disadvantages of each type of detector are summarized.

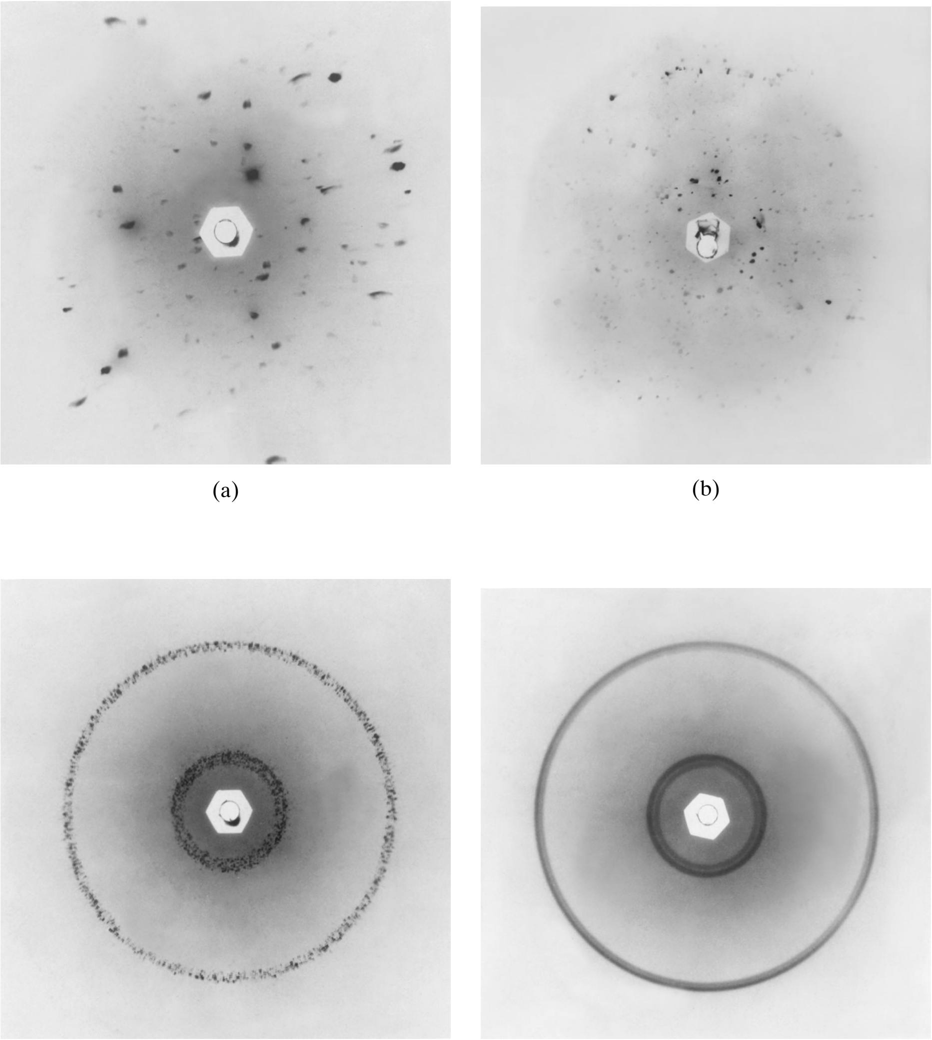

(a) (b)

(c) (d)

Figure 1 Back-reflection pinhole patterns of recrystallized aluminum specimens; grain size decreases in the order (a), (b), (c), (d). Filtered copper radiation.

The nature of the changes produced in pinhole photographs by progressive reductions in specimen grain size is illustrated in Fig. 1. The governing effect here is the number of grains which take part in diffraction. This number is in turn related to the cross-sectional area of the incident beam, and its depth of penetration (in back reflection) or the specimen thickness (in transmission). When the grain size is quite coarse, as in Fig. 1(a), only a few crystals diffract and the photograph consists of a set of superimposed Laue patterns, one from each crystal, due to the white radiation present. A somewhat finer grain size increases the number of Laue spots, and those which lie on potential Debye rings generally are more intense than the remainder, because they are formed by the strong characteristic component of the incident radiation. Thus, the suggestion of Debye rings begins to appear, as in (b). When the grain size is further reduced, the Laue spots merge into a general background and only Debye rings are visible, as in (c). These rings are spotty, however, since not enough crystals are present in the irradiated volume of the specimen to reflect to all parts of the ring. A still finer grain size produces the smooth, continuous Debye rings shown in (d).

Several methods have been proposed for the estimation of grain size purely in terms of various geometrical factors. For example, an equation may be derived which relates the observed number of spots on a Debye ring to the grain size and other such variables as incident-beam diameter, multiplicity of the reflection, and specimen-film distance. However, many approximations are involved and the resulting equation is not very accurate. The best way to estimate grain size by diffraction is to obtain a set of specimens having known ASTM grain-size numbers, and to prepare from these a standard set of photographs of the kind shown in Fig. 1. The grain-size number of an unknown specimen of the same material is then obtained simply by matching its diffraction pattern with one of the standard photographs, *provided both are made under identical conditions*.

When the grain size reaches a value somewhere in the range 10 to 1 μm, the exact value depending on experimental conditions, the Debye rings lose their spotty character and become continuous. Between this value and 0.1 μm (1000 Å), no change occurs in the diffraction pattern. At about 0.1 μm the first signs of line broadening, due to small crystal size, begin to be detectable. There is therefore a size range, from 10 (or 1) to 0.1 μm, where x-ray diffraction is quite insensitive to variations in grain size, at least for an incident beam of normal size. With microbeam techniques, x-ray lines remain spotty down to smaller grain sizes than are mentioned above, allowing spots from individual grains to be observed and counted.

3 CRYSTALLITE SIZE

When the size of the individual crystals is less than about 0.1 μm (1000 Å), the term "particle size" is usually used, but the term "crystallite size" is more precise. Crystals in this size range cause broadening of the Debye rings, the extent of the broadening being given by:

$$B = \frac{0.9\lambda}{t \cos \theta}$$

where B = FWHM (full width at half maximum) of the broadened diffraction line on the 2θ scale (radians) and t = diameter of the crystallites. All diffraction lines have a measurable breadth, even when the crystallite size exceeds 1000 Å, due to such causes as divergence of the incident beam and size of the sample (in Debye cameras) and width of the x-ray source (in diffractometers). The breadth B refers, however, to the *extra* breadth, or broadening, due to the crystallite-size effect alone. In other words, B is essentially zero when the crystallite size exceeds about 1000 Å.

Some investigators prefer to determine the *integral breadth* of a diffraction line rather than the FWHM. The integral breadth is given by the integrated intensity divided by the maximum intensity, i.e., it is the width of a rectangle having the same area and height as the observed line.

The experimental difficulties involved in measuring crystallite size from line broadening increase with the size of the crystallite measured. Roughly speaking, relatively crude measurements suffice in the range 0-500 Å, but very good experimental technique is needed in the range 500-1000 Å. With the diffractometer, the upper limit can approach 2000 Å. Very careful work is required and back-reflection lines are employed, since such lines exhibit the largest crystallite-size broadening.

Application to loose powders is straight-forward, but applying it to the broadened diffraction lines from very fine-grained metal specimens so as to determine the size of the individual grains is not very reliable. The individual grains of such a material are often nonuniformly strained, and this can also broaden the diffraction lines; an uncertainty therefore exists as to the exact cause of the observed broadening. On the other hand, the individual crystals which make up a loose powder of fine particle size can often be assumed to be strain-free, provided the material involved is a brittle (nonplastic) one and all the observed broadening can be ascribed confidently to the crystallite size effects. In such powders, the individual crystallites may be much smaller than the particle size since agglomeration of crystallites often occurs. (But note that loose, unannealed *metal* powders, produced by filing, grinding, ball milling, etc., almost always contain nonuniform strain.) Scherrer's equation has been applied to the measurement of the crystallite size of such materials as carbon blacks, catalysts, and industrial dusts.

Figure 2 shows diffractometer scans (top) of a nanocrystalline composite consisting of a very small concentration of platinum nanocrystals in a matrix of amorphous carbon [1] and (bottom) of a poly crystalline sheet of platinum. A summary of data from this scan appears in Table 1, and the consistent crystallite size determined for each peak, as will be seen in Sec. 5, indicates that crystallite size is the major contribution to broadening in this sample.

Another x-ray method of measuring the size of small particles deserves some mention, although a complete description is beyond the scope of this book. This is the method of *small-angle scattering*. It is a form of diffuse scattering very near the undeviated transmitted beam, i.e., at angles 2θ ranging from 0° up to roughly 2 or 3°. From the observed variation of the scattered intensity vs. angle 2θ, the size, and to some extent the shape, of small particles can be determined, whether they are amorphous or crystalline [G.34, G.35, 2]. Small-angle scattering has also been

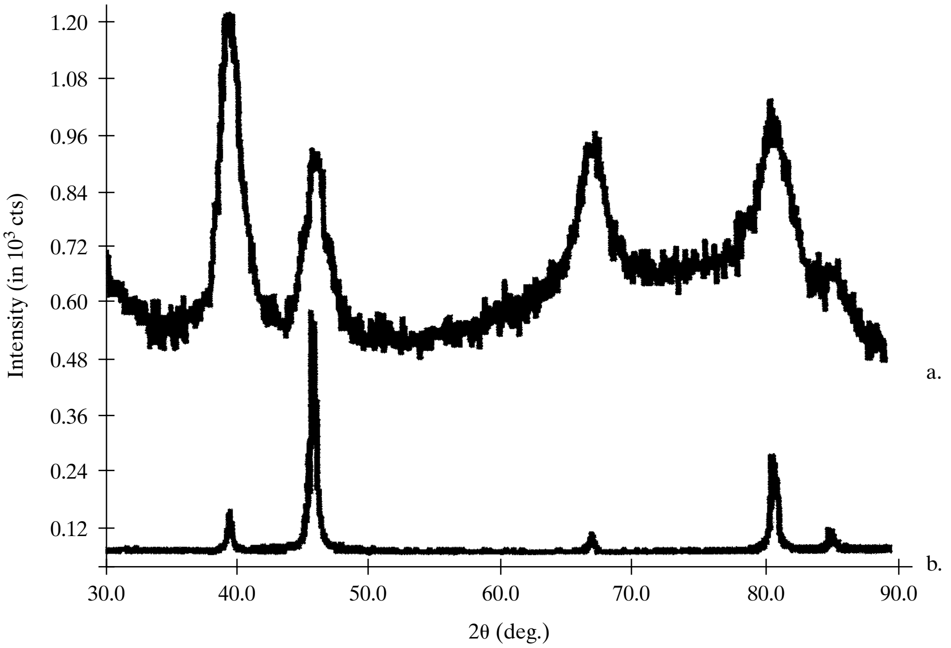

Figure 2 Comparison of θ-2θ diffraction patterns for platinum nanoparticles in a silica matrix [1] (top) and rolled platinum sheet showing strong preferred orientation (bottom).

TABLE 1

hkl	FWHM (°2θ)	t (Å)
111	1.9	50
200	1.7	55
220	2.1	50
311	2.5	45-50

used to study precipitation effects in metallic solid solutions.

4 CRYSTAL QUALITY (MICROSTRAIN)

Nonuniform strain is characteristic of the *cold-worked state* of metals and alloys and has been observed in ceramics and semiconductors. When a polycrystalline piece of metal is plastically deformed, for example by rolling, slip occurs in each grain and the grain changes its shape, becoming flattened and elongated in the direction of rolling. The change in shape of any one grain is determined not only by the forces applied to the piece as a whole, but also by the fact that each grain retains contact on its boundary surfaces with all its neighbors. Because of this interaction between grains, a single grain in a polycrystalline mass is not free to deform in the same way as an isolated crystal would, if subjected to the same deformation by rolling. As a result of this constraint by its neighbors, a plastically deformed grain in a solid aggregate usually has regions of its lattice left in an elastically bent or twisted condition or, more rarely, in a state of uniform tension or compression. The metal is then said to contain *residual stress*. (Such stress is often called “internal stress” but the term is not very informative since all stresses, residual or externally imposed, are internal. The term “residual stress” emphasizes the fact that the stress remains after all external forces are removed.)

When an annealed metal or alloy is cold worked, its diffraction lines become broader. This is a well-established, easily verified experimental fact, but its explanation was for many years a matter of controversy. Some investigators felt that the chief effect of cold work was to fragment the grains to a point where their small size alone was sufficient to account for all the observed broadening. Others concluded that the nonuniformity of strain produced by cold work was the major cause of broadening, with grain fragmentation possibly a minor contributing cause. This controversy revolved around the measurement of line widths and their interpretation in terms of either “particle-size broadening,” according to “strain broadening”.

In 1949, however, Warren pointed out that there was important information about the state of a cold-worked metal in the *shape* of its diffraction lines, and that to base conclusions only on line *width* was to use only part of the experimental evidence. If the observed line profiles, corrected for instrumental broadening, are expressed as Fourier series, then an analysis of the Fourier coefficients discloses both particle size and strain, without the necessity for any prior assumption as to the existence of either [G.17, G.20]. Warren and Averbach [4] made the first measurements of this kind, on brass filings, and many similar studies followed [5]. Somewhat later, Paterson [6] showed that the Fourier coefficients of the line profile could also disclose the presence of stacking faults caused by cold work. (In FCC metals and alloys, for example, slip on {111} planes can here and there alter the normal stacking sequence $ABCABC\ldots$ of these planes to the faulted sequence $ABCBCA\ldots$.) Thus three causes of line broadening are now recognized: small crystallite size, nonuniform strain, and stacking faults.

These studies of line shape showed that it was impossible to generalize about the causes of line broadening in cold-worked metals and alloys. In some materials all three causes contribute, in others only one.

The broadening of a diffraction line by deformation cannot always be observed by simple inspection of a photograph or a diffractometer scan unless some standard is available for comparison. However, the separation of the $K\alpha$ doublet furnishes a very good “internal standard.” In the back-reflection region, a relatively strain-free material produces a well-resolved doublet, one component due to $K\alpha_1$ radiation and the other to $K\alpha_2$. For a given set of experimental conditions, the separation of this doublet is constant and independent of the amount of microstrain. But as the amount of deformation is increased, the broadening increases, until finally the two components of the doublet overlap to such an extent that they appear as one unresolved line. An unresolved $K\alpha$ doublet can therefore be taken as evidence of cold work, if the same doublet is resolved when the material is in the annealed or strain-free condition.

With this background, consider some of the diffraction effects associated with the processes of *recovery, recrystallization*, and *grain growth*. When a cold-worked metal or alloy is annealed at a low temperature, recovery takes place; at a somewhat higher temperature, recrystallization; and at a still higher temperature, grain growth. Or at a sufficiently high constant temperature, these processes may be regarded as occurring consecutively in time. During recovery, both macro- and micro-residual stress are reduced in magnitude, but strength and hardness remain high; much of this stress relief appears to be due to polygonization, which can occur in the individual grains of an aggregate just as in a single crystal. During recrystallization, new grains form, residual stress is practically eliminated, and strength and hardness decrease rather abruptly. During grain growth some grains grow larger by swallowing neighboring grains.

Because the nonuniform strain due to residual microstress is the major cause of deformation-induced line broadening, the broad diffraction lines characteristic of cold-worked metal partially sharpen during recovery. When recrystallization occurs, the lines attain their maximum sharpness. During grain growth, the lines become increasingly spotty as the grain size increases.

The hardness curve and diffraction patterns of Fig. 3 illustrate these changes for an alpha brass, a solid solution of zinc in copper, containing 30 percent zinc by weight. The hardness remains practically constant, for an annealing period of one hour, until a temperature of 200ºC is exceeded, and then decreases rapidly with increasing temperature, as shown in (a). The diffraction pattern in (b) exhibits the broad diffuse Debye lines produced by the cold-rolled, unannealed alloy. These lines become somewhat narrower for specimens annealed at 100º and 200ºC, and the $K\alpha$ doublet becomes partially resolved at 250ºC. At 250ºC, therefore, the recovery process appears to be substantially complete in one hour and recrystallization is just beginning, as evidenced by the drop in Rockwell B hardness from 98 to 90. At 300ºC the diffraction lines are quite sharp, and the doublets are completely resolved, as shown in (c). Annealing at temperatures above 300ºC causes the lines to become increasingly spotty, indicating that the newly recrystallized grains are increasing in size. The pattern of a specimen annealed at 450ºC, when the hardness had dropped to 37 Rockwell B, appears in (d).

Diffractometer measurements made on the same specimens disclose both more, and less, information. Some automatically recorded profiles of the 331 line, the outer ring of the patterns shown in Fig. 3, are reproduced in Fig. 4. It is much easier to follow changes in line shape by means of these curves than by inspection of pinhole photographs. Thus the slight sharpening of the line at 200ºC is clearly evident in the diffractometer record, and so is the doublet resolution which occurs at 250ºC. But note that the diffractometer cannot “see” the spotty diffraction lines

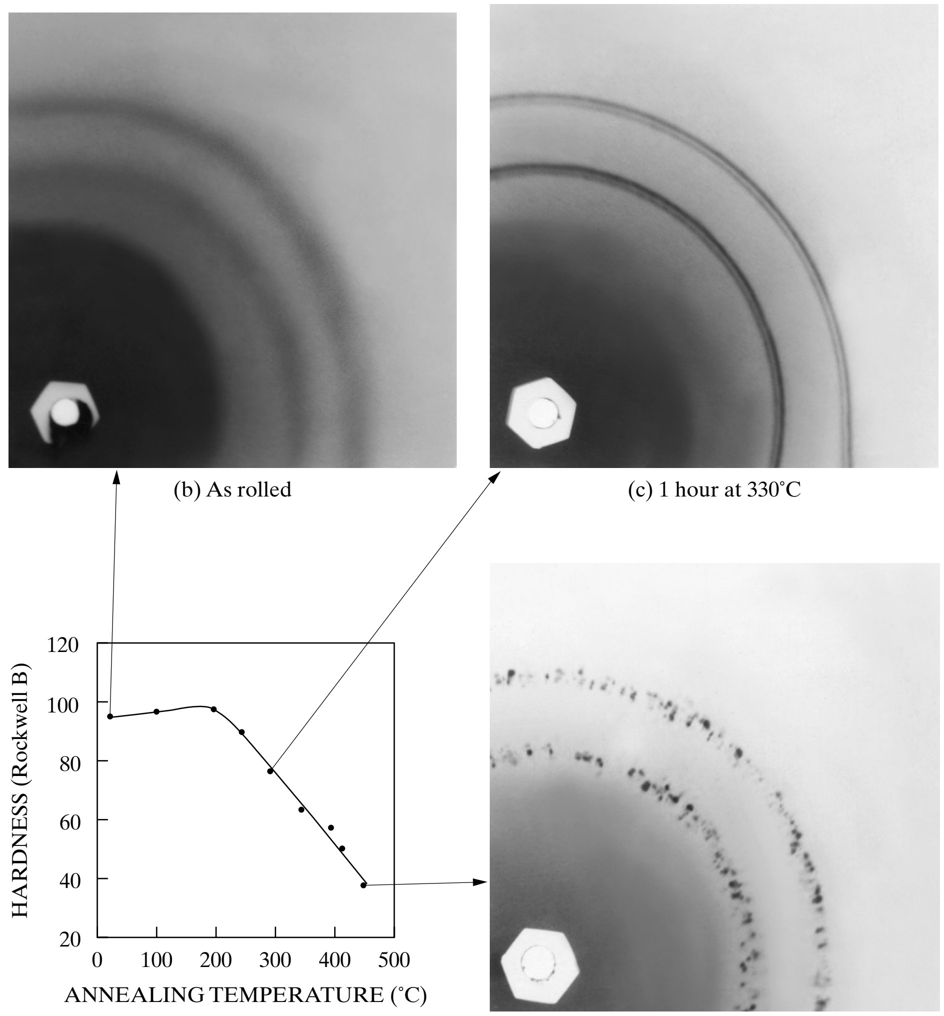

(b) As rolled

(c) 1 hour at 330°C

(a) Hardness curve

(d) 1 hour at 450°C

Figure 3 Changes in hardness and diffraction lines of 70 Cu-30 Zn specimens, reduced in thickness by 90 percent by cold rolling, and annealed for 1 hour at the temperatures indicated in (a), (b), (c), and (d) are portions of back-reflection pinhole patterns of specimens annealed at the temperatures stated (filtered copper radiation).

caused by coarse grains. There is nothing in the diffractometer records made at 300° and 450°C which would immediately suggest that the specimen annealed at 450°C had the coarser grain size, but this fact is quite evident in the pinhole patterns shown in Figs. 3(c) and (d).

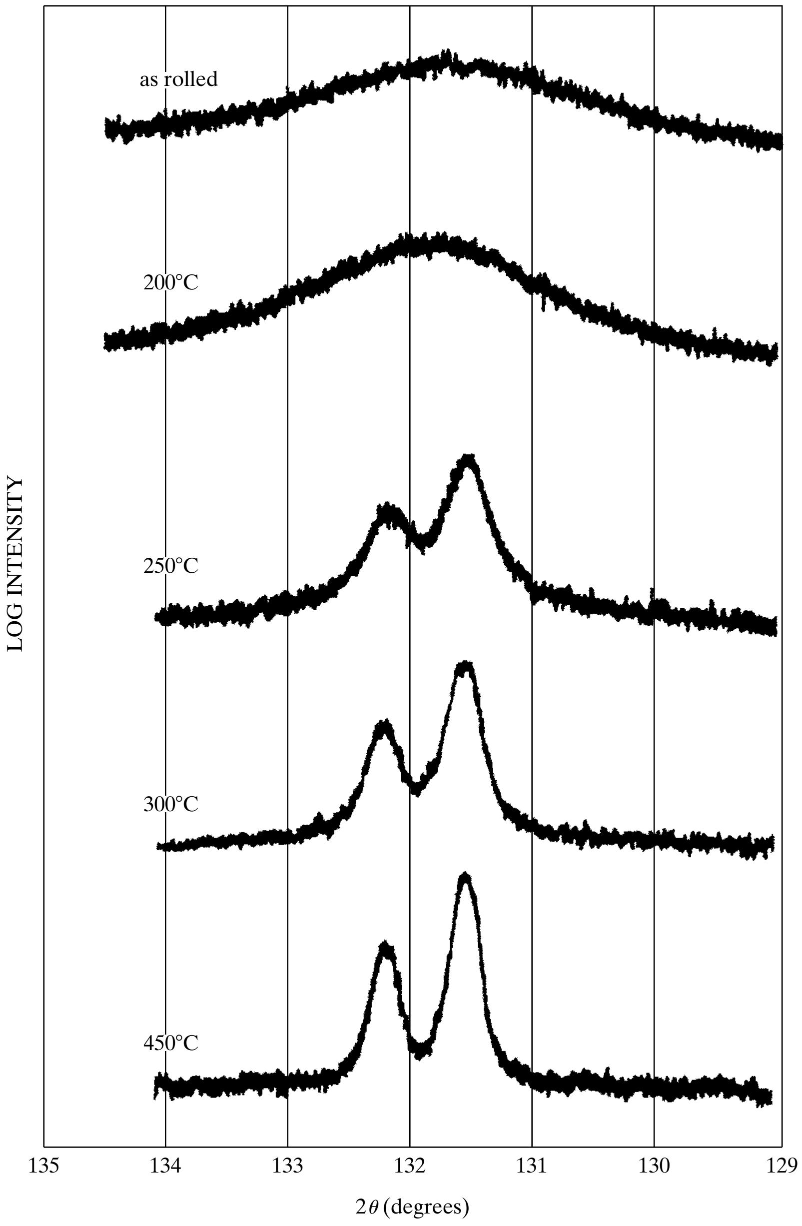

Figure 4 Diffractometer traces of the 331 line of the cold-rolled and annealed 70-30 brass specimens described in Fig.3. Filtered copper radiation. Logarithmic intensity scale. All curves displaced vertically by arbitrary amounts.

If an x-ray camera or two-dimensional detector are not available, a piece of dental film can be placed just in front of the detector slit of the diffractometer can disclose whether or not the diffraction lines are spotty. (Dental x-ray film, available from dental supply houses, comes in the form of a single piece of film, typically about 4×5 cm, enclosed in a thin envelope of light-tight plastic.[2]) If a diffraction line is spotty on a photograph, the grain size of the specimen is too large for accurate intensity measurements with the diffractometer.

Figures 3 and 4 illustrate line sharpening by annealing. Conversely, when an annealed metal is progressively deformed, the x-ray lines progressively broaden and the hardness increases. In fact, the hardness of a particular metal or alloy can be rather accurately measured from the breadth of its diffraction lines. The relation between line breadth and hardness is not general, but must be determined experimentally for each particular material. (Very slight degrees of deformation can be detected by observation of the $K\alpha$ doublet. Rather than attempting to measure a slight increase in line width, one measures the ratio of the height of the "valley" between $K\alpha_1$ and $K\alpha_2$ to the height of $K\alpha_2$. This ratio increases rapidly as the lines broaden.)

When steel is hardened by quenching, the x-ray lines become very broad because of the microstrains due to the formation of martensite. Subsequent tempering causes progressive softening and line sharpening. Here again, a useful relation can be established experimentally between line width and hardness, applicable to a particular type of steel.

Line-width observations are often made in back reflection, whether by a photographic technique (Fig. 3) or by the diffractometer (Fig. 4). It is then necessary to remember that the observation applies only to a thin surface layer of the specimen. For example, Fig. 5(a) was obtained from a piece of copper and exhibits unresolved doublets in the high-angle region. The inexperienced observer might conclude that this material was highly cold worked. What the x-ray "sees" *is* cold worked, but it sees only to a limited depth. Actually, the bulk of this specimen is in the annealed condition, but the surface from which the x-ray pattern was made had had 50 μm removed by grinding on a belt sander after annealing. This treatment cold worked the surface to a considerable depth. By successive etching treatments and diffraction patterns made after each etch, the change in structure of the cold-worked layer could be followed as a function of depth below the ground surface. Not until a total of 75 μm had been removed did the diffraction pattern become characteristic of the bulk of the material; see Fig. 5(b), where the spotty lines indicate a coarse-grained, recrystallized structure.

---

[2] Even if no photographic work is done in the x-ray laboratory in which one is working, and hence no developing and fixing solutions are on hand, it is possible to use a small amount of developer and fixer from a TEM darkroom or from a darkroom for printing positives from microscopy negatives.

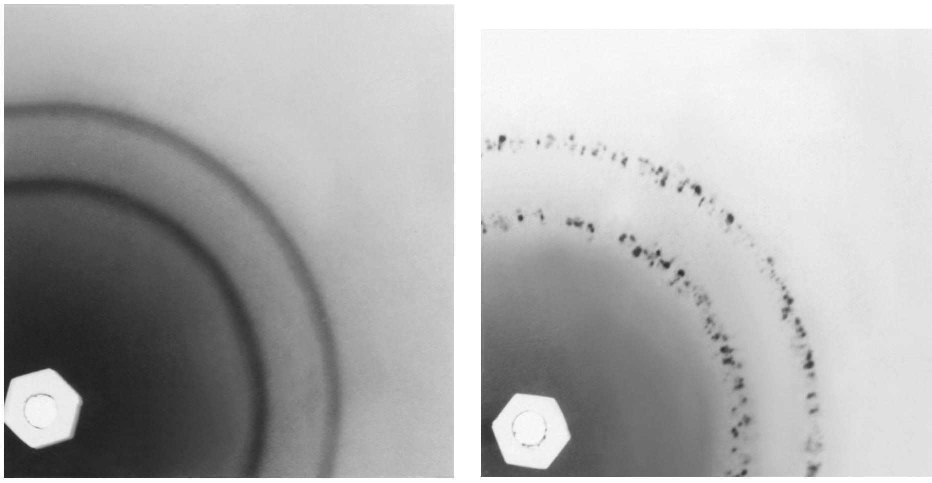
(a) (b)

Figure 5 Back-reflection pinhole patterns of coarse-grained recrystallized copper. Unfiltered copper radiation: (a) from surface ground on a belt sander; (b) after removal of 0.003 in. (75 μm) from this surface by etching.

5 DEPTH OF X-RAY PENETRATION

Observations of this kind suggest that it might be well to consider in some detail the general problem of x-ray penetration. Most metallurgical specimens strongly absorb x-rays, and the intensity of the incident beam is reduced almost to zero in a very short distance below the surface. The diffracted beams therefore originate chiefly in a thin surface layer whenever a reflection technique, as opposed to a transmission technique, is used, i.e., whenever a diffraction pattern is obtained in a back-reflection camera of any kind, a Seemann-Bohlin camera, or a diffractometer as normally used. The example of Fig. 5 just showed how a back-reflection pinhole photograph of a ground surface discloses the cold-worked condition of a thin surface layer and gives no information whatever about the bulk of the material below that layer.

These circumstances naturally pose the following question: what is the effective depth of x-ray penetration? Or, stated in a more useful manner, to what depth of the specimen does the information in such a diffraction pattern apply? This question has no precise answer because the intensity of the incident beam does not suddenly become zero at any one depth but rather decreases exponentially with distance below the surface. Building on the results, one can express the intensity diffracted by the layer at depth α as a fraction of the total integrated intensity diffracted by a specimen of infinite thickness (a few thousandths of an inch for most metals). Call this fraction G_x. Then

$$G_x = \frac{\int_{x=0}^{x=x} dI_D}{\int_{x=0}^{x=\infty} dI_D} = [1 - e^{-\mu x(1/\sin\gamma + 1/\sin\beta)}] \tag{3}$$

permits calculatation of the fraction G_x of the total diffracted intensity which is contributed by a surface layer of depth x. Suppose that a contribution from this surface layer of 95 percent (or 99 or 99.9 percent) of the total is enough so that the contribution from the material below that layer can be ignored then x is the effective depth of penetration. The information recorded on the diffraction pattern (or, more precisely, 95 percent of the information) then refers to the layer of depth x and not to the material below it. As was seen before for the parafocusing diffractometer, $\gamma = \beta = \theta$, and Eq. (3) reduces to

$$G_x = (1 - e^{-2\mu x/\sin\theta}), \tag{4}$$

which shows that the effective depth of penetration decreases as θ decreases and therefore varies from one diffraction line to another. In back-reflection cameras, $\gamma = 90°$, and

$$G_x = [1 - e^{-\mu x(1 + 1/\sin\beta)}], \tag{5}$$

where $\beta = 2\theta - 90°$.

For example, the conditions applicable to the outer diffraction ring of Fig. 5 are $\mu = 473\ \text{cm}^{-1}$ and $2\theta = 136.7°$. By using Eq. (5), G_x can be determined as function of x (Fig. 6). Note that 95 percent of the information on the diffraction pattern refers to a depth of only about 25 μm. It is therefore not surprising that the pattern of Fig. 5(a) discloses only the presence of cold-worked metal, since repeated etching treatments showed that the depth of the cold-worked layer was about 75 μm. Of course, the information recorded on the pattern is heavily weighted in terms of material just below the surface; thus 95 percent of the recorded information applies to a depth of 25 μm, but 50 percent of *that* information originates in the first 25 μm. (Note that an effective penetration of 25 μm means that a surface layer only one grain thick is effectively contributing to the diffraction pattern if the specimen has an ASTM grain-size number of 8. This layer contains some 300,000 reflecting lattice planes for the 331 diffraction line considered here.)

Equation (4) can be put into the following form, which is more suitable for calculation:

$$\frac{2\mu x}{\sin\theta} = ln\left(\frac{1}{1 - G_x}\right) = K_x,$$

$$x = \frac{K_x \sin\theta}{2\mu}. \qquad \text{[Diffractometer]}$$

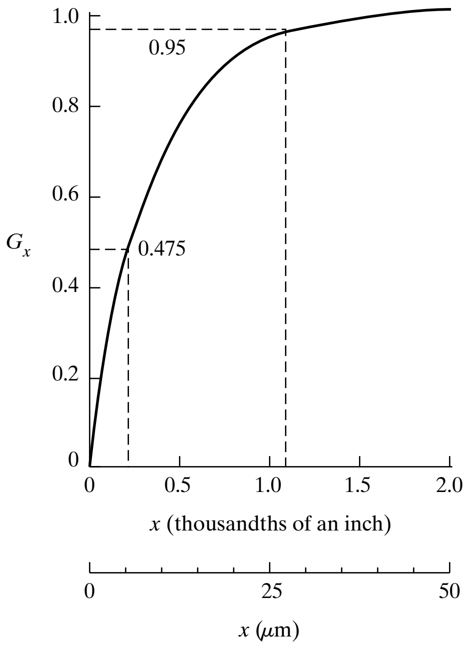

Figure 6 The fraction G_x of the total diffracted intensity contributed by a surface layer of depth x, for $\mu = 473\ \text{cm}^{-1}$, $2\theta = 136.7^{o}$, and normal incidence.

Similarly, Eq. (5) becomes

$$\mu x\left(1 + \frac{1}{\sin\beta}\right) = ln\left(\frac{1}{1 - G_x}\right) = \mathrm{K}_{\mathrm{x}},$$

$$x = \frac{K_x \sin\beta}{\mu(1 + \sin\beta)}. \qquad \text{[Back-reflection camera]}$$

Values of K_x for various assumed values of G_x are given in Table 2.

Calculations of the effective depth of penetration can be valuable in many applications of x-ray diffraction. The effective depth of penetration must be made as large as possible in some applications. Then γ and β in Eq. (3) must be as large as possible, indicating the use of high-angle lines, and μ as small as possible, indicating short-wavelength radiation. Other applications may demand very little penetration, as when information, e.g., chemical composition or lattice parameter, is needed from a very thin surface layer. Then μ must be made large, by using radiation which

TABLE 2

G_x	0.50	0.75	0.90	0.95	0.99	0.999
K_x	0.69	1.39	2.30	3.00	4.61	6.91

is highly absorbed, and γ and β small, by using a diffractometer at low values of 2θ.[3] By these means the depth of penetration can often be made surprisingly small. For instance, if a steel specimen is examined in a diffractometer with Cu $K\alpha$ radiation, 95 percent of the information afforded by the lowest angle line of ferrite (the 110 line at $2\theta = 45^o$) applies to a depth of only 2 μm. There are limits, of course, to reducing the depth of x-ray penetration, and when information is required from very thin surface films, electron diffraction, glancing angle diffraction, or x-ray reflectivity are far more suitable tools.

Although the diffracted beam in any reflection method comes only from a very thin surface layer, it must not be supposed that the information on a diffraction pattern obtained by a transmission method is truly representative of the entire cross section of the specimen. Calculations such as those given above show that a greater proportion of the total diffracted energy originates in a layer of given thickness on the back side of the specimen (the side from which the transmitted beam leaves) than in a layer of equal thickness on the front side. If the specimen is highly absorbing, a transmission method can be almost as nonrepresentative of the entire specimen as a back-reflection method, in that most of the diffracted energy will originate in a thin surface layer. See Problem 5.

6 SIZE AND STRAIN SEPARATION

As indicated in Sec. 4, separating the different contributions to line broadening, if present, requires use of multiple diffraction peaks and analysis of the peaks' shapes. The quality of the diffraction pattern, or more specifically the diffraction peaks and their tails, must be very high if the somewhat involved Fourier analysis pioneered by Warren is to be worthwhile [e.g., 3-6]. Other simpler approaches using peak widths have their place in analyzing size and strain broadening.

It is important to realize that crystallite sizes obtained from peak width measurements give volume-average sizes whereas those from peak shape analysis give number-averages. This can be seen by comparing a histogram of average crystallite diameters observed with TEM (Fig. 7) with the average diameter determined from diffractometry and the Scherrer equation [7]. The sample was a dilute mixture of platinum nanoparticles in an amorphous silica matrix, the diffraction pattern of the sample appears in Fig. 2 and Table 1 lists the crystallite sizes obtained from the x-ray diffraction peaks and Scherrer's equation. The crystallite size averaged 38 Å from TEM and 50 Å from the FWHM of the x-ray diffraction peaks. A small number of very large crystallites were noted during TEM of the samples, and simulation of the diffraction peaks [8] produced by a small number of large crystallites mixed with a much larger number of 35-40 Å crystallites reveals that this is the probable origin of the difference between TEM and X-ray FWHM sizes.

---

[3] Some of these requirements may be contradictory. For example, in measuring the lattice parameter of a thin surface layer with a diffractometer, a compromise must be found between the low value of θ required for shallow penetration and the high value of θ required for precise parameter measurements.

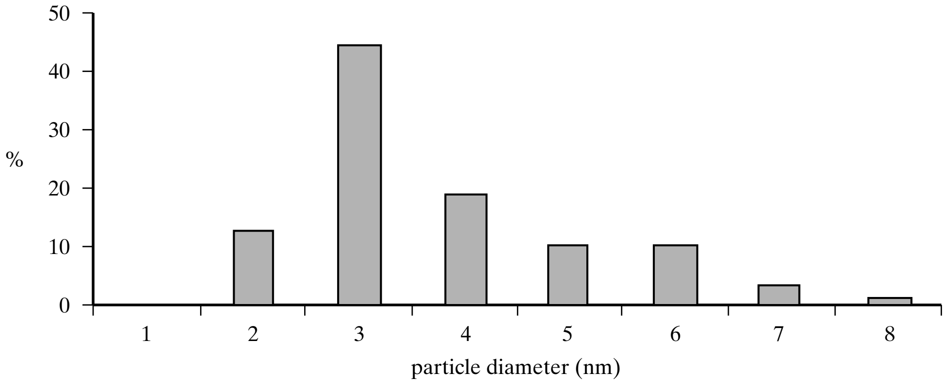

Figure 7 Histogram of Pt nanocluster size as observed by TEM in a Pt/silica xerogel nanocomposite [10].

Contributions from crystallite size, micro strain and instrumental effects can be separated in a straight-forward fashion if the peaks are Lorentzian- or Gaussian-shaped. If

B_{exp} is the experimentally measured FWHM,
B_{size} is the FWHM due to crystallite size,
B_{strain} is the FWHM due to micro strain and
B_{inst} is the FWHM due to the instrument,

then for Lorentzian peaks

$$B_{exp} = B_{size} + B_{strain} + B_{inst} \tag{8}$$

and for Gaussian peaks

$$B^2_{exp} = B^2_{size} + B^2_{strain} + B^2_{inst}. \tag{9}$$

Correction for the instrumental width in either case can be obtained by recording a diffraction pattern, under identical conditions, of the same substance but in a well-annealed, large-grained condition.

Separation of size and strain components can be done by plotting B cos θ as a function of sin θ (Fig. 8); this type of plot is known as a Williamson-Hall plot [9] and implicitly assumes that peak shapes are Lorentzian. Rearranging the terms produces

$$B \cos\theta = 0.9\lambda/t \tag{10}$$

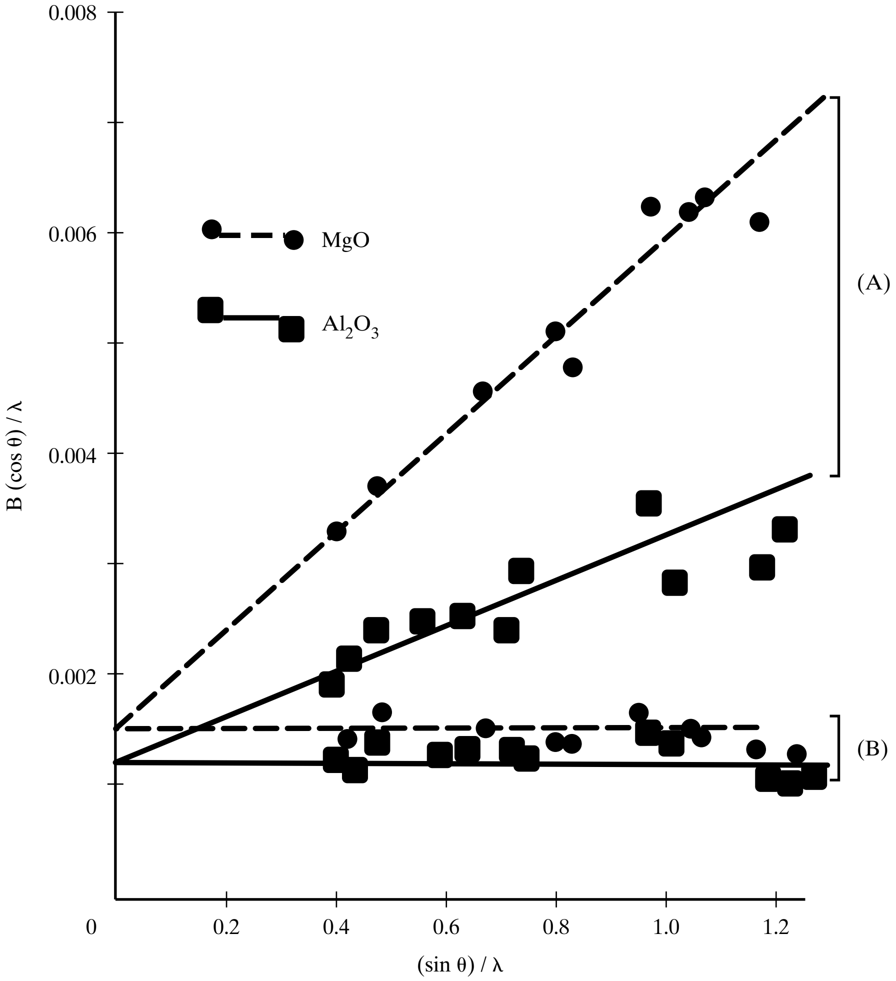

Figure 8 Williamson-Hall plot for MgO and Al_2O_3, curves (A) ball milled for 2 hours and (B) ball milled for 2 hours, then annealed for 2 hours at 1350° C. After Lewis and Lindley [10].

$$\beta \cos\theta = -2(\Delta d/d) \sin\theta \tag{11}$$

If size broadening is the only significant contribution to peak width, then $B_{exp} \cos\theta$ is a constant for all peaks (i.e., its Williamson-Hall plot is a horizontal line). If strain broadening is the important contribution, $B_{exp} \cos\theta$ is a linear function of $\sin\theta$. Figure 8 shows data for two oxide ceramics in two conditions: after ball milling and ball milling followed by annealing at 1350 C for 2 hr [10]. As one would expect, ball milling produces less microstrain in Al_2O_3, a substance which is often used to polish solid samples prior to optical microscopy, and the crystallite size of the two oxides is similar. The crystallite size remained constant after annealing, but virtually all of the strain was relieved.

CRYSTAL ORIENTATION

7 GENERAL

Each grain in a polycrystalline aggregate normally has a crystallographic orientation different from that of its neighbors. Considered as a whole, the orientations of all the grains may be randomly distributed in relation to some selected frame of reference, or they may tend to cluster, to a greater or lesser degree, about some particular orientation or orientations. Any aggregate characterized by the latter condition is said to have a *preferred orientation, or texture*, which may be defined simply as a condition in which the distribution of crystal orientations is nonrandom Preferred orientation can have a profound effect on diffracted intensities measured by diffractometry.

Preferred orientation is a very common condition. Among metals and alloys it is most evident in wire and sheet, and the kinds of texture found in these products are treated below. The preferred orientation that is produced by the forming process itself (wire drawing or sheet rolling) is called a *deformation texture*. It is due to the tendency of the grains in a polycrystalline aggregate to rotate during plastic deformation; each grain undergoes slip and rotation in a complex way that is determined by the imposed forces and by the slip and rotation of adjoining grains; the result is a preferred, nonrandom orientation. When the cold-worked metal, possessed of a deformation texture, is recrystallized by annealing, the new grain structure usually has a preferred orientation too, often different from that of the cold-worked material. This is called a *recrystallization texture* or *annealing texture*. It is due to the influence which the texture of the cold-worked matrix has on the nucleation and/or growth of the new grains in that matrix.

Preferred orientation is not confined to metallurgical products. It also exists in rocks, in ceramics, in semiconductor thin films and other coatings and in both natural and artificial polymeric fibers and sheets. In fact, preferred orientation is generally the rule, not the exception, and the preparation of an aggregate with completely random crystal orientations is a difficult matter.

The industrial importance of preferred orientation lies in the effect, often very marked, which it has on the overall, macroscopic properties of materials. Given the fact that all single crystals are anisotropic, i.e., have different properties in different directions, it follows that an aggregate having preferred orientation must also have directional properties to a greater or lesser degree. Such properties may or may not be beneficial, depending on the intended use of the material. For example, sheet steel for the cores of small electric motors should have, for magnetic reasons, all grains oriented with their {100} planes parallel to the sheet surface. But this texture would not be satisfactory if the steel were to be formed into a cup by deep drawing: here a texture with {111} planes parallel to the surface would make the steel less likely to crack during the severe deformation of deep drawing; however, if the part to be formed by deep drawing has an unsymmetrical shape, a still different texture, or none at all, might yield better results. Some control of texture is possible by the proper choice of production variables such as degree of deformation and annealing temperature, but metallurgists do not yet understand texture formation well enough to produce any desired texture in any particular metal at will.

Because of its technological importance, the literature on observed textures and an texture prediction is extensive. For information on deformation and recrystallization textures observed in specific materials in wire and sheet form, the reader should consult Barrett and Massalski [G.10] and Dillamore and Roberts [11]. Here the focus is on the nature of textures and with their determination by x-ray methods. Detailed coverage of the various techniques, special experimental methods and computational techniques appears elsewhere [G.36 and G.37].

As was noted before in this book, a pinhole photograph made of a polycrystalline specimen with characteristic radiation consists of concentric Debye rings. The implicit assumption has been that these rings are always continuous and of constant intensity around their circumference, but actually such rings are not formed unless the individual crystals in the specimen have completely random orientations.[4] If the specimen exhibits preferred orientation, the Debye rings are of nonuniform intensity around their circumference (if the preferred orientation is slight), or actually discontinuous (if there is a high degree of preferred orientation). In the latter case, certain portions of the Debye ring are missing because the orientations which would diffract to those parts of the ring are simply not present in the specimen. Nonuniform Debye rings can therefore be taken as conclusive evidence for preferred orientation, and analyzing the nonuniformity allows determination of the kind and degree of preferred orientation present. (This nonuniformity is evident even in some Hull/Debye–Scherrer patterns: if a wire having preferred orientation is examined in a Hull/Debye–Scherrer camera, the nonuniformity of Debye rings is usually apparent even though such a camera records only a portion of the rings.)

Fiber Texture

The individual crystals in wire are so oriented that the same crystallographic direction [*uvw*] in most of the grains is parallel or nearly parallel to the wire axis. Because a similar texture occurs in natural and artificial fibers, it is called a *fiber texture* and the axis of the wire is called the *fiber axis*. Materials having a fiber texture have rotational symmetry about an axis: all crystal orientations about this axis are equally probable, like those of beads on a string. A fiber texture is therefore to be expected in any material formed by forces that have rotational symmetry about an axis, for example, in wire and rod formed by drawing, swaging, or extrusion. Less common examples of fiber texture are sometimes found in sheet formed by simple

---

[4] See the next section for one exception to this statement.

compression, in coatings formed by hot dipping, electroplating, and evaporation, and in castings among the columnar crystals next to the mold wall. The fiber axis in these is perpendicular to the plane of the sheet or coating, and parallel to the axis of the columnar crystals.

Fiber textures vary in perfection, i.e., in the scatter of the direction [*uvw*] about the fiber axis, and both single and double fiber textures have been observed. Thus, cold-drawn aluminum wire has almost a single [111] texture, but copper, also FCC, has a double [111] + [100] texture; i.e., in drawn copper wire there are two sets of grains, the fiber axis of one set being [111] and that of the other set [100].

Sheet Texture

In its simplest, most highly developed form, the texture of sheet is such that most of the grains are oriented with a certain crystallographic plane (*hkl*) roughly parallel to the sheet surface, and a certain direction [*uvw*] in that plane roughly parallel to the direction in which the sheet was rolled. Such a texture is described by the shorthand notation (*hkl*)[*uvw*]. In an ideal texture of this kind, the grain orientations in the sheet are fixed with respect to axes in the sheet; there is none of the rotational freedom of grain orientation possessed by a fiber texture.

The notation (*hkl*)[*uvw*] specifies what is called an *ideal orientation*. Some metals and alloys have sheet textures so sharp that they can be adequately described by stating the ideal orientation to which the grains of the sheet closely conform. Most sheet textures, however, have so much scatter that they can be approximated symbolically only by the sum of a number of ideal orientations or texture components, and even such a description is inadequate. Thus, the deformation texture of brass sheet (70 Cu-30 Zn) is very near the ideal orientation (110)[$\bar{1}$12]. But both the deformation and recrystallization textures of low-carbon sheet steel have so much scatter that the grain orientations present can be represented accurately only by a graphical description, such as a *pole figure*.

Pole Figures

A pole figure is a stereographic projection, with a specified orientation relative to the specimen, that shows the variation of pole density with pole orientation for a selected set of crystal planes. This method of describing textures was first used by the German metallurgist Wever in 1924 [12], and its meaning can best be illustrated by the following example. Suppose a very coarse-grained sheet of a cubic metal contains only 10 grains, and the orientation of each of these 10 grains has been determined by one of the Laue methods. The orientations of all of these grains can be summarized by plotting the positions of their {100} poles on a single stereographic projection, with the projection plane parallel to the sheet surface. Since each grain has three {100} poles, there will be a total of $3 \times 10 = 30$ poles plotted on the projection. If the grains have a completely random orientation, these poles

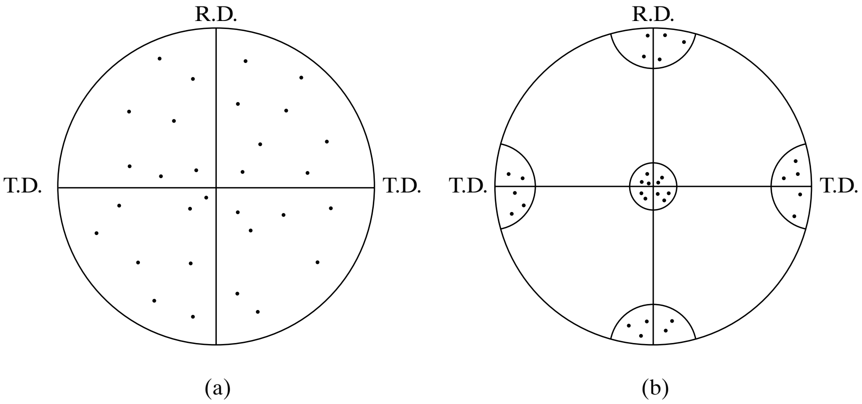

Figure 9 (100) pole figures for sheet material, illustrating (a) random orientation and (b) preferred orientation. R.D. (rolling direction) and T.D. (transverse direction) are reference directions in the plane of the sheet.

will be distributed uniformly[5] over the projection, as indicated in Fig. 9(a). But if preferred orientation is present, the poles will tend to cluster is certain areas of the projection, leaving other areas virtually unoccupied. For example, this clustering might take the particular form shown in Fig. 9(b). This is called the "cube texture," because each grain is oriented with its (100) planes nearly parallel to the sheet surface and the [001] direction in these planes nearly parallel to the rolling direction. (This simple texture, which may be described by the shorthand notation (100)[001], actually forms as a recrystallization texture in many face-centered cubic metals and alloys under suitable conditions.) If a (111) pole figure were constructed by plotting only {111} poles, the resulting pole figure would look entirely different from Fig. 9(b) for the same preferred orientation; in fact, it would consist of four "high-intensity" areas, one near the center of each quadrant. This illustrates the fact that the appearance of a pole figure depends on the indices of the poles plotted, and that the choice of indices depends on which aspect of the texture one wishes to show most clearly. For example, if the plastic deformation of a certain face-centered cubic material in sheet form were of concern, a (111) pole figure would be plotted because it would show at a glance the orientation of the {111} slip planes. Similarly, if the magnetic behavior of iron sheet is of interest, a (100) pole figure would be preferred, because the directions of high magnetic permeability in iron are $\langle 100 \rangle$ directions.

The pole figure of a fiber texture necessarily has rotational symmetry about the fiber axis (Fig. 10). The degree of scatter of this texture is given by the angular width

---

[5] If the orientation is random, there will be equal numbers of poles in equal areas on the surface of a reference sphere centered on the specimen. There will not be equal numbers, however, on equal areas of the pole figure, since the stereographic projection is not area-true. This results, for randomly oriented grains, in an apparent clustering of poles at the center of the pole figure, since distances representing equal angles are much smaller in this central region than in other parts of the pole figure.

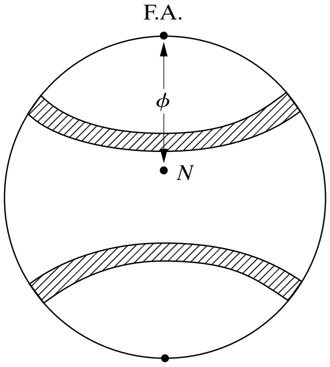

Figure 10 (111) pole figure for an imperfect [100] fiber texture. F.A. = fiber axis. Cross-hatched areas are areas of high (111) pole density.

of the bands that show where (111) poles are located. The angle ϕ is the angle between the fiber axis and the general position N of any pole being considered. For the texture shown the bands are centered on ϕ values, measured from the top and bottom of the projection, of 54.7^o, because this is the angle between the [100] fiber axis and the (111) poles being displayed.

Because of its rotational symmetry a pole figure of a fiber texture displays redundant information, in the sense that the pole density along any longitude line (meridian) is the same as along any other. Thus a plot of pole density vs. angle ϕ between 0 and 90^0 is a simpler description of the texture; for the texture shown in Fig. 10, such a plot would show a single maximum at 54.7°.

When the grain size of the specimen is small, as it normally is, separate determination of the orientations of a representative number of grains, as suggested by Fig. 9, is out of the question. Instead, x-ray methods are used in which the diffraction effects from thousands of grains are automatically averaged. The (*hkl*) pole figure of a fine-grained material is constructed by analyzing the distribution of intensity around the circumference of the corresponding *hkl* Debye ring. Two methods of doing this are available, the area detector[6] and the diffractometer method, and both are time consuming.

Although only a pole figure can provide a complete description of preferred orientation, some information can be obtained fairly quickly by a comparison of calculated diffraction line intensities with those observed on an ordinary diffractometer scan. As stated relative line intensities are given accurately only when the crystals of the specimen have completely random orientations. Therefore any radical disagreement between observed and calculated intensities is immediate evidence of preferred orientation in the specimen, and, from the nature of the disagreement, certain limited conclusions can usually be drawn concerning the

---

[6] The term “area detector” has been substituted here for the earlier designation of “photographic.” Before the development of modern x-ray detectors, photographic emulsions were the only such detectors. Now image plates, CCD detectors or multiwire detectors would be used in place of film, and the more inclusive “area detector” seems more appropriate.

nature of the texture. For example, if a sheet specimen is examined in the diffractometer in the usual way (the specimen making equal angles with the incident and diffracted beams the parafocusing geometry), then the only grains which can contribute to the *hkl* reflection are those whose (*hkl*) planes are *parallel to the sheet surface*. If the texture is such that there are very few such grains, the intensity of the *hkl* reflection will be abnormally low. In another case, a given reflection may have abnormally high intensity, which would indicate that the corresponding planes were preferentially oriented parallel or nearly parallel to the sheet surface. As an illustration, the 200 diffractometer reflection from a specimen having the cube texture is abnormally high, and from this fact alone it is possible to conclude that there is a preferred orientation of (100) planes parallel to the sheet surface. The bottom diffractometer scan of Fig. 2 shows a platinum sheet with cube texture. However, no conclusion is possible as to whether or not there is a preferred direction in the (100) plane parallel to some reference direction on the sheet surface. Such information can be obtained only by making a pole figure.

8 THE TEXTURE OF WIRE (AREA DETECTOR METHOD)

The chief problem presented by a fiber texture is the identification of the fiber axis [*uvw*]. This can be done fairly easily with a single two-dimensional pinhole diffraction pattern, and the procedure is described in this section. If, in addition, the amount of scatter in the texture must be determined, a diffractometer method is preferable (Sec. 10) although image plates appear to provide a convenient alternative [13, 14].

The wire is examined in a transmission pinhole camera with filtered or crystal-monochromatized radiation and with the wire axis vertical, parallel to one edge of the flat area detector. The problem of finding the indices [*uvw*] of the fiber axis is best approached by considering the diffraction effects associated with an ideal case, for example, that of a wire of a cubic material having a perfect [100] fiber texture. Consider the 111 reflection. In Fig. 11, the wire specimen is at *C* with its axis along *NS*, normal to the incident beam *IC*. *CP* is the normal to a set of (111) planes. Diffraction from (111) can occur only when they are inclined to the incident beam at an angle θ which satisfies Bragg's law, and this requires that the (111) pole lie somewhere on the circle *PUQV*, since then the angle *PCI* between the plane normal and the incident beam will always be $90^\circ–0$. For this reason, *PUQV* is called the *reflection circle*. If the grains of the wire had completely random orientations, then (111) poles would lie at all positions on the sphere surface and therefore at all positions on the reflection circle, and the 111 reflection would consist of the complete Debye ring indicated in the drawing. But if the wire has a perfect [100] fiber texture, then the diffraction pattern produced by a stationary specimen is identical with that obtained from a single crystal rotated about the axis [100], because of the rotational symmetry of the wire. During this rotation, the (111) pole is confined to the small circle *PAQB*, all points of which make a constant angle $\phi = 54.7^\circ$ with the [100] direction *N*. Therefore, the only (111) planes in the specimen that are able to

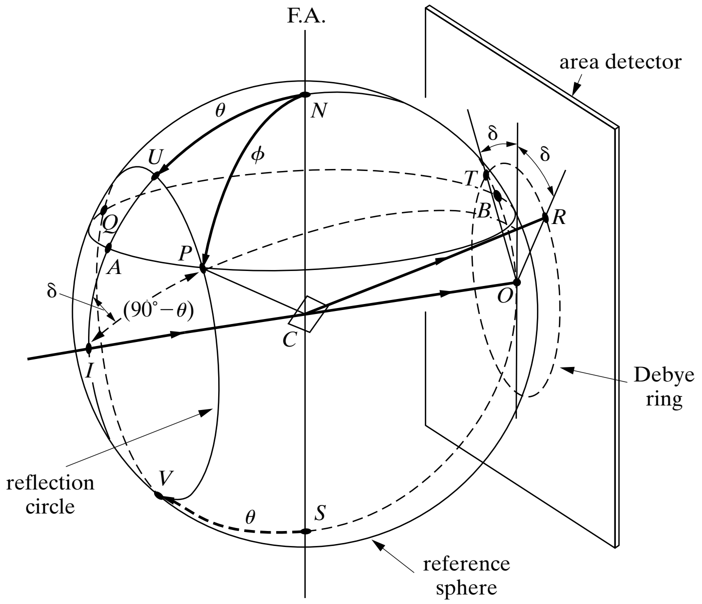

Figure 11 Geometry of diffraction from material having a fiber texture. F.A. = fiber axis.

diffract are those with poles at the intersections of the reflection circle and the circle *PAQB*. These intersections are located at *P* and *Q*, and the corresponding diffraction spots at *R* and *T*, at an azimuthal angle δ from a vertical line through the center of the film. Two other spots, not shown, are located in symmetrical positions on the lower half of the film. If the texture is not perfect, each of these spots will broaden peripherally into an arc whose length is a function of the degree of scatter in the texture.

By solving the spherical triangle *IPN*, results the following general relation results between the angles ϕ, θ, and δ:

$$\cos \phi = \cos \theta \cos \delta \tag{8}$$

These angles are shown stereographically in Fig. 12, projected on a plane normal to the incident beam. The (111) pole figure in (a) consists simply of two arcs which are the paths traced out by {111} poles during rotation of a single crystal about [100]. In (b), this pole figure has been superimposed on a projection of the reflection circle in order to find the locations of the diffraction plane normals. Radii drawn through these points (*P, Q, P´*, and *Q´*) then enable the angle δ to be measured and the appearance of the diffraction pattern to be predicted.

An unknown fiber axis is identified by measuring the angle δ on the film or area detector and obtaining ϕ from Eq. (8). When this is done for a number of different *hkl* reflections, a set of ϕ values is obtained from which the indices [*uvw*] of the

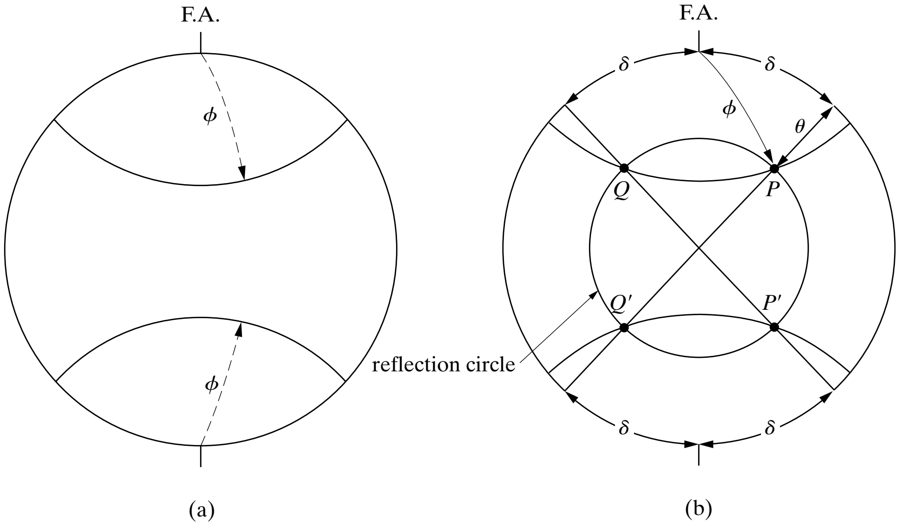

(a)

(b)

Figure 12 Perfect [100] fiber texture (a) (111) pole figure; (b) location of reflecting plane normals.

fiber axis can be determined. The procedure will be illustrated with reference to the diffraction pattern of drawn aluminum wire shown in Fig. 13, which has the incomplete Debye rings typical of a pronounced texture. The first step is to index the Debye rings. Values of θ for each ring are calculated from measurements of ring diameter, and *hkl* indices are assigned by the use "Appendix: Quadratic Forms of Miller Indices." In this way the inner ring is identified as a 111 reflection and the outer one as 200. The angle δ is then measured from a vertical line through the center of the film to the center of each strong Debye arc. The average values of these angles are given below, together with the calculated values of ϕ:

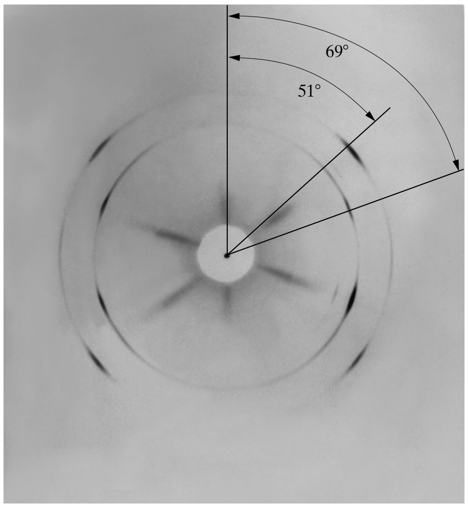

Figure 13 Transmission pinhole pattern of cold-drawn aluminum wire, wire axis vertical. Filtered copper radiation. (The radial streaks near the center are formed by the white radiation in the incident beam.)

Line	*hkl*	δ°	θ°	ϕ°
Inner	111	69	19.3	70
Outer	200	52	22.3	55

The normals to the (111) and (200) planes therefore make angles of 70º and 55º, respectively, with the fiber axis. The indices [*uvw*] of this axis are determined either by the graphical construction by inspection of a table of interplanar angles. In this case, shows that [*uvw*] must be [111], since the angle between $\langle 111\rangle$ and $\langle 111\rangle$ is 70.5 and that between $\langle 111\rangle$ and $\langle 100\rangle$ is 54.7º, and these values agree with the values of ϕ given above within experimental error. The fiber axis of drawn aluminum wire is therefore [111]. There is some scatter of the [111] direction about the wire axis, however, inasmuch as the reflections on the film are short arcs rather than sharp spots. This can be taken into account by measuring the angular range of δ for each arc and calculating the corresponding range of ϕ. A (111) pole figure of the wire would then resemble Fig. 10.

Close inspection of Fig. 13 reveals a weak maximum on the outer ring (200 reflection) at the equator ($\delta = 90º$), indicating a weak [100] component in the texture; there is also evidence of this component on the inner 111 ring. This wire therefore has a double fiber texture: [111] strong and [100] weak. The relative amounts of these components can be measured from the output of as area detector or with a diffractometer (Sec. 10).

If a coating, such as an electrodeposit, on a flat sheet has a fiber texture with the fiber axis [*uvw*] normal to the sheet, then the (*hkl*) planes normal to [*uvw*] will be parallel, or nearly parallel, to the sheet surface. Unusual diffraction effects can then occur:

1. *Parafocusing diffractometer*. The incident and diffracted beams make the same angle with the sheet surface, so that the *hkl* reflection is abnormally strong and all others weak or absent.
2. *Back-reflection pinhole camera*. If the incident beam is normal to the sheet specimen and therefore parallel to the fiber axis, and a projection like that shown in Fig. 12(b) is made (projection plane parallel to sheet), then both the incident beam and the fiber axis coincide with the center of the projection. If the texture is ideally sharp, the (*hkl*) pole figure will consist of one or more concentric circles centered on the center of the projection, and the chance that one of these pole circles will coincide with the concentric reflection circle is essentially zero; no reflection will occur. But if the texture has enough scatter, one of the pole circles will broaden into a band wide enough to touch the reflection circle at all points; a Debye ring of *uniform* intensity will be formed. Thus a uniform Debye ring is not always evidence for randomly oriented grains.

9 THE TEXTURE OF SHEET (DIFFRACTOMETER METHODS)

Prior to about 1950, the texture of sheet materials was determined by a photographic method, in which diffracted x-ray intensities were visually estimated from the degree of film blackening on a series of photographs. The resulting pole figures were qualitative; they were divided by contour lines into areas in which the pole density was designated by terms such as low, medium, and high.

Once the photographic method was regarded as obsolete, because the diffractometer permited direct measurement of diffracted intensities and yielded quantitative pole figures. With the advent of the new area detectors, however, this method many regain its importance.

The essential difference between the area detectors and diffractometer methods can be understood by comparing Figs. 13 and 14. To analyze the information given in Fig. 13, the degree of film blackening, is estimated at points around the Debye ring. With a diffractometer (Fig. 14) the same nonuniform Debye ring exists in space, but the detector cannot be moved around the ring to explore the variation in intensity. Instead, the detector is fixed and *the specimen* is rotated. If the sheet specimen is rotated in its own plane, for example, the Debye ring rotates with it, and the high- and low-intensity regions are successively brought into a position where they can be measured by the detector. At each specimen position the intensity of the diffracted beam is taken to be proportional to the volume of grains then oriented to diffract that beam, except for corrections that may be necessary; this volume is in turn proportional to pole density.

To determine an (*hkl*) pole figure, the detector is fixed at the proper 2θ angle to receive the *hkl* reflection and the sheet specimen is rotated in particular ways described below. The pole figure is a projection made on a plane parallel to the sheet surface and therefore rotates with the sheet. But, whatever the orientation of the sheet, the normal *N* to the diffraction planes (*hkl*) remains fixed in space, bisecting the angle between the incident and diffracted beams. Therefore *N* can be imagined as moving over a fixed projection plane. The position of *N* on the pole figure

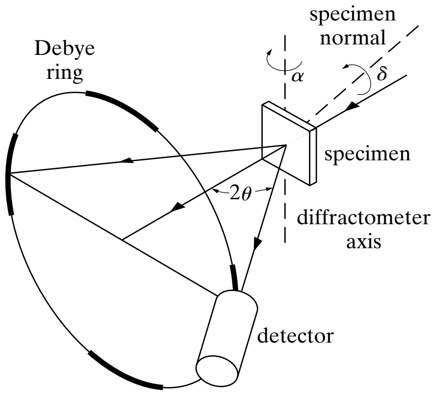

Figure 14 Transmission method for pole-figure determination. After Geisler [15].

is derived from the specimen rotation performed and at each position of N the pole density derived from the detector measurement of x-ray intensity can be plotted.

The ideal diffractometer specimen would be a small sphere cut out of the sheet, because a sphere presents the same aspect to the incident beam whatever its orientation. Normally, however, the sheet is examined directly, and then the paths of incident and diffracted beams within the sheet change with sheet orientation. It is then necessary to correct the measured intensities for these geometrical effects or to design the x-ray optics so that corrections are not required.

There is not one, but several, diffractometer methods for measuring sheet texture. They fall into two groups, transmission and reflection, both being normally necessary for complete coverage of the pole figure.

Transmission Methods

The two methods described below both require a specimen for which μt is of the order of 1, where μ is the linear absorption coefficient and t the thickness. This means a thickness of the order of 35 μm for iron examined with Mo $K\alpha$ radiation or 75 μm for aluminum with Cu $K\alpha$. Thicker sheet has to be thinned by grinding and etching.

The method of *Decker, Asp, and Harker* [16] was the first application of the diffractometer to texture measurements. The sheet specimen, in a special holder, is positioned initially with the rolling direction vertical and coincident with the diffractometer axis,[7] and with the plane of the specimen bisecting the angle between incident and diffracted beams (Figs. 14 and 15). The specimen holder allows rotation of the sheet in its own plane and about the diffractometer axis.

Figure 15 shows how to plot the pole N of the diffraction plane hkl. The angle α measures the amount of rotation about the diffractometer axis, positive when clockwise; α is zero when the sheet bisects the angle between incident and diffracted beams. The angle δ measures the amount by which the sheet is rotated in its own plane and is zero when the transverse direction is horizontal. (Note that other writers often have different symbols and definitions for these angles.) The pole N of the diffraction plane coincides initially, when α and δ are both zero, with the left transverse direction. A rotation of the specimen by δ degrees in its own plane then moves the pole of hkl δ degrees around the circumference of the pole figure, and a rotation of α degrees about the diffractometer axis then moves it α degrees from the circumference along a radius. To explore the pole figure, it is convenient to make intensity readings at intervals of 5° or 10° of α for a fixed value of δ: the pole figure is thus mapped out along a series of radii.[8] By this procedure the entire pole figure can be determined except for a region at the center extending from about

---

[7] For simplicity, the method is described here only in terms of a vertical-axis diffractometer.

[8] The chart shown in skeleton form in Fig. 15(b) is useful for this purpose. It is called a polar stereographic net, because it shows the latitude lines (circles) and longitude lines (radii) of a ruled globe projected on a plane normal to the polar NS-axis. In the absence of such a net, the equator or central meridian of a Wulff net can be used to measure the angle α.

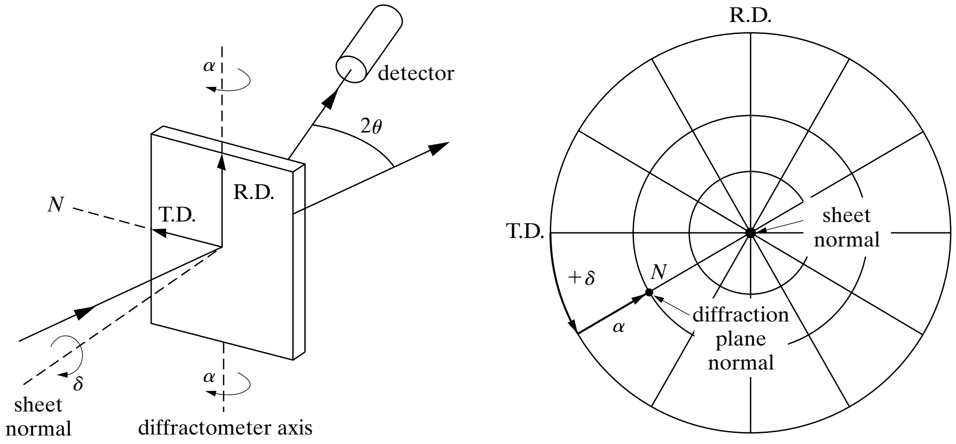

(a) (b)

Figure 15 Angular relations in the transmission method, (a) in space, with $\alpha = \delta = \theta$ and (b) on the projection, with the diffraction plane normal N at $\alpha = \delta = 30^\circ$. R.D. = rolling direction, T.D. = transverse direction.

$\alpha = 50^\circ$ to $\alpha = 90^\circ$; in this region not only does the absorption correction become inaccurate but the frame of the specimen holder obstructs the diffracted x-ray beam; the practical maximum value of α is thus reached before the theoretical, which is $90^\circ - \theta$).

An absorption correction is necessary in this method because variations in α cause variations in both the volume of diffracting material and the path length of the x-rays within the specimen. Variations in δ have no effect. The incident beam in Fig. 16 has intensity I_0 (ergs/cm^2/sec) and is 1 cm square in cross section. It is incident on a sheet specimen of thickness t and linear absorption coefficient μ, and the individual grains of this specimen are assumed to have a completely random orientation. Let a be the volume fraction of the specimen containing grains correctly oriented for diffraction of the incident beam, and b the fraction of the incident energy diffracted by a unit volume. Then the total energy per second in the diffracted beam outside the specimen, originating in a layer of thickness dx located at a depth x, is given by

$$\mathrm{d}I_D = ab(DB)I_o e^{-\mu(AB+BC)}dx \quad \text{(ergs/see)}, \tag{9}$$

where

$$DB = \frac{1}{\cos(\theta - \alpha)}, \quad AB = \frac{x}{\cos(\theta - \alpha)}, \text{ and } BC = \frac{1 - x}{\cos(\theta + \alpha)}.$$

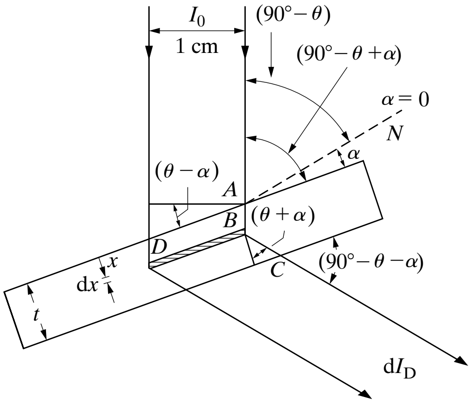

Figure 16 Path length and irradiated volume in the transmission method.

By substitution,

$$dI_D = \frac{ab\mathrm{I}_o}{\cos(\theta - \alpha)} e^{-\mu t/\cos(\theta+\alpha)_\rho} e^{-\mu x[1/\cos(\theta-\alpha) - 1/\cos(\theta+\alpha)]} dx. \tag{10}$$

If $\alpha = 0$ is substituted into Eq. (10) and the integration from $x = 0$ to $x = t$ is performed, the total diffracted energy per second, the integrated intensity, for this position of the specimen is:[9]

$$I_D(\alpha = 0) = \frac{abtI_o}{\cos\theta} e^{-\mu t/\cos\theta}. \tag{11}$$

When α is not zero, the same integration gives

$$I_D(\alpha = \alpha) = \frac{abI_o[e^{-\mu t/\cos(\theta-\alpha)} - e^{-\mu t/\cos(\theta+\alpha)}]}{\mu\{[\cos(\theta - \alpha)/\cos(\theta + \alpha)] - 1\}}. \tag{12}$$

The ratio of these two integrated intensities is needed for the absorption correction and is:

$$R = \frac{I_D(\alpha = \alpha)}{I_D(\alpha = 0)} = \frac{\cos\theta\,[e^{-\mu t/\cos(\theta-\alpha)} - e^{-\mu t/\cos(\theta+\alpha)}]}{\mu t e^{-\mu t/\cos\theta}\{[\cos(\theta - \alpha)/\cos(\theta + \alpha)] - 1\}}. \tag{13}$$

---

[9] Consider that the diffracted beams in any transmission method were of maximum intensity when the thickness of the specimen was made equal to $1/\mu$. This result follows from Eq. (11). If $\theta = \alpha = 0$, then the primary beam will be incident on the specimen at right angles (sec Fig. 16), as in the usual transmission pinhole method, and the result will apply approximately to diffracted beams formed at small angles 2θ. The intensity of such a beam is given by

$$I_D = abtI_0e^{-\mu t}.$$

Differentiating this expression with respect to t and setting the result equal to zero shows that ID is a maximum when $t = 1/\mu$.

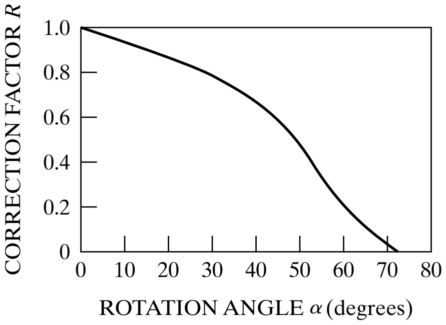

Figure 17 Variation of the correction factor R with α for clockwise rotation from the zero position. $\mu t = 1.0, \theta = 19.25^o$.

A plot of R vs. α is given in Fig. 17 for typical values involved in the 111 reflection from aluminum with Cu $K\alpha$ radiation, namely, $\mu t = 1.0$ and $\theta = 19.25^o$. Figure 17 shows that the integrated intensity of the reflection decreases as α increases in the clockwise direction from zero, even for a specimen containing randomly oriented grains. In the measurement of preferred orientation, it is therefore necessary to *divide* each measured intensity by the appropriate value of the correction factor R in order to arrive at a figure proportional to the pole density. From the way in which the correction factor R was derived, it follows that the *integrated intensity* of the diffracted beam must be measured. To do this with a fixed detector, the detector slits must be as wide as the diffracted beam for all values of α so that the whole width of the beam can enter the detector. The ideal incident beam for this method is a parallel one. However, a divergent beam may be used without too much error, provided the divergence is not too great. There is no question of focusing here: if the incident beam is divergent, the diffracted beam will diverge also and very wide detector slits will be required to admit its entire width. Clockwise rotation of the specimen about the diffractometer axis makes the diffracted beam narrower and is therefore preferred to counterclockwise rotation.

The value of μt used in Eq. (13) must be obtained by direct measurement, since it is not sufficiently accurate to use a tabulated value of μ together with the measured thickness t of the specimen. To determine μt use a strong diffracted beam from any convenient material and measure its intensity when the sheet specimen is inserted in the diffracted beam and again when it is not. The value of μt is then obtained from the absorption equation, $I_t = I_o e^{-\mu t}$, where I_o and I_t are the intensities incident on and transmitted by the sheet specimen, respectively.

The *Schulz transmission method* [17] uses a divergent, rather than a parallel, incident beam and a slit narrow enough to intercept only the central portion of the diffracted beam. For these conditions Schulz derived an equation, analogous to Eq. (12), relating the intensity diffracted by a random specimen (for brevity "random specimen" will be written for "specimen with randomly oriented grains") to the angular setting α. He also showed that the intensity diffracted by a random specimen was constant within a few percent up to an α value of about 30° for a sufficiently thin specimen ($\mu t = 0.4$ to 0.7) and small values of θ (less than about 20°); under these conditions the correction equation is not needed.

In tests of the correction equations by means of random specimens, Newkirk and Bruce [18] found good agreement with Eq. (13) of Decker, Asp, and Harker. On the other hand, the data of Aoki *et al.* [19] show better agreement between experiment and theory for the Schulz method than that of Decker *et al.* However, in judging the validity of correction equations one must always keep in mind the necessity not only of a truly random specimen, but also of a close match between the actual x-ray optics (nature of incident beam and width of detector slit) and those assumed in the derivation of the equations.

Reflection Methods

The central region of the pole figure is inaccessible to any transmission method and can be explored only by a reflection technique. The specimen must be of effectively infinite thickness or extra corrections will be required.

The most popular is the *Schulz reflection method* [20]. It requires a special specimen holder which allows rotation of the specimen in its own plane about an axis normal to its surface and about a horizontal axis; these axes are shown as *BB´* and *AA´* in Fig. 18. The horizontal axis *AA´* lies in the specimen surface and is initially adjusted, by rotation about the diffractometer axis, to make equal angles with the incident and diffracted beams. After this is done, no further rotation about the diffractometer axis is made. Since the axis *AA´* remains in a fixed position during the other rotations of the specimen, the irradiated surface of the specimen is always tangent to a focusing circle passing through the x-ray source and detector slit. A divergent beam may therefore be used since the diffracted beam will converge to a focus at the detector.

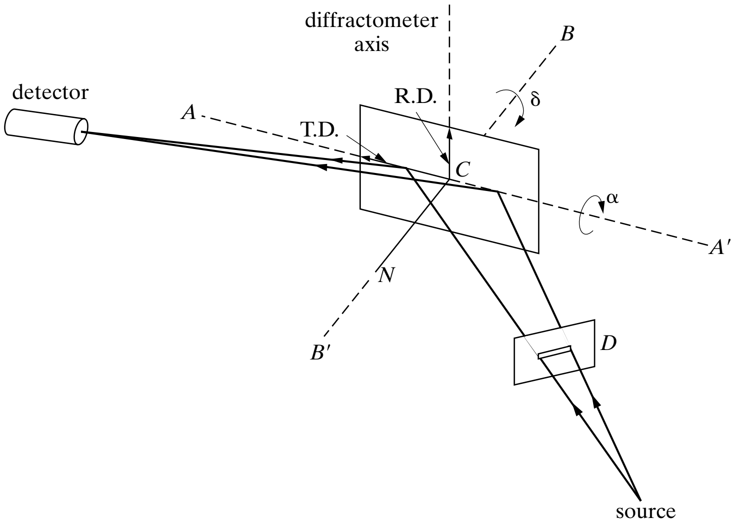

Figure 18 Schulz reflection method.

When the specimen is rotated about the axis AA', the axis BB' normal to the specimen surface rotates in a vertical plane, but CN, the diffraction plane normal remains fixed in a horizontal position normal to AA'. The rotation angles χ and ϕ are shown in Fig. 18.[10] The angle χ is zero when the sheet is horizontal and has a value of 90° when the sheet is in the vertical position shown in the drawing. In this position of the specimen, the diffraction plane normal is at the center of the projection. The angle ϕ measures the amount by which the rolling direction is rotated away from the left end of the axis AA' and has a value of +90° for the position illustrated. With these conventions the angles χ and ϕ may be plotted on the pole figure in the same way as α and δ in the transmission method [Fig. 15(b)].

The great virtue of the Schulz method is that no absorption correction is required for values of χ between 90° and about 40°, i.e., up to about 50° from the center of the pole figure. In other words, a random specimen can be rotated over this range of χ values without any change in the measured intensity of the diffracted beam, provided the specimen has effectively infinite thickness. Under these circumstances, the intensity of the diffracted beam is directly proportional to the pole density in the specimen, without any correction. The constancy of the absorption factor is due essentially to the narrow horizontal slit placed in the primary beam at D (Fig. 18), close to the specimen. The vertical opening in this slit is only about 0.5 mm, which means that the specimen is irradiated only over a long narrow rectangle centered on the fixed axis AA'. It can be shown [20] that a change in absorption does occur, as the specimen is rotated about AA', but it is exactly canceled by a change in the volume of diffracting material, the net result being a constant diffracted intensity for a random specimen when χ lies between 90° and about 40°. To achieve this condition, the reflecting surface of the specimen must be adjusted to accurately coincide with the axis AA' for all values of χ and ϕ. This adjustment is extremely important.

When the specimen is rotated out of the vertical position ($\chi < 90°$) in the sense shown in Fig. 18, the top part moves behind, and the bottom in front of, the focusing circle. The diffracted beam therefore widens at the detector slit and the measured diffracted intensity from a random specimen may decrease as χ departs from 90°. This effect is called the *defocusing error*. It may be minimized by slit adjustment (widening the detector slit and decreasing the vertical opening in slit D) or corrected by calculation [21, 22].

Figure 19 shows a specimen holder suitable for either transmission method and for the Schulz reflection method.

The *Field and Merchant reflection method* [23] is designed for a parallel incident beam, shown simply as a single line in Fig. 20. The specimen is placed initially with the rolling direction vertical, coincident with the diffractometer axis, the transverse direction horizontal, and the plane of the sheet equally inclined to the incident and

---

[10] Designating the rotation angles as χ and ϕ distinguishes the reflection method from the transmission method where the angles are devoted α and δ, respectively.

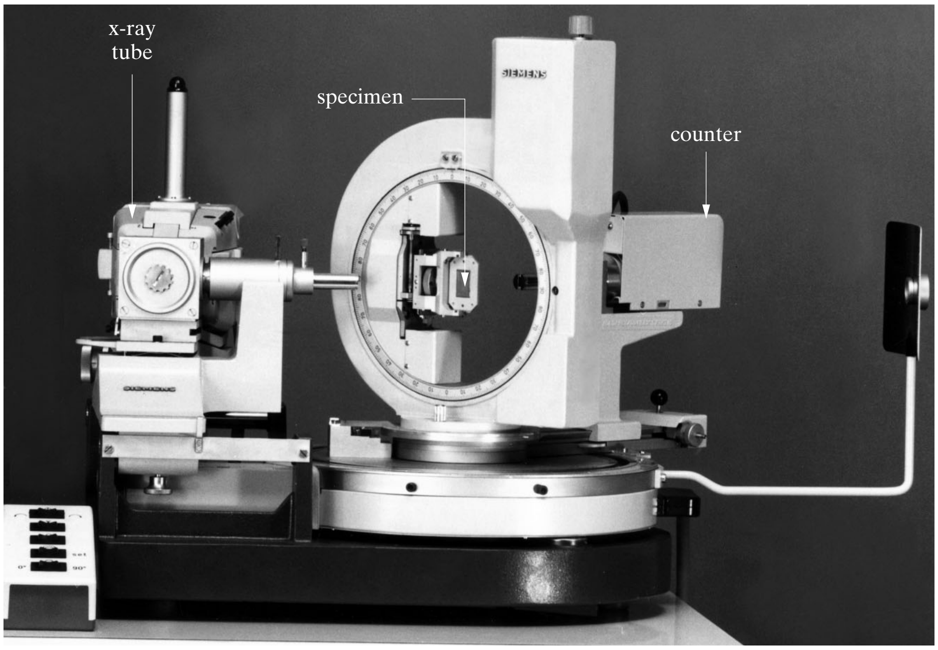

Figure 19 Pole-figure goniometer. The specimen shown is positioned for measurements by the transmission method, and a simple change in the orientation of the specimen holder allows measurements by the Schulz reflection method. The x-ray tube is seen here end-on. This instrument is designed for automatic operation. (Courtesy of Siemens Corporation.)

diffracted beams; the pole *N* of the diffraction planes is then at the center of the projection ($\alpha = 90°$). Counterclockwise rotation of the specimen about the diffractometer axis, which incidentally will narrow the diffracted beam, moves *N* to the left along the equator ($\delta = 0$) of the pole figure. The angle δ is changed by rotating the specimen in its own plane.

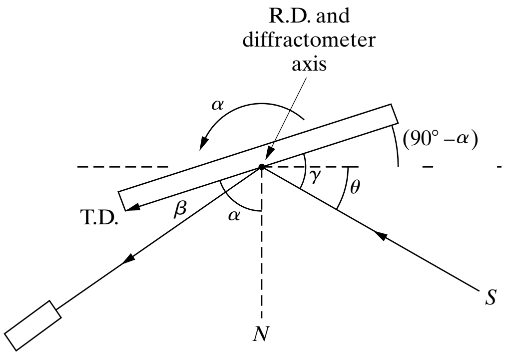

Figure 20 Field and Merchant reflection method. *N* = diffracting plane normal.

Diffracted intensities must be corrected for change in absorption due to change in α. The angles γ and β of incidence and reflection are the same as shown in Fig. 20:

$$dI_D = \frac{I_o ab}{\sin\gamma} e^{-\mu x(1/\sin\gamma + 1/\sin\beta)} dx.$$

For counterclockwise rotation $\gamma = \theta + (90^o - \alpha)$ and $\beta = \alpha - (90^o - \theta)$. Making these substitutions and integrating from x = 0 to ∞, yields the integrated intensity:

$$I_D = \frac{I_O ab}{\mu\{1 - [\cos(\alpha - \theta)/\cos(\alpha + \theta)]\}}. \tag{14}$$

Only the ratio of this quantity to the same quantity for $\alpha = 90^o$ is of interest and it is

$$S = \frac{I_D(\alpha = \alpha)}{I_D(\alpha = 90^\circ)} = 1 - \cot\alpha \cot\theta. \tag{15}$$

Diffracted intensities must be divided by S, which is independent of μ, to give values proportional to pole density. The correction is less severe (S closer to 1), the larger the value of θ; it is therefore advantageous to measure a higher order of the *hkl* reflection measured in transmission. The specimen holder can be identical with that used in the transmission method.

Plotting the Pole Figure

A transmission method yields pole densities covering the outer part of the pole figure, from $\alpha = 0$ to about 50°. A reflection method covers the inner part, from $\alpha =$ about 40° to 90° (i.e., $\chi =$ 90° to 40° in the Schulz method). The pole densities are in arbitrary units, either directly measured diffracted intensities or corrected intensities, depending on the method used. Along those radii of the pole figure where substantial pole density exists in the region of overlap of the two methods ($\alpha =$ 40° to 50°), a normalizing factor is found which will make the pole densities from the transmission method agree with those from the reflection method. The match in the overlap region is rarely perfect, but a substantial disagreement between normalizing factors for different radii points to experimental or computational errors.

Once one set of data is normalized to match the other set contour lines can be constructed on the pole figure at selected levels to connect points of the same pole density, and the result is a pole figure such as Fig. 21. Normally this is done using computer programs such as popLA [25]. Vendor-supplied software or custom written routines. Many, but not all, textures are symmetrical with respect to reflection planes normal to the rolling and transverse directions, and many published pole figures have been determined from measurements made only in one quadrant, with the other quadrants found by assuming symmetry, without supporting data.

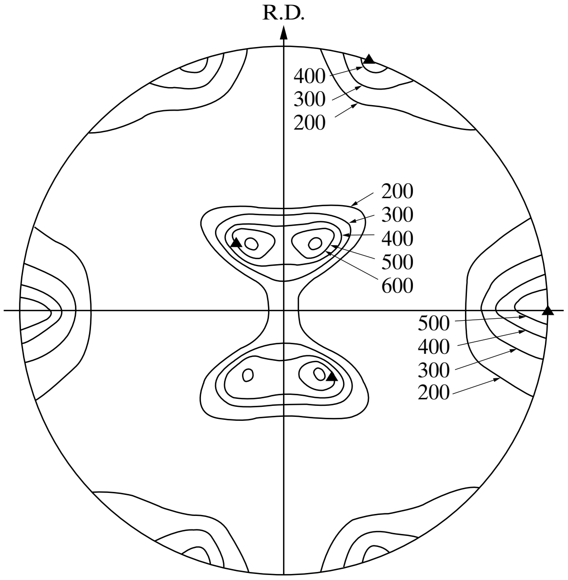

Figure 21 (111) pole figure of alpha brass sheet (70 Cu-30 Zn), cold rolled to a reduction in thickness of 95 percent. Pole densities in arbitrary units. The outer parts of all four quadrants were determined experimentally; the inner parts of the upper right and lower left quadrants were measured, and the other two constructed by reflection. The solid triangles show the (110) [112] orientation. Hu, Sperry, and Beck [24].

The deformation texture of brass sheet (Fig. 21) is fairly sharp, and it is then of interest to know whether or not it can be approximated by an "ideal orientation." To find this orientation successively lay several standard projections over the pole figure, looking for a match between (111) poles and high-density regions. The solid triangles in Fig. 21 show such a match: they represent the (111) poles of a single crystal oriented so that its (110) plane is parallel to the sheet and the [112] direction parallel to the rolling direction. Reflection of these poles in the symmetry planes of the texture, which is equivalent to adding orientations like $(110)[1\bar{1}2]$, will approximately account for all the high-density regions of the pole figure. This texture can therefore be represented by the ideal orientation $\{110\}\langle\bar{1}12\rangle$. It should be emphasized that the pole figure itself is a far better description of the texture than any bare statement of an ideal orientation, which says nothing about the scatter. A quantitative pole figure has about the same relation to an ideal orientation as an accurate contour map of a hill has to a statement of the height, width, and length of the hill.

Pole densities in arbitrary units are not as informative as those expressed in multiples of the pole density of a random specimen, so called "times random" units. The contour lines in Fig. 22 are marked with these units, and one can see at a glance those regions of the pole figure that have a higher, or lower, pole density than random; this pole figure, incidentally, was measured in all four quadrants. The texture represented there, of considerable industrial interest, is messy and cannot be well characterized by ideal orientations. It is approximately a $\langle 111\rangle$ fiber texture, with the fiber axis normal to the plane of the sheet, containing $\{111\}\langle 110\rangle$, called the "cube-on-corner" texture, as its strongest single component [26, 27].

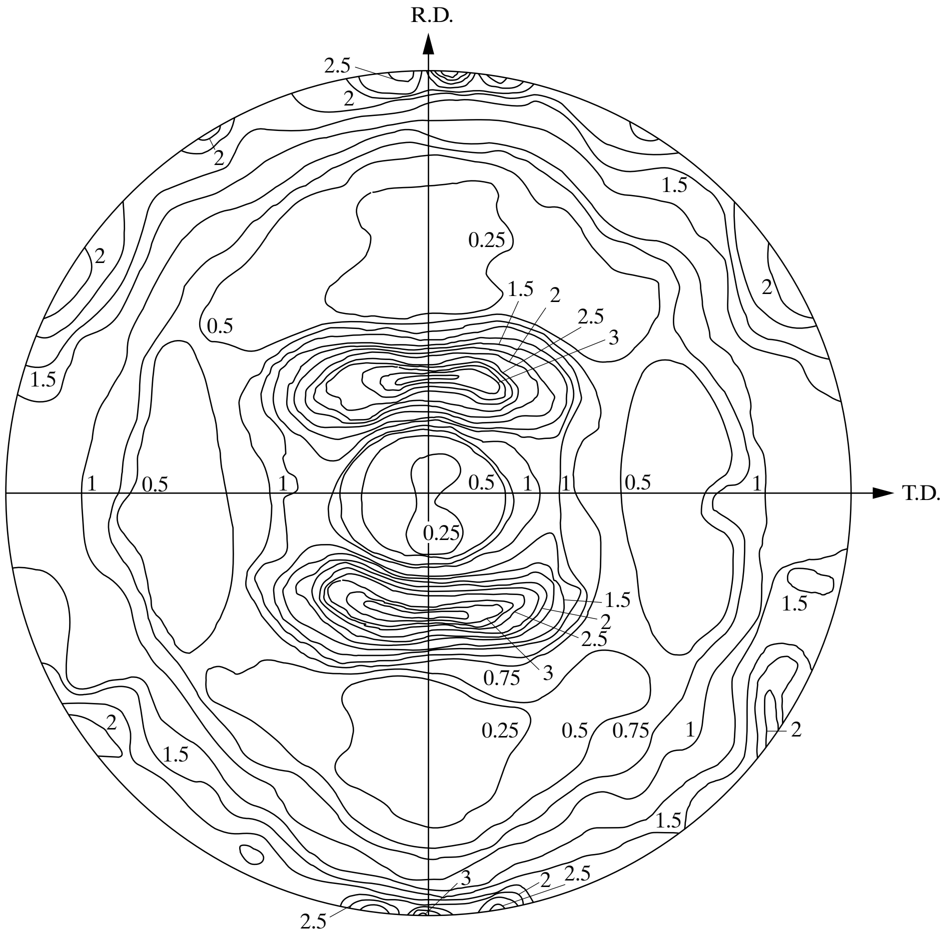

Figure 22 (110) pole figure of recrystallized commercial low-carbon (0.04 percent) sheet steel, aluminum killed, 0.9 mm thick. Pole densities in "times random" units. Determined by a reflection method from composite specimens; see text under "General." Bunge and Roberts [26].

Diffracted intensities, proportional to pole densities, may be put on a times-random basis by comparing them with intensities diffracted by a random specimen [28]. The random specimen should be of the same material as the textured specimen and, for a transmission method, it should have the same value of μt; if not, a correction has to be made that will depend on the transmission method involved. The random specimen itself is usually made by compressing and sintering a power [18, 19]. The randomness of grain orientation in this specimen must be checked by determining its diffraction pattern with a diffractometer in the usual way; the measured integrated intensities of all lines should agree with those calculated.

General

The conditions for optimum specimen thickness in transmission and infinite thickness in reflection are such that the same specimen can serve for both methods. The penalty for exceeding the optimum thickness is not severe: a thickness of double the optimum value for transmission at $\alpha = 0$ reduces the diffracted intensity by only 26 percent (Problem 8).

It may be difficult to make a thin specimen, particularly of a heavy metal, which has the required low, and *uniform*, value of μt throughout. Some investigators have therefore avoided a transmission method altogether by determining only the central portion of the pole figure by reflection; such partial pole figures are useful for some purposes. Others have obtained a complete pole figure by reflecting x-rays from a surface or surfaces inclined to the sheet surface. Several pieces of the sheet are stacked with rolling directions parallel and a composite specimen made by clamping or cementing the stack. If this specimen is cut to expose a surface whose normal makes the same angle, of 54.7°, with the sheet normal and rolling and transverse directions, then measurements on this surface by a reflection method will cover one quadrant of the pole figure [29]. The pole figure of Fig. 22 was derived from reflection measurements on the sheet plane and on sections normal to the rolling and transverse directions.

Errors that can affect texture measurements include the following:

1. If the grain size is too large, as in some recrystallized specimens, the incident beam will not sample enough grains for good statistical accuracy. The specimen holder should then include a mechanical device that will translate the specimen back and forth in its own plane in order to expose more grains to the incident beam.
2. The texture at the surface of a sheet can differ from that in the midplane [24]. When such a texture gradient exists, it must be remembered that the transmission and reflection methods preferentially sample different layers of the same specimen and that the thicknesses of the layers so sampled vary with α in a systematic way.
3. The x-ray optics, particularly slit sizes, must conform to those required by the x-ray method involved. Too narrow a detector slit will exclude a wanted part of the diffraction line; too wide a slit will include some of the background. Too often the background is simply ignored, with the result that measured intensities include both line and background; it would be highly beneficial to eliminate or reduce the background by means of a crystal monochromator, balanced filters, or a pulse-height analyzer. Errors from these sources can be large. They can be almost entirely eliminated by comparing intensities from the textured specimen with intensities measured under identical conditions from a truly random specimen, provided the two specimens differ only in grain orientation. Such a random specimen can be very hard to make. (Note, for example, that an annealed random specimen

will have narrower diffraction lines than a cold-worked textured specimen.)

Because the manual determination of preferred orientation is rather tedious, the process has been automated, and a variety of instruments are available from vendors (Fig. 19). Under computer control, the angular settings α and δ (or χ and ϕ) of the specimen are varied in a prescribed sequence by motor drive, and the diffracted intensity at each setting is recorded, on disk.

The *analysis* of preferred orientation has now gone beyond pole figures, in the direction of a more complete description of the texture. Establishing experimentally that a certain crystal in a sheet has a (100) pole, for example, located at a point on the pole figure specified by the angles α and δ, does not fully specify the orientation of the crystal. These two angles merely describe the orientation of the direction [100], and the crystal might have any rotational position about this axis. A third angle is needed to fix the orientation of the crystal. A full description of the texture would require the specification of three angles (called Ψ, θ, ϕ) for each crystal in the sheet. This information is contained in the *crystal orientation distribution function* or *odf* which is discussed in Sec. 11.

10 THE TEXTURE OF WIRE (DIFFRACTOMETER METHOD)

As mentioned in Sec. 7, if a wire or rod has a true fiber texture, its pole figure will have rotational symmetry about the fiber axis and will resemble Fig. 10 Therefore the pole density must be measured only along a single radius. The angle between the pole N and the fiber axis F.A. is usually called ϕ when dealing with fiber textures.

The Field and Merchant method may be used to measure pole density, and two specimens are required to cover the entire 90° range of ϕ:

1. *Low-ϕ region.* X-rays are diffracted from the cross section of the wire, as in Fig. 23(a). The specimen is a bundle of wires, packed together and cemented into a rectangular hole cut in a thick plastic disc; the wire ends are then ground, polished, and etched. This cross section is made initially parallel to the diffractometer axis and equally inclined to the incident and diffracted beams. The angle ϕ measures the counterclockwise rotation of the specimen about the diffractometer axis from this initial position. Next define a new angle ρ as the acute angle between the specimen surface and the diffraction-plane normal N. The angle α of Eq. (14) and Fig. 20 becomes $\rho = \rho_L = 90^o - \phi$, so that

$$W = \frac{I_D(\rho = \rho)}{I_D(\rho = 90°)} = 1 - \cot\rho\cot\theta. \qquad (16)$$

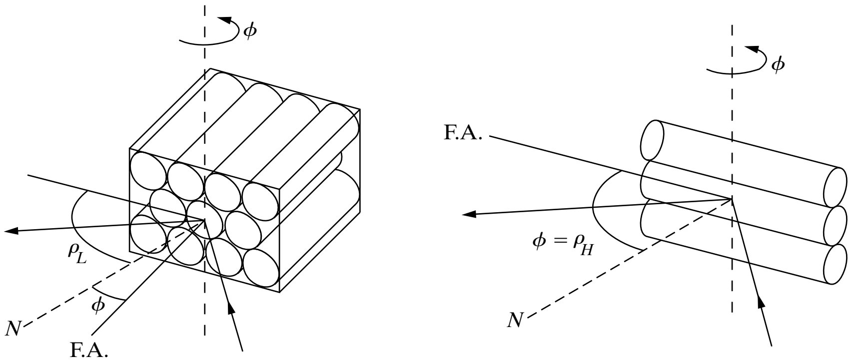

(a) Low-ϕ region

(b) High-ϕ region

Figure 23 Diffraction from composite wire specimens. ϕ is angle between fiber axis F.A. and diffraction-plane normal N. ρ is angle between N and specimen surface.

Diffracted intensities are to be divided by W to obtain numbers proportional to pole density.

2. *High-ϕ region*. X-rays are diffracted from the side of the wire, as in Fig. 23 (b). The specimen is a set of wires glued to a grooved plate. Equation (16) still applies, but now $\alpha = \rho = \rho_H = \phi$.

When the diffracted intensities I_D given by each method have been divided by W and normalized in the region of overlap, a set of numbers I is obtained which is proportional to pole density. Figure 24 shows an I, ϕ curve obtained in this way for the inside texture of cold-drawn aluminum wire. The peaks at $\phi = 0$ and 70^o are due to the strong [111] component of the texture and the peak at 55^o to a weak [100] component.

By analysis of an I, ϕ pole density curve the pole densities can be put on a times-random basis and determine the relative amounts of the components in a double or multiple fiber texture can be determined [31-33].

Imagine a reference sphere of unit radius centered on the wire (Fig. 25). The element of area on the surface is $dA = 2\pi \sin\phi \, d\phi$. If I is the pole density, the number of (hkl) poles in this area is $dn = I \, dA = 2\pi \, I \sin\phi \, d\phi$, and the total number of poles on the surface of a hemisphere is

$$n = 2\pi \int_0^{\pi/2} I \sin\phi \, d\phi. \tag{17}$$

If I_r is the pole density of a random specimen, then $n = I_r(2\pi)$. Therefore

$$I_r = \int_0^{\pi/2} I \sin\phi \, d\phi. \tag{18}$$

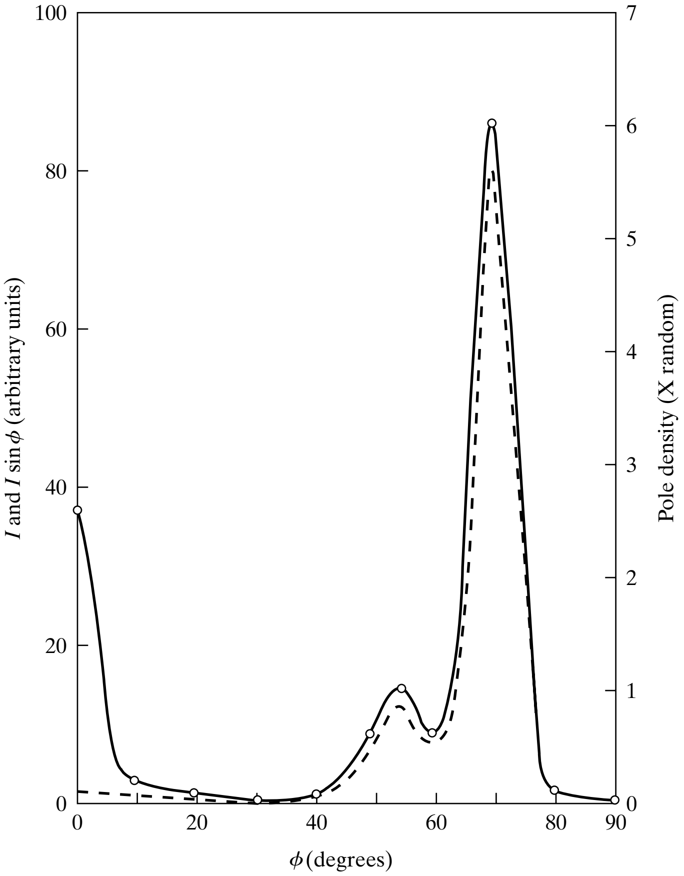

Figure 24 (111) pole density I (full curve) and $I \sin \phi$ (dashed) as a function of ϕ for a cold-drawn aluminum wire, reduced in area 95 percent by drawing, and etched to 80 percent of the as-drawn diameter. Final specimen diameter 1.3 mm, Cr Kα radiation, 222 reflection. Freda *et al.* [30].

This integral is simply the area under a curve of $I \sin \phi$ vs. ϕ, and this area in turn is equal to the average ordinate of the curve $\langle I \sin \phi \rangle_{\text{av}}$ times $\pi/2$. Therefore,

$$I_r = \frac{\pi}{2} \langle I \sin \phi \rangle_{av}. \tag{19}$$

This relation is valid whether the n poles are distributed randomly on the sphere or in some preferred manner, and it allows determination of I_r from measurements on a textured specimen. From experimental I, ϕ data construct a curve of $I \sin \phi$ vs. ϕ, shown dashed in Fig. 24, determine its average ordinate, and find I_r from Eq. 19. Once I_r is known (3 units for this wire), the I, $\sin \phi$ pole density curve can be put on a times-random basis (right-hand ordinate). (Because the angular aperture of the detector slit is not small relative to ϕ when ϕ is small, the true pole density I near

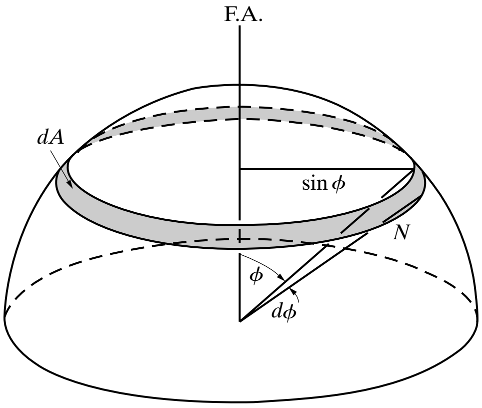

Figure 25 Element of area on reference sphere.

$\phi = 0$ can only be approximated [32]. Therefore extrapolate the $I \sin \phi$ curve near $\phi = 0$ rather than extend it to zero, as is mathematically indicated.)

The amount of each component in a double texture is proportional to the area under the peak(s) due to that component on a curve of $I \sin \phi$ vs. ϕ; knowledge of the multiplicities involved can reduce the number of peaks that need be considered. The multiplicity of {111} poles is 8 for a sphere and 4 for a hemisphere. In Fig. 24 the [100] component puts four {111} poles per grain under the peak at 55º; the [111] component, on the other hand, has one {111} pole at 0º and three at 70º. Because of the uncertainty in the area of the peak at 0º, the area ascribed to the [111] component can be taken as 4/3 times the area of the peak at 70º. Therefore,

$$\frac{\text{Volume fraction of } [111] \text{ component}}{\text{Volume fraction of } [100] \text{ component}} = \frac{\left(\frac{4}{3}\right)(\text{area of } 70^\circ \text{ peak})}{(\text{area of } 55^\circ \text{ peak})}.$$

For the aluminum wire, this calculation led to volume fractions of 0.85 for the [111] component and 0.15 for the [100].

Note that this result was obtained without making any use of the measurements made at ϕ values less than 40°. Thus a complete pole density curve is not necessary for the evaluation of a texture, provided the texture is sharp enough to produce well resolved peaks in the high-ϕ region. This is a fortunate circumstance, because high-ϕ measurements require little or no specimen preparation.

Preferred orientation in wire does not always take the form of a pure fiber texture. For example, the deformation texture of iron wire is usually considered to be a [110] fiber texture, but Leber [34] showed that a *cylindrical texture* was also present. Such a texture may be regarded as a sheet texture, (100) [011] for iron, wrapped around the wire axis. Thus at any point on the wire surface, a (100) plane is tangent to the surface and a [011] direction parallel to the wire axis. The presence of a cylindrical component in a fiber texture is disclosed by anomalies in the $I \sin \phi$ curve:

the areas under the peaks ascribed to the fiber-texture component will not be in the ratio to be expected from the multiplicities [35].

11 INVERSE POLE FIGURES

A pole figure shows the distribution of a selected crystallographic direction relative to certain directions in the specimen. Texture data may also be presented in the form of an *inverse pole figure*, which shows the distribution of a selected direction *in the specimen* relative to the crystal axes. The projection plane for an inverse pole figure is therefore a standard projection of the crystal, of which only the unit stereographic triangle need be shown. Both wire and sheet textures may be represented.

Figure 26(a) is an inverse pole figure for the inside texture of an extruded aluminum rod, showing the density distribution of the rod axis on a times-random basis. It was derived by a trial-and-error method [31] from pole density curves, as in Fig. 24, for the (001), (111), and (113) poles. Note the concentrations of the rod axis at [001] and [111], indicating a double fiber texture; the volume fractions of the [001] and [111] components were estimated as 0.53 and 0.47, respectively. Note that an inverse pole figure shows immediately the crystallographic "direction" of the scatter. In this double texture, there is a larger scatter of each component toward one another than toward [011].

Sheet textures require three separate inverse pole figures to show the distribution of the sheet normal, rolling direction, and transverse direction. Figure 26(b) is such a projection for the normal direction of the steel sheet whose (110) pole figure was given in Fig. 22; it was calculated from the orientation distribution function mentioned in Sec. 9. The distribution of the normal direction is also shown in (c), for the same material, but this distribution was measured directly in the following way. A powder pattern is made of the sheet in a diffractometer by the usual method, with the sheet equally inclined to the incident and diffracted beams i.e., in the normal parafocusing geometry. The intensity of any *hkl* reflection, relative to that from a random specimen, is then proportional to the volume fraction of grains having their (*hkl*) planes parallel to the sheet surface, or to the volume fraction of grains having the sheet normal parallel to the (*hkl*) normal. Stated another way, and with specific reference to Fig. 26(c), the probability of the sheet normal in this steel being parallel to [111] is 3.97 times normal. Similar data for the rolling direction, for example, are obtained by diffracting x-rays from a surface normal to the rolling direction, a surface exposed by sectioning a stack of sheets. This method produces only as many data points in the stereographic triangle as there are lines on the powder pattern and is therefore better suited to materials of low crystal symmetry than to cubic materials.

The inverse pole figures of Figs. 2.6(b) and (c) both show a high density of (111) poles parallel to the sheet normal and are therefore consistent with the [111] quasi-fiber texture mentioned in Sec. 9.

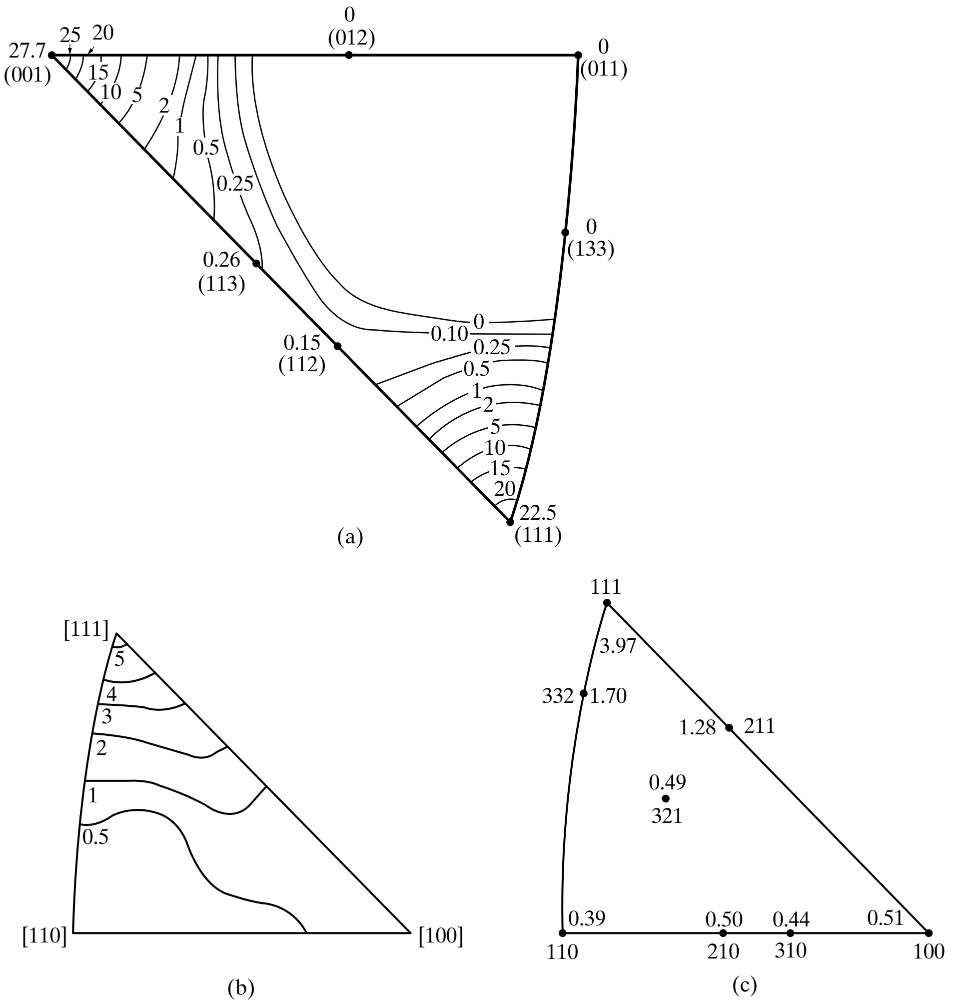

Figure 26 Inverse pole figures. (a) Distribution of axis of aluminum rod, extruded at 450°F to a reduction in area of 92 percent and a final diameter of 23 mm. Jetter, McHargue, and Williams [31]. (b) and (c) show the distribution of the sheet normal for the steel sheet of Fig. 22. Bunge and Roberts [26].

The inverse pole figure is the best way to represent a fiber texture, but it offers no advantage over a direct pole figure in the description of a sheet texture. Inverse or direct, a pole figure is a two-dimensional plot that fixes, at a point, only a direction in space, be it crystal space or specimen space. Only the three-dimensional "plot" afforded by the orientation distribution (see below) can completely describe the orientations present, and this approach, being quite general, is just as applicable to fiber textures as it is to sheet.

12 ORIENTATION DISTRIBUTION FUNCTIONS

In Sec. 9, three angles were seen to be needed to uniquely fix the orientation of a given crystal relative to the sample coordinate system (i.e., rolling direction, sheet normal, etc.). Methods of calculating this orientation distribution function from pole figures have been developed by Roe, Bunge, and Williams [36-39]. The mathematics involved are complex and the calculations extensive, but this approach is powerful and of great generality.

The orientation distribution function for a cubic material in sheet form can be calculated from any two experimental pole figures, for example, the (100) and (110). Once the distribution is known, any other desired pole figure can be calculated, for example, the (111); it need not be measured. It is even possible to calculate the orientation distribution from a set of partial pole figures, determined by a reflection method out of 60° from the center of the pole figure ($\gamma = 30^o$) [40]. The orientation distribution function itself is usually presented in the form of crystal density plots, in which the density is shown as a contour map, for example, in angle space. One method uses spherical polar coordinates θ and ψ to specify the direction of the rotation axis relating the crystal axes to the sample coordinate system and rotation angle ω about the axis. Euler angles φ_1, φ_2 and Φ can also be used (Fig. 27). A series of constant φ_2 is typically used to present all of the information, and Fig. 28 gives an example for rolled brass [41].

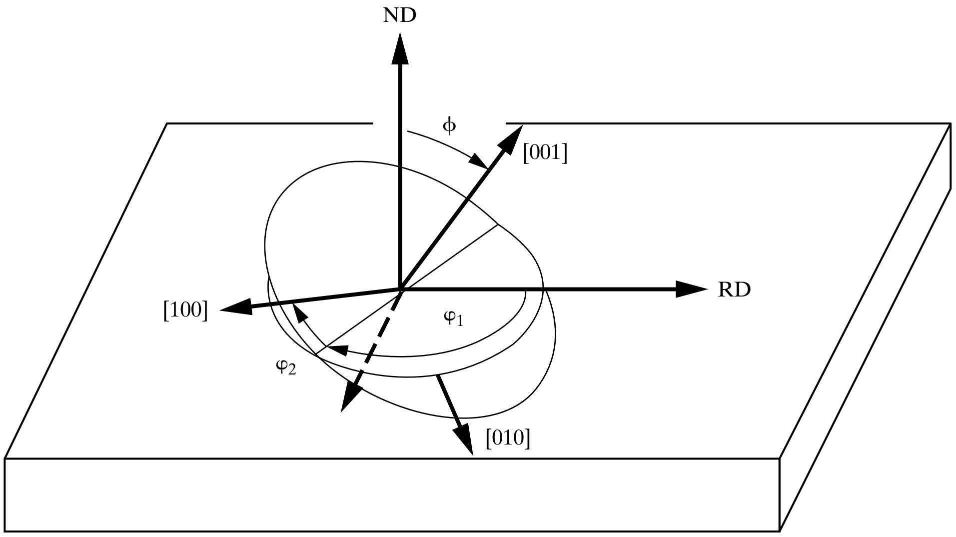

Figure 27 Definition of orientation of crystal axes in terms of Euler angles φ_1, ϕ and φ_2 defined relative to the sample reference directions, here the rolling direction RD and the normal direction ND. After [41].

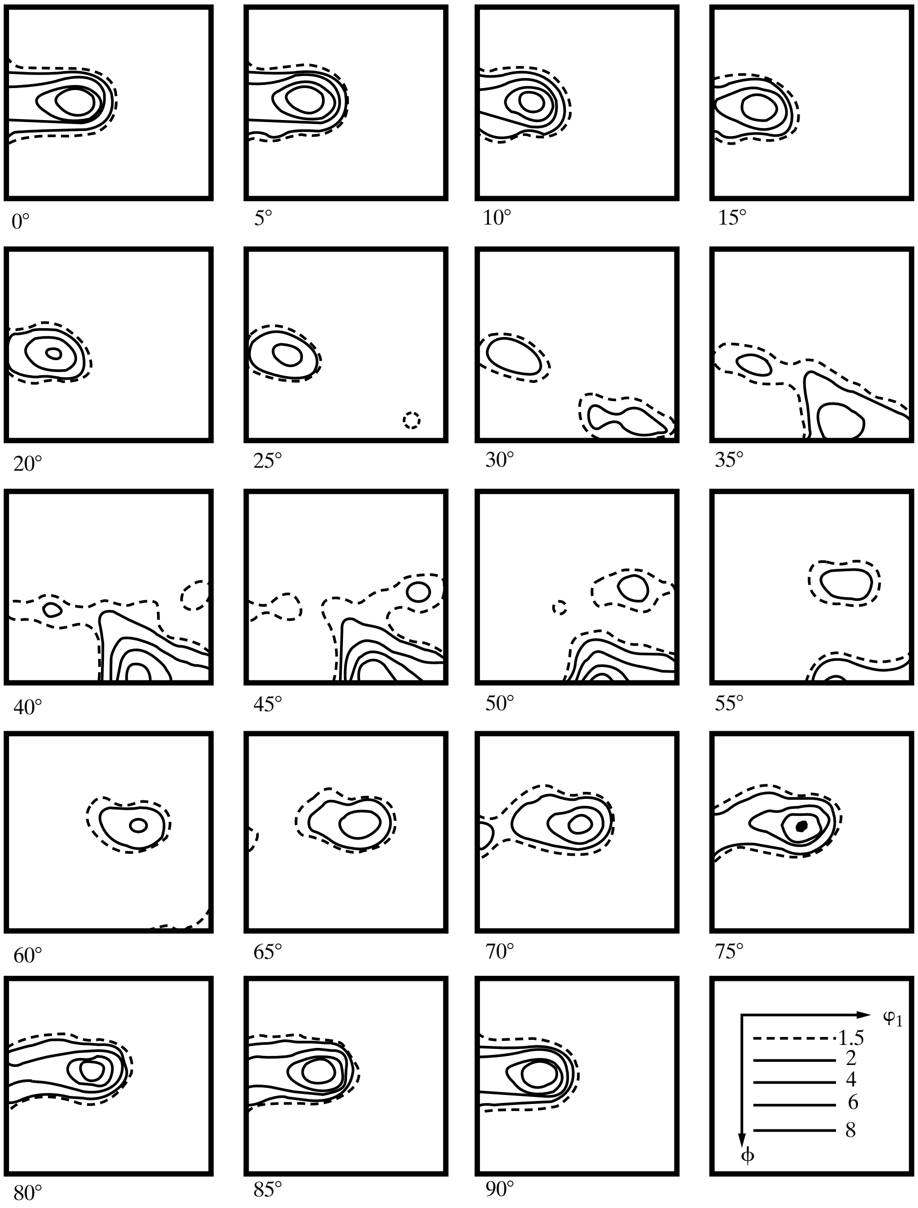

Figure 28 Orientation distribution function for brass cold-rolled 95%. Planes of constant φ_2 spaced every 5° are shown. The contours of equal density (times random) and orientations of φ_1 and ϕ are shown at the lower right. [41].

13 AMORPHOUS AND SEMI-AMORPHOUS SOLIDS

This chapter has concentrated on crystalline materials. X-ray diffraction can also furnish structural information about amorphous and semi-amorphous solids, even though the "structure" is much more diffuse.

Most glasses are amorphous. They yield a pinhole pattern consisting only of a broad, diffuse halo around the central spot, corresponding to the single maximum in the scattering curve of crystalline solids, amorphous solids, liquids, and monatomic gases. Analysis of this curve yields such information as average interatomic distances and average number of atoms around a given atom. The theory of diffraction by amorphous substances is beyond the scope of this chapter and is treated in the books of Guinier [G. 30] and Warren [G. 20].

Many polymeric materials are partly crystalline: They are composed of very long molecules, generally in a state of great disarray but here and there organized into ordered regions usually called "crystallites." These regions, typically very small and highly strained, produce very broad diffraction lines. By comparing the integrated intensity of these lines with that of the broad halo due to the amorphous regions, the volume fraction of crystallites, called the "degree of crystallinity" of the polymer, can be estimated. X-ray diffraction can also disclose crystallite size, usually by means of the Scherrer equation for line broadening and preferred orientation. The latter condition is quite common in fibers and sheets and is studied by one or more of the methods described in this chapter. In fact, the alignment of crystallites in natural fibers like cotton and silk has long been known and is the origin of the term "fiber texture" to describe the preferred orientation found in metal wires. The particular applications of x-ray methods to the study of polymers is the subject of a book by Alexander [42].

14 SUMMARY

In this chapter various aspects of the structure of polycrystalline aggregates and the quantitative effects of variations in crystal size, quality, and orientation on the diffraction pattern have been examined. Although a complete investigation of the structure of an aggregate requires a considerable amount of time and rather complex apparatus, the very great utility of the simple pinhole photograph should not be overlooked. It is surprising how much information an experienced observer can obtain simply by inspection of a pinhole photograph, without making any measurements on the film and without any knowledge of the specimen, i.e., without knowing its chemical identity, crystal structure, or even whether it is amorphous or crystalline. The latter point can be settled at a glance, since Debye rings indicate crystallinity and broad haloes an amorphous condition. If the specimen is crystalline, the conclusions that can be drawn from the appearance of the lines are summarized in Table 3.

TABLE 3

Appearance of diffraction lines	Condition of specimen
Continuous	Fine-grained (or coarse-grained and cold-worked)
Spotty	Coarse-grained
Narrow (1)	Strain-free
Broad (1)	Residual stress and possibly small particle size (if specimen is a solid aggregate) Small particle size (if specimen is a brittle powder)
Uniform intensity	Random orientation (2)
Nonuniform intensity	Preferred orientation

(1) Best judged by noting whether or not the Kα doublet is resolved in back reflection.
(2) Or possibly presence of a fiber texture, if the incident beam is parallel to the fiber axis.

PROBLEMS

1 Prove the statement made in Sec. 4-10 that the effective irradiated volume of a flat plate specimen in a diffractometer is constant and independent of θ.
2 For given values of θ and μ, which results in a greater effective depth of x-ray penetration, a back-reflection pinhole camera or a diffractometer?
3 Assume that the effective depth of penetration of an x-ray beam is that thickness of material which contributes 99 percent of the total energy diffracted by an infinitely thick specimen. Calculate the penetration depth in μm for a low-carbon steel specimen under the following conditions:

a) Diffractometer; lowest-angle reflection; Cu $K\alpha$ radiation.
b) Diffractometer; highest-angle reflection; Cu $K\alpha$ radiation.
c) Diffractometer; highest-angle reflection; Cr $K\alpha$ radiation.
d) Back-reflection pinhole camera; highest-angle reflection; Cr $K\alpha$ radiation.

4 If the same hkl reflection from a given material is examined in a diffractometer with successively different wavelengths, how does the penetration depth x vary with λ? (Assume the wavelengths used lie on the same branch of the absorption curve of the material.)
5 (a)A transmission pinhole photograph is made of a sheet specimen of thickness t and linear absorption coefficient μ. Show that the fraction of the total diffracted energy in any one reflection contributed by a layer of thickness w is given by

$$T = \frac{e^{-\mu[x+(t-x)/\cos 2\theta]}\left[e^{-\mu w(1-1/\cos 2\theta)} - 1\right]}{e^{-\mu t} - e^{-\mu t/\cos 2\theta}},$$

where x is the distance to the side of the layer involved, measured from the side of the specimen on which the primary beam is incident.

b) A transmission pinhole photograph is made of a sheet of aluminum 0.5 mm thick with Cu $K\alpha$ radiation. Consider only the 111 reflection which occurs at $2\theta = 38.4^{\circ}$. Imagine the sheet to be divided into four layers, the thickness of each being equal to one-fourth of the total thickness. Calculate T for each layer.

6 A transmission pinhole pattern is made with Co $K\alpha$ radiation of an iron wire having an almost perfect [110] fiber texture. The wire axis is vertical. How many high-intensity maxima will appear on the lowest-angle 110 Debye ring and what are their azimuthal angles on the film?

7 An electroplated layer of copper on sheet steel is examined in a back-reflection pinhole camera with Cu $K\alpha$ radiation incident at right angles to the sheet surface. Assume the copper has a fiber texture with the fiber axis $[uvw]$ scattered by an angle β in every direction about the sheet normal. How large must β be for the 420 Debye ring to appear on the film if the fiber axis $[uvw]$ is (a) [110], (b) [100]?

8 Consider the diffraction geometry for $\alpha = 0$ in the transmission method for determining preferred orientation and for $\alpha = 90^{\circ}$ in the reflection method. Let t_{inf} be the infinite thickness required in the reflection method, and assume t_{inf} is that thickness which would diffract 99 percent of the intensity diffracted by a specimen of truly infinite thickness. Let t_{opt} be the optimum thickness for the transmission method.

a) Show that $t_{inf}/t_{opt} = 2.30 \tan\theta$.

b) If the thickness t of a transmission specimen is 2topt, by how much is the diffracted intensity decreased?

9 On a stereographic projection parallel to the surface of a rolled sheet, show (a) the positions of the (110) poles, represented by small ellipses, for the ideal orientation $\{111\}\langle 110\rangle$, including the positions due to reflection symmetry, and (b) the lines showing the positions of the (110) poles for a $\langle 111\rangle$ fiber texture, with the fiber axis normal to the plane of the sheet. Compare your result with the experimental (110) pole figure for low-carbon sheet steel in Fig. 22.

REFERENCES

The following books are listed more or less in the order they are encountered in the text

G.10 Charles S. Barrett and T. B. Massalski. *Structure of Metals*, 3rd ed. (New York: McGraw-Hill, 1966). A classic book on the crystallographic aspects of physical metallurgy. Really two books in one, the first part dealing with the theory and methods of diffraction of x-rays, electrons, and neutrons; the second part with the structure of metals in the wider sense of the word.

Very lucid account of stereographic projection. Stress measurement, phase transformations, preferred orientation.

G.17 Harold P. Klug and Leroy E. Alexander. *X-Ray Diffraction Procedures*, 2nd ed. (New York: Wiley, 1974). Contains a great deal of useful detail on the theory and operation of powder cameras and diffractometers. Covers the following topics in depth: chemical analysis by diffraction, parameter measurement, line-broadening analysis, texture determination, stress measurement, and studies of amorphous materials. Single-crystal methods are not included

G.20 B. E. Warren. *X-Ray Diffraction* (Reading, MA: Addison-Wesley, 1969). Excellent advanced treatment, in which the author takes pains to connect theoretically derived results with experimentally observable quantities. Stresses diffraction effects due to thermal vibration, order-disorder, imperfect crystals, and amorphous materials. Includes a treatment of the dynamical theory of diffraction by a perfect crystal.

G.30 A. Guinier. *X-Ray Diffraction in Crystals, Imperfect Crystals, and Amorphous Bodies* (San Francisco: W. H. Freeman, 1963 and reprinted by Dover 1994). Largely theoretical and more advanced than [G.13].

G.34 Andr é Guinier and Gerard Fournet. *Small-Angle Scattering of X-Rays* (New York: Wiley, 1955). A full description of small-angle scattering phenomena, including theory, experimental technique, interpretation of results, and applications.

G.35 G. E. Bacon. *Neutron Diffraction*, 2nd ed. (Oxford: Clarendon Press, 1962). Theory and practice of neutron diffraction, with applications to magnetic materials, structure determination, small-angle scattering, and amorphous materials.

G.36 *Experimental Techniques of Texture Analysis*, H. J. Bunge, ed. (Obervise, Germany: Deutsche Gesellschaft, Metallkunde, 1986). A full description of the various techniques.

G.37 *Quantitative Texture Analysis*, H. J. Bunge and C. Esling, eds. (Obervise, Germany: Deutsche Gesellschaft, Metallkunde, 1986). Analysis of texture.

ANSWERS TO SELECTED PROBLEMS

2. Diffractometer

5. b) 0.11, 0.17, 0.28, and 0.44, listed in the order in which the incident beam traverses the layers

8. b) Decreased by 26 percent

This page intentionally left blank

Stress Measurement

1 INTRODUCTION

When a polycrystalline piece of metal is deformed elastically in such a manner that the strain is uniform over relatively large distances, the lattice plane spacings in the constituent grains change from their stress-free value to some new value corresponding to the magnitude of the applied stress, this new spacing being essentially constant from one grain to another for any particular set of planes similarly oriented with respect to the stress. This uniform macrostrain, causes a *shift* of the diffraction lines to new 2θ positions. On the other hand, if the metal is deformed plastically, the lattice planes usually become distorted in such a way that the spacing of any particular (*hkl*) set varies from one grain to another or from one part of a grain to another. This nonuniform microstrain causes a *broadening* of the corresponding diffraction line. Actually, both kinds of strain are usually superimposed in plastically deformed crystalline materials, and diffraction lines are both shifted and broadened, because not only do the plane spacings vary from grain to grain but their mean value differs from that of the undeformed metal.

The focus here will be the line shift due to uniform strain. From this shift the strain may be calculated and, knowing the strain, the stress can be determined, either by a calculation involving the mechanically measured elastic constants of the material, or by a calibration procedure involving measurement of the strains produced by known stresses. X-ray diffraction can therefore be used as a method of "stress" measurement. Note, however, that stress is not measured directly by the x-ray method or, for that matter, by any other method of "stress" measurement. It is always d that is measured, and, if d_0 is known, the strain: the stress is determined indirectly, by calculation or calibration.

The various methods of "stress" measurement differ only in the kind of strain gauge used. In the electric-resistance method for the measurement of applied stress, the gauge is a short length of fine wire or foil cemented to the surface of the metal being tested; any strain in the metal is shared by the gauge, and any extension or contraction of the gauge is accompanied by a change in its resistance, which can

From Chapter 15 of *Elements of X-Ray Diffraction*, Third Edition. B.D. Cullity, S.R. Stock.

therefore be used as a measure of strain. In the x-ray method, the strain gauge is the spacing of lattice planes.

In principle, the x-ray method is applicable to any crystalline material. While it has had some application to stress measurement in ceramics and rocks, its major use is the measurement of residual stress in metals and alloys, X-ray diffraction, for example, has been used to measure stresses around a fatigue crack [1], in different phases within a sample [2], and crystalline thin films used in microelectronics applications [3]. The availability of synchrotron x-ray microbeans with diameters below 1 μm offers the possibility of measuring stresses as a function of position within individual sub-grains, [4]. Neutron diffraction may also be used to great effect for studying stresses nondestroctively in the interior of large components as can very hard X-ray beams available at synchrotron radiation sources as APS.

X-ray method has been reviewed by Barrett and Massalski [G.16] and, by Klug and Alexander [G.17]. The monograph by Noyan and Coher [G.18] covers x-ray and neutron diffraction techniques in great detail. Another source of papers on the current state of the art is *Advances in X-ray Analysis* [G.39] which appears annually.

2 APPLIED STRESS AND RESIDUAL STRESS

Before the x-ray method is examined in any detail, it is advisable to consider first a more general subject, namely, the difference between applied stress and residual stress, and to gain a clear idea of what these terms mean. Consider a metal bar deformed elastically, for example in uniform tension. The *applied stress* is given simply by the applied force per unit area of cross section. If the external force is removed, the stress disappears, and the bar regains its initial stress-free dimensions. On the other hand, there are certain operations that can be performed on a metal part, which will leave it in a stressed condition even after all external forces have been removed. This stress, which persists in the absence of external force, is called *residual stress*.

For example, consider the assembly shown in Fig. 1(a). It consists of a hollow section through which is passed a loosely fitting bolt with threaded ends. If nuts are screwed on these ends and tightened, the sides of the assembly are compressed and the bolt is placed in tension. The stresses present are residual, inasmuch as there are no external forces acting on the assembly as a whole. Notice also that the tensile stresses in one part of the assembly are balanced by compressive stresses in other parts. This balance of opposing stresses, required by the fact that the assembly as a whole is in equilibrium, is characteristic of all states of residual stress.

An exactly equivalent condition of residual stress can be produced by welding a cross bar into an open section, as shown in Fig. 1(b). It is reasonable to assume that, at the instant the second weld is completed, a substantial portion of the central bar is hot but that the two side members are far enough from the heated zone to be at room temperature. On cooling, the central bar tries to contract thermally but is restrained by the side members. It does contract partially, but not as much as it

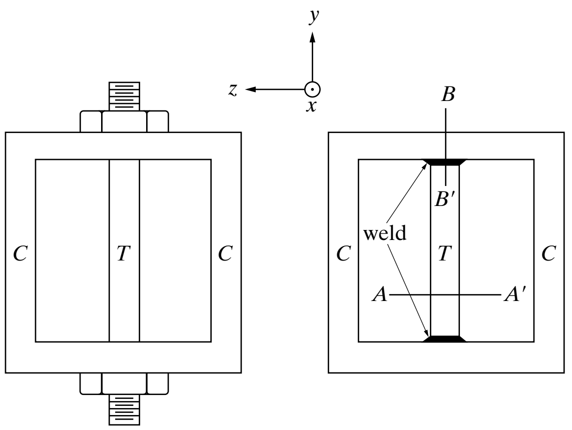

Figure 1 Examples of residual stress. T = tension, C = compression.

(a) (b)

would if it were free, and the end result is that the side members are placed in compression and the central rod in tension when the whole assembly is at room temperature. Residual stress is quite commonly found in welded structures, which are often called *weldments*. Actually, the residual stress state in the weldment of Fig. 1(b) is more complex than might at first appear. Across the section *AA'* the stress σ, is entirely tensile and constant. But on *BB'*, which crosses the weld itself, the stress σ_x in the z direction varies both in magnitude and sign with the position y of the point considered. Numerous studies of welds have shown that σ_y is tensile (positive) in the weld and compressive (negative) on either side.

Plastic flow can also set up residual stresses. The beam shown in Fig. 2(a) is supported at two points and loaded by two equal forces F applied near each end. At any point between the two supports the stress in the outside fibers is constant, tensile on the top of the beam and compressive on the bottom. These stresses are a maximum on the outside surfaces and decrease to zero at the neutral axis, as indicated by the stress diagram at the right of (a). This diagram shows how the longitudinal stress varies across the section *AA'*, when all parts of the beam are below the elastic limit. Suppose the load on the beam is now increased to the point where the elastic limit is exceeded, not only in the outer fibers but to a considerable depth. Then plastic flow will take place in the outer portions of the beam, indicated by shading in (b), but there will be an inner region still only elastically strained, because the stress there is still below the elastic limit. The stresses above the neutral axis are still entirely tensile, both in the elastically and plastically strained portions, and those below entirely compressive. If the load is now removed, these stresses try to relieve themselves by straightening the beam. Under the action of these internal forces, the beam does partially straighten itself, and to such an extent that the stress in the outer regions is not only reduced to zero but is actually changed in sign, as indicated in (c). The end result is that the unloaded beam contains residual compressive stress in its top outside portion and residual tensile stress

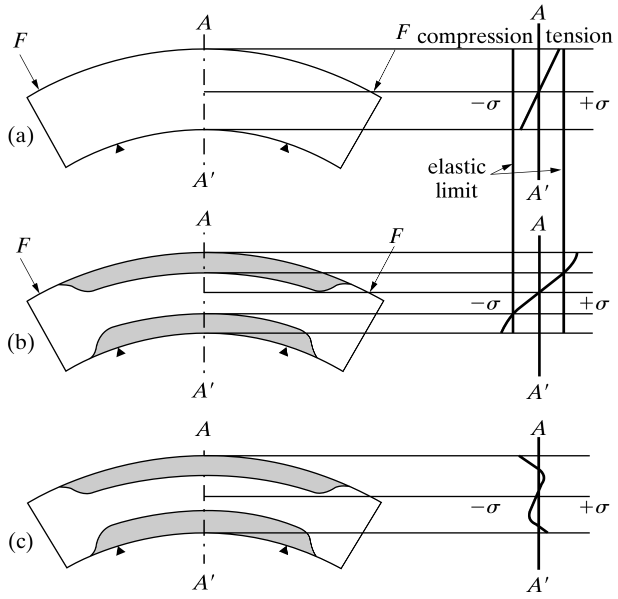

Figure 2 Residual stress induced by plastic flow in bending: (a) loaded below elastic limit; (b) loaded beyond elastic limit; (c) unloaded. Shaded regions have been plastically strained.

in its lower outside portion. It is quite common to find residual stress in metal parts which have been plastically deformed, not only by bending but by rolling, drawing, machining, grinding, etc.

Note that the service stress in any loaded machine or structure is the algebraic sum of the applied stress, due to the service load, and any residual stress that may have existed before the service load was applied. If the residual stress is not known, neither is the service stress. When the service stress reaches dangerous levels, failure occurs. Interest in residual stress stems mainly from the role it plays in three kinds of metal failure: fatigue failure, brittle fractures in general, and stress-corrosion cracking.

Applied stress is easy to measure. An electric-resistance gauge is cemented to the unloaded part, and gauge readings are made before and after the load is applied. The difference in the gauge readings gives the strain, and multiplication of the strain by Young's modulus E gives the applied stress.

Residual stress is more difficult to measure, and there are only three practical methods of doing it:

1. *X-ray diffraction*. This method is nondestructive for the measurement of near-surface stress. If the stress is to be measured at some point below the surface, (generally below depths of $2/\mu$) material must be removed down to that point to expose a new surface for x-ray examination; the x-ray method then becomes destructive. Ordinarily, however, one is most interested in the stress in the near-surface volume of the material, where the applied stress is usually highest and where failures usually originate.

2. *Neutron diffraction* Because neutrons suffer much less attenuation than x-rays in most materials, neutron diffraction can be used to measure nondestructively the stresses within large components. Neutron fluxes, however, are much lower than those for x-rays, and the reactors used to generate the neutrons are scarce.
3. *Dissection (mechanical relaxation)*. This method is inherently destructive, even for the measurement of surface stress, and slow. Part of the residually-stressed object is removed, by cutting or some other method. This removal upsets the pre-existing balance of forces, with the result that the remainder of the object mechanically relaxes (strains) more or less completely. If this strain is measured, the stress originally existing can be computed. For example, suppose the stress in the side members of the weldment in Fig. 1(b) must be measured. A gauge, to measure strain in the y direction is fixed on one of these members. Cutting through the central rod along AA' allows the side members, originally in compression, to elongate to their stress-free length, and the gauge shows a strain of $+\varepsilon_y$. Before the cut was made, the strain relative to the stress-free state must have been $-\varepsilon_y$, so that the original stress σ, was $-\varepsilon_y E$. Similarly, the residual stress at various depths of the bent beam of Fig. 2(c) may be calculated from the change in curvature that results from successive removal of layers parallel to the neutral plane.

The x-ray and neutron methods, being nondestructive, have the great advantage that repeated measurements are possible on the same specimen. For example, one may measure stress before and after some treatment designed to produce or modify residual stress. Or one may measure residual stress on a machine component at various stages in its service life.

Note also that the diffraction method measures the *existing* stress, whether it be solely residual or the sum of residual and applied. It therefore has the capability of measuring the actual service stress in a machine or structure under a service load.

Strictly speaking, neither stresses nor even strains are measured by diffraction. Only changes in d-spacing are measured, and it is important to remember that converting measured d values to strain and strains to stresses involves certain assumptions, and the conversion should never be treated as trivial.

3 GENERAL PRINCIPLES

The x-ray method is best approached by first considering the case of uniaxial stress, where the stress acts only in a single direction, even though this condition is rare in practice. The more general cases of biaxial and triaxial stresses will be covered later.

Consider a cylindrical rod of cross-sectional area A stressed elastically in tension by a force F (Fig. 3). There is a stress $\sigma_y = F/A$ in the y direction but none in the x or z directions. (This stress is the only *normal stress* acting; there are also *shear*

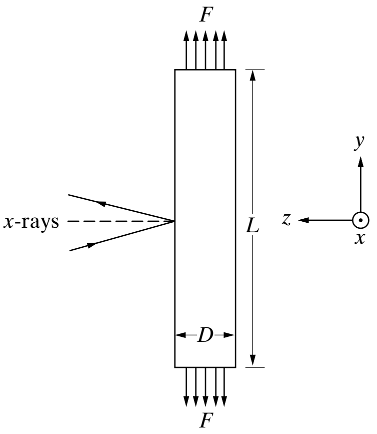

Figure 3 Bar in pure tension, with diffraction planes parallel to axis.

stresses present, but these are not directly measurable by x-ray diffraction.) The stress σ_y, produces a strain ε_y in the y direction given by

$$\varepsilon_y = \frac{\Delta L}{L} = \frac{L_f - L_o}{L_o},$$

where L_o and L_f are the original and final lengths of the bar. This strain is related to the stress by

$$\sigma_y = E\varepsilon_y. \tag{1}$$

The elongation of the bar is accompanied by a decrease in its diameter D. The strains in the x and z directions are therefore given by

$$\varepsilon_x = \varepsilon_z = \frac{D_f - D_o}{D_o},$$

where D_o and D_f are the original and final diameters of the bar. If the material of the bar is isotropic, these strains are related by the equation

$$\varepsilon_x = \varepsilon_z = \nu\varepsilon_y, \tag{2}$$

where ν is Poisson's ratio for the material of the bar. The value of ν ranges from about 0.25 to about 0.45 for most metals and alloys.

To measure ε_y by x-rays would require diffraction from planes perpendicular to the axis of the bar. Since this is usually physically impossible, the diffraction planes parallel to the axis of the bar are used by making the back-reflection x-ray measurement indicated in Fig. 3. (It is essential that a back-reflection technique be used, in order to gain sufficient precision in the measurement of plane spacing. Even quite large stresses cause only a very small change in d.) This provides a measurement of the strain in the z direction since

$$\varepsilon_z = \frac{d_n - d_o}{d_o} \tag{3}$$

where d_n is the spacing of the planes parallel to the bar axis under stress, and d_o is the spacing of the same planes in the absence of stress. (The subscript n describes the fact that the diffraction plane normal is *normal* to the specimen surface.) Combining Eqs. (1), (2), and (3) produces

$$\sigma_y = -\frac{E}{\nu}\left(\frac{d_n - d_o}{d_o}\right), \tag{4}$$

which gives the required stress.

It should be noted that only a particular set of grains contributes to a particular *hkl* reflection in the parafocusing geometry. These are grains whose (*hkl*) planes are parallel to the surface of the bar, as indicated in Fig. 4, and which are compressed by the applied stress, that is, d_n is less than d_o. Grains whose (*hkl*) planes are normal to the surface have these planes extended, as shown in an exaggerated fashion in the drawing.

The variation of d_{hkl} with orientation ψ of the normal of (*hkl*) is shown in polar coordinates in Fig. 5(a). The length and direction of any vector in this diagram show the spacing and plane-normal direction, respectively, of any selected (*hkl*) set of planes. If the specimen were unstressed, the end of the d_o vector would describe the dashed circle shown, because plane spacing is then independent of plane orientation. This is not true when stress is present; if the stress is tensile, d_i increases with ψ along the curve shown by the full line. Figures 5(b) and (c) show the orientations of the x-ray beam required to measure d_n and d_i. The spacing d_{hkl} therefore varies with crystal orientation, and there is thus no possibility of using any of the

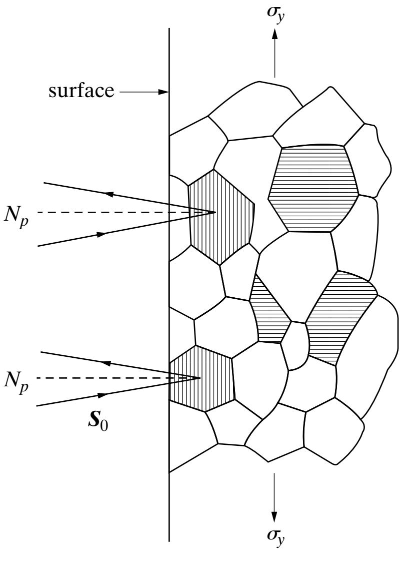

Figure 4 Diffraction from strained aggregate, tension axis vertical. Lattice planes shown belong to the same (*hkl*) set. N_p = diffraction-plane normal.

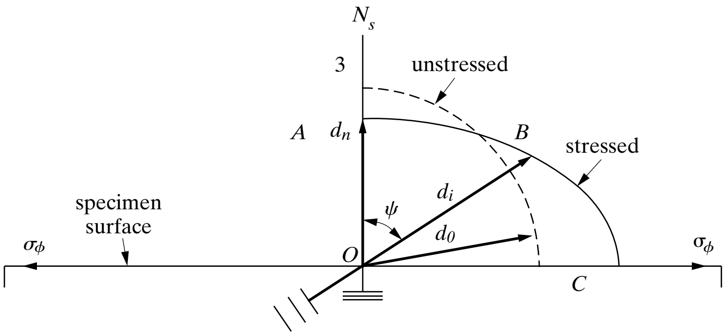

(a) Vector diagram of plane spacings d for a tensile stress σ_ϕ

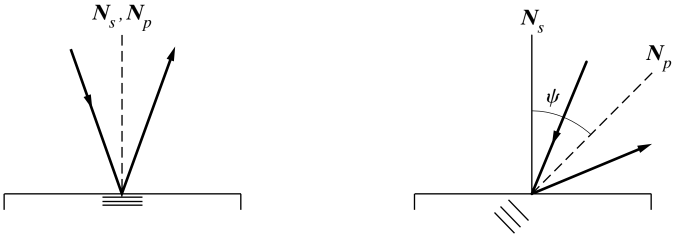

(b) Measurement of d_n

(c) Measurement of d_i

Figure 5 (a) Plane-spacing diagram. (b) and (c) Orientations of x-ray beams relative to specimen. N_s = normal to specimen surface, N_p = *normal to diffraction planes.*

extrapolation procedures to measure d_{hkl} accurately. Instead this spacing must be determined from the 2θ position of a single diffraction line.

Equation (4) shows that knowledge of d_o is required. If the specimen contains only applied stress, d_o can be obtained from a measurement on the unloaded specimen. (Such a stress measurement is rarely made, and then only for certain research purposes; it is far easier to measure applied stress with an electric-resistance gauge.) If the specimen contains residual stress, d_o must be measured on a small stress-free portion cut out of the specimen; the method then becomes destructive and of no interest.

Note that the value of d_o cannot be obtained from measurements on a "similar" stress-free material. If the specimen is iron, for example, it is not sufficiently accurate to look up the lattice parameter of "iron" in a handbook and calculate d_o from that parameter. The specimen may contain more or less impurities than the material for which the parameter is given, and impurities can change the parameter.

Equation (4) is therefore not a practical basis for the measurement of residual stress. At least *two* measurements of plane spacing on the *stressed* specimen are required for a nondestructive determination of stress.

4 ELASTICITY

In a bar subject to pure tension the normal stress acts only in a single direction. But in general there will be stress components in two or three directions at right angles to one another, forming so-called biaxial or triaxial stress systems. While it is true that, the stress at right angles to a free surface is always zero at that surface and that only two normal stress components can exist at the surface, x-rays penetrate a finite depth into a sample, and both triaxial and biaxial stresses can be present in the volume sampled by the x-rays.

The stresses which are present within a body, whatever the stress system, can be related to the set of the three principal stresses σ_1, σ_2, and σ_3. The principal stresses act along the directions normal to the planes on which no shear stresses occur. It will be useful, therefore, to develop the relationship between the strain and stress tensors in a form general enough to allow not only biaxial and triaxial stresses to be related to x-ray diffraction measurements but also to allow transformation of stresses (or strains) from one coordinate system to another.

Typically two rectilinear coordinate systems are used in x-ray diffraction stress measurements: the laboratory coordinate system $\mathbf{L}_i$ and the sample coordinate system $\mathbf{S}_i$ (Fig. 6). The laboratory system consists of the axes with respect to which the diffraction measurements are made; for *hkl* diffraction $\mathbf{L}_3$ is perpendicular to (*hkl*) and $\mathbf{L}_2$ is coplanar with $\mathbf{S}_1$ and $\mathbf{S}_2$. Note that $\mathbf{S}_3$ is perpendicular to $\mathbf{N}_s$ and $\mathbf{S}_1$ and $\mathbf{S}_2$ are in the plane of the sample; $\mathbf{S}_1$ might be chosen parallel to the rolling or machining direction.

In an anisotropic elastic material stress is a second order tensor σ_{ij} related to the strain tensor ε_{ikl} through the equation

$$\sigma_{ij} = C_{ijkl}\,\varepsilon_{kl} \tag{5a}$$

for *i, j, k* and *l* = 1, 2 or 3 and elastic constants matrix C_{ijkl}. Similarly, strain may be defined in terms of the stress components through

$$\varepsilon_{ij} = S_{ijkl}\,\sigma_{kl}, \tag{5b}$$

where S_{ijkl} is the elastic compliance matrix. For an isotropic elastic solid, the elastic constants *E* and *v* relate the stress and strain tensors through

$$\varepsilon_{ij} = \frac{1+\nu}{E}\sigma_{ij} - \delta_{ij}\frac{\nu}{E}\sigma_{kk}, \tag{6}$$

where δ_{ij} is Kroenecker's delta which equals 1 if $i = j$ and 0 if $i \neq j$ and the double subscript "*kk*" indicates the summation $\sigma_{11} + \sigma_{22} + \sigma_{33}$. Written explicitly,

$$\varepsilon_{11} = \frac{1}{E}[\sigma_{11} - \nu(\sigma_{22} + \sigma_{33})],$$

$$\varepsilon_{22} = \frac{1}{E}[\sigma_{22} - \nu(\sigma_{11} + \sigma_{33})],$$

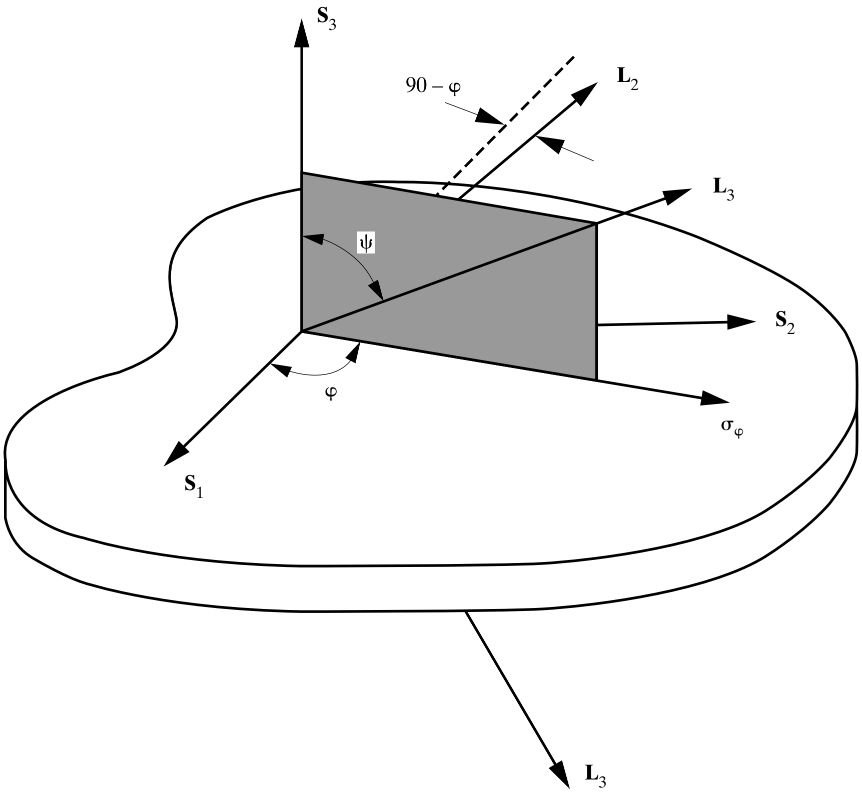

Figure 6 Illustration of the two axes systems used in stress measurements: $\mathbf{S}_i$ sample coordinate system and $\mathbf{L}_i$ laboratory coordinate system.

$$\varepsilon_{33} = \frac{1}{E}[\sigma_{33} - \nu(\sigma_{11} + \sigma_{22})],$$

$$\varepsilon_{23} = \frac{1}{2\mu}\sigma_{23},$$

$$\varepsilon_{31} = \frac{1}{2\mu}\sigma_{31},$$

and

$$\varepsilon_{12} = \frac{1}{2\mu}\sigma_{12} \tag{7}$$

where $\mu = E/(2[1 + \nu])$ is the shear modulus. Stresses normal to a free surface defined by vector $\mathbf{n}_j$ must be zero at the surface, i.e.,

$$\sigma_{ij} \cdot \mathbf{n}_j = 0, \tag{8}$$

and the equations of equilibrium must be satisfied at each point of the material:

$$\sum_{j=1}^{3} \frac{\partial \sigma_{ij}}{\partial \mathbf{x}_j} = 0. \tag{9}$$

It is also necessary to relate ε_{mn} in one coordinate system to that in another system. This is done through direction cosines a_{mi} and a_{nj}, and

$$\varepsilon_{mn} = a_{mi}\, a_{nj}\, \varepsilon_{ij}, \tag{10}$$

where a_{mi} defines the cosine of the angle between $\mathbf{x}_i$ in the old coordinate system and $\mathbf{x}_m$ in the new coordinate system. Thus the relationship between strain ε_{33} in the $\mathbf{S}_i$ coordinate system and ε_{kl} in the $\mathbf{L}_i$ system is

$$\varepsilon'_{33} = a_{3k}\, a_{3l}\, \varepsilon_{kl}, \tag{11}$$

with

$$a_{ik} = \begin{bmatrix} \cos\phi\cos\psi & \sin\phi\cos\psi & -\sin\psi \\ -\sin\phi & \cos\phi & 0 \\ \cos\phi\sin\psi & \sin\phi\sin\psi & \cos\psi \end{bmatrix} \tag{12}$$

for the angles ϕ and ψ defined in Fig. 6. After substituting for a_{3k} and a_{3l}, the result is

$$\varepsilon'_{33} = \varepsilon_{11}\cos^2\phi\sin^2\psi + \varepsilon_{12}\sin 2\phi\sin^2\psi + \varepsilon_{22}\sin^2\phi\sin^2\psi +$$

$$\varepsilon_{33}\cos^2\psi + \varepsilon_{13}\cos\phi\sin 2\psi + \varepsilon_{23}\sin\phi\sin 2\psi. \tag{13}$$

Note that the prime denotes quantities defined in the sample coordinate system $\mathbf{S}_i$, and unprimed quantities refer to $\mathbf{L}_i$. In terms of stresses,

$$\varepsilon'_{33} = \frac{1+v}{E}\{\sigma_{11}\cos^2\phi + \sigma_{12}\sin 2\phi + \sigma_{22}\sin^2\phi - \sigma_{33}\}\sin^2\psi + \frac{1+v}{E}\sigma_{33}$$

$$-\frac{v}{E}(\sigma_{11} + \sigma_{22} + \sigma_{33}) + \frac{1+v}{E}\{\sigma_{13}\cos\phi - \sigma_{23}\sin\phi\}\sin 2\psi \tag{14}$$

The quantity ε'_{33} measured at angles ϕ and ψ in Fig. 6 will be indicated by $(\varepsilon'_{33})_{\phi\psi}$. The difference between $d_{\phi\psi}$, the value of d in the stressed sample and measured for the plane whose normal is at angles ϕ, ψ from $\mathbf{S}_i$, and the value of d_o for the unstressed state is related to $(\varepsilon'_{33})_{\phi\psi}$ by:

$$(\varepsilon_{33}')_{\phi\psi} = \frac{d_{\phi\psi} - d_0}{d_0} \tag{15}$$

This result (Eq. 14 and 15) is the starting point for biaxial and triaxial stress analysis via x-ray diffraction.

5 BIAXIAL AND TRIAXIAL STRESS ANALYSIS

Before proceeding to work through how to use Eq. 14 and 15 to measure stress, it is useful to consider the forms the stress tensor might take.

Biaxial stresses have tensors of the form

$$\begin{bmatrix} \sigma_{11} & 0 & 0 \\ 0 & \sigma_{22} & 0 \\ 0 & 0 & 0 \end{bmatrix} \text{ or } \begin{bmatrix} \sigma_{11} & \sigma_{12} & 0 \\ 0 & \sigma_{22} & 0 \\ 0 & 0 & 0 \end{bmatrix}, \tag{16 a,b}$$

for an isotropic material with the $\mathbf{x}_3$ direction is normal to the sample surface, whereas triaxial stresses include tensors of the form

$$\begin{bmatrix} \sigma_{11} & 0 & 0 \\ 0 & \sigma_{22} & 0 \\ 0 & 0 & \sigma_{33} \end{bmatrix} \text{ or } \begin{bmatrix} \sigma_{11} & \sigma_{12} & 0 \\ 0 & \sigma_{22} & 0 \\ 0 & 0 & \sigma_{33} \end{bmatrix}. \tag{16 c,d}$$

For biaxial stress it is convenient to introduce

$$\sigma_\phi = \sigma_{11}\cos^2\phi + \sigma_{22}\sin^2\phi \tag{17a}$$

for tensor *a* above and

$$\sigma_\phi = \sigma_{11}\cos^2\phi + \sigma_{12}\sin^2\phi + \sigma_{22}\sin^2\phi \tag{17b}$$

for tensor *b* above. This is the stress along the direction $\mathbf{L}_1$ which is at an angle ϕ from $\mathbf{S}_1$. The equation for strain becomes [5]

$$\frac{d_{\phi\psi} - d_0}{d_0} = \frac{1+\nu}{E}\sigma_\phi \sin^2\psi - \frac{\nu}{E}(\sigma_{11} + \sigma_{22}) \tag{18}$$

If d_o, ν and E are known with sufficient precision, measurement of $d_{\phi\psi}$ at two values of ψ would be sufficient to determine σ_ϕ. Multiple ψ and $d_{\phi\psi}$ should be used in the stress determination because this allows the data to be fit with a least squares line, thereby increasing the robustness of the measurement. In this approach, $d_{\phi\psi}$ is plotted as a function of $\sin^2\psi$, (Fig. 7), and, as will be discussed below, this $\sin^2\psi$ method can reveal situations where the assumptions underlying Eq. 18 are

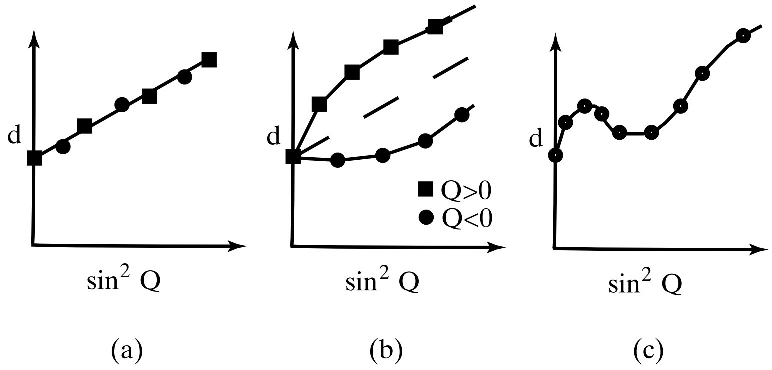

Figure 7 Different types of d vs. $\sin^2\psi$ plots. After [G.38].

not satisfied. In summary, the slope of the plot of $d\phi\psi$ vs. $\sin^2\psi$ gives $\sigma\phi$ providing E, ν and d_o are known.

Next consider the values of d_o, E and ν required for Eq. 18. Normally d_o is taken to equal $d(\psi = 0)$, the experimentally measured d-spacing at $\psi = 0$. This ingenious assumption [5] is reasonable because elastic strains typically introduce a maximum of 0.1% difference between the true d_o and d measured at any ψ [G.38]. Further, d_o is a multiplier to the slope in Eq. 18, and the net effect will, therefore, be less than 0.1%, much less that that from other errors. The x-ray elastic constants should be used for a given material and reflection combination. Values of the x-ray constant $(1 + \nu)/E$ are collected in Table 1. In cases where these are not available, the constants E and ν can be measured experimentally or can be calculated by averaging single crystal constants via the Reuss or Voigt approximations [G.38].

Figure 7 shows three patterns of d vs. $\sin^2\psi$ which might be encountered in practice. The linear plot of d vs. $\sin^2\psi$ (Fig. 7a) shows the behavior expected from biaxial or uniaxial stresses. In this case, determination of the individual stress components may require measurement of $d_{\phi\psi}$ for three values of ϕ, say 0°, 45°, and 90°. The behavior in Fig. 7b is termed "psi-splitting", that is the d-spacings determined for $\psi < 0$, $d_{\phi\psi-}$, are no longer identical with those determined for $\psi > 0$, $d_{\phi\psi+}$. Note that the superscript "+" or "–" for ψ denotes values determined with $\psi > 0$ or $\psi < 0$, respectively. The different curves for $d_{\phi\psi-}$ and $d_{\phi\psi+}$ as a function of $\sin^2\psi$ indicates that triaxial stresses are present and the previous analysis must be modified. Oscillatory d vs. $\sin^2\psi$ curves (Fig. 7c) appear, for example, when significant levels of texture are present. Special approaches, beyond the scope of this text can be used in textured materials [G.38].

TABLE 1 DIFFRACTION DATA AND STRESS CONSTANTS

Alloy	Composition (weight percent)	λ, *hkl*[b]	2θ (deg)	$K_c = \dfrac{E}{1+\nu}$ (10^3 ksi)	K_1[a] (ksi/deg)	Reference
(A) Ferritic and martensitic steels (body-centered cubic)						
Armco iron	Fe + 0.02 C	Cr, 211	156	27.9		[6]
4340 (50 R_c)[c]	Fe + 0.40 C, 1.8 Ni, 0.8 Cr, 0.25 Mo	Cr, 211	156.0	24.5	89.3	[7]
4340	Fe + 0.40 C, 1.8 Ni, 0.8 Cr, 0.25 Mo	Cr, 211	156		122	[8]
4340	Fe + 0.40 C, 1.8 Ni, 0.8 Cr, 0.25Mo	Cr, 211	156		(101)[d]	[9]
4130	Fe + 0.30 C, 1.0 Cr, 0.20 Mo	Cr, 211	156		87	[8]
Railroad steel	Fe + 0.75 C	Cr, 211	156.1		90.9[e]	[10]
D-6AC	Fe + 0.50 C, 1.0 Cr, 0.5 Ni, 1.0 Mo, 0.1 V	Cr, 211	156.2		113.4[e]	[10]
D-6AC	Fe + 0.60 C, 1.0 Cr, 0.5 Ni, 1.0 Me, 0.1 V	Cr, 211	156		(98)[d]	[9]
Vascomax 250	Fe + 18.5 Ni, 6.6 Ca, 4.8 Mo, 0.1 Al, 0.4 Ti	Cr, 211	156		(111)[d]	[9]
4820 (carburized)	Fe + 0.20 C, 2.5 Ni, 0.26 Mo (core composition)	Cr, 211	156	(24.3)[d,g] (26.2)[d,h]		[11]
410 SS[f] (22 R_c)	Fe + 12.5 Cr	Cr, 211	155.1	25.6	98.4	[7]
410 SS (42 R_c)	Fe + 12.6 Cr	Cr, 211	155.1	25.1	96.7	[7]
422 SS (34 R_c)	Fe + 0.22 C, 12.0 Cr, 0.7 Ni, 1.0 Mo, 1.0 W, 0.25 V	Cr, 211	154.8	26.4	103.2	[7]
422 SS (38 R_c)	Fe + 0.22 C, 12.0 Cr, 0.7 Ni, 1.0 Mo, 1.0 W. 0.23 V	Cr, 211	154.8	26.1	103.4	[7]
steel	Fe + 0.39 C	Cr, 220		25.8		[12]
steel	Fe + 0.73 C	Cr, 211		22.8		[12]
steel	Fe + 0.73 C	Co, 310		19.4		[12]
steel	Fe + 4.3 C, 3.96 Mo, 0.57 Si, 3.96 Mo	Fe, 121 (Fe_3C)		21.0		[13]
steel	Fe + 0.1 C, 0.55 Cr, 4.9 Ni, 0.57 Mo, 0.82 Mn, 0.3 Si	Cr, 211		22.8		[13]
200 Maraging steel		Cr, 211		23.5		[10]
HSLA 328		Cr, 211		28.6		[14]
1045		Cr, 211		28.7		[15]
1045		Co, 310		20.0		[5]
(B) Austenitic alloys (face-centered cubic)						
304 SS	Fe + 0.08 C, 18 Cr, 8 Ni, 2 Mn	Cr, 220	129.0	20.2	170.0	[7]
Incoloy 903	Fe + 38 Ni, 15 Co, 3 Nb, 1.4 Ti, 0.7 Al	Cr, 220	128.0	31.2	264.0	[7]
Incoloy 903	Fe + 38 Ni, 16 Co, 3 Nb, 1.4 Ti, 0.4 Al	Cu, 331	146.3		74.6[e]	[10]
Incoloy 800	Fe + 32.5 Ni, 21 Cr, 0.4 Ti, 0.4 Al	Cr, 220	129.0	23.4	196.0	[7]
Incoloy 800	Fe + 32.5 Ni, 21 Cr, 0.4 Ti, 0.4 Al	Cu, 420	147.0	21.5	110.0	[7]
(C) Nickel alloys (face-centered cubic)						
Monel K 500	66.5 Ni, 29.5 Co, 2.7 Al, 1.0 Fe	Cu, 420	150.0	21.0	98.4	[7]
Inconel 600	70 Ni, 15.5 Cr, 8 Fe	Cu, 420	151.0	23.1	105.0	[7]
Inconel 600	70 Ni, 15.5 Cr, 8 Fe	Cr, 220	131.0	21.1	174.0	[7]

TABLE 1 *(Continued)*

Alloy	Composition (weight percent)	λ, hkl^b	2θ (deg)	$K_c = \frac{E}{1+\nu}$ (10^3 ksi)	$K_1{}^a$ (ksi/deg)	Referenc
Inconel 718	52.5 Ni, 19 Cr, 18.5 Fe, 3.1 Mo, 6.0 Nb, 0.9 Ti, 0.4 Al	Cu, 331	145.0	19.7-20.3	109.0-112.0	[7]
Inconel 718	52.5 Ni, 19 Cr, 18.5 Fe, 3.1 Mo, 6.0 Nb, 0.9 Ti, 0.4 Al	Cu, 331	146.1		122.4^e	[10]
Inconel 718	52.5 Ni, 19 Cr, 18.5 Fe, 3.1 Mo, 6.0 Nb, 0.9 Ti, 0.4 Al	Cr, 220	128.0	31.2-31.4	263.0-265.0	[7]
Inconel X750	73 Ni, 15.5 Cr, 7 Fe, 2.5 Ti, 0.9 Nb, 0.8 Al	Cr. 220	131.0	36.8	301.0	[7]
Nickel		Cu, 420		22.9		[12]
Nickel		Cu, 331		20.7		[12]
(D) Aluminum alloys (face-centered cubic)						
2024	Al + 4.4 Cu, 1.5 Mg, 0.6 Mn	Cu, 511	163	8.51		[6]
2024-73	Al + 4.4 Cu, 1.5 Mg, 0.6 Mn	Cr, 311	139		44	[8]
7075	Al + 1.6 Cu, 2.5 Mg. 0.3 Cr, 5.5 Zn	Cr, 311	139.0	8.83	56.9	[7]
7079-T611	Al + 0.6 Cu, 3.7 Mg. 0.2 Cr, 4.7 Zn	Cr. 311	139		50	[8]
2218-T87	Al + 6.3 Cu, 0.3 Mn, 0.18 Zr, 0.1 V, 0.05 Ti	Cr. 311	120.5		55.0^e	[10]
Aluminum		Co, 420		7.10		[12]
5083-H23		Cr, 311		7.98		[16]
5083-H23		Co, 420		7.97		[16]
5083-H23		Cu, 511 /333		7.97		[16]
(E) Copper alloys (face-centered cubic)						
Cu-Ni	85 Cu, 15 Ni	Cu, 420	146.0	18.6	98.8	[17]
α-Brass		Co, 400		9.42		[12]
β-Brass		Co, 310		7.18		[12]
Copper		Co, 400		10.7		[12]
(F) Titanium alloys (hexagonal close - packed)						
Ti-6-4	Ti + 4 Al, 4 v	Cu, 213	142.0	12.2	74.0	[7]
Ti-6-4	Ti + 4 Al, 4 v	Cu, 213	142		70	[7]
Ti-6-2-4-2	Ti + 6 Al, 2 Sn, 4 Zr, 2 Mo	Cu, 213	140.7	14.8	92.3	[7]
Ti-8A1-1Mo-1V		Cu, 213		14.3		[17]
(G) Misc.						
Tungsten		Co, 222		46.5		[12]
Uranium		Cu, 116		39.1		[18]
Zircoloy-2		Cr, 104		11.8		[18]

(a) Value of K_1 from Eq. (16-13) with $\psi = 45°$.
(b) In this only: "Cr" means Cr $K\alpha$: "Cu" means Cu $K\alpha$.
(c) R_c = Rockwell Chardness number.
(d) Calculated from data in referenced paper.
(e) Measured with detector in same radial position, between F and F' of Fig. 9(b), for $\psi = 0$ and 45°.
(f) SS = stainless steel.
(g) As - quenched
(h) Average value after tempering at 200° F and above.
1 ksi = 10^3 p = 10^3 ib/in^2 = 0.7031 kg/mm^2 = 6.895 MPa.
1 kg/mm^2 = 1.422 ksi = 9.807 MP.

In determining triaxal stresses it is convenient to define a_1 and a_2 such that

$$a_1 = \frac{1}{2}[\varepsilon_{\phi\psi^+} + \varepsilon_{\phi\psi^-}] = \frac{d_{\phi\psi^+} + d_{\phi\psi^-}}{2\,d_0} - 1$$

$$= \{\varepsilon_{11}\cos^2\phi + \varepsilon_{12}\sin 2\phi + \phi_{22}\sin^2\phi - \varepsilon_{33}\}\sin^2\psi + \varepsilon_{33}$$

$$= \frac{1+v}{\mathrm{E}}\{\sigma_{11}\cos^2\phi + \sigma_{12}\sin 2\phi + \sigma_{22}\sin^2\phi - \sigma_{33}\}\sin^2\psi$$

$$+\frac{1+v}{\mathrm{E}}\sigma_{33} - \frac{v}{\mathrm{E}}(\sigma_{11} + \sigma_{22} + \sigma_{33}) \text{ and} \tag{19a}$$

$$a_2 = \frac{1}{2}[\varepsilon_{\phi\psi^+} + \varepsilon_{\phi\psi^-}] = \frac{d_{\phi\psi^+} - d_{\phi\psi^-}}{2d_{\mathrm{O}}}$$

$$= \{\varepsilon_{11}\cos\phi + \varepsilon_{23}\sin\phi\}\sin|2\psi|$$

$$= \frac{1+v}{\mathrm{E}}\{\sigma_{13}\cos\phi + \sigma_{23}\sin\phi\}\sin|2\psi|, \tag{19b}$$

with $\psi^- = (-1)\psi^+$ and $\sin 2\psi^+ - \sin 2\psi^- = 2\sin|2\psi|$. Basically, a_1 is defined by the mean of the values of d for $\psi < 0$ and d for $\psi > 0$ and a_2 by the difference of these d. Thus a_1 is a linear function of $\sin^2\psi$ and σ_{11}, σ_{12}, σ_{22}, and σ_{33} are obtained from the slope and intercept of a_1 vs. $\sin^2\psi$ for $\phi = 0, 45$, and 90°. The shear stresses σ_{13} and σ_{23} are obtained from the slope and intercept of a_2 vs. $\sin|2\psi|$ for $\phi = 0, 90°$. Figure 8 shows data for a sample containing a triaxial stress state: a) and b), $d_{\phi\psi}$ and a_1 plotted vs. $\sin^2\psi$ and c) a_2 vs. $\sin|2\psi|$ [19].

6 DIFFRACTOMETER METHOD

Until about 1950, x-ray stress measurements were made only by photographic methods. Today the diffractometer is preferred because it is faster and more precise. The photographic method, and its success of the area detector method, will be described later.

Steel which has been hardened by quenching and tempering produces very broad diffraction lines. Measuring the positions of such lines on a photographic film is difficult and can only be done by making a microphotometer record of the film. However, such measurements can be made in a straightforward fashion with a diffractometer, as was first shown by Christenson and Rowland [20]. Their demon-

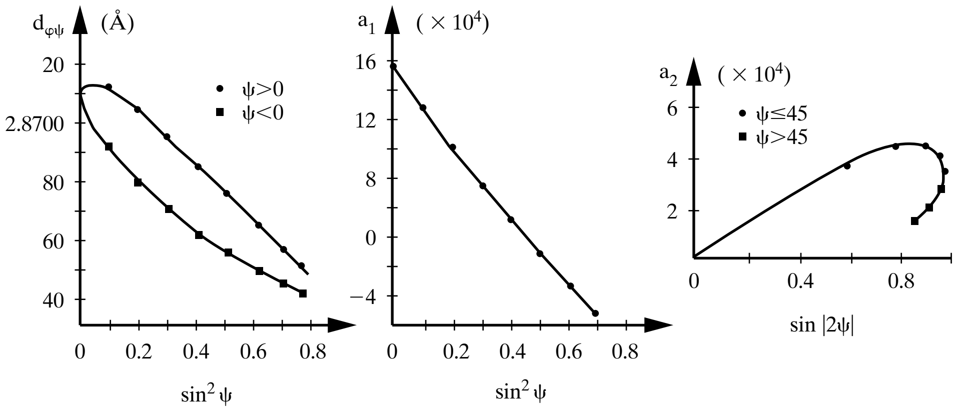

Figure 8 (a) Example of ψ-splitting and corresponding plots of (b) a_1, vs. $\sin^2\psi$ and (c) a_2 vs. $\sin|2\psi|$ for triaxial stress analysis. (After [19]).

stration that residual stress could be accurately measured in hardened steel, an important industrial material, greatly enlarged the scope of the x-ray method.

Most diffractometers must be modified to meet two requirements of stress measurement:

1. The specimen holder must be robust enough to support fairly large and heavy specimens, and it must be possible to rotate the holder about the diffractometer axis independently of the detector rotation, in order to change the angle ψ.
2. In one variant, the detector must be mounted on a radial slide that allows detector movement along a radius of the diffractometer circle. (Some prefer to leave the detector in its usual position and move the detector slit. In the following, when detector movement is mentioned, either practice is meant.)

The second requirement arises from the need to preserve focusing conditions, as shown in Fig. 9. In (a) the specimen is equally inclined to the incident and diffracted beams; ψ is zero and the specimen normal $\boldsymbol{N}_s$ coincides with the diffraction plane normal $\boldsymbol{N}_p$. Radiation divergent from the source S is diffracted to a focus at F on the diffractometer circle. In (b) the specimen has been turned through an angle ψ for the inclined measurement. Because the focusing circle is always tangent to the specimen surface, rotation of the specimen alters the focusing circle both in position and radius, and the diffracted rays now come to a focus at F', located a distance D from the diffractometer axis. If R is the radius of the diffractometer circle, then it may be shown that

$$\frac{D}{R} = \frac{\sin(\theta - \psi)}{\sin(\theta + \psi)}. \qquad (20)$$

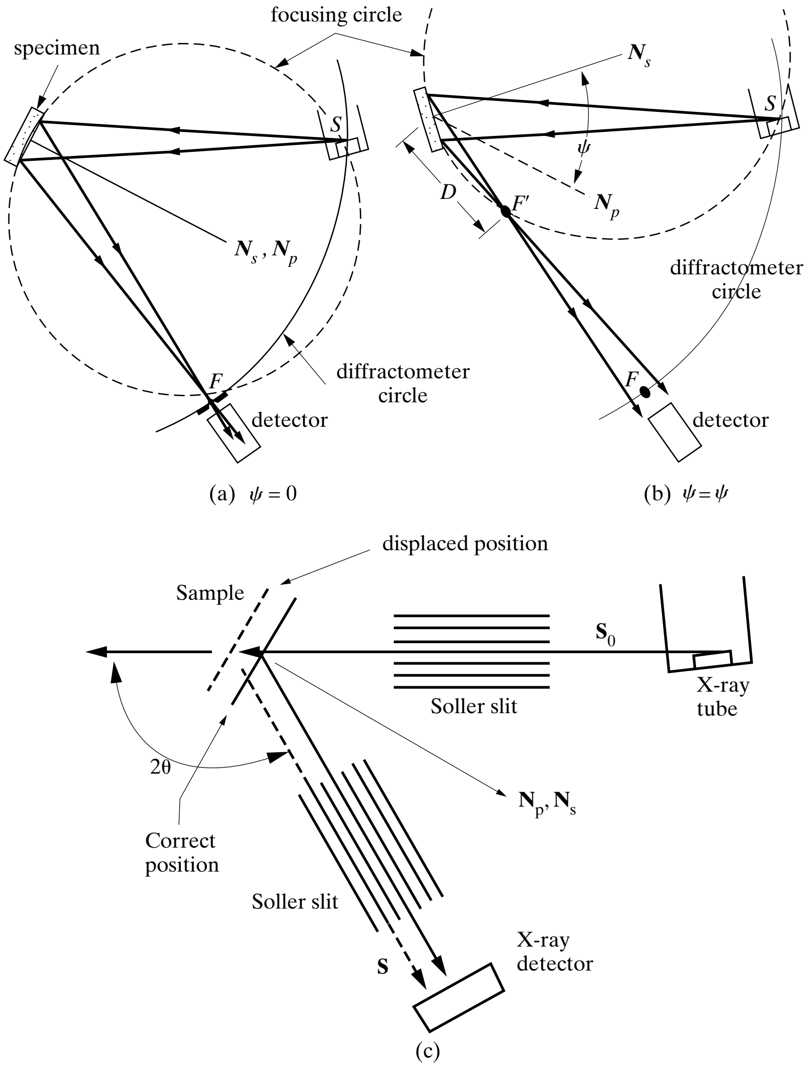

(a) $\psi = 0$ (b) $\psi = \psi$

(c)

Figure 9 Use of a diffractometer for stress measurement (a) and (b) show the focussed beam and (c) shows the parallel beam configurations..

If ψ is 45°, then D/R is 0.70 for $\theta = 80°$ and 0.47 for $\theta = 70°$. When ψ is not zero, the focal point of the diffracted beam therefore lies between F, the usual position of the detector receiving slit, and the specimen. To preserve focusing, the detector should be moved so that the slit is at F'. The cumbersome receiving slit motion required with a focussed beam geometry can be avoided using the parallel beam geometry described below.

Instrument misalignment can introduce small errors which cause a change in 2θ even for a stress-free specimen, when ψ is changed from 0 to 45°. It is therefore necessary to determine this change experimentally and apply it as a correction. If $(\Delta 2\theta)_0$ is the line shift for a stress-free specimen and $(\Delta 2\theta)_{\text{m}}$ the measured shift for a stressed specimen, then the line shift due to stress is

$$\Delta 2\theta = (\Delta 2\theta)_m - (\Delta 2\theta)_0. \tag{21}$$

The correction is best determined on a specimen of fine powder, which is necessarily free of macrostress. The powder should have about the same composition as the material in which stress is to be measured in order that its diffraction line occur at about the same 2θ position, because the correction $(\Delta 2\theta)_0$ itself depends to some extent on 2θ.

A value of $(\Delta 2\theta)_0$ greater than about 0.1° points to the need for better instrument alignment. The general alignment procedure stipulated by the diffractometer manufacturer should be carried out. Two further conditions must be satisfied:

1. The specimen surface must lie on the diffractometer axis and remain there as ψ is changed. Failure to achieve this condition is usually the major source of error in stress measurement. Errors arise, for example, when, the sample is physically displaced from the diffractometer axis; they may also occur if the ψ-axis is offset from the diffractometer's 2θ axis. Some kind of mechanical pointer (feeler gauge) is often used to position the specimen in the proper place.
2. The radial motion of the detector must be truly radial. If the beam from the x-ray tube is restricted by a very narrow incident-beam slit to pass over the diffractometer axis and the detector is positioned at $\theta = 0$ to receive the direct beam, nonradiality of the detector slide will be disclosed by an apparent deviation of the beam from 0° as the detector is moved toward the diffractometer axis.

The effect of sample or ψ-axis displacement can be minimized, however, if a parallel beam geometry (Fig. 9c) is used instead of the focused beam geometry (Fig. 9a,b). In the parallel beam geometry the 2θ position is determined by the angular relationship between parallel slits in the incident and diffracted beams; these slits are Soller slits with baffles perpendicular to the goniometer plane. Then the detector slit can be kept in a stationary position (F in Fig. 9b) instead of translating the slit along the detector arm to keep it at the focal position F' for different ψ; the cost of this procedure is a substantial loss of intensity. The variation of stress with sample or ψ-axis displacement of ± 2mm is nearly negligible with the parallel beam geometry and is substantially less for the stationary slit geometry than for the parafocusing geometry [G.38].

A reasonably strong high-angle diffraction line is needed for the measurement of stress. The combination of (hkl) reflecting planes and wavelength λ that will produce such a line varies from one kind of material to another. These combinations and the approximate 2θ position of the line are listed in Table 1 for various materials.

Measurement of Line Position

Line positions for stress measurements must be determined with the highest possible precision. This is particularly necessary when the lines are broad, as they are from hardened steel; the full width at half-maximum intensity is then $5° - 10°\ 2\theta$. If the line is $8°$ wide for Cr $K\alpha$ and the 211 reflection for steel (E=207 GPa,[1] $\nu = 0.29, \theta = 78°, \psi = 45°$), a stress of 3 MPa will cause the line to shift by only 7 percent of its width when the specimen is turned through $45°$. Measurement of such a small shift requires that the line center be located very accurately at each angle ψ.

The standard method of finding the center of a diffraction line, broad or narrow, is to fit a parabola to the top 15% of the line and take the axis of the parabola as the line center. This method was first used for stress measurement by Ogilvie [21], and it provides a more reproducible measure of peak position than centroid or the mid-point half-maximum methods [22].

When the lines are broad, certain corrections should be applied to the intensity data *before* finding the line center, as pointed out by Koistinen and Marburger [23]. One factor controlling these intensities was the Lorentz-polarization (L-P) factor $(1 + \cos^2 2\theta)/(\sin^2\theta \cos\theta)$. This factor can vary considerably over the width of a single line, when the line is broad and in the high-angle region. However, the L-P factor applies to integrated intensities. To obtain an expression governing intensities at particular values of 2θ within a single line, the $(1/\cos\theta)$term, which relates to line breadth, is eliminated and the resulting modified L-P factor is $(1 + \cos^2 2\theta)/\sin^2\theta$ The variation of this factor with 2θ makes a high-angle line asymmetrical about its center. Absorption in the specimen has a similar effect when $\psi$is not zero, because the absorption factor is then $(1 - \tan\psi \cot\theta)$. If are combined these two factors are combined and termed the LPA factor, then

$$LPA = (\text{modified L-P factor})(\text{absorption factor})$$

$$= \left(\frac{1 + \cos^2 2\theta}{\sin^2\theta}\right)(1 - \tan\psi\ \cot\ \theta) \tag{22}$$

Measured intensities are to be divided by LPA in order to make the lines more nearly symmetrical, before determining the line center. If the background is high, because of fluorescence by the specimen, better accuracy is attainable by subtract-

---

[1] 1 ksi = 10^3 psi = 103 lb/in2 = 0.7031 kg/mm3 = 6.895 MPa. and 1 kg/mm2 = 1.422 ksi = 9.807 MPa.

ing the background, assumed linear across the line, before applying the *LPA* correction and finding the line center.

Specimen Preparation

Ideally, the specimen surface should be clean and smooth. Dirt and scale, if present, must be removed, but any removal of material must be done by a process that does not itself produce residual stress and thereby change the stress to be measured.

Grinding and machining are known to introduce large stresses to depths of at least 0.005 inch (125 μm). The effect of acid etching is less certain; some investigators have reported that etching produces some stress, others that the effect is negligible; at any rate, deep etching is objectionable because of the surface roughness it produces (see below). Electrolytic polishing, i.e., the process in which the specimen is made the anode in an electrolytic cell is another method of removing metal from polycrystalline samples without introducing stresses; details are given in [16] and by Tegart [24].

Surface roughness should be strictly avoided, because the high points in a rough surface are not stressed in the same way as the bulk of the material and yet they contribute most to the diffraction pattern, especially the one made at inclined incidence, as indicated in Fig. 10. Of course, the surface should not be touched at all prior to the stress measurement, if the object is to measure residual surface stresses caused by some treatment such as machining, grinding, shot peening, etc. Such treatments produce steep stress gradients normal to the surface, and the removal of any material by polishing or etching would defeat the purpose of the measurement.

Measurement of Stress as a Function of Depth

When the stress gradients within a specimen are measured with x-ray diffraction, material is removed in layers and the stress is measured at each new exposed surface. These measured stresses are not those previously existing, because the removal of a stressed layer changes the stress in the remaining material. The measured stresses have therefore to be corrected. The layer-removal correction is described by Moore and Evans [25], by [16] and by [G.38].

An example of stress measurements in depth is given in Fig. [11], which shows the residual stress produced in hardened steel by grinding. The extremely steep

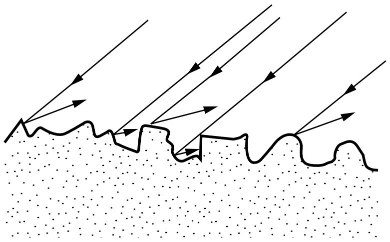

Figure 10 Diffraction from a rough surface when the incident beam is inclined.

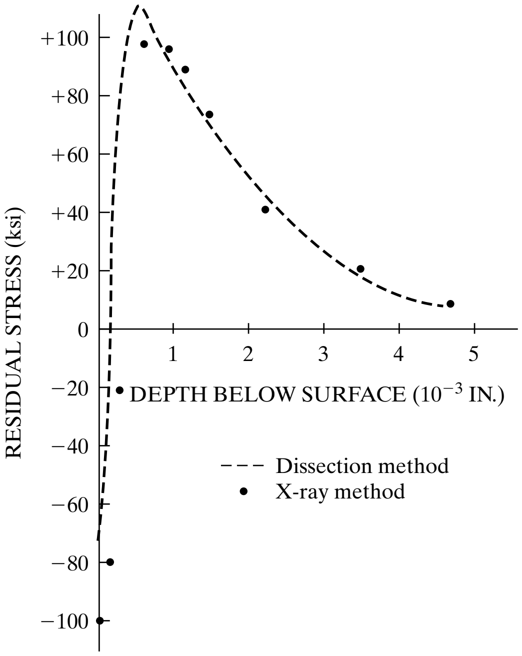

Figure 11 Longitudinal residual stress, parallel to grinding direction, as a function of depth below the ground surface in a steel heat treated to a Rockwell C hardness of 59. X-ray measurements by Koistinen and Marburger [26]; dissection measurements by Letner [27]. Note inability of dissection method to measure stress right at the surface.

stress gradient normal to the surface should be noted; the stress changes from + 100 ksi to - 100 ksi (+ 700 MPa to - 700 MPa) in about 0.0006 inch (15 μm), which means that the gradient is about 3×10^5 ksi/in (90 to 95 MPa/μm. Beam penetration corrections were necessary here, as they generally are when measurements are made on ground or machined surfaces.

Variant Techniques

The following variations of the standard method described above are also in use:

1. Measurements are made at only two values of ψ, normally $0°$ and $45°$ or $60°$. With fever measurements, the precision of the stresses determined decreases compared to the $\sin^2\psi$ method, but the apparatus can thus be very simple. This approach is frequently used for portable stress apparatus, and more details follow below.
2. Side-inclination method. The geometry of the Schulz method for pole-figure determination is adopted. For the measurement of d_n the specimen is positioned so that the direction in which stress is to be measured is parallel to the diffractometer axis. The ψ rotation is then made about the axis AA' for the measurement of d_i. The focal point of the diffracted beam remains on the diffractometer circle as ψ is changed, so that radial motion of the detector is not needed. This method has another advantage for some specimens in which

stress has to be measured at the bottom of a concave region, such as in the space between the teeth of a gear; depending on the shape of the concavity, it may be physically impossible to get an x-ray beam in and out with the standard method, because either the incident or diffracted beam is blocked by the specimen at one ψ angle or another; with the slide-inclination method this problem may not exist. On the debit side, the height of the beam is severely limited.

Special Diffractometers

It is sometimes necessary to measure residual stress in an object that is too large and/or heavy to be accommodated on a standard diffractometer. Or one may wish to measure stress in a large structure, as distinct from a machine component. In either case, it is necessary to bring the diffractometer to the object to be measured rather than vice versa.

Compact, portable diffractometers have been made for this purpose. Because they are intended only for stress measurement, the angular 2θ range of detector movement covers only the high-angle region. The ψ angle is changed by rotating the whole diffractometer (x-ray tube and detector) with respect to the specimen about the diffractometer axis, which is an imaginary axis lying in the surface of the specimen.

Cohen and James [29] adapted a position-sensitive detector to stress measurement. This detector has the great advantage that it can measure the 2θ position of a diffracted beam without a 2θ movement of the detector. Preliminary work was done with the detector mounted on a standard diffractometer [27] Later a portable instrument was made, in which the detector and a miniature, air-cooled x-ray tube are fixed to a single support that moves in a curved guide through an arc of 45° [29]. Three rods fixed to the guide allow the unit to be properly positioned relative to the specimen. Stress is measured by determining the line position at $\psi = 0$, swinging the detector and tube together through 45°, and determining the line position again. This instrument has the following features:

1. It is fast. All the points on the diffraction-line profile are measured simultaneously and stored as I, 2θ data in an MCA. A minicomputer then establishes the line centers for $\psi = 0$ and 45° by least-squares parabola fitting, computes the stress, and displays it. Stress can be measured with a standard deviation of about 35 MPa in 20 seconds or less, depending on line width.
2. It is truly portable, weighing only 23 lb (10 kg) and can be carried by one person, with the aid of a neck strap and two handles, and held in position for a stress measurement. As a fixed instrument, it should be useful for monitoring stress in material coming off a production line.
3. The detector, associated electronics are rather expensive.

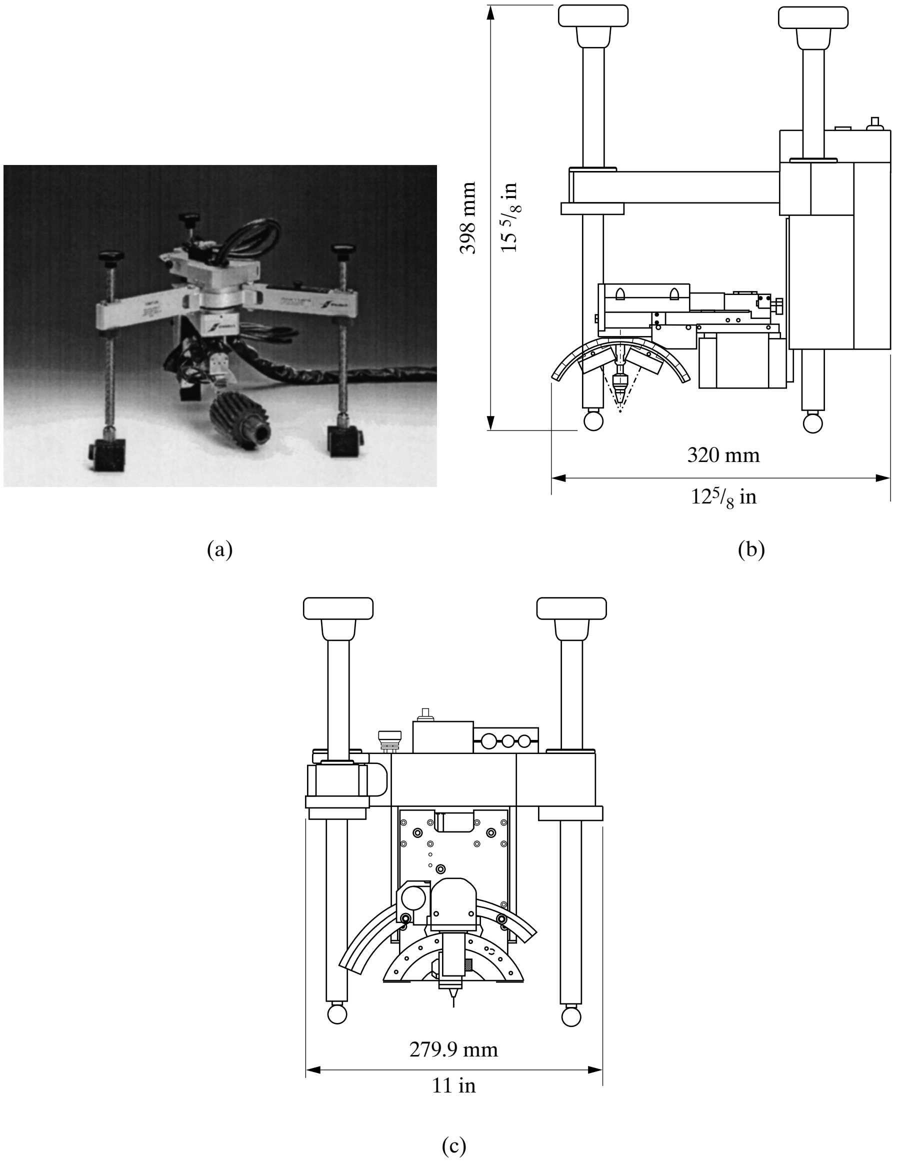

Figure 12. (a) Photograph and (b) schematic views of XSTRESS-3000 portable diffractometer for residual stress measurement (courtesy Stresstech).

Figure 12 shows a photograph (a) and two schematic views (b) of the goniometer of a portable diffractometer for stress measurement (XSTRESS 3000 from Stresstech); the systems provided by other manufacturers are not too dissimilar to this apparatus. The XSTRESS 3000 goniometer sits on three legs so that the x-ray source and detectors are at a fixed distance from the sample's surface; typically the legs are directly on the surface of large samples and control of the separation between goniometer and measurement point is quoted as 0.003 mm. The goniometer incorporates two linear PSD's with 0.029°/detector element angular resolution quoted by the manufacturer; it weighs only 10 kg and the self-contained power supply and tube cooling system module, connected to the goniometer by cables and tubes, weighs an additional 25 kg. A variety of x-ray tubes are available, the system can be operated up to 30 kV and 6.7 mA (200 W) and beam collimators between 1 and 5 mm diameter can be selected by the operator. Diffractometer control, data acquisition and analysis are performed on a standard notebook PC.

7 PHOTOGRAPHIC OR AREA DETECTOR METHOD

The photographic method of stress measurement is not often used today, because it is slower and less precise than the diffractometer method. Stress measurements with area detectors, however, are becoming increasingly popular since the detectors have a wide dynamic range, the data is in digital form and peak positions can be measured with reasonable precision. The photographic method still has some advantages. The required apparatus is very simple: a small back-reflection camera fixed to the head of an x-ray tube. This apparatus is smaller, lighter, more robust, and much cheaper than a mobile diffractometer. It is also more mobile and better suited to work in a confined space.

Two experimental techniques have been used:

1. Two exposures are made, with the incident beam inclined at a different angle to the specimen for each exposure [G.10, 16, 31, 32]. Only one side of the Debye ring on the film is measured in each exposure. This method is entirely analogous to the standard diffractometer method.
2. A single inclined exposure is made, but both sides of the Debye ring are measured.

Norton [31] has analyzed the errors in each technique and has concluded that the single-exposure technique is, in practice, just as precise as the two-exposure technique, besides being twice as fast, even though the precision of the two-exposure technique is theoretically better.

Only the single-exposure technique will be described here for biaxial stresses. The incident beam (Fig. 13) is collimated by a pinhole, not shown, and is inclined at an angle β to the normal $\boldsymbol{N}_s$ to the specimen surface. The diffracted x-rays register on two strips of film held in a curved holder of radius R centered on O. (Flat-film cameras have also been used.) The two x-rays beams shown do not lie on a true Debye cone because they are diffracted by sets of planes, 1 and 2, differently oriented with respect to the stress σ_ϕ and therefore with different spacings. The two sets of planes have slightly different Bragg angles θ_1 and θ_2, and their normals $N_{\rho1}$

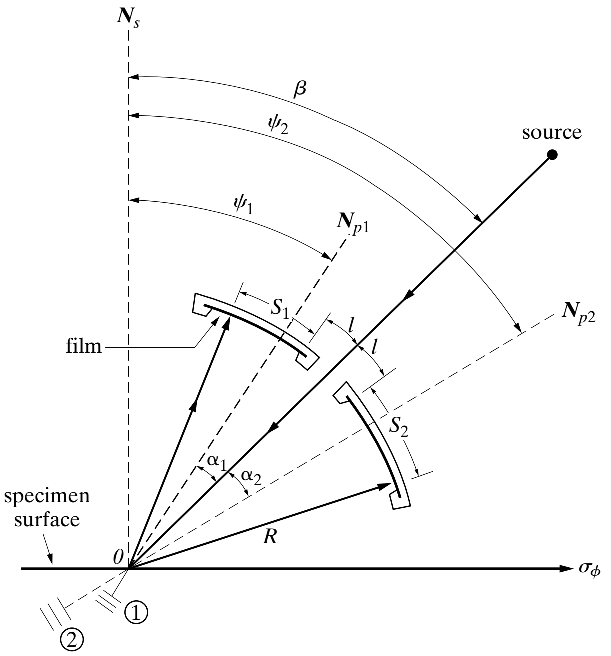

Figure 13 Photographic method of stress measurement (single-exposure technique). After Norton [31].

and $N_{\rho 2}$ make slightly different angles α_1 and α_2 with the incident beam. Equation (18) can then be written for each ψ angle, ψ_1 and ψ_2:

$$\frac{d_{\varphi\psi_1} - d_o}{d_o} = \frac{-\nu}{E}(\sigma_{11} + \sigma_{22}) + \frac{1+\nu}{E}\sigma_\phi \sin^2\psi_1 \tag{23(a)}$$

$$\frac{d_{\varphi\psi_2} - d_o}{d_o} = \frac{-\nu}{E}(\sigma_{11} + \sigma_{22}) + \frac{1+\nu}{E}\sigma_\phi \sin^2\psi_2\,. \tag{23(b)}$$

The difference between Eq. 23(a) and (b) is

$$\frac{d_{\varphi\psi_1} - d_o}{d_o} - \frac{d_{\varphi\psi_2} - d_o}{d_o} = \frac{d_{\varphi\psi_1} - d_{\varphi\psi_2}}{d_o} = \frac{1+\nu}{E}\sigma_\phi[\sin^2\psi_1 - \sin^2\psi_2]\,. \tag{24}$$

Substituting

$$\frac{\Delta d}{d} = -\frac{\cot\theta\,\Delta 2\theta}{2},$$

with $\theta = (\theta_1 + \theta_2)/2$, using $\psi_1 = \beta - \alpha_1$ and $\psi_2 = \beta + \alpha_2$, noting $\alpha_1 - \alpha_2 = \alpha$ and solving for σ_φ yields:

$$\sigma_\phi = \frac{E}{1+v}\left(\frac{\cot\theta}{\sin^2(\beta+\alpha) - \sin^2(\beta-\alpha)}\right)\Delta\theta, \tag{24}$$

which is usually expressed as

$$\sigma_\phi = \mathrm{K}\Delta\theta, \tag{25}$$

where K, the stress constant, is given by

$$\mathrm{K} = \frac{\pi}{180}\,\frac{\mathrm{E}}{1 + v}\,\frac{1}{2\sin 2\beta \sin^2\theta} \tag{26}$$

for $\Delta\theta$ in deg.

The quantities measured are the distances S_1 and S_2 between the diffraction lines and the shadows of the inside knife edges, which are at a distance l from the incident beam. Therefore,

$$2\alpha_1 R = 2[(\pi/2) - \theta_{i1}]R = l + S_1,$$

$$2\alpha_2 R = 2[(\pi/2) - \theta_{i2}]R = l + S_2. \tag{27}$$

By subtraction

$$2R(\theta_{i2} - \theta_{i1}) = S_1 - S_2 \tag{28}$$

or

$$(\theta_{i2} - \theta_{i1}) = \frac{S_1 - S_2}{2R}.$$

Replacing $\Delta\theta$ in Eq. 25 by Eq. 28 results in the working equation

$$\sigma_\varphi = K_3(S_2 - S_1), \tag{29}$$

where the stress constant is given by

$$K_3 = \frac{E}{4R(1 + \nu)\sin^2\theta \sin 2\beta}. \tag{30}$$

If β is chosen to be $45°$, the $\sin 2\beta$ term drops out.

The stress camera shown in Fig. 14 has a radius of 70.0 mm. It takes two standard packets of dental x-ray film which slide into curved slots in the film holder; thus film can be inserted and removed for processing without disturbing the camera alignment. Knife edges in the film holder cast sharp x-ray shadows at each end of each film strip; these serve as fiducial marks for the measurement of line position and for the correction of film shrinkage. The correct distance between specimen and film is set by replacing the collimator aperture with a retractable pointer, not shown; the tip of this pointer lies on the axis of the incident beam at the right distance from the film, i.e., at the point O of Fig. 13. Line positions on the film are measured with a conventional viewing box and scale, such as those used to read Hull/Debye–Scherrer films, or with a microphotometer. If the standard deviation of the quantity (S_2 - S_1) is 0.04 mm, which can be achieved by careful, repeated measurements on each film, then the standard deviation in stress for steel is about 30 MPa [31].

General purpose planar area detectors (e.g., a flat image plate [32]) can be used very effectively to record the entire diffraction cone in a single exposure. Multiwire or CCD detectors can also be used [33]. With the detector placed perpendicular to the incident beam, the diffraction cone from the stressed sample is not circular, and the variation of radius with azimuthal angle is related, through trigonometry, to the angle $180° - 2\theta$ for the different orientations of the diffraction planes. Thus, all ϕ orientations ϕ are measured for a single ψ in a single exposure; obtaining multiple ψ requires tilting the sample and recording multiple exposures [32]. The components of the stress tensor are then obtained using the methods described above. Textured and large-grained samples may be studied by this technique as well as samples with randomly oriented grains. The image plate technique has produced results on a ground steel sample comparable to those from conventional methods [32].

The small diameter of the incident beam from a stress camera a portable diffractometer Fig. 14 is an advantage when one wishes to measure stress variations

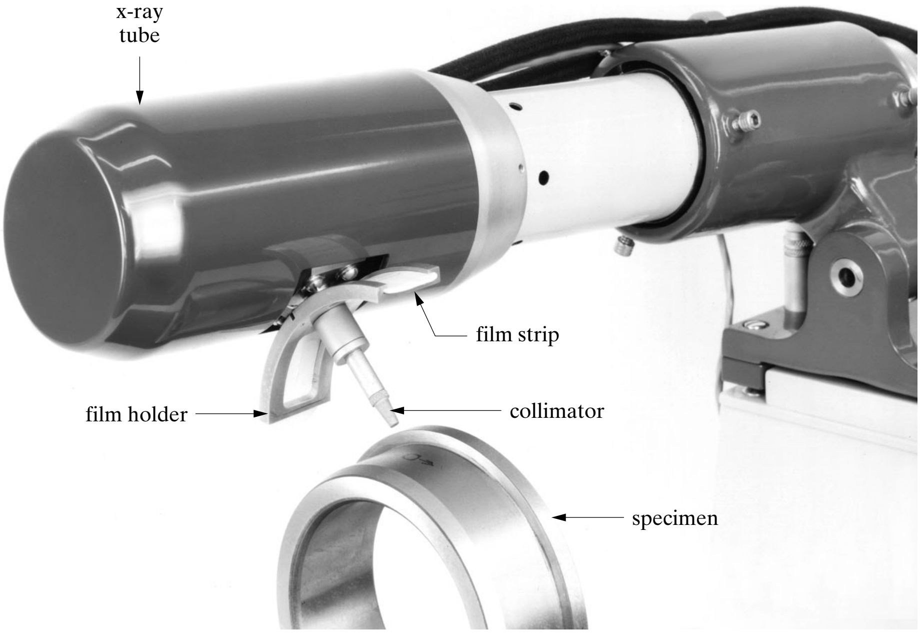

Figure 14 Stress camera in position for a stress measurement by the single-exposure technique. The head of the x-ray tube is enclosed in a protective cover. (Courtesy of Advanced Metals Research Corporation.)

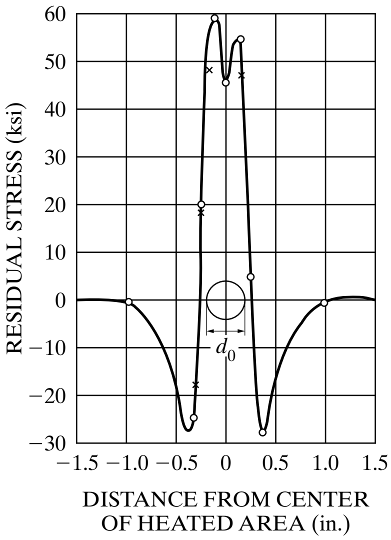

Figure 15 Longitudinal residual stress in the surface of a steel strip, due to localized heating, d_0 is diameter of heated area. Norton and Rosenthal [34].

from point to point on a surface, as in the region near a weld. The stress distribution shown in Fig. 15 determined by a photographic method, simulates the residual stresses due to spot welding. The specimen was a steel strip $25 \times 8 \times 0.6$ cm. A circular area of about 1 cm diameter, whose size is indicated on the graph, was heated locally to about 700ºC for a few seconds by clamping the strip at its center between the two electrodes of a spot welding machine. The central area rapidly expanded but was constrained by the relatively cold metal around it. Plastic flow occurred in the hot central region, and residual stress was set up during cooling. The stresses shown in Fig. 15 are longitudinal stresses at points along a line through the heated area across the 80 mm width of the strip. Tensile residual stress, almost equal to the yield stress of this steel (415 MPa), exists in the heated area.

Other investigations by the photographic method include measurements on Al [35-37], Ti [34] and steel [34, 38, 39].

8 CALIBRATION

The measurement of stress by x-rays depends on the assumption that the material under stress was an isotropic body obeying the laws of elasticity. The quantity $E/(1 + \nu)$, is required to convert strains to stresses and the tacit assumption was that the values of E and ν measured in the ordinary way during a tensile test are to be used. These mechanically measured values are not necessarily the correct ones to apply to a diffraction measurement. In the latter, strains are measured in particular crystallographic directions, namely, the directions normal to the (*hkl*) diffraction planes, and both E and ν vary with crystallographic direction. This anisotropy of elastic properties varies from one metal to another: for example, measurements on single crystals of α-iron show that E has a value of 284 GPa along [111] and 132

GPa along [100], whereas the values of E for aluminum show very little variation, being 75 GPa along [111] and 63 GPa [100]. The mechanically measured values are 207 and 69 GPa for polycrystalline iron and aluminum, respectively. These latter values are evidently average values for aggregates of contiguous grains having random orientation. In the x-ray method, however, only grains having a particular orientation relative to the incident beam, and therefore a particular orientation with respect to the measured stress, are able to diffract. There is therefore no good reason why the mechanically measured values of E and ν should be applied to these particular grains. Stated alternately, an aggregate of randomly oriented grains may behave isotropically but individual grains of particular orientations in that aggregate may not.

These considerations are amply supported by experiment. By making x-ray measurements on materials subjected to known stresses, the ratio $E/(1 + \nu)$ can be determined experimentally and can differ substantially from the values calculated from the mechanically measured elastic constants. Moreover, for the same material the measured values of $E/(1 + \nu)$ usually vary with the indices (hkl) of the diffraction planes.

Methods have been proposed for calculating the proper values of E and ν to use with x-ray stress measurements from values measured in various directions in single crystals. Examples include the Voigt [40] and Reuss [41] averages, and software is commercialy available for applying a wide range of models for elastic constants [e.g., 41a]. These and other approaches are summarized elsewhere [G.38]. The safest procedure is to measure $E/(1 + \nu)$ on a specimen subjected to known stresses, and this specimen should be the same material as the sample in which the stresses are to be measured. Specific examples of calibration procedures may be found in [6-9, 11, 16, G.38].

One practice is to set up known stresses in body by bending. The specimen is a flat strip, seen edge-on in Fig. 16, at two points and loaded by the forces F at two other points. This four-point bending produces a tensile stress in the front surface, and this stress is constant in magnitude between the two inner supports. If the calibration is performed on a diffractometer, the bending fixture must be so designed that the front surface of the specimen coincides with the diffractometer axis at any ψ angle and at any degree of bending.

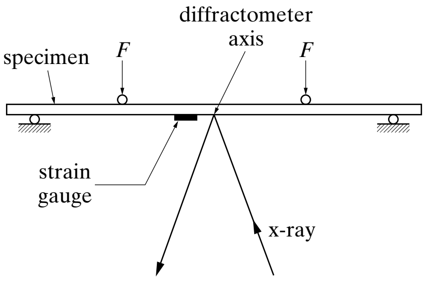

Figure 16 Specimen loaded in bending for calibration of the x-ray method.

The strain due to bending is measured by an electrical-resistance strain gauge mounted near the region examined by x-rays. The product of this strain and the mechanically measured elastic modulus E of the material is the surface longitudinal stress σ_ϕ needed for the calibration. (Any uncertainty in E will cause a corresponding uncertainty in the stress constant K, the proportionality constant linking peak shift as a function of ψ with stress. The best approach is to measure E on the same specimen by direct loading of the same kind as that used in the x-ray calibration, e.g., by four-point bending.)

After a range of known stresses σ_ϕ, not exceeding the elastic limit, are measured by x-rays, the data are plotted in the form of a calibration curve. If, for example, a diffractometer is used, the calibration curve is a plot of σ_ϕ vs. $\Delta 2\theta = (2\theta_n - 2\theta_i)$, and the slope of the line is equal to the stress constant. (If the line does not go through the origin, it indicates that the calibrating member itself contained residual stress before a bending moment was applied.)

The x-ray technique used in calibration should match the technique to be used later for the measurement of unknown stresses. For example, the stress constant determined with the focusing technique is not expected to agree with the stress constant determined by the parallel-beam technique (Fig. 9).

Experimentally determined stress constants are given in Table 1 for a variety of industrial alloys, ferrous and nonferrous. All have been determined with the diffractometer.

9 PRECISION AND ACCURACY

As in most measurements, precision (reproducibility) is easier to attain than accuracy (approach to the "true" value).

Precision

High precision requires that the random errors involved in measuring diffraction line position be minimized, and these errors are larger, the wider the line.

Diffractometer

Precision in establishing the profile, and hence the position, of a diffraction line is governed mainly by the statistical error in counting. As shown by Eq. (6-8), this error is proportional to $1/\sqrt{N}$, where N is the number of counts. Many investigators use a fixed-count technique and count long enough at each 2θ position to accumulate 10^5 counts. The relative standard deviation of such a count is 0.3 percent. Ways of estimating the standard deviation of the measured stress from the errors involved in counting and curve fitting are treated in [16]. James and Cohen [12] have made an experimental study of the precision attainable by different techniques; they show, for example, that better precision is attained by fitting a parabola to a number of points, seven or more, by least squares than by fitting it to three points, even when the total time spent in counting is identical. It is difficult to give a single figure for the precision attainable in a stress measurement in a reasonable measuring time without hedging it about with many qualifications, but, for measurements on steel, standard deviations of 2 ksi-3 ksi (i.e., 15-20 MPa for narrow diffraction lines) and 4 ksi-5 ksi (30-35 MPa for broad lines) are probably conservative estimates. The reader is refered to [G.38] for further details.

Stress camera

Precision is increased by making repeated measurements on each film and averaging the results. Using the single-exposure technique, Norton [31] obtained a standard deviation on steel (narrow lines) of 4.5 ksi (30-35 MPa).

Accuracy

High accuracy requires that systematic errors be minimized. These errors are chiefly of two kinds, those of a geometrical nature and those involved in the elastic-constant portion of the stress constant. The systematic errors cause an error in the measured stress which is proportional to the magnitude of the stress.

In a diffractometer measurement by the standard focusing technique, the chief geometrical error is a displacement of the specimen surface from the diffractometer axis. If the specimen is displaced by an amount x along the reflecting-plane normal, then a line shift will occur even for a stress-free specimen, as it is rotated from $\psi = 0$ to $\psi = \psi$. This shift, in radians, is given by [43]

$$2\theta_n - 2\theta_l = \Delta 2\theta = \frac{2x\cos\theta}{R}\left[1 - \frac{\sin\theta}{\sin(\theta - \psi)}\right], \tag{31}$$

where R is the diffractometer radius and x is taken as positive when the displacement is in front of the axis. For $x = 10^{-2}$ inch (250 μm), $\theta = 78°$, $\psi = 45°$, and $R = 5.73$ in. (14.55 cm), $\Delta 2\theta = -0.033$ deg.

In the single-exposure camera method, faulty positioning of the camera relative to the specimen causes errors in R and β.

Given careful experimental technique, an inaccurate value of $E/(1+\nu)$, remains as the largest source of error. Inspection of the data in Table 1 shows rather poor agreement between certain investigators for the value of $E/(1+\nu)$ for the same or similar material. The investigator who does not have the time or facilities to measure $E/(1+\nu)$, before making stress measurements has two options: (1) he or she can select a value, or a mean value, from a list such as that of Table 1, with a possible error of up to about 10 percent, or (2) he or she can calculate $E/(1+\nu)$ from the mechanically measured values of E and ν, with a possible error of about 30 percent. While such errors would be intolerably large in some measurements, they do not necessarily impair the value of residual stress measurements. As Norton [31] points out, the investigator is usually more concerned with precision than accuracy, in that he or she wants to know how the stress varies from one point to another on the specimen or how the stress at a particular point varies with the treatment of the specimen. An error of even 30 percent in the absolute magnitude of the measured stresses would seldom change the conclusions reached in the investigation.

(In certain nickel alloys Prevey [7] has found abnormally large differences between the x-ray and mechanical values of the elastic constants; for these alloys his x-ray values are up to 80 percent larger than the mechanical values reported in the literature.)

10 PRACTICAL DIFFICULTIES

Certain conditions inherent in the specimen can affect the accuracy, and even the possibility, of x-ray stress measurements. Deviations from the regular d vs $\sin^2\psi$ behavior (Fig. 7) can be assessed qualitatively and the validity of the underlying assumptions tested statistically [44]; this can be very important in determining whether any of the following conditions are present.

Large Grain Size

If the grains are large, the diffraction line is spotty and its position not well defined. This condition is obvious with a photographic, but not with a diffractometric, technique. If this condition is suspected, a back-reflection pinhole photograph should be made before stress measurements with a diffractometer are attempted. Or the line may be recorded on a dental film placed in front of the detector slit.

Some industrial products have grains so large that x-ray stress measurements are impossible with techniques intended for polycrystalline samples. In borderline cases, oscillation of the specimen during the measurement, by ±2–5 degrees about an axis lying in the specimen surface, will increase the number of reflecting grains enough to produce a measurable line.

Techniques for precision measurement of lattice parameters in single crystals can be used to determine stresses in the individual grams.

Preferred Orientation

A moderate degree of preferred orientation causes no difficulty, but a fairly sharp texture has two effects:

1. The diffraction line selected for the stress measurement may be strong at $\psi = 0$ and virtually absent at $\psi = 45°$, or vice versa. The texture will then control the possible ψ angles.
2. If the material is elastically very anisotropic, the mechanically measured value of E will depend markedly on direction in the specimen. Oscillations result in plots of d vs. $\sin^2\psi$ and complicate stress determination [G.38]. Serious errors can result if the biaxial or traxial methods are applied blindly.

Plastic Deformation

If the specimen has been plastically deformed in a particular way in the region examined by x-rays, the x-ray method does not indicate the true macrostress. (If the plastic deformation causing the residual stress is remote from the region examined, the accuracy of the x-ray method is not affected; this condition exists, for example, in surface measurements on quenched specimens, where residual stress in the outer surface is due to plastic flow in the interior.)

When a specimen is stretched plastically a few percent and then unloaded, x-ray measurements show a line shift indicating residual compressive macrostress in the direction of prestrain. The effect is symmetrical: after plastic compression, x-rays indicate residual tensile stress. It is not a surface effect, because x-ray measurements made after successive removal of surface layers show that the stress persists throughout the specimen. On the other hand, dissection measurements show that a true macrostress does not exist, and, in fact, none would be expected after uniform deformation. The stress indicated by x-rays is called *pseudo-macrostress*, "pseudo" because it is not a true macrostress causing strain on dissection and "macro" because it causes an x-ray line shift. Pseudo-macrostress is actually, an unusual kind of microstress, in which the portions of the material that are in tension and in compression are unequal in volume. It has been discussed in various reviews [12, 45, 46 G.38].

The effect was first observed after uniaxial deformation, but such deformation is not restricted to pure tension and compression. Plastic bending, for example, causes true macrostress (Fig. 2), but the deformation mode is predominantly a tension or compression of layers parallel to the neutral axis of the beam. The longitudinal residual stress indicated by x-rays is therefore the sum of true macrostress and pseudo-macrostress, and the x-ray result will be numerically larger at either surface than the result obtained by dissection.

Deformation by rolling or die drawing has a certain uniaxial character, but the forces on the material at the roll or die surface are inclined to the specimen axis. Macrostress is produced, superimposed on a complex system of microstresses; the latter probably include a pseudo-macrostress. As a result, the x-ray method does not measure the true macrostress, but rather the sum of macrostress and some component of the microstress that causes an additional line shift.

On the other hand, plastic deformation by grinding or shot peening produces macrostresses that are accurately measurable by x-rays, as shown by excellent agreement between x-ray and dissection measurements. Figure 11 shows an example. Deformation by these processes appears to be multiaxial, rather than uniaxial, and pseudo-macrostress is accordingly absent.

In summary, the x-ray method does not reveal the true macrostress in specimens that have been plastically deformed by tension, compression bending, rolling, or die drawing. It would be wrong to conclude, however, that the x-ray method is in error. Pseudo-macrostress is just as real as macrostress. X-rays indicate the sum of the two, dissection only the latter.

PROBLEMS

*__1__ A uniaxial tensile stress of 100 ksi is being measured in iron by 211 diffraction of x-rays at $\psi = 0$ and 45°. Take the lattice parameter a of the stress-free iron to be 2.8665 Å, $E = 30 \times 10^6$ psi, and $\nu = 0.29$. (a) Calculate $d_{\phi\psi}$ and d_o to five significant figures. (b) What percent error is made in replacing $(d_{\phi\psi} - d_O)/d_O$ by $[d_{\phi\psi} - d(\psi = 0)]/d(\psi = 0)$ in Eq. (18)?

2 Derive Eq. (20).

3 Show that the absorption factor for the diffractometer method is $(1 - \tan\psi \cot\theta)$.

***4** The circumferential (hoop) stress in a cylinder of 1045 steel, due to water quenching followed by glass bead peening, is measured with a diffractometer (Cr $K\alpha$ radiation, 211 reflection). The line shift $\Delta 2\theta$ when a stress-free specimen is rotated from $\psi = 0$ to $\psi = 45°$ is $-0.10°$. Take the stress constant K_1 as 90 ksi/deg. The time t given below is the time required to accumulate 20,000 counts at each angle.

Calculate the residual stress with and without correction for line asymmetry by the LPA factor.

ψ	2θ	t(sec)	LPA
0	155.00°	69.20	1.910912
	155.80	54.47	1.916158
	156.60	71.64	1.921281
45°	156.00	35.84	1.509882
	156.50	32.35	1.521150
	157.00	33.83	1.532391

REFERENCES

The following books are listed more or less in the order they are encountered in the text

G.10 Charles S. Barrett and T. B. Massalski. *Structure of Metals*, 3rd ed. (New York: McGraw-Hill, 1966). A classic book on the crystallographic aspects of physical metallurgy. Really two books in one, the first part dealing with the theory and methods of diffraction of x-rays, electrons, and neutrons; the second part with the structure of metals in the wider sense of the word. Very lucid account of stereographic projection. Stress measurement, phase transformations, preferred orientation.

G.16 Leonid V. Azaroff. *Elements of X-Ray Crystallography* (New York: McGraw-Hill, 1968). Crystallography, diffraction theory (kinematic and dynamic), structure analysis, single-crystal and powder methods.

G.17 Harold P. Klug and Leroy E. Alexander. *X-Ray Diffraction Procedures*, 2nd ed. (New York: Wiley, 1974). Contains a great deal of useful detail on the theory and operation of powder cameras and diffractometers. Covers the following topics in depth: chemical analysis by diffraction, parameter measurement, line-broadening analysis, texture determination, stress measurement, and studies of amorphous materials. Single-crystal methods are not included.

G.18 W. Parrish, ed. *Advances in X-ray diffractometry and X-ray Spectrography* (Eindhoven: Centrex Pub. Co., 1962).

G.38 I. C. Noyan and J. B. Cohen, Residual Stress: *Measurement by Diffraction and Interpretation* (New York: Springer-Verlag, 1987). A very complete treatment of stress and stress tensors and how stresses are measured in polycrystalline samples.

G.39 *Advances in X-ray Analysis*, International Centre for Diffraction Data.

ANSWERS TO SELECTED PROBLEMS

1. a) $d_0 = 1.1702$ Å, $d_n = 1.1691$ Å, $d_i = 1.1716$ Å
b) –0.1 percent

4. –65 ksi without, and –63 ksi with, correction by the *LPA* factor

Orientation of Single Crystals

1 INTRODUCTION

Many of the properties of polycrystalline materials have been explained by studies of isolated single crystals, since such studies permit measurement of the properties of the individual building blocks in the composite mass. Because single crystals are anisotropic, research of this kind always requires accurate knowledge of the orientation of the single crystal test specimen in order that measurements may be made along known crystallographic directions or planes. By varying the crystal orientation, data on the property measured (e.g., yield strength, electrical resistivity, corrosion rate) is obtained as a function of crystal orientation.

There is also an increasing production of single crystals, not for research studies, but for use as such in various devices, mainly electrical, optical and magnetic. One example is silicon crystals for central processor units and random access memory in computers and for semiconductor based consumer products. Another example is single-crystal nickel-based super alloy turbine blades which have very high creep resistance. These crystals must all be produced with particular orientations.

Described below are the three main methods of determining orientation; back-reflection Laue, transmission Laue, and diffractometer methods. Nor should the old etch-pit method be overlooked. This is an optical method, involving the reflection of visible light from the flat sides, of known Miller indices, of etch pits in crystal surfaces. Although not universally applicable, this method is fast and requires only simple apparatus [G.10].

2 BACK-REFLECTION LAUE METHOD

The Laue pattern of a single crystal consists of a set of diffraction spots on the film and the positions of these spots depend on the orientation of the crystal. This is true of either Laue method, transmission or back-reflection, so either can be used to determine crystal orientation. However, the back-reflection method is the

From Chapter 16 of *Elements of X-Ray Diffraction*, Third Edition. B.D. Cullity, S.R. Stock.

more widely used of the two because it requires no special preparation of the specimen, which may be of any thickness, whereas the transmission method requires relatively thin specimens of low absorption.

In either case, since the orientation of the specimen is to be determined from the location of the Laue spots on the film, it is necessary to orient the specimen relative to the film in some known manner. The single crystal specimens encountered in materials work are usually in the form of wire, rod, sheet, or plate, but crystals of irregular shape must occasionally be analyzed. Wire or rod specimens are best mounted with their axis parallel to one edge of the square or rectangular film; a fiducial mark on the specimen surface, for example on the side nearest the film, then fixes the orientation of the specimen completely. It is convenient to mount sheet or plate specimens with their plane parallel to the plane of the film and one edge of the sheet or plate parallel to an edge of the film. Irregularly shaped crystals must have fiducial marks on their surface which will definitely fix their orientation relative to that of the film.

The problem now is to determine the orientation of the crystal from the position of the back-reflection Laue spots on the film. The Bragg angle θ corresponding to each Laue spot could be determined, but that would be no help in identifying the planes producing that spot, since the wavelength of the diffracted beam is unknown. The orientation of the normal to the planes causing each spot, is fixed, however because the plane normal always bisects the angle between incident and diffracted beams. The directions of the plane normals can then be plotted on a stereographic projection, the angles between them measured, and the planes identified by comparison with a list of known interplanar angles for the crystal involved.

The first problem, therefore, is to derive, from the measured position of each diffraction spot on the film, the position on a stereographic projection of the pole of the plane causing that spot. In doing this it is helpful to recall that all of the planes of one zone diffract beams which lie on the surface of a cone whose axis is the zone axis and whose semi-apex angle is equal to the angle ϕ at which the zone axis is inclined to the transmitted beam (Fig. 1). If ϕ does not exceed 45°, the cone will not intersect a film placed in the back-reflection region; if ϕ lies between 45° and 90°,

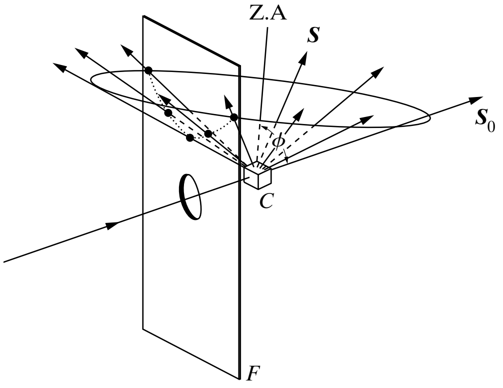

Figure 1 Intersection of a conical array of diffracted beams with a film placed in the back-reflection position. C = crystal, F = film, Z.A. = zone axis.

the cone intersects the film in a hyperbola; and, if ϕ equals 90°, the intersection is a straight line passing through the incident beam. (If ϕ exceeds 90°, the cone shifts to a position below the transmitted beam and intersects the lower half of the film, as may be seen by viewing Fig. 1 upside down.) Diffraction spots on a back-reflection Laue film therefore lie on hyperbolas or straight lines, and the distance of any hyperbola from the center of the film is a measure of the inclination of the zone axis.

In Fig. 2 the film is viewed from the crystal. Coordinate axes are defined such that the incident beam proceeds along the z-axis in the direction Oz and the x- and y-axes lie in the plane of the film. The diffracted beam by the plane shown strikes the film at S. The normal to this plane is CN and the plane itself is assumed to belong to a zone whose axis lies in the yz-plane. If this plane were rotated about the zone axis, it would pass through all the positions at which planes of this zone in an actual crystal might lie. During this rotation, the plane normal would cut the film in the straight line AB and the diffracted beam in the hyperbola HK. AB is therefore the locus of plane normal intersections with the film and HK the locus of diffracted beam intersections. The plane which diffracts a beam to S, for example, has a normal which intersects the film at N, since the incident beam, plane normal, and diffracted beam are coplanar. Since the orientation of the plane normal in space can be described by its angular coordinates γ and δ, the problem is to determine γ and δ from the measured coordinates x and y of the diffraction spot S on the film.

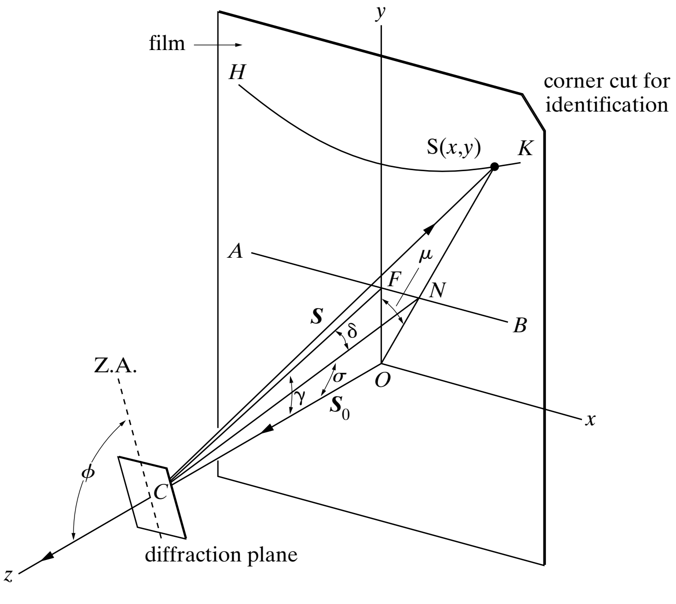

Figure 2 Location of back-reflection Laue spot. Note that $\gamma = 90° - \phi$.

A graphical method of doing this was devised by Greninger [1] who developed a chart which, when placed on the film, gives directly the γ and δ coordinates corresponding to any diffraction spot. To plot such a chart, note from Fig. 2 that

$$x = OS \sin \mu,\ y = OS \cos \mu, \text{ and } OS = OC \tan 2\sigma, \tag{1}$$

where $OC = D$ = specimen-film distance. The angles μ and σ are obtained from γ and δ as follows:

$$\tan \mu = \frac{FN}{FO} = \frac{\mathrm{CF} \tan \delta}{CF \sin \gamma} = \frac{\tan \delta}{\sin \gamma} \tag{2}$$

$$\tan \sigma = \frac{ON}{OC} = \left(\frac{\mathrm{FN}}{\sin \mu}\right)\left(\frac{1}{CF \cos \gamma}\right) = \left(\frac{CF \tan \delta}{\sin \mu}\right)\left(\frac{1}{CF \cos \gamma}\right)$$

$$= \frac{\tan \delta}{\sin \mu \cos \gamma} \tag{3}$$

With these equations, the position (in terms of x and y) of any diffraction spot can be plotted for given values of γ and δ and any desired specimen-film distance D. The result is the Greninger chart, graduated at 2° intervals shown in Fig. 3 for D = 3.0 cm. The hyperbolas running from left to right are curves of constant γ, and any one of these curves is the locus of diffraction spots from planes of a zone whose axis is tilted away from the plane of the film by the indicated angle γ. If points having the same value of δ are joined together, another set of hyperbolas running from top to bottom is obtained. The lower half of the chart contains a protractor whose use will be described later. Greninger charts should have dark lines on a transparent background and are best printed on overhead projector transparencies using a computer plotting package and Eq. (1)-(3).

In use, the chart is placed over the film with its center coinciding with the film center and with the edges of chart and film parallel. The γ and δ coordinates corresponding to any diffraction spot are then read directly. Note that use of the chart avoids any measurement of the actual coordinate distances x and y of the spot. The chart gives directly, not the x and y coordinates of the spot, but *the angular coordinates γ and δ of the normal to the diffraction planes causing the spot.*

Knowing the γ and δ coordinates of any plane normal, for example *CN* in Fig. 2, the pole of the plane can be plotted on a stereographic projection. Imagine a reference sphere centered on the crystal in Fig. 2 and tangent to the film, and let the projection plane coincide with the film. The point of projection is taken as the intersection of the transmitted beam and the reference sphere. Since the plane normal *CN* intersects the side of the sphere nearest the x-ray source, the projection must be viewed from that side and the film "read" from that side. In order to know, after processing, the orientation the film had during the x-ray exposure, the upper right-

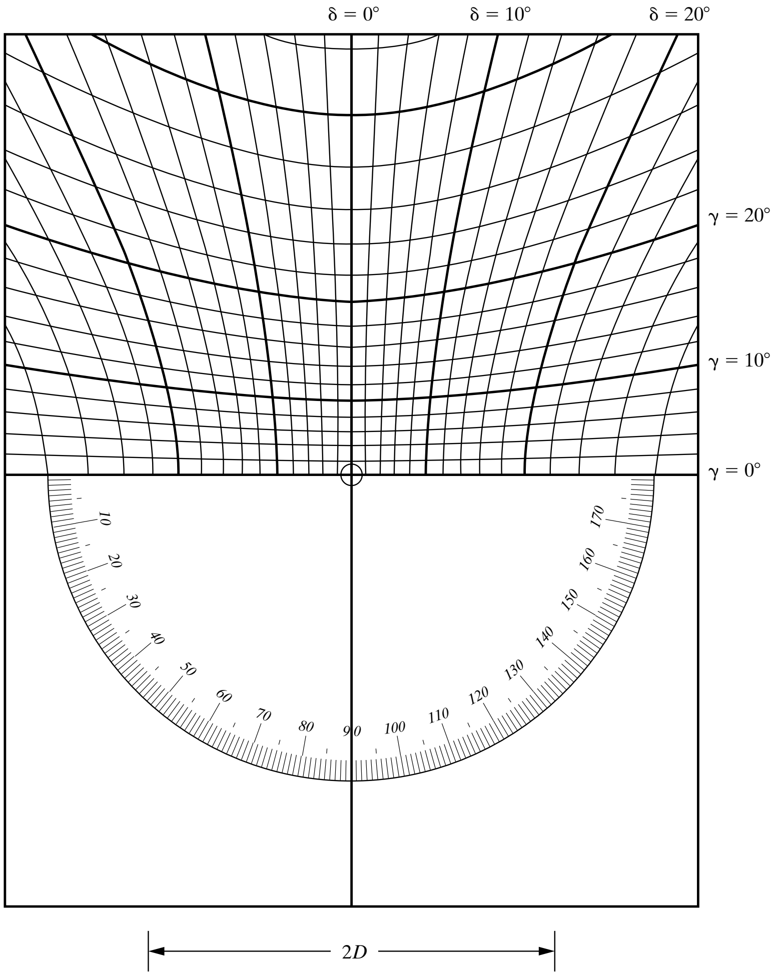

Figure 3 Greninger chart for the solution of back-reflection Laue patterns, reproduced in the correct size for a specimen-to-film distance *D* of 3 cm.

hand corner of the film (viewed from the crystal) is cut away before it is placed in the cassette, as shown in Fig. 2. When the film is read, this cut corner must therefore be at the upper left, as shown in Fig. 4(a). The angles γ and δ, read from the chart, are then laid out on the projection as indicated in Fig. 4(b). Note that the underlying Wulff net must be oriented so that its meridians run from side to side, not top to bottom. The reason for this is the fact that diffraction spots which lie on curves

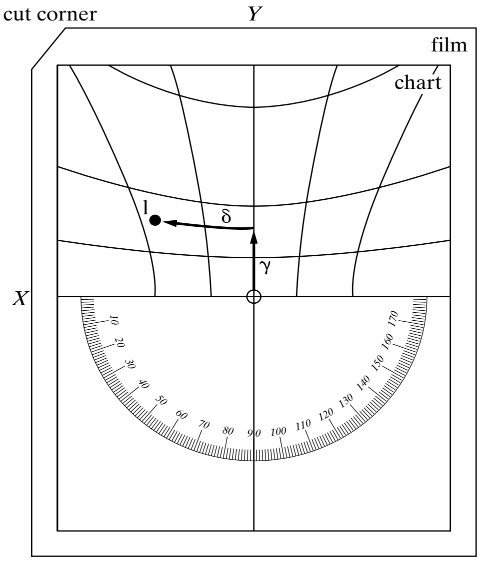

(a)

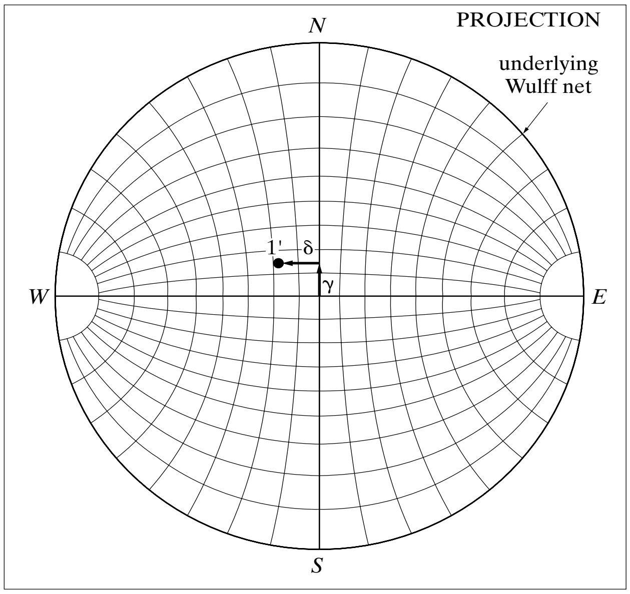

(b)

Figure 4 Use of the Greninger chart to plot the pole of a reflecting plane on a stereographic projection. Pole 1´ ln (b) is the pole of the plane causing diffraction spot 1 in (a).

of constant γ come from planes of a zone, and the poles of these planes must therefore lie on a great circle on the projection. The γ, δ coordinates corresponding to diffraction spots on the lower half of the film are obtained simply by reversing the Greninger chart end for end.

It helps to remember that there are two frames of reference involved in analyzing Laue patterns. The first is the coordinate system of the laboratory, and the second is the coordinate system of the crystal. When the crystal is reoriented, this second system is also reoriented relative to the laboraotry coordinate system. The Wulff net and Greninger chart are in the laboratory frame of reference while the film and the tracing paper or transparency on top of the Wulff net represent the crystal. Since the laboratory, the x-ray generator and the Laue camera remain fixed in position, it is perhaps less confusing to keep the orientation of the Greninger chart and Wulff net fixed and to rotate only the film on the Greninger chart and the stereographic projection of the poles of the crystal on the Wulff net.

The procedure may be illustrated by determining the orientation of the aluminum crystal whose back-reflection Laue pattern. Fig. 5 is a tracing of this photograph, showing the more important spots numbered for reference. The poles of the planes causing these numbered spots are plotted stereographically in Fig. 6 by the method of Fig. 4 and are shown as solid circles.

The problem now is to "index" these planes, i.e., to find their Miller indices, and so disclose the orientation of the crystal. With the aid of a Wulff net, great circles are drawn through the various sets of poles corresponding to the various hyperbolae of spots on the film. These great circles connect planes of a zone, and planes lying at their intersections are generally of low indices, such as {100}, {110}, {111}, and {112}. The axes of the zones themselves are also of low indices, so it is helpful

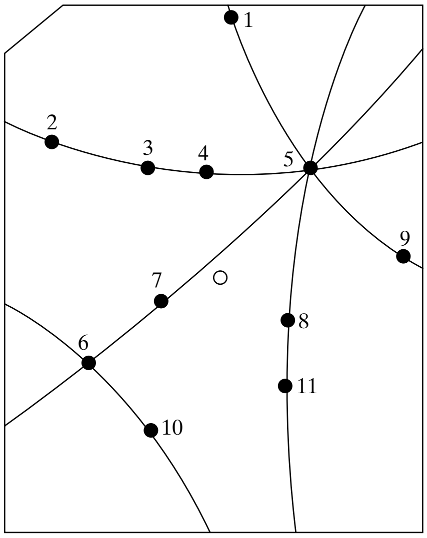

Figure 5 Selected diffraction spots of back-reflection Laue pattern of an aluminum crystal, traced.

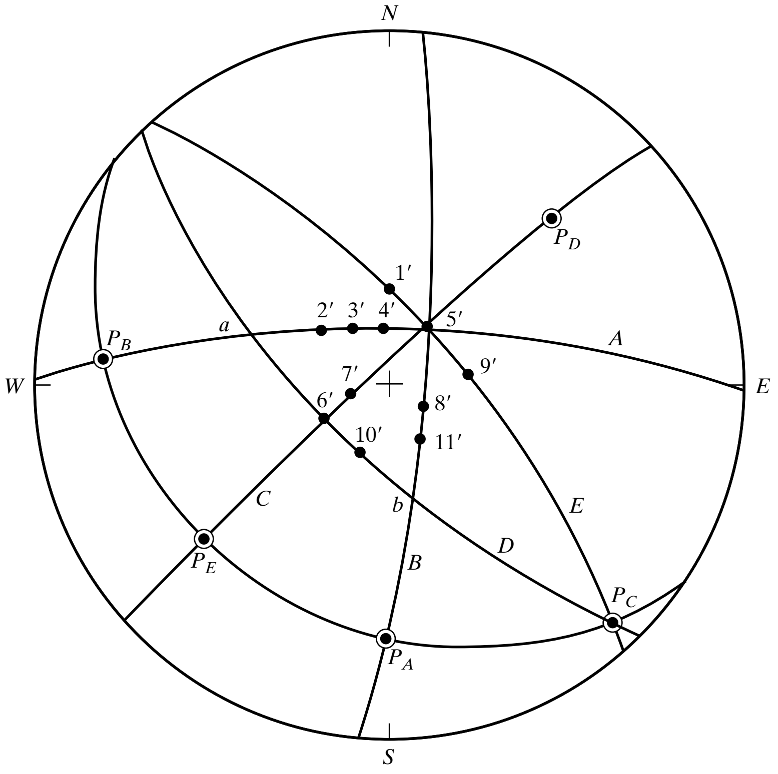

Figure 6 Stereographic projection corresponding to back-reflection pattern of Fig. 5.

to locate these axes on the projection. They are shown as open circles in Fig. 6, P_A being the axis of zone A, P_B the axis of zone B, etc. The angles between important poles (zone intersections and zone axes) are measured next and the poles are identified by comparing of these measured angles with those calculated for cubic crystals. The method is essentially one of trial and error. Note, for example, that the angles P_A - P_B, P_A - 5′, and P_B - 5′ are all 90°. This suggests that one or more of these poles might be {100} or {110}, since the angle between two {100} poles or between two {110} poles is 90°. Suppose P_A, P_B, and 5′ are all {100} poles.[1] Then P_E, which lies on the great circle between P_A and P_B and at an angular distance of

---

[1] The reader may detect an apparent error in nomenclature here. Pole 5′ for example, is assumed to be a {100} pole and spot 5 on the diffraction pattern is assumed, tacitly, to be due to a 100 reflection. Aluminium, however, is face-centered cubic, and there is no 100 reflection from such a lattice, since *hkl* must be unmixed for diffraction to occur. In this case, spot 5, is due to overlapping diffracted beans from second, fourth, sixth, etc. orders of 100 diffraction. But these Bragg planes are all parallel and are represented on the stereographic projection by one pole, which is conventionally designated as {100}. The corresponding diffraction spot is also called, conventionally but loosely, the 100 spot.

45° from each, must be a {110} pole. Next consider zone *C*; the distance between pole 6´ and either pole 5´ or P_E is also 45°. But reference to a standard projection shows that there is no important pole located midway on the great circle between {100}, identified with 5´, and {110}, identified with P_E. The original assumption is therefore wrong. A second assumption is required which is consistent with the angles measured so far, namely that 5´ is a {100} pole, as before, but that P_A and P_B are {110} poles. P_E must then be a {100} pole and 6´ a {110} pole. This assumption is checked by measuring the angles in the triangle *a* - *b* - 5´. Both *a* and *b* are found to be 55° from 5´, and 71° from each other, which conclusively identifies *a* and *b* as {111} poles. Note also, from a standard projection, that a {111} pole must lie on a great circle between {100} and {110}, which agrees with the fact that *a*, for example, lies on the great circle between 5´, assumed to be {100}, and P_B, assumed to be {110}. The second assumption is therefore shown to be consistent with the data.

Figure 7 shows the stereographic projection in a more complete form, with all poles of the type {100}, {110}, and {111} located and identified. Note that it was not

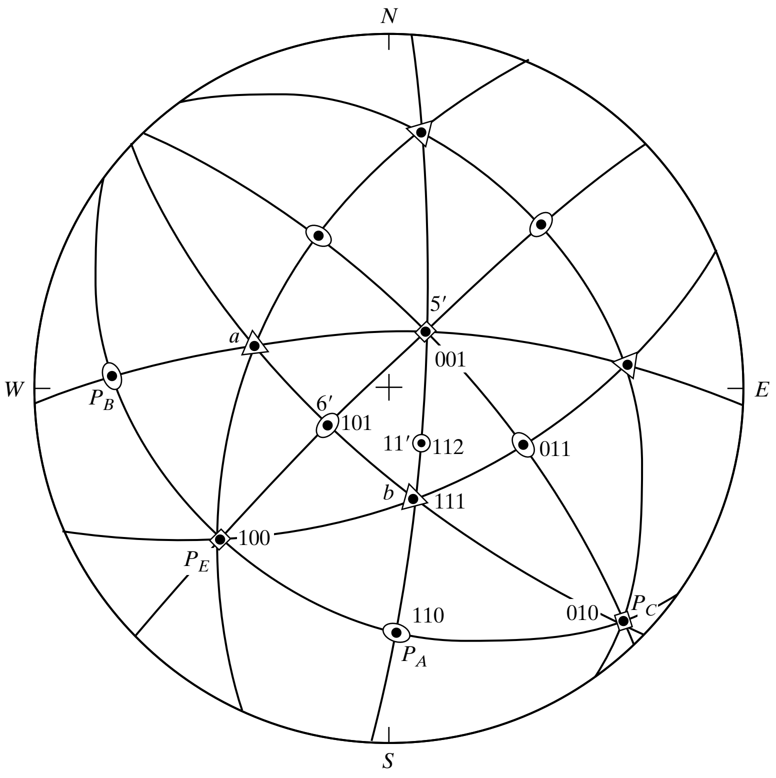

Figure 7 Stereographic projection of Fig. 6 with poles identified.

necessary to index all the observed diffraction spots in order to determine the crystal orientation, which is specified completely, in fact, by the locations of any two {100} poles on the projection. The information given in Fig. 7 is therefore all that is commonly required. Occasionally, however, it may be necessary to determine the Miller indices of a particular diffraction spot on the film, spot 11 for example. To find these indices, note that pole 11´ is located 35° from (001) on the great circle passing through (001) and (111). Reference to a standard projection and a table of interplanar angles shows that its indices are (112).

As mentioned above, the stereographic projection of Fig. 7 is a complete description of the orientation of the crystal. Other methods of description are also possible. The crystal to which Fig. 7 refers had the form of a square plate and was mounted with its plane parallel to the plane of the film (and the projection) and its edges parallel to the film edges, which are in turn parallel to the *NS* and *EW* axes of the projection. Since the (001) pole is near the center of the projection, which corresponds to the specimen normal, and the (010) pole near the edge of the projection and approximately midway between the *E* and *S* poles, a rough description of the crystal orientation is as follows: one set of cube planes is approximately parallel to the surface of the plate while another set passes diagonally through the plate and approximately at right angles to its surface.

Another method of description may be used when only one direction in the crystal is of physical significance, such as the plate normal in the present case. For example, a compression test of this crystal may be required with the axis of compression normal to the plate surface. The interest is then in the orientation of the crystal relative to the compression axis (plate normal) or, stated inversely, in the orientation of the compression axis relative to certain directions of low indices in the crystal. Now inspection of a standard projection shows that each half of the reference sphere is covered by 24 similar and equivalent spherical triangles, each having {100}, {110}, and {111} as its vertices. The plate normal, i.e., the direction along which the polychromatic bean was incident on the crystal, will fall in one of these triangles and it is necessary to draw only one of them in order to describe the precise location of the normal. In Fig. 7, the plate normal lies in the (001)-(101)-(111) triangle which is redrawn in Fig. 8 in the conventional orientation, as though it formed part of a (001) standard projection. To locate the plate normal on this new drawing, measure the angles between the center of the projection in Fig. 7 and the three adjacent 001, 101, and 111 poles. Let these angles be ρ_{001}, ρ_{101}, and ρ_{111}. These angles are then used to determine the three arcs shown in Fig. 8. These are circle arcs, but they are *not* centered, in general, on the corresponding poles; rather, each one is the locus of points located at an equal *angular* distance from the pole involved and their intersection therefore locates the desired point. Another method of arriving at Fig. 8 from Fig. 7 consists simply in rotating the whole projection, poles and plate normal together, from the orientation shown in Fig. 7 to that of a standard (001) projection.

Similarly, the orientation of a single-crystal wire or rod may be described in terms of the location of its axis in the unit stereographic triangle. Note that this

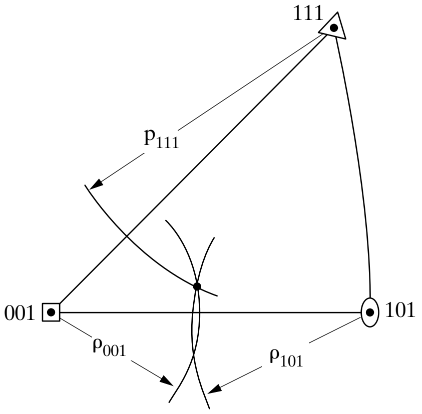

Figure 8 Use of the unit stereographic triangle to describe crystal orientation. The point inside the triangle is the normal to the single crystal plate whose orientation is shown in Fig. 7.

method does not completely describe the orientation of the crystal, since it allows one rotational degree of freedom about the specimen axis. This is of no consequence, however, if only the value of some measured physical or mechanical property is needed along a particular direction in the crystal.

There are other ways of manipulating both the Greninger chart and the stereographic projection, and the particular method used is purely a matter of personal preference. For example, the individual spots on the film may be ignored, and the various hyperbolae on which they lie may be used. The spots on one hyperbola are due to diffracted beams from planes of one zone and, by means of the Greninger chart, the axis of this zone can be plotted directly without plotting the poles of any of the planes belonging to it. The procedure is illustrated in Fig. 9. Keeping the centers of film and chart coincident, rotate the film about this center until a particular hyperbola of spots coincides with a curve of constant γ on the chart, as in (a). The amount of rotation required is read from the intersection of a vertical pencil line, previously ruled through the center of the film and parallel to one edge, with the protractor of the Greninger chart. Suppose this angle is ε. Then the projection is rotated by the same angle ε with respect to the underlying Wulff net and the zone axis is plotted on the vertical axis of the projection at an angle γ from the *circumference*, as in (b).[2] Note that zone A itself is represented by the great circle located at an angle γ above the *center* of the projection. Many investigators use only the zone axes in solving the orientation of the crystal; they will ordinarily not plot the zone (great) circle. Others prefer to plot all zone circles and to use the intersections of multiple circles as additional information. In either case, once all the zone axes or great circles of the important zones are plotted, analysis focuses on the most important poles, i.e., those poles at the intersection of a number of hyperbolas and

---

[2] Note that, when a hyperbola of spots is lined up with a horizontal hyperbola on the chart as in [Fig. 9(a)], the vertical hyperbolae can be used to measure the difference in angle δ for any two spots and that this angle is equal to the angle between the planes causing those spots, just as the angle between two poles lying on a meridian of a Wulff net is given by their difference in latitude.

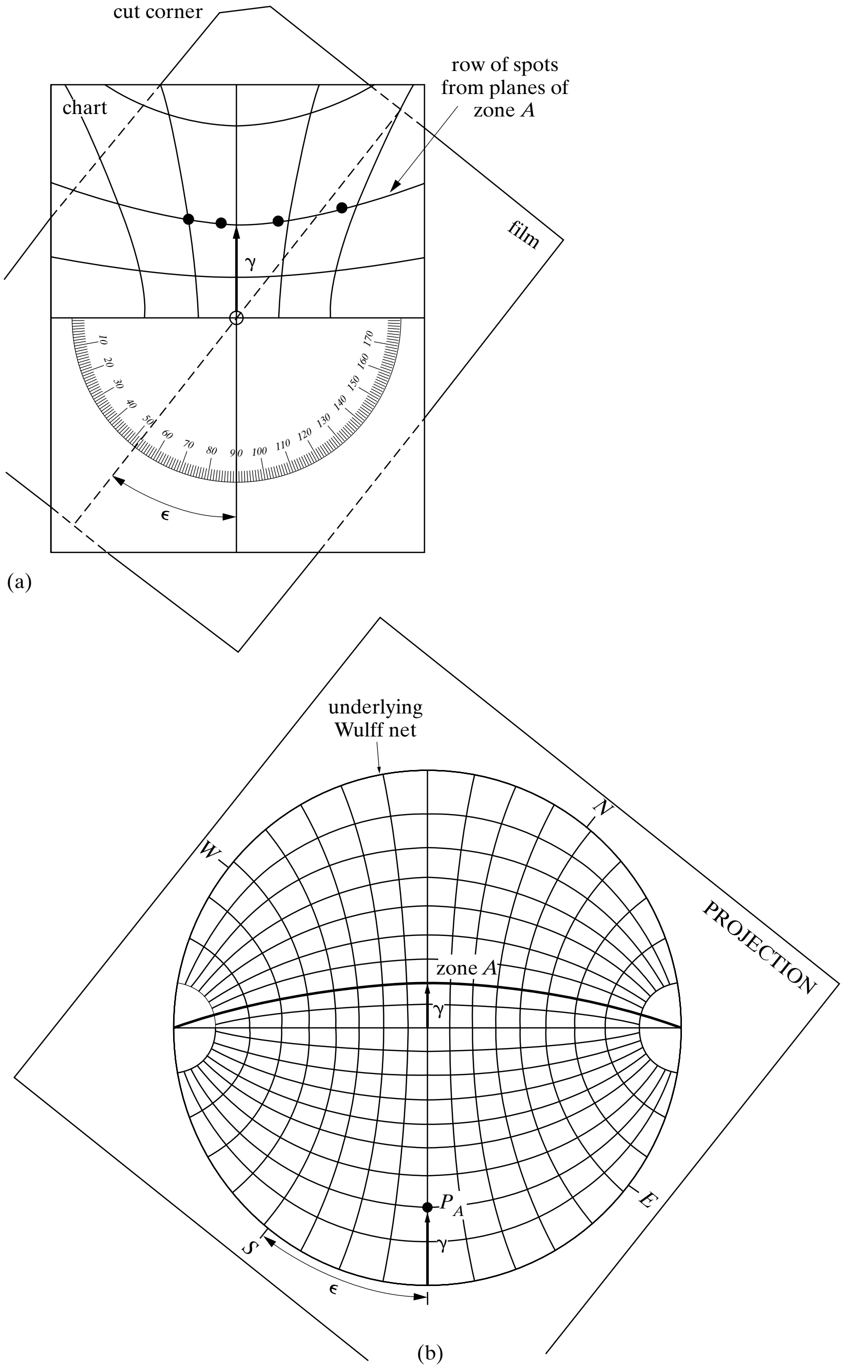

Figure 9 Use of the Greninger chart to plot the axis of a zone of planes on the stereographic projection. P_A is the axis of zone A.

which are well-separated from neighboring diffracted beams are always of low indices and can usually be indexed without difficulty.

An experienced investigator working with a familiar material can often recognize the symmetry of Laue patterns from low-index or near-low-index directions, and compilations of Laue patterns from specific directions [G.40] or commercially available computer simulation programs are very handy in this context (e.g., [2]). Figure 10a was traced from film (note the "UR" labeled the upper right of the original film is now flipped), and the pattern of spots exhibits mirror symmetry across the row of spots labeled with "1" at each end (of course some distortion appears since the incident beam is slightly off zone 1). Mirror-related pairs of hyperbolas are indicated in Fig. 10b and include zones 3 and 4, 5 and 6, 7 and 8, 9 and 10, and 11 and 12. Prominent hyperbola intersections are outlined by circles in Fig. 10a, and important intersections are labeled A-G in Fig. 10b. The pair of intersections C and D are mirror related as are E and F. The intersection matching G lies off the film. Use of sets of symmetry related and crystallographically equivalent zones can speed identification of symmetry related zone intersections greatly since these must necessarily be the same type of *hkl*.

Measurement of the angles between intersections A-G (directly with the Greninger chart or after transfer to the stereographic projection) reveals A and B correspond to 111 and 110 type reflections, respectively, while the pair C and D are 210 type reflections, the pair E and F are 211 reflections and G is a 311 type reflection. Inspection of the calculated 441 and 331 Laue patterns shown in Fig. 10c and d, respectively, confirms the identification given above. Note that the intensities of the symmetry-related spots may vary for different crystallographically equivalent zones due to the tilt of the crystal, and hyperbolae may not appear to be identical due to such differences in intensity or to distortions produced by incident beams along high index directions (e.g., 2 mm symmetry is associated with Laue pattern recorded with the incident beam along 110 and this is far from apparent at B in Fig. 10a). For patterns recorded with the beam along a low index direction such as 100 or 111, several parallel, closely-spaced hyperbolas may be visible and care is required when selecting symmetry related sets.

Another method of indexing plotted poles depends on having available a set of detailed standard projections in a number of orientations, such as {100}, {110}, and {111} for cubic crystals. It is also a trial and error method and may be illustrated with reference to Fig. 6. First, a prominent zone is selected and an assumption is made as to its indices: for example, assume that zone *B* is a $\langle 100 \rangle$ zone i.e., its zone axis P_B is $\langle 100 \rangle$. This assumption is then tested by (a) rotating the projection about its center until P_B lies on the equator of the Wulff net and the ends of the zone circle coincide with the *N* and *S* poles of the net, and (b) rotating all the important points on the projection about the *NS*-axis of the net until P_B lies at the center and the zone circle at the circumference. The new projection is then superimposed on a {100} standard projection and rotated about the center until all points on the projection coincide with those on the standard. If no such coincidence is obtained, P_B is unlikely to be $\langle 100 \rangle$, and another standard projection should be tried. For the par-

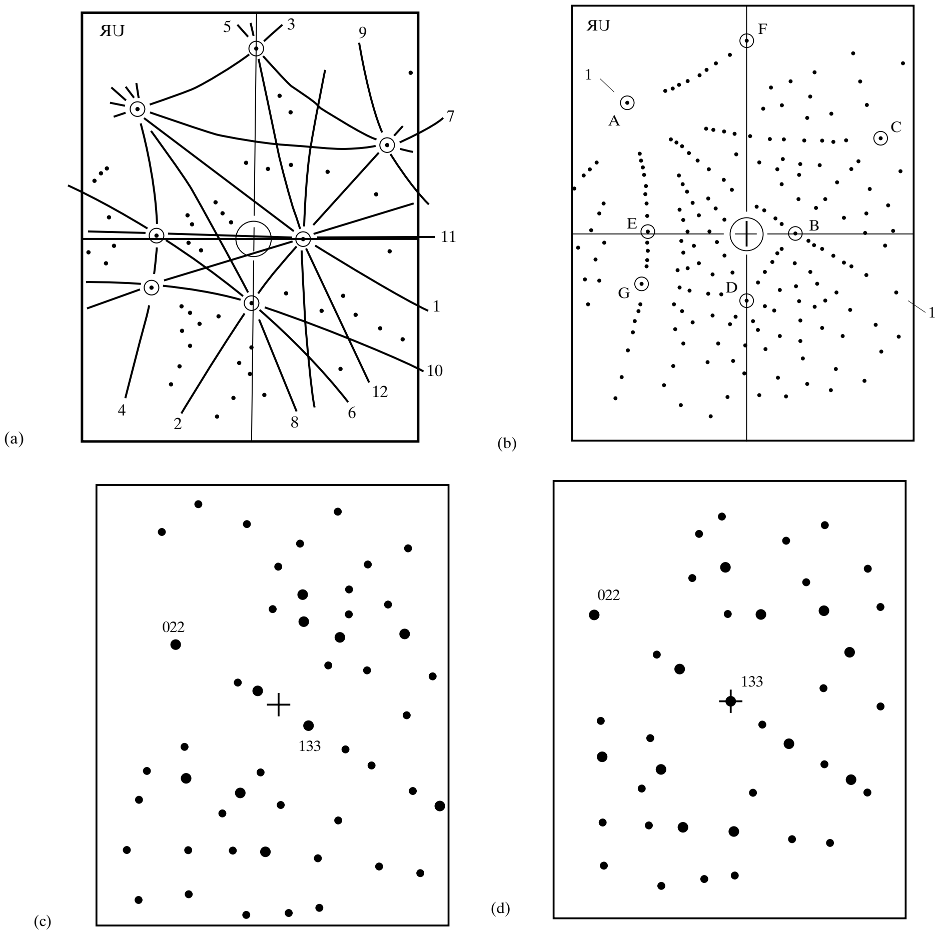

Figure 10 Back reflection Laue patterns for analysis by consideration of symmetry. (a) Pattern traced from the originial. (b) Zones indicated on the pattern. (c) Simulation of 144 pattern and (d) Simulation of 133 pattern (after G.P.). The larger filled circles represent more intense diffracted beams in the simulations.

ticular case of Fig. 6, a coincidence would be obtained only on a {110} standard, since P_B is actually a {110} pole. Once a match has been found, the indices of the unknown poles are given simply by the indices of the poles on the standard with which they coincide.

In the absence of a Greninger chart, the pole corresponding to any observed Laue spot may be plotted by means of an easily constructed "stereographic ruler." The construction of the ruler is based on the relations shown in Fig. 11. This drawing is a section through the incident beam *OC* and any diffracted beam *CS*. Here it is convenient to use the plane normal *CN'* rather than *CN* and to make the projec-

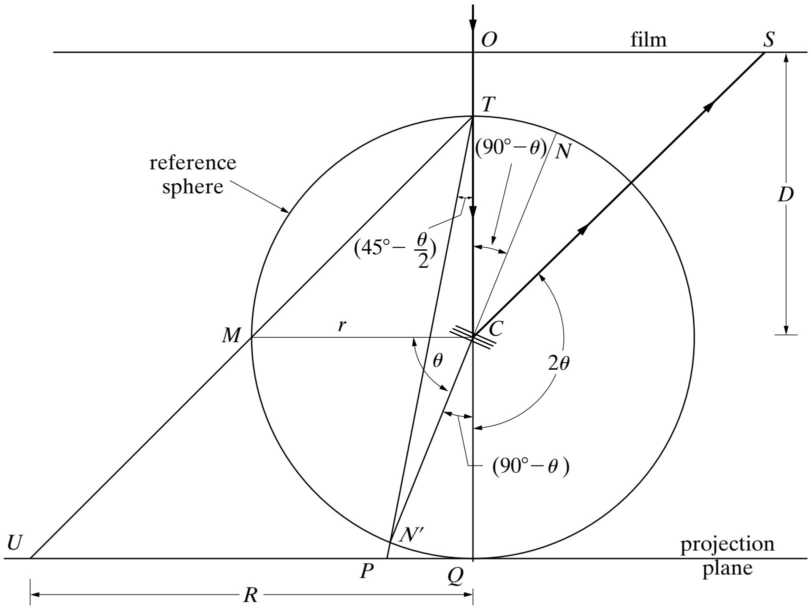

Figure 11 Relation between diffraction spot *S* and stereographic projection *P* of the plane causing the spot, for back reflection.

tion from *T*, the intersection of the reference sphere with the incident beam. The projection of the pole *N'* is therefore at *P*. From the measured distance *OS* of the diffraction spot from the center of the film,

$$OS = OC \tan(180° - 2\theta) = D \tan(180° - 2\theta), \tag{4}$$

the distance *PQ* of the projected pole from the center of the projection is

$$PQ = TQ \tan\left(45° - \frac{\theta}{2}\right) = 2r \tan\left(45° - \frac{\theta}{2}\right), \tag{5}$$

where *D* is the specimen-film distance and *r* the radius of the reference sphere. The value of *r* is fixed by the radius *R* of the Wulff net used, since the latter equals the radius of the basic circle of the projection. If the pole of the plane were in its extreme position at *M*, then its projection would be at *U*. The point *U* therefore lies on the basic circle of the projection, and *UQ* is the radius *R* of the basic circle. Because the triangles *TUQ* and *TMC* are similar, $R = 2r$ and

$$PQ = R \tan\left(45° - \frac{\theta}{2}\right). \tag{6}$$

The ruler is constructed by marking off, from a central point, a scale of centimeters by which the distance *OS* may be measured. The distance *PQ* corresponding to each distance *OS* is then calculated from Eqs. (4) and (6), and marked off from the center of the ruler in the opposite direction. Corresponding graduations are given the same number and the result is the ruler shown in Fig. 12, which also illustrates the method of using it. [Calculation of the various distances *PQ* can be avoided by use of the Wulff net itself. Figure 11 shows that the pole of the reflecting plane is located at an angle θ from the edge of the projection, and θ is given for each distance *OS* by Eq. (13). The ruler is laid along the equator of the Wulff net, its center coinciding with the net center, and the distance *PQ* corresponding to each angle θ is marked off with the help of the angular scale on the equator.]

From the choice of plane normal made in Fig. 11, it is apparent that the projection must be viewed from the side opposite the x-ray source. This requires that the film be read from that side also, i.e., with its cut corner in the upper right-hand position. The projection is then placed over the film, illuminated from below, as shown in Fig. 12. With the center of the ruler coinciding with the center of the projection, the ruler is rotated until its edge passes through a particular diffraction spot. The distance *OS* is noted and the corresponding pole plotted as shown, on the other side of center and at the corresponding distance *PQ*. This procedure is repeated for each important diffraction spot, after which the projection is transferred to a Wulff net and the poles indexed by either of the methods previously described. Note that this procedure gives a projection of the crystal from the side opposite the x-ray source, whereas the Greninger chart gives a projection of the crystal as seen from the x-ray source. A crystal orientation can, of course, be described just as well from one side as the other, and either projection can be made to coincide with the other by a 180°

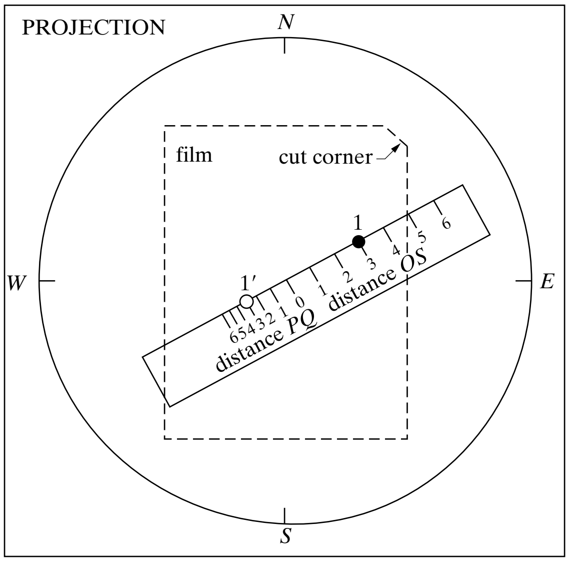

Figure 12 Use of a stereographic ruler to plot the pole of a reflecting plane on a stereographic projection in the back-reflection Laue method. Pole 1′ is the pole of the plane causing diffraction spot 1.

rotation of the projection about its *EW*-axis. Although simple to use and construct, the stereographic ruler is not as accurate as the Greninger chart in the solution of back-reflection patterns.

The methods of determining and describing crystal orientation have been presented here exclusively in terms of cubic crystals, because these are the simplest kind to consider and the most frequently encountered. These methods are quite general, however, and can be applied to a crystal of any system as long as its interplanar angles are known.

However, a noncubic crystal may have such low symmetry and/or be so oriented that the Laue pattern shows only one spot, or none at all, from a low-index plane. Plane indexing can then be difficult. Methods of coping with this problem include the following:

1. The crystal is re-oriented, in a manner suggested by the Laue pattern, and examined in a diffractometer. See Sec. 5.
2. A set of simulated Laue patterns, covering the unit stereographic triangle of the crystal, is generated by a computer [2]. The simulated pattern which most nearly matches the unknown yields tentative (*hkl*) indices for three prominent spots. Measurements on the film of the angles between these spots and the film center (incident x-ray beam) yield tentative indices for the crystal plane normal to the incident beam. A simulated pattern is then generated for this special orientation and compared with the unknown pattern to verify the plane indexing.

Specialized books on the Laue methods are those of Amoros *et al.* [G.31] and Preuss *et al.* [G.40]. The latter contains a catalog of back-reflection patterns, many generated by a computer.

3 TRANSMISSION LAUE METHOD

Given a specimen of sufficiently low absorption, a transmission Laue pattern can be obtained and used, in much the same way as a back-reflection Laue pattern, to reveal the orientation of the crystal.

In either Laue method, the diffraction spots on the film, due to the planes of a single zone in the crystal, always lie on a curve which is some kind of conic section. When the film is in the transmission position, this curve is a complete ellipse for sufficiently small values of ϕ, the angle between the zone axis and the transmitted beam (Fig. 13). For somewhat larger values of ϕ, the ellipse is incomplete because of the finite size of the film. When $\phi = 45°$, the curve becomes a parabola; when ϕ exceeds 45°, a hyperbola; and when $\phi = 90°$, a straight line. In all cases, the curve passes through the central spot formed by the transmitted beam.

The angular relationships involved in the transmission Laue method are illustrated in Fig. 14. Here a reference sphere is described about the crystal at *C*, the incident beam entering the sphere at *I* and the transmitted beam leaving at *O*. The

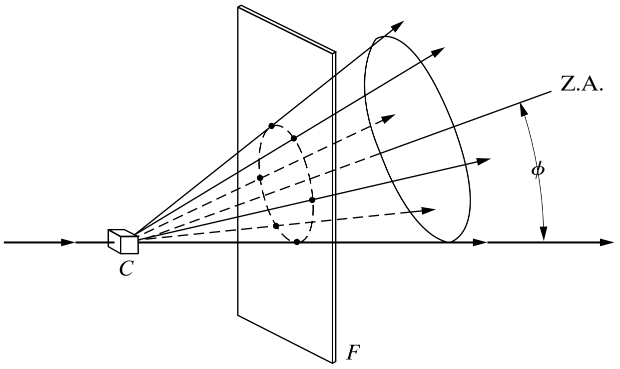

Figure 13 Intersection of a conical array of diffracted beams with a film placed in the transmission position. C = crystal, F = film, Z.A. = zone axis.

film is placed tangent to the sphere at O, and its upper right-hand corner, viewed from the crystal, is cut off for identification of its position during the x-ray exposure. The beam diffracted as plane shown strikes the film at R, and the normal to this diffraction plane intersects the sphere at P.

Consider diffraction from planes of a zone whose axis lies in the yz-plane at an angle ϕ to the transmitted (or incident) beam. If a single plane of this zone is

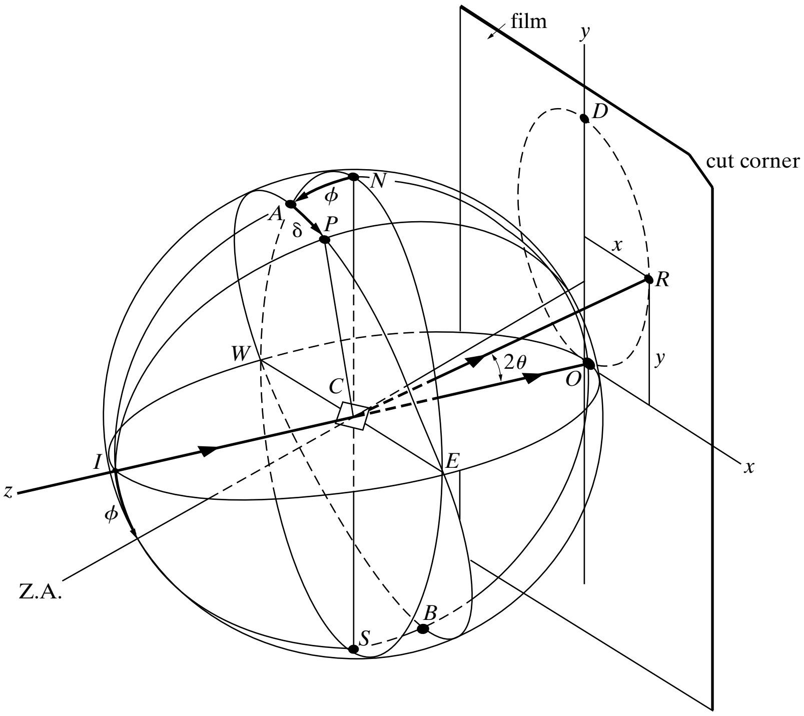

Figure 14 Relation between plane normal orientation and diffraction spot position in the transmission Laue method.

rotated so that its pole, initially at A, travels along the great circle $APEBWA$, then it will pass through all the orientations in which planes of this zone might occur in an actual crystal. During this rotation, the diffraction spot on the film, initially at D, would travel along the elliptical path $DROD$ shown by the dashed line.

Any particular orientation of the plane, such as the one shown in the drawing, is characterized by particular values of ϕ and δ, the angular coordinates of its pole. These coordinates in turn, for a given crystal-film distance D ($= CO$), determine the x,y coordinates of the diffraction spot R on the film. The plane orientation follows from the spot position, and one way of proceeding is by means of the Leonhardt chart shown in Fig. 15.

This chart is exactly analogous to the Greninger chart for solving back-reflection patterns and is used in precisely the same way. It consists of a grid composed of two sets of lines: the lines of one set are lines of constant ϕ and correspond to the

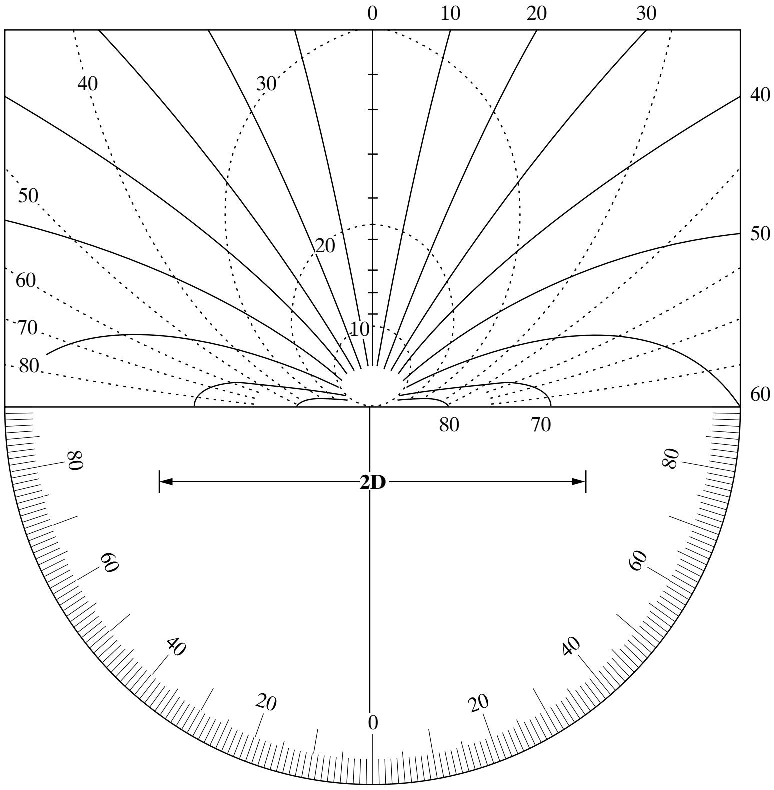

Figure 15 Leonhardt chart for the solution of transmission Laue patterns, reproduced in the correct size for a specimen-to-film distance of 3 cm. The dashed lines are lines of constant ϕ, and the solid lines are lines of constant δ. (Courtesy of C. G. Dunn [3].)

meridians on a Wulff net, and the lines of the other are lines of constant δ and correspond to latitude lines. By means of this chart, the pole of a plane causing any particular diffraction spot may be plotted stereographically. The projection plane is tangent to the sphere at the point I of Fig. 14, and the projection is made from the point O. This requires that the film be read from the side facing the crystal, i.e., with the cut corner at the upper right. Figure 16 shows how the pole corresponding to a particular spot is plotted when the film and chart are in the parallel position. An alternate way of using the chart is to rotate it about its center until a line of constant ϕ coincides with a row of spots from planes of a single zone, as shown in Fig. 17; knowing ϕ and the rotation angle ε, allows the axis of the zone to be plotted directly.

A stereographic ruler may be constructed for the transmission method and will give greater plotting accuracy than the Leonhardt chart, particularly when the angle ϕ approaches 90°. Figure 18, which is a section through the incident beam and any diffracted beam, shows that the distance of the diffraction spot from the center of the film is given by

$$OS = D \tan 2\theta. \tag{7}$$

The distance of the pole of the diffraction plane from the center of the projection is given by

$$PQ = R \tan\left(45^\circ - \frac{\theta}{2}\right). \tag{8}$$

Figure 19 illusrates the use of a ruler constructed according to these equations. In this case, the projection is made on a plane located on the same side of the crystal as the film and, accordingly, the film must be read with its cut corner in the upper left-hand position.

Whether the chart or the ruler is used to plot the poles of diffraction planes, they are indexed in the same way as back-reflection patterns. The location of the projected poles is quite different for the two x-ray methods. The poles of planes responsible for observed spots on a transmission film are all located near the edge of the projection, since such planes must necessarily be inclined at small angles to the incident beam. The reverse is true of back reflection patterns.

4 DIFFRACTOMETER METHOD

Still another method of determining crystal orientation involves the use of the diffractometer and a procedure radically different from that of either Laue method. With the essentially monochromatic radiation used in the diffractometer, a single crystal will diffract only when its orientation is such that a certain set of diffraction planes is inclined to the incident beam at an angle θ which satisfies Bragg's law for that set of planes and the characteristic radiation employed. But when the detector, fixed in position at the corresponding angle 2θ, discloses that diffraction *is*

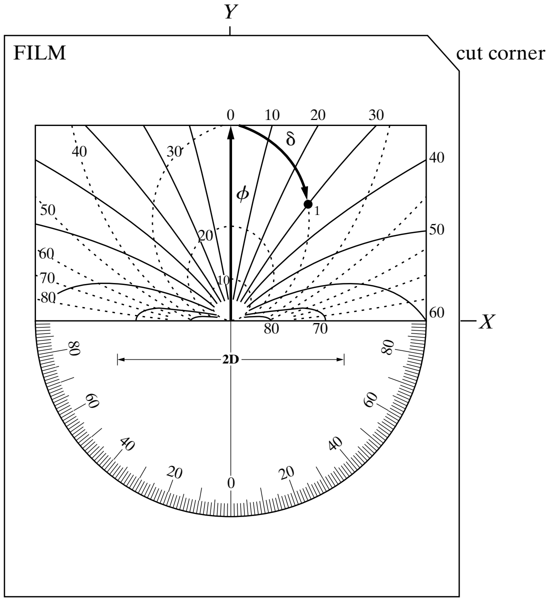

(a)

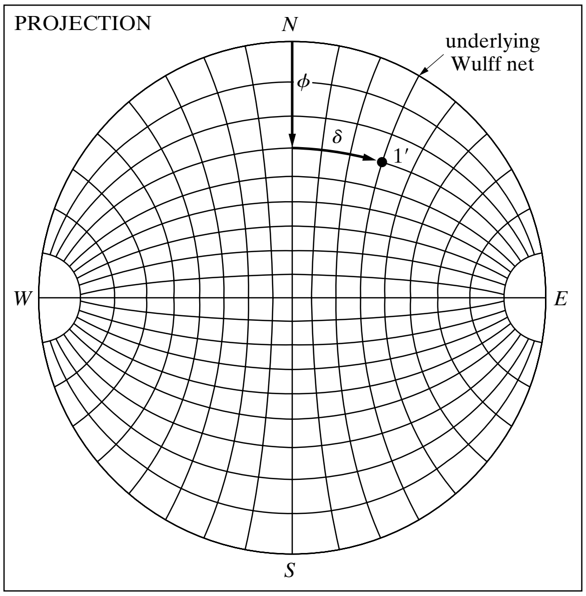

(b)

Figure 16 Use of the Leonhardt chart to plot the pole of a plane on a stereographic projection. Pole 1' in (b) is the pole of the plane causing diffraction spot 1 in (a).

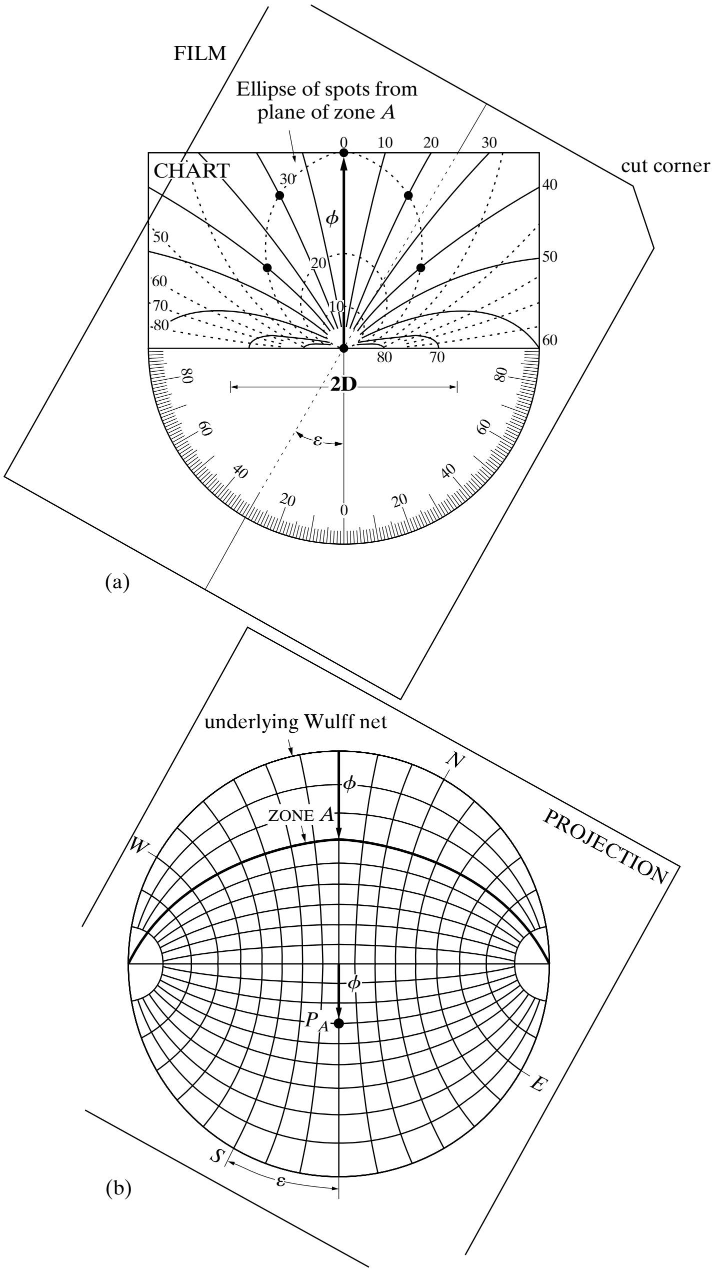

Figure 17 Use of the Leonhardt chart to plot the axis of a zone of planes on the projection. P_A is the axis of zone A.

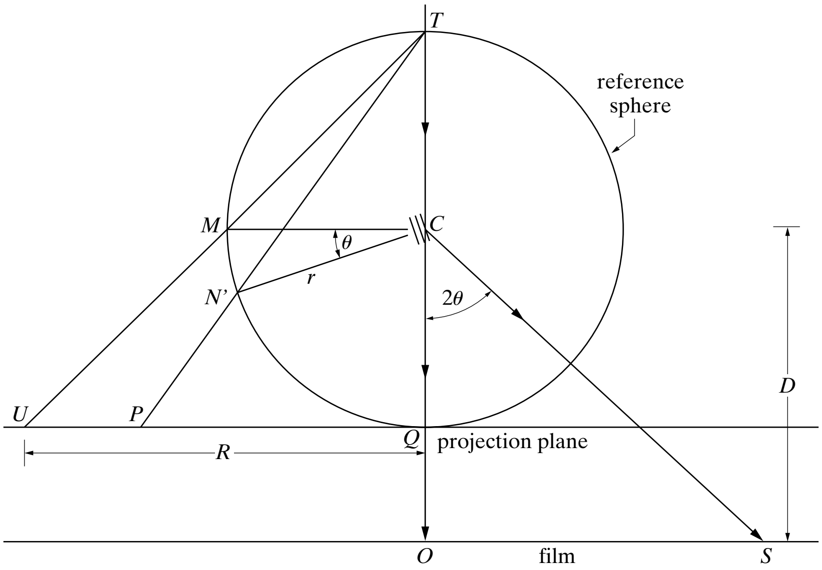

Figure 18 Relation between diffraction spot *S* and stereographic projection *P* of the plane causing the spot, in transmission.

produced, then the inclination of the diffraction plane relative to any chosen line or plane on the crystal surface is known from the position of the crystal. Two kinds of operation are required:

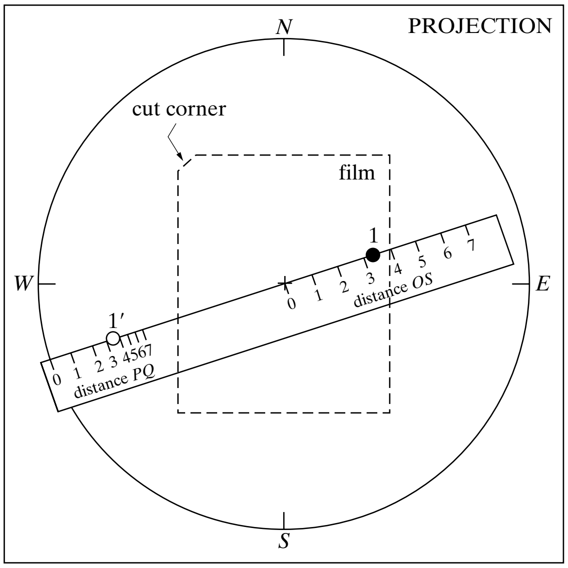

Figure 19 Use of a stereographic ruler to plot the pole of a diffracting plane on a stereographic projection in the transmission Laue method. Pole 1' is the pole of the plane causing diffraction spot 1.

1. rotation of the crystal about various axes until an angular position is found for which diffraction occurs.
2. location of the pole of the diffraction plane diffraction on a stereographic projection from the known angles of rotation.

The diffractometer method has many variations, depending on the particular kind of goniometer used to hold and rotate the specimen. Only one of these variations will be described here, that involving the goniometer used in the reflection method of determining preferred orientation, since that is the kind most generally available in materials laboratories. This specimen holder needs very little modification for use with single crystals, the chief one being an increase in the width of the primary beam slits in a direction parallel to the diffractometer axis in order to increase the diffracted intensity. This type of holder provides the three possible rotation axes shown in Fig. 20: one coincides with the diffractometer axis, the second (*AA'*) lies in the plane of the incident beam *I* and diffracted beam *D* and tangent to the specimen surface, shown here as a flat plate, while the third (*BB'*) is normal to the specimen surface.

Suppose the orientation of a cubic crystal is to be determined. For such crystals it is convenient to use {111}: there are four sets of these and their diffracting power is usually high. First, the 2θ value for the 111 reflection (or, if desired, the 222 reflection) is computed from the known spacing of the {111} planes and the known wavelength of the radiation used. The detector is then fixed in this 2θ position. The specimen holder is now rotated about the diffractometer axis until its surface, and the rotation axis *AA'*, is equally inclined to the incident beam and the diffracted beam, or rather, to the line from crystal to detector with which the diffracted beam, when formed, will coincide. The specimen holder is then fixed in this position, no further rotation about the diffractometer axis being required. Then, by rotation about the axis *BB'*, one edge of the specimen, or a line drawn on it is made parallel to the diffractometer axis. This is the initial position illustrated in Fig. 20.

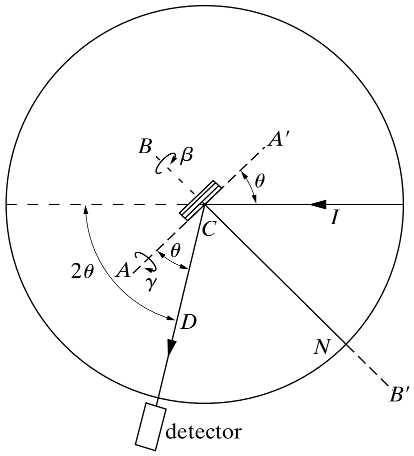

Figure 20 Crystal rotation axes for the diffractometer method of determining orientation

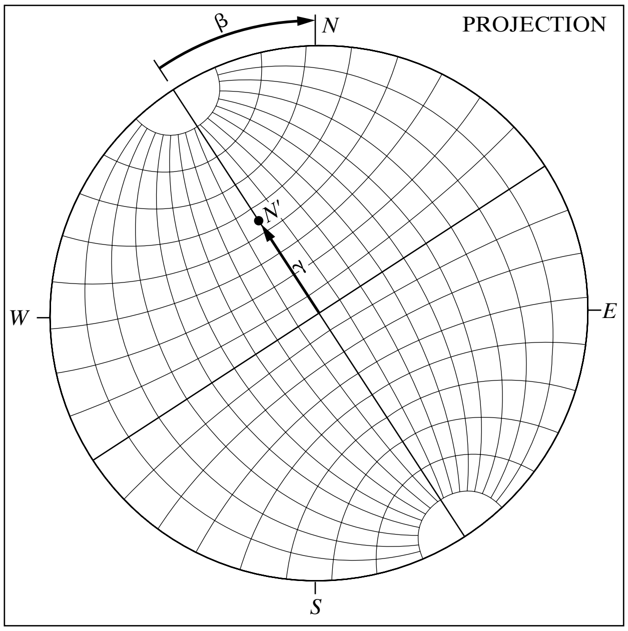

Figure 21 Plotting method used when determining crystal orientation with the diffractometer. (The directions of the rotations shown here correspond to the directions of the arrows in Fig.20.)

The crystal is then slowly rotated about the axes *AA*' and *BB'* until an indication of a reflection is observed on the rate meter. Computerized diffractometers allow this search to be automated; the computer systematically checks different combinations of notations about axes AA' and BB' until a peak is found, whereupon the search ends and the computer awaits further instructions. The increases in productivity which result from the ability to align crystals while the operator is elsewhere should not be underestimated.

Once the position of the crystal for diffraction has been found, the normal to one set of {111} planes coincides with the line *CN*, that is, lies in the plane of the diffractometer circle and bisects the angle between incident and diffracted beams. The pole of these diffracting planes may now be plotted stereographically, as shown in Fig. 21. The projection is made on a plane parallel to the specimen surface, and with the *NS*-axis of the projection parallel to the reference edge or line mentioned above. When the crystal is rotated β degrees about *BB'* from its initial position, the projection is also rotated β degrees about its center. The direction *CN*, which might be called the normal to "potential" diffraction planes, is represented by the pole *N*´, which is initially at the center of the projection but which moves γ degrees along a radius when the crystal is rotated γ degrees about *AA*´.

The object is to make *N*´ coincide with a {111} pole and so disclose the location of the latter on the projection. The search may be made by varying γ continuously for fixed values of β 4 or 5° apart; the projection is then covered point by point along a series of radii. It is enough to examine one quadrant in this way since there will always be at least one {111} pole in any one quadrant. Once one pole has been located, the search for the second is aided by the knowledge that it must be 70.5° from the first. Although two {111} poles are enough to fix the orientation of the crystal, a third should be located as a check.

Parenthetically, it should be noted that the positioning of the crystal surface and the axis AA' at equal angles to the incident and diffracted beams is done only for convenience in plotting the stereographic projection. There is no question of focusing when monochromatic radiation is diffracted from an undeformed single crystal, and the ideal incident beam for the determination of crystal orientation is a parallel beam, not a divergent one.

In the hands of an experienced operator, the diffractometer method is faster than either Laue method. Furthermore, it can yield results of greater accuracy if narrow slits are used to reduce the divergence of the incident beam, although the use of extramely narrow slits will make it more difficult to locate the diffracting positions of the crystal. On the other hand, the diffractometer method furnishes no permanent record of the orientation determination, whereas Laue patterns may be filed away for future reference. This is true even with most computer automated systems for diffractometer-based crystal orientation. But what is more important, the diffractometer method does not readily disclose the state of perfection of the crystal, whereas a Laue pattern yields this kind of information at a glance and in many investigations the relative perfection of a single crystal is of as much interest as its orientation.

All things considered the Laue methods are preferable when only occasional orientation determinations are required, or when there is any doubt about the quality of the crystal. When the orientations of large numbers of crystals have to be determined in a routine manner, the diffractometer method is superior. In fact, this method was developed largely for just such an application during World War II, when the orientation of large numbers of quartz crystals had to be determined. These crystals were used in radio transmitters to control, through their natural frequency of vibration, the frequency of the transmitted signal. For this purpose quartz wafers had to be cut with faces accurately parallel to certain crystallographic planes, and the diffractometer was used to determine the orientations of these planes in the crystal.

5 SETTING A CRYSTAL IN A REQUIRED ORIENTATION

After the orientation of a crystal is found by x-rays, it is often necessary to rotate it into some special orientation, such as one with $\langle 100 \rangle$ along the incident beam, for the purpose of either (a) subsequent x-ray examination in the special orientation, or (b) subsequent cutting along some selected plane. To obtain this orientation, the crystal is mounted in a three-circle goniometer, whose arcs have been set at zero, and its orientation is determined by, for example, the back-reflection Laue method. A projection of the crystal is then made, and from this projection the goniometer rotations which will bring the crystal into the required orientation are determined.

For example, suppose it is required to rotate the crystal whose orientation is given by Fig. 7 into a position where [011] points along the incident beam and [100] points horizontally to the left, i.e., into the standard (011) orientation if the latter were rotated 90° about the center. The initial orientation (Position 1) is shown in Fig. 22 by the open symbols, referred to *NSEW*-axes. Since (011) is to be brought to the center of the projection and (100) to the left side, (010) will lie on the vertical axis of the projection when the crystal is in its final position. The first step therefore is to locate a point 90° away from (011) on the great circle joining (010) to (011), because this point must coincide with the north pole of the final projection. This is simply a construction point; in the present case it happens to coincide with the $(0\bar{1}1)$ pole, but generally it is of no crystallographic significance. The projection is then rotated 22° clockwise about the incident-beam axis to bring this point onto the vertical axis of the underlying Wulff net. (In Fig. 22, the latitude and longitude lines of this net have been omitted for clarity.) The crystal is now in Position 2, shown by open symbols referred to *N´S´E´W´*-axes. The next rotation is

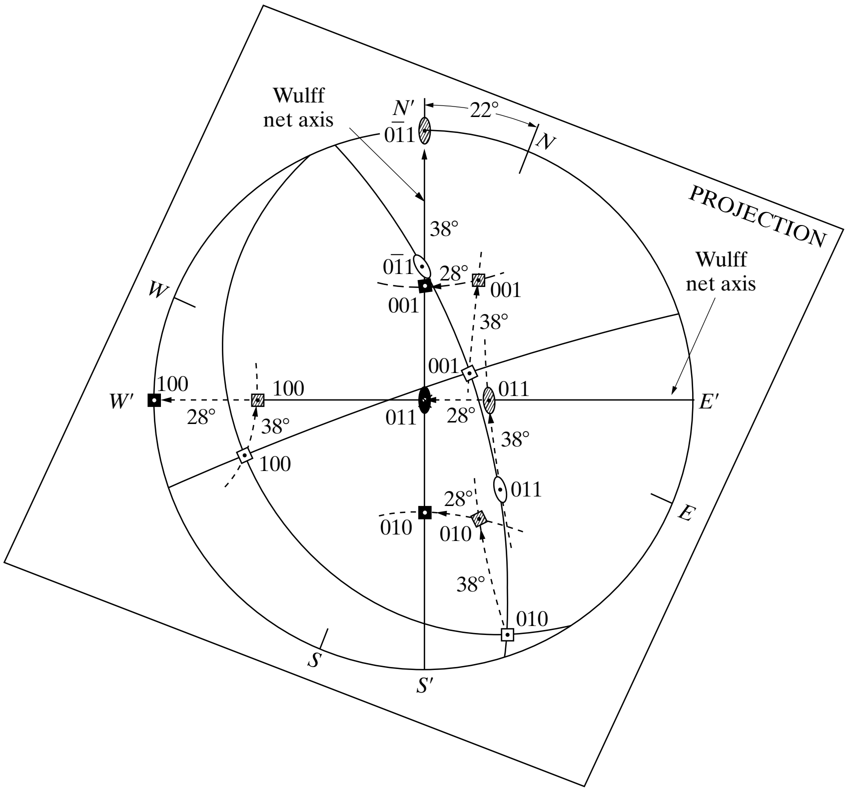

Figure 22 Crystal rotation to produce specified orientation. Position 1 is shown in Fig 7, position 2 is indicated by open symbols, position 3 by shaded symbols, and position 4 by solid symbols.

performed about the $E'W'$-axis, which requires that the underlying Wulff net be arranged with its equator vertical so that the latitude lines will run from top to bottom. This rotation, of 38°, moves all poles along latitude lines, shown as dashed small circles, and brings $(0\bar{1}1)$ to the N'-pole, and (100) and (011) to the $E'W'$-axis of the projection, as indicated by the shaded symbols (Position 3). The final orientation is obtained by a 28° rotation about the $N'S'$-axis, with the equator of the underlying Wulff net now horizontal; the poles move to the positions shown by solid symbols (Position 4).

The necessity for selecting a construction point 90° from (011) should now be evident. If this point, which here happens to be $(0\bar{1}1)$, is brought to the N'-pole, then (011) and (100) must of necessity lie on the $E'W'$-axis; the final rotation about $N'S'$ will then move the latter to their required positions without disturbing the position of the $(0\bar{1}1)$ pole, since $(0\bar{1}1)$ coincides with the $N'S'$-axis.

The order of these three rotations is not arbitrary. The sterographic rotations correspond to physical rotations on the goniometer and must be made in such a way that one rotation does not physically alter the position of any axis about which a subsequent rotation is to be made. The goniometer used here was initially set with the axis of its uppermost arc horizontal and coincident with the primary beam, and with the axis of the next arc horizontal and at right angles to the incident beam. The first rotation about the beam axis therefore did not disturb the position of the second axis (the $E'W'$-axis), and neither of the first two rotations disturbed the position of the third axis (the vertical $N'S'$-axis). Whether or not the stereographic orientations are performed in the correct order makes a great difference in the rotation angles found, but once the right angles are determined by the correct stereographic procedure, the actual physical rotations on the goniometer may be performed in any sequence.

The back-reflection Laue pattern of an aluminum crystal rotated into the orientation described above is shown in Fig. 23. Note that the arrangement of spots has 2-fold rotational symmetry about the primary beam, corresponding to the 2-fold rotational symmetry of cubic crystals about their $\langle 110 \rangle$ axes. (Conversely, the observed symmetry of the Laue pattern of a crystal of unknown structure is an indication of the kind of symmetry possessed by that crystal. Thus the Laue method can be used as an aid in the determination of crystal structure.)

The crystal-setting procedure illustrated in Fig. 22 can be carried out whether or not the indices of the various poles are known. If the Laue pattern of a crystal is difficult to solve, any spot on it can be indexed by using a Laue camera and a diffractometer in sequence [4]. In addition, a goniometer is required that fits both instruments. The procedure is as follows:

1. Make a Laue pattern and a stereographic projections of the poles corresponding to a few important spots.
2. By the procedure of Fig. 22, rotate the pole to be indexed to the center of the projection. The corresponding rotation on the goniometer will make the unknown plane (hkl) normal to the incident beam of the Laue camera.

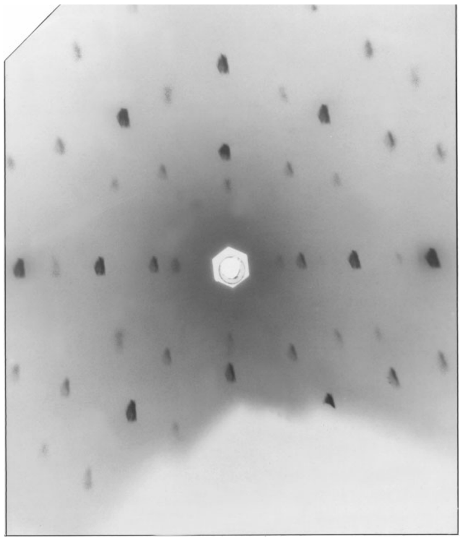

Figure 23 Back-reflection Laue pattern of an aluminum crystal. The incident beam is parallel to [011], points vertically upward, and [100] points horizontally to the left. Tungsten radiation, 30 kV, 19 mA, 40 min exposure, 5 cm specimen-to-film distance. (The light shadow at the bottom is that of the goniometer which holds the specimen.)

3. Transfer the goniometer and crystal to the diffractometer, in such a way that the (*hkl*) plane normal bisects the angle between the incident and (potential) diffracted beams.
4. Make a diffractometer scan to find the angle 2θ at which diffraction occurs from the (*hkl*) planes. [Higher-order reflections may also be observed, i.e., diffraction from (*nh nk nl*) planes.]
5. Calculate the spacing d of the (*hkl*) planes from 2θ and the known value of λ.
6. From this value of d determine (*hkl*) by calculation from the known crystal structure or by examining a list of known d spacings for the substance involved.

There is another method of setting a crystal in a standard orientation, which does not require either photographic registration of the diffraction pattern or stereographic manipulation of the data. This involves real-time observation of the Laue pattern: the diffracted beams formed in the transmission Laue method are so intense, for a crystal of the proper thickness that the spots they form on a fluorescent screen are readily visible in a dark room. The observer merely rotates the crystal about the various arcs of the goniometer until the pattern corresponding to the required orientation appears on the screen. Obviously, this pattern must be recognized when it appears, but a little study of a few Laue photographs made of crystals in standard orientations provides enough experience.

Various area detectors are available (see below) and would be employed if the job of crystal setting occurs frequently enough to justify the expense. An alternative is the construction of a light-and x-ray-tight viewing box. This box encloses the fluorescent screen which the observer views through a binocular eyepiece set in the wall of the box, either directly along the direction of the transmitted beam, or indirectly in a direction at right angles by means of a mirror or a right-angle prism. For x-ray protection, the optical system should include lead glass, and the observer's hands should be shielded during manipulation of the crystal if the goniometer axes cannot be controlled remotely. Direct manipulation of the goniometer head is very undesirable while the x-ray tube is energized (even if "reliable" shutters are closed during manipulation): there is too great a risk of operator carelessness. Even without motorized axes controlled outside the radiation enclosure, flexible cables can be attached to the knobs of the goniometer allowing remote rotation.

More elaborate apparatus permits electronic amplification of transmission Laue spots formed on a fluorescent screen. An image of the spot pattern on the screen can be projected by a lens on to the front (input) face of an image-intensifier tube. The intensified image appears on the rear (output) face of the tube and is bright enough to be observed directly or photographed in 1/220 second [5-7]. This large gain in image intensity permits photography, by a motion picture or television camera, of rapid changes in a Laue pattern caused, for example, by a phase change in the crystal. (The image-intensifier tube has also made it possible to obtain a transmission Laue photograph with a single 30-nanosecond pulse from a high-power pulsed x-ray tube [8].) Multiple wire area detectors can be used to record Laue patterns as can charge-coupled-device (CCD) detectors coupled to fluorescent screens; an additional advantage of these systems is that the data is recorded in digital form, ready for further analysis on a computer.

PROBLEMS

***1** A back-reflection Laue photograph is made of an aluminum crystal with a crystal- to-film distance of 3 cm. When viewed from the x-ray source, the Laue spots have the following *x, y* coordinates, measured (in inches) from the center of the film, see table at the top of the next page. Plot these spots on a sheet of graph paper graduated in inches. By means of a Greninger chart, determine the orientation of the crystal, plot all poles of the form {100}, {110}, and {111}, and give the coordinates of the {100} poles in terms of latitude and longitude measured from the center of the projection.

2 A transmission Laue photograph is made of an aluminum crystal with a crystal-to-film distance of 5 cm. To an observer looking through the film toward the x-ray source, the spots have the following *x, y* coordinates (in inches):

x	*y*	*x*	*y*
+0.26	+0.09	−0.44	+1.24
+0.45	+0.70	−1.10	+1.80
+1.25	+1.80	−1.21	+0.40
+1.32	+0.40	−1.70	+1.19
+0.13	−1.61	−0.76	−1.41
+0.28	−1.21	−0.79	−0.95
+0.51	−0.69	−0.92	−0.26
+0.74	−0.31		

x	*y*	*x*	*y*
+0.66	+0.88	−0.10	+0.79
+0.94	+2.44	−0.45	+2.35
+1.24	+0.64	−0.77	+1.89
+1.36	+0.05	−0.90	+1.00
+1.39	+1.10	−1.27	+0.50
+0.89	−1.62	−1.75	+1.55
+1.02	−0.95	−1.95	+0.80
+1.66	−1.10	−0.21	−0.58
		−0.59	−0.28
		−0.85	−1.31
		−1.40	−1.03
		−1.55	−0.36

Proceed as in Prob. 1, but use a stereographic ruler to plot the poles of diffraction planes.

***3** Determine the necessary angular rotations about (a) the incident beam axis, (b) the east-west axis, and (c) the north-south axis to bring the crystal of Prob. 2 into the "cube orientation."

REFERENCES

The following books are listed more or less in the order they are encountered in the text

G.10 Charles S. Barrett and T. B. Massalski. *Structure of Metals*, 3rd ed. (New York: McGraw-Hill, 1966). A classic book on the crystallographic aspects of physical metallurgy. Really two books in one, the first part dealing with the theory and methods of diffraction of x-rays, electrons, and neutrons; the second part with the structure of metals in the wider sense of the word. Very lucid account of stereographic projection. Stress measurement, phase transformations, preferred orientation.

G.31 J. L. Amoros, M. J. Buerger, and M. L. Canut de Amoros. *The Laue Method* (New York: Academic Press, 1974). Describes the various projections used with the Laue method and the application of this method to studies of crystal symmetry and diffuse scattering.

G.40 E. Preuss, B. Krahl-Urban, and R. Butz. *Laue Atlas* (New York: Wiley, 1974). Atlas of computer-generated back-reflection Laue patterns of most elements and many important compounds.

ANSWERS TO SELECTED PROBLEMS

1. 8°N, 23°E; 74°S, 90°E; 16°S, 64°W

3. 26° about beam axis, clockwise, looking from crystal to x-ray source; 3° about EW, clockwise, looking from E to W; 9° about NS, counterclockwise, looking from N to S

Crystal Quality

1 INTRODUCTION

The quality of what is nominally a "single" crystal can vary over an enormous range. At one extreme, the crystal may have undergone gross plastic deformation by bending and/or twisting, such that some portions of it are disoriented from other portions by angles as large as tens of degrees, and the dislocation density is high. At the other extreme, some carefully grown crystals are free of dislocations and other line or planar imperfections, and their crystal planes are flat to less than 10^{-4} degrees over distances of the order of a centimeter. In general, metal crystals tend to be more imperfect than crystals of covalent or ionic substances.

Various x-ray methods of assessing crystal quality are described below. These methods differ in sensitivity, and the least sensitive will be covered first.

2 LAUE METHODS

Either Laue method, transmission or back-reflection, easily discloses gross plastic deformation. Any change in the orientation of the diffraction planes is accompanied by a corresponding change in the direction, and wavelength, of the diffracted beam. In fact, Laue diffraction of x-rays is often compared to the reflection of visible light by a mirror. An undistorted crystal gives sharp Laue spots. In a bent or twisted crystal, the continuous change in orientation of the diffraction planes smears the Laue spots into streaks, just as a spot of light reflected onto a screen by a flat mirror becomes elongated when the mirror is curved.

Ordinary Laue Methods

If a crystal has been bent about a single axis, both the Miller indices of the bending axis and the extend of the bending can usually be determined stereographically; each Laue streak is plotted as an arc representing the range of orientation of the corresponding lattice plane, and a rotation axis that will account for the directions of these arcs on the projection is found. The angular lengths of the arcs are a measure of the amount of bending which has occurred. In measuring the amount of

From Chapter 17 of *Elements of X-Ray Diffraction*, Third Edition. B.D. Cullity, S.R. Stock.

bending by this method, it must be remembered that the wavelengths present in the incident beam do not cover an infinite range. There is no radiation of wavelength shorter than the short-wavelength limit, and on the long-wavelength side the intensity decreases continuously as the wavelength increases. This means that, for a given degree of lattice bending, some Laue streaks may not be as long as they might be if a full range of wavelengths were available. The amount of bending estimated from the lengths of these streaks would therefore be smaller than that actually present.

Transmission and back-reflection Laue patterns made from the same deformed region usually differ markedly in appearance. The photographs in Fig. 1 were made, under identical conditions, of the same region of a deformed aluminum crystal having the same orientation relative to the incident beam for each photograph. Both show elongated spots, which are evidence of lattice bending, but the spots are elongated primarily in a radial direction on the transmission pattern while on the back-reflection pattern they tend to follow zone lines. The term *asterism* (from the Greek *aster* = star) was used initially to describe the starlike appearance of a transmission pattern such as Fig. 1(a), but it is now used to describe any form of streaking, radial or nonradial, on either kind of Laue photograph.

The striking difference between these two photographs is best understood by considering a very general case. Suppose a crystal is so deformed that the normal to a particular set of diffraction planes describes a small cone of apex angle 2ε, i.e., in various parts of the crystal the normal deviates by an angle ε in all directions from its mean position. This is equivalent to rocking a flat mirror through the same angular range and, as Fig. 2 shows, the diffracted spot S is roughly elliptical on a film placed in the transmission position. When the plane normal rocks through the angle

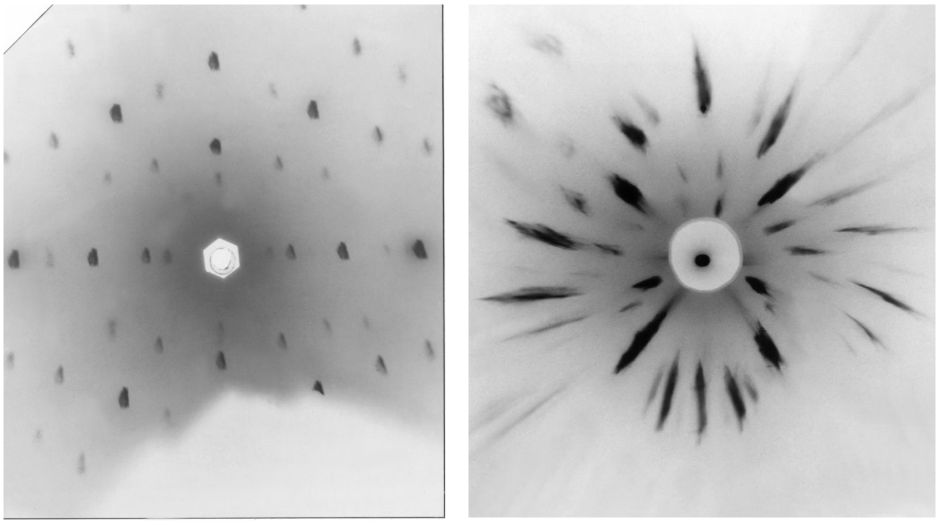

Figure 1 Laue photographs of a deformed aluminum crystal. Specimen-to-film distance 3 cm, tungsten radiation, 30 kV.

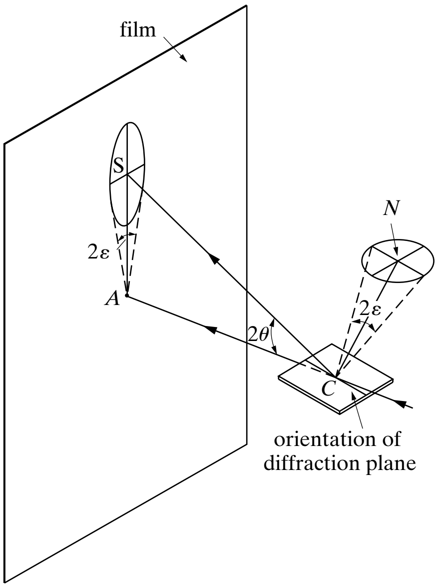

Figure 2 Effect of lattice distortion on the shape of a transmission Laue spot. *CN* is the normal to the diffracting plane.

2ε in the plane ACN, the diffracted beam moves through an angle 4ε, and the major axis of the ellipse is given approximately by $4\varepsilon(AC)$ when 2θ is small. On the other hand, when the plane normal rocks through the angle 2ε in a direction normal to the plane ACN, the only effect is to rock the diffraction planes through the same angle 2ε about the incident beam. The minor axis of the elliptical spot is therefore given by $2\varepsilon(AS) \approx 2\varepsilon(AC)\tan 2\theta \approx 2\varepsilon(AC)2\theta$. The shape of the spot is characterized by the ratio

$$\frac{\text{Major axis}}{\text{Minor axis}} = \frac{4\varepsilon(AC)}{2\varepsilon(AC)2\theta} = \frac{1}{\theta}.$$

For $2\theta = 10°$, the major axis is some 12 times the length of the minor axis.

In the back-reflection region, the situation is entirely different and the spot S is roughly circular, as shown in Fig. 3. Both axes of the spot subtend an angle of approximately 4ε at the crystal. Therefore, the shape of a back-reflection spot is more directly related to the nature of the lattice distortion than is the shape of a transmission spot since, in the general case, circular motion of the end of the (hkl) plane normal causes circular motion of the backward-reflected beam but elliptical motion of the forward-reflected beam. For this reason, the back-reflection method is generally preferable for studies of lattice distortion. It must not be supposed, however, that only radial streaking is possible on transmission patterns. The direction of streaking depends on the orientation of the axis about which the lattice planes are bent and if, for example, they are bent only about an axis lying in the plane ACN of Fig. 2, then the spot will be elongated in a direction at right angles to the radius AS.

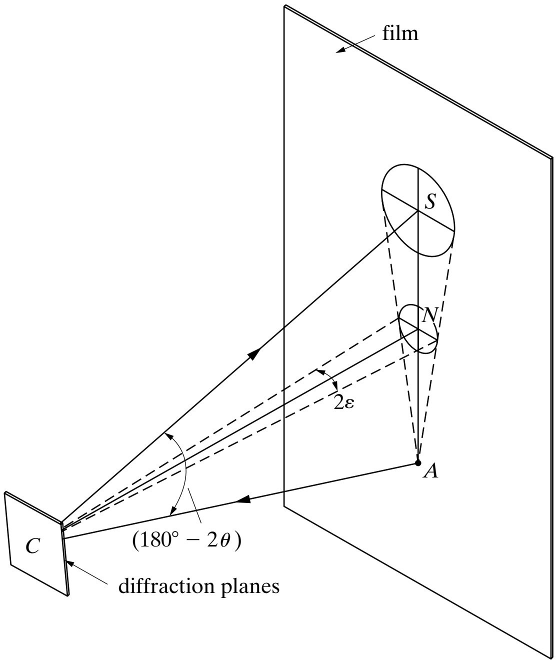

Figure 3 Effect of lattice distortion on the shape of a back-reflection Laue spot. *CN* is the normal to the diffracting plane.

One feature of the back-reflection pattern Fig. 1 deserves some comment, namely, the short arcs, concentric with the film center, which pass through many of the elongated Laue spots. These are portions of Debye rings, such as one might expect on a pinhole photograph made of a polycrystalline specimen with characteristic radiation. With a polycrystalline specimen of randomly oriented grains a complete Debye ring is formed, because the normals to any particular set of planes (*hkl*) have all possible orientations in space; in a deformed single crystal, the same normals are restricted to a finite range of orientations with the result that only fragments of Debye rings appear. Imagine a circle on the film along which a Debye ring would form if a polycrystalline specimen were used, as indicated in Fig. 4. If a Laue spot then becomes enlarged as a result of lattice deformation and spreads over the

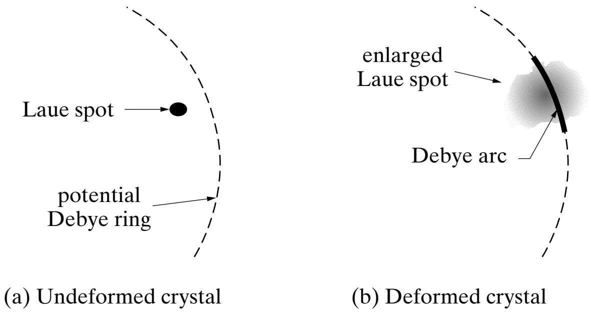

(a) Undeformed crystal

(b) Deformed crystal

Figure 4 Formation of Debye arcs on Laue patterns of deformed crystals.

potential Debye ring, then a short portion of a Debye ring will form. It will be much darker than the Laue spot, since the characteristic radiation[1] which forms it is much more intense than the wavelengths immediately adjacent to it in the continuous spectrum. In fact, if the x-ray exposure is not sufficiently long, only the Debye arcs may be visible on the film, and the observer may be led to erroneous conclusions regarding the nature and extent of the lattice deformation.

1. Since the asterism on the transmission pattern is predominantly radial, lattice planes inclined at small angles to the incident beam are bent about a number of axes, in such a manner that their plane normals are confined to a small cone in space.
2. Since the asterism on the back-reflection pattern chiefly follows zone lines, the major portion of planes inclined at large angles to the incident beam are bent about a single axis. However, the existence of Debye arcs shows that there are latent Laue spots of considerable area superimposed on the visible elongated spots, and that a small portion of the planes referred to are therefore bent about a number of axes.

Laue photographs can also disclose *polygonization*, which is a process that some deformed crystals undergo when annealed at an elevated temperature. If the deformation is not too severe, plastically bent portions of the crystal break up into smaller blocks, which are relatively strain-free and disoriented by approximately the same total amount (never more than a few degrees) as the bent fragment from which they originate, as suggested by Fig. 5. (The term “polygonization” describes the fact that a certain crystallographic direction [*uvw*] forms part of an are before annealing and part of a polygon afterwards.) Moreover, the mean orientation of the blocks is the same as that of the parent fragment. The effect of polygonization on a Laue pattern is therefore to replace an elongated Laue streak (from the bent lattice) with a row of small sharp spots (from the individual blocks) occupying the same position on the film, provided each block is sufficiently disoriented from its neighbor so that the beams reflected by adjoining blocks are resolved one from another. Figure 6 shows an example of polygonization in a crystal of silicon ferrite. A single elongated Laue spot from the deformed crystal appears in (a), while (b) and (c) show the breakup of this spot caused by annealing.

With these facts in mind, re-examination of the patterns shown in Fig. 1 leads to the following conclusions:

A polygonized crystal such as this may be regarded as an extreme example of the mosaic structure depicted, extreme in the sense that the average angle between adjacent blocks (subgrains) of the polygonized crystal is much larger than normal.

---

[1] In Fig. 1(b), the characteristic radiation involved is tungsten L radiation. The voltage used (30 kV) is too low to excite the K lines of tungsten (excitation voltage = 70 kV) but high enough to excite the L lines (excitation voltage = 12 kV).

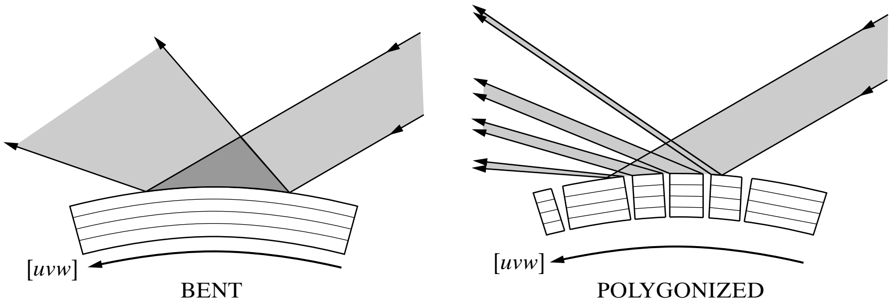

Figure 5 Reflection of white radiation by bent and polygonized lattices (schematic).

The sensitivity of the ordinary Laue method in the detection of crystal disorientation may be estimated as follows. Suppose the crystal-to-film distance is 5 cm, and assume that the minimum detectible broadening of a Laue spot is 1 mm. Then the

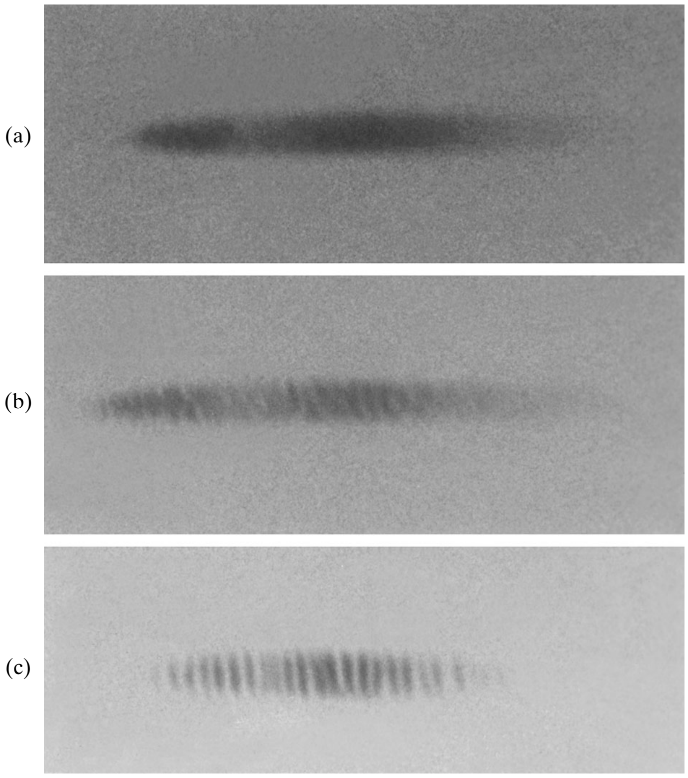

Figure 6 Enlarged transmission Laue spots from a thin crystal of silicon ferrite (α − iron containing 3.3 percent silicon in solid solution): (a) as bent to a radius of 9 mm., (b) after annealing 10 min at 950°C, (c) after annealing 4 hr at 1300°C. Dunn and Daniels [1].

diffracted beam has diverged by about 1/50 radian or 1°. This divergence corresponds to a disorientation of the reflecting planes of about 0.5°. This disorientation applies only to the area irradiated by the incident beam, which is typically 1 mm in diameter; the irradiated area is therefore only 10^{-2} cm^2.

Guinier-Tennevin Method

This method [2, 3] is a variant of the transmission Laue method and exploits the focusing effect. A large increase in sensitivity is obtained by increasing the source-to-crystal and crystal-to-film distances to the order of 50 cm. One therefore has a rather long "optical lever" that can disclose slight disorientations of the crystal.

Figure 7 shows the geometry of the method. This drawing is a horizontal section and shows white radiation diverging from a source S, either a point focus or a fine vertical-line focus on the x-ray tube target, and incident on a thin crystal. The horizontal divergence angle α is 1°-3°. If the crystal is perfect, as in (a), the rays diffracted by the transverse planes shown converge to a focus at F. The Laue spot on the film is then a thin vertical line, as in Fig. 8 (a). Note that only *one* Laue spot is of concern and not the arrangement of spots as in an ordinary Laue pattern.

If the crystal is bent or polygonized, as in Fig. 7 (b), the diffracted beam will broaden and the Laue spot on the film will be a rectangle of width w. (The dashed lines in this drawing will be discussed later.) The disorientation of the crystal may be calculated from the magnitude of w and the other dimensions involved. Disorientations as small as 5×10^{-3} degree are detectible, and this value pertains

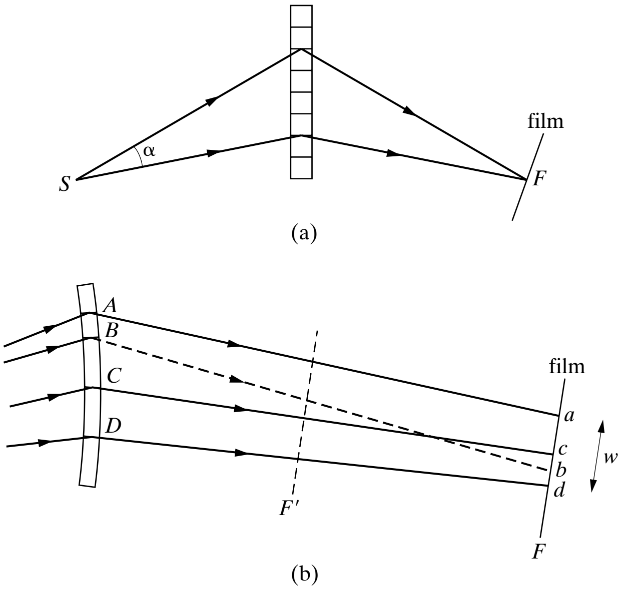

Figure 7 Guinier-Tennevin method. (a) Perfect crystal. Focused diffracted beam. (b) Bent or polygonized crystal. Enlarged view of nonfocused beam.

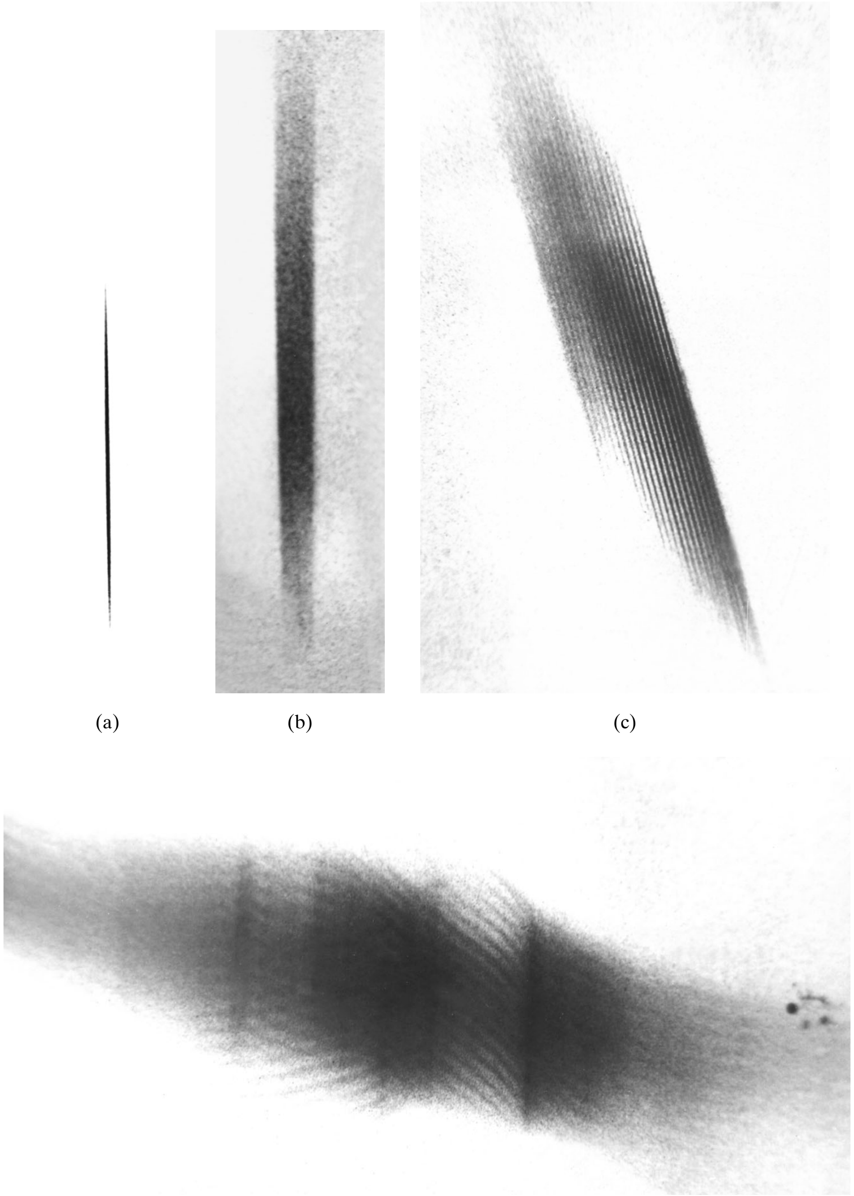

(a) (b) (c)

(d)

Figure 8 Single Laue spots obtained by the Guinier-Tennevin method on a film placed at the focusing position *F*. Spots (a), (b), and (c) are from the transverse planes of a quartz crystal plate, 37 × 13 × 0.5 mm: (a) unstrained, magnification 2X, (b) elastically bent, 2X, (c) elastically twisted, 5X. Spot (d) is from an aluminum crystal after plastic deformation, 4X. Julien *et al*. [4-6].

to an irradiated crystal area of 1-2 cm^2. Fig. 8 (b) shows a broadened reflection of this kind.

A modification of the Guinier-Tennevin method can reveal additional information about a deformed crystal [4, 5]. If a Soller slit with horizontal plates is placed in the incident beam and the crystal is twisted about a vertical axis, the original vertical-line Laue spot broadens into a striated region composed of fine inclined lines, and the inclination of these lines is a measure of the torsional strain in the crystal (Fig. 8 (c)).

Spot (d) of Fig. 8 is from a plate-shaped aluminum crystal that had been plastically deformed a small amount. This spot contains considerable internal detail. The striations show that portions of the crystal are twisted, and the dark vertical lines, of which two are prominent, show that fragmentation (polygonization) has occurred. Each line is a focused reflection from a nearly perfect portion of the crystal.

3 TOPOGRAPHIC AND OTHER METHODS

In methods designed mainly for the examination of nearly perfect crystals, the interest is not so much in measuring the angular disorientation of one part of the crystal with respect to another, but rather in disclosing the presence of individual imperfections, such as dislocations. All of these emplying radiation from x-ray tubes methods involve diffraction of $K\alpha$ radiation. Synchrotron radiation-based techniques can use either the continuous spectrum or monoclvornatized radiation. A number of interesting variants have been devised [7, G22].

The methods described below are called *topographic*, in the sense that the diffraction "spot" has a fine structure that is an image or map of the crystal examined. To be topographic, a one-to-one correspondence must exist between points within the diffraction spot and points on the crystal.

X-ray diffraction topography has sometimes been called *x-ray microscopy*,[2] because the image formed by diffracted x-rays, often only a few millimeters wide, is subsequently examined, and photographed, with an optical microscope at magnifications of 10-100 X. Such magnification is useful only if the detail in the x-ray image is sufficiently fine, and fine detail is obtained by recording the image, not on ordinary x-ray film, but on special high-resolution plates. These are glass plates coated with a thin, photographically slow, high-resolution emulsion. As a rule of thumb, individual dislocations can be resolved in carefully prepared topographs once the dislocation density is blow 10^6 cm^{-2}.

---

[2] Other techniques of x-ray imaging also qualify as microscopy, for example, those employing Fresnel plates for focussing x-rays [8], and it would be better to use x-ray topography and x-ray diffraction microscopy as synonyms

Effect of Extinction

The phenomenon of extinction plays a major role in image formation in x-ray topography. Extinction has its maximum effect in perfect crystals. As a crystal becomes *more imperfect*, its diffracting power for x-rays *increases*. Thus, when a crystal is examined by a topographic method, the crystal's imperfect regions will diffract more strongly, and the dark regions on the topograph will reveal where the imperfections are located in the crystal.

It is not usually the imperfections themselves that are imaged on the topograph (they are much too small) but rather the strain fields around the imperfections; these strains cause the plane spacings d to vary from their equilibrium value, thereby modifying the x-ray scattering process. White [9] has given a vivid demonstration, on the macroscopic level, of the effect of lattice strain on diffracting power, such as occurs in x-ray topography on a microscopic scale. He diffracted crystal-monochromatized Mo $K\alpha$ radiation from the surface of a thin quartz plate, elastically bent by increasing amounts, and measured the integrated intensity of the reflection (Fig. 9). The intensity for the unbent crystal was near the value calculated for a perfect crystal, and it increased with bending strain up to almost the value calculated for an "ideally imperfect" crystal (one in which extinction is absent). The effect was reversible and independent of whether the bending was convex or concave relative to the incident beam. The crystal plate was 0.5 mm thick, so that the surface strain was about 2×10^{-4} for the maximum bending shown in Fig. 9 The x-ray penetration depth was greater than half the thickness of the bent crystal, so that the x-rays saw strains varying from zero at the neutral axis to a maximum at the surface.

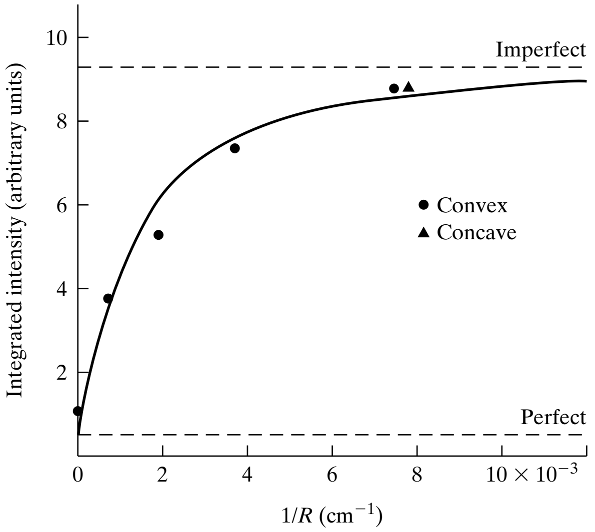

Figure 9 Integrated intensity of the 202 reflection of Mo $K\alpha$ radiation from a quartz plate as a function of the amount of bending. R is the radius of curvature. The quartz plate was cut parallel to the (202) planes. After White [9].

Not only does this important experiment demonstrate quite directly the relation between nonuniform lattice strain and x-ray diffracting power, but it also shows that extinction can be reversibly varied in an almost perfect crystal.

Diffraction Contrast

Contrast within x-ray topographs can arise from differences in diffracting power of crystal defects, such as dislocations, and the perfect lattice. As can be inferred from Fig. 9, the highly strained material around the core of a dislocation diffracts more intensely than the positions farther away. Thus, contrast is produced between the material immediately adjacent to the defect and the material far from the defect. In certain orientations of the defect relative to the incident and diffracted beams, however, the contrast produced by the defect disappears. Use of this "invisibility criterion" is the principal way in which defect character is deduced in x-ray topography and in transmission electron microscopy. The formula for the invisibility criterion can be obtained in the same way that the interference function was obtained: the intensity observed depends on the phase difference between scattering atoms, in this case, displaced from their equilibrium positions.

The structure factor is given by

$$\mathrm{F}_{\mathrm{hkl}} = \Sigma_{\mathrm{n}} \mathrm{f}_{\mathrm{n}} \exp\{2\pi \mathrm{i}[(\mathbf{S} - \mathbf{S_0})/\lambda \cdot \mathbf{r_n}]\}$$

$$= \Sigma_n \mathrm{f}_{\mathrm{n}} \exp\{2\pi \mathrm{i}(\mathbf{H} \cdot \mathbf{r_n})\},$$

where n denotes the different atoms in the unit cell, $\mathbf{H} = h\,\mathbf{b}_1 + k\,\mathbf{b}_2 + l\,\mathbf{b}_3$ and $\mathbf{r}_{\mathrm{n}}$ is the direct space vector from the origin of the unit cell to the *nth* atom in that unit cell. In practice, diffracted intensity does not drop to zero at angles slightly different from the Bragg angle θ_B, and setting $(\mathbf{S} - \mathbf{S_0}/\lambda = \mathbf{H} + \mathscr{s}$ allows for this. In other words, the vector $(\mathbf{S} - \mathbf{S_0})/\lambda$ no longer must be the sum of integral multiples of the reciprocal lattice vectors b_{i}. Remember also that the formula for the amplitude diffracted by the entire crystal is

$$\mathrm{A}_{\mathrm{hkl}} = \Sigma_{\mathrm{m}} \mathrm{F}_{\mathrm{hkl}} \exp\{2\pi \mathrm{i}([\mathbf{H} + \mathscr{s} \cdot \mathbf{R}_{\mathrm{m}}]\},$$

where the summation is over the m unit cells in the crystal, F is the structure factor which is the same for each unit cell, and $\mathbf{R}_{\mathrm{m}}$ is the direct space vector from the origin to the *mth* unit cell. The effect of deformation, either from a continuously varying elastic field or from a discrete defect such as a dislocation can be treated in the same fashion. If $\mathbf{R}'_{\mathrm{m}}$ is the position of the mth unit cell in the deformed crystal,

$$\mathrm{A}_{\mathrm{hkl}} = \Sigma_{\mathrm{m}} \mathrm{F}_{\mathrm{hkl}} \exp\{2\pi \mathrm{i}([\mathbf{H} + \mathscr{s}] \cdot \mathbf{R}'_{\mathrm{m}})\}. \qquad (1)$$

Writing the displacement of the unit cell due to the deformation as $d\mathbf{R}_m$, then

$$A_{hkl} = \Sigma_m F_{hkl} \exp \{2\pi i([\mathbf{H} + \mathscr{s}] \cdot [\mathbf{R}_m + d\mathbf{R}_m])\}$$

$$= \Sigma_m F_{hkl} \exp 2\pi i(\mathbf{H} \cdot \mathbf{R}_m) \exp 2\pi i(\mathscr{s} \cdot \mathbf{R}_m) \text{ x}$$

$$\exp 2\pi i(\mathbf{H} \cdot \mathbf{R}_m) \exp 2\pi i(\mathscr{s} \cdot d\mathbf{R}_m) \qquad (2)$$

Note that $d\mathbf{R}_m$ is a function of position and is defined relative to the nearest position a unit cell would have in a perfect crystal.

The four vector products $\mathbf{H} \cdot \mathbf{R}_m$, $\mathscr{s} \cdot \mathbf{R}_m$, $\mathbf{H} \cdot d\mathbf{R}_m$ and $\mathscr{s} \cdot d\mathbf{R}_m$ must now be considered to deduce the effect of the defect, if any, on contrast. The first and third terms have already been encountered in the structure factor and interference function, respectively. Note that $\mathscr{s}$ and $d\mathbf{R}_m$ are both small quantities, i.e., $d\mathbf{R}_m \ll \mathbf{R}_m$ and $\mathscr{s} \ll \mathbf{H}$. Thus the fourth term can be neglected, and only the term $\mathbf{H} \cdot d\mathbf{R}_m$ produces contrast. If $\mathbf{H} \perp d\mathbf{R}_m$, then $\mathbf{H} \cdot d\mathbf{R}_m = 0$ and there is no effect on diffracted intensity. This condition $\mathbf{H} \cdot d\mathbf{R}_m = 0$ is known as the *invisibility criterion*, Stated another way, the defect will not produce contrast if its displacement field is solely parallel to the diffraction planes. If, however, the displacement field has one or more components out of these planes, the strain will affect the diffracted intensity and produce a local increase in diffracted intensity.

As examples of the use of the invisibility criterion in TEM or x-ray topographic defect identification, consider a pure screw dislocation and a pure edge dislocation. The displacement field u_i around a stationary screw dislocation whose unit line vector **t** is parallel to $\mathbf{x}_3$ depends on the Burgers vector b and is given by [10]:[3]

$$u_1 = 0,$$

$$u_2 = 0, \text{ and}$$

$$u_3 = \frac{-b}{2\pi} \tan^{-1} \frac{x_2}{x_1}. \qquad (3)$$

Around a stationary edge dislocation parallel to $\mathbf{x}_3$, the displacement field is:

$$u_1 = -\frac{b}{2\pi}\left[\tan^{-1}\frac{x_2}{x_1} + \frac{\Lambda + \mu}{\Lambda + 2\mu}\,\frac{x_1 \cdot x_2}{x_1^2 + x_2^2}\right],$$

$$u_2 = -\frac{b}{2\pi}\left[-\frac{\mu}{2(\Lambda + 2\mu)} \log \frac{x_1^2 + x_2^2}{C} + \frac{\Lambda + \mu}{\Lambda + 2\mu}\,\frac{x_2^2}{x_1^2 + x_2^2}\right], \quad \text{and}$$

$$u_3 = 0. \qquad (4)$$

---

[3] Note that the Burgers vector b is different from the reciprocal lattice vectors whose magnitudes are also designated by b. However reciprocal lattice vectors are written b_n in general and b_1, b_2 and b_3 specifically while the Burgers vector is written b.

The term C is a constant required to make the argument of the natural logarithm term dimensionless, and Λ and μ are the Lamé constants. In terms of more commonly encountered elastic constants, μ is the shear modulus and Young's modulus $E = \mu(3\Lambda + 2\mu)/(\Lambda + \mu)$. Even though **t** may change for a given dislocation line as it winds through the crystal, its Burgers vector b must remain constant unless it intersects another dislocation. Note that these equations apply to an isotropic elastic solid, and the displacement fields will differ in anisotropic materials.

For screw dislocations the invisibility criterion is very simple: $\mathbf{H} \cdot \mathbf{b} = 0$. Many authors, particularly those working in TEM replace **H** with **g**. This equation states that the screw dislocation will be invisible if **b** is parallel to the diffracting planes, i.e., if **b** is a direction within this plane. For edge dislocations, the two non-zero displacement terms require that $\mathbf{H} \cdot \mathbf{b} = 0$ and $\mathbf{H} \cdot (\mathbf{b} \times \mathbf{t}) = 0$ must be satisfied for the dislocation to go out of contrast. Examples of the use of the invisibility criterion in x-ray topography follow in this section; Section 20-8 covers examples in TEM.

Consider the curved dislocation pictured in Fig. 10; it is in an fcc material. If its Burgers vector is $a/2\,[110](\bar{1}11)$ and its line direction is given by unit vector **t**, the section AA′ where $\mathbf{t} = [110]$ has pure screw character and BB′ where $t = [1\bar{1}1]$ has pure edge character. Between A′ and B′ the dislocation character is mixed, varying from predominantly screw to predominantly edge. For the pure edge section $\mathbf{b} \times \mathbf{t} = [\bar{1}11]$. An image produced with $\mathbf{H} = 200$, i.e., an image formed with the beam diffracted from (100), would have $\mathbf{H} \cdot \mathbf{b} \neq 0$. The entire length of the dislocation would be visible. An image produced with $H = 002$, however, would have $\mathbf{H} \cdot \mathbf{b} = 0$. Note that (001) is in the same zone as $(\bar{1}11)$ and $(1\bar{1}2)$, having zone axis [110], and is rotated 54.7° from $(\bar{1}11)$. The pure screw segment AA′ would not produce contrast, but the pure edge section BB′ might since $\mathbf{H} \cdot (\mathbf{b} \times \mathbf{t}) = [001]. [\bar{1}11] \neq 0$. Generally, the contrast produced when $\mathbf{H} \cdot \mathbf{b} \neq 0$ is greater than that produced when $\mathbf{H} \cdot \mathbf{b} = 0$ but $\mathbf{H} \cdot (\mathbf{b} \times \mathbf{t}) \neq 0$, so that contrast from the latter con-

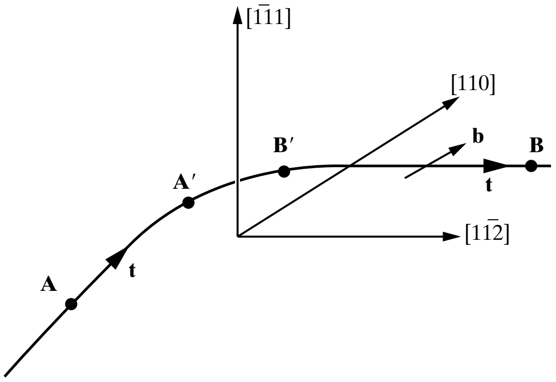

Figure 10 Schematic of a curved dislocation line lying on $(1\bar{1}0)$ with tangent vector **t** and Burgers vector parallel to [110].

dition is termed residual contrast. If the dislocation were imaged with $\mathbf{H} = [\mathbf{1}\bar{\mathbf{1}}2]$ both $\mathbf{H} \cdot \mathbf{b}$ and $\mathbf{H} \cdot (\mathbf{b} \times \mathbf{t})$ would be zero and the dislocation would be invisible.

Finding invisibilities from two non-colinear **H** insures that a dislocation's character can be identified. In many situations, however, only one type of Burgers vector is expected, and only one invisibility may be required to establish the character of the dislocations. In a bcc system, for example, the expected slip system is $\{110\}\langle 111\rangle$, and $b \| [111]$, $[\bar{1}11]$, $[1\bar{1}1]$, or $[11\bar{1}]$, must be distinguished. Imaging with $\mathbf{H} = \langle 110\rangle$ allows rapid identification of **b** in the bcc system. The schematic of Fig. 11 shows a progression of steps which might be used in the identification process. With *a priori* knowledge of the type of slip system, only two images must be recorded to determine **b**. Images from at least three different **H** must be recorded to reveal all of the dislocations present (e.g., $\mathbf{H} = [101]$ in addition to $\mathbf{H} = [110]$ and $[011]$ in the schematic of Fig. 11).

As was noted above, residual contrast can be seen if $\mathbf{H} \cdot \mathbf{b} = 0$ but $\mathbf{H} \cdot (\mathbf{b} \times \mathbf{t}) \neq 0$. In some cases this residual contrast can be nearly as strong *in the same micrograph* as that for dislocations with $\mathbf{H} \cdot \mathbf{b} \neq 0$, or it can so weak as to be negligible. An additional complication can occur for situations where $\mathbf{H} \cdot \mathbf{b} > 1$: the intensity produced for dislocations for which $\mathbf{H} \cdot \mathbf{b} \geq 2$ can be much higher than that when the product equals 1. The possibility exists, therefore, that dislocations which are in contrast can be mistaken for dislocations exhibiting residual contrast. These potential pitfalls are mentioned to illustrate that some caution is required in interpreting contrast in x-ray topographs and TEM micrographs; normally analysis of defect character using the invisibility criterion is straight-forward.

Under conditions of high absorption and in perfect crystals, the contrast of defects such as dislocations reverses from that in thinner crystals. Imperfections locally destroy the crystal perfection that causes the anomalously high transmission of the Borrmann effect, thereby producing less blackening of the photographic emulsion and casting a white "shadow" on the film.

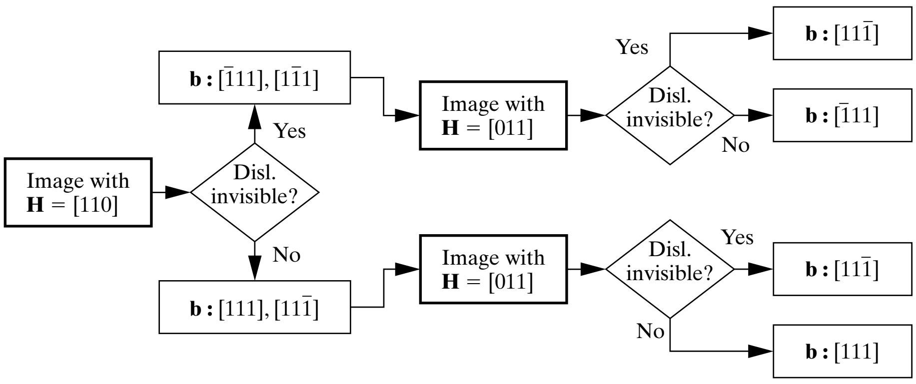

Figure 11 Flow chart illustrating the use of the invisibility criterion.

Berg-Barrett Method

This method involves the diffraction of $K\alpha$ radiation from the face of the specimen crystal [7.11-7.13]. There is therefore no restriction on specimen thickness but the depth from which the x-rays sample may range from one micrometer to hundreds of micrometers or more.

Unfiltered radiation from the x-ray tube passes through a, long collimator (Fig. 12), which defines a broad beam that will flood the specimen crystal. In a darkened room the crystal is adjusted so that a selected (*hkl*) plane makes the correct Bragg angle for diffraction, as judged by the appearance of a bright spot on an adjacent fluorescent screen. The screen is then replaced by a photographic plate. For maximum resolution of detail the plate should be as close to the crystal as possible, preferably less than 1 mm, without touching the incident beam. This prevents the images of the same defect from $K\alpha_2$ and $K\alpha_2$ from diverging too much and smearing the image of the defect. The diffraction planes, as suggested in the drawing, are not normally parallel to the crystal surface; the angle 2θ should be about 90° so that

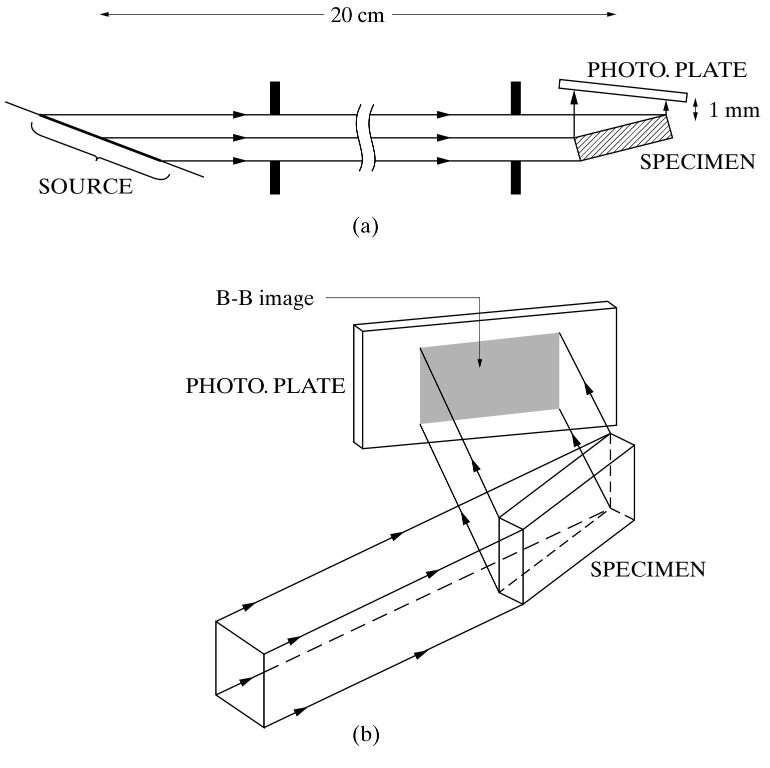

(a)

(b)

Figure 12 Berg-Barrett method. (a) Plan view. The source is the focal spot on the x-ray tube target, seen "end on" from the specimen, so that the source appears square. (b) Perspective view.

the diffracted rays strike the plate at right angles.

A perfect crystal would produce a uniformly dark Berg-Barrett image. Crystal imperfections affect the image mainly in two ways:

1. As discussed before, local regions of the crystal with low extinction, such as those with nonuniform strain, will diffract more strongly and cause *darker* regions on the image, an effect called "extinction contrast."
2. Local regions that are rotated out of parallelism with the rest of the crystal will be set not quite, or not at all, at the exact Bragg angle and will diffract of $K\alpha$ less strongly or not at all, causing *lighter* regions on the image.

The Berg-Barrett method has a maximum resolution of about 5 μm, and it can disclose such imperfections as subgrain boundaries, twins, and individual dislocations where they intersect or pass close to the crystal surface.

The Berg-Barrett topographs in Fig. 13 show how the choice of diffracting plane governs dislocation visibility [13]. The specimen is a lithium fluoride crystal, cleaved parallel to a (100) face and slightly bent. Dislocations that emerge on this face are revealed by tiny etch pits in the optical micrograph (a). Pits forming diagonal lines

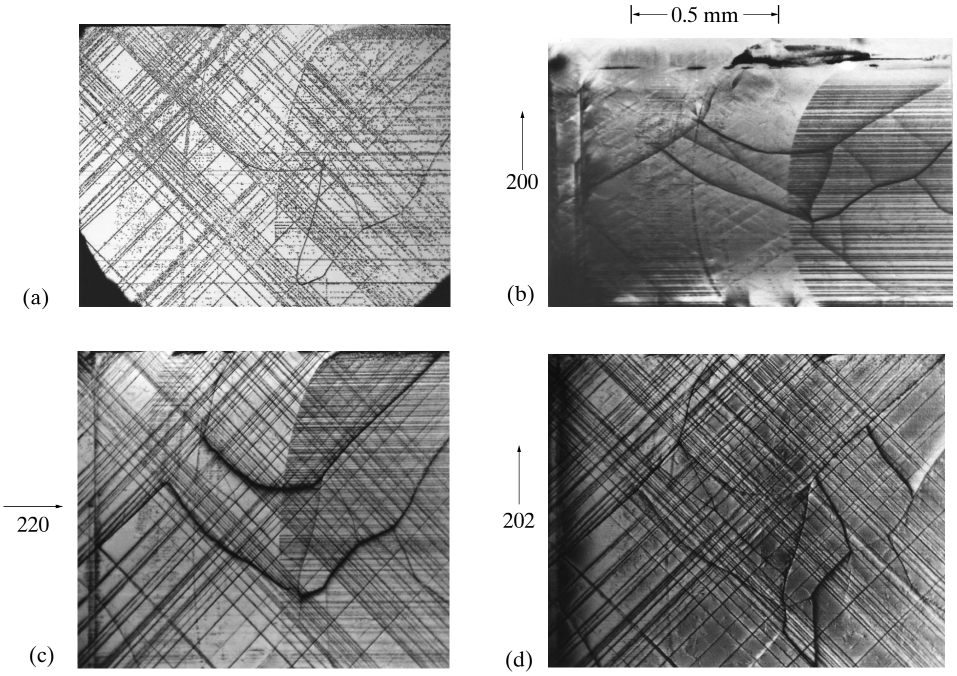

Figure 13 Different aspects of the (100) face of a LiF crystal. (a) Optical micrograph of the etched surface. (b), (c), (d) Berg-Barrett x-ray topographs of the same area of the *unetched* surface, made with three different *hkl* reflections; the arrow on each topograph is the projection of the incident-beam direction on the (100) face. Newkirk [13].

are due to edge dislocations; those forming horizontal lines are due to screw dislocations; both kinds of dislocations lie on {110} slip planes and have **b** = $\langle 110 \rangle$. Most of the screw dislocations are located to the right of the curved vertical line at the center; this line is thought to mark the place where the cleavage crack, moving from right to left, began to move so fast that dislocations had no time to form ahead of it. The x-ray topographs of the unetched surface in (b), (c), (d) reveal dislocations selectively. In (b), a 200 reflection, the emergent points of screw dislocations form dark horizontal lines, and edge dislocations are virtually invisible. One can conclude, therefore, that the edge dislocations have **b** = [011] or [011]. On the other hand, if the image is formed by a 202 reflection, as this means that the screw dislocations have **b** = [101] in (c), only edge dislocations are revealed, as evidenced by the dark diagonal lines. As expected from the **b** identified above, the 220 image in (d) shows both edge and screw dislocations. The thick, irregular dark lines in all three topographs are subgrain boundaries. One should remember that the horizontal and diagonal lines in Fig. 13 are not the images of individual dislocation lines running parallel to the crystal's surface; rather, the lines result from closely spaced dislocations emerging from the surface.

Lang Method

This method involves the diffraction of of $K\alpha$ radiation in *transmission* [14, 15] The diffracted beam will therefore be too weak if the crystal is either too thin or too thick. The optimum thickness t corresponds to $\mu t \approx 1$, where of μ is the linear absorption coefficient.

X-rays from the source S, a point or a line, pass through the narrow slit S_t in Fig. 14 before hitting the crystal. The incident beam therefore has the shape of a very thin ribbon, intersecting the crystal along the plane AB. This beam has very little divergence in the plane of the drawing, because S_1 is a narrow slit and the source-to-slit distance D is large, several tens of centimeters. The diffracting planes, for the beam directions shown, are at right angles to the crystal surface, and these planes must make the right Bragg angle for the characteristic radiation involved. Slit assembly S_2 passes the diffracted beam but prevents the transmitted beam from striking the plate.

If the crystal is fixed, the image on the plate is a *section topograph*, revealing the distribution of imperfections on the section AB of the crystal: these defects form "direct images," that is they diffract more strongly than the perfect regions of the crystal and produce more darkening of the photographic emulsion. Remember that a ribbon of radiation is striking the crystal, and the image of the section topograph recorded on the film is, for a parallel-sided crystal, a long narrow rectangle. The two Bloch waves excited in the Borrmann triangle interfere, and, in the absence of defects or strain, the section topograph consists of a set of light and dark fringes parallel to the sides of the topograph (Fig. 15a). More precisely, the waves interfere within the Borrmann *prism* consisting of the stack of many contiguous Borrmann triangles. These fringes are termed Pendellösung fringes from the German words

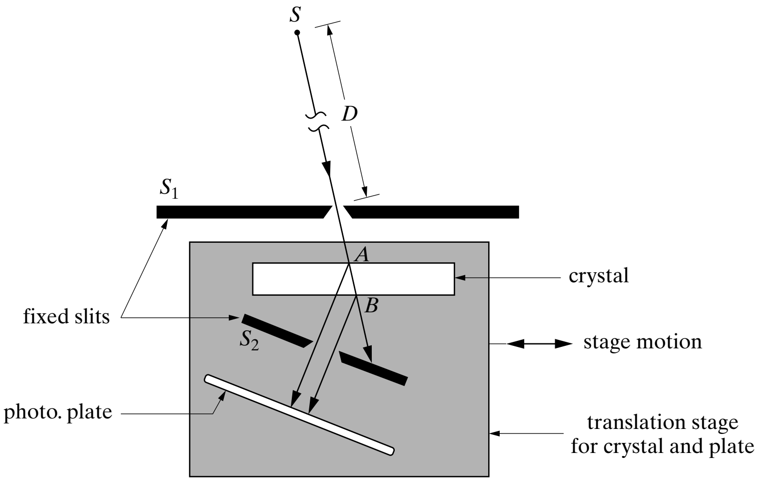

Figure 14 Lang method. Slits S_1 and S_2 are fixed. The crystal and the photographic plate are mounted on a stage that can be slowly traversed in the directions shown.

for "pendulum" and "solution" which describes the mathematical treatment of the energy transfer from one Bloch wave to the other. The fringes are very sensitive to small strain gradients which affect the pattern of fringes first by producing additional periods of the fringes (left side of Fig. 15a) and second, at high elastic strains, by destroying the Pendellösung fringes altogether (Fig. 15b). Dislocations within the Borrmann triangle ABC, but not intersecting the direct beam (AB), cast shadow within the section topograph or distort the pattern of fringes. A significant density of oxide precipitates within an otherwise defect-free silicon wafer is sufficient to obscure the fringes, and back surface damage, introduced to getter point defects within the silicon wafer, is also sufficient to destroy the conditions required to observe fringes. The length of the crystal may be explored by making a series of section topographs, the crystal and plate being moved stepwise between exposures. Section topographs are most useful when the crystal is rather thick. The first images of individual dislocations were obtained by this method, and very beautiful section topographs have been produced of synthetic crystals such as silicon and of naturally occurring crystals such as diamond. Pendellösung fringe measurements have been used to provide very precise measurement of the atomic scattering factor in crystals as diverse as silicon [18] and aluminum [19] and of the thermal expansion coefficient of silicon [20]. Section topographs may also be recorded with monochromatic synchrotron radiation as well as polychromatic synchrotron radiation.

The crystal may be continuously explored from end to end by moving crystal and plate together, back and forth, during the exposure. The resulting image is a *projection topograph*; it is most informative when the crystal is fairly thin and the density of imperfections not too large, so that images of imperfections do not overlap.

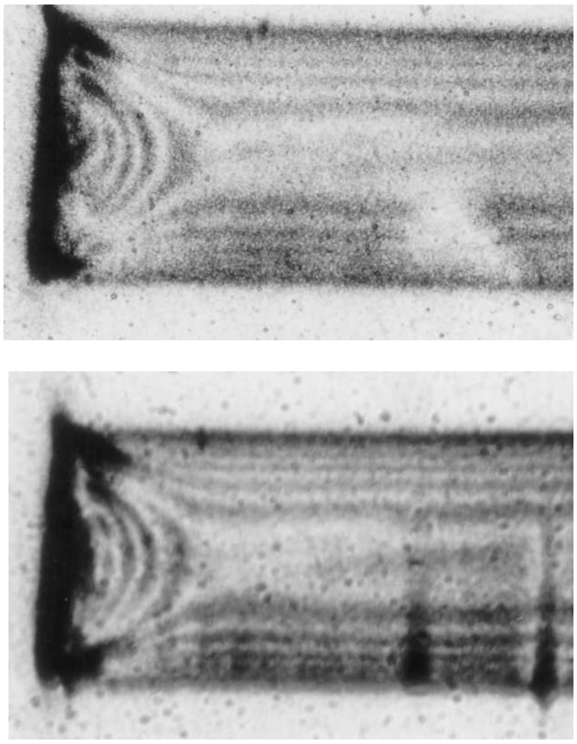

Figure 15 Two section topographs of a 0.5 mm Si wafer recorded with synchrotron radiation at two adjacent positions. The Pendellösung fringes run horizontally. The left edge of the image corresponds to the position where the wafer was cut with a diamond dicing blade; extra fringes result because of the elastic strain gradients left by the cutting operations. Small amounts of strain from surface scratches, etc. can completely destroy the interference producing the fringes (white blur in the top topograph and black, vertical black streaks in the bottom topograph) [16].

Figure 16 shows a topograph containing images of dislocations. Spatial resolution can approach 1 μm, although this is not often attained.

The Lang method can also reveal magnetic domains in ferromagnetic and ferrimagnetic materials [22]. Here, spontaneous magnetostrictive strains in domains and domain walls are enough to upset the regularity of the lattice and constitute crystal imperfections.

Lang cameras are commercially available and can be used to great effect for quality control of silicon crystals. Such crystals are often may centimeters wide. If a wide crystal happens to be very slightly bent, Bragg's law will not be satisfied for the highly parallel incident beam during a complete traverse of the crystal. To ensure continuous diffraction Schwuttke [23] oscillated the crystal and plate through a very small angle about a vertical axis through A of Fig. 14 during the traverse, and Silver and Turner [24] devised an automatic control of the oscillation angle.

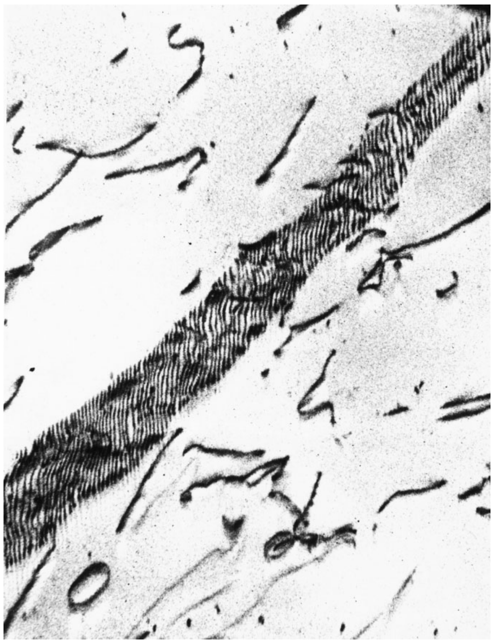

Figure 16 Lang topograph of a thin crystal of lithium fluoride. Dark lines are dislocations, some randomly arranged and some nearly parallel. The latter form the band running diagonally across the photograph; these dislocations, which intersect the top and bottom surfaces of the crystal, constitute a small angle boundary between two subgrains. of Mo $K\alpha_1$, radiation, 200 reflection. (Courtesy of A. R. Lang [21].)

Polychromatic or White Beam Topography

Laue patterns of nearly perfect crystals can produce many topographs simultaneously: the structure within each spot is a map of the diffracting power of the area of the crystal irradiated (Fig. 17). Section and projection topographs can be recorded as well as reflection topographs. Topographic imaging with polychromatic x-rays is practical only with synchrotron radiation, since only it possesses the needed intensity and parallelism. The disadvantages of experimenting away from one's home laboratory and of being able to record topographs only during several tightly scheduled periods each year are offset by several advantages.

In addition to being able to record multiple reflections simultaneously, that is, to record much of the information required to identify defect character, each set of topographs requires an exposure of seconds compared to hours required for topographs recorded with x-ray generators. This is essential for following dynamic processes such as phase transformations or plastic deformation. A number of investigators have developed x-ray cameras for recording topographs at video rates, and spatial resolutions down to $10 - 20\ \mu$m have been reported [25-27]. Plastic deformation emanating from a notch during in situ loading has been studied, for example, in thin niobium crystals containing a low density of dislocations [28]. Dislocations emitted from notches in silicon under different loading conditions is another example of in situ studies only practical with synchrotron radiation.

Another advantage of polychromatic topography is that crystals containing a range of orientations can be imaged in their entirety: different portions of the crys-

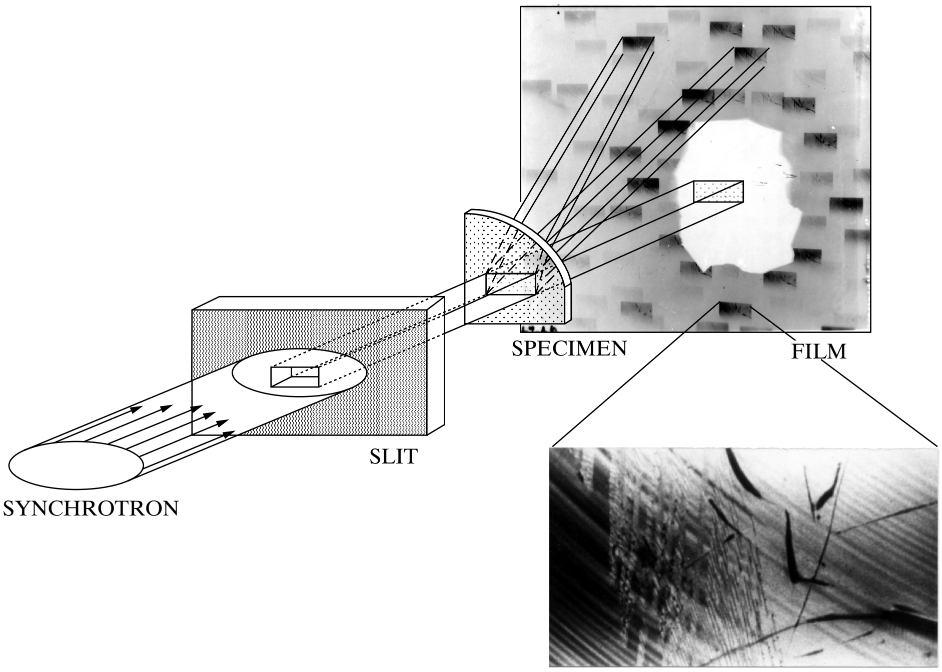

Figure 17 White or polychromatic beam topography illustrated for a crystal of GaAs alloyed with $\sim 2\%$ In. The slit defined the area imaged, and the irregular white area at the center of this 001 Laue pattern is the beam stop. The enlarged topograph shows contrast from surface scratches (heavy running from upper left to lower right) and individual dislocation lines (short, sharply difined black images).

tal diffract slightly different wavelengths. Bent or otherwise distorted crystals are one application where polychromatic topography is particularly valuable. This method is also quite useful in determining the misorientation between subgrains (i.e., the rotation axis and the magnitude of rotation).

Misorientations may be mapped by observing a sharp change in contrast in a crystal possessing a K-absorption edge within the range of wavelengths diffracted from the crystal. Those parts of the crystal diffracting wavelengths lower than that of the absorption edge contribute little intensity to the topograph while those positions where diffracted wavelengths are greater than that of the edge produce much greater darkening of the topograph [29]. The locus of positions where the large change in contrast occurs is termed an absorption edge contour, and the position of this contour for different crystals orientations maps the strain and/or bending in the sample [30]. If the crystal does not possess a suitable absorption edge, a filter with a suitable edge can be placed in the polychromatic beam before or after the sample and can produce the desired change of contrast. A molybdenum filter in a polychromatic beam, for example, provides different transmissivities for wavelengths above and below 0.62 A; the change in contrast allows one to quickly characterize texture in flat plate diffraction patterns of polycrystalline systems as diverse as $TaSi_2$/Si eutectic composites [31] and plates of Al-Li 2090 [32].

Cross-sections of crystals as large as of 5 mm × 20 mm are often imaged in transmission; in the reflection geometry, much larger areas can be studied in single exposures by directing the incident beam at an angle nearly parallel to the surface of the sample. Recording multiple reflections simultaneously requires large sheets of film, and a much larger sample-to-film separation is needed than in the Lang method so that the different Laue "spots" do not overlap. Because the emulsions must be thick in order to record topographs in a reasonable period of time, some smearing of defect images such as dislocations is inevitable in this technique: the diffracted beams cannot everywhere be perpendicular to the plane of the film. The normal compromise in transmission polychromatic topography is either to place the film perpendicular to the direct beam $\mathbf{S}_0$ (Fig. 17) or to position the film perpendicular to the diffracted beam of greatest interest.

Double Crystal Topography

A dislocation-free, undeformed crystal can be used as a monochromator or beam conditioner for recording x-ray topographs of samples. Figure 18 illustrates this technique, double crystal topography, and shows how a divergent beam of of $K\alpha$ radiation from an x-ray tube or a nearly parallel beam of polychromatic synchrotron radiation is incident on the monochromator and how those x-ray photons oriented at the appropriate angle diffract first from the monochromator (through angle of $2\theta_M$) and then from the sample (through angle $2\theta_C$) in transmission (Fig. 18(d)) or reflection (Fig. 18(a)). Because the perfect monochromator crystal has a very narrow acceptance angle for x-rays of a given wavelength, double crystal topographs often require much longer exposure times than other types of topographs. Even small elastic curvatures prevent large portions of the irradiated volume from diffracting. This effect has been used to measure changes in dilational and shear strains as a function of position in a GaAs wafer. In cases with considerably greater strains, the resulting topograph consists of only a narrow contour which can be used to map the distribution of deformation around stress concentrators. Figure 19a shows a single contour from diffraction of the niobium matrix which was deformed by a nearby niobium hydride precipitate, and Fig. 19b, of the same sample, shows multiple contours recorded on a single piece of film using rotations of 210 arc sec between exposures [21].

The high strain sensitivity intrinsic to double- or triple- crystal topography can be very useful in revealing subtle changes in orientation, defect character or strain. Fewster [34], for example, has used triple crystal topography[4] to explain that the diffuse intensity observed around Bragg peaks in triple axis diffractometry can be due to incompletely removed scratches on the sample and not necessarily to point defects.

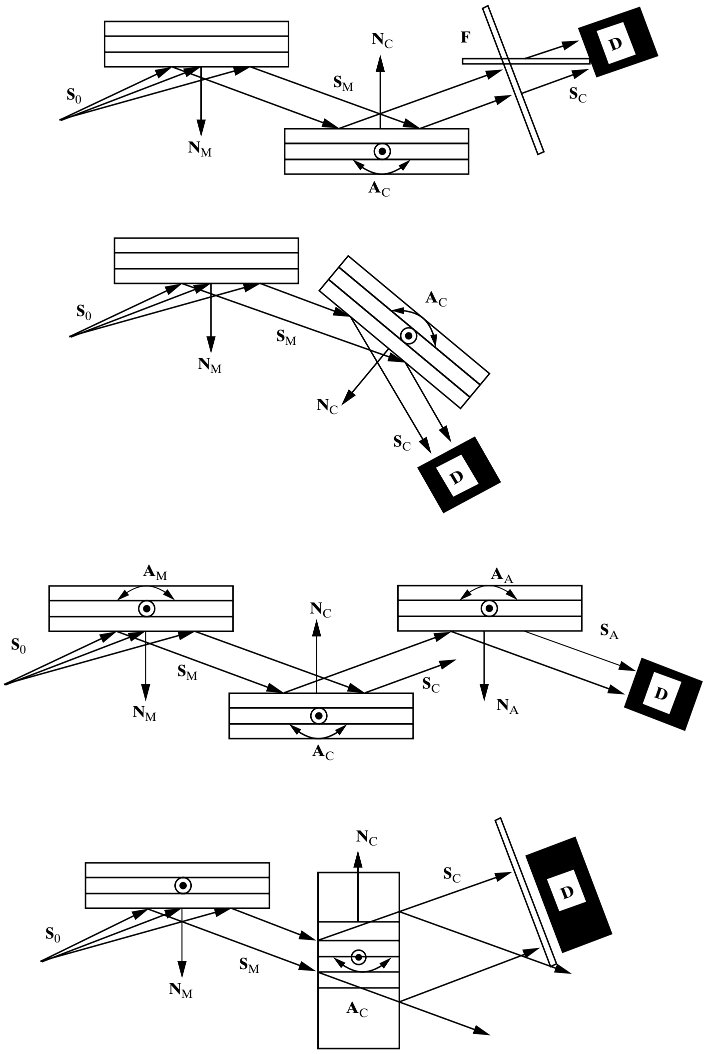

Figure 18 Illustration of different multiple axis geometries; S, N and A are the directions of x-ray beams, crystal normals and rotation axes, respectively, while subscripts 0, M, C and A denote initial, monochromator, sample crystal and analyzer, respectively. Double axis diffractometry/topography in the non-dispersive or (+,-) mode and reflection geometry is illustrated at the top; film is placed at "F", either orientation, for topographic imaging while the detector "D" is used to record diffracted intensity as a function of sample rotation about A_c. Double axis diffractometry is the dispersive or (+,+) mode and reflection geometry appears in the diagram second from the top. Triple axis diffractometry is shown in the diagram third from the top; the analyzer crystal is used to separate strain and misorientation contributions to the diffraction peak. The bottom diagram shows double axis diffractometry/topography in the transmission geometry.

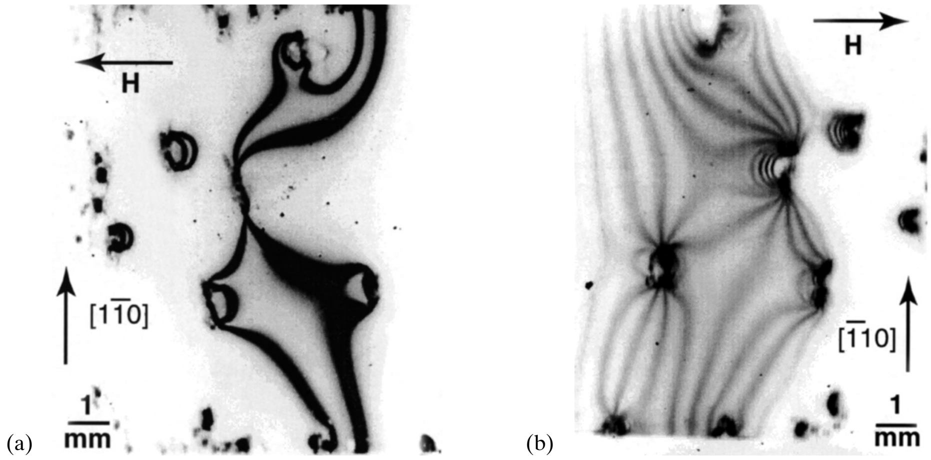

Figure 19 Transmission double crystal topographs recorded with Mo $K\alpha$ radiation with diffraction vector **H** = [002]. A number of NbH precipitates nucleated and grew within the niobium single-crystal matrix; these produce the large deflections in the set of positions diffracting. (a) was recorded with a single sample orientation and shows the positions within the crystal diffracting $K\alpha_1$ and $K\alpha_2$ wavelengths. (b) was recorded with multiple 210 arc sec sample rotations. [28, 29].

4 MULTIPLE AXIS DIFFRACTOMETRY

In order to measure the diffraction peak profile of nearly perfect crystals or epitaxial layers, an experimental arrangement different from that of the parafocusing θ–2θ diffractometer is required: the instrumental profile for such an instrument is far broader than the width typical of a dislocation-free crystal. Instead, a perfect reference crystal (or set of crystals) is used as a beam conditioner so that the sample's diffraction peak profile contains little contribution from sources other than the sample itself. In double axis diffractometry,[5] shown in Fig. 18, the monochromator M, which should be as nearly perfect as possible, is set to diffract $K\alpha$ radiation in the direction of crystal C, which is to be examined. Crystal C is then rotated ("rocked") through the Bragg angle θ_C, while the beam diffracted by it is measured in a fixed detector with a wide slit. The resulting curve of intensity vs. θ is called a *rocking curve*.

There are two settings of the monochromator and sample crystal can be used, the (+,–) and the (+,+) geometries which are shown in Fig. 18 (a) and (b), respectively;

---

[4] Triple crystal topography uses an analyzer crystal or set of crystals, placed within the beam diffracted from the sample, to separate orientation effects from strain effects within the topographic image. The geometry is that in Fig. 18(c) if film replaces the detecter.

[5] Double axis diffractometry is also called double crystal diffractometry.

the first "+" denotes the direction of the normal of the diffraction planes of the monochromator, and the second symbol denotes the direction of the normal to the diffraction planes of the sample crystal relative to the monochromator crystal. The (+,–) arrangement is also termed the non-dispersive and the (+,+) arrangement the dispersive setting. If the *d*-spacings of the diffraction planes of the monochromator and sample are idenitcal, the beam $\mathbf{S}_C$ diffracted from the sample in the (+,–) geometry will be parallel to the beam incident on the monochromator $\mathbf{S}_0$. An additional consequence is that $K\alpha_1$ and $K\alpha_2$ radiation diffract at exactly the same angle. For differing *d*-spacings, $\mathbf{S}_C$ and $\mathbf{S}_0$ will no longer be parallel, and $K\alpha_1$ and $K\alpha_2$ peaks will be separated by the angle:

$$\Delta\theta = \frac{\Delta\lambda}{\lambda}\left[\tan\theta_M - \tan\theta_C\right] \qquad \text{(rad.)}, \tag{5}$$

where $\Delta\lambda$ is the difference in wavelength between $K\alpha_1$ and $K\alpha_2$, λ is the average wavelength of the $K\alpha$ doublet and θ_m and θ_C are the Bragg angles for the monochromator and sample, respectively. The $K\alpha_1$ peak may appear at a higher angle than the $K\alpha_2$ peak, or it may appear at lower angles depending on the relative sizes of θ_m and θ_C. In the (+,+) geometry the minus sign in Eq. (5) is replaced by a plus sign, and $K\alpha_1$ and $K\alpha_2$ are always separated. There are, therefore, two reasons to use the (+,–) geometry and a monochromator matched to the sample: the pattern is simpler to interpret and superposition of the $K\alpha_1$ and $K\alpha_2$ radiation at the same angle increases the peak intensity.

The double axis diffractometer was much used in the early days of x-ray diffraction to compare the width and height of the rocking curve for a real crystal with the values predicted by dynamical theory for a perfect crystal [G.19, G.20]. Note that the perfect crystal rocking curve predicted by dynamical diffraction theory for an incident plane wave is not what is measured by the double axis diffractometer. Instead, experimental rocking curves are the convolution of the monochromator and sample reflection profiles. After accounting for convolution of the two crystals, dynamical theory predicted a width of the order of 10 arc sec. (0.003°) for typical experimental conditions, and some crystals were found with rocking-curve widths approaching this value. However, most natural crystals exhibit widths 10 to 100 times greater.

The width of a rocking curve is a direct measure of the range of orientation and, to a lesser extent, the amount of strain present in the irradiated area of the crystal, because the instrumental contribution to the width of the diffraction peaks is so low, peaks from individual blocks (subgrains) often can be resolved in a rocking curve (Fig. 20).

The width of a rocking curve can also be very sensitive to the surface condition of the crystal. Etching the surface of a calcite crystal produces a rocking curve width in transmission of 12 arc sec (0.003°), very near the perfect crystal value while grinding the surface of a similar crystal on emery paper produces a width of about 120 arc sec (0.03°) [36].

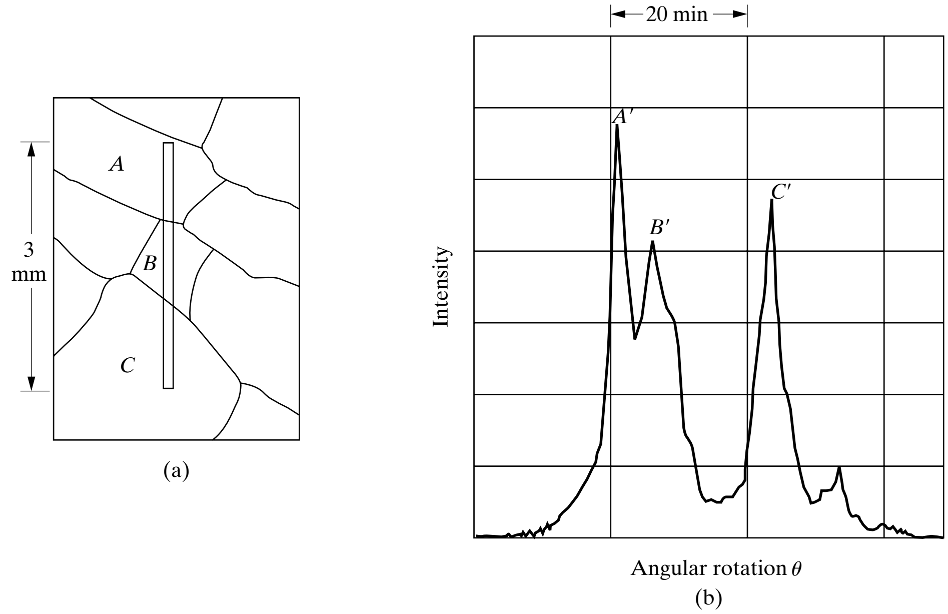

Figure 20 Double axis diffractometer data and subgrain peaks. (a) Tracing of optical photomicrograph of a polygonized aluminum crystal, etched to reveal large subgrains, produced by bending the crystal to a radius of 2 cm and annealing at 645 C for 21 hours; the superimposed rectangle shows the area irradiated (3 × 0.1 mm) by the incident x-ray beam. (b) Rocking curve (200 reflection, (+,-) setting) of the crystal in (b); the maxima *A', B', C'* correspond to subgrains *A, B, C* in (b). Intrater and Weissmann [25].

With the advent of the transistor age and the enabling advances in crystal growth, particularly of silicon, more and more laboratories incorporated double axis diffractometers into their quality control programs. Rocking curve widths routinely are those predicted by dynamical theory. The availability of low cost personal computers in the 1980's led, by 1990, to a high degree of automation of the tedious alignment required for double axis diffractometry, and relatively inexpensive, user-friendly computer-integrated systems became available. The impact of this technical development has been that rocking curves can now be obtained by the crystal growers themselves, after a few hours of training, without the intervention of x-ray diffraction specialists. Since that time it has become the rule rather than the exception for rocking curve data to be reported in the literature.

Rocking curves from silicon and other, well-established wafer materials, however, are no longer of particular interest because quality control has become so good; growth issues are better addressed by x-ray topography, described in the previous section, or triple axis diffractometry, described later in this section. Instead, rocking curves of epitaxial layers grown by such techniques as metallo-organic chemical vapor deposition and molecular beam epitaxy (MBE) are now the focus of much of the characterization effort with double axis diffractometry.

Figure 21 shows rocking curves from two different multiple quantum well structures of $\mathrm{Al_xGa_{1\text{-}x}As/GaAs}$; the nominal structure for each is shown schematically to the right of each rocking curve [37]. The reader should note that the logarithm of the intensity is plotted and not the intensity; this increases the visibility of the smaller peaks. Large peaks from the substrate and buffer layer (labeled “s” and “b”, respectively) appear as well as a series of peaks from the periodic $\mathrm{Al_xGa_{1\text{-}x}As/GaAs}$ structure (labeled “0, $\pm$ 1, $\pm$ 2, … ”). This type of structure is loosely termed a superlattice, and the average *d*-spacing of the artificial superlattice determines the Bragg angle of the fundamental or “0” peak of this structure. If the superlattice and substrate diffraction planes are both parallel to the sample’s surface, the separation between the superlattice’s fundamental peak and substrate peak is given by

$$\Delta\theta_0 = \frac{\Delta a}{a_s} \tan\theta, \tag{6}$$

where $\Delta a = a_{SL} - a_S$, a_{SL} is the average lattice parameter of the superlattice and a_S is that of the unstrained substrate. Satellite peaks also appear, and the period of the superlattice determines the separation between satellites: the smaller the period in

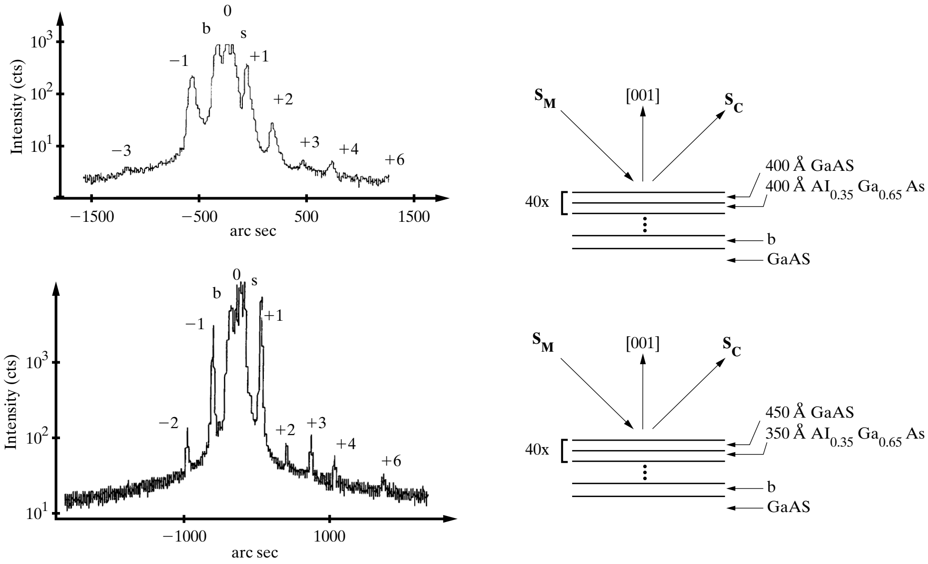

Figure 21 Rocking curves (left) from two 40 period $\mathrm{Al_xGa_{1\text{-}x}As/GaAs}$ superlattices grown on (001) GaAs. The 004 reflection and Cu $K\alpha$ radiation were used. The nominal structures are shown to the right of the rocking curves: the superlattice period and composition were intended to be 800 Å and x=0.35. The best fit found for the top rocking curve (a) was 360 Å GaAs and 500 Å $\mathrm{A_{l0.33}Ga_{0.67}As}$ and for the bottom rocking curve (b) 423 Å GaAs and 286 Å $\mathrm{A_{l0.38}Ga_{0.62}As}$. [37], reprinted courtesy of *Advances in X-ray Analysis*. The numbers show the order of the superlattice satellite reflections, “b” and “s” label the buffer layer and substrate reflections, respectively, and the x-ray beams incident on and exiting from the sample are $\mathbf{S}_\mathrm{M}$ and $\mathbf{S}_\mathrm{C}$ respectively.

direct space, the larger the peak separation in a diffraction pattern (i.e., in reciprocal space). Kinematical diffraction theory accurately predicts, in most circumstances, the superlattice period t from the satellite peak separation $\Delta\theta_p$ and this relation is

$$t = \frac{\lambda}{\Delta\theta_\rho \sin 2\theta} \tag{7}$$

for different diffraction geometries [37, G.22]. For the sample producing the data in Fig. 21a, the period is 860 Å and for that in Fig. 21b the period is 709 Å. The periods were intended to be 800 Å in both cases.

The number and relative thicknesses of the layers within each period of the superlattice produce a modulation of satellite peak intensity in much the same way that the atoms and their positions within the unit cell determine the structure factor and affect the diffracted intensity. For the samples described in Fig. 21, the layers are $Al_xGa_{1-x}As$ and GaAs. Changes in the relative thicknesses of the two layers, while keeping the composition and period of the superlattice constant, leads to different patterns of interference and to some satellite peaks disappearing. For example, the ±1 peaks are strong in both structures of Fig. 21. In Fig. 21a, the +2 peak is prominent, –2 cannot be seen and ±3 peaks are small; in Fig. 21b the –2 peak is reasonably strong, and more prominent than the +2 peak, and the +3 peak is about as intense as the –2 peak. Numerical simulation of the superlattice diffraction patterns reveals that a structure of 360 Å GaAs/500 Å $Al_{0.33}Ga_{0.67}As$ within each period is consistent with the observed intensities of Fig. 21a and that 423 Å GaAs/286 Å $Al_{0.38}Ga_{0.62}As$ is consistent with Fig. 21b.

In the schematics of Fig. 21, the diffraction planes are parallel to the crystal surface. This geometry is termed the symmetric Bragg setting, and only those strains $\varepsilon_\perp$ along the direction of the surface normal are measured. Often $\varepsilon_\parallel$, the strain parallel to the surface, must be determined in order to understand the nature of any relaxation processes in the thin layer. In this case, diffraction planes are selected which make a small angle with the surface; these are termed asymmetric reflections since the plane normal is no longer symmetric with respect to the sample surface, i.e., it is no longer parallel to the sample surface normal. The angular separation between layer and substrate peaks is now a function of both $\varepsilon_\parallel$ and $\varepsilon_\perp$. Comparison of data from symmetric and asymmetric peaks, therefore, allows direct quantification of $\varepsilon_\parallel$. For layers grown on 001 GaAs or Si, {511} are frequently used asymmetric reflections.

The lateral variation of epilayer quality is often assessed by stepping the sample across the beam. Sampling from areas as small as 1 mm^2 is routine with tube-produced x-radiation. With synchrotron radiation rocking curves can be obtained without difficulty with 25 μm diameter microbeams [38]. Rocking curves have been obtained from areas less than 1 μm^2 [39, 40].

Another approach is that developed by Weissmann and coworkers [41] who obtained semitopographic information by phtographing the beam diffracted by crystal C for various angular positions of this crystal. These type of measurements can be made topographic by recording the diffracted beams on film for several carefully measured film-to-sample separations [42].

Several aspects of the design of most double axis diffractometers limit their ability to measure accurate *absolute* lattice parameters. Because these units are primarily intended for measuring rocking curve widths and separations between closely spaced peaks of epilayers and their substrates or of superlattice peaks of multiple quantum well samples, the x-ray optics are not designed with precise measurement of absolute diffraction angles. The sample holder or stage is generally intended to accommodate different sized samples and not to place the sample precisely in the center of the beam. The receiving slits are wide in order to allow all diffraction beams to be observed without rotating the detector. Calibration of the zero angle precise enough for lattice parameter determinations is impractical. Mis-cuts of the sample face of a fraction of a degree are routinely present as are misorientations introduced during mounting of the sample on the second axis stage. Thus, without special procedures, the Bragg angle of the sample can only be taken as approximate.

If one can assume that the top micrometers of the substrate are not strained by the layer(s) on top of it, the difference in diffraction angles between the substrate and layer peaks can be related to the difference in lattice parameter through Bragg's law. Because the unstrained lattice parameter of the substrate is generally known to reasonable level of accuracy, the layer lattice parameter(s) may be determined if *there is no misorientation (i.e., rotation) between the diffraction planes of layer and substrate*. These assumptions are often unjustified, and the resulting uncertainty is simply too great for most applications. Obviously, this short cut does not apply to monolithic samples, i.e., bare wafers or other bulk crystals.

The Bond method [13.7-13.9] allows precise measurement of lattice parameters (Fig. 22). A special rotation stage is needed which permits the position of the *hkl* peak to be measured on either side of the incident beam (i.e., at detector positions d_1 and d_2 in Fig. 22). The average 2θ value from these two measurements yields the precise lattice parameter (without requiring a precise measurement of the beam's zero position). Such diffractometers are rarely encountered.

It is fortunate that there is a simple procedure, suitable for most double axis systems, which allows determination of absolute lattice parameters. The technique [43, 44], which can be termed the 0°/180° sample/reference method, provides accuracy comparable to the Bond method [13.8] but requires measurements be made on a reference crystal as well as the crystal of interest. Both crystals are mounted on the sample stage and are left undisturbed throughout the measurement (Fig. 23). First, the diffraction peak position $\theta_S(0)$ is determined for the sample in the 0° orientation of the sample stage. Then the sample stage is rotated (about $\mathbf{z}$, the bisector of $\mathbf{S}_M$ and $\mathbf{S}_S$) to the 180° orientation and the diffraction peak position $\theta_S(180)$ is measured. In general, $\theta_S(0)$ and $\theta_S(180)$ will be unequal due to miscut or to incidental tilt of the sample on the stage. These steps are repeated for the reference crystal, and $\theta_R(0)$ and $\theta_R(180)$ are obtained. The average positions of the sample and reference peaks are:

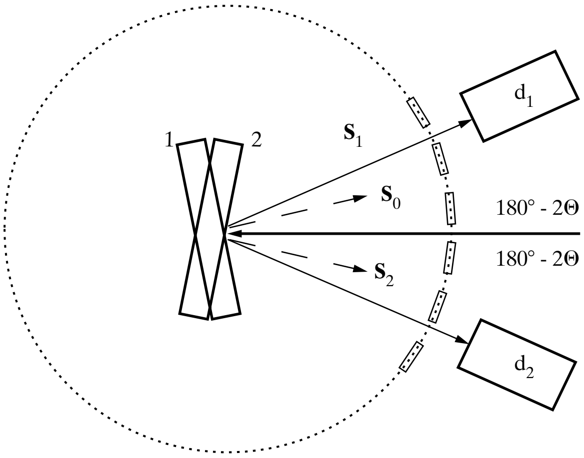

Figure 22 Schematic illustrating the Bond technique. The *hkl* peak position is measured at detector positions d_1 and d_2 for crystal orientations 1 and 2, respectively. The dashed lines show the normals to (*hkl*) for each orientation, and the angle needed to rotate the detector from d_1 to d_2 is 4θ.

$$\theta_S = [\theta_S(0) + \theta_S(180)]/2$$

and

$$\theta_R = [\theta_R(0) + \theta_R(180)]/2$$

The difference between θ_S and θ_R is related directly to the difference in lattice parameter between the reference and unknown sample crystals.

Double axis diffractometry collects data from a large region of reciprocal space. As a result, contributions from tilt (i.e., misorientation) and from dilation combine to form the observed rocking curve. Figure 24 shows how a misoriented portion of a crystal with a slightly different lattice parameter can diffract simultaneously with the remainder of the crystal, so that diffracted beams from both can pass through the wide aperture of the detector. In this example, the two regions have a common direction [110], and region 2 (right of Fig. 24) is rotated by ϕ from region 1. The beam incident on both parts of the crystal is along $\mathbf{S}_M$, the proper direction for 004 diffraction, and, with $d_2 > d_1, 2\theta_2 < 2\theta_1$ and $\mathbf{S}_1$ exits at a greater angle than $\mathbf{S}_2$. Many assumptions are required, therefore, for quantitative interpretation of double crystal rocking curves.

The normal method of separating the misorientation from dilation uses a perfect (unstrained) analyzer crystal positioned between the sample crystal and the detector (Fig. 18(d)). The rotation axes of the monochromator M, the sample crystal and the analyzer A are denoted A_M, A_C, and A_A, respectively. Normally, A_A and the analyzer crystal are mounted on an arm that pivots around A_C. The analyzer crystal functions as an ideal detector slit and greatly decreases the region of reciprocal space sampled for any given orientation of the sample.

The basic scan in triple axis diffractometry involves rotating the analyzer crystal

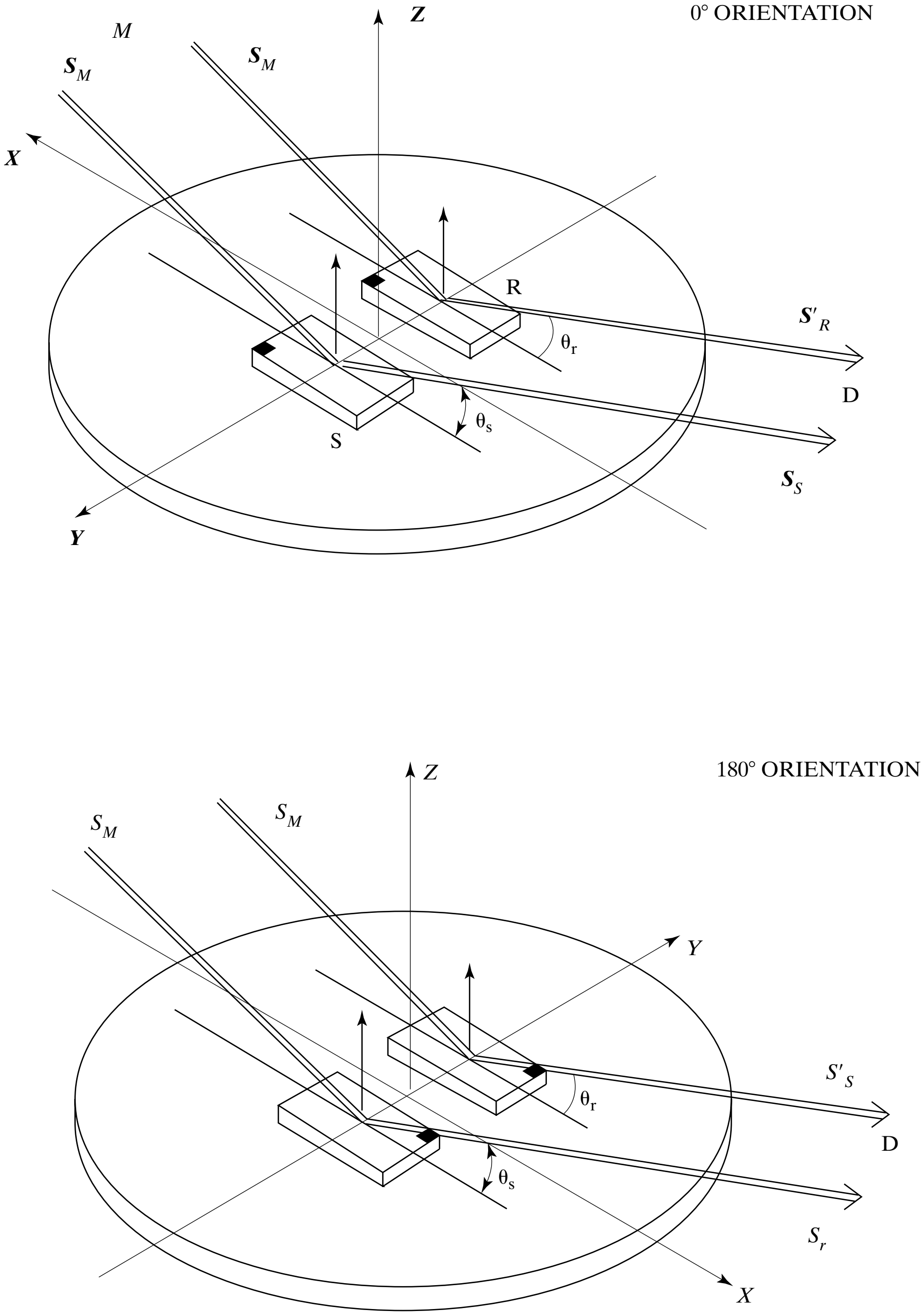

Figure 23 Sample orientations for the 0°/180° sample/reference method for double axis diffractometers described in the text. Note the position of the dark mark in the corner of the sample and reference crystals.

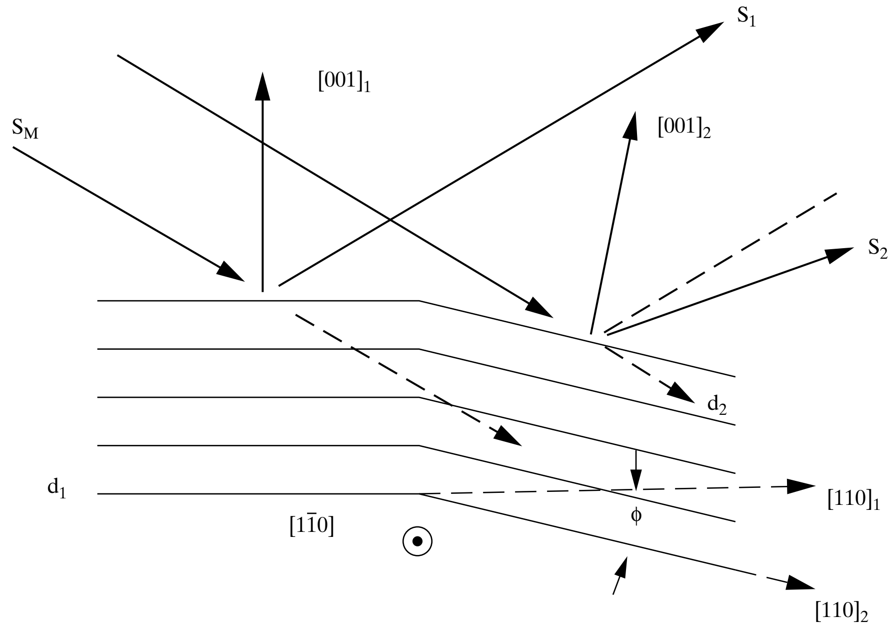

Figure 24 Illustration of how misorientation between closely oriented domains can contribute to broadening in double axis diffractometry.

by angle ω for a sample rotation 2ω. In order to separate the contributions from lattice parameter variation and misorientation, a series of ω–2ω scans are recorded, each being offset from the preceding scan by a sample rotation δω. In effect, the sample rotation δω aligns another misoriented domain for diffraction, and the ω–2ω scan records only changes in *d* from regions with this misorientation in much the same fashion as a *θ*–2*θ* scan in the parafocusing diffractometer reveals changes in *d*-spacings. The result is that only changes in lattice parameter appear in any one ω–2ω scan, and the changes or spread of misorientation are seen by comparing offset ω–2ω scans.

Figure 25 compares a 111_{si} double crystal rocking curve with a triple crystal ω–2ω for a $TaSi_2$/Si *in situ* composite crystal [45]; both were recorded with Cu $K\alpha$ radiation. The sample consists of a parallel array of ~1 μm diameter silicide rods in a single crystal silicon matrix; there are about 10^6 cm^{-2} rods with spacing of $7 - 8$ μm in samples containing ~4 wt. % Ta [46]. The rod axes are $[0001]_{TaSi2}$, and the rods are parallel to $[111]_{Si}$. It is remarkable that the rocking curve of a sample with two phases intimately mixed throughout its volume can be so narrow: 93 arc sec compared to the expected width of 7.4 arc sec. The ω–2ω scan in Fig. 25 is much narrower than the double crystal rocking curve (20-25 arc sec) and indicates that the strain and misorientation contribute to the rocking curve.

In heavily dislocated samples it is sometimes impossible to distinguish peaks in

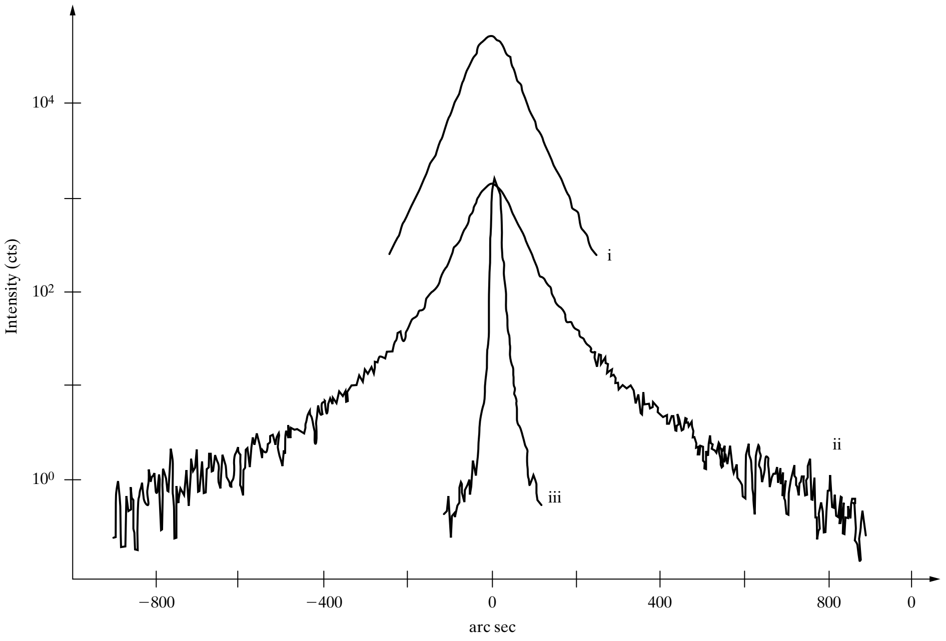

Figure 25 Comparison of 333_{Si} double axis rocking curve (i), triple axis ω scan (ii) and triple axis ω–2ω curve for a crystal of $TaSi_2$-Si recorded on the same diffractometer using Cu $K\alpha$ radiation. Curve (i) was recorded without the analyzer crystal, (ii) was recorded with the analyzer crystal in a single orientation and (iii) was recorded with the analyzer rotated 2 Δω for every Δω rotation of the sample crystal. [15]

double axis rocking curves while the peaks are quite clear in triple axis ω–2ω scans (Fig. 26). The sample consisted of five silicon-germanium layers, each 0.5 μm thick, with germanium contents of 10, 20, 30, 40, and 50%. In the double crystal rocking curve (top), only a broad peak, spanning the 0-50% germanium composition range, is visible: the individual layers are not resolved. In the triple axis curve (bottom) the layers are clearly revealed [G.22].

The distribution of diffracted intensity around a Bragg peak is normally represented by a reciprocal space map constructed of a series of triple axis ω–2ω scans, each of which has the analyzer crystal offset by an angle δω from the other scans in the series. In the map, one axis is the variation in strain and the second, orthogonal axis is the variation in tilt; contours of intensity for these two variables comprise the map. For the example of Fig. 24, the variation of strain in the reciprocal space map would be labeled Δq_{001} and the variation in tilt would be designated Δq_{110}; what would be plotted would be the change in scattering vector **q** along each of these directions. In a single ω–2ω scan, the change in intensity is measured as the diffraction vector changes along [001]. A rotation δω about $[\bar{1}10$ changes the diffraction vector from being parallel to [001] to having a component along [110].

Figure 27 shows two 224-type reciprocal space maps for a sample consisting of a

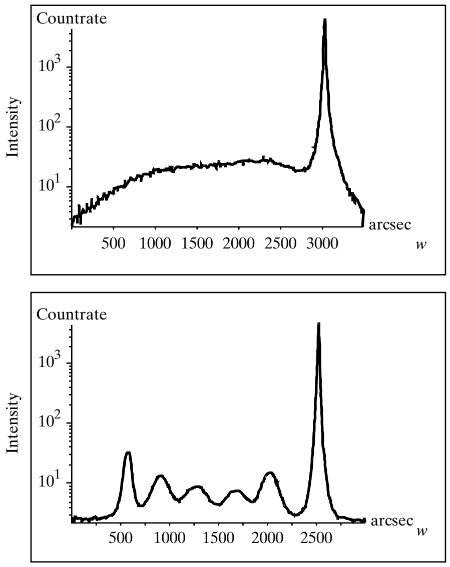

Figure 26 Double crystal rocking curve (top) and triple crystal rocking curve (bottom) from a heavily dislocated silicon germanium multi layer [G.22].

GaAs substrate {2° offcut (001)}, a compositionally graded InGaAs buffer layer and a 40 period AlGaAs/InGaAs superlattice [47]. Recording two 224-type reciprocal space maps gives a much more complete picture of the strain and misorientation in the sample than a single map would. The different shades of gray indicate intensity contours. In addition to the periodically spaced superlattice peaks (labeled –4, –3, etc.), there is a broad peak consisting of the graded layer and the substrate. The left side of the broad peak is the top of the graded layer, and the substrate peak is at the right. The breadth of the central peak (spreading left from the substrate peak shows the range of compositions in the buffer layer, and the vertical shift in the plot between the substrate and graded layer peaks indicates there is a tilt between the two, a tilt measured as 0.17° along the nearest $\langle 110 \rangle$ to the miscut direction.

It would not have been possible with double axis diffractometry to isolate the tilt and composition differences between substrate and graded buffer layer seen in Fig. 27, even with the 0°/180° sample/reference method or with rocking curve simulations. The inclined dark bar in the lower left of the $(\bar{2}24)$ reciprocal space map of Fig. 27 right represents the reciprocal space sampling region for a typical double axis diffractometer. The intensity measured at an one sample angle in a double axis scan is the integral of intensities along this line, and the intensity at the next angle in the scan is found by translating the sampling region from the position shown in the figure and integrating the intensities along the new line. The small bar indicates the reciprocal space sampling region for triple crystal diffraction and shows the improved strain and tilt resolution.

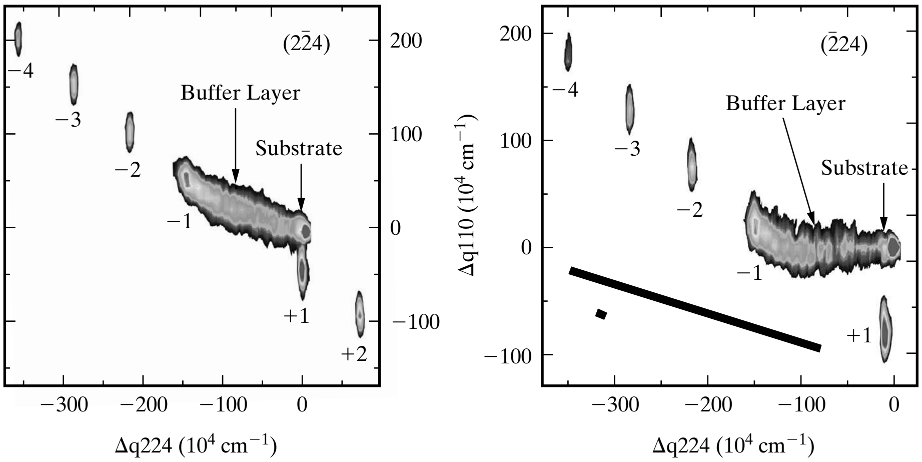

Figure 27 Two 224 reciprocal space maps for a sample consisting of a 2° offcut 001 GaAs substrate, a graded buffer layer and superlattice. The contours of different shades of gray map different levels of intensity [41]. The pair of diagonal black bands (lower left of right-hand map) schematically indicate the regions of reciprocal space sampled, with the longer band corresponding to double axis and the shorter band to triple axis diffractometry.

5 REMARKS

Table 1 summarizes some of the features of the methods just described. Note that a crystal of any thickness can be examined in reflection, but the information received applies only to a shallow surface layer. The range of techniques is wide, and any crystal growth program may employ several during different stages of developing production techniques. Transmission methods, on the other hand, are restricted to rather thin crystals, of the order of 1 mm or less, but these methods reveal imperfections throughout the volume. Note also that the "area irradiated," which is related to the area of the incident beam, may differ from the "area examined" if the crystal is traversed across the beam, as in the Lang projection method.

Incidentally, the reader should note a possible confusion in terminology. When monochromatic radiation is diffracted by a single crystal in reflection the experimental geometry is B termed the *Bragg case or Bragg* setting. When the monochromatic beam is diffracted in transmission it is called the *Laue case or Laue* setting even though white radiation is not involved.

Further information about the methods listed and about other methods assessing crystal quality may be found in various review papers [41, 48-51] and in the books cited in [G.22, G.43 and G.44]. The production of good x-ray topographs can demand considerable experimental skill; the experimental side of the Berg-Barrett and Lang methods, including processing technique for special photographic emul-

TABLE 1

Method	Type*	Radiation**	Area examined	Strain sensitivity
Ordinary Laue	R, T	poly	small	low
Guinier-Tennevin	T	poly	large	low
X-ray Topography				
Berg-Barrett	R	mono	large	low to moderate
Lang	T	mono	small (section) large (projection)	high moderate
Double crystal	T,R	mono	large	high
Polychromatic	T,R	poly	large	low to moderate
Diffractometry				
Double axis	T,R	mono	large or small	high
Triple axis	T,R	mono	large or small	very high

* R=reflection T=transmission
** Poly=polychromatic, Mono=monochromatic

sions, is described by Austerman and Newkirk [54] and by Tanner [G.43].

Finally, a comparison is in order between TEM and x-ray topography as means of studying crystal imperfections. The TEM has the advantage of very much higher resolution of fine detail, but with some danger that what is seen in the thin-foil specimen does not represent the bulk crystal; dislocations may move into or out of the foil or rearrange themselves during the process of thinning the specimen. The lower resolution of x-ray topography is balanced by the facts that one topograph represents a relatively enormous area of the specimen and that x-ray topography is much more sensitive to strain variation than TEM. Roughly stated, one technique looks at the trees., the other at the forest.

PROBLEMS

1 In the Berg-Barrett topographs of Fig. 13, explain why only screw dislocations are revealed in (b), only edges in (c), and screws and edges in (d). Give the indices of the operating slip systems. i.e., the indices of each slip plane and of the slip direction in that plane. (Slip in a LiF crystal occurs on {110} planes in $\langle 110 \rangle$ directions, but the experimental observations in Fig. 13 are inconsistent with the assumption that slip occurred on all possible slip systems. Note also that only those dislocations which intersect a crystal face will be distinctly observed by x-ray examination of that face.)

REFERENCES

The following books are listed more or less in the order they are encountered in the text

G.19 R. W. James. *The Optical Principles of the Diffraction of X-Rays* (Woodbridge; CT: Ox Bow Press, 1982). Excellent book on advanced theory of x-ray diffraction. Includes thorough treatments of diffuse scattering (due to thermal agitation, small particle size, crystal imperfections, etc.), the use of Fourier series in structure analysis, and scattering by gases, liquids, and amorphous solids.

G.20 B. E. Warren. *X-Ray Diffraction* (Reading, MA: Addison-Wesley, 1969). Excellent advanced treatment, in which the author takes pains to connect theoretically derived results with experimentally observable quantities. Stresses diffraction effects due to thermal vibration, order-disorder, imperfect crystals, and amorphous materials. Includes a treatment of the dynamical theory of diffraction by a perfect crystal.

G.22 D. Keith Bowen and Brian K. Tanner. *High Resolution X-ray Diffractometry and Topography* (London: Taylor and Frances, 1998). Excellent emphasis on applications: x-ray diffraction topography and multi-axis diffractometry.

This page intentionally left blank

Polymers

1 INTRODUCTION

Diffraction and scattering from polymers presents a set of problems different from those encountered with crystalline materials or even amorphous materials such as inorganic glasses. The difference is not merely that polymers are very large molecules with large molecular weights. The structure of many, very large bio-active molecules such as proteins and DNA has been determined by x-ray diffraction in a straight-forward albeit laborious fashion. The origin of the word "polymer" illustrates an important difference between materials. Many (*poly*) repeats units (*mers*) of the same building block link repetitively, normally in a long, flexible chain.

As flexible chains, polymers can be crystalline, semi-crystalline or amorphous. The amount of crystallinity (or its absence) determines to a large extent whether a particular piece of polymeric material is useful for a given application. Different polymers crystallize or order to different extents, and measuring the amount and the anisotropy of ordering in polymer samples is a very important application of diffraction and scattering studies.

Because the "structure" of amorphous materials are rather different from that of the crystalline materials discussed above, this chapter begins by describing the structure of some common polymers and compares these building blocks with those of inorganic glasses. Because polymers are frequently encountered in the form of fibers, with preferred orientation similar to the fiber texture in crystalline materials, examples used in the present chapter are drawn from fiber studies. X-ray studies of polymer structure naturally divide into wide angle diffraction, wide angle scattering ($2\theta > 5°$) and small angle scattering ($2\theta < 5°$), and Sec. 3 and 4, respectively, introduce the first two topics. Since long range order is required for diffraction, studies of the crystalline portion of polymer samples are covered in Sec. 3. Amorphous polymers and the amorphous portions of semi-crystalline polymers produce significant scattered intensities in the wide-angle range and provide the examples in Sec. 4. While small angle scattering is a frequently-used technique with

From Chapter 18 of *Elements of X-Ray Diffraction*, Third Edition. B.D. Cullity, S.R. Stock.

polymers, it finds application in crystalline as well as amorphous materials systems; for this reason its application to polymers is beyond the scope of this chapter.

2 POLYMER STRUCTURE

In order to understand why polymers in solids "pack" so differently than other classes of materials, consider first the structure of SiO_2. The molecule SiO_2 forms several crystalline phases (e.g., cristoballite, quartz) as well as the amorphous phase silica. The repeat unit or mer for silica is the $(Si0_4)^{4-}$ tetrahedron, and, in this unordered state, the several linked tetrahedra pictured in Fig. 1 can be con sidered part of a long chain. Each oxygen atom needs to be shared with a silicon atom; the oxygen atoms at the tetrahedra corners are not free to dangle. This sharing produces a three-dimensional network of silicon and oxygen, and two-dimensional representations of possible crystalline and amorphous atomic arrangements are also shown in Fig. 1. Short-range order but not long-range order is present in the silica glass while long-range order is the characteristic of the crystalline phase.

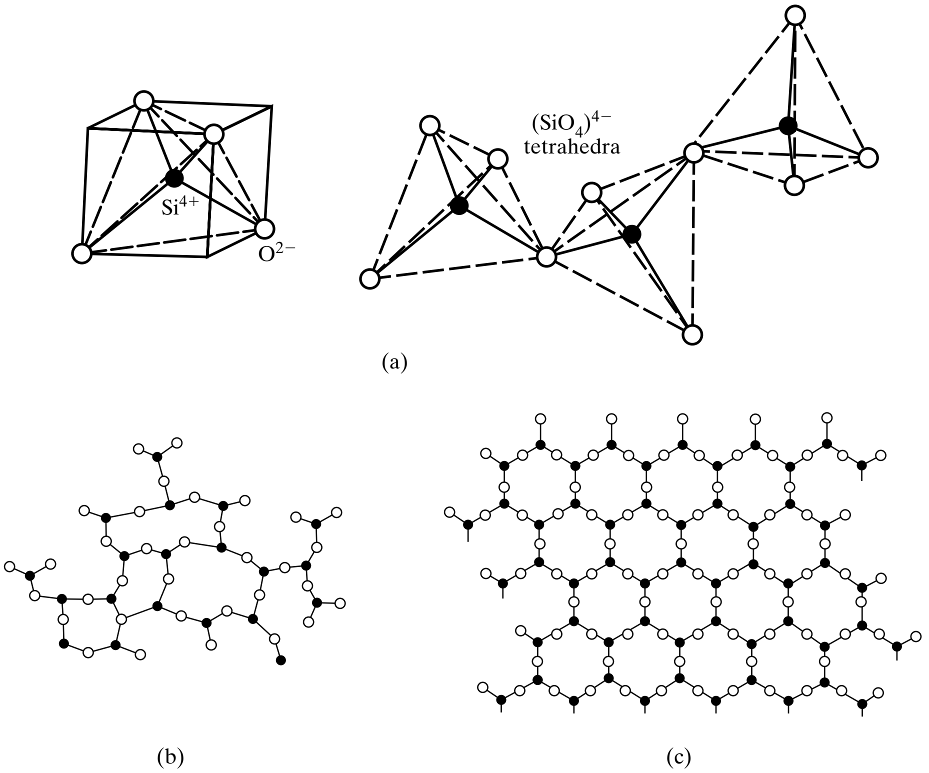

Figure 1 Repeat units in different SiO_2 structures: (a) $(SiO_4)^4$-tetrahedral and two-dimensional representations of (b) silica glass and (c) crystalline SiO_2. (After Schaffer, Saxena, Antolovich, Sanders and Warner [1].)

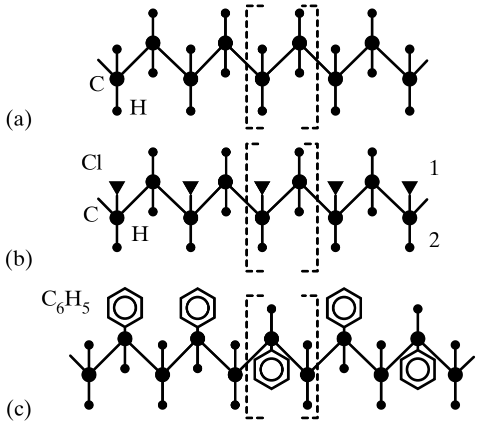

Figure 2 Three polymers based on the mer C_2H_3R where R is a single hydrogen atom in polyethylene (a), a single chlorine atom in polyvinylchloride (b) and a C_6H_5 ring in polystyrene (c). The simplified planar representation is used. (After Schaffer, Saxena, Antolovich, Sanders and Warner [1].)

Figure 2(a) shows a section of a polyethylene molecule with the C_2H_4 mer enclosed in square brackets. Note that this two-dimensional linear representation simplifies the actual three-dimensional structure. The structure of polyethylene is often abbreviated as $-[-CH_2-CH_2-]_n-$, where n represents the number of repeat units (or monomers) and is on the order of 10^5.

The backbones of polymers consist of covalent bonds, for example, the chain of carbon single bonds in polyethylene (Fig. 2a). Polyesters, on the other hand, contain the ester linkage in the backbone:

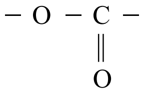

$$-O-\underset{\displaystyle O}{\underset{\|}{C}}-$$

In some families of polymers, one of the hydrogen atoms attached to the carbon backbone in Fig. 2a is replaced by a more complicated sidegroup R. For a vinyl polymer, the generic formula is

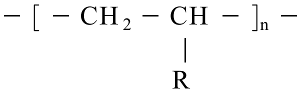

$$-[-CH_2-\underset{\displaystyle R}{\underset{|}{CH}}-]_n-$$

Polypropylene results when R is a CH_3 group and polyvinylchloride when R is a chlorine atom (Fig.2b). Polystyrene is more complex, with R being a C_6H_5 ring (Fig. 2c). Hydrocarbon rubbers share the form $-[-CH_2-CH=CR-CH_2-]_n-$ and have a double bond in the backbone.

Examining the polyvinylchloride and polystyrene structures shown in Fig. 2 reveals alternating carbon atoms with a sidegroup R different from hydrogen. In these structures there are, however, two hydrogens which can be replaced, and these can be distinguished as sites 1 and 2. Figure 2b and c show configurations where R is randomly distributed between sites 1 and 2, and this is the atactic configuration. In the isotactic configuration, all R occupy site 1 (alternatively, all R might occupy site 2 , and in the syndiotactic configuration R alternates regularly

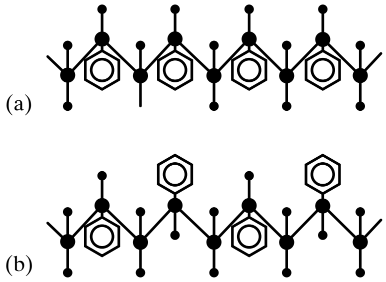

Figure 3 (a) Isotactic and (b) syndiotactic configurations of polystyrene. Note that the C_6H_5 rings are much larger than indicated in the drawing. The atactic configuration is shown in Fig 2c. (After Schaffer, Saxena, Antolovich, Sanders and Warner [1].)

between the two sites (Fig. 3). As will be discussed shortly, the type of polymer configuration largely determines the extent to which it can be crystallized.

The facts that polymer backbones are covalently bonded and that covalent bonds have specific bond angles have important consequences for the three-dimensional structure (conformation) of polymers. In polyethylene, the carbon atom forms four covalent bonds, two with other carbon atoms and two with hydrogen atoms. The resulting tetrahedral bond angles of 109.5° are shown in Fig. 4. Note that the C-C bonds are free to rotate about an axis which preserves the bond angle; therefore, the carbon atoms adjacent to the pair in the center of Fig. 4b are free to occupy any position on the cones shown. Conformations from planar zig-zag (Fig. 4c) to random coil (Fig. 4d) may occur for a chain of covalently bonded carbon atoms; the latter conformation is the lower energy, more common form of polyethylene. Polymer molecules in solution, in melts and in noncrystalline solids seek to coil randomly, and energy can be lowered in solids only if the polymers crystallize.

Polymer chains are not independent of their neighbors in solids; they can interact and bond. At one extreme are the hydrocarbon rubbers

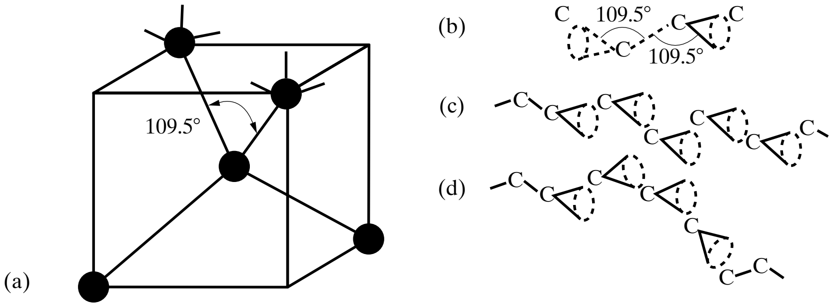

Figure 4 Three-dimensional structure (conformation) of a polyethlene chain. (a) the C-C-C bond angle, (b) restriction of adjacent carbon atoms to specific cones of rotation, (c) planar zig-zag conformation resulting when all of the C atoms in the chain backbone lie in the same plane and (d) the more common (lower energy) random coil conformation. (After Schaffer, Saxena, Antolovich, Sanders and Warner [1].)

-[-CH_2-CH=CR-CH_2-]$_n$- where a double bond exists in the center of each mer; under certain conditions this bond can be broken and can link adjacent chains. Such cross-links are primary bonds and are characteristic of thermoset polymers: the concept of individual chains no longer applies. In the absence of primary bonds, strong secondary bonds can form. In polyvinylchloride the electronegative chlorine side groups bond to the electropositive hydrogen sidegroups of a neighboring chain, and Fig. 5 illustrates possible bonding for isotactic and syndiotactic configurations for this thermoplastic polymer.

In general thermoset polymers do not crystallize, and the factors influencing the crystallinity of thermoplastic polymers are those which affect the efficiency with which molecules can pack: the size of sidegroups, the extent and degree of chain branching, tacticity and the complexity of monomer or repeat unit. Even in the most favorable circumstances, a polymer with small, polar sidegroups in a regular configuration, the tangling and low diffusion rates of the long molecules in the melt prevent fully crystalline material from solidifying.

Three possible crystallite arrangements are shown in Fig. 6; a polymer chain with length up to 50,000 Å can extend through multiple 50-500 Å long crystallites. It is not surprising that a chain might run from a disordered region through a bundle of well-organized, parallel chains (micelle) back through an amorphous volume, etc. Nor is it unexpected that oriented crystallites might be produced in drawn fibers. In some instances polymers form folded chains and reasonably-sized single crystals. Polyethylene single crystals have been observed with lengths along a single direction of up to 10 μm [2]; in this case, the orientation of covalent chain backbones are perpendicular to the longer dimensions of the crystal (Fig. 7). A unit cell of polyethylene is shown in Fig. 8. Usually planar ribbon-like structures crystallize in orthorhombic or monoclinic unit cells; rod-like and helical polymer chains often pack in a hexagonal or trigonal unit cell [4]. Once again note that many molecules may be present in a single crystal.

Bulk semi-crystalline polymers often have structures composed of aggregates of folded chain crystalline and non-crystalline material; these spherulites possess radii

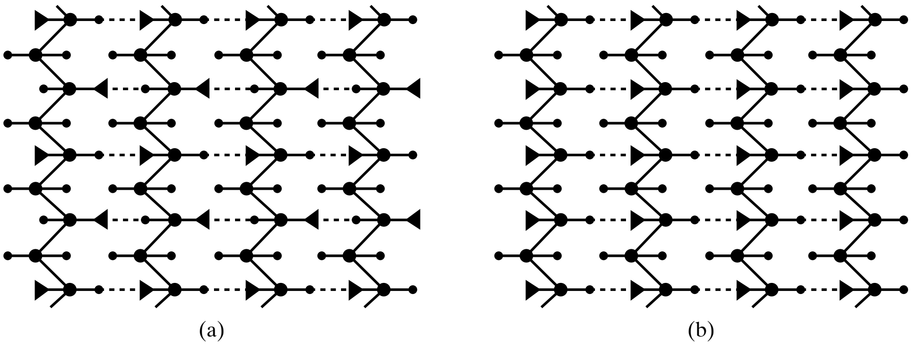

Figure 5 Secondary bonds (dashed lines) which can result for (a) isotactic and (b) syndiotactic configurations of polyvinylchloride. (After Schaffer, Saxena, Antolovich, Sanders and Warner [1].)

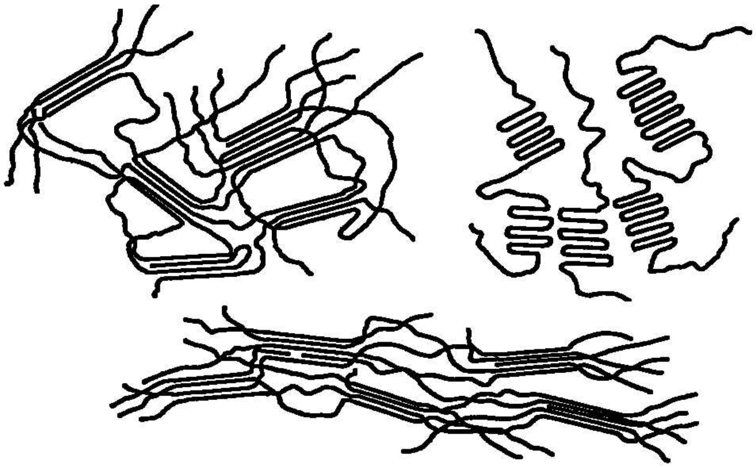

Figure 6 Three polymer chain arrangements producing crystallites, (top left) fringed micelles, (top right) folded chains. Possible arrangement of oriented crystallites (bottom). (After Rodriguez [2].)

of up to 100 μm (Fig. 9) and each grows out from a separate nucleation point [2]. In spherulites the folded chains within the crystalline material are oriented normal to the spherulites' radii. A primary concern is the fraction of crystallinity present.

3 WIDE-ANGLE DIFFRACTION

A common arrangement for diffraction from polymer samples employs the same geometry as is used in recording transmission Laue patterns: a flat piece of film or an area detector sits perpendicular to the incident x-ray beam $\mathbf{S}_0$ and at a distance D from the sample (Fig. 10). A monochromatic beam, however, is normally used for polymer diffraction instead of the polychromatic beam required to

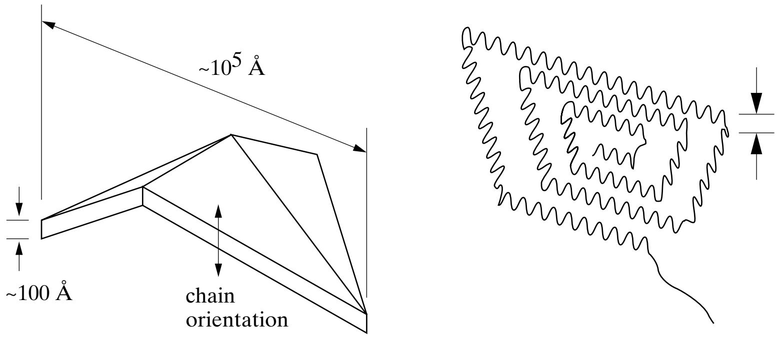

Figure 7 Illustration of dimensions and chain orientations in a large single crystal of polyethylene. (After Rodriguez [2].)

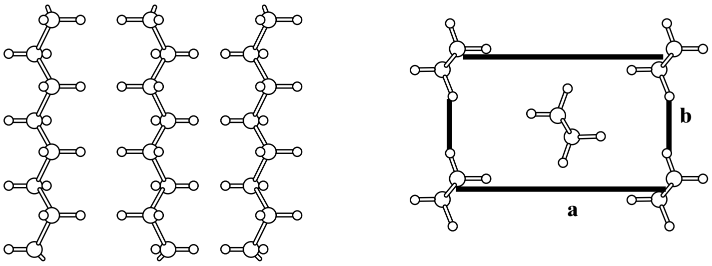

Figure 8 Unit cell of crystalline polyethylene, a = 7.41 Å, b = 4.94 Å and successive pendant atoms are 2.55 Å apart along the chain axis (After Natta and Corradini, [3].)

produce Laue patterns. The most common arrangement is with the monochromator placed between the x-ray source and the sample. The diffracted beams $\mathbf{S}_i$ emerge from the back surface of the sample at angles $2\theta_i$ and expose the film/detector at a separation R_i from the position where the incident beam would have encountered the film if it were not intercepted by the beam stop. The transmission geometry is normally used since most polymer samples are not highly absorbing, being composed of relatively low atomic number elements such as carbon and hydrogen, and since these elements' scattering powers drop rapidly with increasing angle. For example, a sample of polymethylmethacrylate (PMMA) has a linear attenuation coefficient $\mu = 6\ \text{cm}^{-1}$ for Cu $K\alpha$ radiation [5]. Samples with thicknesses t $\sim 1/\mu$ are optimum for transmission diffraction, and for PMMA this thickness is about 1.5 mm, a thickness which is readily obtained.

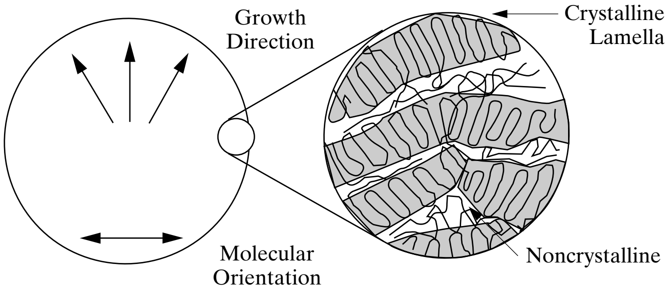

Figure 9 Schematic of spherulite structure.

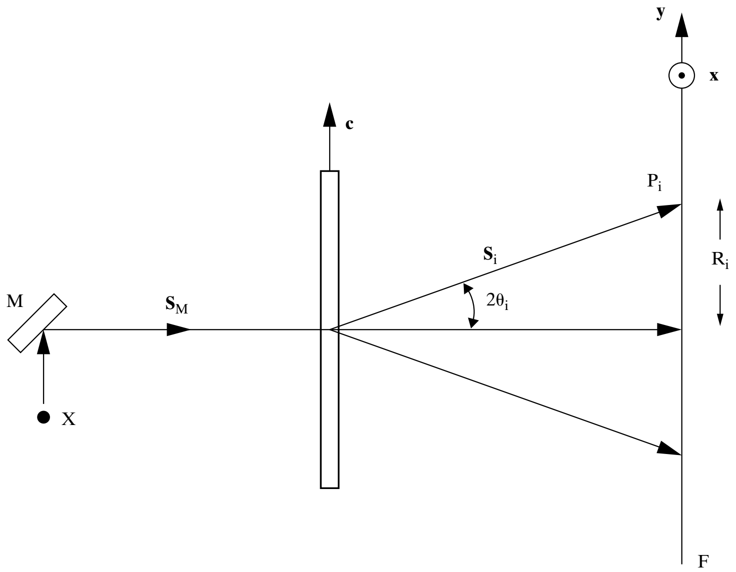

Figure 10a Illustration of the diffraction geometry (transmission) often used for polymers.

The value of D must be accurately known if the R_i are to be converted into reliable d_i and the reflections assigned their proper *hkl* indices. The most reliable technique for determining D for a particular diffraction pattern is to dust an internal standard onto the sample. Using a fine powder such as calcite, which produces a strong diffraction ring at $d = 3.035$ Å, is more reliable than having a standard specimen-to-film separation since sample position variability on the order of 5% are typical in flat plate apparatus [4]. Direct measurement of R_i is impractical since a beam stop must be used in this geometry, but $2R_i$ can be measured accurately using diffraction spots or arcs P_i on opposite sides of the transmitted beam. Simple trigonometry applied to Fig 10 yields:

$$\tan 2\theta_i = R_i/D \quad (1)$$

or solving for the Bragg angle

$$\theta_i = 1/2 \tan^{-1}(R_i/D) \qquad (2)$$

When this angle is substituted into Bragg's law, the interplanar spacing is

$$d_i = \lambda/(2 \sin[\{\tan^{-1}(R_i/D)\}/2]) \quad (3)$$

for diffraction of x-rays with wavelength λ.

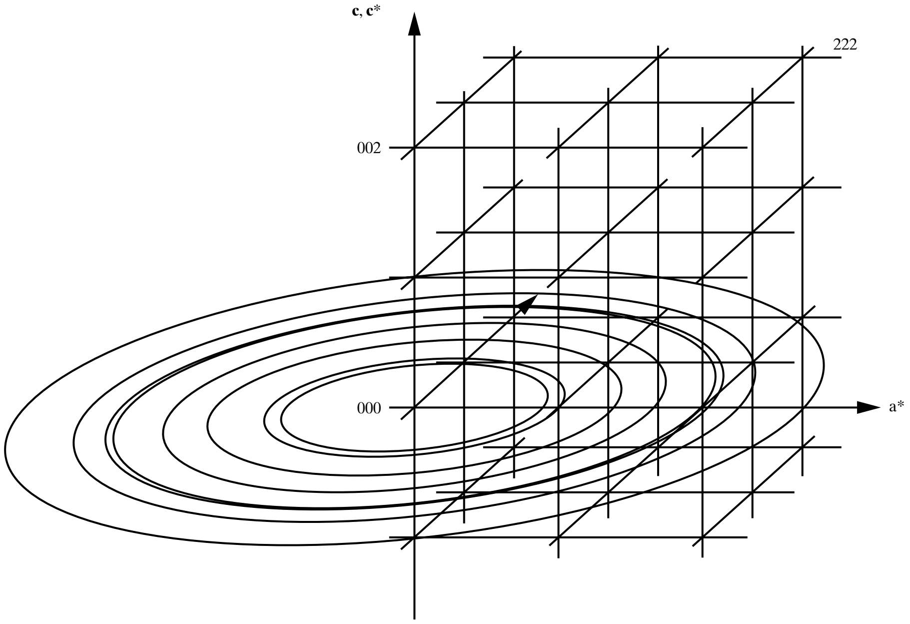

Figure 10b Reciprocal lattice for polymer fiber(s) with concentric circular distribution of reciprocal lattice points in the equatorial plane (a*b*); note the similarity with rotation photographs.

Indices *hkl* need to be assigned to the reflections recorded on the film or area detector, and this process is speeded greatly if one makes use of what is known about preferred orientation in the sample. For fibers, the simplest case is where the crystallites are uniformly distributed at all orientations about a common axis termed the fiber axis (**FA** in Fig. 10) which is usually denoted **c**. An analogy is a single crystal rotated with constant angular velocity about **c**, i.e., to the results of a rotation camera. Each reciprocal lattice point will trace a circle centered on **c** (more precisely **c*** which is taken to be parallel to **c**), and Fig. 10 illustrates this geometry as well as the Ewald sphere construction representing diffraction from a uniaxially oriented fibrous sample. The diffraction conditions are satisfied where these reciprocal lattice rings (*rel rings*) intersect the Ewald sphere. If the fiber axis is positioned perpendicular to the incident beam, the resulting diffraction pattern consists of spots arrayed in layer lines (Fig. 10c) just like a rotation camera pattern. The presence of the layer lines allow periodicities along the fiber axis **c** to be separated from periodicities along the other lattice vectors.

The meridian and the equator shown in the schematic diffraction pattern in Fig. 10d are important in the indexing procedure. The diffracted beams forming spots on the equator are coplanar with $\mathbf{S}_0$ and perpendicular to **c** and **c***. The indices of these equatorial reflections must be of the form *hk*0 since the rel rings producing these reflections are centered on point 0,0,0 of the reciprocal lattice. On the

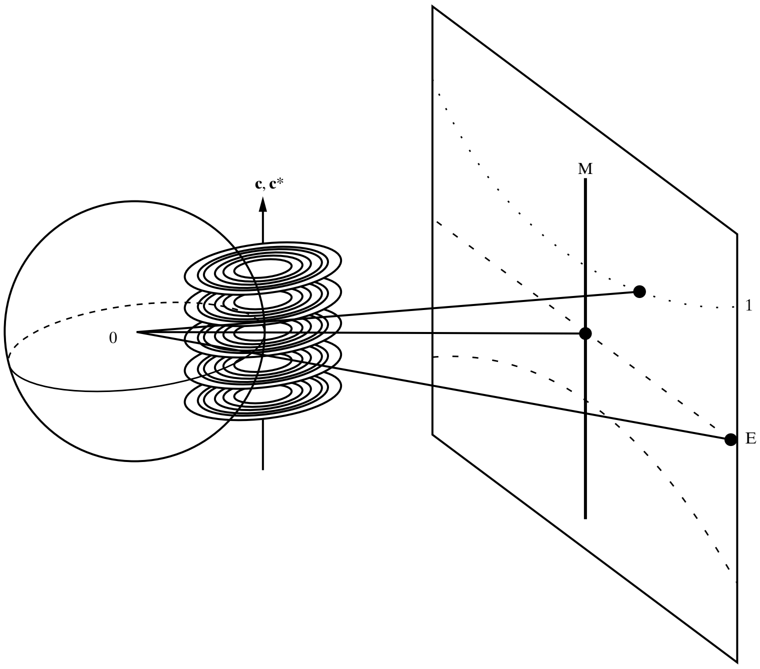

Figure 10c Geometric relationship between the distribution of reciprocal lattice points and the fiber diffraction pattern.

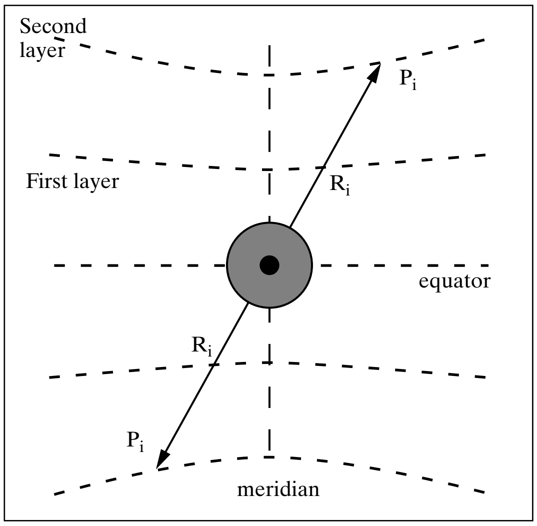

Figure 10d Schematic of the resulting diffraction pattern.

adjacent first layer line, the rel ring centers are point 0,0,1 of the reciprocal lattice, and the reflections have indices *hk*1. On the meridian, the diffraction vector is parallel to **c***, and the reflections must have indices 00*l*.

Even if the rel rings were continuous, each ring would only intersect the Ewald sphere over a narrow range. The resulting reflection would not, therefore, extend too far along the layer line. As shown in the enlargement of the reciprocal lattice near **c*** (Fig. 11), higher order meridional 00*l* rel rings, however, do not intersect the Ewald sphere as long as the fiber axis is perpendicular to $\mathbf{S}_0$. Further, limited crystallite size and imperfect fiber texture often broaden the reciprocal lattice points so that *hkl* rel rings can produce diffraction spots on the meridian.

The problem of determining whether a given reflection is meridional or not is solved by simply tilting the sample (i.e., the fiber axis) and, hence, the reciprocal lattice, so that a particular 00*l* rel ring touches the Ewald sphere. This angle is the Bragg angle for the 00*l* reflection. Once the tilt is executed 00*l* should appear and $00\bar{l}$ should be absent. Figure 12 shows data for poly-(p-phenylene terephthalamide) with and without tilting of the fiber [6]. Any *hkl* reflection appearing on the meridian in the untilted fiber will split into two off-meridional reflections upon tilting. Note also that tilting does distort the equatorial line.

Using the layer line spacing allows relatively straight-forward determination of the value of the lattice constant *c*. In addition, all of the reflections on the equator have $l = 0$, those on the first layer line have $l = 1$, etc. What remains is the determination of *h* and *k* for each reflection, something which can be done using the methods outlined.

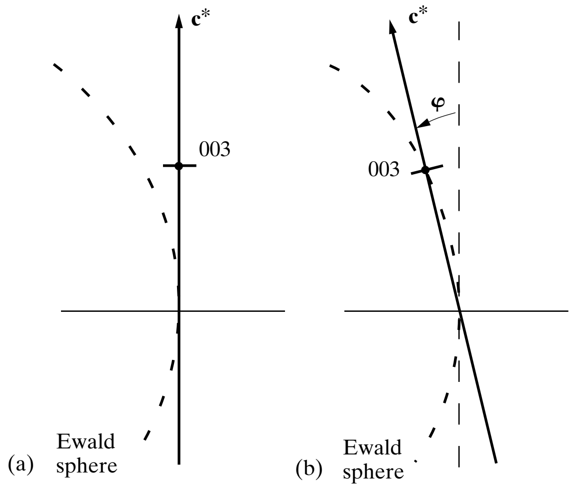

Figure 11 Illustration of the tilt φ needed to bring meridional reflections into the orientation for diffraction. (a) Beam perpendicular to fiber axis **c***, and (b) fiber axis tilted by φ to bring 003 to the Ewald sphere.

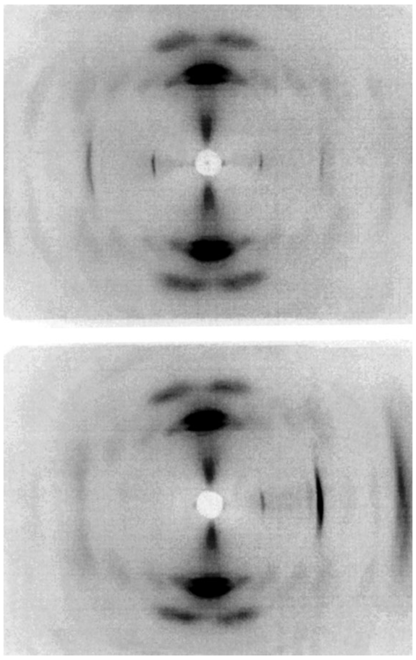

Figure 12 Diffraction patterns of Kevlar fibers recorded on an image plate. (Top) Beam incident perpendicular to the fiber axis (vertical), and (bottom) with 16 tilt of the fibers.(Courtesy of S. Jerkins).

Clues concerning crystal morphology can be gained by observing the morphology of the spots in a diffraction pattern. The sharpness of the equatorial diffraction peaks compared with the arcs on the layer lines can indicate chain-folded lamellae [4].

4 WIDE-ANGLE SCATTERING

It would be quite unexpected to find a polymer sample which was totally crystalline or which had perfect fiber texture. Sharp diffraction peaks would not be observed, but considerable amounts of scattering would be expected. Fluctuations in electron density over lengths less than about 100 Å produce maxima in scattered intensity at diffraction angles greater than about 5°. Figure 13 shows x-ray scattering curves for poly tetrafluoroethylene in the crystal phase at 18 C and in the molten phase at 350 C [5]; note that intensity $I(\mathscr{S})$ is plotted as is conventional in scattering experiments, as a function of the scattering vector $\mathscr{S}\,' = 4\pi(\sin\theta)/\lambda$ where the angle 2θ lies between the incident and scattered beams. The sharp peaks in the 18 C pattern indicate the crystal structure, but there are also broad peaks superimposed on the diffraction peaks. The broad peaks accompanying the diffraction peaks are very similar to those in the pattern from the melt and demonstrate that a substantial fraction of the sample is non-crystalline at 18 C.

Apparatus for wide angle scattering studies of polymers generally make use of the symmetric transmission geometry with pinhole collimation and with a monochromator positioned between sample and x-ray source. Use of the symmetric θ–2θ

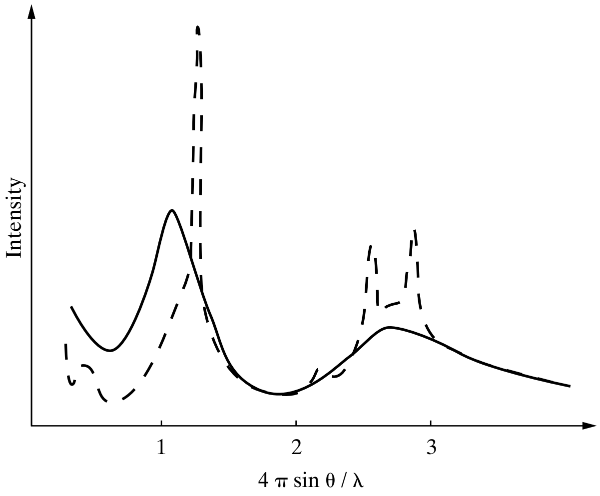

Figure 13 X-ray scattering curve for poly (tetrafluoroethylene) in the crystalline phase (dashed line) and in the molten phase (solid line). (After Warren, Krutter and Morningstar [7].)

transmission geometry requires intensity corrections which are much less involved than those in the reflection geometry and produce an undistorted map of reciprocal space. Obtaining this latter condition prevents use of area detectors for anything other than qualitative scattering studies of aligned polymers when the range of scattering angles spans $2\theta > 30°$ [5]. Therefore, a simple scintillation detector is adequate for $\theta - 2\theta$ diffractometry. In scattering studies of preferred molecular orientation, the sample must be rotated in its own plane; without this provision only a single line through reciprocal space can be scanned. Experimental scattering data needs to be corrected carefully for a variety of effects, and the reader is directed to the references for an introduction to these details.

Of the total intensity scattered by organic polymers, a large fraction is incoherent or Compton scattering. In addition, the large x-ray path lengths inherent in polymer samples allow significant multiple scattering. The relative amount of incoherent scattering relative to coherent scattering increases as $\mathcal{S}'$ becomes large, and this causes problems if coherent scattering must be measured out to large $\mathcal{S}'$ in order to provide radial distribution functions with high resolution. Since radial distribution functions have somewhat limited application in the area of organic polymers, the scattering vector range can be limited to $\mathcal{S}' \sim 6 - 7$ Å^{-1} [5]. Ordinarily, much more information can be gained from inorganic non-crystalline materials (glasses), and the complexity of Fig. 14, the radial distribution function determined for an inorganic glass [7], demonstrates the difficulties encountered when applying this procedure to interpreting scattering from the inherently more complex polymers.

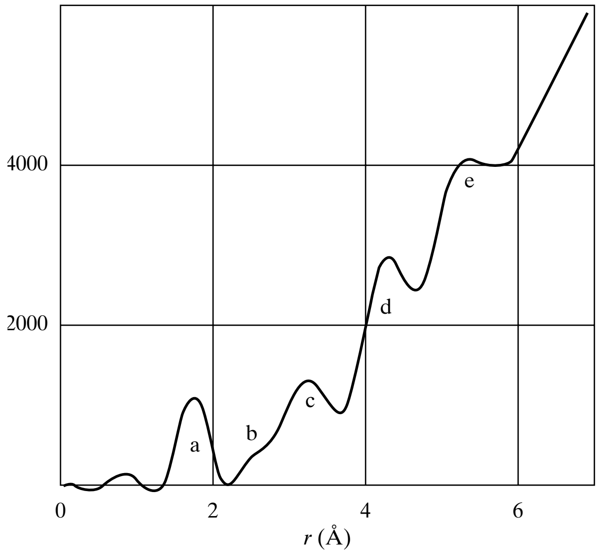

Figure 14 Radial distribution curve for SiO_2 glass, with the letters indicating various characteristic atomic separations. (After Warren, Krutter and Morningstar [7].)

Preparing a sample with some amount of average preferred orientation, is one route to unraveling the diffuse x-ray scattering from disordered polymers. Mechanical methods including extrusion produce significant preferred orientation, and plotting $I(\alpha, \mathscr{S}')$, where α is the angle between $\mathscr{S}'$ and the deformation axis, reveals the ordering present. Figure 15 shows a contour map of $I(\alpha, \mathscr{S}')$ for a partially-aligned, non-crystalline sample of extruded PEEK (poly ether ether ketone) and $I(\mathscr{S}')$ for $\alpha = 0°$ meridional and for $\alpha = 90°$ equatorial orientations [5]. The diffuse peak at $\mathscr{S}' \sim 1.3$ Å^{-1} is the most intense for $\alpha = 90°$ while the other peaks at higher $\mathscr{S}'(\sim 3$ and 5.5 Å^{-1}) are more intense for $\alpha = 0°$. Since the largest peak is most intense in the plane perpendicular to the mechanical axis (equator), it represents correlations between PEEK chain segments. The peaks at $\mathscr{S}'(\sim 3$ and 5.5 Å^{-1} are most intense along a direction parallel to the direction of alignment (meridian) and arise from correlations within molecular chains. Use of aligned polymer samples is particularly revealing with polymers possessing substantial sidechains [5].

Scattering studies have shown that the chain conformation in molten polyethylene is irregular and ‘random-coil’-like [8]; this result was obtained by partitioning the scattering into interchain (producing broad oscillations) and intrachain (more sharply defined maxima) components.

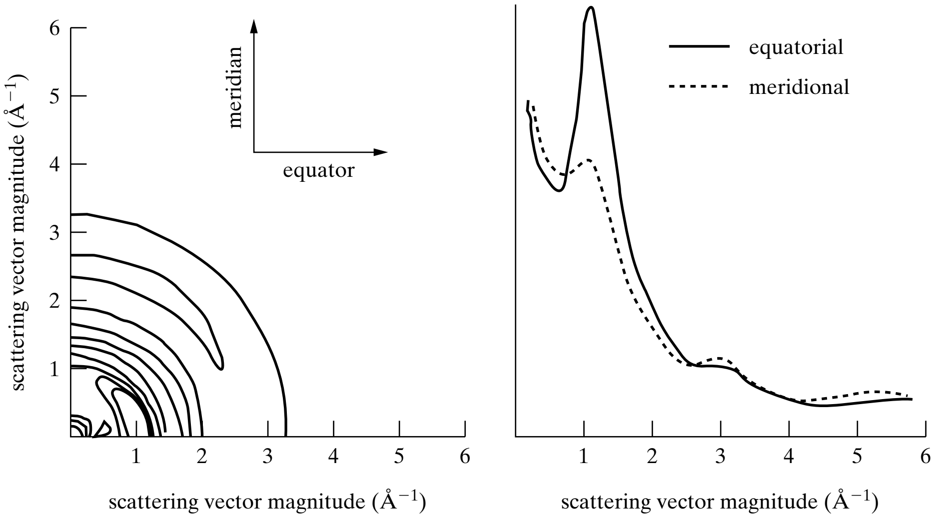

Figure 15 (Left) Scattered x-ray intensity function for partially aligned non-crystalline PEEK prepared by extrusion (extrusion axis vertical) and (right) two-dimensional surfaces along the indicated setions. (After G.R. Mitchell [5].)

5 SUMMARY

Diffraction patterns from polymers incorporate features normally encountered in very different contexts in metals or ceramics. Improved computational methods for quantifying the amount of crystallinity and for refining lattice parameters offer the prospect for better process control and development of strategies for economic manufacturing; discussion of these methods is beyond the scope of a volume such as this; Alexander's monograph, although dated, remains a very useful reference [9]. Additional helpful information is provided in the recent book by Roe [10].

PROBLEMS

1 For the polyethylene crystal structure shown in Fig. 8, calculate the diffraction peak positions for the ten lowest-angle reflections. Assume the crystals are randomly oriented. What is the maximum width the diffraction peaks could have and still be resolved? How might processing of a sample with fairly wide peaks allow better analysis of the underlying crystal structure?

This page intentionally left blank

Small Angle Scattering

1 INTRODUCTION

Strong diffraction peaks result from constructive interference of x-rays scattered from ordered arrays of atoms and molecules. Much can be learned from the angular distribution of scattered intensity at low angles, and the treatment of scattering covered previously can be extended without overly much work to cover small angle scattering. Fluctuations in electron density over lengths on the order of 100 Å or larger can be great enough to produce appreciable scattered x-ray intensities at angles $2\theta < 5°$. These variations can be from differences in density, from differences in composition or from both, and do not need to be periodic.

Long period structures can produce peaks in intensity in the small angle range. The anisotropic distribution of intensity can be analyzed in much the same way as wide angle diffraction patterns, texture photographs, or pole figures. Examples of analysis of long period structures appear in Sec. 2.

The amount and angular distribution of scattered intensity also provides information such as the size of very small particles or their surface area per unit volume, regardless of whether the sample or particles are crystalline or amorphous. Section 3 develops the scattering formalism used to interpret results from small angle scattering experiments. In Sec. 4 analysis of one of the scattering regions, the *Guinier* region, is discussed, and in Sec. 5 another portion of the scattering curve, the *Porod* region, is covered. Small angle scattering apparatus are discussed in Sec. 6, and examples appear in Sec. 7.

The reader will note that the discussion begins with long period structures which are often encountered in polymers and in biological materials. These long period structures and their analysis, however, are largely foreign to those working with metals, ceramics, or semiconductors. Readers primarily concerned with metals and ceramics will find Sec. 3 through the end of the chapter more applicable. The reason for covering long period structures early in the chapter (Sec. 2) and starting the discussion of scattering with diffraction equations (the first part of Sec. 3) is to provide

From Chapter 19 of *Elements of X-Ray Diffraction*, Third Edition. B.D. Cullity, S.R. Stock.

a bridge from earlier coverage of *diffraction* from periodic arrays of scatterers to scattering from random arrays of entities which can be sharply or poorly defined.

2 LONG PERIOD STRUCTURES

Long period structures produce maxima in scattered intensity, and the sharpness and angular distribution of these peaks reflect the regularity of the variation in electron density along different directions. There are differences with respect to the more often encountered wide angle diffraction. In what follows, the distribution of scattered intensity recorded on film or other area detector is linked to specific structures using examples of polymers comprised of lamellar crystallites [1]. It is important to remember the inverse relationship between periodicity in direct space and diffraction angle in reciprocal space, between crystallite size and the width of diffraction peaks.

The left side of Fig. 1 shows the features in small angle scattering patterns expected from different microstructures of stacked lamellar crystallite (right side) [1]. When ring patterns are observed (Fig. 1a), spherically symmetric assemblies of crystallites, e.g., spherulites, or unoriented assemblies of stacked lamellar crystallites can be responsible. Such rings sometimes are distorted into ellipses, and these elliptical ring patterns can be encountered at intermediate stages of deformation of

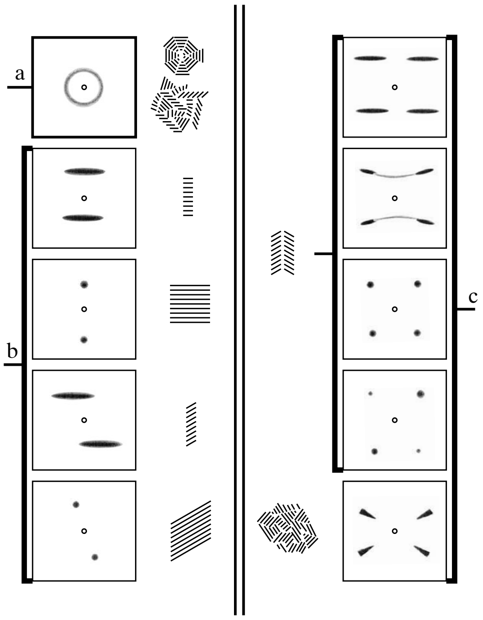

Figure 1 Schematic of long-range ordered structures (right side of each column) and corresponding diffraction patterns in the small angle region (left side of each column). Pattern types a-c discussed in the text. (After Kakudo and Kasai [1].)

drawn or compressed samples; the corresponding microstructures might be deformed spherulites or stacked lamellar crystallites. Many orders can be observed if the long period structure is regular enough. Spherical latex particles 2780 Å in diameter and suspended in water produced thirteen rings, for example, when a pinhole monochromator and Cu Kα radiation were used [2].

Scattering in layer lines is a frequent feature in long period patterns of polymers. Two-point (Fig. 1b) and four-point (Fig. 1c) layer line patterns reveal the orientation of stacks of lamellar crystallites. The maxima appear along the direction of stacking, and the lateral width of the spots depends on the dimensions of the lamellae along the corresponding direction, being larger for smaller direct space dimensions. Inclined stacks of crystallites, i.e., parallel lamellae inclined with respect to the fiber direction, sometimes result in necked regions of drawn fibers or in sheets drawn in two different directions. The resulting rotation of the direction of stacking alters the position of the scattered intensity maxima (Fig. 1b), and small crystallite size broadening can be superimposed. Figure 2 was recorded from turkey leg tendon, and multiple small angle peaks are observed on either side of the direct beam [3].

Four-point layer line geometry reflects doubly oriented structure in the sample (Fig. 1c). Patterns with four points on straight horizontal lines or convex with respect to the equator are best regarded as the superposition of two two-point layer line patterns related by mirror symmetry. The corresponding texture could be an assembly of two crystallite stacks with mirrored inclinations. The bottom pattern of Fig. 1c shows what might be produced by a doubly-oriented structure. The inclination from the vertical axis reveals the directions along which the lamellae are stacked, and one material producing such a pattern is doubly oriented Nylon 6 obtained by solid state polymerization [1]. Sometimes the four maxima lie on a curve concave with respect to the equator, and this can be thought of as a distortion of the symmetry producing an elliptical ring pattern.

3 SCATTERED INTENSITY

The "exact" equation for the relative intensities of different diffracted lines measured in a diffractometer was given previously as

$$I = |\mathrm{F}|^2 \mathrm{p} \left(\frac{1 + \cos^2 2\theta}{\sin^2 \theta \cos \theta} \right) \exp(-2\mathrm{M})$$

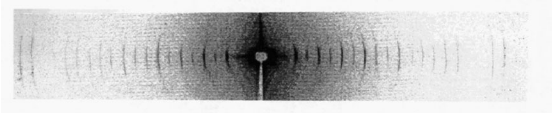

Figure 2 Low angle x-ray diffraction pattern of turkey leg collagen recorded on an image plate. (Courtesy of Snigirev *et al* [3].)

where I = relative integrated intensity, p = multiplicity factor, θ = Bragg angle, exp (–2M) = temperature factor and F = structure factor defined by

$$F_{hkl} = \Sigma f_n \exp[2\pi i(hu_n + kv_n + lw_n)],$$

where the summation extends over all n atoms of the unit cell, u_n, v_n, w_n are the fractional coordinates of the nth atom within the unit cell and f_n are the atomic scattering factors. Implicit in writing the summation is that each atom scatters as a well-defined entity.

As seen by incident x-ray photons, a sample consists of a spatially inhomogeneous sea of electrons. In fact, quantum mechanics indicates that each electron is itself spread into a diffuse cloud of negative charge. The important quantity is the charge density ρ which is normally expressed in electron units so that the quantity $\rho\, dV$ is the ratio of charge in volume dV to the charge of one electron. Thus, for each electron $\int \rho\, dV = 1$. The scattering from a single atom must take into account the phase differences for scattering from different "portions" of the atom, and f the atomic scattering factor is made up of the contributions from individual electrons f_e given by

$$f_e = \int \exp[(2\pi i/\lambda)(\mathbf{S} - \mathbf{S}_0) \cdot \mathbf{r}]\rho\, dV. \tag{1}$$

Calculation of the precise values of $f = \Sigma_n(f_e)_n$ depends on detailed knowledge of the charge distribution ρ.

While it may not be precisely true, assuming that the charge distribution of electrons in an atom is spherical and equals $\rho = \rho(r)$ is a very useful approximation and allows a simple expression to be obtained for f. Using $k = (4\pi/\lambda)\sin\theta$ and Fig. 3, $(\mathbf{S} - \mathbf{S_0}) \cdot \mathbf{r} = 2r \sin\theta \cos\phi$ and

$$f = \sum_n (f_e)_n = \sum\nolimits_n \int_r^{\infty} \int_{\phi}^{\pi} \exp(ikr \cos\phi)\, \rho_n(r)\, 2\pi r^2 \sin\phi\, d\phi\, dr$$

$$= \sum_n \int_0^{\infty} 4\pi r^2 \rho_n(r) \frac{\sin kr}{kr}\, dr, \tag{2}$$

Note that at small angles, i.e., small k or $(\sin\theta)/\lambda$, sin (kr)/kr approaches unity. If Z is the number of electrons in the atom,

$$\sum\nolimits_n \int_0^{\infty} 4\pi r^2 \rho_n(r) dr = Z \tag{3}$$

and f approaches Z at small values of $\sin\theta/\lambda$. Thus, changes in electron density affect the amplitude of scattered x-radiation regardless of the ordering or lack of ordering of the scattering atoms.

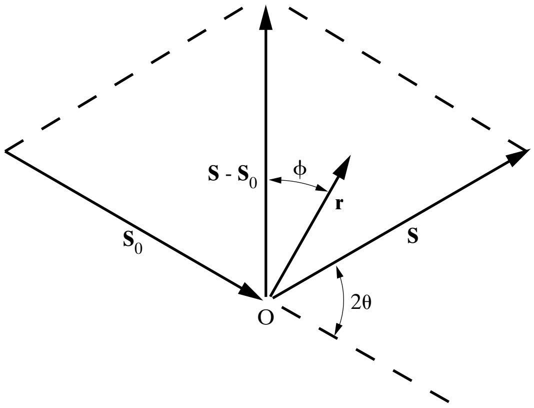

Figure 3 Illustration of qualities used in the transformation of Eq. 1 to 2.

Suppose there are small regions of constant composition different from the surrounding matrix. If the regions, hereafter designated particles, are dispersed at random and the concentration of particles is not too high, the amplitude scattered by the particle (in electron units) relative to the matrix is given by the difference in electron density through:

$$A(\mathscr{s}) = \Delta\rho \int \exp(2\pi i[\mathscr{s}\cdot \mathbf{r}])dV_r, \tag{4}$$

With reference to Fig. 4, r_s is the magnitude of r along $\mathscr{s} = (\mathbf{S} - \mathbf{S_0})$ and $\mathscr{s} \cdot \mathbf{r} = \mathbf{s}\mathbf{r}_s$. At small angles $\mathscr{s} \cong 2\theta/\lambda$ and r_s is the component of r along a line perpendicular to $\mathbf{S}_0$. If A_{rs} is the cross-sectional area of the particle along r_s, the scattered amplitude is

$$A(\mathscr{s}) = \Delta\rho \int \exp(2\pi i \mathscr{s} r_s) A_{rs} dr_s \tag{5}$$

There are two regions of small angle scattering are important in many applications, the Guinier and Porod regions. The angular limits of these regions and what can be learned from analysis of scattering in each is covered in the next two sections.

4 GUINIER REGION

Equation 5 expresses scattering from a single particle as a function of the scattering vector $\mathscr{s}$, and, in the small angle region, the exponential function can be expanded as a power series in $\mathscr{s}$, and terms of order higher than $\mathscr{s}^2$ can be discarded, leaving

$$A(\mathscr{s}) = \Delta\rho\left[\int A_{rs} dr_s + \int 2\pi i \mathscr{s}\, r A_{rs} dr_s - \int 2\pi^2\, \mathscr{s}^2 r_s^2 A_{rs} dr_s \right]. \tag{6}$$

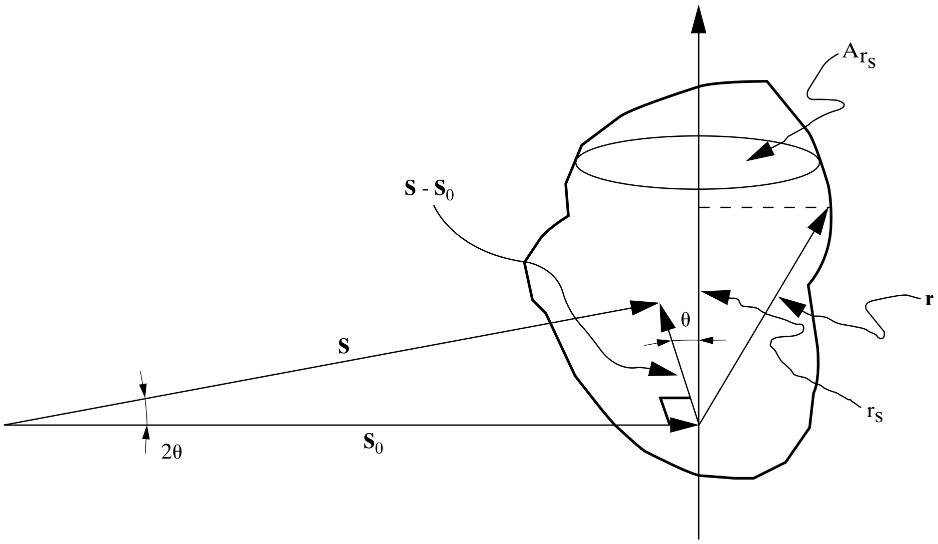

Figure 4 Illustration of the approximations used in obtaining Eq. 5.

The most convenient origin to choose for the particle is its center of gravity; the second term of Eq. 6 goes to zero. The first term is the product of the volume per particle V and $\Delta\rho$ while the third term is related to R_{gs} the radius of gyration of the particle. This relationship is

$$R_{gs}^2 = V^{-1}\int r_s^2 A_{rs} dr_s, \tag{7}$$

and yields for the amplitude of scattering for the particle

$$A(\mathscr{I}) = \Delta\rho\,(V - 2\pi^2 V \mathscr{I}^2 R_{gs}^2)$$

$$= \Delta\rho V(1 - 2\pi^2 \mathscr{I}^2 R_{gs}^2). \tag{8}$$

Normally the term in the parenthesis is approximated as an exponential function:

$$A(\mathscr{I}) = \Delta\rho V \exp(-2\pi^2[2\theta/\lambda]^2 R_{gs}^2). \tag{9}$$

For n independently scattering particles,

$$I(\mathscr{I}) = |A(\mathscr{I})|^2 \simeq n(\Delta\rho)^2 V^2 \exp[-4\pi^2(2\theta/\lambda)^2 R_{gs}^2] \tag{10}$$

and the slope of the plot of ln I vs. $16\pi^2\theta^2/\lambda^2$ yields a slope of $-R_{gs}^2$ (Fig. 5) and is termed a Guinier plot after A. Guinier who pioneered this approach. Guinier's

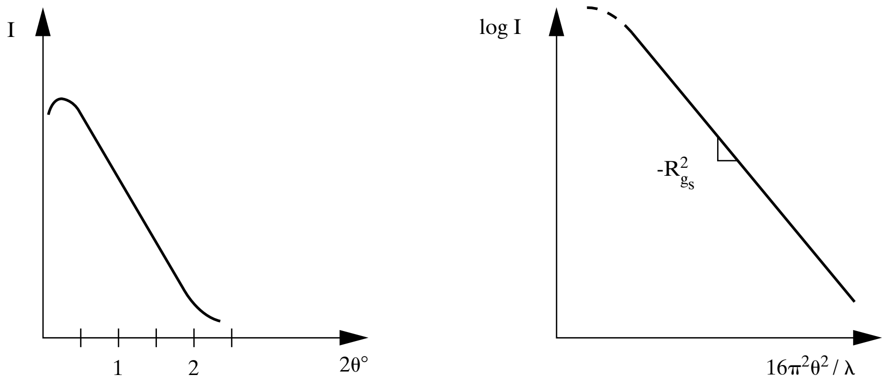

Figure 5 Variation of scattered intensity in the small angle region (left) and Guinier plot for determining the radius of gyration R_{gs} of the scatters.

name should already be familiar through the Guinier camera. Guinier-Preston or G-P zones in Al-Cu alloys also bear his name. Note that Eq. 10 holds for scatterers which are small enough so that their maximum diameter $D_{\max}$ satisfies the inequality $kD_{\max} \leq 1$.

If the particles have a range of sizes and take all possible orientations, then the particle dimensions along the two orthogonal axes x_1 and x_2 perpendicular to $\mathscr{S}$ also are reflected in the slope of the Guinier plot. The distance to a point r is related to its coordinates via $r^2 = X^2 + y^2 + \mathscr{S}^2$ and the average radius of gyration $< R_g^2 >$ is given by

$$< R_g^2 > \; = \; < R_{gx}^2 > + < R_{gy}^2 > + < R_{gs}^2 > . \tag{11}$$

If all orientations are equally possible, then $\langle R_g^2 \rangle /3$ replaces R_{gs}^2 in Eq. 10, where

$$< R_g^2 > \; = \int r^2 dV/V. \tag{12}$$

In practice, Guinier plots do not have a linear region which extends to $2\theta = 0°$ (Fig. 5). Normally the slope is taken where the curve is linear and excludes the very lowest angles. A bump in the plot of Fig. 5b, for example, can be caused by interparticle interference: the particles may not be randomly arranged or the density of particles may be too high. If a range of particle sizes are present, this will be indicated by a range of slopes in the Guinier plot, and, in some cases, the size distribution can be determined.

When particles of varying sizes are present, the radius of gyration determined from the slope of the Guinier plot is heavily weighted towards those with the largest sizes. For n different sizes present each with weight fraction w_n and volume V_n, the term V R_g^2 represents the scattered amplitude and

$$< R_g^2 > \ = \frac{\sum_n w_n(\Delta\rho)^2 V_n^2 (R_g^n)^2}{\sum w_n(\Delta\rho)^2 V_n^2}. \tag{13}$$

Since $\Delta\rho^2 V^2$ is the square of the number of electrons per particle and this is proportional to R^6,

$$< R_g^2 > \ = \ < R^8 > / < R^6 > \tag{14}$$

which is heavily-weighted toward large *R* of the distribution of particle sizes.

5 POROD REGION

For a solid sphere of radius *a*, the amplitude scattered can be found by terms of spherical coordinates and setting $\rho = 1$ inside the sphere and $\rho = 0$ elsewhere:

$$\int \exp(-2\pi i s \cdot \mathbf{r}) dV_r \int_0^{2\pi}\int_0^{\pi}\int_0^{a} \exp(-2\pi i\, s\, r \cos\alpha) r^2 \sin\alpha\, d\alpha\, d\phi\, dr \tag{15}$$

Writing the exponential function in terms of cosines and sines and letting $u = 2\pi s\, r \cos\alpha$ (so that $du = -2\pi s\, r \sin\alpha\, d\alpha$) allows the integral in Eq. 15 to be altered to

$$\int_0^{2\pi}\int_{2\pi s\, r}^{-2\pi s\, r}\int_0^{a} [\cos u - i \sin u]\left[-\frac{1}{2}\pi s \cdot\right] r\, d\phi\, dr\, du. \tag{16}$$

Note that as α varies from 0 to π, u varies from $+2\pi s r$ to $-2\pi s r$. The value of the integral with respect to ϕ is 2π. After integrating with respect to u and then r, the result is:

$$\int \exp 2\pi i \Big(s \cdot \mathbf{r} dV_r = \frac{4}{3}\pi a^3 \left\{ \frac{3[\sin 2\pi s\, a - 2\pi s\, a \cos 2\pi s\, a]}{(2\pi s\, a)^3} \right\} \Big). \tag{17}$$

This result is proportional to the amplitude of scattering, and one can, therefore, write for the intensity in electron units:

$$I(s) = [\Delta\rho 4\pi a^3]^2 (3)^2 \left[\frac{\sin 2\pi a s - 2\pi a s \cos 2\pi a s}{(2\pi s\, a)^3} \right]^2. \tag{18}$$

Computing the square of the term in the parentheses and setting $2 \sin x \cos x = \sin 2x$ and $1 - \cos^2 x = \sin^2 x$ produces:

$$I(s) = \frac{16(\Delta\rho)^2}{64\pi^4 s^6}[1 + (4\pi^2 a^2 s^2 - 1)\cos^2 2\pi a s - 2\pi a s \sin 4\pi a s], \tag{19}$$

and applying $\cos^2 x = (1 + \cos 2x)/2$ yields

$$I(s) = \frac{(\Delta\rho)^2}{8\pi^3}\left[\frac{1}{\pi s^6} + \frac{4\pi a^2}{s^4} + \left(\frac{4\pi a^3}{s^4} - \frac{1}{\pi s^6}\right)\cos 4\pi a s - \frac{4a}{s^5}\sin 4\pi a s\right]. \tag{20}$$

Two factors allow further simplification. First, in the presence of a size distribution of scatterers, which is usually the case, the trigonometric terms cancel due to the contributions of the various size scatterers. Second, $s^{-6} \ll s^{-4}$. Therefore, for each size having frequency w_a,

$$I(s) = \frac{(\Delta\rho)^2}{8\pi^3}\frac{\sum_a w_a 4\pi a_a^2}{s^4} = \frac{(\Delta\rho)^2}{8\pi^3}\frac{S_T}{s^4}, \tag{21}$$

where S_T is the total surface area in the volume irradiated. Approximations made in obtaining Eq. 21 are valid where a plot of ln I vs. ln s has a slope of -4. A plot of the quantity $s^4 I(s)$ vs. s yields a horizontal region where $kR_g > 3$ and from which the value $\Delta\rho^2\, S_T$ can be obtained. This Porod plot (Fig. 6)
can have oscillations at low s when there is a narrow size distribution of particles; these are due to the trigonometric factors in Eq. 20. For a narrow distribution of particle sizes and for equiaxed particles, equal areas are found at small s above and below the line defining $\Delta\rho^2\, S_T$. If the particles are angular or if they are very small in one direction, the areas will not be equal and a horizontal line is never quite achieved [4].

The inverse of the surface to volume ratio S_V is related to an average dimension termed the Porod radius R_P. Since R_p is related to $< R^3 > / < R^2 >$, it is numerically different from R_G [4].

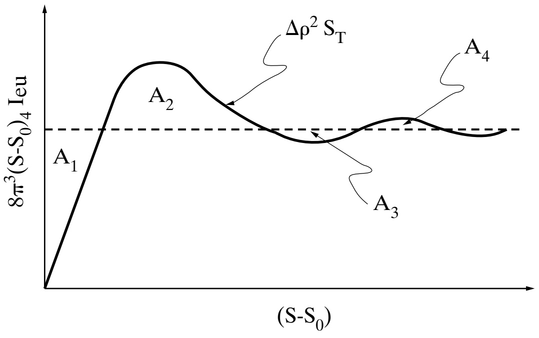

Figure 6 Porod plot for determining S_T the total surface area of the scatteres in the irradiated volume. If the size distribution is narrow, the total area below the dashed line will equal that above the line (i.e., $A_1 + A_3 + \ldots = A_2 + A_4 + \ldots$).

Absolute intensities do not need to be measured in order to determine S_T using Eq. 21. It can be shown that Eq. 10 can be used to determine that the integrated small angle intensity equals $N\Delta\rho^2$ V, i.e.,

$$\int I(s)\,dV_s = N(\Delta\rho)^2V, \tag{22}$$

where N is the total number of particles and V is the volume of each particle. Therefore,

$$\frac{I(0)}{\int I(s)\,dV_s} = \frac{N(\Delta\rho)^2V^2}{N(\Delta\rho)^2V} = V, \tag{23}$$

which is another measure of particle size. Dividing Eq. 21 by Eq. 22 eliminates the constants, and the relative scattered intensity is

$$\left(\frac{(\Delta\rho)^2 S_T}{8\pi^3 s^4}\right)\frac{1}{N(\Delta\rho)^2V} = \frac{S_T/V_{total}}{8\pi^3 s^4}, \tag{24}$$

where $V_{total} = N\,V$, the total volume for all particles in the beam.

6 SMALL ANGLE SCATTERING APPARATUS

Apparatus for measuring the distribution of small angle scattering generally employ the transmission geometry because of the difficulty in making intensity measurements near the direct beam in the reflection geometry. The measurements require a fine x-ray beam with small flare so that the direct beam can be intercepted without blocking much of the range of scattered intensity. Monochromatic radiation is required, and a crystal monochromator between the x-ray source and sample is used frequently. The balanced filter approach can also be used to determine the scattering from Kα radiation only. The smaller and/or more parallel the incident beam, however, the lower the intensity. Therefore, simultaneously achieving adequate resolution and intensity is a significant challenge. Three successful approaches to data collection are slit collimation, pinhole collimation and crystal monochromator collimation.

Consider a beam emanating from a source and defined by two collimating slits (C1 and C2 in Fig. 7a). Cross-fire from the source illuminates not only the area AB defined by parallel rays from the source and passing through C1 and C2 but also the penumbral region to either side of AB. Between D and E of Fig. 7a, therefore, it is impossible to measure the scattered intensity. In fact, there is almost always a halo of parasitic radiation accompanying the direct beam, and the region where the incident intensity cannot be measured extends beyond D and E. The angles in Fig. 7a are greatly exaggerated, but it is important to remember that there is some divergence $\Delta\theta$ contributing to the scattered intensity at P and that this divergence, as well as the physical dimensions of the beam and what part of the source area is used, is defined by the slits C1 and C2. Slit C1 is placed as close as possible to the

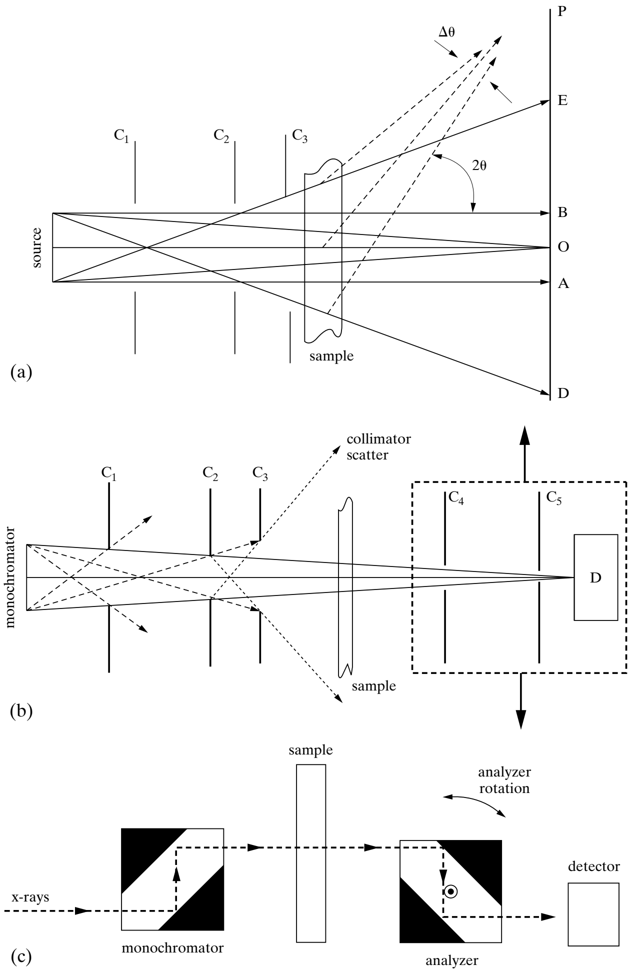

Figure 7 (a) Illustration of the finite source size producing a penumbral area where the scattered intensity cannot be measured (after Guinier, [G.30]). (b) Laboratory small angle scattering apparatus designed to scan the detector and receiving slits across the scattered beam. With Cu $K\alpha$ radiation and the configuration shown, the beam is about 0.05° 2θ wide, scattering from the slits becomes small beyond $\sim 0.075°$ 2θ and *d*-approaching 500 Å are observable. In order to achieve this performance, collimators $C_1 \ldots C_5$ have openings 0.1 mm, 0.05 mm, $0.1 - 0.15$ mm, 0.1 mm, and 0.05 mm, respectively. The separations between C_1 and C_2, C_3, the sample, and as shown above. C_5 are about 200 mm, 300 mm, 350 mm and 500 mm, respectively. (after Schwartz and Cohen, [G.7]). (c) Bonse-Hart geometry. The monochromator and analyzer are channel-cut crystals, that is crystals through which a specially-oriented channel has been cut. The x-ray bean diffracts twice in both the monochromator and in the analyzer crystals, thereby narowing the range of angles incident on the sample and the angular range of scattered radiation measured at any one setting of the analyzer.

x-ray source, and sometimes a third slit C3 is added near the sample. The third slit is slightly wider than C1 and C2 so that it does not quite intersect the direct beam but does eliminate most of the scatter from C2.

Because the scattering is at such small angles, the slit geometry and dimensions can strongly affect the results. Rectangular slits, used to increase intensity, can be a particularly problem since the top, middle and bottom portions of the slit sample inherently different angles. Even data collected with a narrow pinhole must be carefully corrected for the effect of finite slit width as well as for other effects such as parasitic scattering (from sources other than the sample).

Small angle scattering is quite weak, and vacuum paths from the x-ray source to the detector are a practical necessity to minimize beam attenuation and air scattering. Very thin foils, which themselves do not produce small angle scattering, can be used to seal the vacuum where the x-ray beam enters and leaves the scattering apparatus. Sample thicknesses $t = 1/\mu$, where μ is the linear attenuation coefficient, produce maximum intensity. This result is common to other x-ray transmission experiments and represents a reasonable compromise between increasing attenuation with increasing thickness and increasing number of scatterers encountered by the beam. Thicknesses of $2/\mu$ and $3/\mu$, however, are still useful since the variation of scattered intensity $\mathrm{I} \propto \mathrm{I}_0\, t \exp[-(\mu/\rho)\rho \mathrm{t}]$ varies slowly with t.

In simpler apparatus, the detector may pivot about the center of the sample, in the same fashion as a transmission diffractometer. Alternatively, the scatter slit, receiving slit and detector may be translated perpendicular to the incident beam. Figure 7b illustrates such an apparatus and shows dimensions and separations of slits typical of such a small angle system [4]. Note that only a simple, single-channel detector (proportional or scintillation) and simple electronics are required. Data collection rates can be improved dramatically if a linear position sensitive detector replaces the slit and detector system. More complex electronics and increased susceptibility to parasitic scatter are the trade-offs when using such a multiple channel detector. Use of a single channel or linear position sensitive detector suffices for isotropic samples where the scattering (and structure) does not vary with direction. If this is not the case, then the sample must be rotated about the beam axis to align different directions with the scattering plane defined by the detector and its plane of rotation. Thus data collection can be very slow although high quality numerical data can be produced.

Earlier the method of choice for non-isotropic samples employed photographic emulsions as area detectors, and the older scattering literature contains many fine examples. The limited dynamic range and long exposure times led to use of multiwire proportional area detectors, image storage plates or CCD detectors. These digital media are down-loaded directly to computers, provide orders of magnitude increase in dynamic range and at least two orders of magnitude increase in data collection rates. Real time observation of dynamic phenomena are possible as a result.

The Bonse-Hart geometry (Fig. 7c) offers very important advantages [5]. A perfect crystal monochromator system provides monochromatic, nearly parallel radiation. A perfect crystal analyzer system takes the place of the slits following the sample in the single channel system (Fig. 7a). As the analyzer is rotated, the intensity at different scattering angles is recorded. Thus, with the parallel beam optics, large sample areas can be irradiated. Scattering angles very close to the direct beam can be investigated, and some researchers, therefore, refer to this as ultra-small-angle scattering. Generally more than one reflection in the monochromator is required to provide a sharply-enough defined direct beam. Similarly, multiple bounces in one or two channel-cut analyzer crystal may be employed.

7 EXAMPLES

Applications of small angle scattering span fields from biological structures to porosity in coals to dispersoids in structural engineering materials. In some cases complementary information can be gathered by techniques such as TEM. In others such as pore evolution during heating of coal, the information is unobtainable by other methods.

It is instructive to first consider small angle scattering from various coals because a wide range of scattering behavior has been documented [7, 8]. One complication is that both pores and mineral matter exist in coal and contribute to scattering. Low temperature ashing of several coals was used to eliminate the effect of porosity, the scattering curves of the ash (including the mineral matter) were observed to always be proportional to k^{-4} for a range of mineral contents, and the contribution of mineral matter was estimated to be less than a few percent in most cases and never more than twenty-five percent. Two effects allow the scattering from the mineral matter to be neglected. First, the contribution to the total scattering of the mineral matter must be even smaller than that in the ashed samples, and the intensity from smaller pores decreases less rapidly than k^{-4}. Second, specific surfaces calculated from the k^{-4} portions of the scattering curve normally have systematic errors or statistical uncertainties on the order of ten percent [7, 8].

Scattering curves from fifty coal samples were recorded six times with Cu Kα radiation and corrected for various factors. All of the coals examined were found to produce one of four distinct types of scattering curves (Fig. 8). Curve 1 (dash-dotted line) showed scattered intensity proportional to θ^{-4} for the inner portion of the curve; pores exist, therefore, that are so large that $kD_{\min} \geq 3.5$ is always satisfied. Scattering from these macropores, whose dimensions exceed 10^3 Å, decays very rapidly, and the relatively weak scattering from micropores, whose dimensions average less than ~ 25Å, produces the nearly constant scattered intensity in the outer portion of the curve [7, 8].

Curve 2 (solid line in Fig. 8) shows, in addition to the features of curve 1, a shoulder in the scattered intensity curve at intermediate angles. The shoulder can be interpreted as evidence for 100 to 300 Å diameter transitional pores. For there to be a shoulder, the transitional pores must have been small enough to satisfy $kD_{\max} \leq 1$ in the inner portion of the scattering curve and must have produced scattering much weaker than that of the macropores (whose θ^{-4} scattering underlies the shoulder. With the presence of the shoulder, there were two regions seen where

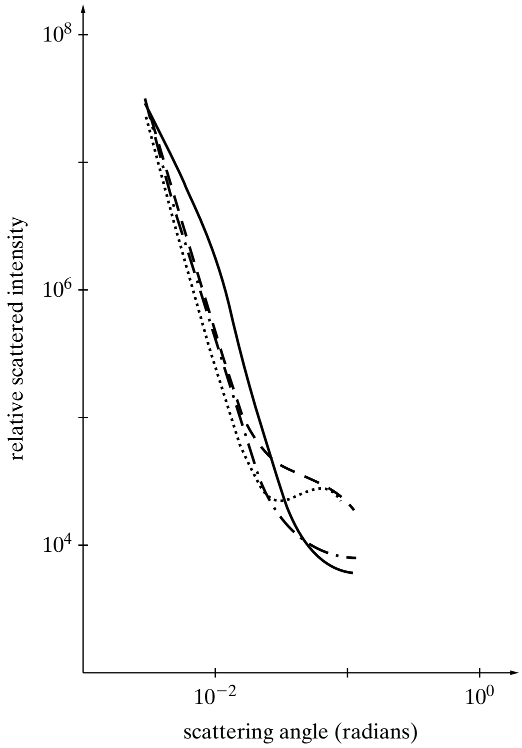

Figure 8 Small angle scattering typical of coal. Four types of behaviour are observed, and an explanation of each is given in the text. (After Kalliat, Kwak, Schmidt and coworkers [7, 8].)

intensity decreased as θ^{-4} : the inner range reflected the surface area of the macropores and the outer range reflected the sum of the surface area of the macropores and transition pores [7, 8].

In the third type of coals, represented by curve 3 (dotted line) in Fig. 8, a rather broad peak was observed in the outermost portion of the scattering curve. At lower angles the scattering was proportional to θ^{-4} , as in the coal types discussed above, and the macropore structure was, therefore, taken to be equivalent for all three types. The peak corresponded to a Bragg spacing of about 20 Å and has been interpreted as being from scattering units consisting of a few layers of planar aggregates containing aromatic rings. The fourth type of scattering curve (dashed line) appeared quite similar to the third, except that the scattering curve showed significant inflection instead of a peak at the highest angles [7, 8].

Consolidation of nanometer-sized metal particles provides a second example of the application of small angle scattering. Consolidation of such powders is one route to obtaining nanocrystalline metallic samples, and the volume fraction and size distribution of voids are important in determining the densities which can be obtained. The crystallite size is obtained easily from diffraction peak widths, and small angle neutron scattering can be used to measure the distribution of void dimensions [9].

Dispersoid volume fraction and size frequency distribution play an important role in strengthening many alloys, both at room and elevated temperatures, and the diameters of the dispersoids are frequently in the range which may profitably be studied with small angle scattering. Oxide dispersion strengthened Ni-based alloys, for example, have been studied in this way, and, not only were histograms of dispersoid size found to be in good agreement with results from TEM, but the resulting calculated creep strengths also agreed reasonably well with experiment [10].

Small angle scattering has been used to great effect to study formation and evolution of metastable coherent precipitates, such as Guinier Preston zones, during the early stages of decomposition of alloys. Small angle neutron scattering of Al-3% Ag samples [11], for example, has helped clarify the shape of the metastable miscibility gap in this alloy as well as the composition variation within the zones as they evolve. The variation (during aging) of Ti composition in coherent precipitates in Ni-rich Ni-Ti alloys [12] is a second example of how small angle (neutron) scattering can be employed profitably.

Position-resolved small angle x-ray scattering is possible, and synchrotron radiation sources such as APS or ESRF should make such scattering studies possible with 25 μm or smaller diameter beams. As an example, hydroxy apatite crystallite orientation in human vertebral bone and cellulose semi-crystalline fibril orientation distribution in wood has been quantified at the 200 μm level [13]. In both materials the measured crystallite orientations agreed with those expected to develop in response to the applied stresses.

Other biological materials also can be studied profitably by small angle scattering. Phase transitions in cell membrane lipids, for example, are thought to be the mechanism whereby mass transfer occurs into/out of cells, and the kinetics and mechanisms have been studied [14]. Position-resolved ultra small angle scattering clearly reveals the changes between calcified and non-calcified regions of the tendon [3]; data from this study is shown in Fig. 2; the data was obtained from an irradiated area less than 10 μm in diameter.

Ultra small angle scattering has found application in the observation of latex particle degeneration in water and in the ordering of the particles into an fcc array for low concentrations [15]. Measurement of radii of gyration for polypropylene samples clearly differentiated between translucent and opaque samples: microcrystallite radii of two translucent samples were 600 and 400 Å, respectively, while that of a turbid sample was 1400 Å [15]. Temporal resolution at the 100 ms level has been obtained for heating and quenching of polymers and the growth of starch particle during gelatinization [16]. Polymer superstructure during deformation has been observed during stretching to change gradually from lamellar to fibrillar [17].

REFERENCES

The following books are listed more or less in the order they are encountered in the text

G.7 L.H. Schwartz and J.B. Cohen. *Diffraction from Materials*, 2nd ed. (Berlin: Springer-Verlag). Wider ranging thorough coverage of crystallography, instruments and techniques and diffraction theory.

G.30 A. Guinier. *X-Ray Diffraction in Crystals, Imperfect Crystals, and Amorphous Bodies* (San Francisco: W. H. Freeman, 1963 and reprinted by Dover 1994). Largely theoretical and more advanced than [G.13].

Transmission Electron Microscopy

1 INTRODUCTION

Transmission electron microscopy (TEM) is the pre-eminent method for determining dislocations' and other crystallographic defects character and for performing chemical and crystallographic analysis of micrometer and smaller precipitates and other microstructures. Use of TEM in materials science/engineering can be introduced in only a few additional pages and is well worth the small increment of effort. Since most defect characterization requires an understanding of diffraction contrast, this is an important constituent of this chapter.

A TEM can be used to image either a planar section through reciprocal space (i.e., the diffraction pattern) or the sample itself. Diffraction contrast can be used to identify defect character; this introduction was in the context of x-ray diffraction topography, the x-ray imaging analog of TEM. The treatment of TEM, therefore, builds on what was already presented, with the four sections on the TEM, its components and operation followed by four sections on analysis of information obtained using TEM.

Section 2 discusses the interaction of electrons with electric and magnetic fields, Sec. 3 covers electron guns (i.e., sources), Sec. 4 discusses magnetic lenses and Sec. 5 introduces electron optics, focusing on the lenses in a generic TEM and their differences from glass lenses used in optical microscopes. The subject of Sec. 6 is Kikuchi lines, of Sec. 7 is convergent beam diffraction, of Sec. 8 is imaging and amplitude contrast and of Sec. 9 is imaging and phase contrast.

2 ELECTRON INTERACTIONS WITH ELECTRIC AND MAGNETIC FIELDS

In an electric field **E** and magnetic field **H**, the electrons experience the Lorentz force **F** given by

$$\mathbf{F} = -e(\mathbf{E} + \mathbf{v} \times \mathbf{H}) \tag{1}$$

From Chapter 20 of *Elements of X-Ray Diffraction*, Third Edition. B.D. Cullity, S.R. Stock.

where e is the charge and $\mathbf{v}$ is the velocity vector of the electron. When combined with Newton's expression

$$\mathbf{F} = m\mathbf{a} = md^2\mathbf{x}/dt^2 \qquad (2)$$

where t denotes time and m is the mass, $\mathbf{a}$ is the acceleration vector and $\mathbf{x}$ is the position vector of the electron, an expression for particle optics results. In TEM, the first term of Eq. 1, the electric field interaction, applies to the electron gun where the electrons produced by the filament are accelerated to the energy to be used in the microscope. The second term of Eq. 1, describing the magnetic field interaction, governs the operation of TEM lenses. In particular, it is important to remember that the spatial variation of **E** and **H** is essential in the operation of the TEM electron gun and lenses.

3 ELECTRON GUN

Figure 1 shows a schematic of an electron gun. The filament is the cathode (C in Fig. 1) and is at a potential $\phi_C = -U$ relative to the anode A (i.e., $\phi_A = 0$). Many of the electrons emitted from the filament strike the anode and are lost, but some pass through the hole and proceed along the optic axis. Between the cathode and anode, the cup-like Wehnelt cylinder improves the uniformity of electron emission from the gun: the cylinder has a slight positive bias ϕ_W with respect to the cathode.

The relationship between **E** and the potential is

$$\mathbf{E} = -\nabla\phi = -(\partial\phi/\partial x, \partial\phi/\partial y, \partial\phi/\partial z) \qquad (3)$$

lines of constant potential ϕ appear in Fig. 1a and the corresponding electron trajectories are shown in Fig. 1b. Control of the electron trajectories within the gun are important in obtaining good imaging performance, but the energy of the electrons depends only on the potential through which they are accelerated not their trajectories. Acceleration through 100 kV produces electrons with 100 keV energy, and

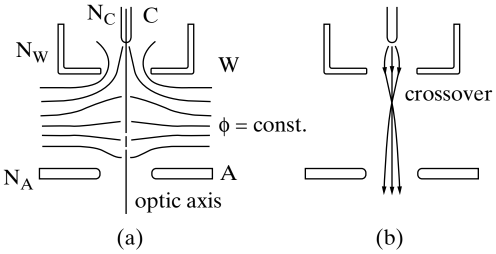

Figure 1 Illustration of the electron gun. (a) Lines of constant potential ϕ and (b) electron trajectories in relation to the cathode C, the Wehnelt cylinder W, and anode A. After [7].

the relationship between accelerating potential and electron wavelength λ, correcting for relativistic effects, is

$$\lambda = h[2m_0\, eU(1 + eU/\{2\, m_0\, c^2\})]^{-0.5} \tag{4}$$

where m_0 is the electron rest mass, c is the speed of light and h is Planck's constant. Accelerating potentials of 100 kV or greater are normally used, and Table 1 lists potentials and corresponding wavelengths. Note that, unlike in x-ray diffraction, wavelengths and *d*-spacings in electron microscopy conventionally are given in nm.

Filaments can be made from W or more exotic materials such as LaB_6. In most TEM's, electrons are produced by thermionic emission as they are in x-ray tubes. Field emission of electrons from a very sharp W tip can also be used in the gun; no heating is required. Field emission guns provide much greater current density but require a much better vacuum than thermionic emission guns.

4 MAGNETIC LENSES

In considering the operation of the magnetic lenses of a TEM, the focus is on the second term of Eq. 1 which states that the force **F** from a magnetic field **H** on an electron moving with velocity **v** is perpendicular to both **v** and the component of **H** perpendicular to **v**. Note that any component of **H** parallel to **v** produces no force. If $\mathbf{v} \perp \mathbf{H}$, a circular trajectory results. More complex helical paths result when uniform motion along the field is superimposed on uniform rotation in the plane perpendicular to the field. This occurs when **v** makes a slight angle α with the magnetic field **H** (Fig. 2a); at z=0 the electron is r away from the **z**-axis, and the force at any instant deflects the electron toward the **z**-axis (in a direction out of the plane of the page) as it spirals around a cylinder of radius r.

A spatially varying magnetic field is required for focusing, and a typical field distribution is shown in Fig. 2b for a magnetic lens. The **z**-axis is the center of the cylindrically symmetric lens, and **H** has mirror symmetry across the plane z=0. Below the diagram of $\mathbf{H}(r,z)$, the values of the components H_z and H_r are plotted

Table 1

Accelerating voltage (kV)	Wavelength (nm)
100	0.00370
150	0.00335
200	0.00251
300	0.00197
400	0.00164
1000	0.00087

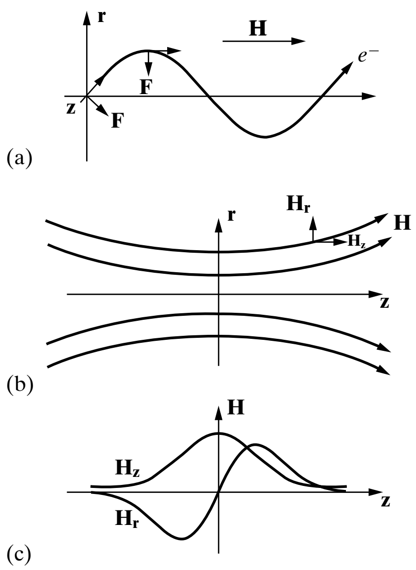

Figure 2 (a) Projection of the electron trajectory in a constant magnetic field **H**, with the direction of the force **F** on the electron indicated. (b) Variation of **H** in a magnetic lens, showing components $\mathbf{H}_r$ and $\mathbf{H}_z$ (radial and along the optic axis, respectively), as a function of z. (c) Projection of the electron path on the initial plane, showing lenses and crossover point $\mathbf{z}_0$. After [1].

for a position near the optic axis (i.e., *r* approaching 0). This magnetic field distribution is obtained using a coil carrying electrical current centered on the optic axis (Fig. 3). The gap in the iron pole piece containing the windings allows magnetic field leakage not only directly across the gap but also out into the bore of the pole piece. The design of magnetic lenses has become quite sophisticated, and more detailed discussion of lenses and their design appears in texts on electron microscopy [1, 2].

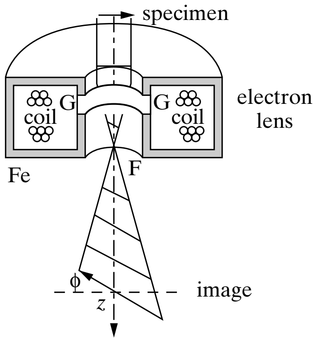

Figure 3 Illustration of concentration of a rotationally symmetric magnetic field by the gap in the electron lens and the resulting image rotation. After [7].

The dashed line in Fig. 2c illustrates schematically the trajectory of electrons traveling parallel to but off of the optic axis. Actually, the electron spirals toward the optic axis and then crosses it with r steadily decreasing and then increasing again; therefore, the dashed line is the projection of the electron's path onto the initial plane (r,z) containing the electron. The closer the electrons are to the optic axis, the smaller their deflection, and electrons traveling exactly on the optic axis experience no deflection. Note that the electrons off the plane shown and off the optic axis in Fig. 2c also spiral toward the optic axis. If the focussing action of the lens is perfect, all of the electrons traveling parallel to **z** and lying on the plane intersecting the page along the line $z = z'$ (Fig. 2c) will converge to a point at $z = z_0$, and the line $z = z'$ will rotate as the electrons travel through the lens (Fig. 3). In other words, the image of the sample formed by the electrons rotates as it travels through the lens. If the strength of the lens changes, i.e., if **H** increases or decreases, the amount rotation will alter must be known for correct interpretation of diffraction patterns and images. This rotation is not present in glasses lenses.

Various aberrations exist in all lenses, to a greater or lesser degree, and spherical and chromatic aberrations, astigmatism and distortion all contribute to degrading image quality. Spherical aberration results because the lens field acts inhomogeneously on electrons following off-axis paths and spreads the image of a point into a disk. Chromatic aberration exists because a lens deflects lower energy electrons more strongly than higher energy electrons; the range of energy $\Delta E < 1$ eV for the incident beam and increases to 15-20 eV for some of the electrons emerging from a 50-100 nm thick sample [2]. Astigmatism arises from the inevitable deviations of the lens from cylindrical symmetry. Finally, image distortion can sometimes occur, e.g., a set of orthogonal lines can appear concave inward to the center of the image (pincushion) or bulge outward (barrel).

5 TRANSMISSION ELECTRON MICROSCOPES

Any TEM is a complex assembly of magnetic lenses (in addition to an electron gun described in Sec. 3), several apertures, a sample holder and an image recording/viewing system (Fig. 4). The magnetic lenses can be grouped into those of the illumination system between the electron gun and sample and those of the imaging system after the sample. Typically one finds two condenser lenses in the illumination system and three lenses in the imaging system; the descriptions below refer to this kind of TEM.

Consider first the illumination system, shown at the top of Fig. 4. The traditional TEM mode adjusts the condenser lenses C1 and C2 to illuminate the sample with a nearly parallel beam (convergence angle $\alpha < 10^{-4}$ rad compared to electron diffraction angles on the order of 10^{-2} rad). This beam covers sample areas several micrometers in diameter at magnifications between 20,000X and 100,000X. Without the action of the condenser lens concentrating the electron beam into the area of interest, the images would be too dim to be useful. For applications other than imaging, highly convergent beams can be produced, but discussion of this is post-

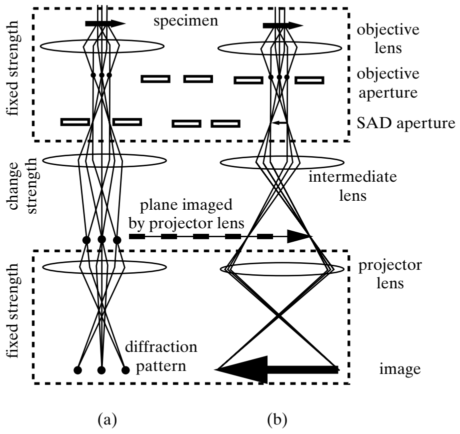

Figure 4 Ray diagram for viewing the diffraction pattern (a) and the image of the sample (b). The strength of the intermediate lens is changed to focus on the back focal plane or on the image plane, respectively. After [2].

poned until Sec. 7. Pre-specimen scanning or deflection coils are often used to control beam position or angle.

When the electrons encounter the sample, some are diffracted in various directions depending on the orientation of the crystal(s) through which the incident beam travels. The formation of the diffraction pattern, i.e., the action of the objective lens bringing parallel rays to a point focus in the back focal plane (see also Fig 4). The objective lens simultaneously brings differently directed rays (that is, electrons) emanating from a single point on the sample back to a single point in the first intermediate image plane.

In TEM one can switch between imaging the sample and viewing its diffraction pattern by changing the strength of the intermediate lens. To see the diffraction pattern, the intermediate lens is adjusted to focus on the back focal plane of the objective lens; i.e., the back focal plane acts as the object plane for the intermediate lens. In the imaging mode the intermediate lens is adjusted so that its object plane is the image plane of the objective lens.

When viewing a diffraction pattern, an aperture limiting the area contributing to the pattern is typically inserted into the first intermediate image plane; this diffraction mode is therefore called selected area diffraction or SAD, and the aperture is called the SAD aperture. While SAD is the most common diffraction mode, other modes including convergent beam diffraction can be very valuable. A typical SAD pattern was shown, and experienced microscopists can readily recognize patterns recorded with the electron beam along high symmetry, low index directions.

Depending on the amount of magnification provided by the intermediate and projector lenses, 1 cm on the diffraction pattern recorded on film may correspond to various nm^{-1}. Convenience dictates using standardized settings for most work, and the camera length L is used to describe the magnification of the diffraction pattern. While L is a calculated rather than a physical distance, the concept of a camera length arose from x-ray diffraction projection cameras which operate without lenses and in which the diffraction pattern is magnified by moving the recording medium farther from the sample. Figure 5 shows the Ewald sphere construction and the direct space diagram relating distance R between the incident beam **O** and the diffracted beam **G** (on the film) and the camera length L. From the figure,

$$\tan 2\theta_{hkl} = R/L = (1/d)/(1/\lambda)$$

and

$$Rd = \lambda L \tag{5}$$

with λ and L known from the TEM's operating parameters, simple measurement of distances R on the film is sufficient to determine d for the diffraction spot of interest. Each investigator should do this calibration for her- or himself and should not rely on factory calibrations because the conditions used may be different. If the sample is of a known material, the indices of two non-collinear spots $\mathbf{G}_1$ and $\mathbf{G}_2$ can be quickly assigned, and the incident beam direction **B** can be determined from the cross product of $\mathbf{G}_1$ and $\mathbf{G}_2$. An example is provided in Fig. 6.

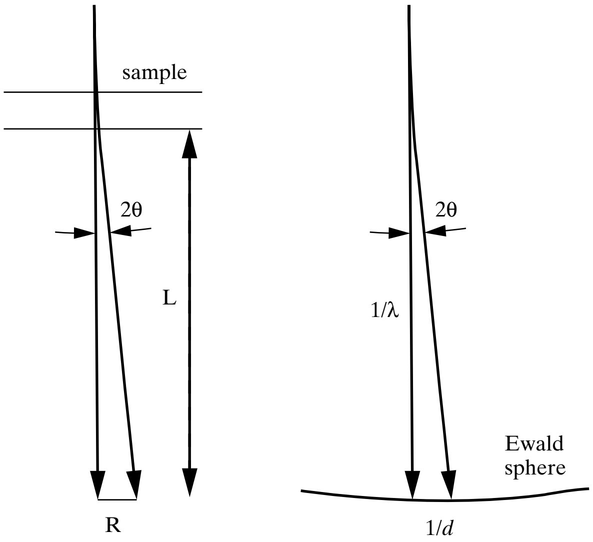

Figure 5 Direct space and reciprocal space illustrations of the camera length L.

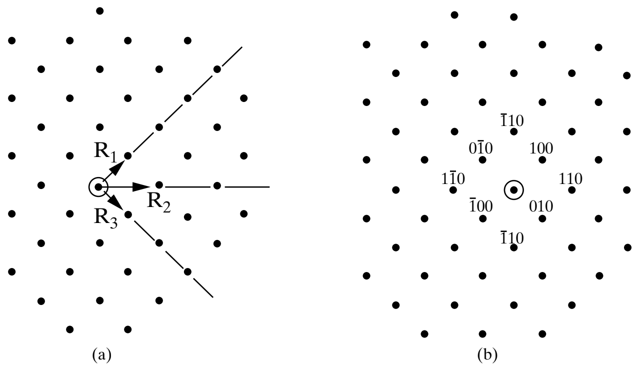

(a)

(b)

CsCI structure

allowed *hkl*: 100, 110, 111, 200, ...

spot	R_i	R_i^2	R_i^2/R_1^2	*hkl*
1	1.25	1.56	1.00	100
2	1.28	1.64	1.05	100
3	1.78	3.17	2.03	110

g $R_1, R_2 = 46°$
g $R_1, R_3 = 91°$

$$\mathbf{B} = \mathbf{R}_2 \times \mathbf{R}_1 = \begin{vmatrix} \mathbf{i} & \mathbf{j} & \mathbf{k} \\ 1 & 1 & 0 \\ 1 & 0 & 0 \end{vmatrix} = -\mathbf{k} = [\bar{1}00]$$

(c)

Figure 6 Indexing the diffraction pattern (NiAl which has the CsCl structure). The diffraction pattern is reproduced in (a), and a schematic of it appears in (b) with separations R_i between O and three diffracted beams indicated. In (c) the values of R_i^2 and of the angles between R_i are used to determine the incident beam direction **B**. The resulting indices for several diffraction spots are shown in (b).

If all of the diffracted beams and the transmitted beam were allowed to recombine in the first intermediate image plane, there would be relatively little contrast in the resulting image. Some contrast might exist because varying thickness or varying composition would lead to different amounts of absorption, but relatively little could be learned. Instead, an objective aperture is placed around one of the spots in the back focal plane. Bright field (BF) imaging centers the aperture around the transmitted or **O** beam while dark field (DF) imaging positions the aperture around one of the diffracted beams $\mathbf{G}_i$ (Fig. 7). Centered dark field (CDF) imaging, depicted in Fig. 7b, improves DF images by tilting the incident beam (via the pre-sample deflection coils) to an angle $2\theta_{hkl}$ from the optic axis so that the *hkl* diffracted beam exits the sample parallel to the TEM's optic axis. Thus, the *hkl* diffracted beam would appear on the viewing screen where the **O** beam would be seen normally. The aperture is placed around the centered diffracted beam, and the effect of the various lens aberrations on the DF image is reduced considerably from that in conventional DF imaging.

A wide variety of sample holders are available including heating, cooling and straining stages. Holders for multiple specimens find use as well as bulk sample holders for samples larger than the conventional 3 mm diameter disks. Most TEM's now incorporate side entry specimen holders, and these provide at least one axis of sample rotation (about the axis of the rod-like holder). This single degree of free-

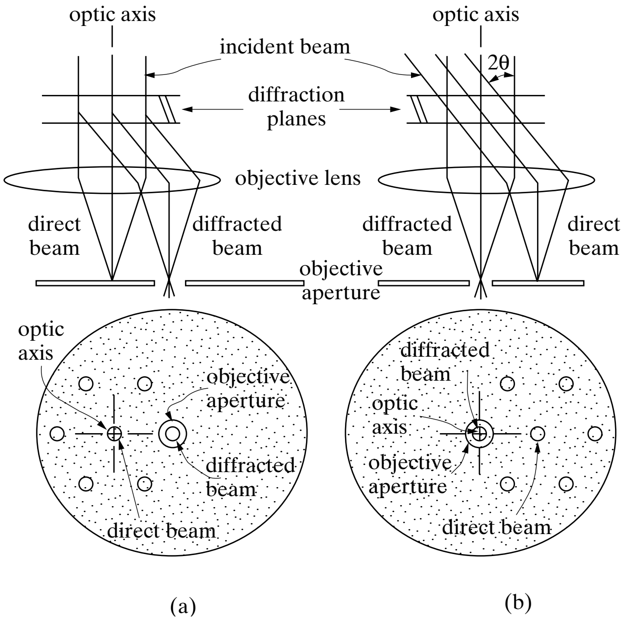

Figure 7 Aperture position and ray paths for (a) conventional dark field (DF) imaging and (b) centered dark field (CDF) imaging.

dom is enough to allow identification of defect character in some cases. Often, however, tilt-rotate holders or double tilt holders are more convenient for defect studies.

Real time observation is invaluable when surveying a sample or when adjusting viewing conditions, and fine-grained screens such as ZnS are used to convert the two-dimensional distribution of electrons comprising the image or diffraction pattern into light which can be viewed by the operator. The TEM viewing screen can be observed directly by eye or through a low light TV camera (which is a real advantage for faint images or for recording dynamically changing images). Recording images on photographic emulsions continues for the vast majority of TEM work. The resolving power of photographic emulsions is no better than about 10 μm due to electron spreading which is a factor of about two greater than the grain size of the film. Nonetheless, there are more than 10^7 pixels (picture elements) in a 10 cm × 10 cm image. The two chief drawbacks of photographic emulsions are their inherently limited dynamic range and the necessity of digitizing the images for quantitative comparison with simulations. Charge-coupled device (CCD) chips have been incorporated into a few TEM's and can provide more than 10^6 pixels, orders of magnitude higher dynamic range and direct digitization of images. Conventional read-out speeds of CCDs and related detector arrays can be bothersomely slow for viewing, but most chips allow rapid, albeit noisy readout.

6 KIKUCHI LINES

Kikuchi lines are an important feature of diffraction patterns, and, because they are used so frequently to orient samples precisely, it is worth describing their origin. They appear as pairs of parallel light and dark lines in diffraction patterns. Inelastically scattered electrons are responsible for the phenomenon, and Kikuchi lines are, therefore, more prominent in thicker rather than thinner sections of foils. The electrons scatter (inelastically) in all directions, but there is a much greater probability of scattering close to the forward direction than in other directions. The intensity scattered inelastically in each direction is represented by the length of the vector in the polar plot of Fig. 8a. The amount of energy lost by the scattered electrons is, however, not very great.

The diagram in Fig. 8b shows that some of the inelastically scattered electrons travel in directions where they can be re-scattered elastically through $2\theta_{\mathrm{hkl}}$. Since the inelastic scattering has a three-dimensional distribution, the locus of the resulting Bragg diffracted electrons are a pair of cones, which intersect the Ewald sphere as a pair of parallel arcs which are so slightly curved as to appear straight. There will be a pair of lines for diffraction vectors $\pm \mathbf{g}$, $\pm \mathbf{2g}$, etc. The intensity of one of the pair of lines is greater than background (excess line) and the other is less than background (deficient line). Figure 8b shows that the inelastically scattered electrons on path 1 (OB) are closer to the incident beam direction than those along path 2 (OA); before the second scattering event (diffraction), the intensity along path 1 is higher. Diffraction redirects the intensities as shown in Fig. 8b, and the result is that the left-most Kikuchi line, from path 1, has the larger intensity.

Geometry dictates that the projection of (*hkl*) lies midway between the excess and deficient (*hkl* and $\overline{hkl}$, respectively) Kikuchi lines. The angle between the excess and deficient lines is twice the Bragg angle and not four times the Bragg angle. As the crystal is rotated, the projection of (*hkl*) onto the diffraction pattern

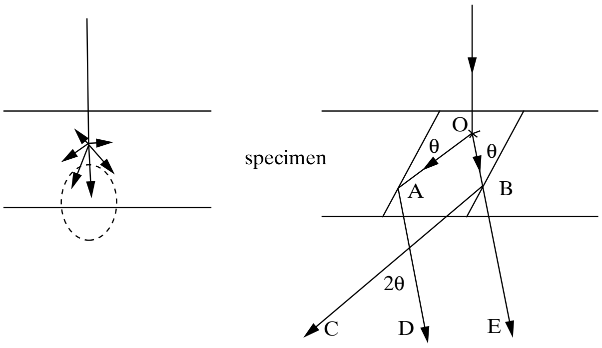

(a) (b)

Figure 8 Simplified illustration of the production of Kikuchi lines. (a) Polar plot of the magnitude of inelastic electron scattering as a function of scattering angle. (b) Diffraction of the inelastically scattered electrons and the production of excess and deficient lines.

moves and the pair of Kikuchi lines move with it. This last point has enormous consequences in TEM of crystalline materials, and this section will end with a discussion of what these are.

At the exact Bragg condition for reflection *hkl*, where the deviation parameter s is zero, the excess or *hkl* Kikuchi line passes through the center of the diffraction spot **G** and the deficient or $\overline{hkl}$ Kikuchi line passes through the incident beam spot **O**. If the sample is rotated so that the direct beam is exactly parallel to (*hkl*), the *hkl* and $\overline{hkl}$ Kikuchi lines are symmetrically displaced about **O** with the excess line lying midway between **O** and G and the deficient line midway between **O** and -**G** (here $s < 0$).[1] Figure 9a shows a diffraction pattern recorded with $s > 0$, and Ewald sphere diagrams for $s < 0$, , $s = 0$ and $s > 0$ appear in Fig. 9b. In other words, $s > 0$ whenever the excess line is on the same side of **O** as **G** and the excess line is farther from **O** than **G**. Optimum defect contrast, as will be seen later, requires aligning the sample to certain s, so Kikuchi lines are an invaluable tool.

Small changes in specimen orientation are very difficult to see in SAD patterns, but the displacement of Kikuchi lines from the spot centers are easy to see and allows straight-forward calculation of the magnitude of the deviation parameter. Knowing the diffracted beam's indices, the magnitude of $1/d$ for the reflection, the separation between the centers of the **O** and **G** spots and the displacement of the pair of Kikuchi lines from their positions at $s = 0$ and forming appropriate ratios allows calculation of the magnitude of s.

So far the discussion focused on one pair of Kikuchi lines, but many pairs appear simultaneously especially when the beam direction **B** is close to a low index direction. The pattern of Kikuchi lines reflects the symmetry of the crystal, and Kikuchi maps are often constructed to help microscopists rotate/tilt from one low index **B** to another. With the TEM in the SAD mode, a pair of Kikuchi lines leading to the desired low index direction are found and followed to the desired low index direction. One essentially "drives" along the lines by rotating/tilting the crystal. Some workers find it faster to construct a stereographic projection representing the foil orientation (if **B** is at the center of the projection, the various **G** in the diffraction pattern lie on the projection's perimeter) and to use it to tilt directly to the new beam direction.

7 CONVERGENT BEAM DIFFRACTION PATTERNS

Convergent beam electron diffraction (CBED) offers considerable advantages over SAD, and its development transformed electron crystallography into a technique with power comparable to neutron or x-ray crystallography. To demonstrate how features arise within CBED patterns, differences between CBED and SAD are discussed first, the existence of higher order diffraction zones are described

---

[1] In this geometry the simple model of excess and deficient lines presented above predicts that the lines will have intensities indistinguishable from the background. The lines are visible, however, and a more complex explanation is required than can be presented here.

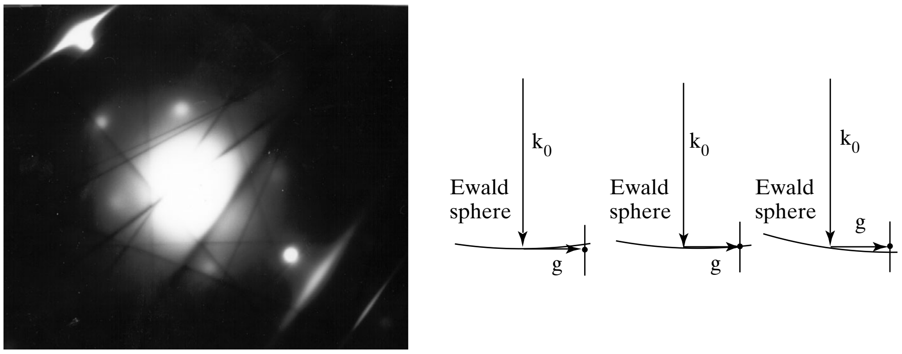

(a) (b)

Figure 9 (a) Diffraction pattern recorded with the deviation parameter of greater than zero. (b) Orientation of the incident beam, the Ewald sphere, **g** and *hkl* relrod for deviation parameter less than zero (left), equal to zero (middle) and greater than zero (right).

next and the use of higher order Kikuchi lines to determine point and space groups is covered last.

A spatially wide ($1 - 10\ \mu$m diameter) nearly parallel beam (with a single incident wave vector **k** and a very small convergence angle α) is normally used in SAD while CBED uses a convergent beam (range of **k** and $2\alpha \lesssim 2\theta_B$) and a relatively small area ($\sim 10 - 100$ nm diameter). Parallel illumination means that an SAD pattern consists of an array of sharp maxima in the back focal plane of the objective lens. A convergent beam, however, produces disks of high intensity in the back focal plane, and at some point, increasing α leads to overlap of disks. For thin samples, kinematical diffraction dominates and the disks are featureless. Thicker samples allow dynamical diffraction effects to be observed, and complex contrast appears within the disks. Figure 10 compares α 111 SAD pattern from Si and the corresponding CBED pattern, and both are most useful when **B** is along a zone axis of the crystal.

To understand the origin of the dark lines in the CBED disks, one needs to consider diffraction spots other than those near the direct beam. The section of the Ewald sphere in Fig. 11a shows the incident beam along 001 and demonstrates that the diffraction spots near the incident beam are from relrods extending from the *hk*0 plane. The farther from **O**, the farther the Ewald sphere curves from (*hk*0), until the *hk*0 spots from the zero order Laue zone (ZOLZ) are no longer prominent. Still farther from the origin of reciprocal space, the relrods from the *hk*1 reciprocal lattice plane begin to intersect the Ewald sphere and produce the spots of the first order Laue Zone (FOLZ). Normally, SAD and CBED patterns do not include FOLZ spots because the camera length L is too large, i.e., the angular field of view is too small to record these large reciprocal distances (Fig. 11b).

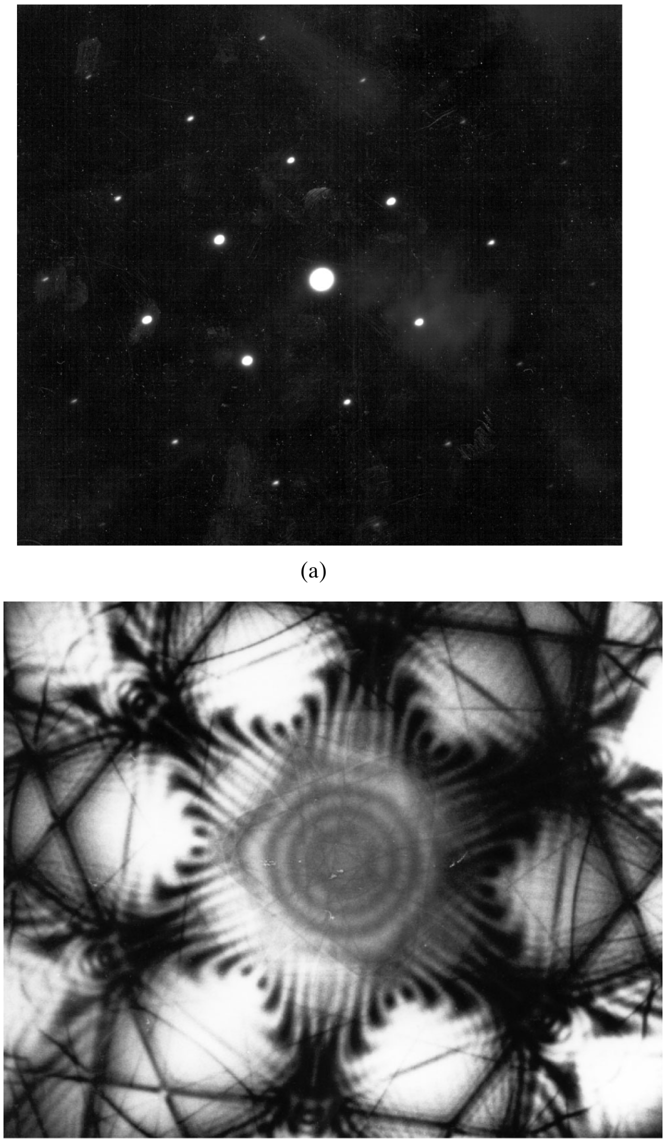

(a)

(b)

Figure 10 Silicon 111 diffraction patterns: (a) Selected area diffraction (SAD) pattern and (b) Convergent beam electron diffraction (CBED) pattern.

Each of the FOLZ and higher order Laue zones (HOLZ) reflections has Kikuchi lines associated with them. In zone axis patterns, many reflections appear at the exact Bragg condition, including HOLZ reflections which have small s. The excess HOLZ Kikuchi lines, as well as the HOLZ spots, are outside the image field

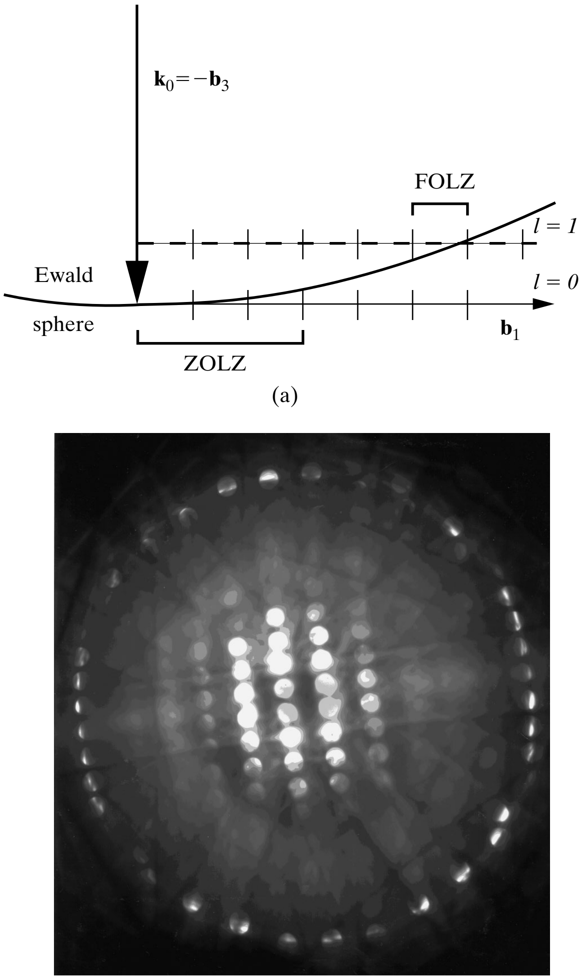

(a)

(b)

Figure 11 Origin of the zero order Laue zone (ZOLZ) and first order Laue zone (FOLZ). (a) Section of reciprocal lattice showing intersection of relrods in ZOLZ and FOLZ. (b) Diffraction pattern recorded with a much smaller than normal camera length L and showing appearance of the Laue zones.

normally used in CBED while the deficient Kikuchi lines lie near the direct beam; in fact the deficient HOLZ Kikuchi lines cut the disks of the CBED pattern. The symmetry of the HOLZ lines reflects the space group of the sample: the three-dimensional crystallography of the sample can be inferred because the HOLZ lines include information off the *hk*0 plane of the reciprocal lattice. Exactly how this is done and how foil thickness is precisely measured is thoroughly covered elsewhere [2, 3].

8 IMAGING AND AMPLITUDE CONTRAST

As mentioned in Sec. 5, defect characterization is normally done by allowing only one beam to form the image: the objective aperture is centered around either the transmitted beam **O** for BF imaging or a diffracted beam for DF imaging. Good defect visibility results for two-beam conditions, that is, when the crystal is tilted so that only one diffracted beam has $s \sim 0$ and has strong intensity and the other diffracted beams have $s \ll 0$ or $s \gg 0$. The length of the relrods, due to the small sample thickness normal to the plane of the foil, dictates that SAD patterns never consist of only two spots, but the intensity of one diffracted beam can be made much stronger than that of all of the others.

During a typical TEM session, the microscopist finds a transparent area of the sample and alters the specimen orientation until a low-index zone axis is seen in SAD patterns. This assumes, of course, that there are features of interest to be seen. Slight tilts from the zone axis are then required to obtain several different two-beam conditions. For an incident beam direction **B** = [001], **g** = [200], [020], [110], and $[\bar{1}10]$ are readily obtained two-beam conditions (Fig. 12).

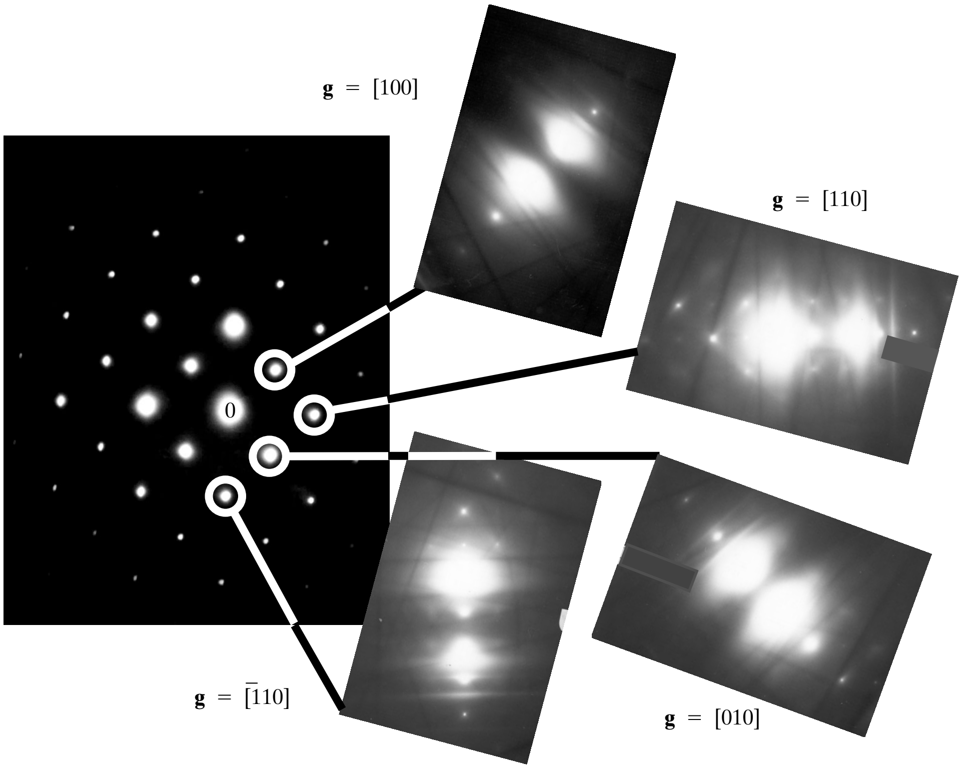

Figure 12 Diffraction pattern recorded with **B** = [001] (upper left). Small tilts are used to obtain the two beam conditions shown.

An important advantage of imaging under two-beam conditions is the simplicity in calculating how different factors alter how defects appear. Also, BF and DF images show complementary contrast under conditions where absorption can be neglected. Tilting to $s \gtrsim 0$ produces best defect contrast. Remembering that high contrast describes situations where there is a large difference in signal from the feature of interest and its surroundings, Fig. 13 a)-d) show micrographs of dislocations in NiAl for various s and e) illustrates why s slightly positive (i.e., the excess Kikuchi line just outside of **G**) offers best contrast. Near the dislocation core, the strain field locally distorts the planes into the Bragg condition for $\pm$ **g**. Far from the core, the planes do not satisfy the Bragg condition, and only the existence of relrods leads to any intensity being diffracted at positions away from the dislocation core. At larger $|s|$ too little of the volume around the core can diffract; while such "weak beam" imaging is useful in high resolution TEM, it typically limits contrast too much to be desirable for everyday imaging. The fact that imaging with $s < 0$ makes the defects difficult to see is a consequence of dynamical diffraction and of absorption, and, after some development, this will be seen below.

For two-beam dynamical diffraction of electrons, the intensity I_g of the Bragg diffracted beam is given by

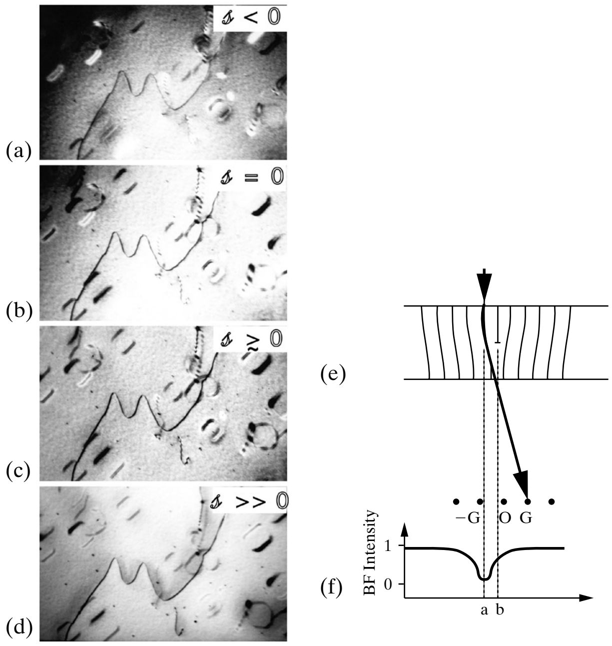

Figure 13 (a-d) Illustration of the effect of deviation parameter on contrast from dislocations. (e) Local distortions around a dislocation core allow that volume to continue to diffract strongly when the crystal is tilted slightly from the exact Bragg condition. (f) Intensity profiles showing displacement of dislocation image from its projected position. (e and f after [2]).

$$I_g = 1 - I_0 = (\pi t/\xi_g)^2 \frac{\sin^2(\pi t s_{\mathrm{eff}})}{(\pi t s_{\mathrm{eff}})^2} \tag{6}$$

where I_0 is the intensity of the incident beam, t is thickness of the sample through which the electrons have traveled, ξ_g is a constant called the extinction distance and has units of inverse length and s_{eff} is the effective deviation parameter given by

$$s_{\mathrm{eff}} = \sqrt{(s^2 + \xi_g^{-2})} \tag{7}$$

Note the similarity of Eq. 6 to the interference function defined; also, the diffracted intensity is periodic in two independent quantities t and s_{eff} and the treatment neglects absorption. In the absence of absorption, Eq. 6 predicts that BF and DF images will be complementary.

The extinction distance ξ_g can be regarded as a characteristic length for diffraction vector **g**, and this scalar quantity is given by

$$\xi_g = (\pi V_c \cos\theta_B)/(\lambda F_g) \tag{8}$$

The value of ξ_g depends on the lattice parameter(s) of the specimen through V_c, the volume of the unit cell, on the atomic number of the sample through F_g, the structure factor for diffraction vector **g**, and the kV through λ. Table 2 lists values of ξ_g for commonly used reflections of some frequently encountered materials.

Because diffracted intensity is a function of deviation parameter, small specimen tilts can change the appearance of images substantially. This result is very important in TEM since the foils are so thin that some bending seems inevitable. As the ori-

Table 2 (a) Values of the extinction distance ξ_g (in nm) for several commonly encountered materials and diffraction vectors **g** after [2]. The dashes mark reflections with F=0, and all values are for 100 keV electrons. Multiplication by the correction term v/v_{100}, see (b), is needed to convert the values listed below to an energy E other than 100 keV [6].

(a)

Material	Extinction distance ξ_g				
	hkl = 110	111	200	220	400
Al	–	56.3	68.5	114.4	202.4
Au	–	18.3	20.2	27.8	43.5
Si	–	60.2	–	75.7	126.8
MgO	–	272.6	46.1	66.2	103.3
Fe	28.6	–	41.2	65.8	116.2
W	18.0	–	24.5	35.5	55.6

(b)

E (keV)	v/v_{100}
30	0.5990
50	0.7528
80	0.9164
100	1
200	1.268
300	1.416
400	1.510
1000	1.717

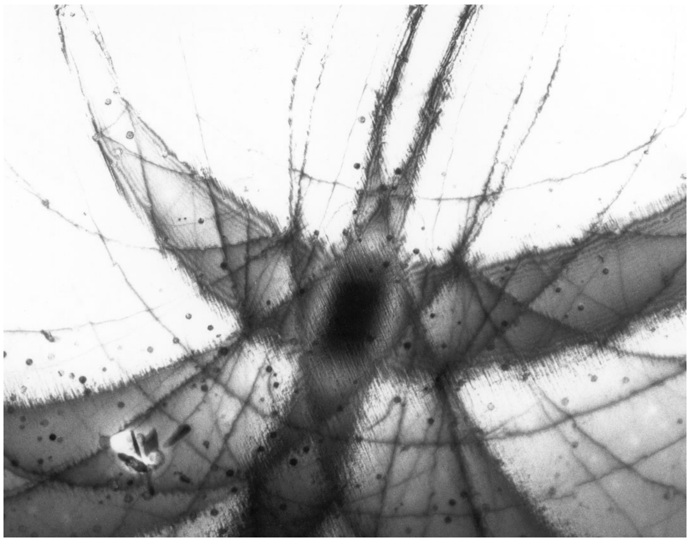

Figure 14 Bend contours. (Courtesy of Z.L. Wang).

entation in a bent sample varies with position, i.e., s varies locally, diffracted intensity can change quite abruptly and the resulting bend contours can overwhelm contrast from other features. An example of bend contours appears in Fig. 14; these contours are often a nuisance but can also be a useful tool.

Plots of intensity I vs. $s \cdot \xi_g$ are termed rocking curves and are a good way of seeing why imaging of defects is best done with s slightly positive. When absorption is considered in the dynamical diffraction calculations, the BF rocking curve no longer is symmetric around $s = 0$ while the DF rocking curve remains symmetric (Fig. 15). In BF images, s should be small and positive: better transmission and sharper images are obtained than if $s = 0$ or $s < 0$. Indeed, BF images with $s < 0$ show very low average intensity.

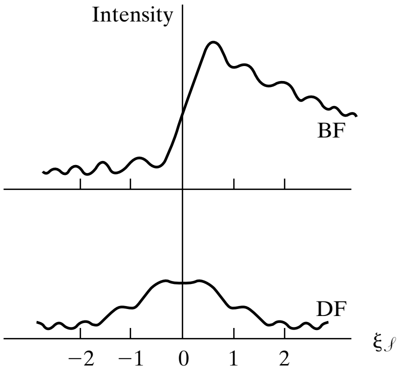

Figure 15 Bright field (BF) and dark field (DF) rocking curves, very schematic (After [5]).

Periodicity in t means that the intensity of both the **O** and **G** beams oscillates with depth below the surface on which the beam is incident. Initially I_0 starts at unity (it is normalized to one) and gradually decays while I_g gradually increases from zero until it contains all of the intensity after traveling $\xi_g/2$ into the specimen. The process then repeats with I_g decreasing while I_0 increases. These oscillations can be visualized as thickness fringes in wedge-shaped crystals but not in samples with constant thickness. The intensity that the **G** or **O** beam has at the exit surface dictates the intensity of that beam outside the sample, that is, when the beam is observed. It is possible, therefore, that an image may appear to be black or white depending on the thickness of the sample. Defects which might otherwise be visible in images, may not produce contrast if they lie parallel to the entrance surface of the foil and at a depth where the intensity is zero in that beam.

Defects which extend through different depths often show alternating light and dark contrast; this is a result of the oscillation in intensity between diffracted and incident beam. In dislocations this modulation in intensity is termed zig-zag contrast. In stacking faults or other planar defects alternating light and dark fringes are seen. Comparison of BF and DF images of stacking faults and other planar defects (changes of fringes from light to dark in corresponding micrographs) is an important part of identifying the character of these faults [2 - 6]. The contrast between light and dark thickness fringes in wedge-shaped crystals decreases to zero for thicknesses $t \gtrsim 5\xi_g$, and this phenomenon is also seen in contrast from stacking faults extending through foils. Explaining this effect, termed anomalous absorption in TEM and anomalous transmission in x-ray diffraction, requires referring to results from dynamical diffraction theory.

In many respects, dynamical diffraction theory for electrons and for x-rays are quite similar. The interference of the two Bloch waves (for two beam conditions which are difficult to avoid for x-rays and require some effort to achieve for electrons) set up by the dynamic transfer of energy to/from the diffracted beam leads to the dependence of intensity on thickness described in Eq. 6. Consideration of where these Bloch waves localize spatially in the specimen reveals that the maxima in the probability distribution function for one Bloch wave coincides with the rows of atoms of the diffracting planes while that of the second centers on the channel between the planes of atoms. Because interaction between electrons of the beam and electrons of the sample's atoms leads to scattering and absorption, the former Bloch wave is heavily attenuated while the latter suffers relatively little absorption. After several ξ_g of propagation only one Bloch waves remains, and the interference leading to intensity oscillation with depth disappears.

The BF images of Fig. 16 show several dislocations in NiAl, a material with the CsCl structure. Dislocations B and F are clearly in contrast with $\mathbf{g} = [\bar{1}10]$, [010] and [001] and cannot be seen with $\mathbf{g}$ = [110]. In the $\mathbf{g} = [\bar{1}10]$ image, the contrast along the length of dislocations B and F is uniform while zig-zag contrast appears for dislocation B and for the lower right-hand portion of dislocation F in the other

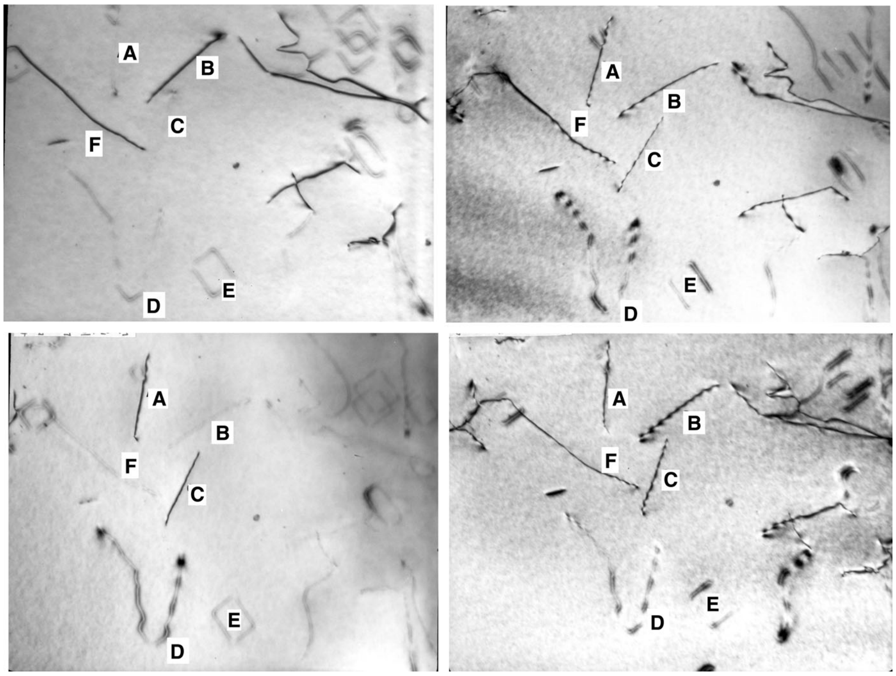

Figure 16 Bright field micrographs of a NiAl sample recorded with four diffraction vectors. Identification of the Burgers vectors of dislocations **A-F** are discussed in the text. Clockwise from upper left, $\mathbf{g} = [\bar{1}10]$, [010], [100], and [110].

two images. Dislocations A and C exhibit no contrast with $\mathbf{g} = [\bar{1}10]$ and are visible in the other three BF images shown in Fig. 16.

Contrast of well-separated dislocation dipole D and dislocation loop E is more complex. Double images are seen for all **g** of Fig. 16, and this shows that the value of $\mathbf{g}\cdot\mathbf{b}$ differs for D and E compared to A, B, C, and F. Very strong zig-zag contrast of D is seen with $\mathbf{g} = [100]$. Two sides of the square loop E are completely extinct with $\mathbf{g} = [100]$ and [010] while opposite corners of the loop disappear completely with $\mathbf{g} = [110]$ and $[\bar{1}10]$. The references give more details.

When discussing whether images appear light or dark, it is important to know whether BF or DF images are under discussion. Because dislocations diffract greater intensities than the perfect regions of the crystal, there should be more intensity at the dislocation positions in DF images and less at these positions in BF images. Thus, the expected BF dislocation images in Fig. 12 and 16 consist of white lines against a dark background. In fact, this is what is seen on BF *negatives*. Printing positives from the negatives, therefore, produces dark dislocations images on a light background.

9 IMAGING AND PHASE CONTRAST

Thus far in the discussion of imaging, consideration has been limited to only one beam passing through the objective aperture. If two or more beams are allowed through the aperture, phase contrast can result. While detailed understanding of various modes of TEM phase contrast imaging requires a somewhat lengthy development (e.g., [2]), a straight-forward and short explanation for this type of imaging is possible [6].

Let the aperture allow the incident plus one diffracted beam to reach the image. The total wave function for the electrons (i.e., the amplitude) is

$$\Psi = \exp(2\pi i\mathbf{k}\cdot\mathbf{r}) + \phi_g \exp(2\pi i\mathbf{k}'\cdot\mathbf{r}) \tag{9}$$

where the incident wave has unit amplitude and wave vector $\mathbf{k}$ in the crystal and $\mathbf{k}' = \mathbf{k} + \mathbf{g}$ is the wave vector of the diffracted wave in the crystal. Factoring produces

$$\Psi = \exp(2\pi i\mathbf{k}\cdot\mathbf{r})[\mathbf{1} + \phi_g \exp(2\pi i\mathbf{g}\cdot\mathbf{r}) \tag{10}$$

and the intensity is, for $\phi_g = \mathrm{R}\ \exp(i\delta)$,

$$\mathrm{I} = \mathbf{1} + \mathrm{R}^2 + 2\mathrm{R}\ \cos\,(2\pi\mathbf{g}\cdot\mathbf{r} + \delta) \tag{11}$$

Both R and δ are functions of s and thickness t, and from Eq. 6,

$$\mathrm{R} = (\pi/\xi_g)\frac{\sin \pi\ \mathrm{t}\ s}{\pi\ s} \tag{12}$$

and

$$\delta = \pi/2 - \pi\, t\, s \tag{13}$$

Next consider how intensity varies along direction $\mathbf{x}$ (in direct space, i.e., in the image) chosen parallel to $\mathbf{g}$, that is in the plane normal to the incident beam $\mathbf{B}$. Since $\mathbf{g}$ is nearly perpendicular to $\mathbf{B}$, little error is introduced. The result of Eq. 11 then becomes

$$\mathrm{I} = 1 + \mathrm{R}^2 - 2\mathrm{R}\ \sin\,(\{2\pi \mathrm{x}/d\} - \pi\, s\, t) \tag{14}$$

Thus, a modulation in intensity exists along $\mathbf{x}$ with periodicity *proportional* to d, a spacing in the crystal, and the lattice is “resolved” if the TEM has sufficient resolving power.

When more beams reach the image, the interference sharpens, and more details are visible in the pattern. One-dimensionally modulated lattice fringe images (from collinear diffraction spots plus the incident beam) are rarely used. More often noncollinear **G** contribute to form two-dimensional lattice fringe images

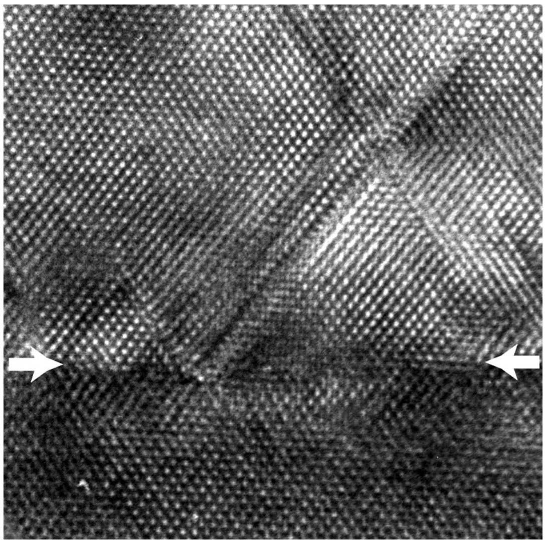

Figure 17 110 lattice fringe image of an epitaxial layer (ZnS, top) grown on a GaAs substrate; the boundary, identified with an arrow, is parallel to the bottom of the micrograph. (Courtesy Z.L. Wang.)

(Fig. 17).The reader should always remember that the visibility of fringes depends on orientation and on foil thickness and should never forget that individuals atoms (or even columns of atoms are not being imaged. Image simulation is often required for correct interpretation of lattice fringe and other phase contrast images. Discussion of this topic and of other interesting topics in TEM is beyond the scope of this chapter and can be found elsewhere (e.g., [2], [7], [8]).

Appendix

Electron and Neutron Diffraction

A1 INTRODUCTION

Just as a beam of x-rays has a dual wave-particle character so, inversely, does a stream of particles have certain properties peculiar to wave motion. In particular, such a stream of particles can be diffracted by a periodic arrangement of scattering centers. This was first predicted theoretically by de Broglie in 1924 and demonstrated experimentally by Davisson and Germer in 1927 (for electrons) and by Von Halban and Preiswerk in 1936 (for neutrons).

If a stream of particles can behave like wave motion, it must have a wavelength associated with it. The theory of wave mechanics indicates that this wavelength is given by the ratio of Planck's constant $\hbar$ to the momentum of the particle, or

$$\lambda = \frac{\hbar}{mv}, \tag{1}$$

where m is the mass and v the velocity of the particle. If a stream of particles is directed at a crystal under the proper conditions, diffraction will occur in accordance with Bragg's law just as for x-rays, and the directions of diffraction can be predicted by the use of that law and the wavelength calculated from Eq. (1). Numerous applications of electron and neutron diffraction have been found in materials science/engineering, solid state physics and chemistry. The differences between x-ray, electron, and neutron diffraction by crystals are such that these three techniques supplement one another to a remarkable degree, each giving a particular kind of information which the others are incapable of supplying.

A2 ELECTRON DIFFRACTION

A stream of fast electrons is obtained in a tube operating on much the same principles as an x-ray tube. The wavelength associated with the electrons depends on the applied voltage, since the kinetic energy of the electrons is given by

$$\tfrac{1}{2}mv^2 = eV \tag{2}$$

where e is the charge on the electron and V the applied voltage. Combination of Eqs. (1) and (2) shows the inverse relation between wavelength and voltage:

$$\lambda = \sqrt{\frac{150}{V}},$$

where λ is in angstroms and the applied voltage V is in volts. This equation requires small relativistic corrections at high voltages, due to the variation of electron mass

From Appendix 2 of *Elements of X-Ray Diffraction*, Third Edition. B.D. Cullity, S.R. Stock.

with velocity. At an operating voltage of 100 kV, the electron wavelength is about 0.04 Å, or considerably shorter than the wavelength of x-rays used in diffraction.

Electron diffraction differs from x-ray diffraction in the following ways:

1. Electrons interact much more strongly with matter than x-rays. Therefore, electrons are much less penetrating than x-rays. They are easily absorbed by air, which means that the specimen and the photographic film on which the diffraction pattern is recorded must both be enclosed within the evacuated tube in which the electron beam is produced. Transmission patterns can be made only of specimens so thin as to be classified as foils or films. Reflection patterns from thick specimens are recorded by a glancing-angle technique; such a pattern will be representative only of a thin surface layer, because diffraction occurs over a depth of only a few hundred angstroms or less. The angular pattern of back scattered electrons also supplies crystallographic information and has received increasing attention recently. Electron diffraction is therefore well suited to the study of thin surface layers.
2. Electrons are scattered much more intensely than x-rays, so that even a very thin layer of material gives a strong diffraction pattern in a short time.
3. The intensity of electron scattering decreases as 2θ increases, as with x-rays, but much more rapidly. This circumstance, coupled with the very short wavelength of the electron beam, causes the entire observable diffraction pattern to be confined to an angular region of about $\pm 4° 2\theta$.

Experimentally, electron diffraction has developed in three stages:

1. The earlier work, before the invention of the transmission electron microscope, was done with homemade apparatus called “electron diffraction cameras.” Many important studies were made of the structures of metal foils, electrodeposits, films deposited by evaporation, oxide films on metals, and surface layers due to polishing.
2. Much work is done with the transmission electron microscope. Here, microscopy and diffraction go hand in hand. The diffraction pattern discloses the orientation of the crystal (grain) under examination and thus the proper imaging conditions required to disclose what the microscopist wishes to see. Another application is in the determination of the structure of very small crystals revealed by the microscope.
3. Still another application is low-energy electron diffraction, called LEED, carried out in special apparatus with an operating voltage of the order of 100 volts. The electron beam then has such low energy that it can penetrate only a monolayer or so of atoms at the specimen surface. The resulting diffraction pattern reveals the arrangement of these surface atoms, an arrangement often quite different from that of the underlying material.

Such studies are important in the understanding of phenomena such as catalysis.

A3 NEUTRON DIFFRACTION

By making a small opening in the wall of a nuclear reactor, a beam of neutrons can be obtained. The neutrons in such a beam have kinetic energies extending over a considerable range, but a "monochromatic" beam, i.e., a beam composed of neutrons with a single energy, can be obtained by diffraction from a single crystal and this diffracted beam can be used in diffraction experiments. If E is the kinetic energy of the neutrons, then

$$E = \tfrac{1}{2}mv^2, \tag{3}$$

where m is the mass of the neutron (1.68×10^{-27} kg) and v is its velocity. Combination of Eqs. (1) and (3) gives the wavelength of the neutron beam:

$$\lambda = \frac{h}{\sqrt{2mE}}. \tag{4}$$

The neutrons issuing from a reactor have their kinetic energies distributed in much the same way as those of gas molecules in thermal equilibrium; i.e., they follow the Maxwell distribution law. The largest fraction of these so-called "thermal neutrons" therefore has kinetic energy equal to kT, where k is Boltzmann's constant and T the absolute temperature. If this fraction is selected by the monochromating crystal, inserting $E = kT$ in Eq. (4) yields

$$\lambda = \frac{h}{2mkT}. \tag{5}$$

T is of the order of 300 to 400K, which means that λ is about 1 or 2 Å, i.e., of the same order of magnitude as x-ray wavelengths. Diffraction experiments are performed with a neutron diffractometer, in which the intensity of the beam diffracted by the specimen is measured with a defectors optimized for neutrons.

Neutron diffraction differs markedly from x-ray or electron diffraction in several ways:

1. A neutron beam is highly penetrating. An iron plate, 1 cm thick, is opaque to electrons, virtually opaque to 1.5 Å x-rays, but transmits 35 percent of 1.5 Å neutrons which diffract at the same θ as the x-rays. Note that synchrotron radiation from insertion devices at storage rings such as the Advanced Photon Source can produce x-ray photon energies high enough to penetrate considerably more than 1 cm of iron; the corresponding 2θ angles are quite small for these photons, which may be a disadvantage for certain applications.

2. The intensity of neutron scattering varies quite irregularly with the atomic

number Z of the scattering atom. Elements with almost the same values of Z may have quite different neutron-scattering powers, and elements with widely separated values of Z may scatter neutrons equally well. Furthermore, some light elements, such as carbon, scatter neutrons more intensely than some heavy elements, such as tungsten. It follows that structure analyses can be carried out with neutron diffraction that are impossible, or possible only with great difficulty, with x-ray or electron diffraction. In a compound of hydrogen or carbon, for example, with a heavy metal, x-rays will not "see" the light hydrogen or carbon atom because of its relatively low scattering power, whereas its position in the lattice can be determined with ease by neutron diffraction. Neutrons can also distinguish in many cases between elements differing by only one atomic number, elements which scatter x-rays with almost equal intensity; neutron diffraction, for example, shows strong superlattice lines from ordered FeCo, whereas with x-rays they are practically invisible.

3. Neutrons have a small magnetic moment. If the scattering atom also has a net magnetic moment, the two interact and modify the total scattering. In substances that have an ordered arrangement of atomic moments (antiferromagnetic, ferrimagnetic, and ferromagnetic materials) neutron diffraction can disclose both the magnitude and direction of the moments. Only neutron diffraction can furnish such information, and it has had a major impact on studies of magnetic structure.

Diffuse scattering at small angles (in transmission), also occurs with neutrons. Neutron small-angle scattering has certain advantages over x-rays as a means of studying inhomogeneities in materials, particularly because thick specimens, rather than thin foils, can be examined.

Neutron diffraction would doubtless have wider application if all potential investigators had easy access to high-intensity neutron sources, but the number of such sources is very limited.

Appendix

Lattice Geometry

A1 PLANE SPACINGS

The value of d, the distance between adjacent planes in the set (hkl), may be found from the following equations.

Cubic:
$$\frac{1}{d^2} = \frac{h^2 + k^2 + l^2}{a^2}$$

Tetragonal:
$$\frac{1}{d^2} = \frac{h^2 + k^2}{a^2} + \frac{l^2}{c^2}$$

Hexagonal:
$$\frac{1}{d^2} = \frac{4}{3}\left(\frac{h^2 + hk + k^2}{a^2}\right) + \frac{l^2}{c^2}$$

Rhombohedral:

$$\frac{1}{d^2} = \frac{(h^2 + k^2 + l^2)\sin^2\alpha + 2(hk + kl + hl)(\cos^2\alpha - \cos\alpha)}{a^2(1 - 3\cos^2\alpha + 2\cos^3\alpha)}$$

Orthorhombic:
$$\frac{1}{d^2} = \frac{h^2}{a^2} + \frac{k^2}{b^2} + \frac{l^2}{c^2}$$

Monoclinic:
$$\frac{1}{d^2} = \frac{1}{\sin^2\beta}\left(\frac{h^2}{a^2} + \frac{k^2\sin^2\beta}{b^2} + \frac{l^2}{c^2} - \frac{2hl\cos\beta}{ac}\right)$$

Triclinic:
$$\frac{1}{d^2} = \frac{1}{V^2}(S_{11}h^2 + S_{22}k^2 + S_{33}l^2 + 2S_{12}hk + 2S_{23}kl + 2S_{13}hl)$$

In the equation for triclinic crystals,

V = volume of unit cell (see below),

$S_{11} = b^2c^2\sin^2\alpha,$

$S_{22} = a^2c^2\sin^2\beta,$

$S_{33} = a^2b^2\sin^2\gamma,$

$S_{12} = abc^2(\cos\alpha\cos\beta - \cos\gamma),$

$S_{23} = a^2bc(\cos\beta\cos\gamma - \cos\alpha),$

$S_{13} = ab^2c(\cos\gamma\cos\alpha - \cos\beta).$

From Appendix 3 of *Elements of X-Ray Diffraction*, Third Edition. B.D. Cullity, S.R. Stock.

A2 CELL VOLUMES

The following equations give the volume V of the unit cell.

Cubic: $V = a^3$

Tetragonal: $V = a^2 c$

Hexagonal: $V = \frac{\sqrt{3}a^2 c}{2} = 0.866a^2 c$

Rhombohedral: $V = a^3\sqrt{1 - 3\cos^2\alpha + 2\cos^2\alpha}$

Orthorhombic: $V = abc$

Monoclinic: $V = abc\sin\beta$

Triclinic: $V = abc\sqrt{1 - \cos^2\alpha - \cos^2\beta - \cos^2\gamma + 2\cos\alpha\,\cos\beta\,\cos\gamma}$

A3 INTERPLANAR ANGLES

The angle ϕ between the plane $(h_1k_1l_1)$, of spacing d_1, and the plane $(h_2k_2l_2)$, of spacing d_2, may be found from the following equations. (V is the volume of the unit cell.)

Cubic:

$$\cos\phi = \frac{h_1h_2 + k_1k_2 + l_1l_2}{\sqrt{(h_1^2 + k_1^2 + l_1^2)(h_2^2 + k_2^2 + l_2^2)}}$$

Tetragonal:

$$\cos\phi = \frac{\dfrac{h_1h_2 + k_1k_2}{a^2} + \dfrac{l_1l_2}{c^2}}{\sqrt{\left(\dfrac{h_1^2 + k_1^2}{a^2} + \dfrac{l_1^2}{c^2}\right)\left(\dfrac{h_2^2 + k_2^2}{a^2} + \dfrac{l_2^2}{c^2}\right)}}$$

Hexagonal:

$$\cos\phi = \frac{h_1h_2 + k_1k_2 + \frac{1}{2}(h_1k_2 + h_2k_1) + \dfrac{3a^2}{4c^2}l_1l_2}{\sqrt{\left(h_1^2 + k_1^2 + h_1k_1 + \dfrac{3a^2}{4c^2}l_1^2\right)\left(h_2^2 + k_2^2 + h_2k_2 + \dfrac{3a^2}{4c^2}l_2^2\right)}}$$

Rhombohedral:

$$\cos\ \phi = \frac{a^4 d_1 d_2}{V^2}[\sin^2\alpha(h_1h_2 + k_1k_2 + l_1l_2)$$
$$+(\cos^2\alpha - \cos\alpha)(k_1l_2 + k_2l_1 + l_1h_2 + l_2h_1 + h_1k_2 + h_2k_1)]$$

Orthorhombic:
$$\cos\phi = \frac{\dfrac{h_1h_2}{a^2} + \dfrac{k_1k_2}{b^2} + \dfrac{l_1l_2}{c^2}}{\sqrt{\left(\dfrac{h_1^2}{a^2} + \dfrac{k_1^2}{b^2} + \dfrac{l_1^2}{c^2}\right)\left(\dfrac{h_2^2}{a^2} + \dfrac{k_2^2}{b^2} + \dfrac{l_2^2}{c^2}\right)}}$$

Monoclinic:

$$\cos\phi = \frac{d_1d_2}{\sin^2\beta}\left[\frac{h_1h_2}{a^2} + \frac{k_1k_2\sin^2\beta}{b^2} + \frac{l_1l_2}{c^2} - \frac{(l_1h_2 + l_2h_1)\cos\beta}{ac}\right]$$

Triclinic:

$$\cos\phi = \frac{d_1d_2}{V^2}[S_{11}h_1h_2 + S_{22}k_1k_2 + S_{33}l_1l_2$$
$$+S_{23}(k_1l_2 + k_2l_1) + S_{13}(l_1h_2 + l_2h_1) + S_{12}(h_1k_2 + h_2k_1)]$$

This page intentionally left blank

Appendix

The Rhombohedral-Hexagonal Transformation

The lattice of points shown in Fig. A1 is rhombohedral, that is, it possesses the symmetry elements characteristic of the rhombohedral system. The primitive rhombohedral cell has axes $\mathbf{a}_1(\mathbf{R})$, $\mathbf{a}_2(\mathbf{R})$, and $\mathbf{a}_3(\mathbf{R})$. The same lattice of points, however, may be referred to a hexagonal cell having axes $\mathbf{a}_1(\mathbf{H})$, $\mathbf{a}_2(\mathbf{H})$, and $\mathbf{c}(\mathbf{H})$. The hexagonal cell is no longer primitive, since it contains three lattice points per unit cell (at $0\ 0\ 0$, $\frac{2}{3}\frac{1}{3}\frac{1}{3}$, and $\frac{1}{3}\frac{2}{3}\frac{2}{3}$), and it has three times the volume of the rhombohedral cell.

If one wishes to know the indices $(HK \cdot L)$, referred to hexagonal axes, of a plane whose indices (hkl), referred to rhombohedral axes, are known, the following equations may be used:

$$H = h - k,$$

$$K = k - l,$$

$$L = h + k + l.$$

Thus, the (001) face of the rhombohedral cell (shown shaded in the figure) has indices$(0\bar{1} \cdot 1)$. when referred to hexagonal axes.

Since a rhombohedral lattice may be referred to hexagonal axes, it follows that the powder pattern of a rhombohedral substance can be indexed as a hexagonal substance. How then can the true nature of the lattice be recognised? From the equations given above, it follows that

$$-H + K + L = 3k.$$

If the lattice is really rhombohedral, then k is an integer and the only lines appearing in the pattern will have hexagonal indices $(HK \cdot L)$ such that the sum $(- H + K + L)$ is always an integral multiple of 3. If this condition is not satisfied, the lattice is hexagonal.

When the pattern of a rhombohedral substance has been so indexed, i.e., with reference to hexagonal axes, and the true nature of the lattice determined, the indices (hkl) of the diffraction peeks referred to rhombohedral axes often are required. The transformation equations are

$$h = \tfrac{1}{3}(2H + K + L),$$

$$k = \tfrac{1}{3}(-H + K + L),$$

$$l = \tfrac{1}{3}(-H - 2K + L).$$

From Appendix 4 of *Elements of X-Ray Diffraction*, Third Edition. B.D. Cullity, S.R. Stock.

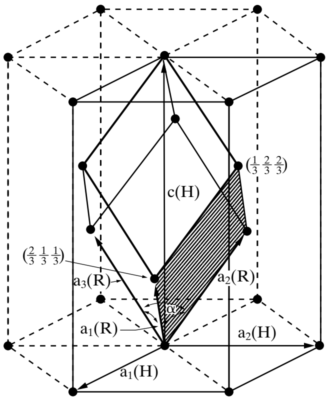

Figure A1 Rhombohedral and hexagonal unit cell in a rhombohedral lattice.

There is then the problem of determining the lattice parameters a_R and α of the rhombohedral unit cell. But the dimensions of the rhombohedral cell can be determined from the dimensions of the hexagonal cell, and this is an easier process than solving the rather complicated plane-spacing equation for the rhombohedral system. The first step is to index the pattern on the basis of hexagonal axes. Then the parameters a_H and c of the hexagonal cell are calculated in the usual way. Finally, the parameters of the rhombohedral cell are determined from the following equations:

$$a_R = \frac{1}{3}\sqrt{3a_H^2 + c^2}\,,$$

$$\sin\frac{\alpha}{2} = \frac{3}{2\sqrt{3 + (c/a_H)^2}}$$

Finally, it should be noted that, if the *c/a* ratio of the hexagonal cell in Fig. A1 takes on the special value of 2.45, then the angle α of the rhombohedral cell will equal 60° and the lattice of points will be face-centered cubic.

Further information on the rhombohedral-hexagonal relationship and on unit cell transformations in general may be obtained from the *International Tables for X-Ray Crystallography* [G1].

REFERENCES

The following books are listed more or less in the order they are encountered in the text

G.1 *International Tables for Crystallography*, Ed. A.J.C Wilson, Vol. A-C (Dordrecht Kluwer Academic Pub. for International Union of Crystallography, 1995). The reference ''book'' for crystallography and diffraction.

This page intentionally left blank

Appendix

X-Ray Wavelengths

All the following values are extracted from much longer tables on pp. 6-43 of Vol. 4 of the *International Tables for X-Ray Crystallography* [G.1], which are in turn taken from J. A. Bearden, *Rev. Mod. Phys.*, **39**, 78 (1967).

E($K\alpha$) is the energy *hv* of the unresolved $K\alpha$ line to the nearest 0.01 keV. (The values in [G.1] are of higher accuracy.) In computing E($K\alpha$), $K\alpha_1$ is given twice the weight of $K\alpha_2$.

The wavelengths are given in Å* units. This unit is *defined* by the wavelength of the W$K\alpha_1$ line = 0.2090100 Å*. The Å* unit is believed to be equal to the angstrom Å to within 5 parts per million and involves a conversion factor of 1.002056 ± 0.000005 Å/*kX*. Because of the still remaining uncertainty in this conversion factor, it was decided to introduce the Å* unit. The distinction between Å and Å* is negligible except in work of the very highest accuracy.

Wavelengths (in Å* units) and Energies (in keV) of Some Characteristic Emission Lines and Absorption Edges

Element	E($K\alpha$) (keV)	$K\alpha_2$ strong	$K\alpha_1$ very strong	$K\beta_1$ week	K edge	$L\alpha_1$	L_{111} edge
1 H							
2 He							
3 Li	0.05	228			226.5		
4 Be	0.11	114			111		
5 B	0.18	67.6					
6 C	0.28	44.7			43.68		
7 N	0.39	31.6			30.99		
8 O	0.52	23.62			23.32		
9 F	0.68	18.32					
10 Ne	0.85	14.610		14.452	14.3018		
11 Na	1.04	11.9101		11.575	11.569		405
12 Mg	1.25	9.8900		9.521	9.5122		250.7
13 Al	1.49	8.34173	8.33834	7.960	7.94813		170.4
14 Si	1.74	7.12791	7.12542	6.753	6.738		123
15 P	2.01	6.160	6.157	5.796	5.784		94
16 S	2.31	5.37496	5.37216	5.0316	5.0185		
17 Cl	2.62	4.7307	4.7278	4.4034	4.3971		
18 A	2.96	4.19474	4.19180	3.8860	3.87090		
19 K	3.31	3.7445	3.7414	3.4539	3.4365		42.1
20 Ca	3.69	3.36166	3.35839	3.0897	3.0703	36.33	35.49
21 Sc	4.09	3.0342	3.0309	2.7796	2.762	31.35	
22 Ti	4.51	2.75216	2.74851	2.51391	2.49734	27.42	27.29
23 V	4.95	2.50738	2.50356	2.28440	2.2691	24.25	
24 Cr	5.41	2.293806	2.28970	2.08487	2.07020	21.64	20.7
25 Mn	5.90	2.10578	2.101820	1.91021	1.89643	19.45	
26 Fe	6.40	1.939980	1.936042	1.75661	1.74346	17.59	17.525
27 Co	6.93	1.792850	1.788965	1.62079	1.60815	15.972	15.915
28 Ni	7.47	1.661747	1.657910	1.500135	1.48807	14.561	14.525
29 Cu	8.04	1.544390	1.540562	1.392218	1.38059	12.336	13.288
30 Zn	8.63	1.439000	1.435155	1.29525	1.2834	12.254	12.131

From Appendix 7 of *Elements of X-Ray Diffraction*, Third Edition. B.D. Cullity, S.R. Stock.

Appendix: X-Ray Wavelengths

Element	E($K\alpha$) (keV)	$K\alpha_2$ strong	$K\alpha_1$ very strong	$K\beta_1$ week	K edge	$L\alpha_1$	L_{111} edge
31 Ga	9.24	1.34399	1.340083	1.20789	1.1958	11.292	11.100
32 Ge	9.88	1.258011	1.254054	1.12894	1.11658	10.4361	10.187
33 As	10.53	1.17987	1.17588	1.05730	1.0450	9.6709	9.367
34 Se	11.21	1.10882	1.10477	0.99218	0.97974	8.9900	8.646
35 Br	11.91	1.04382	1.03974	0.93279	0.9204	8.3746	7.984
36 Kr	12.63	0.9841	0.9801	0.8785	0.86552	7.817	7.392
37 Rb	13.38	0.92969	0.925553	0.82868	0.81554	7.3183	6.862
38 Sr	14.14	0.87943	0.87526	0.78292	0.76973	6.8628	6.387
39 Y	14.93	0.83305	0.82884	0.74072	0.72766	6.4488	5.962
40 Zr	15.75	0.79015	0.78593	0.70173	0.68883	6.0705	5.579
41 Nb	16.58	0.75044	0.74620	0.66576	0.06298	5.7243	5.230
42 Mo	17.44	0.713590	0.709300	0.632288	0.61978	5.40655	4.913
43 Tc	18.33	0.67932	0.67502	0.60130	0.58906	5.1148	4.630
44 Ru	19.24	0.647408	0.643083	0.572482	0.58061	4.84575	4.389
45 Rh	20.17	0.617630	0.613279	0.545605	0.53395	4.59743	4.1299
46 Pd	21.12	0.589821	0.585448	0.520520	0.6092	4.36767	3.9074
47 Ag	22.11	0.563798	0.5594075	0.497069	0.48589	4.15443	3.6999
48 Cd	23.11	0.539422	0.535010	0.475105	0.48407	3.95635	3.5047
49 In	24.14	0.516544	0.512113	0.454545	0.44371	3.77192	3.3237
50 Sn	25.20	0.495053	0.490599	0.435236	0.42467	3.59994	3.1557
51 Sb	26.28	0.474827	0.470354	0.417085	0.40868	3.43941	3.0003
52 Te	27.38	0.455784	0.451295	0.399995	0.30074	3.28920	2.8555
53 I	28.51	0.437829	0.433318	0.383905	0.37381	3.14860	2.7196
54 Xe	29.67	0.42087	0.41634	0.36872	0.3584	3.0166	2.5926
55 Cs	30.86	0.404835	0.400290	0.354364	0.36451	2.8924	2.4740
56 Ba	32.07	0.389668	0.385111	0.340811	0.33104	2.77595	2.3629
57 La	33.31	0.375313	0.370737	0.327983	0.31844	2.66570	2.261
58 Ce	34.57	0.361683	0.357092	0.315816	0.30643	2.5615	2.166
59 Pr	35.87	0.348749	0.344140	0.304261	0.29518	2.4630	2.0791
60 Nd	37.19	0.336472	0.331846	0.293299	0.28453	2.3704	1.9967
61 Pm	38.54	0.324803	0.320160	0.28290	0.27431	2.2822	1.9191
62 Sm	39.92	0.313698	0.309040	0.27301	0.26464	2.1998	1.8457
63 Eu	41.33	0.303118	0.298446	0.263577	0.25553	2.1209	1.7761
64 Gd	42.77	0.293038	0.288353	0.25460	0.24681	2.0468	1.7117
65 Tb	44.24	0.283423	0.278724	0.24608	0.23841	1.9765	1.6497
66 Dy	45.73	0.274247	0.269533	0.23788	0.23048	1.90881	1.5916
67 Ho	47.26	0.265486	0.260756	0.23012	0.22291	1.8450	1.5368
68 Er	48.83	0.257110	0.252365	0.22266	0.21567	1.78425	1.4835
69 Tm	50.42	0.249095	0.244338	0.21556	0.20880	1.7268	1.4334
70 Yb	52.04	0.241424	0.236655	0.20884	0.20224	1.67189	1.3862
71 Lu	53.70	0.234081	0.229298	0.20231	0.19595	1.61951	1.3405
72 Ht	55.40	0.227024	0.222227	0.19607	0.18982	1.56958	1.2972
73 Ta	57.11	0.220305	0.215497	0.190089	0.18394	1.52197	1.2553
74 W	58.87	0.213828	0.2090100	0.184374	0.17837	1.47639	1.2155
75 Re	60.67	0.207611	0.202781	0.178880	0.17302	1.43230	1.1773
76 Os	62.50	0.201639	0.196794	0.173611	0.16787	1.39121	1.1408
77 Ir	64.36	0.195904	0.191047	0.168542	0.16292	1.35128	1.1058
78 Pt	66.26	0.190381	0.185511	0.163675	0.15818	1.31304	1.0723
79 Au	68.20	0.185075	0.180195	0.158982	0.153693	1.27640	1.04000
80 Hg	70.18	0.179958	0.175068	0.154487	0.14918	1.24120	1.0091
81 Ti	72.19	0.175036	0.170136	0.150142	0.14495	1.20739	0.9793
82 Pb	74.25	0.170294	0.165376	0.145970	0.140880	1.17501	0.95073
83 Bi	76.34	0.165717	0.160789	0.141948	0.13694	1.14386	0.9234
84 Po	78.48	0.16130	0.15636	0.13807		1.11386	
85 At	80.66	0.15705	0.15210	0.13432		1.08500	
86 Rn	82.88	0.15294	0.14798	0.13069		1.05723	
87 Fr	85.14	0.14896	0.14399	0.12719		1.03049	
88 Ra	87.46	0.14512	0.14014	0.12382		1.00473	0.8028
89 Ac	89.81	0.14141	0.136417	0.12055		0.97993	
90 Th	92.22	0.137829	0.132813	0.117396	0.11307	0.95600	0.7607
91 Pa	94.67	0.134343	0.129325	0.114345		0.93284	
92 U	97.18	0.130968	0.125947	0.111394	0.10723	0.910639	0.7223

Appendix: X-Ray Wavelengths

Some commonly used K wavelengths

Element	$K\alpha$ (weighted average)*	$K\alpha_2$ strong	$K\alpha_1$ very strong	$K\beta_1$ week
Cr	2.29100	2.293606	2.28970	2.08487
Fe	1.937355	1.939980	1.936042	1.75661
Co	1.790260	1.792850	1.788965	1.62079
Cu	1.541838	1.544390	1.540562	1.392218
Mo	0.710730	0.713590	0.709300	0.632288

*$K\alpha_1$ is given twice the weight of Ka_2.

Characteristic L Lines of Tungsten

Line	Relative Intensity	Wavelength
$L\alpha_1$	Very Strong	1.47639
$L\alpha_2$	Weak	1.48743
$L\beta_1$	Strong	1.281809
$L\beta_2$	Medium	1.24460
$L\beta_3$	Weak	1.26269
$L\gamma_1$	Weak	1.09855

REFERENCES

The following books are listed more or less in the order they are encountered in the text

G.1 *International Tables for Crystallography*, Ed. A.J.C Wilson, Vol. A-C (Dordrecht Kluwer Academic Pub. for International Union of Crystallography, 1995). The reference ''book" for crystallography and diffraction.

This page intentionally left blank

Appendix

Quadratic Forms of Miller Indices

	Cubic				Hexagonal	
$h^2 + k^2 + l^2$	*hkl*				$h^2 + hk + k^2$	*hk*
	Simple	Face-centered	Body-centered	Diamond		
1	100				1	10
2	110	. . .	110		2	
3	111	111	. . .	111	3	11
4	200	200	200		4	20
5	210				5	
6	211	. . .	211		6	
7					7	21
8	220	220	220	220	8	
9	300, 221				9	30
10	310	. . .	310		10	
11	311	311	. . .	311	11	
12	222	222	222		12	22
13	320				13	31
14	321	. . .	321		14	
15					15	
16	400	400	400	400	16	40
17	410, 322				17	
18	411, 330	. . .	411, 330		18	
19	331	331	. . .	331	19	32
20	420	420	420		20	
21	421				21	41
22	332	. . .	332		22	
23					23	
24	422	422	422	422	24	
25	500, 430				25	50
26	510, 431	. . .	510, 431		26	
27	511, 333	511, 333	. . .	511, 333	27	33
28					28	42
29	520, 432				29	
30	521	. . .	521		30	
31					31	51
32	440	440	440	440	32	
33	522, 441				33	
34	530, 433	. . .	530, 433		34	
35	531	531	. . .	531	35	
36	600, 442	600, 442	600, 442		36	60
37	610				37	43
38	611, 532	. . .	611, 532		38	
39					39	52
40	620	620	620	620	40	
41	621, 540, 443				41	
42	541	. . .	541		42	
43	533	533	. . .	533	43	61
44	622	622	622		44	
45	630, 542				45	
46	631	. . .	631		46	
47					47	
48	444	444	444	444	48	44
49	700, 632				49	70, 53

From Appendix 9 of *Elements of X-Ray Diffraction*, Third Edition. B.D. Cullity, S.R. Stock.

	Cubic				Hexagonal	
$h^2 + k^2 + l^2$	*hkl*				$h^2 + hk + k^2$	*hk*
	Simple	Face-centered	Body-centered	Diamond		
50	710, 550, 543	. . .	710, 550, 543		50	
51	711, 551	711, 551	. . .	711, 551	51	
52	640	640	640		52	62
53	720, 641				53	
54	721, 633, 552	. . .	721, 633, 552		54	
55					55	
56	642	642	642	642	56	
57	722, 544				57	71
58	730	. . .	730		58	
59	731, 553	731, 553	. . .	731, 553	59	

Appendix

Atomic Scattering Factors

$\frac{\sin\theta}{\lambda}(\mathring{\mathrm{A}}^{-1})$	0.0	0.1	0.2	0.3	0.4	0.5	0.6	0.7	0.8	0.9	1.0	1.1	1.2
H	1	0.81	0.48	0.25	0.13	0.07	0.04	0.03	0.02	0.01	0.00	0.00	
He	2	1.88	1.46	1.05	0.75	0.52	0.35	0.24	0.18	0.14	0.11	0.09	
Li^{+}	2	1.96	1.8	1.5	1.3	1.0	0.8	0.6	0.5	0.4	0.3	0.3	
Li	3	2.2	1.8	1.5	1.3	1.0	0.8	0.6	0.5	0.4	0.3	0.3	
Be^{+2}	2	2.0	1.9	1.7	1.6	1.4	1.2	1.0	0.9	0.7	0.6	0.5	
Be	4	2.9	1.9	1.7	1.6	1.4	1.2	1.0	0.9	0.7	0.6	0.5	
B^{+3}	2	1.99	1.9	1.8	1.7	1.6	1.4	1.3	1.2	1.0	0.9	0.7	
B	5	3.5	2.4	1.9	1.7	1.5	1.4	1.2	1.2	1.0	0.9	0.7	
C	6	4.6	3.0	2.2	1.9	1.7	1.6	1.4	1.3	1.16	1.0	0.9	
N^{+5}	2	2.0	2.0	1.9	1.9	1.8	1.7	1.6	1.5	1.4	1.3	1.16	
N^{+3}	4	3.7	3.0	2.4	2.0	1.8	1.66	1.56	1.49	1.39	1.28	1.17	
N	7	5.8	4.2	3.0	2.3	1.9	1.65	1.54	1.49	1.39	1.29	1.17	
O	8	7.1	5.3	3.9	2.9	2.2	1.8	1.6	1.5	1.4	1.35	1.26	
O^{-2}	10	8.0	5.5	3.8	2.7	2.1	1.8	1.5	1.5	1.4	1.35	1.26	
F	9	7.8	6.2	4.45	3.35	2.65	2.15	1.9	1.7	1.6	1.5	1.35	
F^{-}	10	8.7	6.7	4.8	3.5	2.8	2.2	1.9	1.7	1.55	1.5	1.35	
Ne	10	9.3	7.5	5.8	4.4	3.4	2.65	2.2	1.9	1.65	1.55	1.5	
Na^{+}	10	9.5	8.2	6.7	5.25	4.05	3.2	2.65	2.25	1.95	1.75	1.6	
Na	11	9.65	8.2	6.7	5.25	4.05	3.2	2.65	2.25	1.95	1.75	1.6	
Mg^{+2}	10	9.75	8.6	7.25	5.95	4.8	3.85	3.15	2.55	2.2	2.0	1.8	
Mg	12	10.5	8.6	7.25	5.95	4.8	3.85	3.15	2.55	2.2	2.0	1.8	
Al^{+3}	10	9.7	8.9	7.8	6.65	5.5	4.45	3.65	3.1	2.65	2.3	2.0	
Al	13	11.0	8.95	7.75	6.6	5.5	4.5	3.7	3.1	2.65	2.3	2.0	
Si^{+4}	10	9.75	9.15	8.25	7.15	6.05	5.05	4.2	3.4	2.95	2.6	2.3	
Si	14	11.35	9.4	8.2	7.15	6.1	5.1	4.2	3.4	2.95	2.6	2.3	
P^{+5}	10	9.8	9.25	8.45	7.5	6.55	5.65	4.8	4.05	3.4	3.0	2.6	
P	15	12.4	10.0	8.45	7.45	6.5	5.65	4.8	4.05	3.4	3.0	2.6	
P^{-3}	18	12.7	9.8	8.4	7.45	6.5	5.65	4.85	4.05	3.4	3.0	2.6	
S^{+6}	10	9.85	9.4	8.7	7.85	6.85	6.05	5.25	4.5	3.9	3.35	2.9	
S	16	13.6	10.7	8.95	7.85	6.85	6.0	5.25	4.5	3.9	3.35	2.9	
S^{-2}	18	14.3	10.7	8.9	7.85	6.85	6.0	5.25	4.5	3.9	3.35	2.9	
Cl	17	14.6	11.3	9.25	8.05	7.25	6.5	5.75	5.05	4.4	3.85	3.35	
Cl^{-}	18	15.2	11.5	9.3	8.05	7.25	6.5	5.75	5.05	4.4	3.85	3.35	
A	18	15.9	12.6	10.4	8.7	7.8	7.0	6.2	5.4	4.7	4.1	3.6	
K^{+}	18	16.5	13.3	10.8	8.85	7.75	7.05	6.44	5.9	5.3	4.8	4.2	
K	19	16.5	13.3	10.8	9.2	7.9	6.7	5.9	5.2	4.6	4.2	3.7	3.3
Ca^{+2}	18	16.8	14.0	11.5	9.3	8.1	7.35	6.7	6.2	5.7	5.1	4.6	
Ca	20	17.5	14.1	11.4	9.7	8.4	7.3	6.3	5.6	4.9	4.5	4.0	3.6
Sc^{+3}	18	16.7	14.0	11.4	9.4	8.3	7.6	6.9	6.4	5.8	5.35	4.85	
Sc	21	18.4	14.9	12.1	10.3	8.9	7.7	6.7	5.9	5.3	4.7	4.3	3.9
Ti^{+4}	18	17.0	14.4	11.9	9.9	8.5	7.85	7.3	6.7	6.15	5.65	5.05	
Ti	22	19.3	15.7	12.8	10.9	9.5	8.2	7.2	6.3	5.6	5.0	4.6	4.2
V	23	20.2	16.6	13.5	11.5	10.1	8.7	7.6	6.7	5.9	5.3	4.9	4.4
Cr	24	21.1	17.4	14.2	12.1	10.6	9.2	8.0	7.1	6.3	5.7	5.1	4.6
Mn	25	22.1	18.2	14.9	12.7	11.1	9.7	8.4	7.5	6.6	6.0	5.4	4.9

From Appendix 10 of *Elements of X-Ray Diffraction*, Third Edition. B.D. Cullity, S.R. Stock.

Appendix: Atomic Scattering Factors

$\frac{\sin\theta}{\lambda}(\mathring{A}^{-1})$	0.0	0.1	0.2	0.3	0.4	0.5	0.6	0.7	0.8	0.9	1.0	1.1	1.2
Fe	26	23.1	18.9	15.6	13.3	11.6	10.2	8.9	7.9	7.0	6.3	5.7	5.2
Co	27	24.1	19.8	16.4	14.0	12.1	10.7	9.3	8.3	7.3	6.7	6.0	5.5
Ni	28	25.0	20.7	17.2	14.6	12.7	11.2	9.8	8.7	7.7	7.0	6.3	5.8
Cu	29	25.9	21.6	17.9	15.2	13.3	11.7	10.2	9.1	8.1	7.3	6.6	6.0
Zn	30	26.8	22.4	18.6	15.8	13.9	12.2	10.7	9.6	8.5	7.6	6.9	6.3
Ga	31	27.8	23.3	19.3	16.5	14.5	12.7	11.2	10.0	8.9	7.9	7.3	6.7
Ge	32	28.8	24.1	20.0	17.1	15.0	13.2	11.6	10.4	9.3	8.3	7.6	7.0
As	33	29.7	25.0	20.8	17.7	15.6	13.8	12.1	10.8	9.7	8.7	7.9	7.3
Se	34	30.6	25.8	21.5	18.3	16.1	14.3	12.6	11.2	10.0	9.0	8.2	7.5
Br	35	31.6	26.6	22.3	18.9	16.7	14.8	13.1	11.7	10.4	9.4	8.6	7.8
Kr	36	32.5	27.4	23.0	19.5	17.3	15.3	13.6	12.1	10.8	9.8	8.9	8.1
Rb^+	36	33.6	28.7	24.6	21.4	18.9	16.7	14.6	12.8	11.2	9.9	8.9	
Rb	37	33.5	28.2	23.8	20.2	17.9	15.9	14.1	12.5	11.2	10.2	9.2	8.4
Sr	38	34.4	29.0	24.5	20.8	18.4	16.4	14.6	12.9	11.6	10.5	9.5	8.7
Y	39	35.4	29.9	25.3	21.5	19.0	17.0	15.1	13.4	12.0	10.9	9.9	9.0
Zr	40	36.3	30.8	26.0	22.1	19.7	17.5	15.6	13.8	12.4	11.2	10.2	9.3
Nb	41	37.3	31.7	26.8	22.8	20.2	18.1	16.0	14.3	12.8	11.6	10.6	9.7
Mo	42	38.2	32.6	27.6	23.5	20.8	18.6	16.5	14.8	13.2	12.0	10.9	10.0
Tc	43	39.1	33.4	28.3	24.1	21.3	19.1	17.0	15.2	13.6	12.3	11.3	10.3
Ru	44	40.0	34.3	29.1	24.7	21.9	19.6	17.5	15.6	14.1	12.7	11.6	10.6
Rh	45	41.0	35.1	29.9	25.4	22.5	20.2	18.0	16.1	14.5	13.1	12.0	11.0
Pd	46	41.9	36.0	30.7	26.2	23.1	20.8	18.5	16.6	14.9	13.6	12.3	11.3
Ag	47	42.8	36.9	31.5	26.9	23.8	21.3	19.0	17.1	15.3	14.0	12.7	11.7
Cd	48	43.7	37.7	32.2	27.5	24.4	21.8	19.6	17.6	15.7	14.3	13.0	12.0
In	49	44.7	38.6	33.0	28.1	25.0	22.4	20.1	18.0	16.2	14.7	13.4	12.3
Sn	50	45.7	39.5	33.8	28.7	25.6	22.9	20.6	18.5	16.6	15.1	13.7	12.7
Sb	51	46.7	40.4	34.6	29.5	26.3	23.5	21.1	19.0	17.0	15.5	14.1	13.0
Te	52	47.7	41.3	35.4	30.3	26.9	24.0	21.7	19.5	17.5	16.0	14.5	13.3
I	53	48.6	42.1	36.1	31.0	27.5	24.6	22.2	20.0	17.9	16.4	14.8	13.6
Xe	54	49.6	43.0	36.8	31.6	28.0	25.2	22.7	20.4	18.4	16.7	15.2	13.9
Cs	55	50.7	43.8	37.6	32.4	28.7	25.8	23.2	20.8	18.8	17.0	15.6	14.5
Ba	56	51.7	44.7	38.4	33.1	29.3	26.4	23.7	21.3	19.2	17.4	16.0	14.7
La	57	52.6	45.6	39.3	33.8	29.8	26.9	24.3	21.9	19.7	17.9	16.4	15.0
Pr	59	54.5	47.4	40.9	35.2	31.1	28.0	25.4	22.9	20.6	18.8	17.1	15.7
Nd	60	55.4	48.3	41.6	35.9	31.8	28.6	25.9	23.4	21.1	19.2	17.5	16.1
Pm	61	56.4	49.1	42.4	36.6	32.4	29.2	26.4	23.9	21.5	19.6	17.9	16.4
Sm	62	57.3	50.0	43.2	37.3	32.9	29.8	26.9	24.4	22.0	20.0	18.3	16.8
Eu	63	58.3	50.9	44.0	38.1	33.5	30.4	27.5	24.9	22.4	20.4	18.7	17.1
Gd	64	59.3	51.7	44.8	38.8	34.1	31.0	28.1	25.4	22.9	20.8	19.1	17.5
Tb	65	60.2	52.6	45.7	39.6	34.7	31.6	28.6	25.9	23.4	21.2	19.5	17.9
Dy	66	61.1	53.6	46.5	40.4	35.4	32.2	29.2	26.3	23.9	21.6	19.9	18.3
Ho	67	62.1	54.5	47.3	41.1	36.1	32.7	29.7	26.8	24.3	22.0	20.3	18.6
Er	68	63.0	55.3	48.1	41.7	36.7	33.3	30.2	27.3	24.7	22.4	20.7	18.9
Tm	69	64.0	56.2	48.9	42.4	37.4	33.9	30.8	27.9	25.2	22.9	21.0	19.3

$\frac{\sin\theta}{\lambda}(\mathring{A}^{-1})$	0.0	0.1	0.2	0.3	0.4	0.5	0.6	0.7	0.8	0.9	1.0	1.1	1.2
Yb	70	64.9	57.0	49.7	43.2	38.0	34.4	31.3	28.4	25.7	23.3	21.4	19.7
Lu	71	65.9	57.8	50.4	43.9	38.7	35.0	31.8	28.9	26.2	23.8	21.8	20.0
Hf	72	66.8	58.6	51.2	44.5	39.3	35.6	32.3	29.3	26.7	24.2	22.3	20.4
Ta	73	67.8	59.5	52.0	45.3	39.9	36.2	32.9	29.8	27.1	24.7	22.6	20.9
W	74	68.8	60.4	52.8	46.1	40.5	36.8	33.5	30.4	27.6	25.2	23.0	21.3
Re	75	69.8	61.3	53.6	46.8	41.1	37.4	34.0	30.9	28.1	25.6	23.4	21.6
Os	76	70.8	62.2	54.4	47.5	41.7	38.0	34.6	31.4	28.6	26.0	23.9	22.0
Ir	77	71.7	63.1	55.3	48.2	42.4	38.6	35.1	32.0	29.0	26.5	24.3	22.3
Pt	78	72.6	64.0	56.2	48.9	43.1	39.2	35.6	32.5	29.5	27.0	24.7	22.7
Au	79	73.6	65.0	57.0	49.7	43.8	39.8	36.2	33.1	30.0	27.4	25.1	23.1
Hg	80	74.6	65.9	57.9	50.5	44.4	40.5	36.8	33.6	30.6	27.8	25.6	23.6
Ti	81	75.5	66.7	58.7	51.2	45.0	41.1	37.4	34.1	31.1	28.3	26.0	24.1
Pb	82	76.5	67.5	59.5	51.9	45.7	41.6	37.9	34.6	31.5	28.8	26.4	24.5
Bi	83	77.5	68.4	60.4	52.7	46.4	42.2	38.5	35.1	32.0	29.2	26.8	24.8
Po	84	78.4	69.4	61.3	53.5	47.1	42.8	39.1	35.6	32.6	29.7	27.2	25.2
At	85	79.4	70.3	62.1	54.2	47.7	43.4	39.6	36.2	33.1	30.1	27.6	25.6
Rn	86	80.3	71.3	63.0	55.1	48.4	44.0	40.2	36.8	33.5	30.5	28.0	26.0
Fr	87	81.3	72.2	63.8	55.8	49.1	44.5	40.7	37.3	34.0	31.0	28.4	26.4
Ra	88	82.2	73.2	64.6	56.5	49.8	45.1	41.3	37.8	34.6	31.5	28.8	26.7
Ac	89	83.2	74.1	65.5	57.3	50.4	45.8	41.8	38.3	35.1	32.0	29.2	27.1
Th	90	84.1	75.1	66.3	58.1	51.1	46.5	42.4	38.8	35.5	32.4	29.6	27.5
Pa	91	85.1	76.0	67.1	58.8	51.7	47.1	43.0	39.3	36.0	32.8	30.1	27.9
U	92	86.0	76.9	67.9	59.6	52.4	47.7	43.5	39.8	36.5	33.3	30.6	28.3
Np	93	87	78	69	60	53	48	44	40	37	34	31	29
Pu	94	88	79	69	61	54	49	44	41	38	34	31	29
Am	95	89	79	70	62	55	50	45	42	38	35	32	30
Cm	96	90	80	71	62	55	50	46	42	39	35	32	30
Bk	97	91	81	72	63	56	51	46	43	39	36	33	30
Cf	98	92	82	73	64	57	52	47	43	40	36	33	31
	99	93	83	74	65	57	52	48	44	40	37	34	31
	100	94	84	75	66	58	53	48	44	41	37	34	31

From Peiser, Rooksby, and Wilson (see [10]). More extensive tables, at smaller intervals of (sin θ)/λ, are given in [G.1].

REFERENCES

The following books are listed more or less in the order they are encountered in the text

G.1 *International Tables for Crystallography*, Ed. A.J.C Wilson, Vol. A-C (Dordrecht Kluwer Academic Pub. for International Union of Crystallography, 1995). The reference ''book'' for crystallography and diffraction.

This page intentionally left blank

Appendix

Multiplicity Factors for the Powder Method

Cubic:	hkl	hhl	$0kl$	$0kk$	hhh	$00l$	
	48*	24	24*	12	8	6	
Hexagonal and Rhombohedral:	$hk \cdot l$	$hh \cdot l$	$0k \cdot l$	$hk \cdot 0$	$hh \cdot 0$	$0k \cdot 0$	$00 \cdot l$
	24*	12*	12*	12*	6	6	2
Tetragonal:	hkl	hhl	$0kl$	$hk0$	$hh0$	$0k0$	$00l$
	16*	8	8	8*	4	4	2
Orthorhombic:	hkl	$0kl$	$h0l$	$hk0$	$h00$	$0k0$	$00l$
	8	4	4	4	2	2	2
Monoclinic:	hkl	$h0l$	$0k0$				
	4	2	2				
Triclinic:	hkl						
	2						

Note that, in cubic crystals, for example, *hhl* stands for such indices as 112 (or 211), 0*kl* for such indices as 012 (or 210), 0*kk* for such indices as 011 (or 110), etc.

[*] These are the usual multiplicity factors. In some crystals, planes having these indices comprise two forms with the same spacing but different structure factor, and the multiplicity factor for each form is half the value given above. In the cubic system, for example, there are some crystals in which permutations of the indices (*hkl*) produce planes which are not structurally equivalent; in such crystals (AuBe is an example), the plane (123), for example, belongs to one form and has a certain structure factor, while the plane (321) belongs to another form and has a different structure factor. These are 48/2 = 24 planes in the first form and 24 planes in the second. This question is discussed more fully by Henry, Lipson, and Wooster [G.15].

From Appendix 11 of *Elements of X-Ray Diffraction*, Third Edition. B.D. Cullity, S.R. Stock.

REFERENCES

The following books are listed more or less in the order they are encountered in the text

G.15 N. F. M. Henry, H. Lipson, and W. A. Wooster. *The Interpretation of X-Ray Diffraction Photographs* (London: Macmillan, 1951). Rotating and oscillating crystal methods, as well as powder methods, are described. Good section on analytical methods of indexing powder photographs.

Appendix
Lorentz-Polarization Factor $\left(\dfrac{1 + \cos^2 2\theta}{\sin^2 \theta \cos \theta}\right)$

Θ°	.0	.1	.2	.3	.4	.5	.6	.7	.8	.9
2	1639	1486	1354	1239	1138	1048	968.9	898.3	835.1	778.4
3	727.2	680.9	638.8	600.5	565.6	533.6	504.3	477.3	452.3	429.3
4	408.0	388.2	369.9	352.7	336.8	321.9	308.0	294.9	282.6	271.1
5	260.3	250.1	240.5	231.4	222.9	214.7	207.1	199.8	192.9	186.3
6	180.1	174.2	168.5	163.1	158.0	153.1	148.4	144.0	139.7	135.6
7	131.7	128.0	124.4	120.9	117.6	114.4	111.4	108.5	105.6	102.9
8	100.3	97.80	95.37	93.03	90.78	88.60	86.51	84.48	82.52	80.63
9	78.79	77.02	75.31	73.66	72.05	70.49	68.99	67.53	66.12	64.74
10	63.41	62.12	60.87	59.65	58.46	57.32	56.20	55.11	54.06	53.03
11	52.04	51.06	50.12	49.19	48.30	47.43	46.58	45.75	44.94	44.16
12	43.39	42.64	41.91	41.20	40.50	39.82	39.16	38.51	37.88	37.27
13	36.67	36.08	35.50	34.94	34.39	33.85	33.33	32.81	32.31	31.82
14	31.34	30.87	30.41	29.96	29.51	29.08	28.66	28.24	27.83	27.44
15	27.05	26.66	26.29	25.92	25.56	25.21	24.86	24.52	24.19	23.86
16	23.54	23.23	22.92	22.61	22.32	22.02	21.74	21.46	21.18	20.91
17	20.64	20.38	20.12	19.87	19.62	19.38	19.14	18.90	18.67	18.44
18	18.22	18.00	17.78	17.57	17.36	17.15	16.95	16.75	16.56	16.36
19	16.17	15.99	15.80	15.62	15.45	15.27	15.10	14.93	14.76	14.60
20	14.44	14.28	14.12	13.97	13.81	13.66	13.52	13.37	13.23	13.09
21	12.95	12.81	12.68	12.54	12.41	12.28	12.15	12.03	11.91	11.78
22	11.66	11.54	11.43	11.31	11.20	11.09	10.98	10.87	10.76	10.65
23	10.55	10.45	10.35	10.24	10.15	10.05	9.951	9.857	9.763	9.671
24	9.579	9.489	9.400	9.313	9.226	9.141	9.057	8.973	8.891	8.810
25	8.730	8.651	8.573	8.496	8.420	8.345	8.271	8.198	8.126	8.054
26	7.984	7.915	7.846	7.778	7.711	7.645	7.580	7.515	7.452	7.389
27	7.327	7.266	7.205	7.145	7.086	7.027	6.969	6.912	6.856	6.800
28	6.745	6.692	6.637	6.584	6.532	6.480	6.429	6.379	6.329	6.279
29	6.230	6.183	6.135	6.088	6.042	5.995	5.950	5.905	5.861	5.817
30	5.774	5.731	5.688	5.647	5.605	5.564	5.524	5.484	5.445	5.406
31	5.367	5.329	5.292	5.254	5.218	5.181	5.145	5.110	5.075	5.040
32	5.006	4.972	4.939	4.906	4.873	4.841	4.809	4.777	4.746	4.715
33	4.685	4.655	4.625	4.595	4.566	4.538	4.509	4.481	4.453	4.426
34	4.399	4.372	4.346	4.320	4.294	4.268	4.243	4.218	4.193	4.169
35	4.145	4.121	4.097	4.074	4.052	4.029	4.006	3.984	3.962	3.941
36	3.919	3.898	3.877	3.857	3.836	3.816	3.797	3.777	3.758	3.739
37	3.720	3.701	3.683	3.665	3.647	3.629	3.612	3.594	3.577	3.561
38	3.544	3.527	3.513	3.497	3.481	3.465	3.449	3.434	3.419	3.404
39	3.389	3.375	3.361	3.347	3.333	3.320	3.306	3.293	3.280	3.268
40	3.255	3.242	3.230	3.218	3.206	3.194	3.183	3.171	3.160	3.149
41	3.138	3.127	3.117	3.106	3.096	3.086	3.076	3.067	3.057	3.048
42	3.038	3.029	3.020	3.012	3.003	2.994	2.986	2.978	2.970	2.962
43	2.954	2.946	2.939	2.932	2.925	2.918	2.911	2.904	2.897	2.891
44	2.884	2.878	2.872	2.866	2.860	2.855	2.849	2.844	2.838	2.833

From Appendix 12 of *Elements of X-Ray Diffraction*, Third Edition. B.D. Cullity, S.R. Stock.

Θ°	.0	.1	.2	.3	.4	.5	.6	.7	.8	.9
45	2.828	2.824	2.819	2.814	2.810	2.805	2.801	2.797	2.793	2.789
46	2.785	2.782	2.778	2.775	2.772	2.769	2.766	2.763	2.760	2.757
47	2.755	2.752	2.750	2.748	2.746	2.744	2.742	2.740	2.738	2.737
48	2.736	2.735	2.733	2.732	2.731	2.730	2.730	2.729	2.729	2.728
49	2.728	2.728	2.728	2.728	2.728	2.728	2.729	2.729	2.730	2.730
50	2.731	2.732	2.733	2.734	2.735	2.737	2.738	2.740	2.741	2.743
51	2.745	2.747	2.749	2.751	2.753	2.755	2.758	2.760	2.763	2.766
52	2.769	2.772	2.775	2.778	2.782	2.785	2.788	2.792	2.795	2.799
53	2.803	2.807	2.811	2.815	2.820	2.824	2.828	2.833	2.838	2.843
54	2.848	2.853	2.858	2.863	2.868	2.874	2.879	2.885	2.890	2.896
55	2.902	2.908	2.914	2.921	2.927	2.933	2.940	2.946	2.953	2.960
56	2.967	2.974	2.981	2.988	2.996	3.004	3.011	3.019	3.026	3.034
57	3.042	3.050	3.059	3.067	3.075	3.084	3.092	3.101	3.110	3.119
58	3.128	3.137	3.147	3.156	3.166	3.175	3.185	3.195	3.205	3.215
59	3.225	3.235	3.246	3.256	3.267	3.278	3.289	3.300	3.311	3.322
60	3.333	3.345	3.356	3.368	3.380	3.392	3.404	3.416	3.429	3.441
61	3.454	3.466	3.479	3.492	3.505	3.518	3.532	3.545	3.559	3.573
62	3.587	3.601	3.615	3.629	3.643	3.658	3.673	3.688	3.703	3.718
63	3.733	3.749	3.764	3.780	3.796	3.812	3.828	3.844	3.861	3.878
64	3.894	3.911	3.928	3.946	3.963	3.980	3.998	4.016	4.034	4.052
65	4.071	4.090	4.108	4.127	4.147	4.166	4.185	4.205	4.225	4.245
66	4.265	4.285	4.306	4.327	4.348	4.369	4.390	4.412	4.434	4.456
67	4.478	4.500	4.523	4.546	4.569	4.592	4.616	4.640	4.664	4.688
68	4.712	4.737	4.762	4.787	4.812	4.838	4.864	4.890	4.916	4.943
69	4.970	4.997	5.024	5.052	5.080	5.109	5.137	5.166	5.195	5.224
70	5.254	5.284	5.315	5.345	5.376	5.408	5.440	5.471	5.504	5.536
71	5.569	5.602	5.636	5.670	5.705	5.740	5.775	5.810	5.846	5.883
72	5.919	5.956	5.994	6.032	6.071	6.109	6.149	6.189	6.229	6.270
73	6.311	6.352	6.394	6.437	6.480	6.524	6.568	6.613	6.658	6.703
74	6.750	6.797	6.844	6.892	6.941	6.991	7.041	7.091	7.142	7.194
75	7.247	7.300	7.354	7.409	7.465	7.521	7.578	7.636	7.694	7.753
76	7.813	7.874	7.936	7.999	8.063	8.128	8.193	8.259	8.327	8.395
77	8.465	8.536	8.607	8.680	8.754	8.829	8.905	8.982	9.061	9.142
78	9.223	9.305	9.389	9.474	9.561	9.649	9.739	9.831	9.924	10.02
79	10.12	10.21	10.31	10.41	10.52	10.62	10.73	10.84	10.95	11.06
80	11.18	11.30	11.42	11.54	11.67	11.80	11.93	12.06	12.20	12.34
81	12.48	12.63	12.78	12.93	13.08	13.24	13.40	13.57	13.74	13.92
82	14.10	14.28	14.47	14.66	14.86	15.07	15.28	15.49	15.71	15.94
83	16.17	16.41	16.66	16.91	17.17	17.44	17.72	18.01	18.31	18.61
84	18.93	19.25	19.59	19.94	20.30	20.68	21.07	21.47	21.89	22.32
85	22.77	23.24	23.73	24.24	24.78	25.34	25.92	26.52	27.16	27.83
86	28.53	29.27	30.04	30.86	31.73	32.64	33.60	34.63	35.72	36.88
87	38.11	39.43	40.84	42.36	44.00	45.76	47.68	49.76	52.02	54.50

From Henry, Lipson, and Wooster [G.15].

REFERENCES

The following books are listed more or less in the order they are encountered in the text

G.15 N. F. M. Henry, H. Lipson, and W. A. Wooster. *The Interpretation of X-Ray Diffraction Photographs* (London: Macmillan, 1951). Rotating and oscillating crystal methods, as well as powder methods, are described. Good section on analytical methods of indexing powder photographs.

This page intentionally left blank

Appendix

Data for Calculation of the Temperature Factor

Values of $\phi(x) = \frac{1}{x}\int_0^x \frac{\xi}{e^{\xi} - 1}\,d\xi$ as a Function of x

x	.0	.1	.2	.3	.4	.5	.6	.7	.8	.9
0	1.000	0.975	0.951	0.928	0.904	0.882	0.860	0.839	0.818	0.787
1	0.778	0.758	0.739	0.721	0.703	0.686	0.669	0.653	0.637	0.622
2	0.607	0.592	0.578	0.565	0.552	0.539	0.526	0.514	0.503	0.491
3	0.480	0.470	0.460	0.450	0.440	0.431	0.422	0.413	0.404	0.396
4	0.388	0.380	0.373	0.366	0.359	0.352	0.345	0.339	0.333	0.327
5	0.321	0.315	0.310	0.304	0.299	0.294	0.289	0.285	0.280	0.276
6	0.271	0.267	0.263	0.259	0.255	0.251	0.248	0.244	0.241	0.237

For x greater than 7, $\phi(x)$ is given to a good approximation by $(1.642/x)$. (From [G.1].)

Debye Temperatures
James [G.19] gives the following values of the characteristic Debye temperature Θ for some cubic metals

Metal	Θ(K)	Metal	Θ (K)
Al	390	Ta	245
Ca	230	Pb	88
Cu	320	Fe	430
Ag	210	Co	410
Au	175	Ni	400
Cr	485	Pd	275
Mo	380	Ir	285
W	310	Pt	230

From Appendix 13 of *Elements of X-Ray Diffraction*, Third Edition. B.D. Cullity, S.R. Stock.

REFERENCES

The following books are listed more or less in the order they are encountered in the text

G.1 *International Tables for Crystallography*, Ed. A.J.C Wilson, Vol. A-C (Dordrecht Kluwer Academic Pub. for International Union of Crystallography, 1995). The reference ''book'' for crystallography and diffraction.

G.19 R. W. James. *The Optical Principles of the Diffraction of X-Rays* (Woodbridge; CT: Ox Bow Press, 1982). Excellent book on advanced theory of x-ray diffraction. Includes thorough treatments of diffuse scattering (due to thermal agitation, small particle size, crystal imperfections, etc.), the use of Fourier series in structure analysis, and scattering by gases, liquids, and amorphous solids.

Index

Page references followed by "f" indicate illustrated figures or photographs; followed by "t" indicates a table.